The University of Sheffield

Effect of Magnetic Saturation in Fractional Slot PM Machines with Particular Reference to Terminal Voltage Distortion

Di Wu

A thesis submitted for the degree of Doctor of Philosophy

Department of Electronic and Electrical Engineering

The University of Sheffield

Mappin Street, Sheffield, S1 3JD, UK

July 2015

ABSTRACT

This thesis investigates the influence of magnetic saturation on the electromagnetic performance of fractional slot permanent magnet (FS PM) machines, with particular reference to the influence of local magnetic saturation on terminal voltage distortion. The terminal voltage in this thesis is the voltage measured between the machine winding terminals, especially referring to the on-load condition. All theoretical analyses are carried out by the 2-dimensional finite element method and validated by experiments made on several prototypes.

The mechanisms of terminal voltage distortion in FS surface-mounted PM (SPM) machines and interior PM (IPM) machines are investigated with the aid of frozen permeability method. The results show that the change in local magnetic saturation caused by tooth-tip leakage flux is the main reason for the terminal voltage distortion in both SPM and IPM machines when current advance angle (β) is around 0° especially when small or closed slot openings are adopted. Meanwhile, the local magnetic saturation affected by the variation of rotor flux paths is also responsible for the terminal voltage distortion in IPM machines particularly when β approaches 90°. Furthermore, the influences of slot and pole number ($N_s/2p$) combinations are systematically investigated. It shows that all FS SPM machines exhibit higher voltage distortion than the integer slot SPM machines, whilst all FS IPM machines suffer less voltage distortion than the integer slot machines. For FS machines appearing in pairs, e.g. $N_s=2p\pm2$, the ones with $N_s>2p$ always have less voltage distortion than their counterparts with $N_s<2p$. The machines suffering more from voltage distortion usually have higher distortions of on-load back-EMF, on-load cogging torque, *dq*-axis inductances and torque ripple, while their torque speed characteristics will be more deteriorated from the ideal curves calculated by the fundamental voltage only. Finally, the minimisation methods of terminal voltage distortion are investigated. It shows that design trade-offs should be made in order to balance different machine performances according to the most frequent operation load conditions.

ACKNOWLEDGEMENTS

Foremost, I would like to extend my sincere thanks to my supervisor Professor Zi-Qiang Zhu for his continuous encouragement and support throughout my PhD study, and for his invaluable advice and guidance to my career.

I would also like to thank all my fellows of Electrical Machines and Drives Group at The University of Sheffield for their help and inspired discussions. Particularly, I would like to express my thanks to Mr. John A. Wilkinson for his assistance in prototyping, and to Mr. Beomseok Lee for his aid of experiments.

I would also like to thank Welling Motor Manufacturing Co., Ltd, China, for their sponsorship and the opportunity to boost my career.

Finally, I would like to thank my parents and all my family members, for their love, understanding and encouragement to conquer all difficulties in my life.

CONTENTS

NOMENCLATURE

E_1	Fundamental open-circuit phase back-EMF (V)
E_n	n^{th} harmonic open-circuit phase back-EMF (V)
GCD	Greatest common divisor
I_1	Fundamental phase current (A)
I_d	D-axis current (A)
I_q	Q-axis current (A)
I_{max}	Current amplitude (A)
K_w	Flux weakening factor
L_d	D-axis inductance (H)
L_q	Q-axis inductance (H)
LCM	Lowest common multiple
LVDR	Voltage distortion ratio calculated by terminal line voltage
MMF	Magneto Motive Force
MTPA	Maximum torque per ampere
MTPV	Maximum torque per volt
N_c	Number of turns per coil
T_{all}	Resultant electromagnetic torque (Nm)
T_{avg}	Average torque (Nm)
T_{cog}	On-load cogging torque (Nm)
T_{max}	Maximum torque (Nm)
T_{min}	Minimum torque (Nm)
T_{pm}	Permanent magnet torque (Nm)
T_r	Reluctance torque (Nm)
T_{ripple}	Torque ripple (%)
THD	Total harmonic distortion (%)
N_s	Number of stator slots
N_{s0}	Number of stator slots for unit machine
U_{DC}	DC link voltage (V)
U_{error}	Voltage error (V)
U_{fund}	Fundamental terminal phase voltage (V)
U^{line}_{fund}	Fundamental terminal line voltage (V)

U^{line}_{peak}	Peak terminal line voltage (V)
U_n	n^{th} harmonic voltage (V)
U_{peak}	Peak terminal phase voltage (V)
U_{resp}	Maximum response voltage (V)
$U_{vec\text{-}fund}$	Fundamental value of voltage vector (V)
$U_{vec\text{-}peak}$	Peak value of voltage vector (V)
VDP	Voltage distortion pattern
VDR	Voltage distortion ratio calculated by terminal phase voltage
b_0	Slot opening width (mm)
d_s	Stator shaping depth (mm)
g_0	Airgap length (mm)
h_r	Thickness of iron region above PM in IPM rotor (mm)
h_t	Thickness of tooth-tips (mm)
i_a	Instantaneous phase current (A)
i^k	Current of the slot k (A)
k	Slot number
k_a	Rotor shaping depth factor
k_{ap}	Rotor pole arc/pole pitch ratio
k_{pv}	v^{th} winding pitch factor
k_{w1}	Fundamental winding factor
m	Number of phases
p	Number of rotor pole pairs
pk-pk	Peak to peak
q	Number of slots per pole per phase
q_e	Number of adjacent Type I slots
r_a	Phase resistance (Ω)
u^a_{tip}	Phase voltage ripple by tooth-tip leakage flux
w_r	IPM rotor centre beam width (mm)
Λ_{b0}	Permeance of slot opening (N/A^2)
Λ^k	Permeance of tooth-tips belonged to slot k (N/A^2)
α_t	Tooth-tip angle (°)
β	Current advance angle (°)
θ_r	Rotor position (°)

σ_v	Voltage error ratio (%)
τ_r	Rotor pole pitch (rad)
τ_s	Stator slot pitch (rad)
ω	Electrical angular speed (rad/s)
ω_m	Mechanical angular speed (rad/s)
ψ_a^{arm}	Phase armature flux linkage (Wb)
ψ_a^{pm}	Phase PM flux linkage (Wb)
ψ_d^{arm}	D-axis armature flux linkage (Wb)
ψ_{PM}	PM flux linkage (Wb)
ψ_q^{arm}	Q-axis armature flux linkage (Wb)
ψ_d^{pm}	D-axis PM flux linkage (Wb)
ψ_q^{pm}	Q-axis PM flux linkage (Wb)
$\psi^a_{tip\sigma}$	Tooth-tip leakage flux of one phase (Wb)
$\psi^k_{tip\sigma}$	Tooth-tip leakage flux linked with one coil side (Wb)

CHAPTER 1

GENERAL INTRODUCTION

1.1 PM Brushless AC Machines with Fractional Slot Concentrated Windings

1.1.1 Basic Concepts

With the development of new permanent magnet (PM) materials and power electronics technologies, PM brushless machines have been investigated extensively during the last three decades due to inherent advantages such as high torque and power densities, as well as high efficiency [JAH86], [ZHU93], [BIA06], [ELR10], [ZHU14]. By adopting proper winding configurations and/or rotor designs, the open-circuit back-EMFs of PM brushless machines could be designed to be either more sinusoidal or more trapezoidal [HOA86], [PIL91], [ZHU01], [KIM07], [EVA10], as typically shown in Fig. 1.1. Thus, in order to maximize the torque density and minimize the torque ripples, their relatively preferred driving current waveforms are sinusoidal and rectangular, respectively, Fig. 1.1, [PIL91], [JAH96], [ZHU14], which can be respectively designated as brushless AC (BLAC) drive and brushless DC (BLDC) drive [HEN94]. In fact, ideal trapezoidal back-EMF is difficult to achieve, which may increase the torque ripples of machines under BLDC drive [HOA86]. Meanwhile, BLDC drive exhibits more current harmonics which result in high iron loss and magnet eddy current loss [DEN97], [ISH05] as well as noise and vibration [KO04], [ZHU07]. Therefore, machines with BLAC drives are more popular for high precision servo drives, traction and propulsion drives especially when vector control is adopted [JAH87], [VAS90], [MOR94]. For convenience, the machines under BLAC drives will be designated as BLAC machines in the following parts of this thesis.

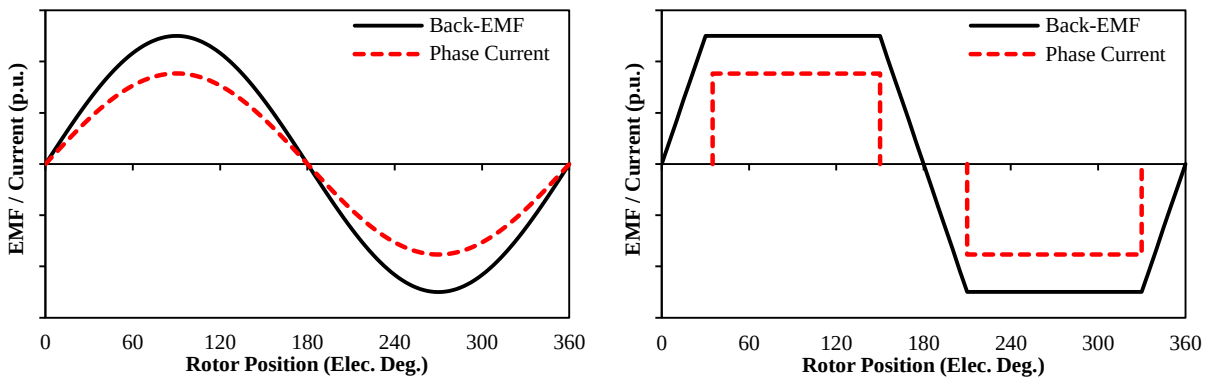

(a) BLAC (b) BLDC

Fig. 1.1 Illustration of open-circuit back-EMF shapes and relative driving currents [ZHU07].

According to the number of slots per pole per phase (q), the radial field PM BLAC machines can be simply classified as integer slot machines, i.e. q equals an integer, or fractional slot machines, i.e. q equals a fraction. Although fractional slot machines become more popular recently, its history can date back to 100 years ago [SMI16], [CAL38]. However, before 1980s, most of the investigated fractional slot machines equipped with distributed overlapping windings, e.g. q>1, which have much longer end-windings compared with the machines with fractional slot concentrated windings (FSCW), e.g. q<1. In order to emphasise the difference of winding types, two 8-pole machines with different stator slot numbers and winding arrangements are compared in Fig. 1.2. Fig. 1.2(a) and (c) show a 48-slot stator with overlapping windings for Toyota Prius 2010 [OAK11], while Fig. 1.2(b) and (d) show a typical 12-slot stator with FSCW. Both of them can operate with 8-pole rotors. Meanwhile, both stators have similar stack length (~50mm) and packing factor (~0.6), but the total length of end-windings for the overlapping windings is significantly much larger than that for FSCW. Due to the merits of short end-windings, as well as high packing factor, high efficiency, low cogging torque, and fault tolerance capability, FSCW machines have attracted increasing research interests [ELR10].

In cooperation with an FSCW stator, various rotor topologies have been proposed, which have been reviewed by Zhu and Howe in [ZHU07]. Generally, all these topologies could be ascribed into four basic configurations in Fig. 1.3. As shown in Fig. 1.3(a), SPM rotors are the most widely adopted topologies in FSCW machines [JAH84]. Due to similar rotor flux paths for d-axis and q-axis armature fluxes, their d-axis and q-axis inductances are almost the same, which result in negligible reluctance torque. Due to large equivalent airgap, the armature reaction in SPM machines is normally small. Fig. 1.3(b) shows the IPM rotor which is also widely adopted in FSCW machines [RED12]. The iron parts offer extra q-axis flux paths for armature reaction, which normally lead to higher q-axis inductance compared with d-axis inductance. Thus, such rotor saliency will increase the reluctance torque and improve flux weakening performance. However, since the magnets are embedded in the rotor iron, the leakage fluxes in IPM rotors are significantly larger than those in SPM rotors. Fig. 1.3(c) offers a trade-off between SPM and IPM machines. The surface-inset rotors keep the iron region between magnets but remove the iron region above magnets [GAN00]. Thus, the rotor saliency may also exist and increase the reluctance torque and help to increase flux weakening performance. However, similar to the SPM rotor, surface-inset rotor also faces the mechanical problem in terms of magnets retaining if operating at high speed. Fig. 1.3(d)

shows another commonly adopted spoke type rotor which can be regarded as a special type of IPM rotor and fully utilize the inner space to increase the magnet volume and enhance the torque density [ELR14]. However, due to large iron region above the magnet, the cross-saturation in spoke rotor is always strong, which may influence the machine performance and increase the design difficulties [YAM14].

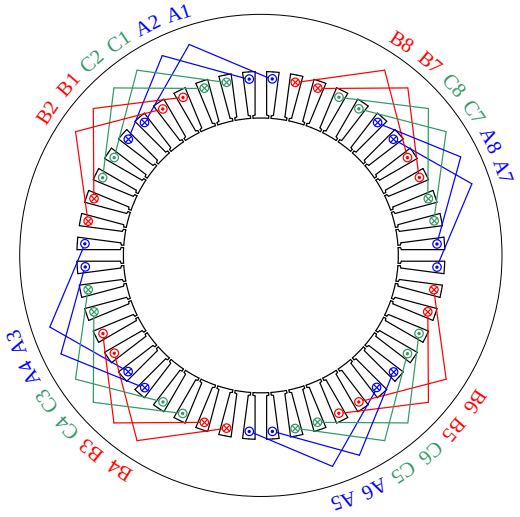

(a) Winding connection, 48-slot overlapping winding

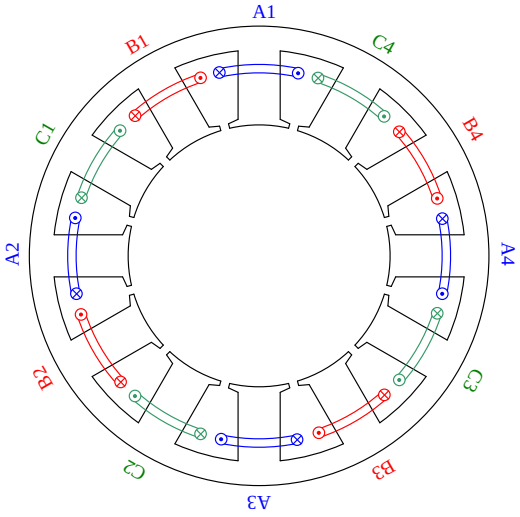

(b) Winding connection, 12-slot FSCW

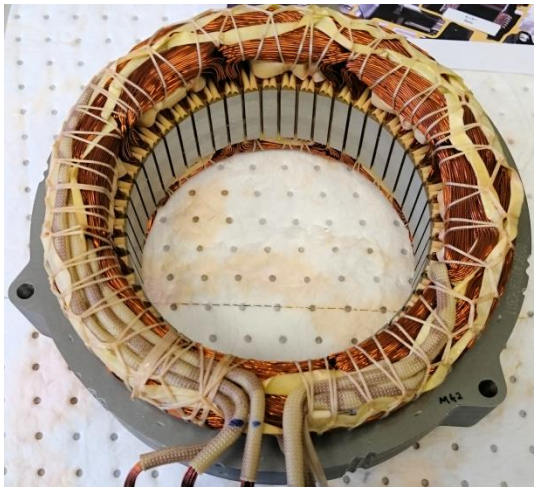

(c) Photo, 48-slot overlapping winding [OAK11]

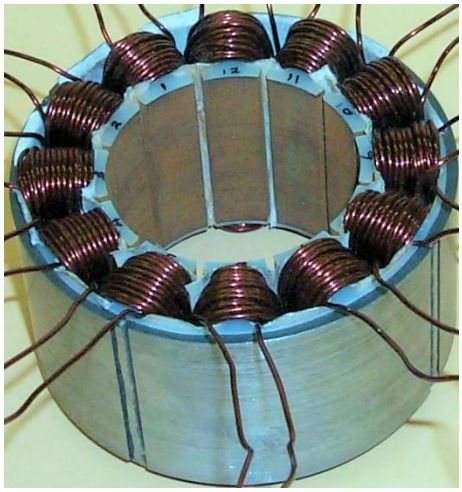

(d) Photo, 12-slot FSCW [ISH06]

Fig. 1.2 Comparison of overlapping and concentrated windings (8-pole).

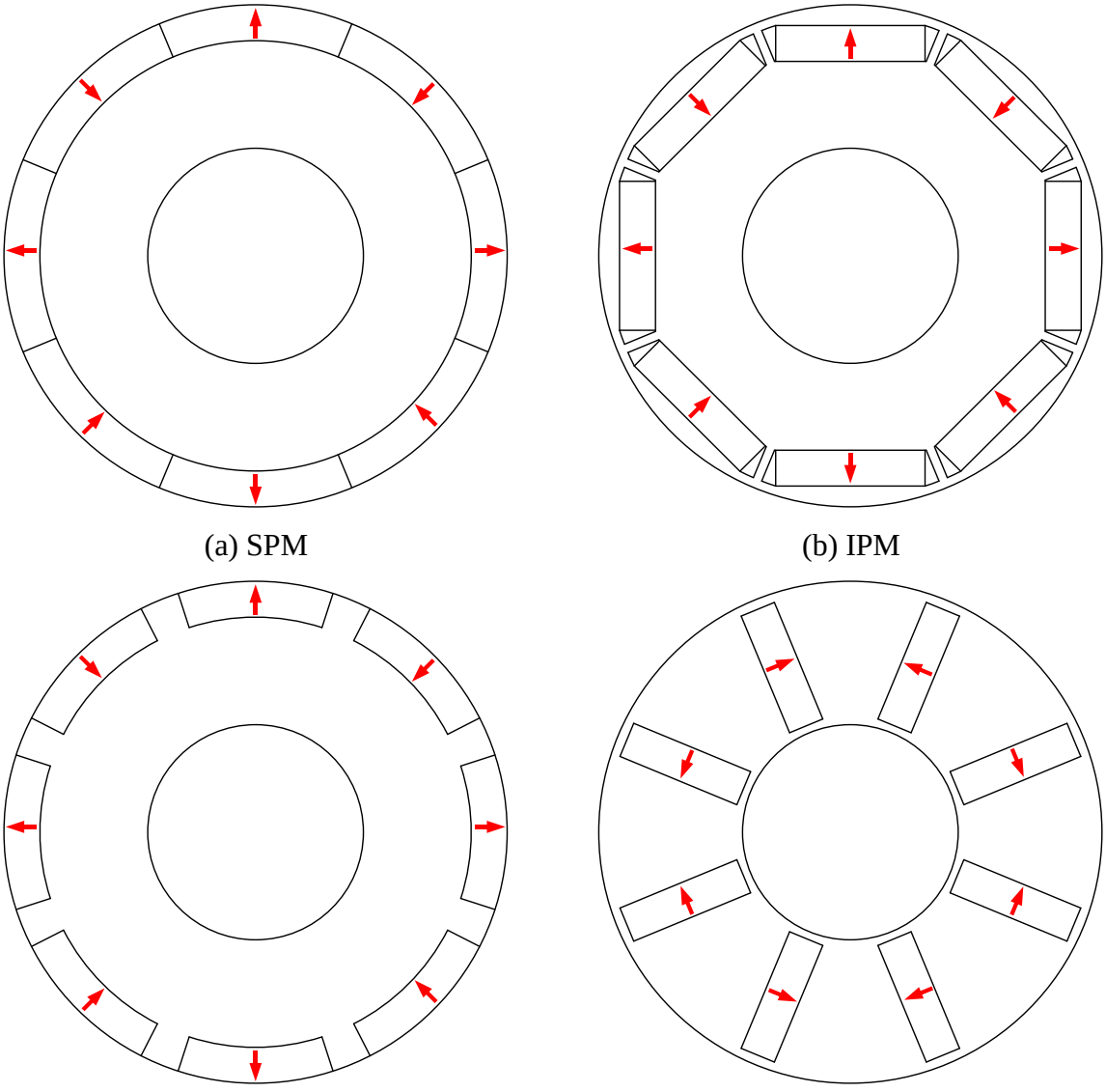

(a) SPM (b) IPM

(c) Surface-Inset (d) Spoke

Fig. 1.3 Comparison of basic rotor configurations for FSCW machines.

1.1.2 Performance of FSCW Machines Influenced by Slot and Pole Number Combinations

Table 1.1 shows typical q for the commonly used FSCW machines with different slot number (N_s) and pole number ($2p$) combinations. Clearly, N_s and $2p$ of all machines having larger winding factors are distributed around the diagonal line of the table, which means the FSCW machines with N_s close to $2p$ are much more preferred. Accordingly, they can be grouped as q=0.5 or 0.25, $2p$=N_s±1 and $2p$=N_s±2 [ZHU14].

In fact, all performances of FSCW machines are sensitive to N_s/$2p$ combinations. The first and most concerned one is the fundamental winding factor k_{w1}. Many papers have paid

attention to the calculation of k_{w1} for FSCW machines with different $N_s/2p$ combinations [CHO99], [CRO02], [SAL04], [TAN10]. The investigation results can be summarized in Fig. 1.4, in which k_{w1} will be achieved when $q \rightarrow 1/3$, i.e. $N_s \rightarrow 2p$, as both pitch and distribution winding factors approach 1. The machines with larger k_{w1} will obtain higher flux linkages and back-EMFs under the same PM excitation, which consequently lead to higher average torques and torque densities. It is noticed that by adopting un-equal tooth width and alternative teeth wound windings, k_{w1} could increase as well [ISH05a], which is worth considering during design stage. Meanwhile, it can be seen that q=0.5 and q=0.25 machines are defined as the boundaries of all the preferred FSCW machines with k_{w1} both equalling 0.866. Thus, any possible $N_s/2p$ combinations beyond the boundaries will have k_{w1} lower than 0.866, which are not cost-effective and seldom adopted. For middle or small sized FSCW machines, neither N_s nor $2p$ could be too large, which limits the maximum values of k_{w1}. Thus, $2p=N_s\pm2$ machines, e.g. 12-slot/10-pole machines with k_{w1} equalling 0.933 are widely adopted for the applications such as servo drive and power steering. However, for some high power direct-drive machines, much larger N_s and $2p$ could be adopted, which makes $q \rightarrow 1/3$, and consequently leads to higher k_{w1}. In example, Valavi *et al.* [VAL14] reported that 120-slot/118-pole design could be adopted for large wind power generator which has q equals 0.34 and k_{w1} equals 0.955.

Table 1.1 Feasible N_s/2p combinations of FSCW machines.

	N_s							
$2p$	3	6	9	12	15	18	21	24
2	1/2							
4	1/4	1/2						
6			1/2					
8		1/4	3/8	1/2				
10			3/10	2/10	1/2			
12			1/4		5/12	1/2		
14				2/7	5/14	3/7	1/2	
16				1/4	5/16	3/8	7/16	1/2
18					5/18		7/18	4/9
20					1/4	3/10	7/20	2/5
22						3/11	7/22	4/11
24						1/4	7/24	

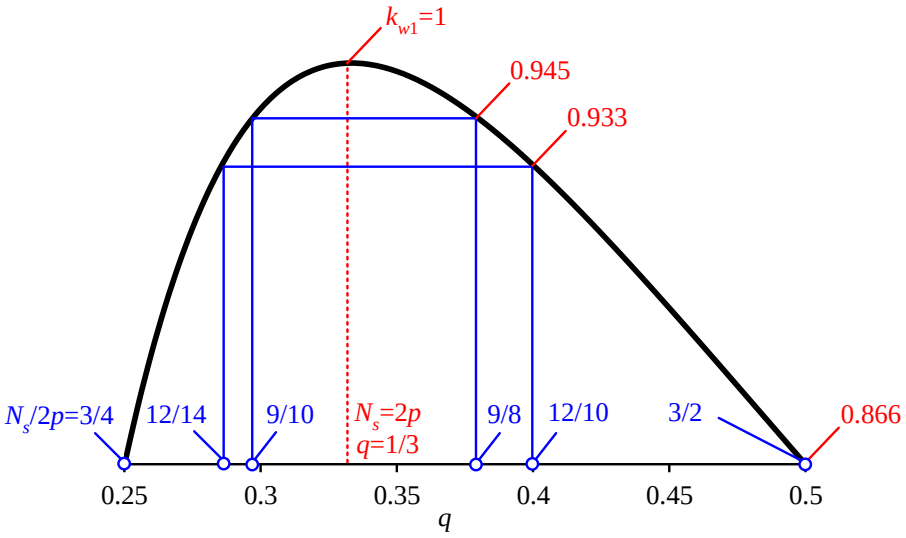

Fig. 1.4 k_{w1} for FSCW machines with different $N_s/2p$ combinations (q=1/3 is a virtual machine for comparison) [TAN10].

The second important performance influenced by $N_s/2p$ combinations is cogging torque, which is widely considered as an important issue for torque quality of FSCW machines [JAN96]. Many papers have focused on the influence of $N_s/2p$ on cogging torque [ZHU00], [BIA02], [ZHU14]. Zhu and Howe [ZHU00] pointed out for the first time that the machines with higher least common multiple between N_s and $2p$, and with smaller values of N_s or $2p$ will obtain smaller cogging torque amplitudes, which can be summarized as goodness factor (1.1).

$$C_T = 2pN_s / LCM(2p, N_s) \tag{1.1}$$

where *LCM* is the least common multiple. Further, Zhu *et al.* [ZHU09] provided precise deduction of the goodness factor, which also shows that $2p=N_s\pm1$ and $2p=N_s\pm2$ machines, e.g. 9-slot/8-pole and 12-slot/10-pole machines, will have much smaller cogging torque amplitudes compared with other FSCW machines with q=0.5. However, this result may change when static or rotating eccentricities occur. Zhu *et al.* [ZHU14a] investigated the cogging torque performances for different $N_s/2p$ combinations with rotor eccentricities by hybrid finite element and analytical method. It shows that $2p=N_s\pm1$ and $2p=N_s\pm2$ machines are much more influenced by rotor eccentricities, while q=0.5 machines are less sensitive to that. Therefore, the machines with q=0.5 may have better consistency of cogging torques considering manufacturing tolerance in mass production.

Besides cogging torque, electromagnetic torque ripples determined by back-EMF harmonics are believed to be another important issue for torque quality [SEB96], [ISL05], [ISL09], [MAG05]. From energy conversion point of view, Islam *et al.* [ISL05] proposed the electromagnetic torque equation can be expressed as (1.2).

$$T_e = 1.5p/\omega[E_1 I_1 \cos\beta - E_5 I_1 \cos(6\omega t + \beta) + E_7 I_1 \cos(6\omega t - \beta)\cdots] \quad (1.2)$$

where ω is the electric angular speed, β is the current advance angle, E_1 and I_1 are the fundamental back-EMF and current, E_5 and E_7 refer to the amplitudes of 5th and 7th back-EMF harmonics. Therefore, the machines with smaller harmonic winding factors will obtain smaller electromagnetic torque ripples as well. Ishak *et al.* [ISH06] offered the detail equations to calculate harmonic winding factors for all feasible $N_s/2p$ combinations of FSCW machines. The results reveal that the $2p=N_s\pm1$ and $2p=N_s\pm2$ machines, e.g. 9-slot/8-pole and 12-slot/10-pole machines, all have small 5th and 7th winding factors. Since such machines also obtain small cogging torque according to the aforementioned review, smooth output torques can be expected for these machines.

Winding inductance is an important parameter of FSCW machines, which also significantly influences the machine performance and is sensitive to $N_s/2p$ combinations. Due to plenty of harmonics in magneto-motive force (MMF), the difference between *dq*-axis inductances reduces, which may influence the torque and flux weakening performance compared with integer slot machines [CHO09], [DUT12]. Ponomarev *et al.* [PON13] calculated the leakage inductances for FSCW machines with different $N_s/2p$ combinations. The results show that $2p=N_s\pm2$ machines have higher leakage inductances than q=0.5 machines, while $2p=N_s+2$ machines have relative higher leakage inductance than its counterparts with $2p=N_s-2$. Further, higher leakage inductance may reduce the torque capabilities of FSCW machines. However, as an important component of total winding inductance [ELR08], the flux weakening performance of FSCW machine may even be improved. El-Refaie *et al.* [ELR05], [ELR06a] proved that the high leakage inductances for $2p=N_s\pm2$ machines, e.g. 12-slot/14-pole machine, can have better flux weakening performance than integer slot machines with q=1, and may realize infinite flux weakening if carefully designed. On the other hand, winding inductances of FSCW machines significantly influence the fault tolerant performance. In order to achieve good fault tolerance capability, the machine phase self-inductance should be designed high enough to limit the potential short-circuit currents, while the mutual inductance among

phases should be as low as possible to prevent the influence of the phase winding under fault [BIA06a]. Mitcham *et al.* [MIT04] compared the mutual inductances for different $N_s/2p$ combinations and phase numbers. It showed that 12-slot/10-pole and 12-slot/14-pole are good choices for 3-phase FSCW machines. El-Refaie *et al.* [ELR08] further proved that all $2p=N_s\pm2$ machines have low mutual inductances, and when N_s is more close to $2p$, i.e. $q\rightarrow1/3$, smaller mutual inductance could be expected. In order to further reduce the winding mutual inductance, alternative teeth winding, also called single layer winding, could be introduced as shown in Fig. 1.5. Bianchi *et al.* [BIA08] proposed that by careful design, the mutual inductance of alternative teeth wound FSCW machines could be zero.

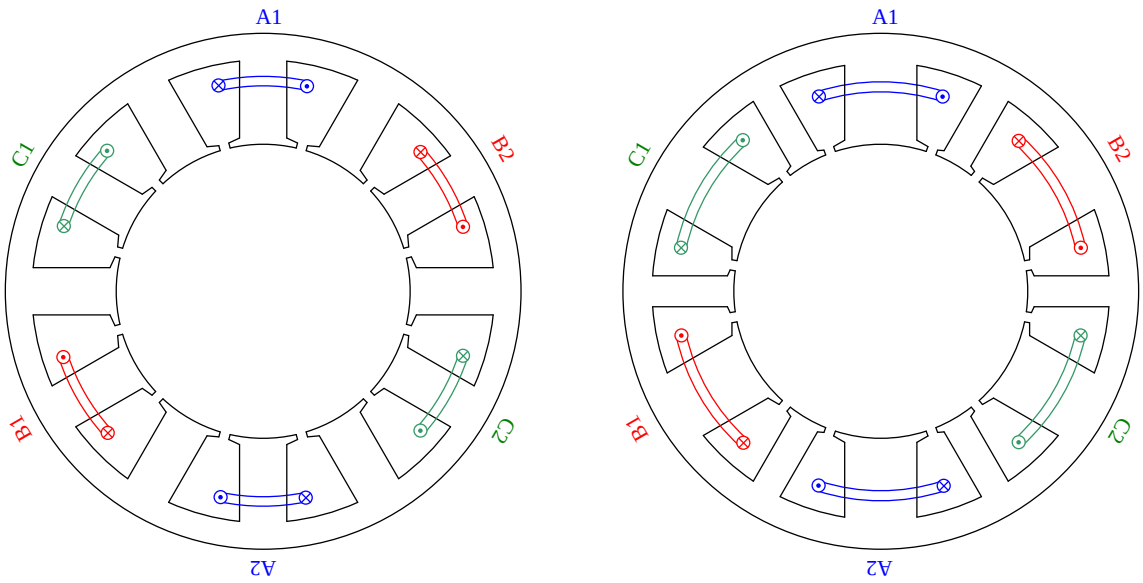

(a) Equal teeth (b) Un-equal teeth

Fig. 1.5 Illustration of alternative teeth wound windings [ISH05a], [ISH06].

Generally, the iron loss and magnet eddy current loss in FSCW machines are significantly influenced by slot harmonics and MMF space harmonics [ALB12]. Fornasieo *et al.* [FOR12] pointed out that the slot harmonics will increase when $N_s\rightarrow2p$, which leads to higher losses in FSCW machines. Bianchi *et al.* [BIA10] claimed that MMF space harmonics in FSCW machines will increase when $N_s\rightarrow$2p, which makes $2p=N_s\pm2$ machines have higher rotor losses than q=0.5 machines. However, according to the aforementioned review, most of the FSCW machine performances will be enhanced when $N_s\rightarrow2p$, which are conflicted with the low losses conditions. Therefore, a trade-off between losses and other performances exists when selecting proper $N_s/2p$ combinations [HAN10].

Last but not the least, noise and vibration in FSCW machines is a more practical issue which is also influenced by $N_s/2p$ combinations. Due to the fractional slot winding, the radial forces under load condition always change with rotor positions, leading to noise and vibration [CHE06]. Generally, the higher the lowest vibration mode of FSCW machine, the lower noise and vibration level will be [CHE06], [ZHU09a]. Thus, q=0.5 machines may have less noise and vibration compared with $2p=N_s\pm2$ machines, but $2p=N_s\pm1$ machines will suffer even more than $2p=N_s\pm2$ machines. In fact, $2p=N_s\pm1$ machines naturally have asymmetric phase windings, which introduces unbalanced magnetic force UMF, and leads to strong noise and vibration [ISH05b]. Zhu *et al.* [ZHU13], [WU13] further proved the conclusion by comparing the UMFs of many $N_s/2p$ combinations. It is found that the UMF in $2p=N_s$-1 machines, e.g. 9-slot/8-pole, are more severe than $2p=N_s$+1 machines, e.g. 9-slot/10-pole, and may even deteriorate if rotor eccentricities occur.

1.1.3 Harmonics Reduction Techniques of FSCW Machines

The aforementioned literature reveals that harmonics in airgap field and armature windings are typical features and common drawbacks in FSCW machines. Therefore, many engineers and scientists have paid great attention to harmonics reduction techniques for FSCW machines. Generally, the harmonics in the airgap field of FSCW machine may come from three different ways, i.e. stator MMF, rotor MMF, and airgap permeance harmonics [LIP04]. From the MMF harmonics point of view, Dajiaku and Gerling [DAJ12] claimed that stator segmentation from the back iron in a 12-slot/10-pole could significantly reduce the sub-harmonics in MMF, Fig. 1.6(a). Meanwhile, they also claimed stator barrier could also be allocated in the stator teeth [DAJ12a] as shown in Fig. 1.6(b). This technique has been further investigated and improved by Li *et al.* [LI14]. However, these methods will reduce the iron region of stator and influence the flux paths, which may reduce the average torque. To fulfil the advantage of this method, proper $N_s/2p$ combination and optimization are demanded [LI14]. In another way, Alberti and Bianchi [ALB13] introduced multi-layer FSCW winding to reduce MMF harmonics, which can be shown in Fig. 1.7 by taking a 12-slot/10-pole machine for example. With the increase of number of coils per phase, the MMF harmonics generated by each coil could be largely cancelled compared with the original double layer windings. Based on that, Kim *et al.* [KIM14a] developed the method and found that MMF harmonics in multi-layer winding could be further reduced by unequal turns for different coils.

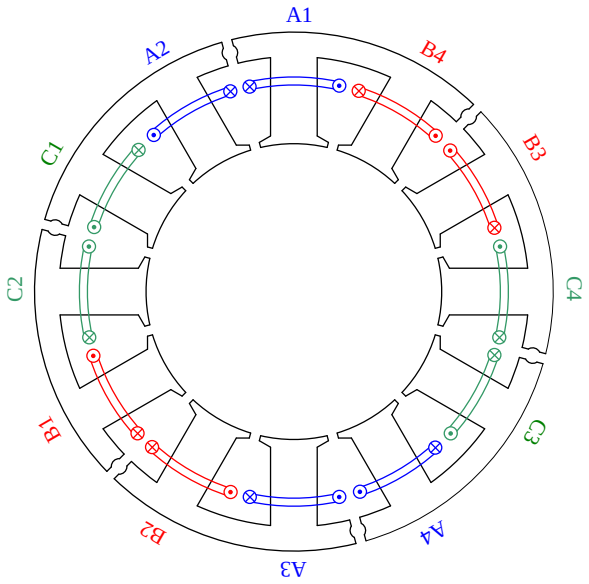

(a) Flux barriers in yoke [DAJ12]

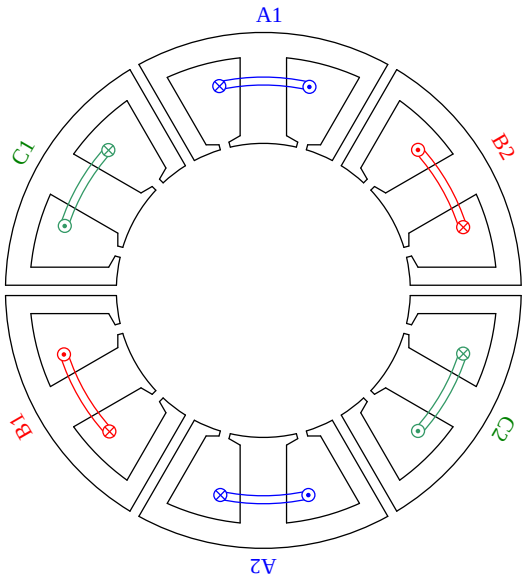

(b) Flux barriers in teeth [DAJ12a], [LI14]

Fig. 1.6 Illustration of stator barrier techniques for 12-slot/10-pole machine.

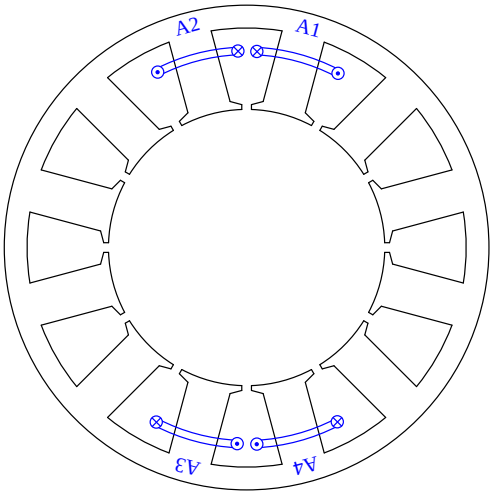

(a) Original double-layer winding

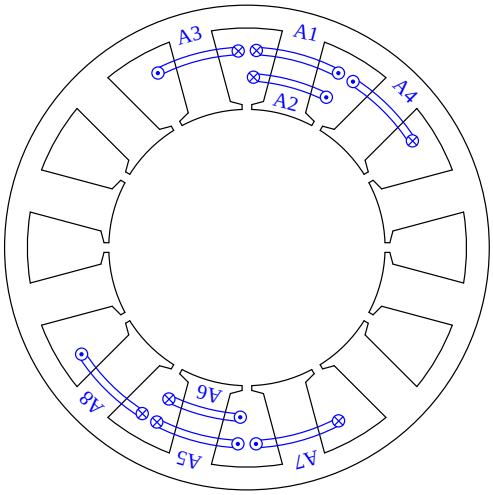

(b) Four-layer winding

Fig. 1.7 Illustration of multilayer FSCW of one phase for 12-slot/10-pole machine [ALB13].

In order to make the rotor MMF more sinusoidal, Halbach [HAL80] proposed an SPM rotor with different magnetization directions as shown in Fig. 1.8(a), which can generate almost sinusoidal airgap field. In order to further improve the harmonic reduction effect, Shen and Zhu [SHE13] proposed unequal magnet height Halbach rotor topology, which reduces the adjacent magnets as shown in Fig. 1.8(b). Besides, rotor pole shaping is another way to reduce the rotor MMF harmonics. The basic method is sinusoidal shaping, which makes the airgap length change following a sinusoidal function [RUA05], [LI08], [TAV10], Fig. 1.9(a).

However, this method may largely reduce the magnet volume and fundamental back-EMF. In order to compensate that, inverse cosine shaping method [HSI05] and 3rd harmonic shaping method [WAN14a], [WAN14c] are proposed as shown in Fig. 1.9(b) and (c). Considering the feature of IPM rotor, the magnet could not be directly shaped like that in SPM rotors. Thus, the IPM rotor shaping methods majorly reduce the harmonics in airgap permeance function, in which inverse cosine [EVA10], [DOG11] and 3rd harmonic shaping [WAN14b] are the best candidates, Fig. 1.10. Meanwhile, the stator tooth could also be shaped to achieve unequal airgap length similar to the rotor shaping, Fig. 1.11. Lee *et al.* [LEE11] claimed that stator shaping can reduce the voltage harmonics caused by MMF harmonics. Junak and Ombach [JUN10] proposed an asymmetric tooth-tip shaping, which could reduce the torque ripples together with rotor shaping.

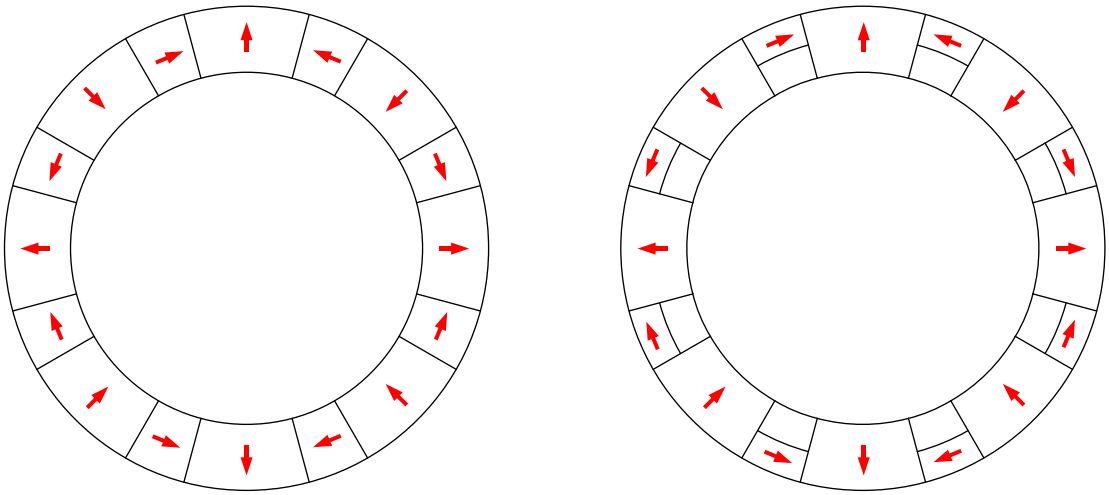

(a) Equal PM Height Halbach [HAL80] (b) Unequal PM Height Halbach [SHE13]

Fig. 1.8 Comparison of different Halbach rotors.

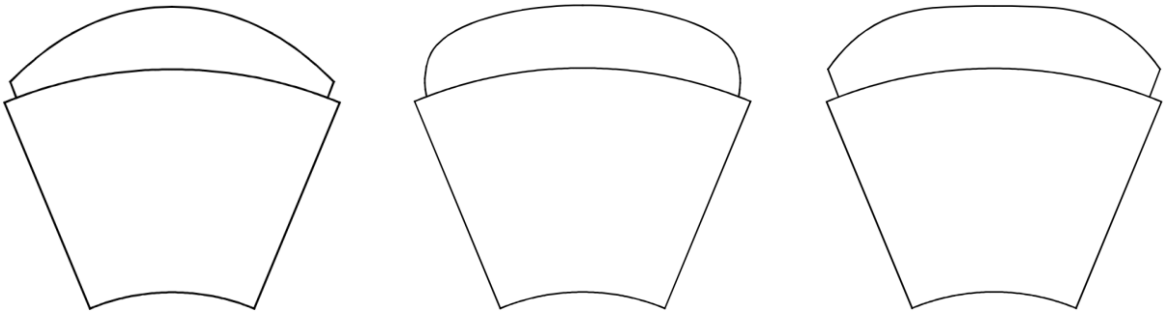

(a) Sinusoidal [RUA05] (b) Inverse cosine [HSI05] (c) 3rd Harmonic [WAN14a]

Fig. 1.9 Comparison of shaping methods for SPM rotors.

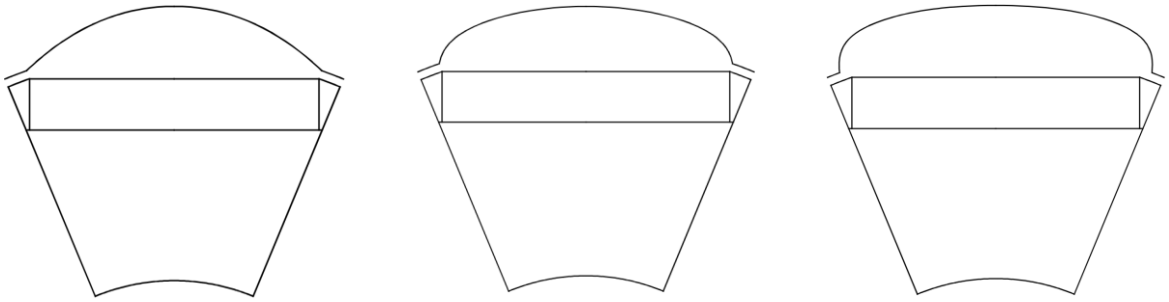

(a) Sinusoidal [RUA05] (b) Inverse cosine [EVA10] (c) 3rd Harmonic [WAN14b]

Fig. 1.10 Comparison of shaping methods for IPM rotors.

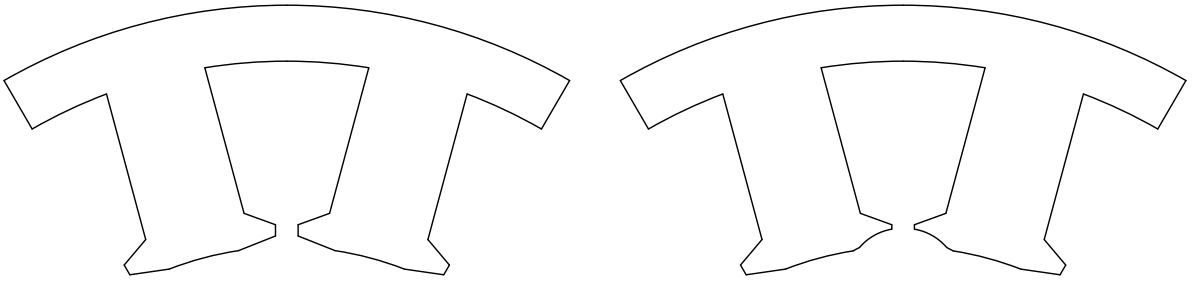

(a) Symmetric shaping [LEE11] (b) Asymmetric shaping [JUN10]

Fig. 1.11 Illustration of stator shaping methods.

1.1.4 FSCW Machines Considering Manufacturing Process

Due to concentrated winding, FSCW machines are more suitable for automatic winding fabrication, which leads to high packing factor and thereafter high efficiency [ELR10]. By adopting pressed wire, Jack *et al.* [JAK00] claimed that the packing factor calculated by pure copper area could reach almost 80%. Meanwhile, in order to fulfil the advantages of FSCW and increase the manufacturing efficiency, modular stator techniques are widely adopted nowadays [ELR10]. A typical modular stator can be shown in Fig. 1.12, in which each segment contains a tooth body and part of the back iron. After automatic winding, the modular segments are assembled together to form a complete stator. There are normally location holes and bumps in order to reduce the manufacturing tolerance, which can be observed from Fig. 1.12 as well. Since the manufacturing tolerance may make the assembled stator not a perfect circle, the plug-in teeth technique has been proposed as shown in Fig. 1.13. For this technique, the back iron is a complete ring without any segmentation, while the teeth or tooth-tips can be plugged in the back-iron after automatic winding [ZEP05], [RIC14]. Nevertheless, although alignment techniques have been introduced, the manufacturing tolerance may still reduce the uniformity of teeth, which introduces undesired non-uniform

airgap and influences the machine performance. Therefore, the advanced plug-in techniques have been developed, which only separate the stator lamination into two parts, e.g. complete back-iron and all teeth linked together by tooth-tips with closed-slot openings, [MUL05], [PAR12], Fig. 1.14. Since the number of stator segments largely reduces, the eccentricities caused by manufacturing tolerance are also minimized. Additionally, it is worth mentioning that by adopting alternative slot openings based on advanced plug-in technique, Fig. 1.15, the cogging torque of FSCW machines could be further reduced or even eliminated [AZA12a].

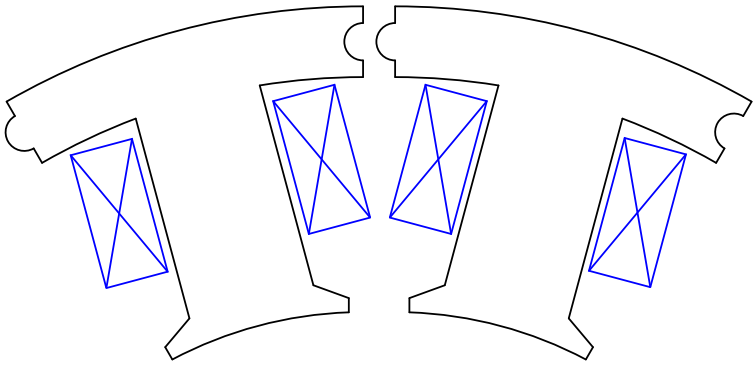

Fig. 1.12 Illustration of conventional modular stator technique [AKI03].

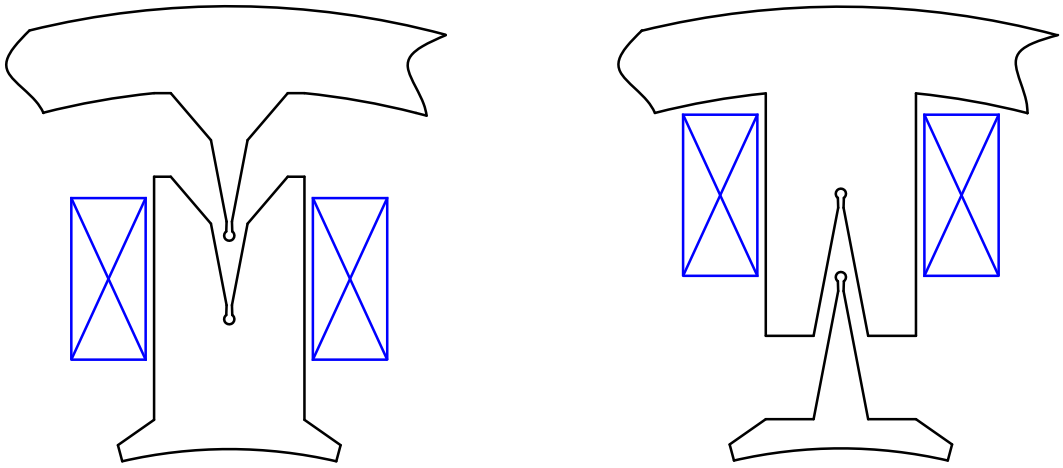

(a) Plug-in tooth [ZEP05] (b) Plug-in tooth-tip [RIC14]

Fig. 1.13 Illustration of plug-in tooth techniques.

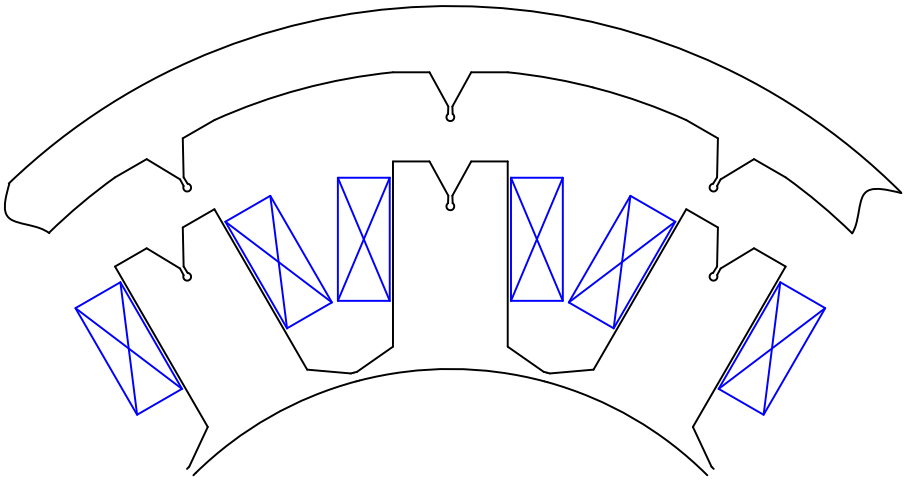

(a) Closed slot tooth plug-in [PAR12]

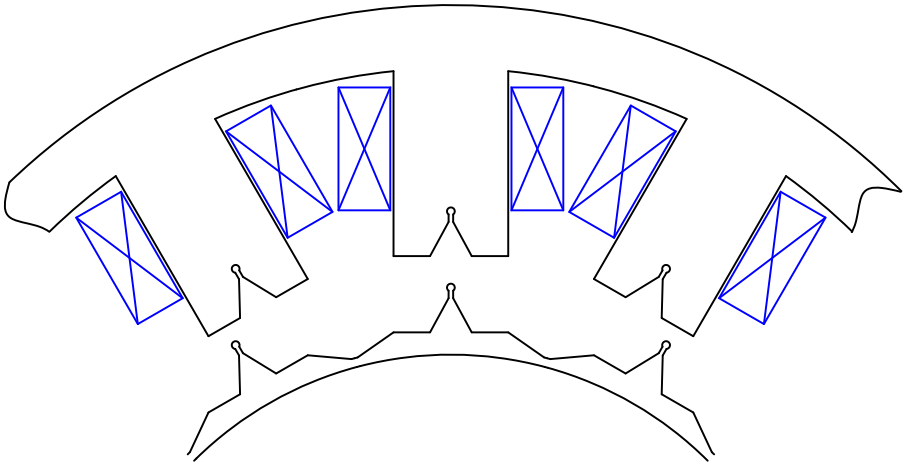

(b) Closed slot tooth-tip plug-in [MUL05]

Fig. 1.14 Illustration of advanced plug-in techniques.

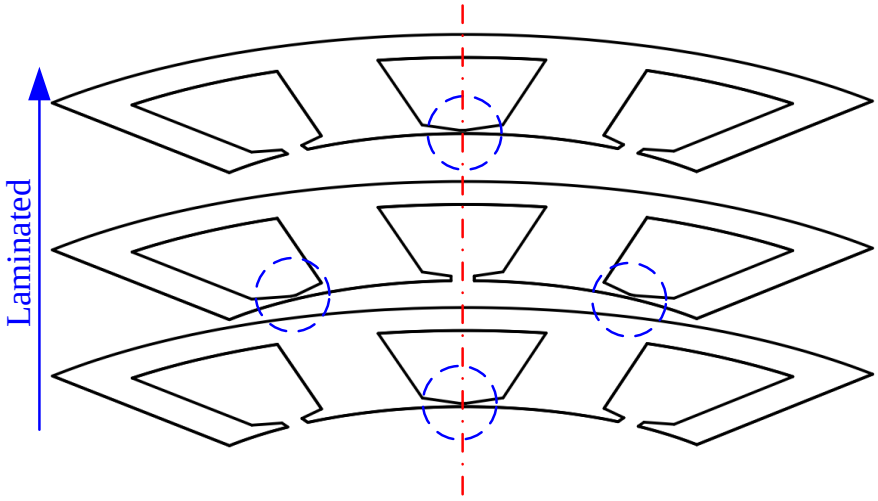

Fig. 1.15 Illustration of alternative closed slot opening techniques (3D drawing) [AZA12a].

1.2 Terminal Voltage Distortion in FSCW Machines

Fig. 1.16 illustrates the typical configuration of a three-phase BLAC machine and drive system, which is basically constituted by four different parts, e.g. electric machine, inverter, controller and sensor, as well as the DC power supply. Based on that, the terminal phase currents and voltages of electric machines directly determine the input energy, which consequently influence the machine torque performances [MIL92]. In order to reduce the current harmonics for BLAC operation, field oriented control, i.e. vector control, is commonly adopted [VAS90]. In this method, the control of torque and excitation field are decoupled and could be adjusted by *dq*-axis currents separately, while the *dq*-axis voltages are maintained within the DC link limitation. Based on that, sinusoidal phase currents could be generated, which makes the terminal voltage distortion more sensitive on machine performance from energy conversion point of view [DEO96], [STA96].

In real applications, all four major parts of the BLAC machine and drive system contribute to the terminal voltage distortion. From drive side, the origins of terminal voltage distortion are well known as inverter nonlinearities, such as voltage drop on power devices, PWM dead time, delay in drive circuit, turn-on and -off delays, parasitic capacitance effect, etc. [GON11]. Meanwhile, due to limited power rating of DC supply, the DC link voltage fluctuation may also introduce terminal voltage distortion and influence machine performances [SIL11]. However, due to strong nonlinear nature of the electric machines, more obvious voltage distortion could be generated from machine side, which is the main concern of this thesis.

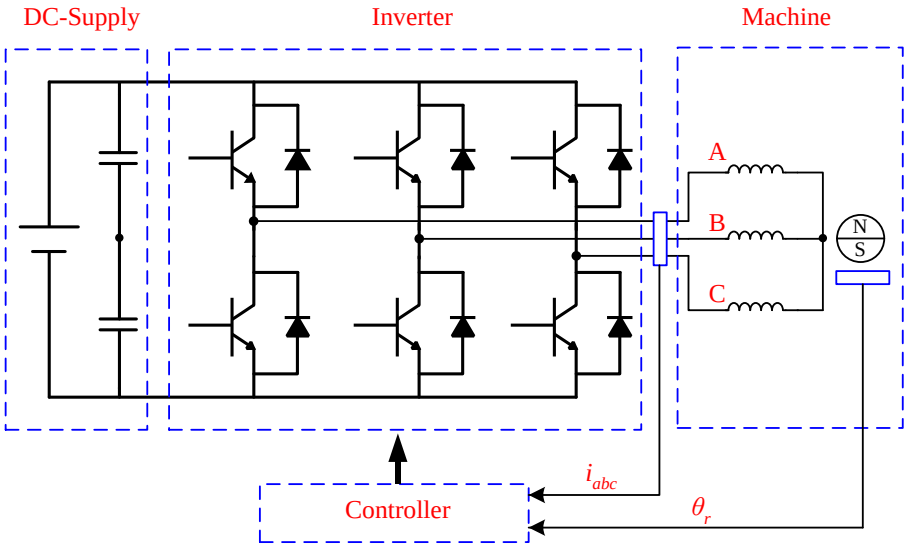

Fig. 1.16 Schematic of BLAC machine drive system.

The nonlinear behaviours of electric machines inherit from the nonlinearity of ferromagnetic lamination material adopted in nearly all electric machines. Since the open-circuit flux density in main flux paths are usually designed around the knee point of lamination material, the saturation majorly influences the on-load performance, which is well known as armature reaction.

Almost right after the invention of electric machine in nineteen century, the magnetic saturation caused by armature reaction began to obtain attentions from engineers and scientists. In some conventional machines, e.g. induction machines, magnetic saturation will increase harmonics in airgap field, which leads to voltage harmonics in both stator and rotor windings [LEE61]. These harmonics will further influence the current harmonics and increase torque ripples and losses [LIP04]. Nevertheless, after the invention of vector control, the phase currents of electric machines could be controlled sinusoidal, which reduce the concern of terminal voltage distortion caused by magnetic saturation, especially for PM machines.

In order to investigate the influence of magnetic saturation on voltage distortion in addition to the classical *dq*-axis theory, Moreira and Lipo [MOR92] introduced the concept of spatial dependent magnetic saturation, which exists in all synchronous machines. In this concept, the magnetic saturation in teeth and back iron synchronously rotates with rotor, and its influence can be treated as an additional virtual rotating airgap, Fig. 1.17. This virtual airgap will influence the airgap permeance function, and introduce flux and voltage harmonics, which consequently influence the machine performance. Orlik *et al.* [ORL11] further developed this concept for PM machines in order to accurately consider the voltage harmonics and its influence on control performance. Based on that, as well as the features of FSCW machine reviewed in the aforementioned sections, the generating process of terminal voltage distortion could be summarized as shown in Fig. 1.18. Ideally, if ignoring the magnetic saturation, the blocks within the dashed green rectangular can be ignored. The stator MMF will not contribute to the terminal voltage distortion since only sinusoidal currents are injected. Thus, the terminal voltage distortion under such condition only comes from the back-EMF harmonics which are generated by the rotor MMF harmonics and the harmonics in airgap permeance function due to stator slotting. Since the harmonic winding factors in FSCW machines are normally small, the terminal voltage distortion is also unobvious under such condition.

However, if magnetic saturation is considered, all blocks in the dashed green rectangle should to be concerned, which makes the generating process of terminal voltage distortion much more complicated. First, the magnetic saturation significantly increases the harmonics of airgap permeance function through 'virtual airgap', which leads to the distortion of on-load back-EMF and increases the harmonics in terminal voltages. Frozen permeability (FP) method could be adopted to prove this result [AZA12]. As the main investigation tool of this thesis, FP method will be introduced briefly in Appendix A. Meanwhile, through the airgap permeance function influenced by magnetic saturation, stator MMFs will also contribute to the on-load terminal voltage distortion. This influence can be represented by the voltage drop on harmonic inductances [YU13]. Further, if the terminal voltage distortion has not been fully tracked by the control system, harmonic currents will be generated, which further increase the harmonics of stator MMFs, and enhance the terminal voltage distortion level.

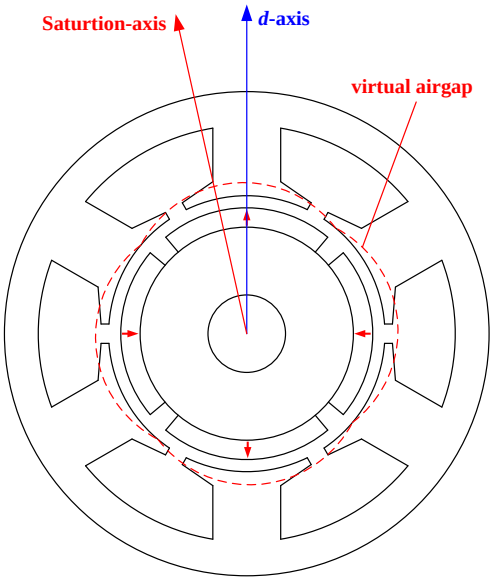

Fig. 1.17 Concept of spatial dependent magnetic saturation in synchronous machines [MOR92], [ORL11].

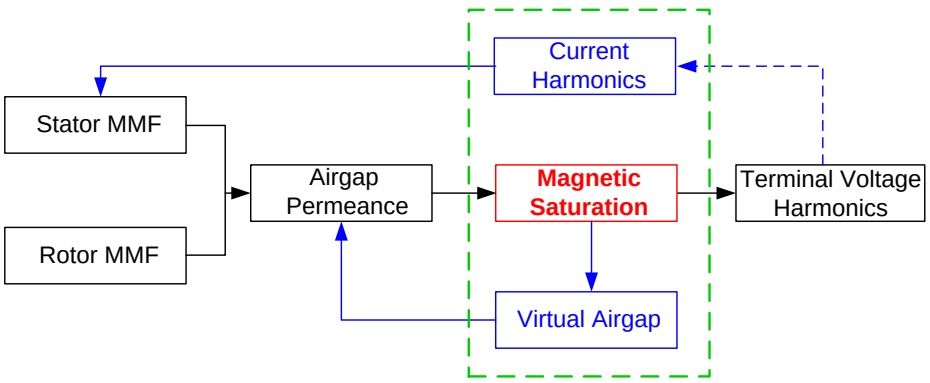

Fig. 1.18 Influence of magnetic saturation on terminal voltage distortion.

Considering the negative impact of on-load magnetic saturation, the operation point of major flux paths under rated currents could be designed around the knee point of the lamination material. However, under fixed machine size, this design demands larger dimension of teeth body and back iron, which definitely reduce the slot area and thereafter the torque capability. In order to balance the conflict between laminated teeth and slot area, tooth-tips are widely adopted in middle or small sized machine. However, this introduces another dilemma since the tooth-tips may also be highly saturated due to limited geometric size, although the saturation in tooth body and back iron could be negligible. Since the stator lamination is locally saturated instead of globally saturated, the saturations in toot-tips are designated as ***local magnetic saturation***, which can be illustrated as the shadowed region in Fig. 1.19(a). Due to limited space in IPM rotors, the lamination region around rotor flux barriers are regionally saturated as well, which can also be called local magnetic saturation, Fig. 1.19(b).

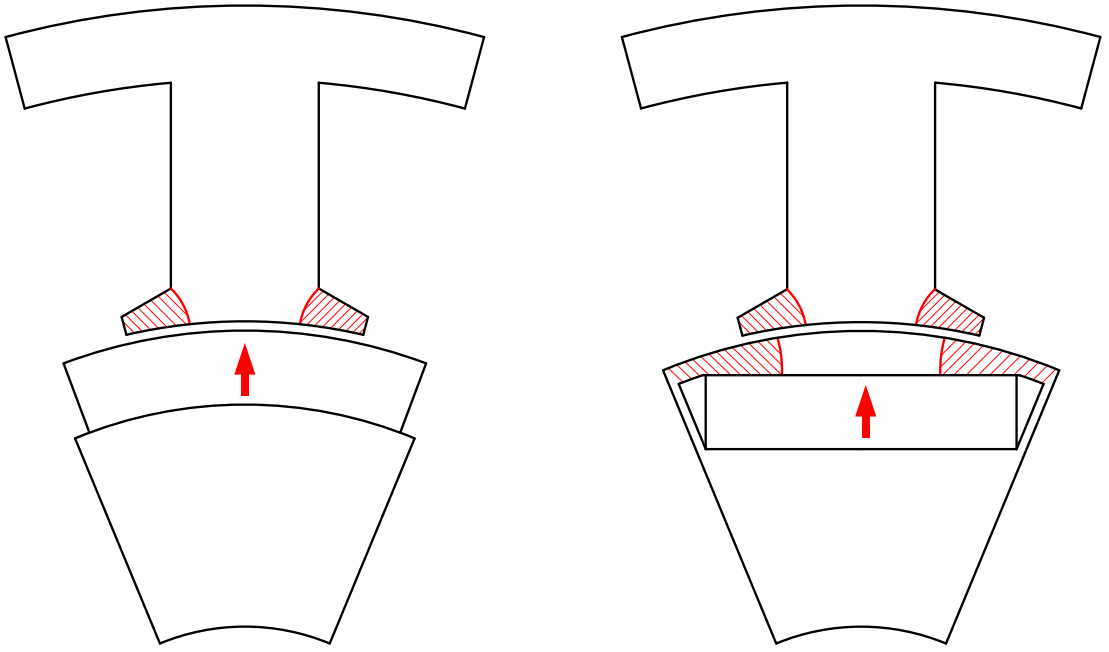

(a) SPM rotor (b) IPM rotor

Fig. 1.19 Illustration of ***local magnetic saturation*** in FSCW machines.

In fact, the local magnetic saturation has attracted increasingly research interest in the last five years, especially with the development of FP method. By FP method, Azar *et al.* [AZA12] found that the on-load cogging torque and on-load back-EMF harmonics are much higher than that under open-circuit condition, which result in on-load torque ripples. Yamazaki and Kumagai [YAM14] calculated the on-load *dq*-axis PM flux linkages by FP

method. It is found that the PM flux linkage phasor will be shifted from *d*-axis due to the asymmetric local magnetic saturation, which reduces the electromagnetic torque especially under I_d=0 control. Chu and Zhu [CHU13], [CHU13b] improved the FP method for on-load cogging torque calculation, and proved that rotor skewing could not sufficiently reduce the on-load torque ripples since the tooth-tips local magnetic saturations in different machine segments along axial direction are different. Ponomarev *et al.* [PON14] claimed that the local magnetic saturations in some tooth-tips are more severe than others based on an 18-slot/16-pole FSCW machine. Thus, by adjusting the designs for such tooth-tips, the overall torque ripples could be reduced. Xuan *et al.* [XUA13] reported that the on-load local magnetic saturation in FSCW SPM machine will increase the equivalent slot opening width, which may increase the slot harmonics and rotor PM eddy current loss. Faggion *et al.* [FAG13] pointed out that local magnetic saturation in tooth-tips will help to increase the high frequency rotor saliency, which increases the sensor-less control performance especially for FSCW SPM machines. According to all these recent investigations, it can be concluded that local magnetic saturation almost influences all kinds of performances for FSCW machines, which show great importance and necessity for further investigation.

Based on the aforementioned review, terminal voltage distortion could also significantly influence the machine performance, which should be investigated together with local magnetic saturation. Nevertheless, it can be barely found in any literature from this point of view. Lee *et al.* [LEE11] found that the local magnetic saturation in tooth-tips of a 12-slot/8-pole IPM machine will increase the maximum value of terminal line voltage. But the phenomenon in other $N_s/2p$ combinations, as well as the influences on other performances such as flux weakening operation are not further investigated. Therefore, this thesis will systematically investigate the mechanism of terminal voltage distortion in both FSCW SPM and IPM machines, with due consideration of the influence of $N_s/2p$ combinations. Meanwhile, other performance such as flux weakening characteristic, on-load back-EMF, on-load cogging torque, *dq*-axis inductance, torque ripple, as well as iron loss will be investigated at the same time.

1.3 Scope of Research and Contribution of the Thesis

This thesis investigates the on-load terminal voltage distortion in FSCW SPM and IPM machines focusing on the influence of local magnetic saturation. All FEA calculations are

carried out based on JMAG version 14. The arrangement of each chapter can be illustrated in Fig. 1.20, while the detail contents of each chapter will be listed as follows.

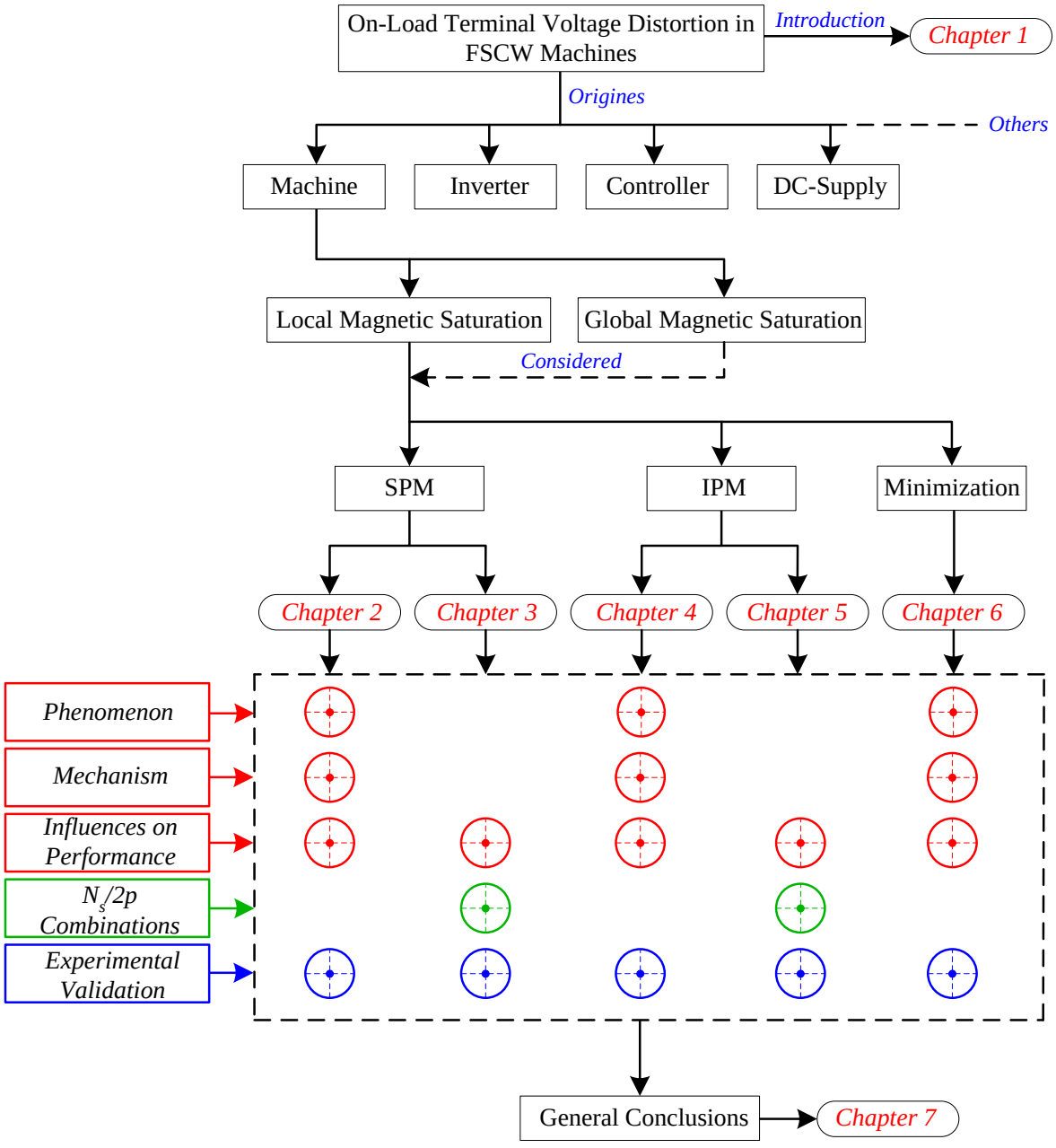

Fig. 1.20 Research scope and arrangement of chapters.

Chapter 1:

This chapter reviews the background literature related with the research topic, and shows the importance and necessity of the investigations in this thesis.

Chapter 2:

With the aid of frozen permeability method, the mechanism of on-load voltage distortion in FSCW SPM machines will be investigated based on a 12-slot/8-pole model for example. Then, its impacts on machine performance under vector control will be investigated, focusing on on-load back-EMF, on-load cogging torque and torque ripple, *dq*-axis inductances, iron loss, and flux weakening performance. The phenomena and influences when the machine operates beyond the base-speed or considering the limited band width of controller and inverter in real systems will also be discussed. Finally, a prototype machine is manufactured and tested to validate the analyses.

Chapter 3:

This chapter focuses on investigating the influence of $N_s/2p$ combinations on on-load terminal voltage distortion in both fractional slot and integer slot SPM machines. Then, a concept of voltage distortion pattern is proposed to analyse the occurring time or rotor positions of voltage ripples and their relative amplitudes according to the winding arrangements of different $N_s/2p$ combinations, with the influence of PM leakage flux considered. By 2D finite element analysis, the voltage distortion of various machines are calculated and compared, such as $N_s \pm 1 = 2p$, $N_s \pm 2 = 2p$, $N_s/2p = 3/2$ (3/4) and integer slot machines with slot number per pole per phase q=1 or 2. Finally, two prototype machines with 12/10, and 12/8 slot/pole numbers are manufactured and tested to validate the analyses.

Chapter 4:

The mechanism and influence of on-load terminal phase voltage distortion in FSCW IPM machines are investigated by taking a 12-slot/8-pole machine as example with the aid of FP method. The influences on other performance are also investigated, such as on-load back-

EMF, on-load cogging torque, *dq*-axis inductances. Finally, a prototype is manufactured and tested to validate the analyses.

Chapter 5:

This chapter investigates the influences of $N_s/2p$ combinations on terminal voltage distortion in IPM machines. Various machines with the same machine size and rated current are compared, such as $N_s \pm 1 = 2p$, $N_s \pm 2 = 2p$, $N_s/2p$ =3/2 (3/4), together with two integer slot machines with q=1 and 2. Meanwhile, their influences on other machine performances are also compared such as such as on-load back-EMF, on-load cogging torque, *dq*-axis inductances. Finally, two prototype machines with 12/10, and 12/8 slot/pole numbers are manufactured and tested to validate the analyses.

Chapter 6:

Rotor skewing and non-uniform airgap methods are investigated focusing on their effectiveness to eliminate terminal voltage distortion in FSCW IPM and SPM machines by taking 12-slot/8-pole machines for example. The design trade-off between machine torque performance and on-load terminal voltage distortion are also discussed. Finally, the design trade-off of SPM machine, and the rotor shaping method of IPM machine are selected for validation by the experiments.

Chapter 7:

General conclusions about the phenomenon and mechanism of voltage distortion in FSCW SPM and IPM machines are drawn, considering the influence of $N_s/2p$ combinations. Meanwhile, several research topics are also presented as the future work based on this thesis.

Appendix A:

The principle and calculation method of frozen permeability method is briefly described.

Appendix B:

The methods for cogging torque and static torque measurement in this thesis are introduced.

Appendix C:

Two traction machines with 42-slot/8-pole and 48-slot/8-pole will be investigated as case study to revel that terminal voltage distortion also exists in high power machines.

Appendix D:

Design trade-off between cogging torque and torque ripple in FSCW SPM machines considering local magnetic saturation are discussed.

Appendix E:

CAD drawings for all prototypes.

Appendix F:

Publications resulted from this PhD study.

<u>Major Contributions of this thesis:</u>

(1) Systematically investigated the mechanism of terminal voltage distortion in FSCW and integer slot winding SPM and IPM machines focusing on local magnetic saturation.

(2) Investigated the influences of $N_s/2p$ combinations on machine performances influenced by terminal voltage distortion and local magnetic saturation.

(3) Investigated the effectiveness of terminal voltage distortion elimination methods from local magnetic saturation point of view.

CHAPTER 2

ON-LOAD TERMINAL VOLTAGE DISTORTION IN FRACTIONAL SLOT SPM MACHINES CONSIDERING LOCAL MAGNETIC SATURATION

The on-load voltage distortion in fractional slot SPM machines refers to the terminal voltage distorted by armature reaction considering local magnetic saturation. With the aid of FP method, the mechanism of this phenomenon will be investigated based on a 12-slot/8-pole model as example in this chapter, while its influences on other machine performances will also be discussed.

2.1 Introduction

Surface-mounted permanent magnet (SPM) machine has been investigated extensively in the last three decades following the development of new PM materials and power electronics technologies [ELR05], [ZHU10], [PEL12], [FAG13], [ELR10]. In this type of machines, fractional-slot concentrated winding is widely adopted due to many inherent merits such as high torque and power densities, fault tolerant capability, low cogging torque, short end-winding, low copper loss, and high efficiency [ELR10].

In order to reduce the current harmonics and enhance the torque performance, field oriented control, i.e. vector control, is commonly adopted [VAS90]. In this method, the control of torque and excitation field are decoupled and could be adjusted by *dq*-axis currents separately, while the *dq*-axis voltages are maintained within the DC link limitation. However, the *dq*-axis voltages are calculated by the *dq*-axis inductances and PM flux linkages, which are usually derived by only considering their fundamental values [ELR05]. Therefore, the influence of harmonics in phase terminal voltage, which is represented by the harmonic inductances and back-EMF harmonics, are normally not considered. Many control methods take the terminal voltage harmonics as disturbances and try to compensate them for better control performance [URA07], [RAU10], [KIM05]. But the origins have been ascribed to the nonlinearities of inverters or control methods rather than machines. Due to the ferromagnetic lamination materials adopted, the fractional slot SPM machines are inherently nonlinear, which also contribute to the on-load voltage distortion [ORL11], [MOR92], [PAU14].

In a conventionally designed SPM machine, the slots and teeth share the stator space, while tooth-tips are adopted to balance the conflicts between them. Owing to the limited geometry sizes and relatively high slot leakage flux of armature reaction field in SPM machines due to large equivalent airgap, the local magnetic saturation in tooth-tips is usually more obvious, especially when small or closed slot openings are adopted [MOM09]. Many papers have paid attention to the design of tooth-tips and slot opening width in fractional slot SPM machines. [BIA02], [DON12], [CHO10] investigate the influence of toot-tips on cogging torque. It reveals that small or closed slot openings can smooth the variation of airgap permeance and consequently reduce the cogging torque. [FOR12], [XUA13] focus on the rotor loss in fractional slot SPM machines, which shows smaller slot opening width will reduce the slot harmonics and the eddy current loss in PMs. [PAP14], [CVE08] claim that the back-EMF harmonics and torque ripples will be alleviated if closed slots are adopted. Furthermore, a new method was employed to improve the manufacturing automation by separating the teeth from back iron, but directly link them together with tooth-tips [MUL05], [PAR12], [ZHU12]. In this way, this method can further increase the packing factor and reduce the fabrication cost. Meanwhile, the sensorless control performance may be also improved since the local magnetic saturation in tooth-tips introduces saliency in fractional slot SPM machines [AKA07], [FAG13].

Although the aforementioned literature illustrates the advantages of small or closed slot openings, their drawbacks are not fully discussed yet. [ORL11], [MOR92] investigate the current and inductance harmonics due to saturation, but the actual location and mechanism of the saturation are not investigated. [MOM09], [XUA13], [PAP14] show the open-circuit back-EMF and average torque will reduce when very small slot openings are adopted due to the increase of slot leakage flux. However, their influences on terminal voltages are not considered. [RED09], [MEI08] report that the small slot opening width will increase the iron loss of the tooth-tips, but they have not paid attention to the influence on other performances.

Therefore, this chapter focuses on the mechanism and influences of on-load voltage distortion in fractional slot SPM machines caused by local magnetic saturation due to small or closed slot openings, with particular reference to torque speed characteristics under limited DC link voltage. Since the fractional slot SPM machines with the number of slots per pole per phase equal to 0.5 are very popular in industry applications, a 12-slot/8-pole prototype will be adopted as an example in this chapter. Influence of slot and pole number combinations will

be investigated in the next chapter. Based on this model, the production mechanism will be investigated by frozen permeability (FP) method [AZA12]. Meanwhile, the voltage distortion appearing conditions and the impact of tooth-tip geometric parameters will be analysed as well. By adopting vector control, the influence of voltage distortion on the performance in constant torque and flux weakening regions are investigated separately. Finally, a prototype with the same dimensions of the analysis model has been manufactured and tested, which validates the analysed results.

2.2 Phenomenon of On-Load Voltage Distortion

2.2.1 Prototype Model

The investigation is carried out on a 3-phase double-layer winding 12-slot/8-pole SPM machine, which is specially designed for servo application in Fig. 2.1 at zero rotor position (θ_r=0°). In order to achieve low cogging torque and torque ripple, closed slot technique is adopted, while the rotor pole arc is optimized to achieve sinusoidal back-EMF. All basic parameters of the machine are shown in Table 2.1.

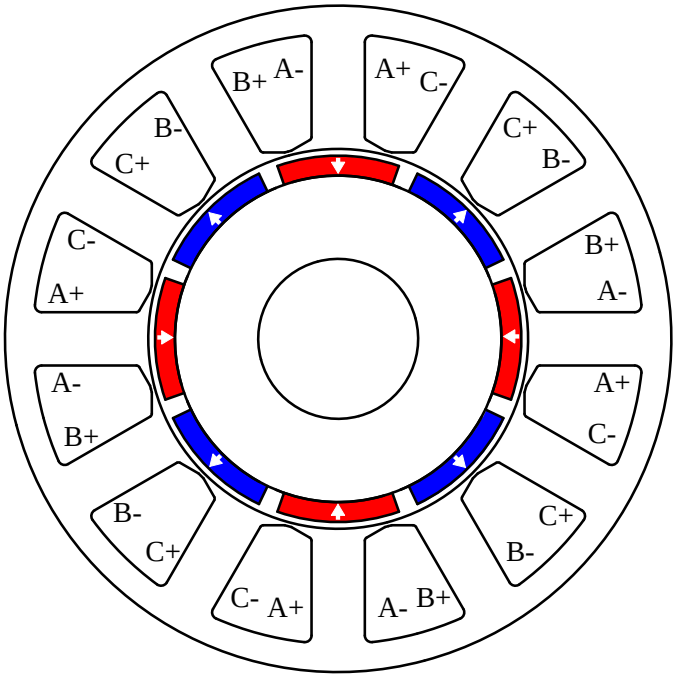

Fig. 2.1 Cross section of 12-slot/8-pole SPM prototype machine (θ_r=0°).

Table 2.1 Basic parameters of 12-slot/8-pole prototype machine

Parameter	***Value***	***Parameter***	***Value***
Stator outer diameter	100mm	Axial length	50mm
Split ratio	0.57	Airgap length	1.0mm
Tooth width	8mm	Back iron thickness	4.2mm
Slot bridge thickness	0.6mm	Turns per phase	184
Magnet thickness	3.0mm	Pole arc/pitch ratio	0.86
Rated current	$7.1A_{rms}$	Phase resistance	0.5Ω
Magnet permeability	1.05	Magnet remanence	1.2T
Magnet material	N35SH	Lamination material	M300
L_d	24.3mH	L_q	8.4mH

2.2.2 On-Load Voltage Distortion

Since the most significant saturation in SPM machines exists in tooth-tips, it is worth investigating their influences on the terminal voltage distortion. A 12/8 machine without tooth-tips is introduced and compared with the original design in Fig. 2.2. Except for the tooth-tips, other parameters of the tip-less model are kept the same as the original 12/8 machine. Fig. 2.3(a) compares the open-circuit and on-load armature flux linkages between the two models, while Fig. 2.3(b) compares their relative voltage waveforms. Although both models have sinusoidal open-circuit back-EMF, their on-load terminal phase voltages are completely different. For the model without tooth-tips, the on-load voltage is almost sinusoidal, with slight harmonics due to the saturation of tooth body and back iron. However, the on-load voltage for the original design is obviously distorted by many spike-like voltage ripples, which can be reflected as strong harmonics shown in Fig. 2.3(c). Since they are $6n\pm1$ time harmonics, the voltage distortion cannot be cancelled in the line voltages. In order to evaluate the level of this phenomenon, the voltage distortion ratio (*VDR*) is defined as

$$VDR = \frac{U_{peak} - U_{fund}}{U_{fund}} \times 100\% \tag{2.1}$$

where U_{peak} and U_{fund} refer to the peak and fundamental values of on-load phase voltages. According to (2.1), *VDR* at rated current is calculated as 94%, which means the peak voltage is nearly twice of the fundamental voltage at rated current. Therefore, the voltage distortion cannot be simply ignored and needs to be carefully investigated. In order to ease the analysis,

the current amplitude (I_{max}) and current advance angle (β) are adopted to describe the driving conditions in the following sections.

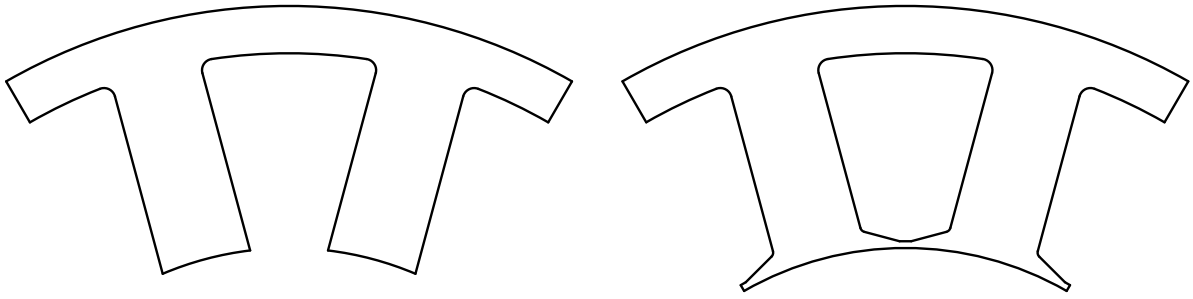

(a) Without tooth-tips (b) With tooth-tips

Fig. 2.2 Illustration of investigated models without tooth-tips for comparison.

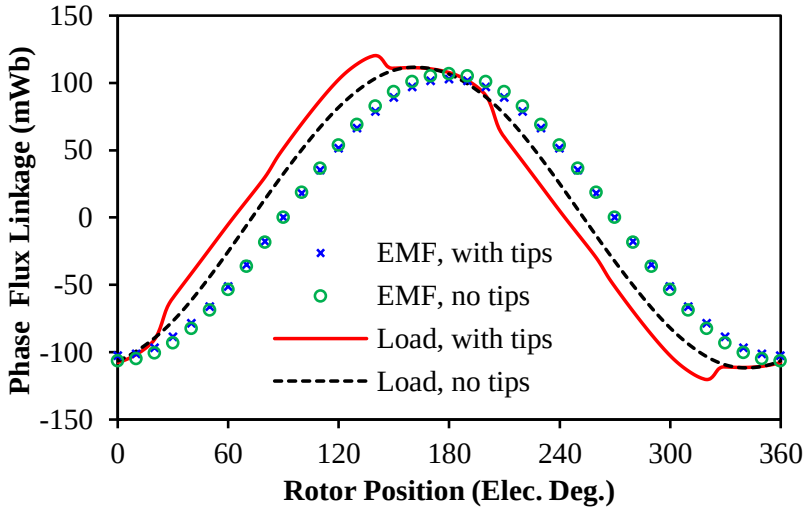

(a) Phase flux linkages

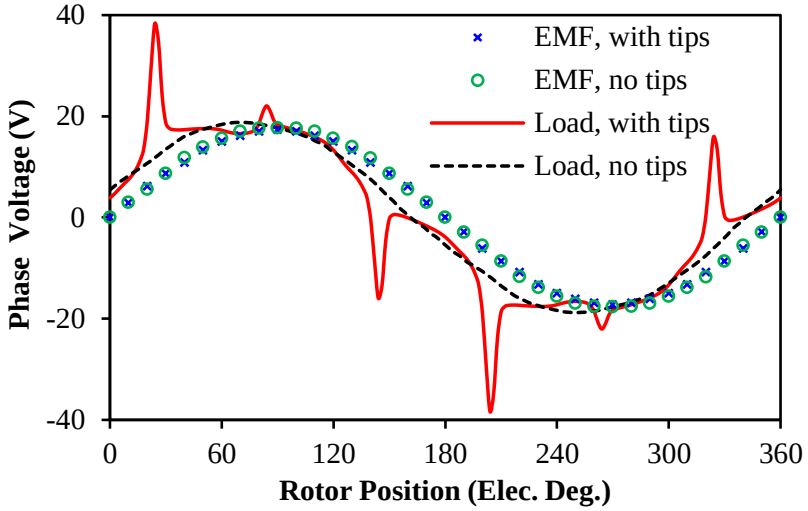

(b) Phase voltage waveforms

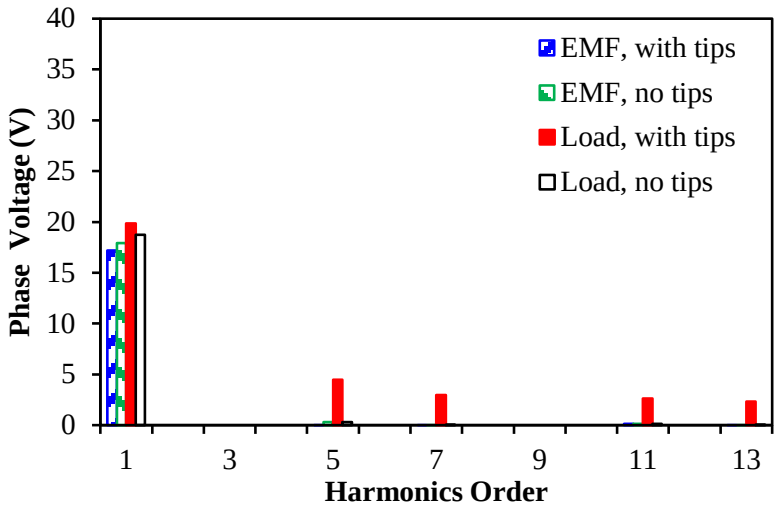

(c) Phase voltage harmonics

Fig. 2.3 Comparison of open-circuit phase back-EMF and on-load phase terminal voltage (I_{max}=10A, β=0°, 400rpm).

2.3 Mechanism of On-Load Voltage Distortion

2.3.1 Mechanism

Since the open-circuit back-EMF does not distort for the prototype machine, the armature reaction plays the main role to trigger this phenomenon. According to Faraday's Law, the on-load voltage distortion should originate from the distortion of on-load flux linkages, which can be revealed by the equation:

$$U_a = r_a i_a + \omega \frac{d(\psi_a^{pm} + \psi_a^{arm})}{d\theta_r} \tag{2.2}$$

where r_a represents the phase resistance, ω is the electric angular speed, $\psi_a{}^{pm}$ and $\psi_a{}^{arm}$ are the on-load PM and armature reaction flux linkage respectively. According to (2.2), the distortion of on-load phase voltage could be generated by the variation of both PM and armature reaction flux linkages. The frozen permeability method is adopted to separate their influences, Fig. 2.4(a). It can be seen that the PM flux linkage rises and falls significantly around certain rotor positions, e.g. 30°, 150°, 210° and 330°, while the armature reaction flux linkage jumps down and soars up simultaneously. Therefore, the phase voltages calculated by the variation of flux linkages are shown in Fig. 2.4(b). The curve marked 'PM only' can be seen as the on-load back-EMF generated by the on-load PM flux linkage, while the curve with 'Armature only' is the voltage drop on winding inductances. It can be observed that both

voltages change dramatically around certain positions where their relative flux linkages vary significantly as well. However, the pulsations of flux linkages are always in the opposite directions, which lead to less distortion in the resultant phase voltage.

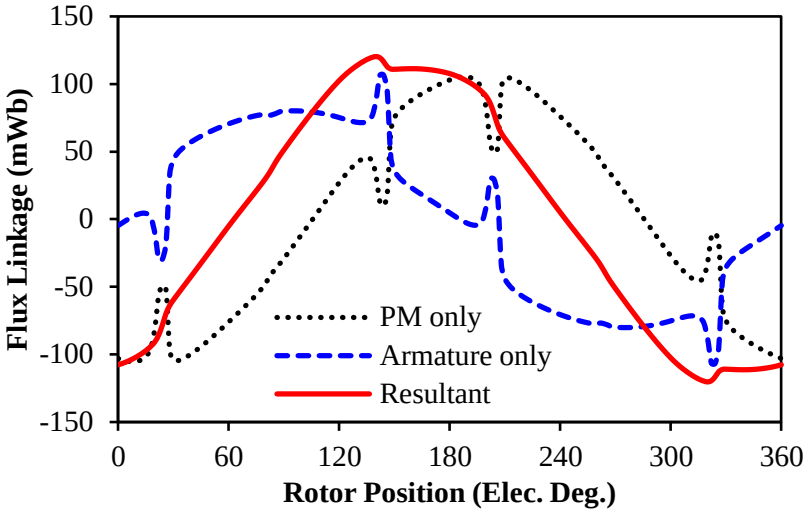

(a) Flux linkages

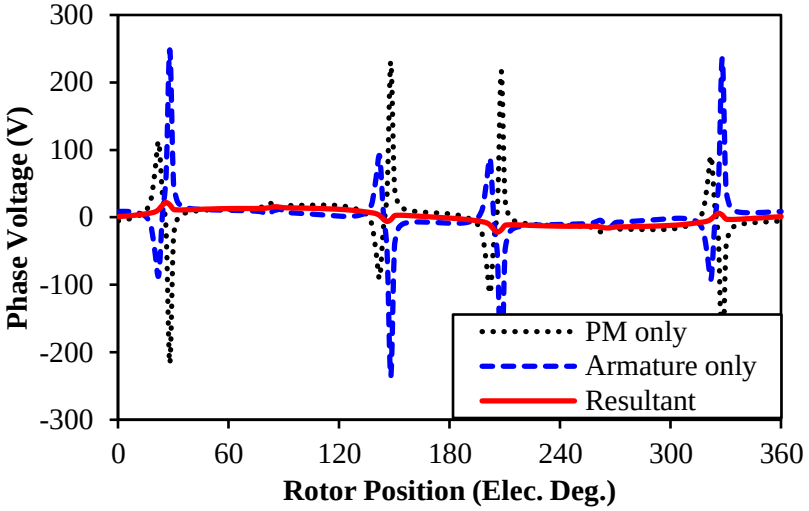

(b) Voltages

Fig. 2.4 On-load phase flux linkage and phase voltage components by FP method (I_{max}=10A, β=0°, 400rpm, 'resultant' is the direct FEA result considering both PMs and armature currents.).

The typical flux paths for both PM and armature reaction fluxes are shown in Fig. 2.5, which shows the tooth-tips are shared by both PM and armature reaction leakage fluxes. Since the main flux paths will not be significantly changed during operation, the pulsation of flux linkages should origin from the local magnetic saturation in tooth-tips. In order to prove this, the permeability of tooth-tips between each tooth coils in the analysis model, e.g. by three

detecting points marked in Fig. 2.6(a), are calculated in Fig. 2.6(b). Clearly, the permeability at each point jumps twice over an electrical period, which is caused by the reversing of leakage flux directions during operation. Fig. 2.7 shows a typical reversing process at rated current, i.e. the process for the first pulsation of P_b in Fig. 2.6. When θ_r=144°, the resultant tooth-tip leakage flux circulates from left to right which is mainly dominated by the armature flux. However, it becomes zero just 1° later, since a balance between PM and armature flux has been achieved. Shortly after that (θ_r=146°), the resultant tooth-tip leakage flux re-establishes and is dominated by PM leakage flux with reversed directions. During this process, both the PM and armature leakage fluxes change dramatically due to the significant changing of tooth-tip local saturation. Consequently, the spike-like voltage ripples generate. It has to be noted that, the leakage flux which dominates the tooth-tip local saturation switches from armature to PM during the above process. Thus, the voltage ripples contributed by two excitation sources always occur simultaneously but in opposite directions (Fig. 2.4). However, since the armature reaction is the origin of local magnetic saturation, the armature leakage flux plays more dominant role during the process, which makes the resultant voltage distortion still obvious.

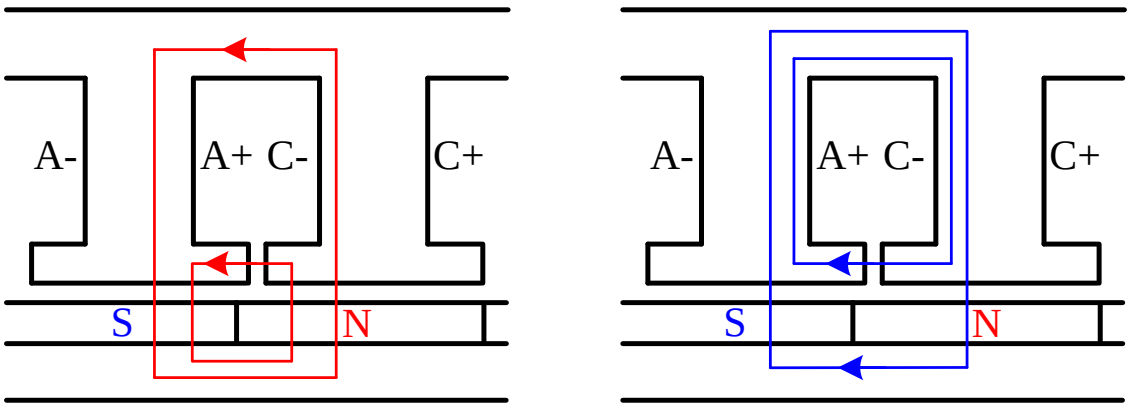

(a) PM (b) Armature

Fig. 2.5 Illustration of typical flux paths for PM and armature, (a) PM, (b) armature.

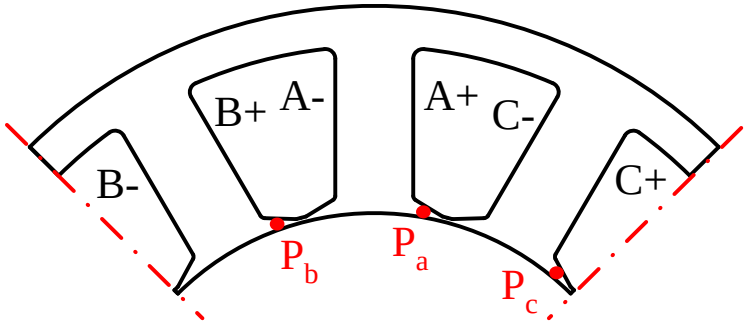

(a) Positions of detecting points

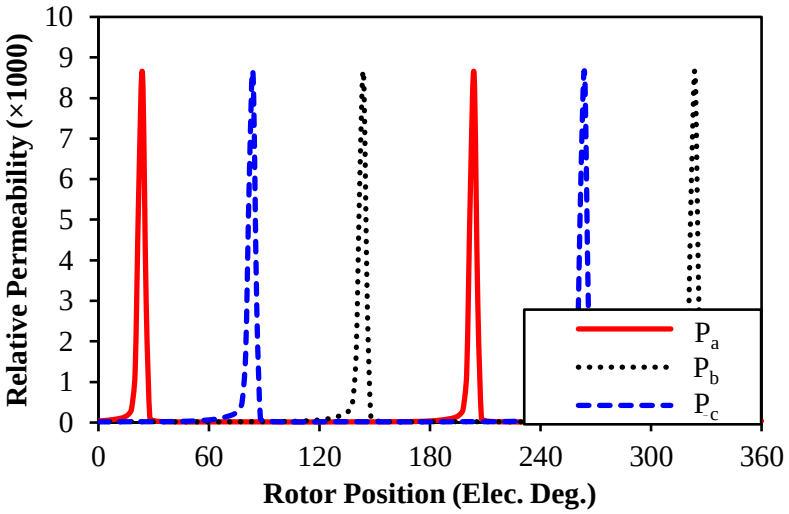

(b) Variation of permeability of tooth-tips

Fig. 2.6 Relative permeability for tooth-tip bridges between each phase coils (I_{max}=10A, β=0°).

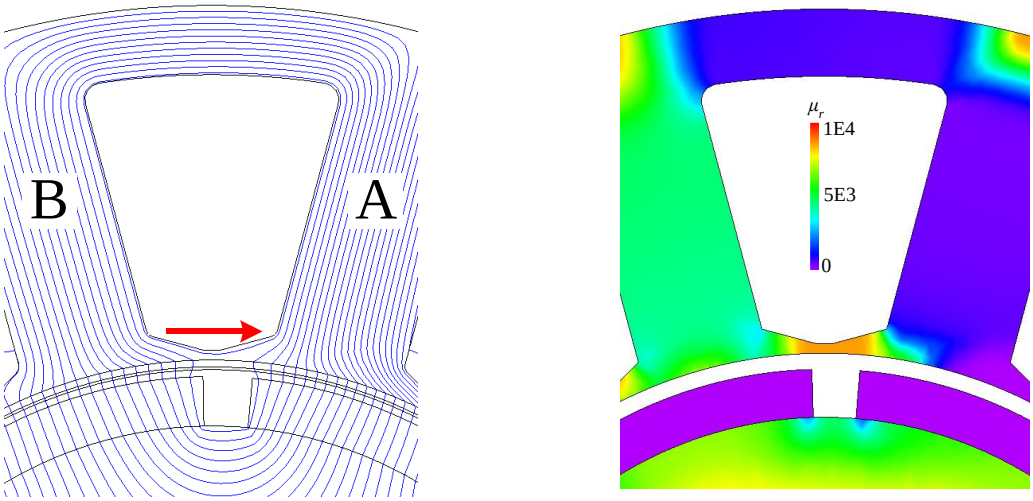

(a) θ_r=144°

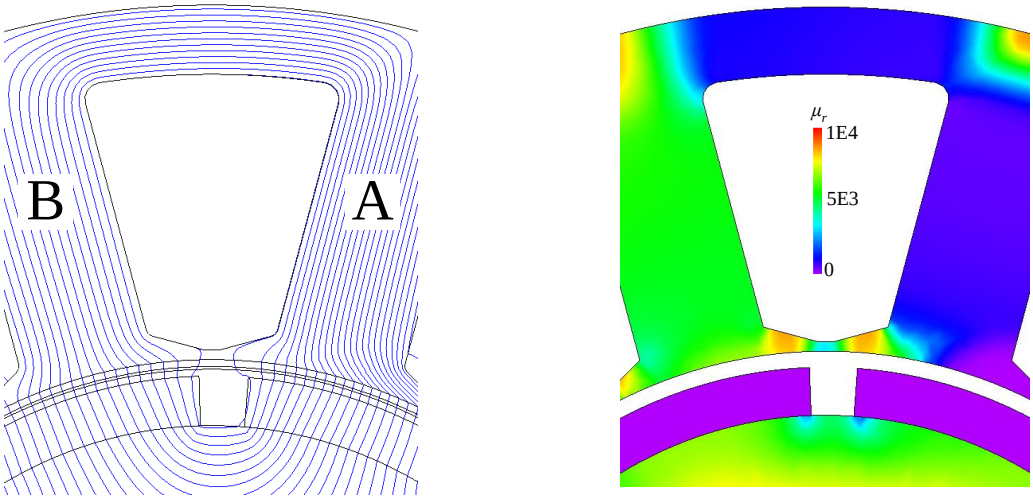

(b) θ_r=145°

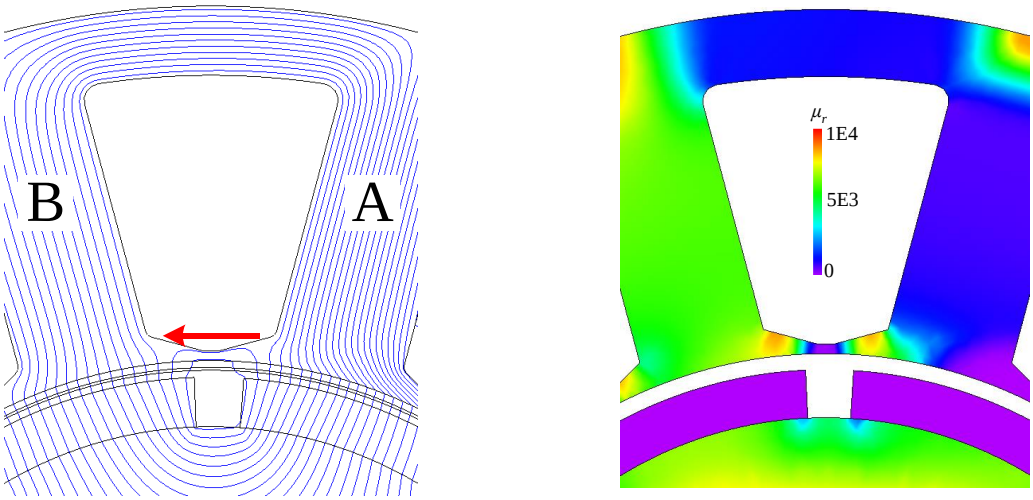

(c) θ_r=146°

Fig. 2.7 Illustration of reversing process of on-load tooth-tip leakage flux (I_{max}=10A, β=0°).

2.3.2 Voltage Ripples Appearing Rotor Positions

The mechanism shows that the flux linkage fluctuates at certain rotor positions will cause the spike-like voltage ripples. These certain positions can be predicted by analysing when the PM and armature leakage fluxes reverse their directions for the same slot opening. If the centre of rotor inter-pole, i.e. the central line of adjacent PMs, faces a slot opening, the PM leakage flux will reverse its polarity around this rotor position. Such rotor positions can be described as

$$\theta_r^{PM} = k\pi, k = 1, 2, 3... \tag{2.3}$$

Meanwhile, when the slot current, e.g. I_A-I_C in Fig. 2.5, crosses zero, the armature tooth-tip leakage flux reverses its polarity as well. Such rotor positions can be expressed as

$$\theta_r^{arm} = m\pi + \beta, m = 1, 2, 3... \tag{2.4}$$

Ideally, when θ_r^{PM} equals θ_r^{arm}, i.e. β=0°, two types of leakage fluxes, i.e. PM and armature fluxes, will reverse simultaneously, which leads to the worst voltage distortion for certain I_{max}. However, the local saturation will influence the ideally predicted positions, and the maximum *VDR* will happen when β is slightly larger than 0°. In order to clarify this, β corresponding to the maximum *VDR* under different I_{max} is shown in Fig. 2.8. It can be seen that when current is low, the maximum voltage spikes happen exactly at β=0° as predicted. With the increase of I_{max}, the relative β for the maximum *VDR* will gradually increase.

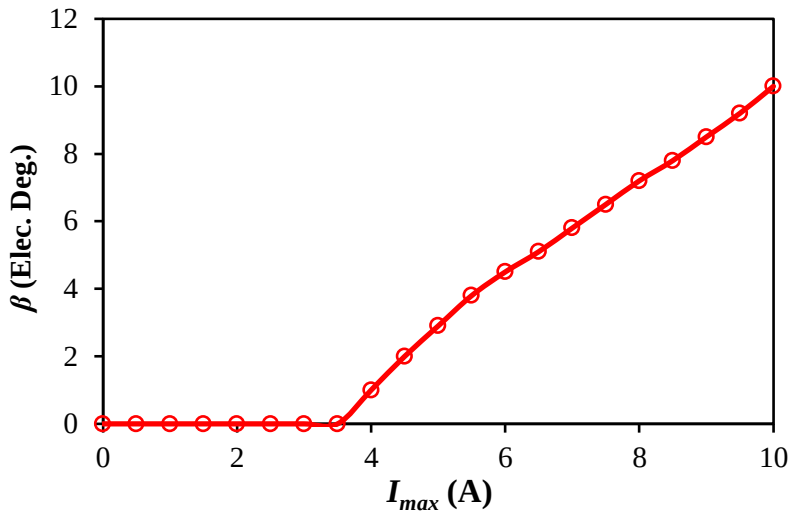

Fig. 2.8 Variation of relative β for the maximum *VDR* against different I_{max}.

2.3.3 Influence of Current Advance Angle and Current Amplitude

The former section shows that when β is not zero, two types of leakage fluxes (PM and armature fluxes) will not reverse at the same time theoretically. Thus, when the armature flux linkage tries to reverse, the tooth-tips may be still saturated by the PM leakage flux, which will reduce the fluctuation of resultant tooth-tip leakage flux and thereafter the voltage distortion. For example, when β=60°, the on-load phase voltage is shown in Fig. 2.9(a) compared with β=0°. Although the voltage is still distorted, its fluctuation level is much smaller, as evidenced by the reduction of harmonics in Fig. 2.9(b).

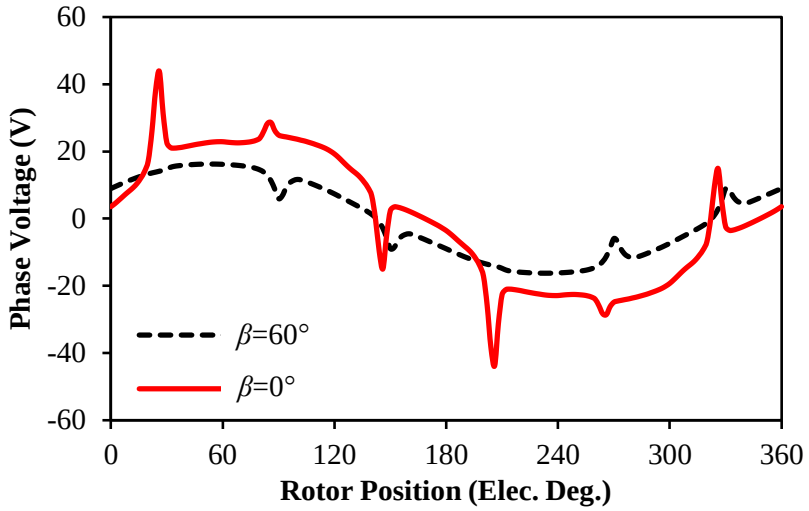

(a) Waveforms

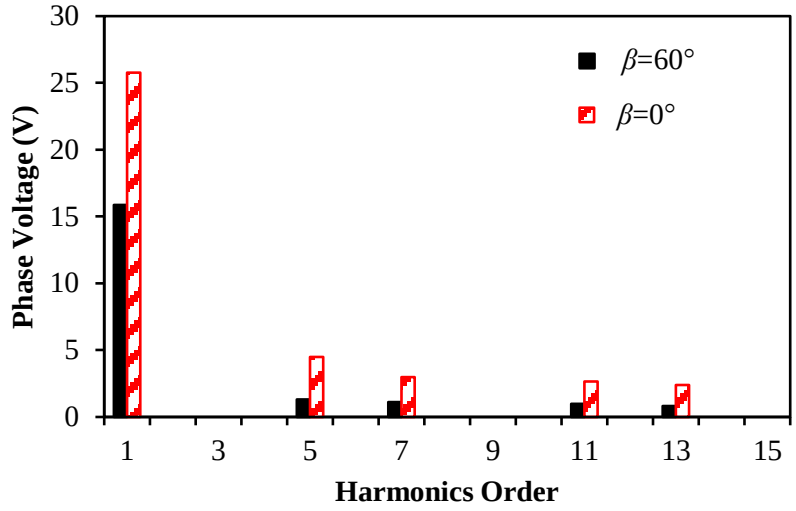

(b) Harmonic components

Fig. 2.9 Comparison of on-load voltage for different β (I_{max}=10A, 400rpm).

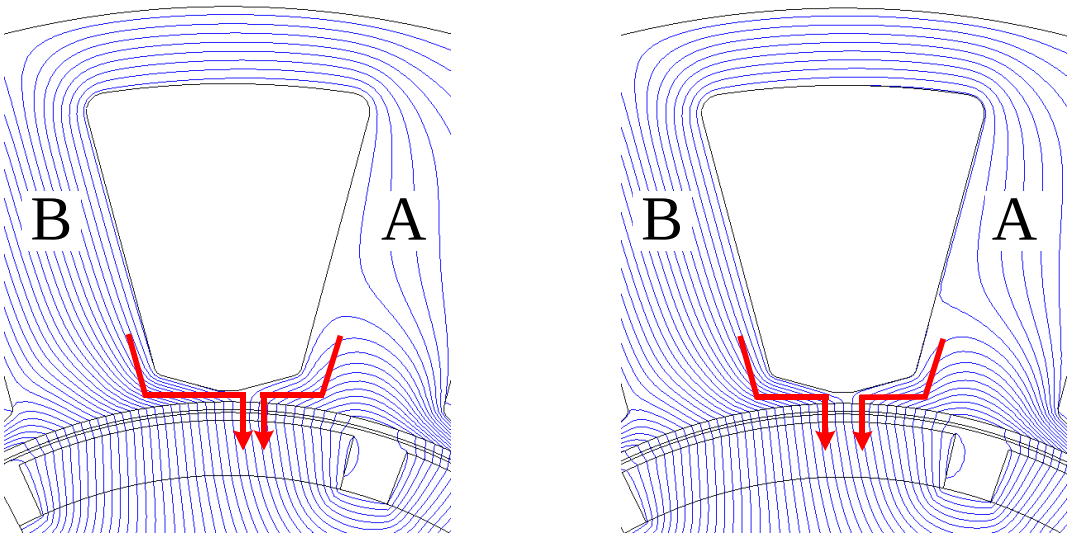

(a) θ_r=84° (b) θ_r=91°

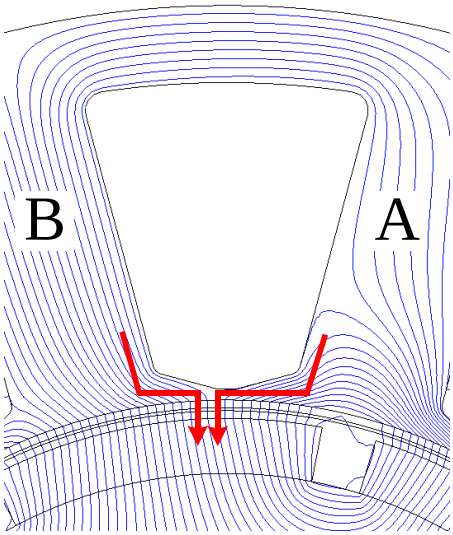

(c) θ_r=98°.

Fig. 2.10 Illustration of on-load tooth-tip leakage flux reversing process for β=60° (I_{max}=10A, 400rpm).

In order to illustrate the mechanism more clearly, the typical process when tooth-tip leakage flux reverses directions at β=60° is shown in Fig. 2.10. Different from Fig. 2.7 when β=0°, this process becomes much more smooth. When θ_r=84°, the resultant leakage flux circulates from left to right crossing the centre line of slot. Until 7° later, the tooth-tip leakage flux becomes zero, while the reversing process is finished until θ_r=98°. This much more smooth process leads to much smaller voltage distortion as already shown in Fig. 2.9. This process could also be reflected by the variation of flux density in tooth-tips in Fig. 2.11(a). When

β=0°, the flux density crosses zero and reaches the saturation point of lamination material (~1.5T) within a very short period. However, when β=60°, this process becomes much slower, which results in less voltage distortion. By observing the differential θ_r between zero-crossing position and the entering saturation position, the variation of local magnetic saturation in tooth-tips could be reflected in Fig. 2.11(b). Clearly, with the increase of β, the gap between two points continuously increases, which relates with the variation of voltage distortion as well. It is worth mentioning that if cobalt steel lamination, which has saturation point ~2.3T, is adopted for the analysis model, the local magnetic saturation will be significantly alleviated. However, in order to fulfil the potential of cobalt steel, the electoral and magnetic loadings of the machine designed with such material will be much higher than that with the normal lamination material, which makes the local magnetic saturation still unavoidable.

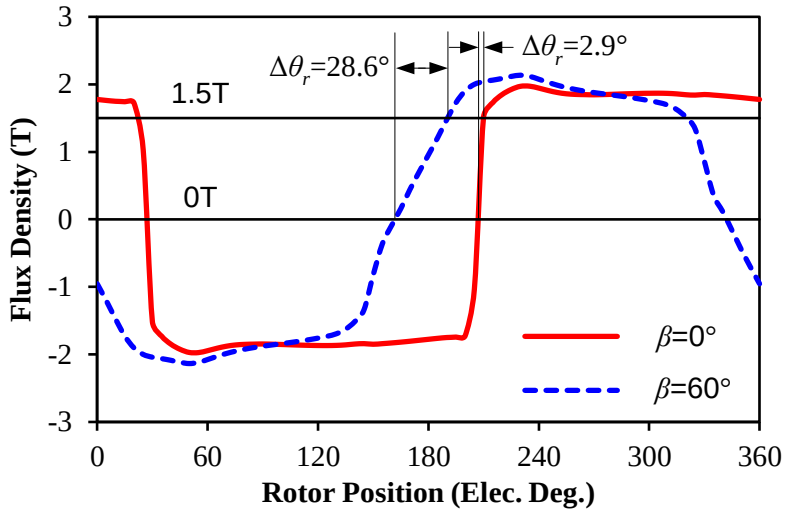

(a) Flux density in detecting points P_a (1.5T refers to lamination steel knee point, P_a defined in Fig. 2.6(a))

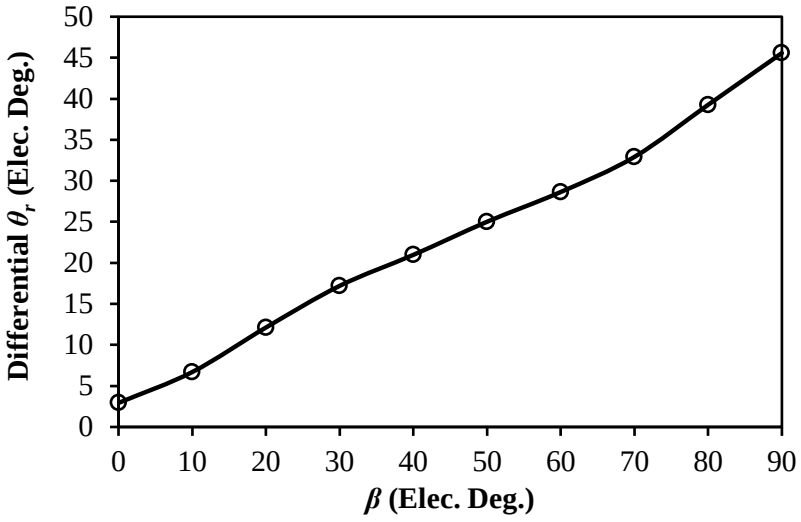

(b) Different angle between zero-crossing and saturation points

Fig. 2.11 Variation of local saturation against β (I_{max}=10A).

The voltage distortion according to different β and I_{max} can be calculated and shown in Fig. 2.12, which shows the maximum *VDR* under rated current is about 110%, while the minimum value is almost zero. Meanwhile, under the same β, *VDR* always increases with I_{max} due to the increasing of local magnetic saturation by armature reaction. For the same I_{max}, *VDR* will slightly increase with β at first, and then decrease immediately after reaching the peak. It is noted that when β approaches 90°, *VDR* slightly increases, which can be explained by the on-load flux linkage and voltage components when β=90° in Fig. 2.13. Although the variation of local magnetic saturation becomes less significant, the tooth-tips are still saturated, which make the PM and armature flux linkages distorted, particularly around 60°, 120°, 240° and 300, Fig. 2.13(a). Accordingly, the PM and armature voltage ripples will occur at such rotor positions, Fig. 2.13(b). With the increase of β, the slot currents zero-crossing positions changes, which generate negative voltage ripples when β approaches 90°. Such negative voltage ripples reduce the fundamental values of the resultant terminal phase voltages, which slightly increase *VDR*.

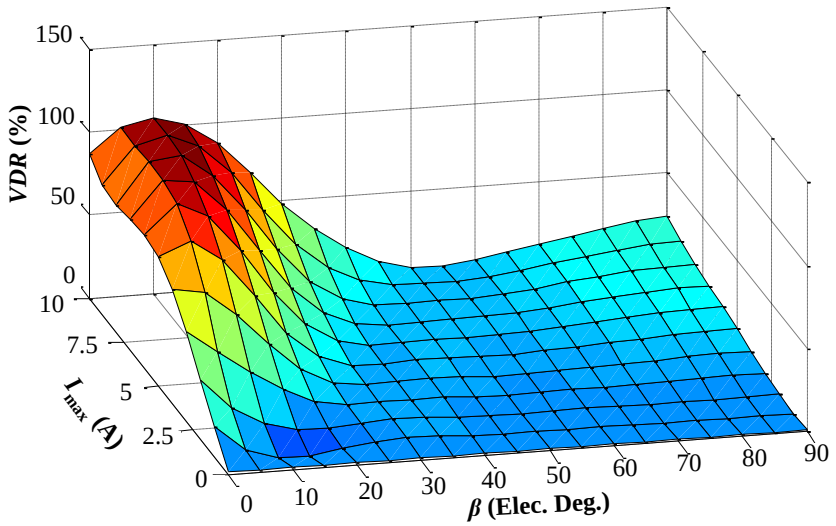

Fig. 2.12 Variation of *VDR* under different current conditions (400rpm).

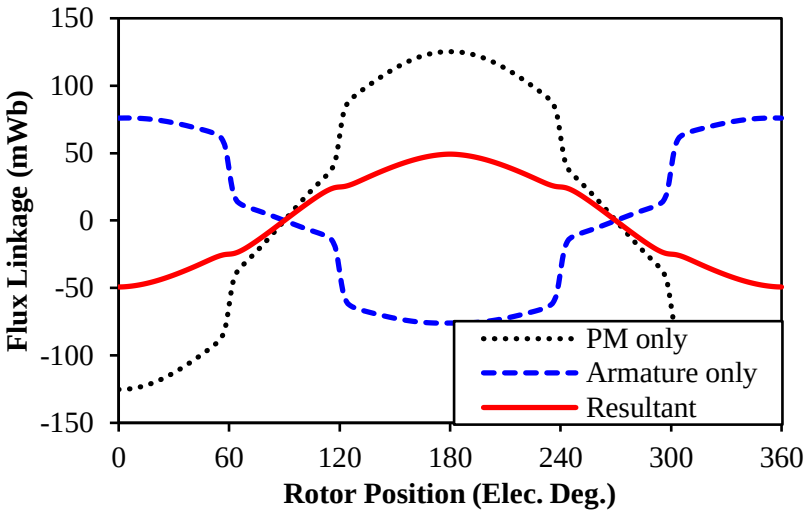

(a) Flux linkages, β=90°

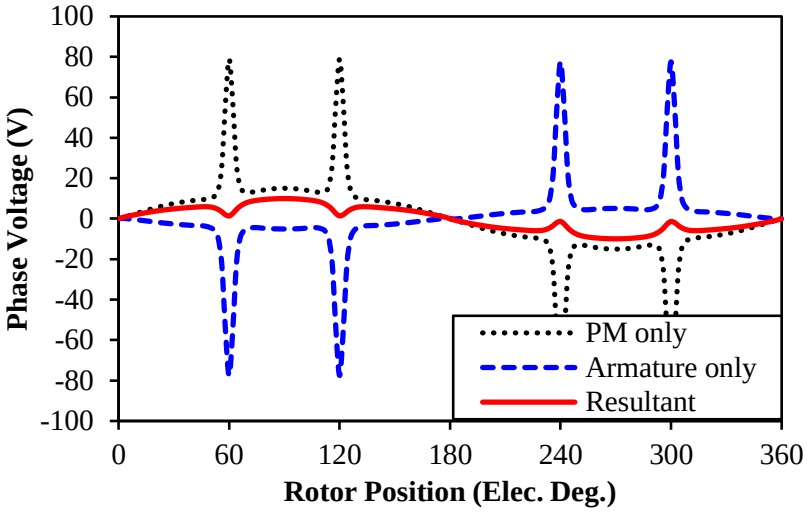

(b) Phase voltages, β=90°

Fig. 2.13 On-load phase flux linkage and phase voltage components by FP method (I_{max}=10A, β=90°, 400rpm).

2.3.4 Influence of Tooth-Tip Geometric Parameters

The production mechanism shows that the terminal voltage distortion is inevitable since local saturation in tooth-tips exists in almost all conventionally designed fractional-slot SPM machines. However, if the amount of leakage flux is not large enough to obviously influence the main flux linkage, the phenomenon could not reach a significant level. For the same current amplitude and rotor magnet design, the tooth-tip flux paths of leakage flux are mainly determined by three geometric parameters, i.e. the slot opening width b_0, tooth-tip thickness h_t, and tooth-tip slope α_t as defined in Fig. 2.14. Therefore, the variation of *VDR* with

different tooth-tip designs at rated current condition can be calculated as Fig. 2.15, in which the other geometric parameters are kept the same as the prototype model.

In Fig. 2.15(a), *VDR* increases with the decrease of b_0 for the same h_t and α_t, and reaches maximum value if b_0=0, i.e. closed slot. With the increase of b_0, the tooth-tip leakage flux will reduce, which leads to smaller *VDR*. Meanwhile, with the decrease of h_t, i.e. approaches open slot, *VDR* will reduce due to the reduction of local saturation area. With the increase of h_t, the leakage flux also increases, which aggravates the local saturation and boosts up the maximum *VDR*. However, if h_t is too large, the leakage flux at fixed driving current would not be sufficient to further increase the local saturation in tooth-tips. Thus, the increasing trend of *VDR* begins to saturate, which makes the maximum values for h_t=1 and h_t=1.5 close. In Fig. 2.15(a), *VDR* increases with the decrease of α_t for the same b_0 and h_t, since the tooth-tips region closed to tooth body become more saturated. With the increase of α_t , the overall local magnetic saturation in tooth tips will release for the same driving current, which reduce the *VDR* as well. However, α_t could not be too large in reality since it reduces the effective slot area for armature windings.

For machines with large geometry sizes, the open slot is usually adopted for fabrication process. Thus, the voltage distortion due to local magnetic saturation in these machines could be negligible. However, the tooth-tips are normally adopted in the design of medium or small sized machines, and hence the on-load voltage distortion and local magnetic saturation may still be introduced.

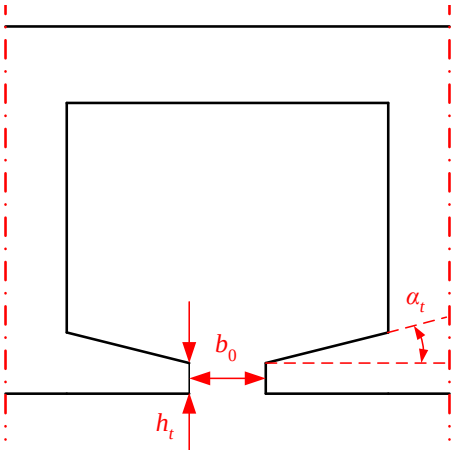

Fig. 2.14 Illustration of main geometric parameters for tooth-tips.

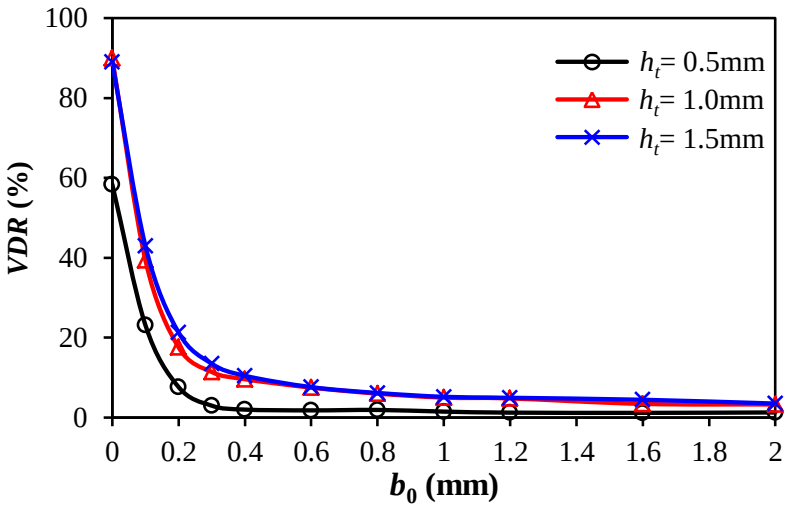

(a) *VDR* against b_0 and h_t, α_t=10°

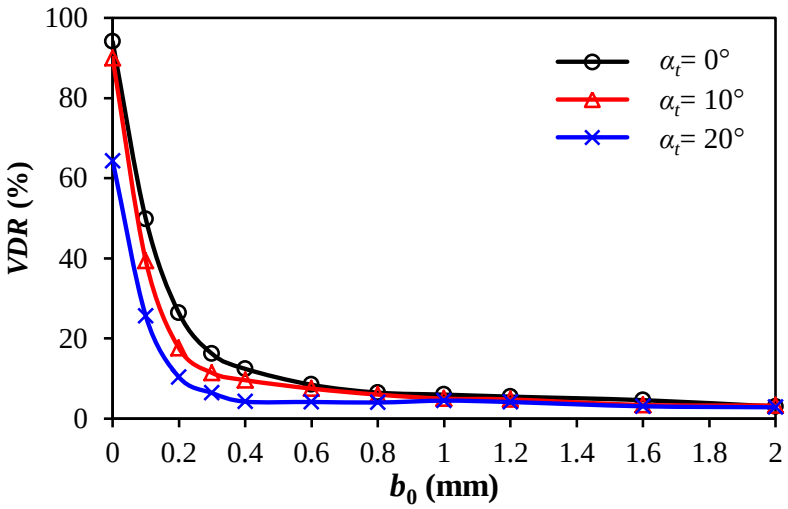

(b) *VDR* against b_0 and α_t, h_t=1mm

Fig. 2.15 Variation of *VDR* against tooth-tip geometric parameters (I_{max}=10A, β=0°, 400rpm).

2.3.5 Influence of Rotor Pole Arc

The aforementioned analyses are carried out based on fixed rotor pole arc. However, the PM leakage flux will change with rotor pole arc, which may lead to different voltage distortion levels. Fig. 2.16 illustrates two rotors with different pole arcs over a large range. Within the certain range, the variation of voltage distortion can be calculated in Fig. 2.17. With the decrease of rotor pole arc, the magnet volume and main PM flux linkage reduce, which decrease the fundamental voltages. Consequently, the PM leakage flux also reduces, which makes the flux reversing process more dominated by armature leakage flux under the same driving current. Thus, both the peak voltage and *VDR* increase with the reduction of rotor pole arc.

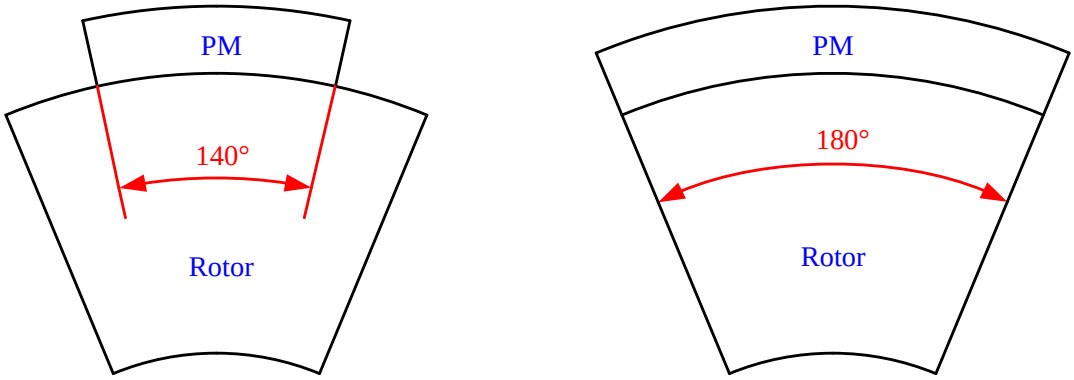

(a) Pole arc=140° (b) Pole arc=180°

Fig. 2.16 Illustration of different rotor pole arcs.

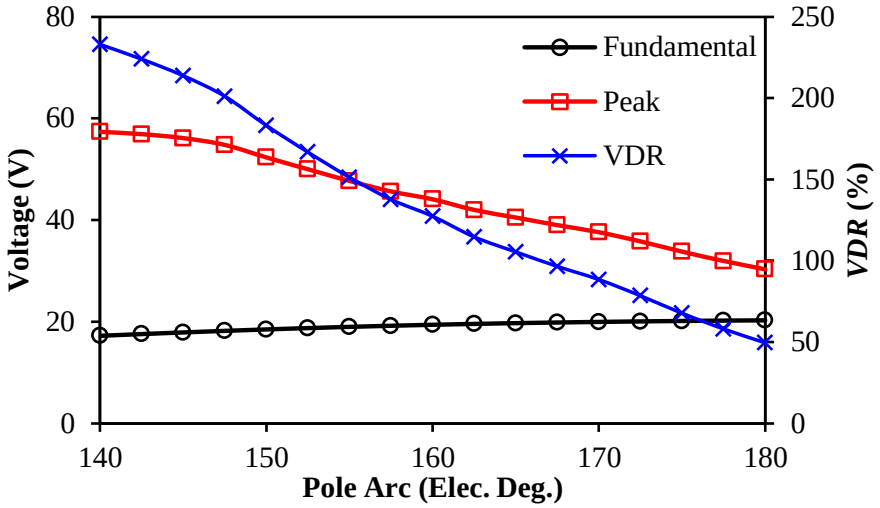

Fig. 2.17 Variation of *VDR* against rotor pole arc (I_{max}=10A, β=0°, 400rpm).

2.4 Electromagnetic Performance Influenced by Voltage Distortion and Local Magnetic Saturation

According to the aforementioned analyses, the on-load voltage distortion represents the variation of local magnetic saturation. Therefore, other electromagnetic performance may be changed accordingly, which will be investigated in this section.

2.4.1 On-Load Back-EMF

The on-load back-EMF is the voltage induced by only PM magnetic field with considering the saturation in lamination. Since the local magnetic saturation in tooth-tips significantly changes the leakage flux, the on-load back-EMF will be largely influenced as well. Similar to Fig. 2.4, the three-phase on-load back-EMFs at rated current with β=0° can be calculated by

FP method in Fig. 2.18(a). Since there are two coil sides from different phases in each slot, the ripples in back-EMFs always occur for two phases together. When β=90°, the on-load back-EMFs can be calculated in Fig. 2.18(b). Since the local saturation and tooth-tip leakage flux still exist, there are voltage ripples as well. Compared with β=0°, the peaks of on-load back-EMF reduce significantly. Fig. 2.18(c) compares the harmonic components for different β. When β=0°, the harmonics are as strong as the fundamental value. When β=90°, the amplitudes of harmonics reduce while the fundamental value increases due to the reduction of leakage fluxes and local magnetic saturation. Thus, with the increase of β, the distortion of on-load back-EMF reduces similar as *VDR*, which can be shown in Fig. 2.19. Meanwhile, since the global magnetic saturation reduces with the increase of β, the fundamental value of on-load back-EMF also increases, which can be observed from Fig. 2.19.

Although the variation of local saturation slows down with the increase of β, the tooth-tips are still highly saturated even when all currents are utilized for flux weakening, e.g. β=90°, which makes peak value still higher than the fundamental one. According to the aforementioned analysis, the distorted back-EMF will be partially cancelled with the armature voltage (Fig. 2.4(b)), which results in small *VDR* when β approaches 90°. Thus, the variation of armature voltage represented by inductances should be investigated further.

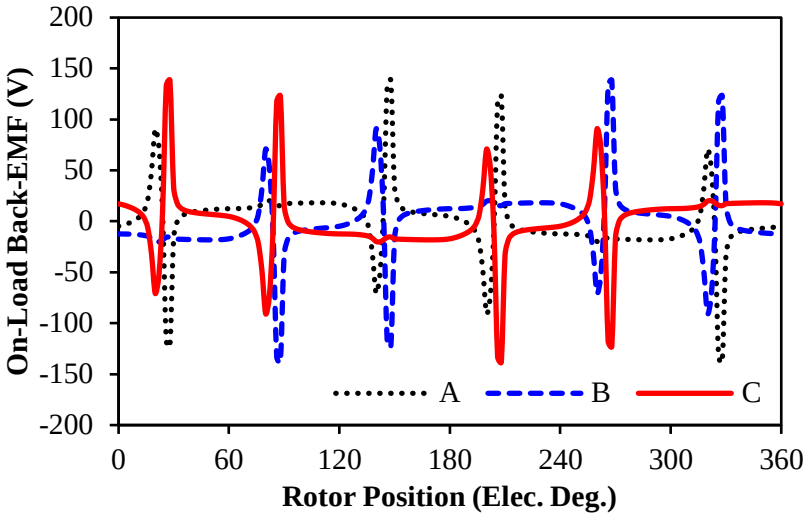

(a) Waveforms, β=0°

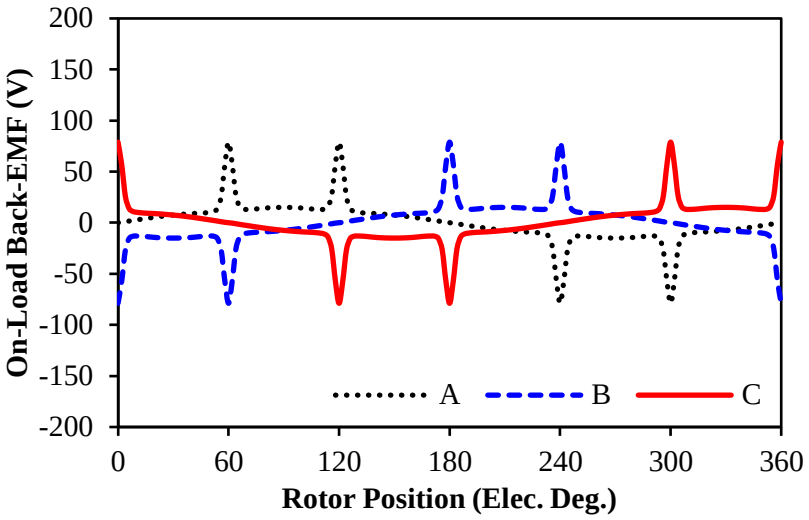

(b) Waveforms, β=90°

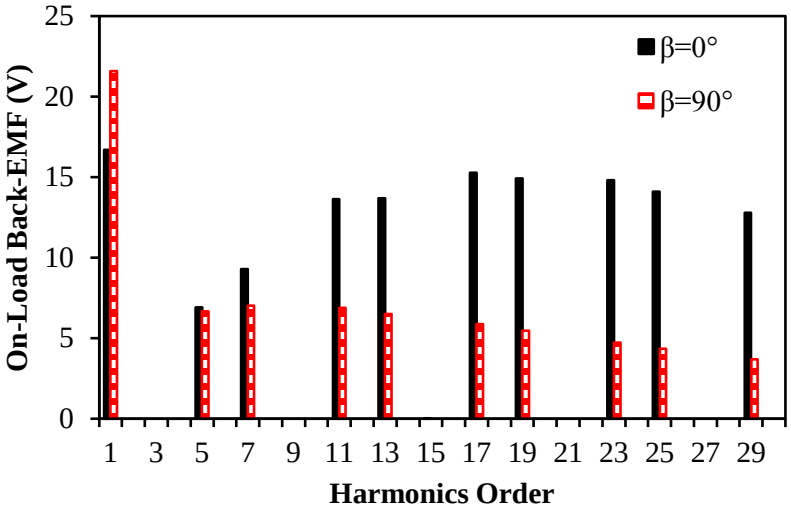

(c) Harmonics

Fig. 2.18 Three-phase on-load back-EMF (I_{max}=10A, 400rpm)

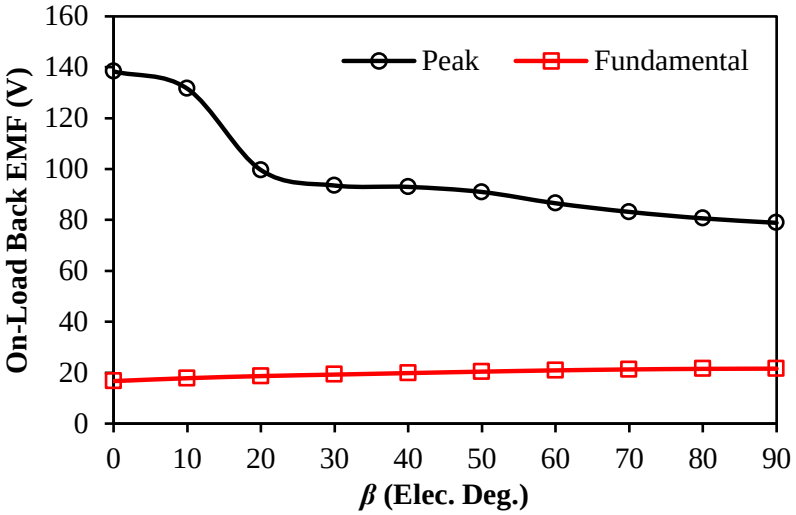

Fig. 2.19 Variation of peak and fundamental on-load back-EMFs against β (I_{max}=10A, 400rpm).

2.4.2 DQ-Axis Inductances

When β=0°, the *dq*-axis flux linkage components vary with rotor position, Fig. 2.20. The PM flux linkages can represent the on-load back-EMF, while the armature flux linkages can represent the voltage drop on armature winding. All flux linkage waveforms significantly change every 60°, but the *d*-axis flux linkages have larger fluctuation amplitudes. Normally, there is no *d*-axis armature flux linkages exist if only injected with I_q, i.e. β=0°. However, the local saturation in tooth-tips of the closed slot design increases the cross saturation effect, which introduces strong ripples of *d*-axis armature flux linkages. Although parts of the ripples in PM and armature flux linkages could be cancelled when combined together, there is still obvious distortion in the resultant *dq*-axis flux linkages.

With the increase of β, the voltage distortion and the variation of local saturation reduce, which influence the inductance as well. Fig. 2.21 shows the *dq*-axis flux linkages when β=90°. Unlike the waveforms for β=0°, the *d*-axis flux linkages become more smooth when β=90°. However, the *q*-axis flux linkages become more fluctuated, which represent the local saturation also shifts with β. Since PM and armature flux linkage ripples are in opposite direction, the resultant *q*-axis flux linkages are still smooth, which reflects less local saturation when β approaches 90°.

Meanwhile, the variation of *dq*-axis armature flux linkages could be represented by *dq*-axis inductances under the same current conditions. By FP method, the *dq*-axis inductance waveforms for different β over an electric period can be shown in Fig. 2.22. It can be seen that when β=0°, there are sharp spikes in L_d which represent the terminal voltage distortion and local magnetic saturation, while L_q is smoother due to less distorted armature *q*-axis flux linkages. On the contrary, when β=90°, L_d becomes more smooth, while L_q fluctuates more obviously, which can also be explained similarly as the *q*-axis flux linkages when β=90°. The peak and fundamental *dq*-axis inductances are shown in Fig. 2.23. With the increase of β, the current phasor shifts from *q*-axis to *d*-axis, which alleviates the saturation of *q*-axis flux paths and leads to the increase of fundamental value of L_q. However, the *d*-axis flux path becomes relatively more saturated, which makes the fundamental value of L_d decrease with β. Due to the same reason, the peak value of L_q continuously increases. Although L_d reaches maximum when β=10° similar to that for *VDR*, the overall variation trend of L_d still reduces with β.

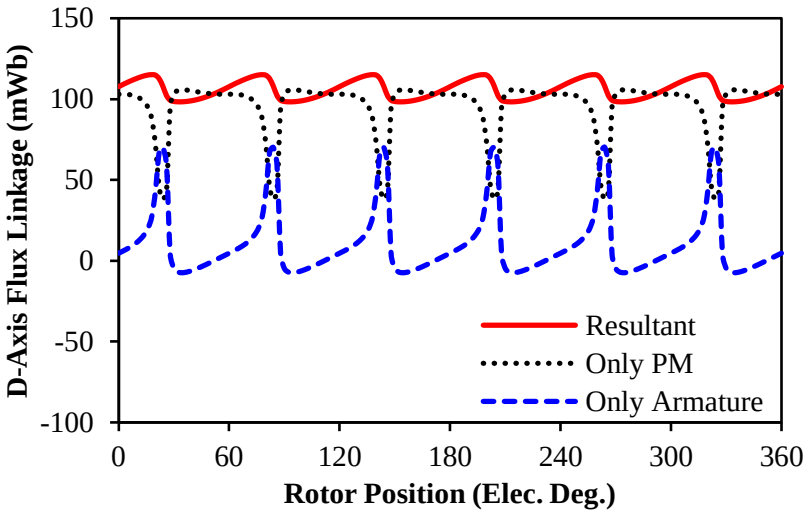

(a) D-axis flux linkages, β=0°

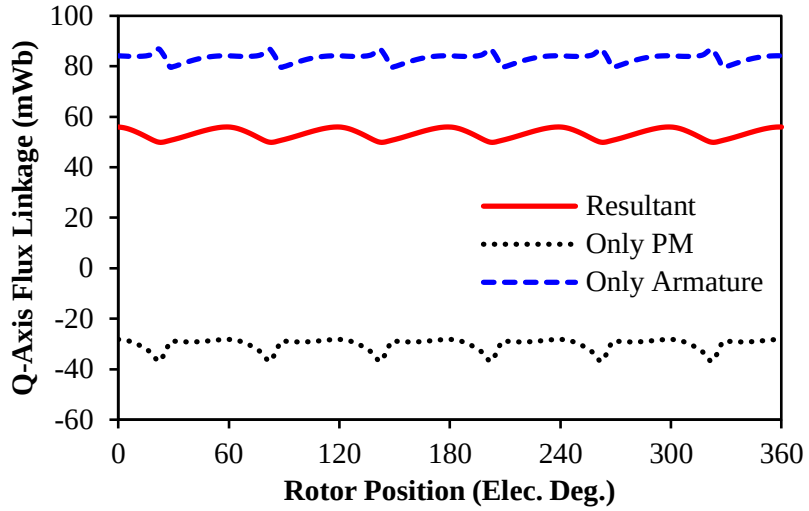

(b) Q-axis flux linkages, β=0°

Fig. 2.20 Variation of *dq*-axis flux linkages by FP method (I_{max}=10A, β=0°)

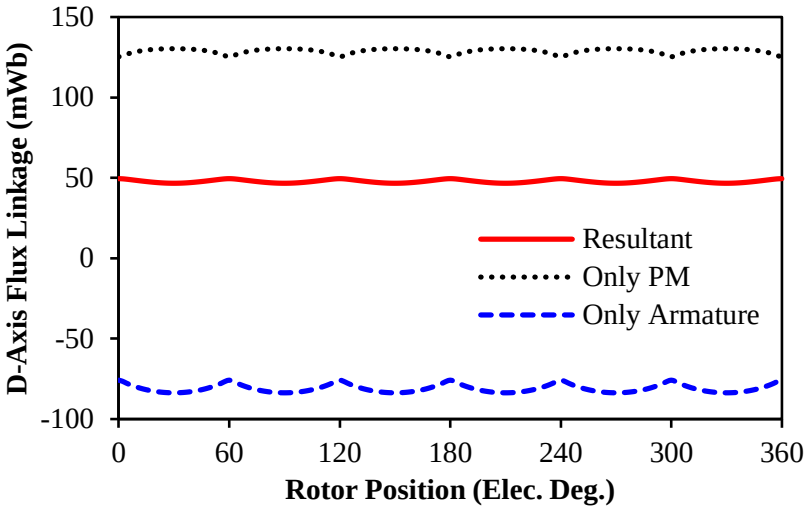

(a) D-axis flux linkages, β=90°

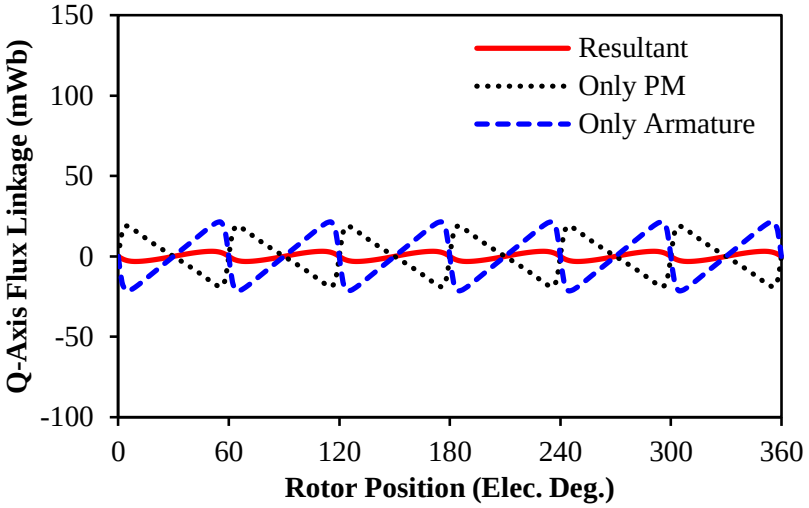

(b) Q-axis flux linkages, β=90°

Fig. 2.21 Variation of *dq*-axis flux linkages by FP method (I_{max}=10A)

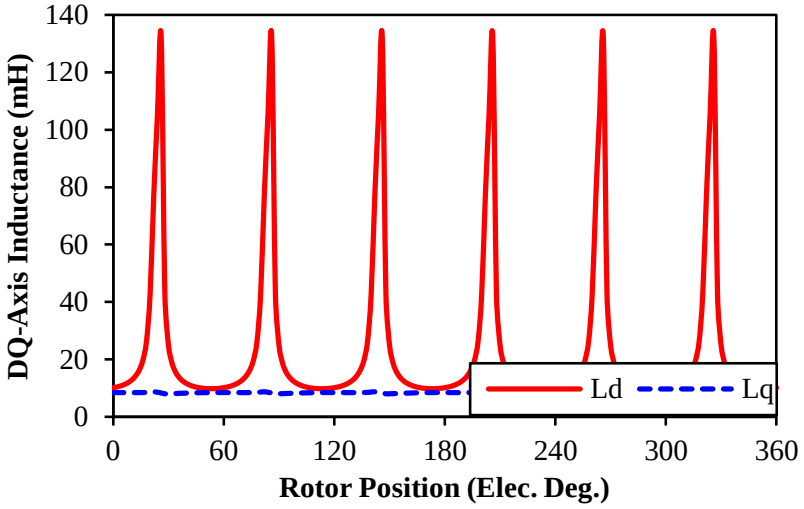

(a) β=0°

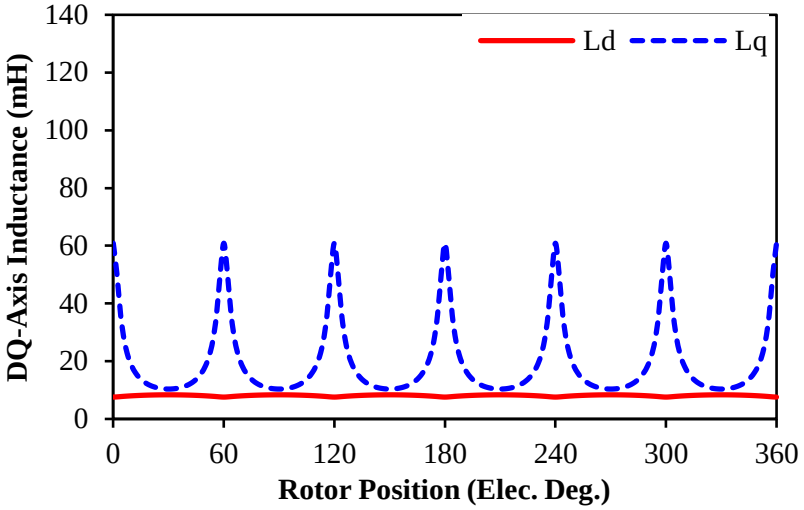

(b) β=90°

Fig. 2.22 Variation of *dq*-axis inductances by FP method (I_{max}=10A).

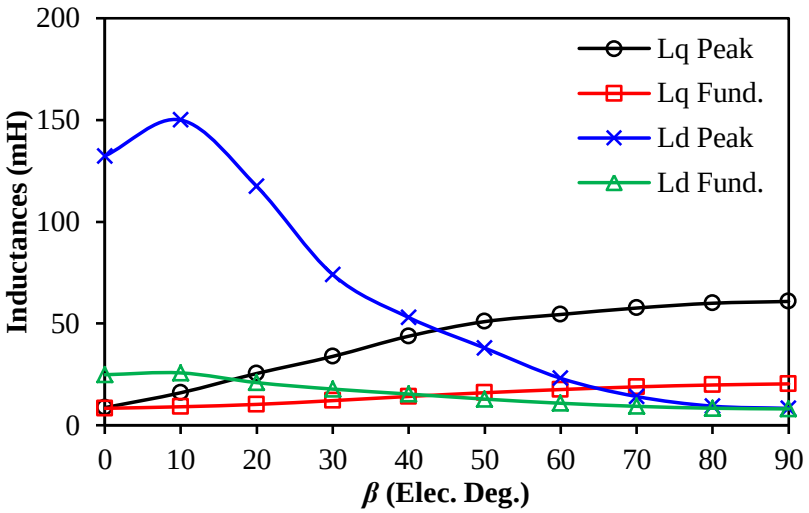

Fig. 2.23 Variation of *dq*-axis inductances against β by FP method (I_{max}=10A).

2.4.3 On-Load Cogging Torque and Torque Ripple

If the DC link voltage (U_{DC}) is sufficient for all the voltage distortion, the driving currents will be sinusoidal under vector control. Thus, the influence of local magnetic saturation and voltage distortion will be mainly reflected on torque ripples. Based on virtual work principle, the on-load torque can be expressed as following equations [LIU05], [CHU13].

$$T_{all} = T_{pm} + T_r + T_{cog} \tag{2.5}$$

$$T_{pm} = \frac{3}{2} p\left(\frac{d\psi_d^{pm}}{d\theta_r} I_d + \frac{d\psi_q^{pm}}{d\theta_r} I_q + \psi_d^{pm} I_q - \psi_q^{pm} I_d\right) \tag{2.6}$$

$$T_r = \frac{3}{2} p\left(\frac{d\psi_d^{arm}}{d\theta_r} I_d + \frac{d\psi_q^{arm}}{d\theta_r} I_q + \psi_d^{arm} I_q - \psi_q^{arm} I_d\right) \tag{2.7}$$

where T_{pm}, T_r and T_{cog} are the PM torque, reluctance torque and on-load cogging torque respectively, p is the number of pole pairs, ψ_d^{pm}, ψ_q^{pm}, ψ_q^{arm} and ψ_d^{arm} are *dq*-axis flux linkages generated by PM and armature respectively, I_q and I_d are the *dq*-axis currents.

By FP method, the on-load cogging torque can be calculated in Fig. 2.24 together with the open-circuit cogging torque. Due to closed slot design, the airgap permeance is smooth, which leads to ignorable open-circuit cogging torque. However, due to the significant local saturation in tooth-tips, the on-load cogging torque becomes much higher with asymmetric waveforms although the average value is still zero. With the increase of β, the variation of local magnetic saturation becomes slower as the aforementioned analyses, which also leads to the reduction of on-load cogging torque in Fig. 2.25.

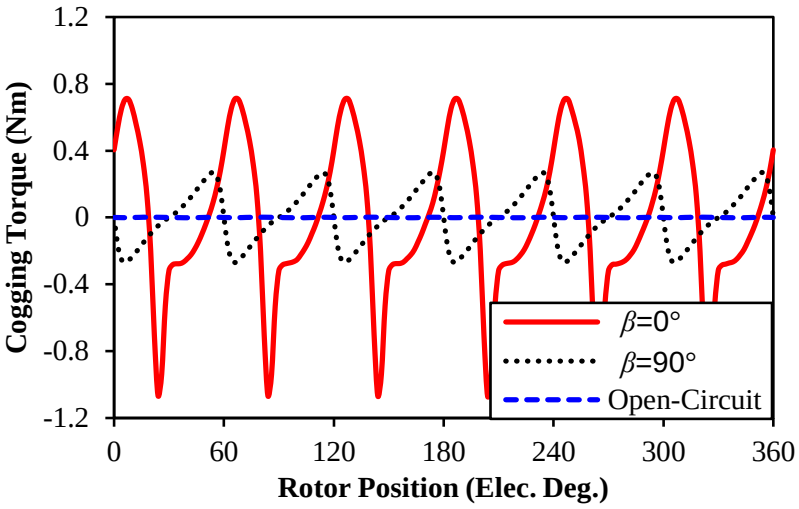

Fig. 2.24 Comparison of open-circuit and on-load cogging torques (I_{max}=10A).

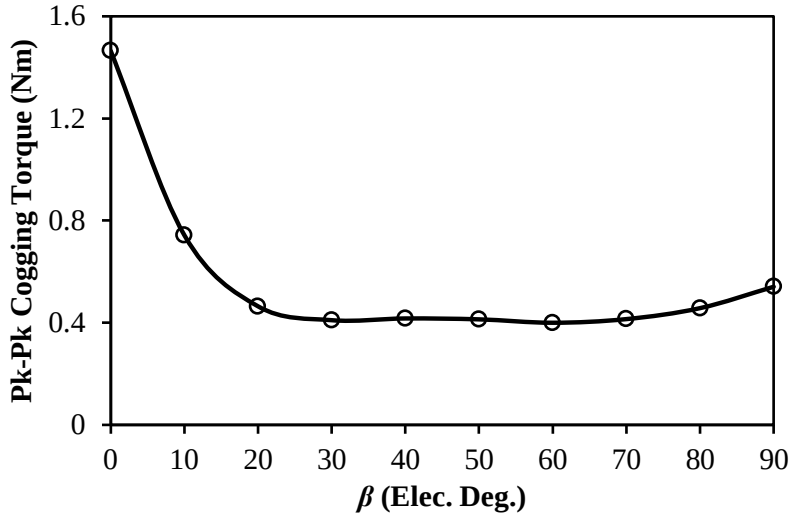

Fig. 2.25 Variation of pk-pk on-load cogging torque against β (I_{max}=10A).

By applying (2.5) to (2.7), the torque components for β=0° can be calculated in Fig. 2.26(a). It can be observed that all components fluctuate significantly, which lead to significant resultant torque ripples (T_{all}). Fig. 2.26(b) shows the harmonics of each torque components, in which the zero order harmonic refers to average torque. Due to local magnetic saturation, the on-load PM flux linkage fluctuates, which makes the T_{pm} dramatically changes and contributes to 6n times torque ripples. Although T_r barely contributes to average torque, it has significant 6n times torque ripples as well. When β=90°, the torque components can be calculated in Fig. 2.27. Similar to the reduction of terminal voltage distortion, the slower variation of local magnetic saturation reduces the amplitudes of torque ripples. However,

since the tooth-tips are still saturated, the on-load cogging torque could not be as small as the open-circuit one although their average values are both zero.

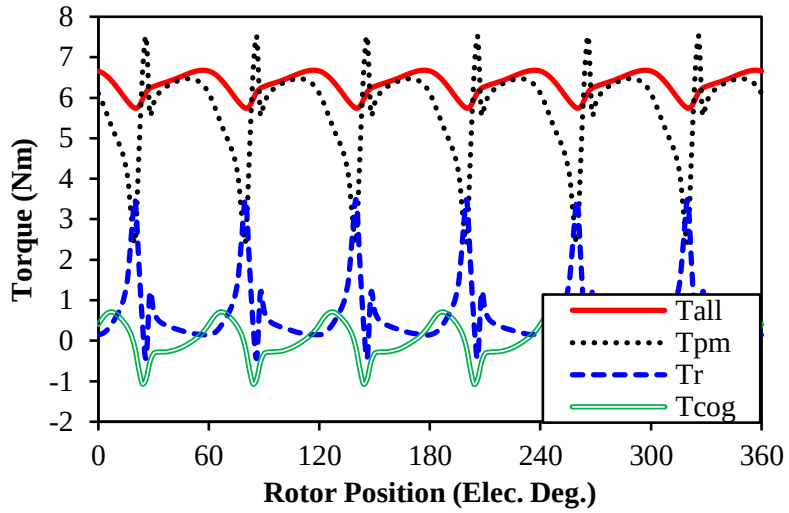

(a) Waveforms, β=0°

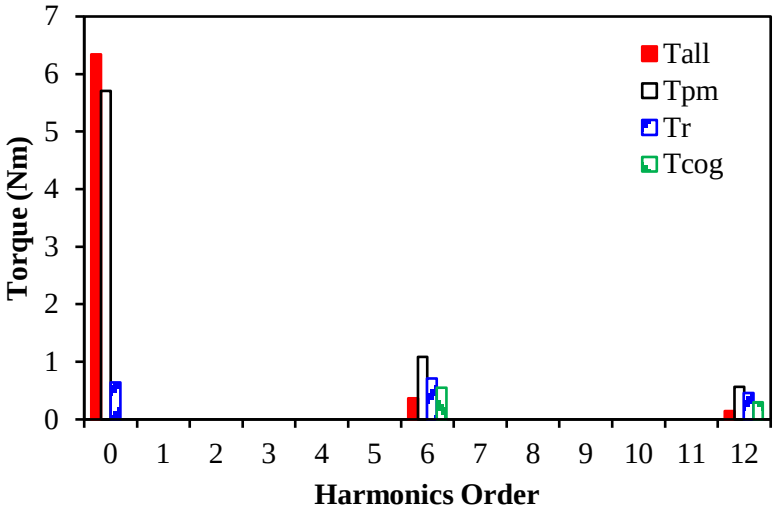

(b) Harmonics, β=0°

Fig. 2.26 Variation of torque components with rotor position by FP method (I_{max}=10A, β=0°).

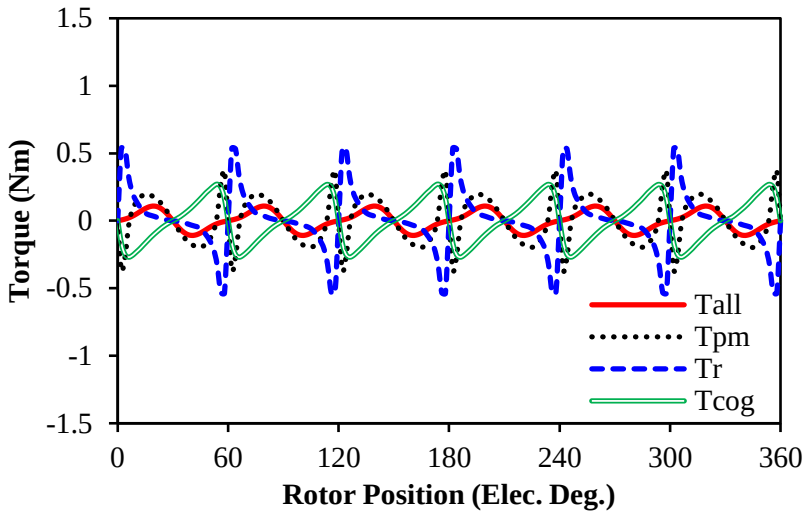

(a) Waveforms, β=90°

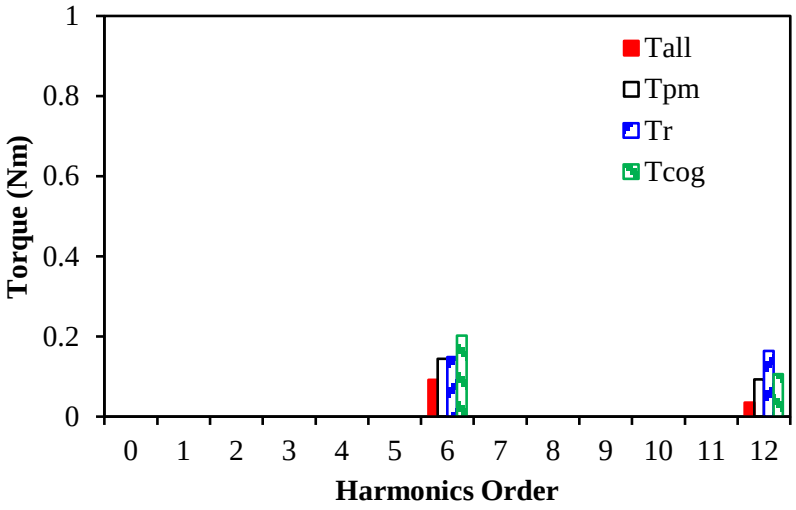

(b) Harmonics, β=90°

Fig. 2.27 Variation of torque components with rotor position (I_{max}=10A, β=90°).

The torque ripple can be defined as the peak to peak torque over the average value, e.g.

$$T_{ripple} = \frac{T_{\max} - T_{\min}}{T_{avg}} \times 100\% \tag{2.8}$$

where $T_{\max}$, $T_{\min}$ and T_{avg} are maximum, minimum and average torques over one electric period. The variation of torque ripple against different β can be calculated and shown in Fig. 2.28. The pk-pk torque reduces quickly at first, while the *VDR* reduces quickly as well. After that, the pk-pk torque only reduces slightly, which increases T_{ripple} since T_{avg} continuously reduces with β.

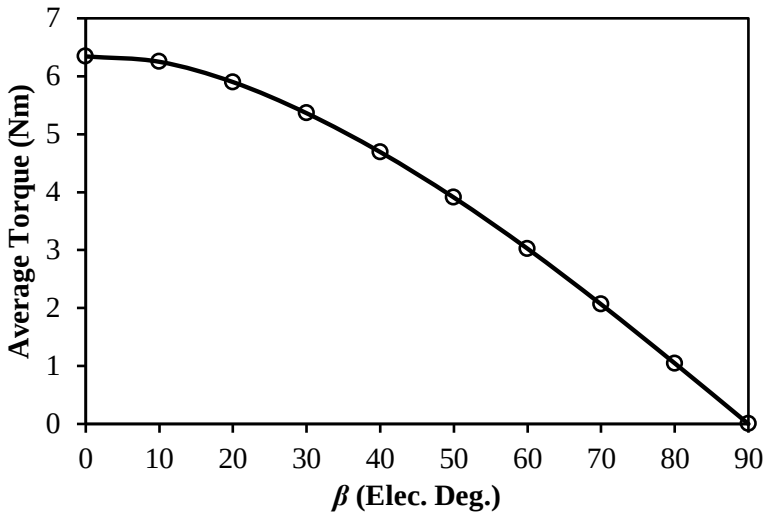

(a) Average torque

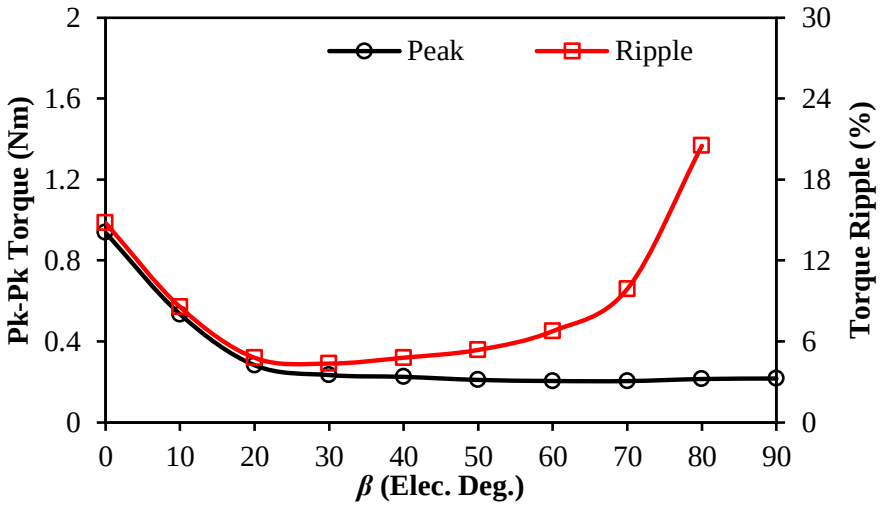

(b) Pk-Pk torque and torque ripple

Fig. 2.28 Variation of torque ripple against β (I_{max}=10A).

2.4.4 Iron Loss

The iron losses in this thesis are calculated by the loss package of JMAG v.14 software, in which both hysteresis loss and eddy current loss are considered as (2.9) [JSO14].

$$W_{iron} = K_h B^{\alpha} f^{\beta} + K_e B^{\gamma} f^{\delta} \tag{2.9}$$

where K_h and K_e are the coefficients of hysteresis loss and eddy current loss respectively, while α, β, γ and δ refer to multipliers for element flux density (B) and its variation frequency (f). All these parameters are interpolated by the software itself from loss-frequency curves of the lamination material according to different operation frequencies.

Since local magnetic saturation changes significantly during one electric period, it may increase the iron loss especially in tooth-tips. In order to investigate the iron loss, the stator of the investigated model has been divided into tooth-tips and tooth body as illustrated in Fig. 2.29. No matter it is constant torque operation or flux weakening operation, the local magnetic saturation in tooth-tips is always significant, which can be shown clearly in Fig. 2.30 by taking β=0° and 90° as examples. At the rated speed, the iron loss of the investigated model can be calculated and compared in Fig. 2.31(a), which shows the iron loss in tooth-tip region has the same variation trend as the *VDR*. Although the area of tooth-tip region is much smaller compared with stator body and rotor core, it takes considerable part of the resultant iron loss. With the increase of β, the global saturation in lamination releases, which reduces the resultant iron loss. However, the iron loss in tooth-tips does not reduce obviously in flux weakening region. As shown in Fig. 2.11, the typical tooth-tip maximum flux densities under different β are similar and have the same variation frequency as well, which lead to the unchanged tooth-tips iron loss even in flux weakening regions. Considering the geometric area of each lamination region, the iron loss density in tooth-tips is much higher than the other parts, which can be revealed in Fig. 2.31(b).

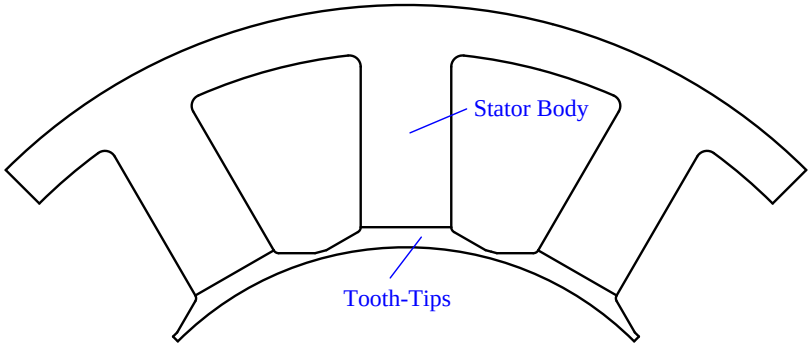

Fig. 2.29 Separation of the investigated model.

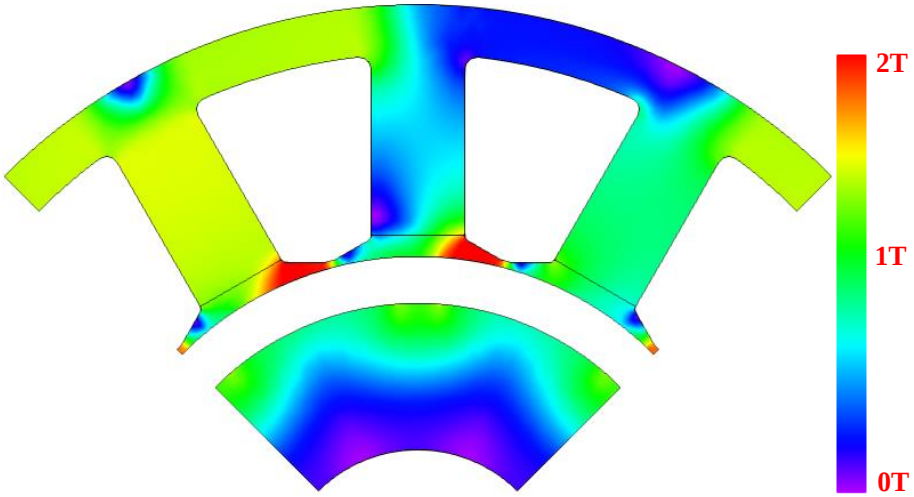

(a) β=0°

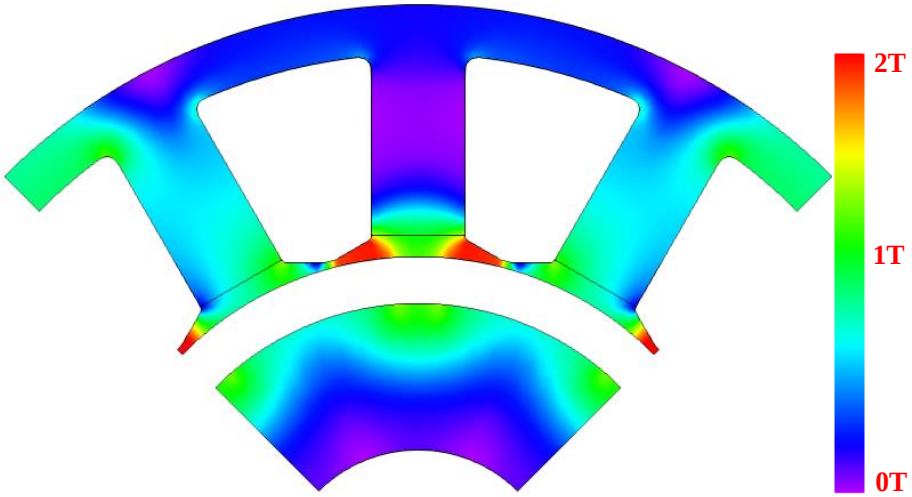

(b) β=90°

Fig. 2.30 On-load flux density distribution (I_{max}=10A, θ_r=90°).

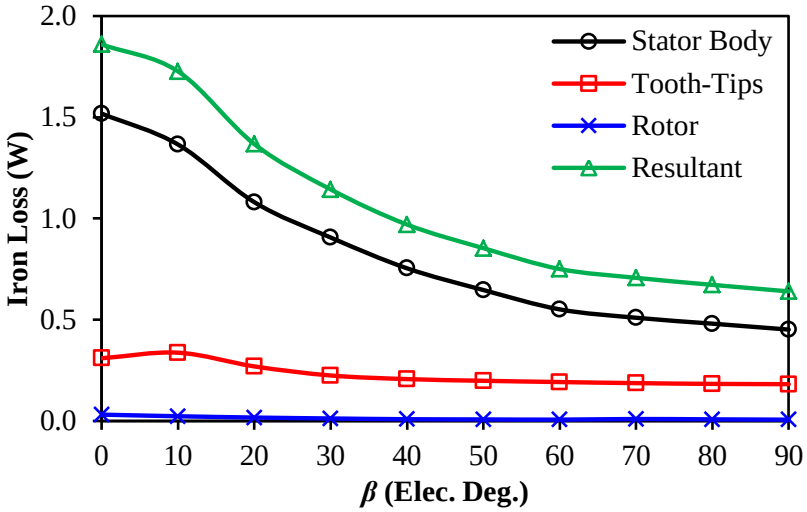

(a) Iron loss

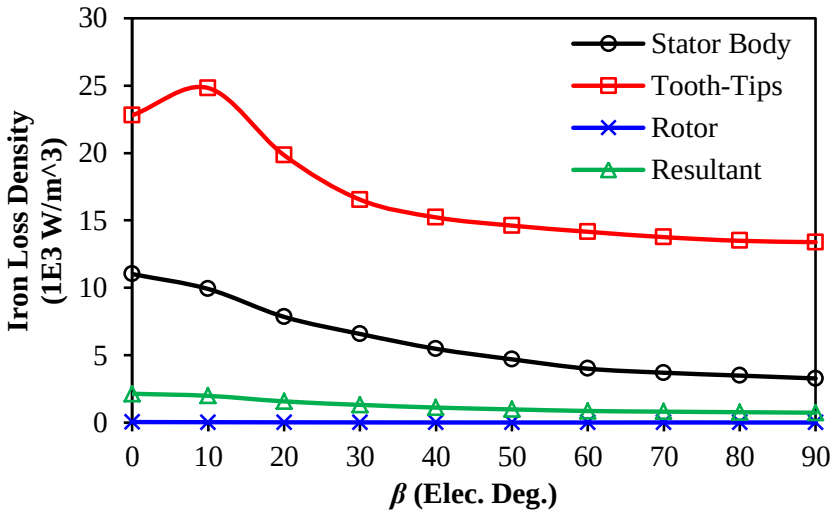

(b) Iron loss density

Fig. 2.31 Iron loss components against β (I_{max}=10A, 400rpm).

2.4.5 PM Eddy Current Loss

SPM machines may suffer from high PM eddy current loss since the PMs are directly exposed in the airgap with various space MMF harmonics due to the feature of FSCW. Amongst these space MMF harmonics, sub-harmonics and slot MMF harmonics are believed to be the main reason [BIA06]. Nevertheless, the local magnetic saturation may increase the variation of slot harmonics even for the closed slot design [XUA13]. In order to prove this, the PM eddy current loss for the investigated machine under rated speed and current are calculated as shown in Fig. 2.32 based on the PM conductivity of 699000 S/m. Similar to the variation of *VDR*, the strong local magnetic saturation introduces high PM eddy current loss even when the closed slot design is adopted. Nevertheless, with the increase of β, the variation of local magnetic saturation reduces, which subsequently reduces the PM eddy current loss. Due to the closed slot design, the PM eddy current loss becomes ignorable under the rated speed in deep flux weakening regions.

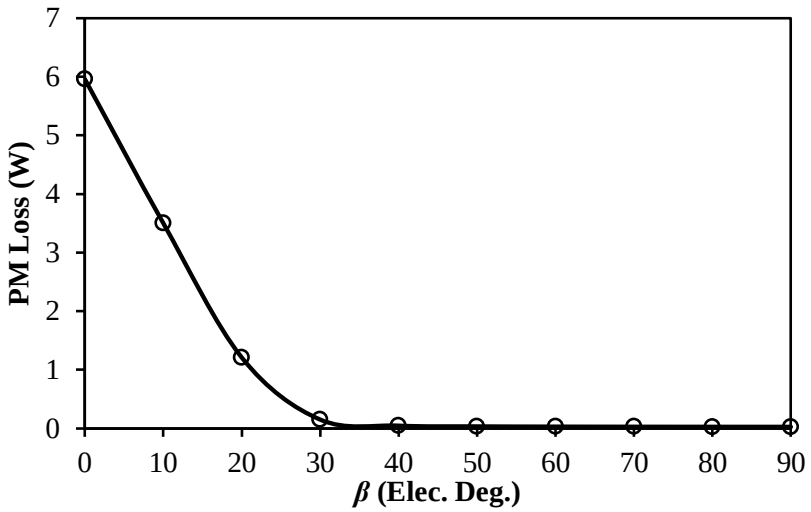

Fig. 2.32 Variation of PM eddy current loss against β (I_{max}=10A, 400rpm).

2.4.6 Flux Weakening Performance

If U_{DC} is not sufficient with the increase of speed, the machine needs to enter flux weakening operation under vector control. Conventionally, the torque-speed characteristics are calculated by only considering the fundamental voltage [ELR05]. However, the voltage distortion will make the peak voltage much larger than the fundamental value, which makes the machine enter flux weakening operation much earlier and significantly reduces the base-speed. This influence can be reflected in Fig. 2.33(a), in which U_{DC} is 42V while I_{max} is 10A. It can be seen that the expected base-speed calculated by the fundamental voltage is around 450rpm, while the actual base-speed considering voltage distortion reduces to only 200rpm. Meanwhile, the variation of torque ripple against speed is also shown in Fig. 2.33(a). Due to different β and flux weakening levels, the torque ripple considering voltage distortion will be much higher than the ideal curve in deep flux weakening region. On the other hand, the variation of average torque and torque ripple can also be reflected on the relative *dq*-axis currents in Fig. 2.33(b). Since *VDR* is very large around β=10° (Fig. 2.12), the current angle increases quickly to maintain the peak voltage within DC link limitation after base-speed. Thus there exists a significant reduction of torque after the base-speed due to the fast increasing of β. After that, the curve decreases slowly until approaching the ideal curve calculated by the fundamental values. With the reduction of fundamental voltage, *VDR* rises again when β>40°, which makes the second drop in deep flux weakening region.

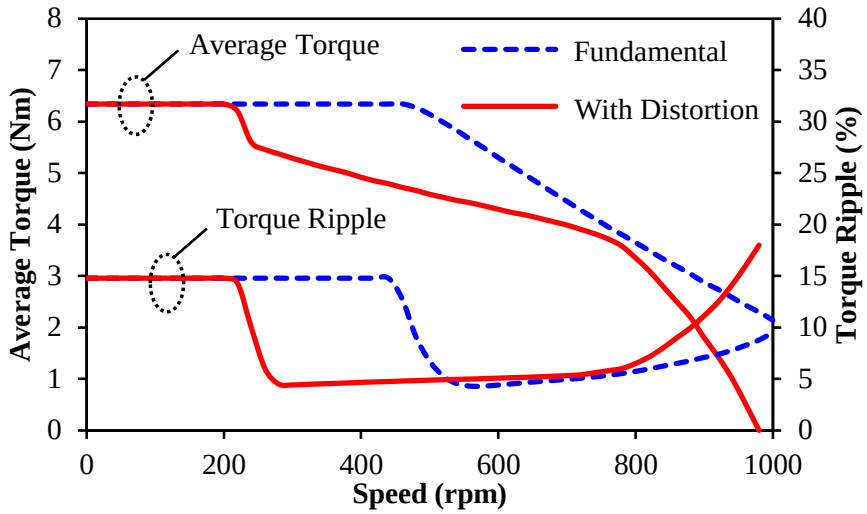

(a) Torque and torque ripple against speed

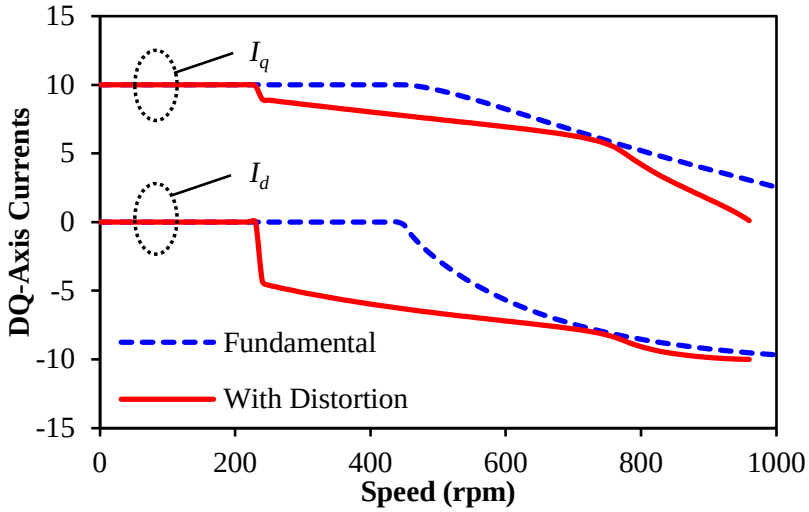

(b) DQ-axis currents against speed

Fig. 2.33 Variation of torque speed characteristics for different calculation methods (I_{max}=10A, U_{DC}=42V).

2.4.7 Voltage Distortion under Limited Band Width

Since the sinusoidal current is the control objective of conventional vector control, the distorted voltage will be the command for controller when the machines suffer from on-load voltage distortion. If U_{DC} is sufficient while the drive system have infinite band-width, the response voltage will fully repeat the command to generate sinusoidal driving currents. However, due to the limited U_{DC} and limited band width in real systems, the response voltage would be less than the peak of command, which generates the control errors and influences the quality of response currents. This phenomenon occurs more commonly for SPM

machines only working in constant torque region with I_d=0 control, since they cannot maintain the peak voltage under U_{DC} by adjusting β beyond the base-speed.

Fig. 2.34 shows the calculated voltage phasor amplitude when driven by pure sinusoidal currents for the analysis model, which has six sharp spikes over an electric period. The maximum response voltage (U_{resp}) is defined on the figure together with the peak and fundamental values of the demand voltage vector ($U_{vec\text{-}peak}$ and $U_{vec\text{-}fund}$). Thus, the voltage error (U_{error}) between $U_{vec\text{-}peak}$ and U_{resp} represents the difference between the command and the response of the driven terminal voltage. In order to show the influence of U_{error} related with on-load voltage distortion, the voltage error ratio can be defined as

$$\sigma_v = \frac{U_{error}}{U_{vec-peak} - U_{vec-fund}} \times 100\% \tag{2.10}$$

According to the definitions above, if σ_v=0%, the response voltage fully repeats the command. However, 0<σ_v<100% in real driving systems. When σ_v=100%, U_{resp} is deteriorated and reduced to the fundamental voltage, which is shown as the dotted line in Fig. 2.35 compared with the command voltage. It can be seen that all the spikes have been partially ignored especially for the one larger than fundamental phase voltage. By injecting such voltage into the analysis model, the response current will be distorted as Fig. 2.36(a), which has significant drop at each voltage spike appearing position. In order to show the distortion more clearly, the reduction of current amplitude and phase shifting are shown in Fig. 2.36(b) with the variation of σ_v. Therefore, the torque performance will be influenced as shown in Fig. 2.37. It can be seen that the average torque will reduce with the increase of σ_v, while the torque ripple changes accordingly.

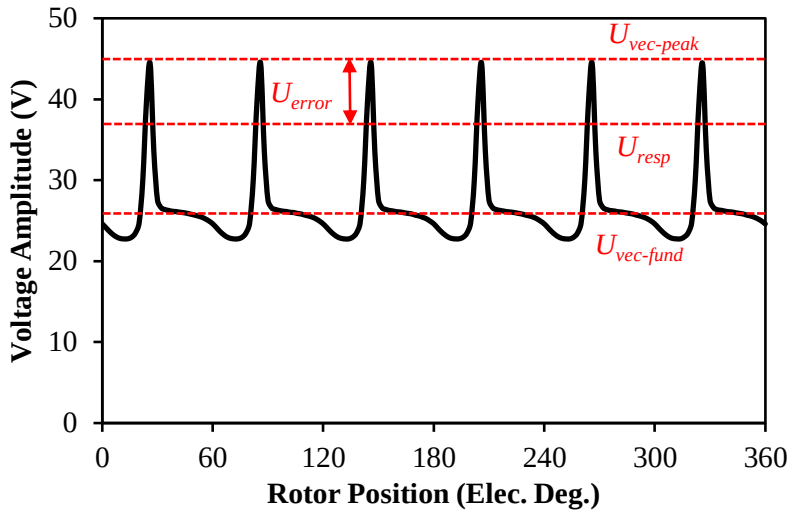

Fig. 2.34 Illustration of command voltage phasor amplitude in *dq*-axis frame (I_{max}=10A, β=0°, 400rpm).

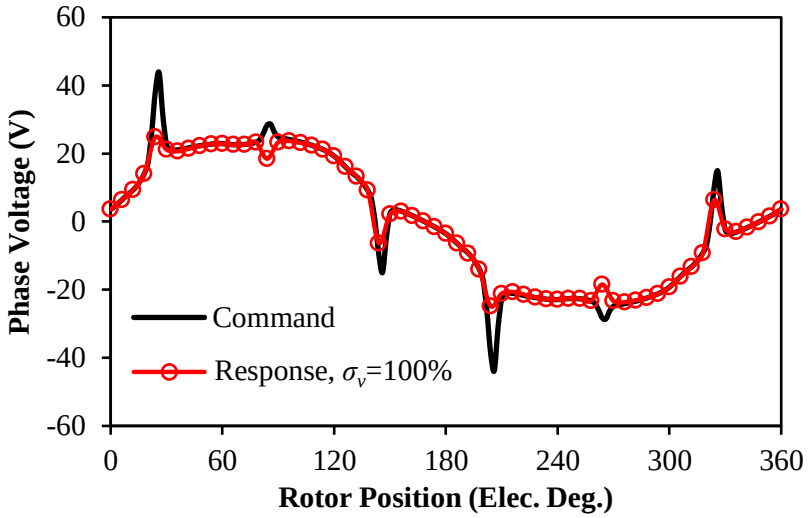

Fig. 2.35 Comparison of command and response phase voltage (demand current: I_{max}=10A, β=0°, 400rpm).

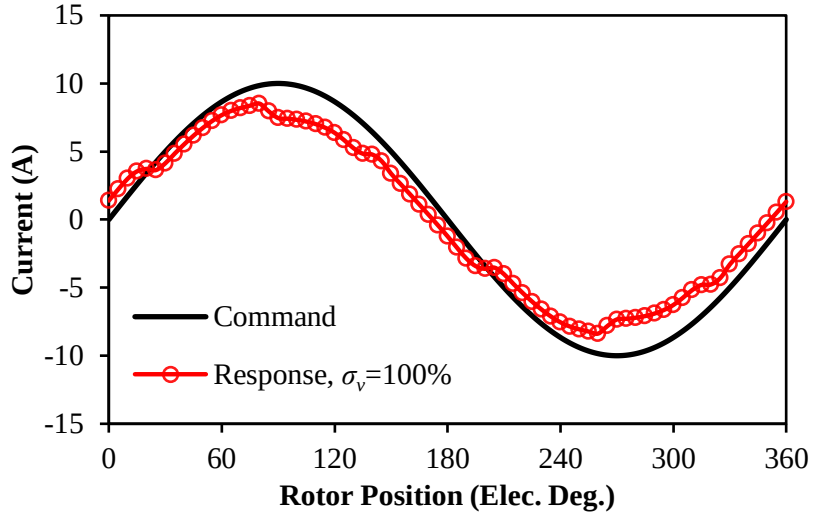

(a) Waveforms

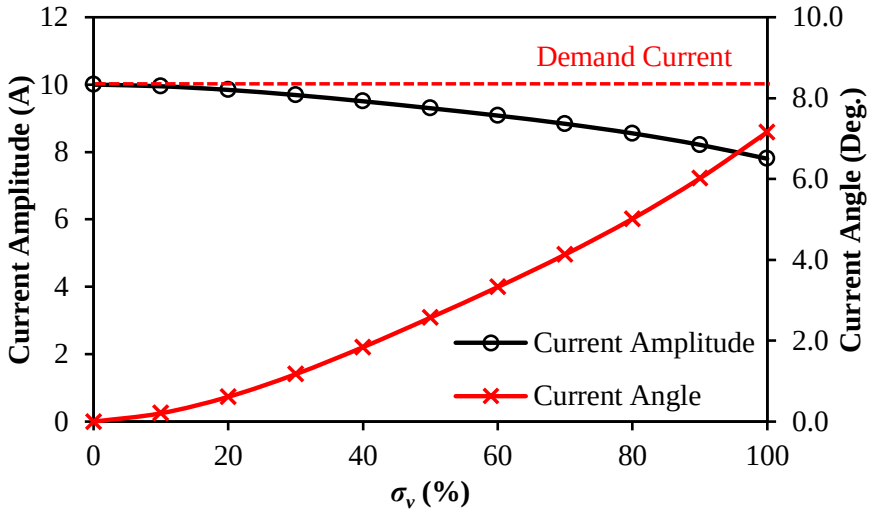

(b) Amplitude and phase shifting for different σ_v.

Fig. 2.36 Ideal and real response phase current (demand current: I_{max}=10A, β=0°).

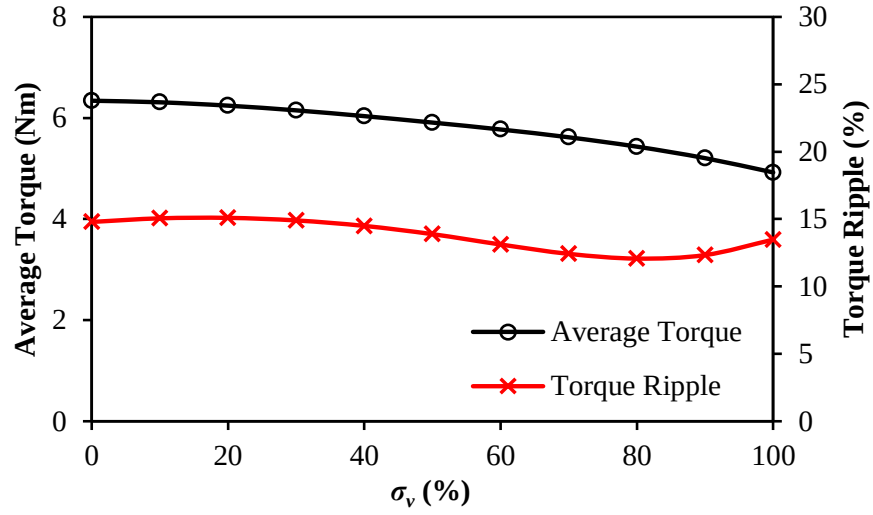

Fig. 2.37 Variation of torque and torque ripple (demand current: I_{max}=10A, β=0°).

2.5 Experimental Validation

2.5.1 Prototype and Test Rig

The prototype machine with the same dimensions in Table 2.1has been manufactured, Fig. 2.38(a) and Fig. 2.38(b). The measured phase resistance under room temperature is 0.64Ω. Considering the hand winding tolerance as well as the extra resistance of coil connections, the measured result is higher than the ideal prediction in Table 2.1. Meanwhile, the test rig is shown in Fig. 2.38(c), which utilizes a DC generator as the load. Due to the inverter limitation, the rated peak current is adjusted to 8A, while the PWM frequency is 10kHz. Further, the measured phase back-EMF at 400rpm is shown in Fig. 2.39(a), which is 5.8% less than the prediction by 2D FEA due to end-effect, manufacturing tolerance and measuring error, Fig. 2.39(b).

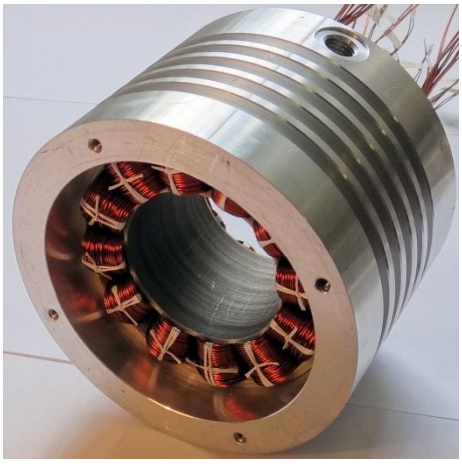

(a) Stator

(b) Rotor

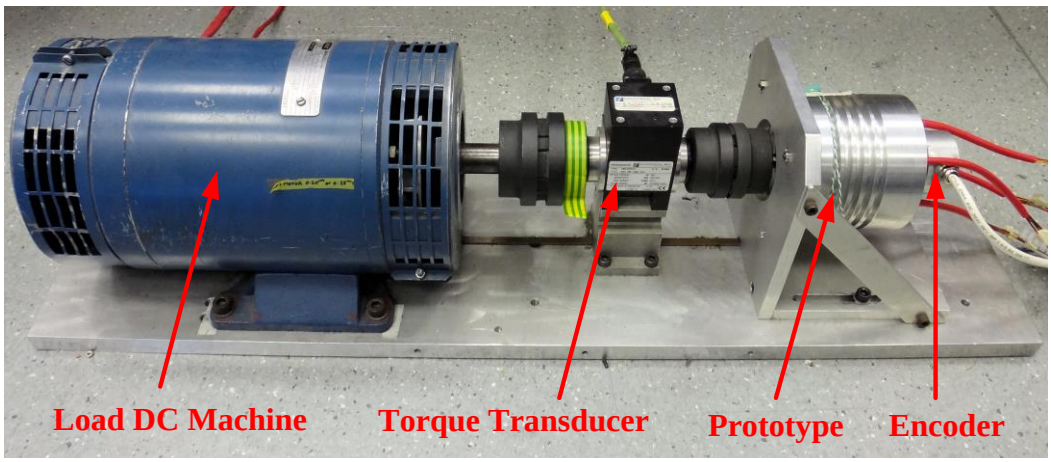

(c) Test rig

Fig. 2.38 Prototype machine and test rig.

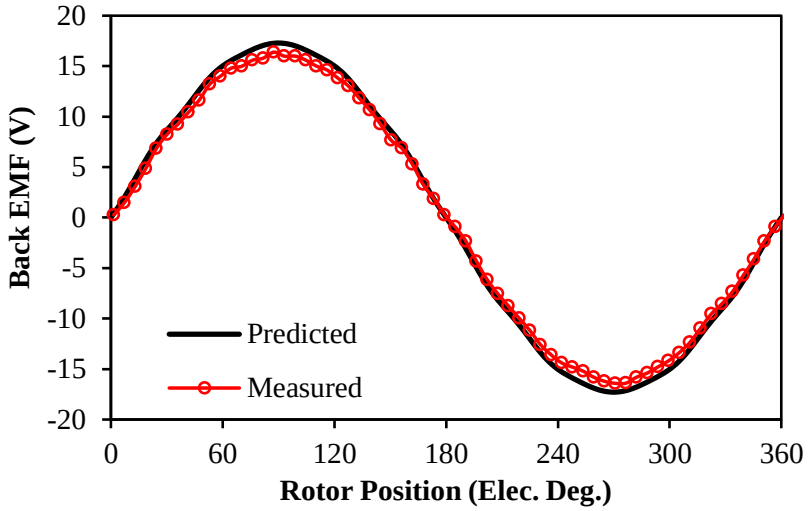

(a) Waveforms

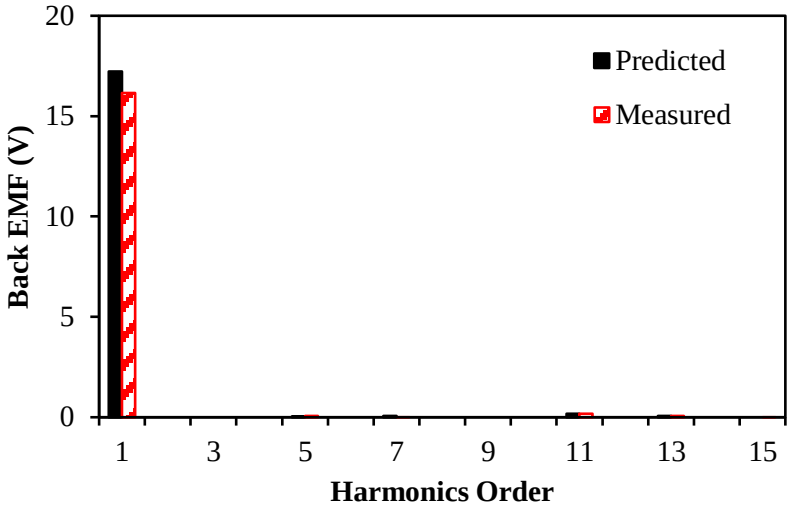

(b) Harmonic components

Fig. 2.39 Measured and predicted open-circuit back-EMFs of prototype machine (400rpm).

2.5.2 Torque Waveforms

The measured and predicted open-circuit cogging toques are compared in Fig. 2.40. The measuring method will be introduced in Appendix B in detail. The amplitude of cogging torque is quite small for the closed slot design, which makes it difficult to measure the value accurately. However, the measured result can still validate the tiny amplitude of open-circuit cogging toque. The measuring method of torque ripple is similar to that for measuring cogging torque, which adopts two DC current sources for the windings to simulate the real driving condition. Thus, the torque waveforms under different current condition could be measured and compared in Fig. 2.41, which shows good agreement considering the end-effect and measuring error.

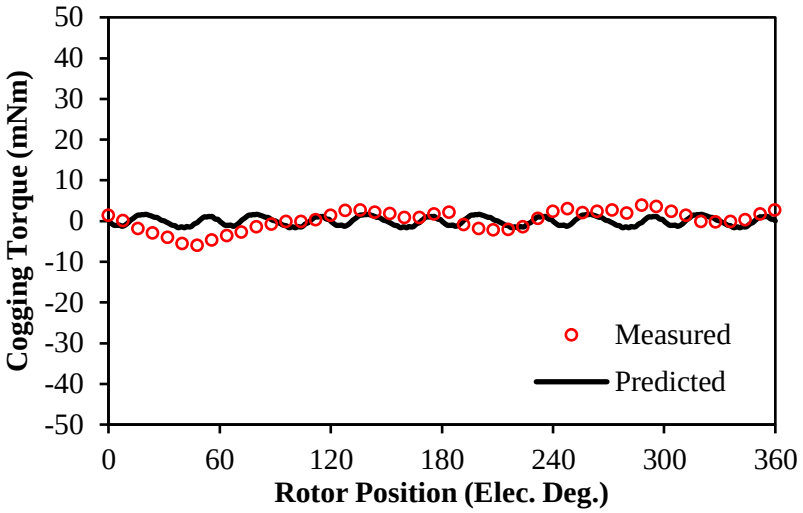

Fig. 2.40 Comparison of measured and predicted open-circuit cogging torque.

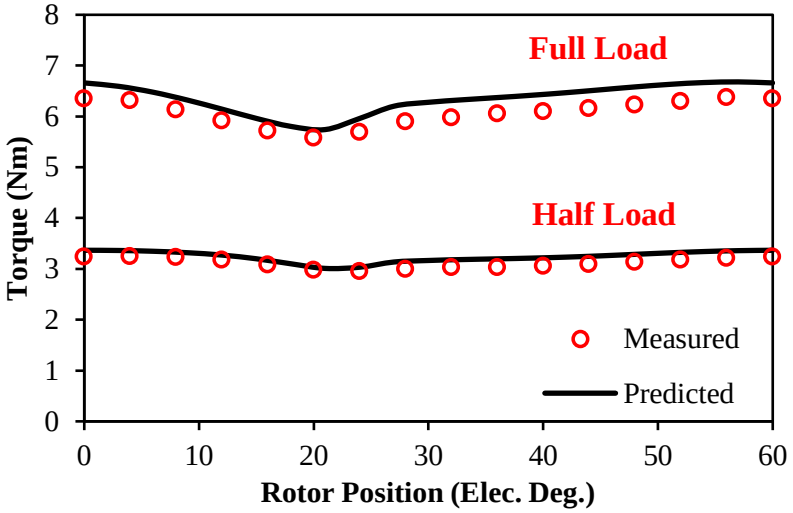

Fig. 2.41 Comparison of measured ant predicted torque waveforms (for full load, I_{max}=10A, β=0°).

2.5.3 Phenomenon of Voltage Distortion

In order to show the voltage distortion clearly, a low pass filter with the cut-off frequency about 1.5kHz has been adopted in order to get rid of PWM for the measurement. Fig. 2.42(a) shows that when β=0°, the phase voltage is distorted obviously while the phase current is almost sinusoidal. By increasing β to 60°, the current is still sinusoidal but the voltage distortion becomes less significant, Fig. 2.42(b). The comparisons in Fig. 2.43(a) and Fig. 2.43(b) reveal that the measured results validate the predictions.

In order to show the influence of σ_v, U_{DC} has been manually reduced to the fundamental phase voltage around 33V under I_d=0 control. When U_{DC}=42V, the response voltage will

approach the peaks of voltage distortion, e.g. $\sigma_v \approx 0\%$. However, when U_{DC}=33V, $\sigma_v \approx 100\%$, which generates the distorted current in Fig. 2.44(a). It can be seen that there are just slightly current harmonics in the measured current for U_{DC}=42V, in which σ_v is nearly zero. However, significant distortion can be found in the measured current when U_{DC}=33V, especially from the FFT result shown in Fig. 2.44(b).

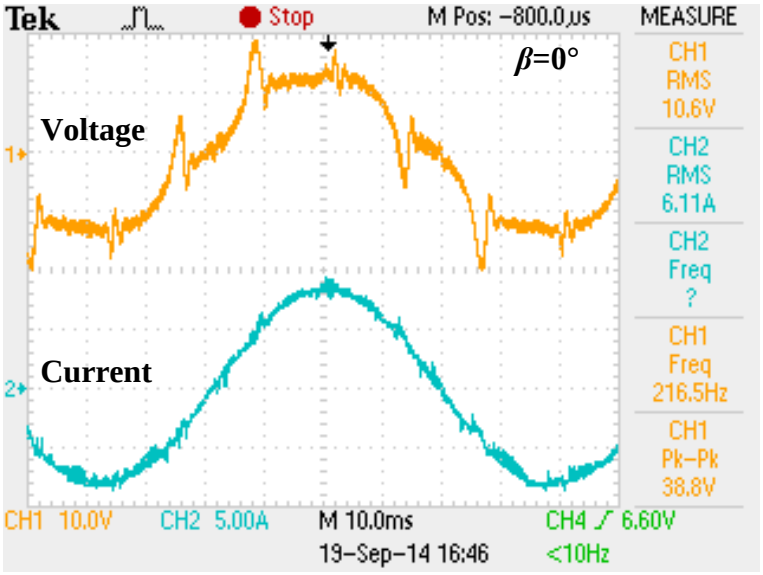

(a) β=0°

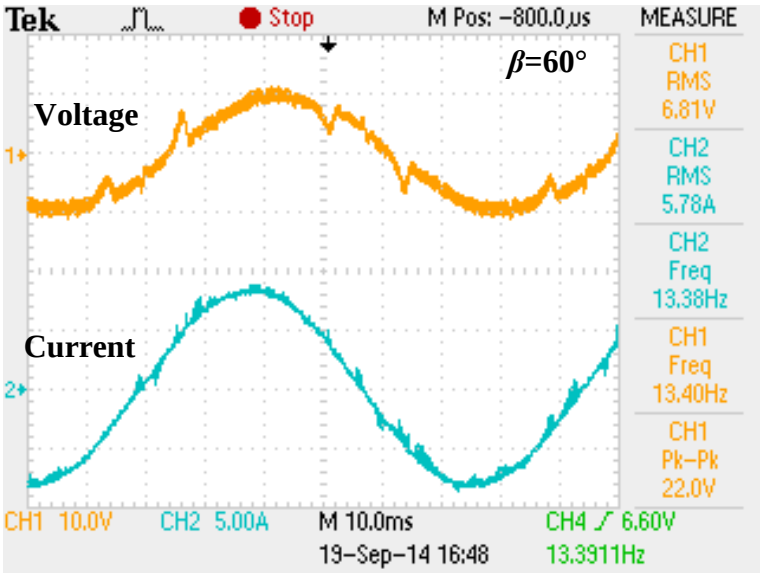

(b) β=60°

Fig. 2.42 Measured terminal phase voltage and currents for different β (I_{max}=8A, 200rpm).

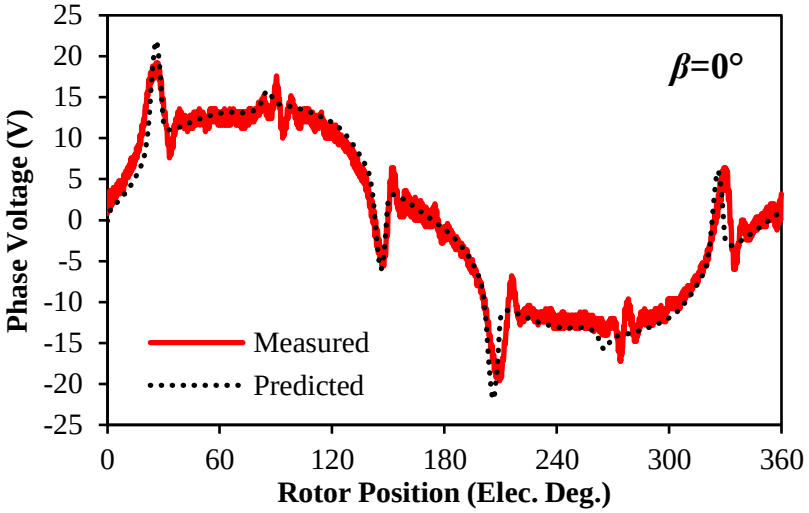

(a) β=0°

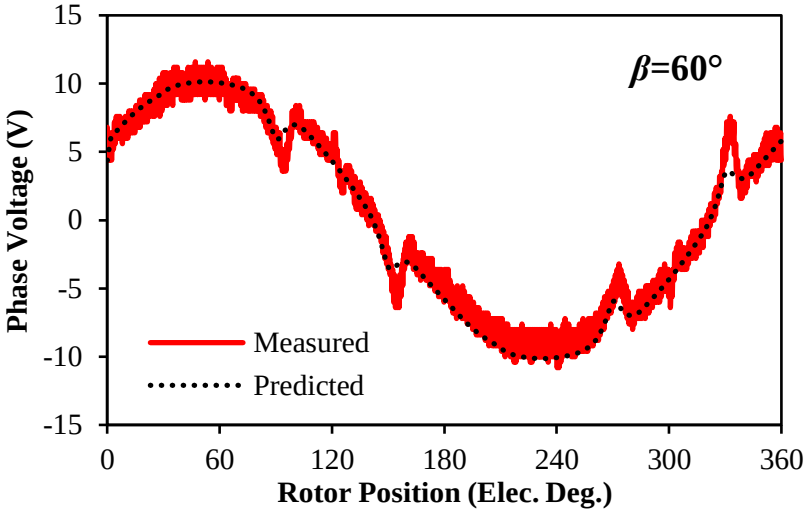

1q

(b) β=60°

Fig. 2.43 Comparison of the influence of different current angle on phase voltage and current (200rpm, U_{DC}=42V, I_{max}=8A).

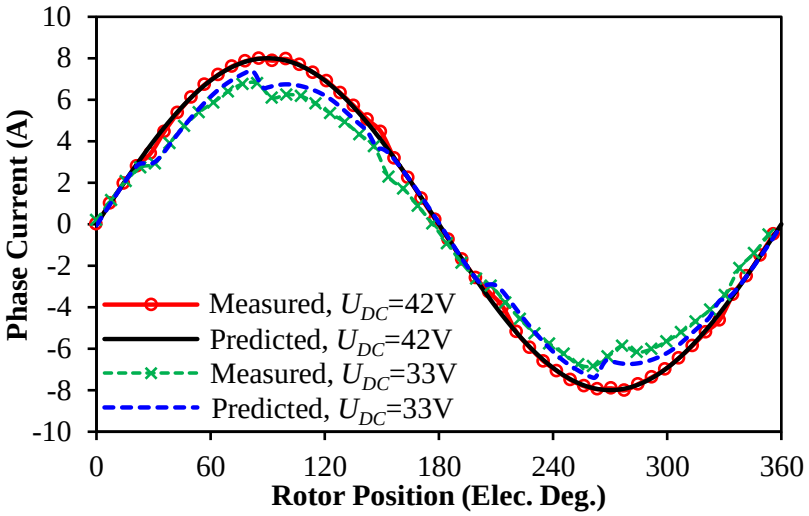

(a) Waveforms

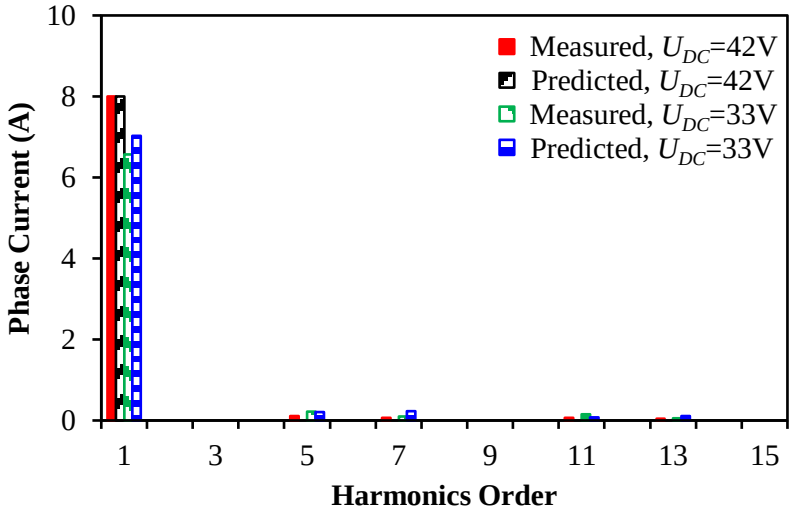

(b) Harmonic components

Fig. 2.44 Comparison of measured and predicted phase currents for different σ_v by adjusting U_{DC} (200rpm, demand current: I_{max}=8A, β=0°).

2.5.4 Torque Speed Characteristics

Feedback voltage regulation method developed in [KIM97] is adopted for the flux weakening experiment. Thus, if the output voltage amplitude of PI controller is larger than U_{DC}, β will be increased automatically to maintain the terminal voltage within U_{DC}. Therefore, the measured torque-speed characteristic can be shown as the circle-dotted line in Fig. 2.45. The dashed line in the figure is the ideal torque-speed curve calculated by only considering the fundamental voltage in 2D FEA, while the predicted line with the same method as measured curve is shown as the cross-dotted line. Considering the difference between measured and predicted back-EMFs as well as the response voltage error due to controller's band width limitation, the reason for the reduction of measured torque in the prototype machine can be clearly explained. Overall, the measured torque-speed curve validates the prediction.

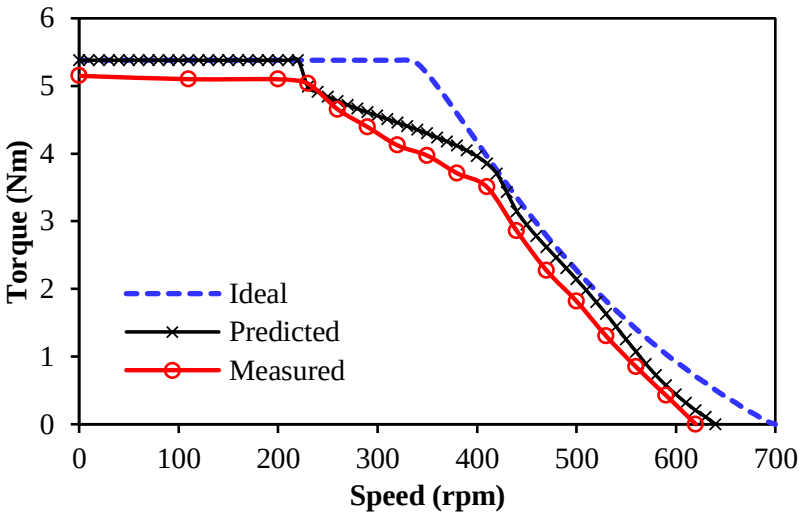

Fig. 2.45 Comparison of predicted and measured torque speed curves (U_{DC}=42V, I_{max}=8A).

2.6 Summary

This chapter focuses on the on-load voltage distortion in fractional slot SPM machines by taking an example of a 12-slot/8-pole analysis model. The phenomenon is introduced and described firstly, while the mechanism is investigated with the aid of frozen permeability method. When the direction of resultant tooth-tip leakage flux reverses, the local magnetic saturation in tooth-tips will change significantly. This changing generates the distortion of both PM and armature reaction flux linkages, and leads to phase voltage distortion. Since tooth-tips exist in most conventionally designed machines, the on-load voltage distortion is inevitable and become much more obvious when small or closed slot openings are adopted. The electromagnetic performance influenced by terminal voltage distortion and local magnetic saturation has been investigated, such as on-load back-EMF, on-load cogging torque and torque ripple, *dq*-axis inductances, and flux weakening performances. When DC link voltage is sufficient, this phenomenon will mainly increase the torque ripple. However, it will cause more side effects when DC link voltage is not enough. Under such a condition, the base-speed will be significantly reduced compared with the one calculated by only considering the fundamental voltage. Besides, the flux weakening performance is also deteriorated and worse than that would be usually expected. Meanwhile, if the response voltage is less than the command when the machine operating beyond base-speed under I_d=0 control or due to limited band-width in a real system, the response current will be distorted, which consequently leads to the reduction of average torque. Finally, a prototype with the same dimensions as the analysis model has been manufactured and tested. All measured results validate the analyses and predictions.

CHAPTER 3

INFLUENCE OF SLOT AND POLE NUMBER COMBINATIONS ON TERMINAL VOLTAGE DISTORTION IN SPM MACHINES WITH LOCAL MAGNETIC SATURATION

Based on the mechanism of terminal voltage distortion investigated in the previous chapter, this chapter focuses on investigating the influence of slot and pole number ($N_s/2p$) combinations in both fractional slot and integer slot SPM machines. Meanwhile, the electromagnetic performance of the investigated machines influenced by voltage distortion and local magnetic saturation are also compared.

3.1 Introduction

Surface-mounted permanent magnet (SPM) machine was introduced many years ago [SAU51]. However, its potential merits were not fully recognized until the PM materials and power electronics technologies were further developed. In recent decades, the SPM machines gain extensive research interests and applications due to the advantages of high power and torque density, high efficiency, and fast dynamic response caused by small winding inductances [BIA06], [CAS09], [ELR10], [ISL09], [FAG13]. Consequently, SPM machines are especially suitable for servo drive and direct drive [HUT05], [BOA14].

As important components in SPM machines, the machine performance is very sensitive to tooth-tips. [BIA02], [DON12], [CHO10] proposes that small or closed slot openings can smooth the fluctuation of air-gap permeance, which effectively reduces the amplitude of cogging torque. [PAP14] and [CVE08] claim that the back-EMF harmonics and torque ripples could be alleviated by employing closed slot. [ELR05] and [ELR08] report that the winding leakage inductance increases with smaller slot opening width but higher tooth-tip thickness, which significantly improves the flux weakening and fault-tolerant performance of SPM machines. In order to adopt automatic winding for concentrated winding machines, modular stator segments with small slot openings, or the techniques that separate the back iron from the stator teeth but link them together with closed slot openings are commonly employed [ZHU12], [MUL005], [PAR12]. Moreover, the sensorless control performance can also benefit from the small or closed slot opening designs since they introduce additional

magnetic saturation saliency for SPM machines [HA08], [FAG13], [YAN11]. Although small or closed slot opening techniques have many advantages, their drawbacks are not sufficiently investigated.

Due to the use of ferromagnetic lamination materials, the SPM machines are naturally nonlinear, which would lead to on-load terminal voltage distortion under brushless AC operation [ORL11], [MOR92], [YU13], [ZHU00]. Particularly, the increase of slot leakage due to small slot opening width will further aggravate the local magnetic saturation in tooth-tips, which may lead to more severe on-load voltage distortion. Since the distorted terminal voltage will significantly influence the performance of machines operating under limited DC link voltage [YU13], the influence of terminal voltage distortion in SPM machines should be further investigated. On the other hand, the machine performance, such as cogging torque [ZHU00], average torque [BIA08], winding inductance [PON13], and noise and vibration [VAL14], etc. are also sensitive to slot and pole number combinations.

In this chapter, the relation between local magnetic saturation in tooth-tips and on-load voltage distortion in SPM machines is investigated, particularly focusing on the influence of slot and pole number ($N_s/2p$) combinations. In order to make it more general, both fractional slot and integer slot SPM machines are investigated. Since $N_s \pm 2 = 2p$, $N_s \pm 1 = 2p$ and $N_s/2p = 3/2$ (3/4) are the most popular combinations for fractional slot SPM machines, the machines with 12/10, 12/14, 9/8, 9/10, 12/8, 12/16 $N_s/2p$ are chosen as examples. Meanwhile, the machines with 12/4 and 24/4 $N_s/2p$ are also investigated as the examples of integer slot machines. In the following sections, the generating process of a single voltage ripple will be investigated based on a 12/10 machine firstly, with the aid of FP method and virtual detecting coils. Then, the voltage distortion patterns are proposed to analyse the influence of different winding arrangements by different $N_s/2p$ combinations. After that, the voltage distortion under constant torque operation and flux weakening operation are investigated separately, while the machine performance influenced by voltage distortion and local magnetic saturation are also compared, such as on-load back-EMF, on-load cogging torque, *dq*-axis inductances, average torque and torque ripple, iron loss, and flux weakening performance. Finally, the 12/10 and 12/8 $N_s/2p$ prototypes are manufactured and tested to validate the analyses.

3.2 Investigated Machines

The investigated SPM machines with small slot openings are designed in Fig. 3.1 at zero rotor position (θ_r=0°). All machines have the same size, air-gap length, magnet thickness, and major tooth-tip parameters (b_0, h_t and α_t). In order to compare the terminal voltage distortion fairly, the turns per phase have been adjusted to acquire similar back-EMFs for all machines at rated speed. Meanwhile, the tooth width and back iron thickness for all machines are adjusted to obtain similar tooth body and back iron flux density around 1.5T at rated current with I_d=0 control. The basic parameters are shown in Table I and Table II respectively.

Table 3.1 Basic common parameters of investigated machines

Parameter	***Value***	***Parameter***	***Value***
Stator outer diameter	100mm	Axial length	50mm
Split ratio	0.57	Airgap length	1.0mm
Rated speed	400rpm	Rated current	7.1A_{rms}
Magnet thickness	3.0mm	Pole arc/pitch ratio	1
Slot opening width	0.2mm	Tooth-tip thickness	1mm
Tooth-tip slot	10°	Lamination material	M300
Magnet permeability	1.05	Magnet remanence	1.2T

Table 3.2 Basic differential parameters of investigated machines

Machine	***A***	***B***	***C***	***D***	***E***	***F***	***G***	***H***
Slot number	12	12	9	9	12	12	12	24
Pole number	10	14	8	10	8	16	4	4
Tooth width, mm	9.0	6.8	12.0	9.6	9.4	5.0	9.9	6.5
Yoke height, mm	4.6	3.5	6.0	4.8	4.7	2.5	10.8	10.3
Turns per phase	184	200	180	192	196	228	172	176

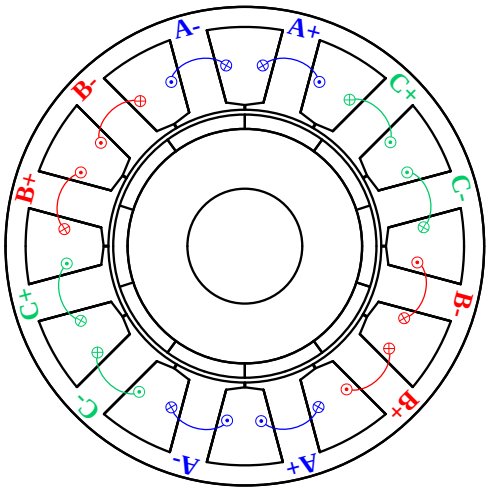

(a) 12/10

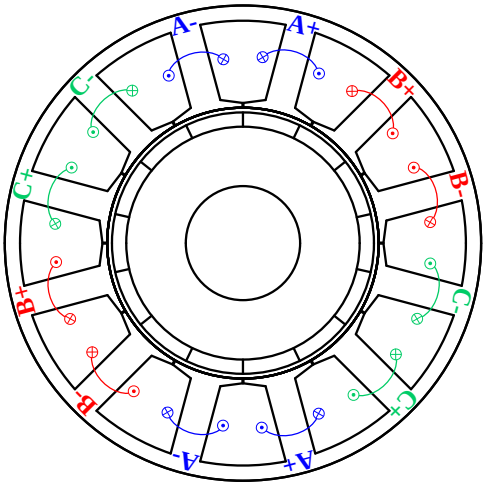

(b) 12/14

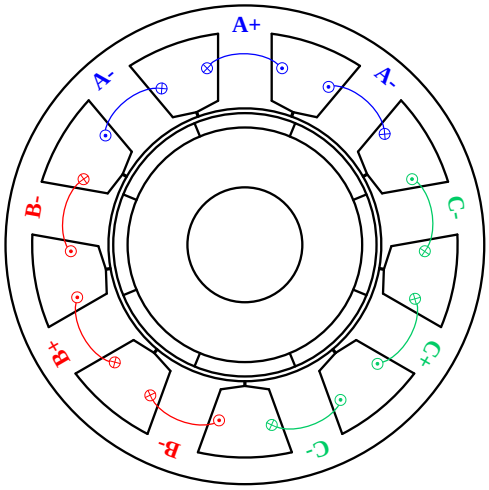

(c) 9/8

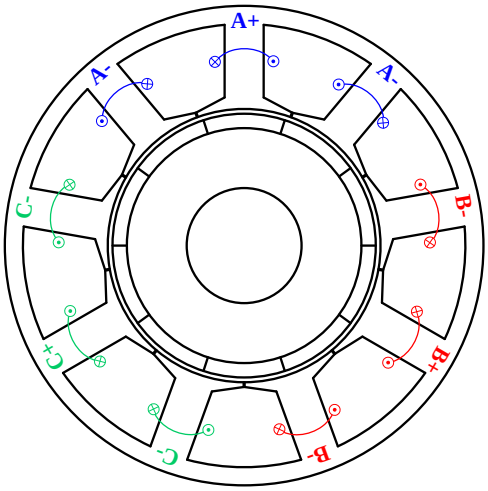

(d) 9/10

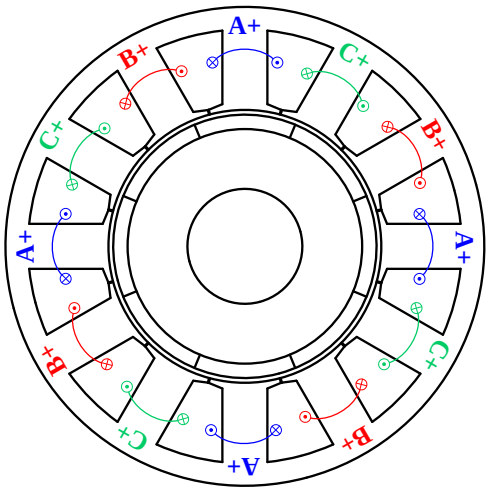

(e) 12/8

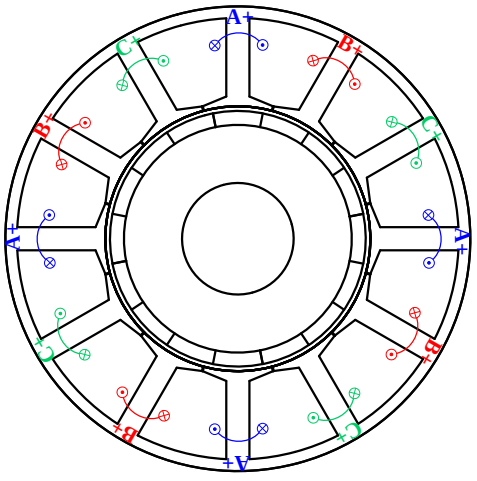

(f) 12/16

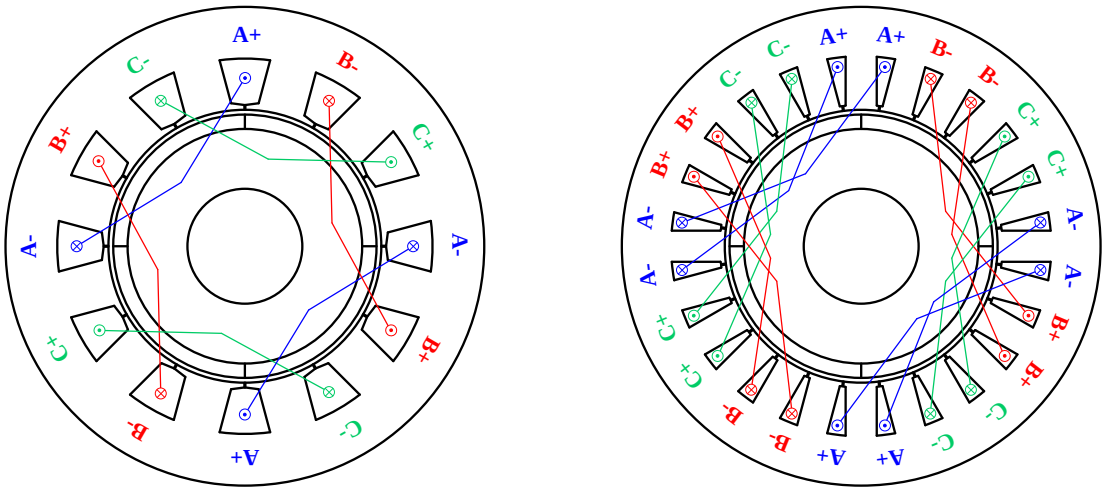

(g) 12/4 (h) 24/4

Fig. 3.1 Configurations of machines with different slot/pole number combinations (Phase A at *d*-axis, θ_r=0°).

3.3 Influence of Slot and Pole Number Combinations on Terminal Voltage Distortion

Due to negligible reluctance torque, SPM machines often operate under I_d=0 control which is also the theoretical current condition for the worst voltage distortion. Thus, this section will investigate the general principle of voltage distortion for different slot and pole number combinations based on I_d=0 control, while the analysis methods and results can be applied for machines driven by different β as well.

3.3.1 Voltage Ripple Occurring Rotor Positions

The mechanism of voltage distortion reveals that the local magnetic saturations of tooth-tips are the origin source of generating terminal voltage ripples. In order to obtain the general principles of voltage distortion for different slot and pole number combinations, a virtual detecting coil is introduced to further reveal the generating process of a single voltage ripple, Fig. 3.2(a), based on the 12-slot/10-pole machine in Fig. 3.1(a). In the FEA model, the virtual detecting coil can be set up around the tooth-tip, Fig. 3.2(b), which has the same number of turns as the major tooth-coil. Since it is an open-circuit detecting coil without conductivity, the simulation result will not be influenced.

By FP method, the leakage fluxes contributed by PM and armature respectively can be reflected in Fig. 3.3(a), in which the PM and armature leakage fluxes cross zero at the same time with opposite directions. Since the local magnetic saturation of tooth-tips change

significantly during this process, a voltage ripple will occur as shown in Fig. 3.3(b). For certain driving currents and winding arrangements, the slot currents zero-crossing time are determined, which makes the voltage ripples always occur at certain rotor positions, Fig. 3.4.

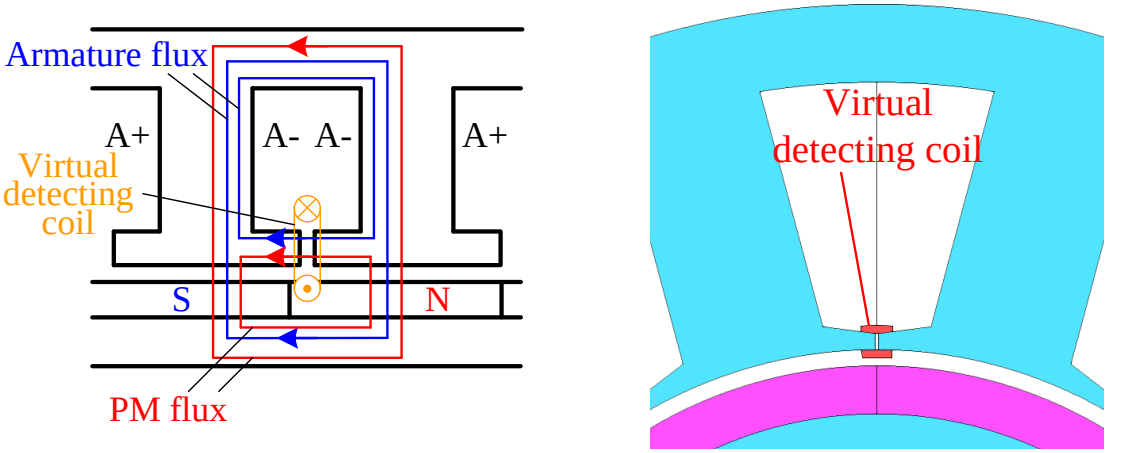

(a) Flux paths (b) Virtual detecting coil in FEA model

Fig. 3.2 Illustration of flux paths and slot leakages through tooth-tips.

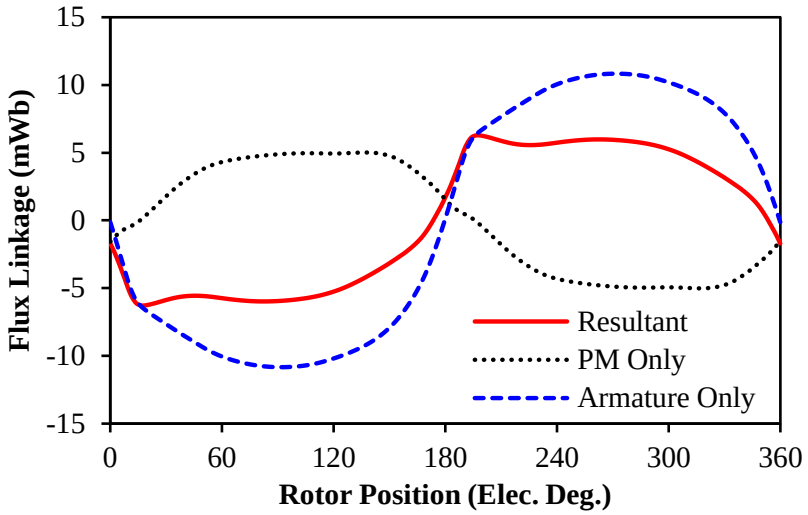

(a) Flux linkages in virtual detecting coil

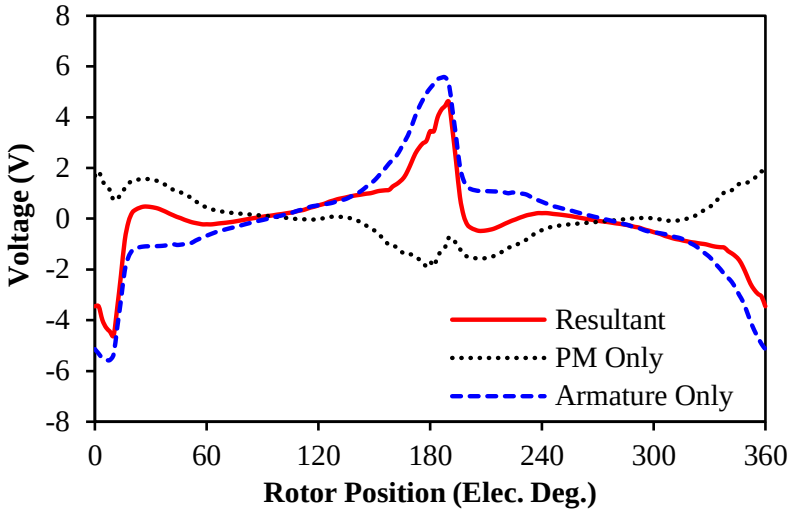

(b) Induced voltage in virtual detecting coil

Fig. 3.3 Tooth-tip leakage fluxes and voltages in virtual detecting coil by FP method (I_{max}=10A, β=0°, 400rpm).

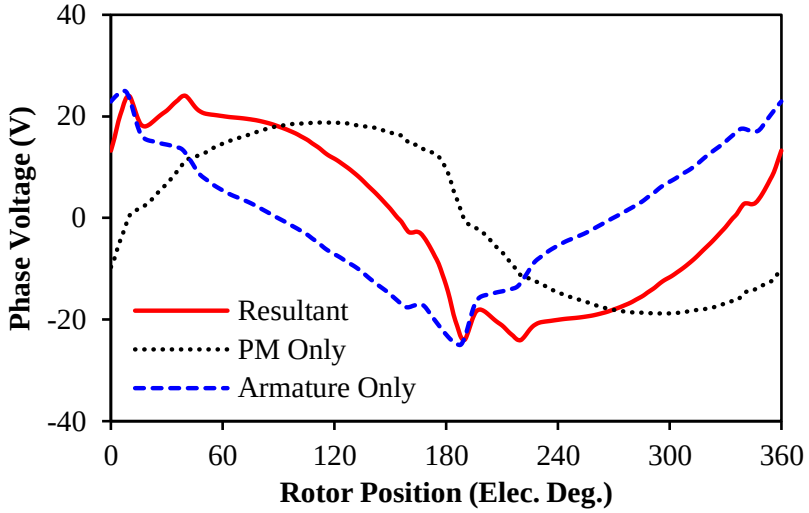

(a) Terminal phase voltages

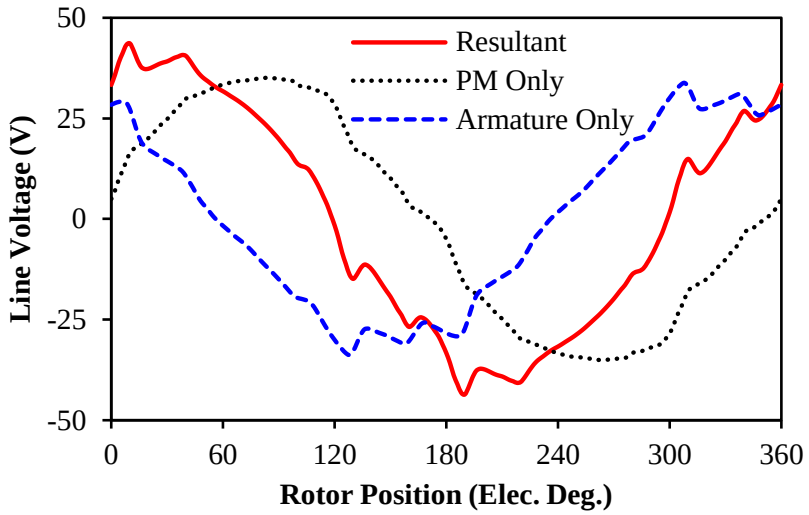

(b) Terminal line voltages

Fig. 3.4 Terminal phase and line voltages by FP method (I_{max}=10A, β=0°, 400rpm).

Fig. 3.5(a) shows the winding arrangement for the 12-slot/10-pole machine, in which the circles pointed out the slots related with phase A. It can be seen that the coil sides of phase A are distributed in six different slots which can be divided into two types. One of them only contains the coil sides of phase A, e.g. slots 1 and 7, which can be designated as Type I slot. The other type contains coil sides from two different phases, e.g. slots 2, 6, 8 and 12, which can be designated as Type II slot. Since their slot currents are different, the zero-crossing time will be different as well. Fig. 3.5(b) compares the terminal phase voltages to illustrate such differences. It can be observed that the voltage ripples caused by Type I slot will only influence the voltage ripple for the belonging phase, i.e. the voltage ripples for phase A around 0° and 180° are caused by slots 1 and 7 which only contain coil sides of phase A. On the contrary, as the dashed circle pointed out, the voltage ripples caused by Type II slots, i.e. slots 6 and 12, will occur simultaneously in both two phases since the leakage flux links with coil sides of both phases at the same time. The relative amplitudes between different voltage ripples will be explained in the following discussions.

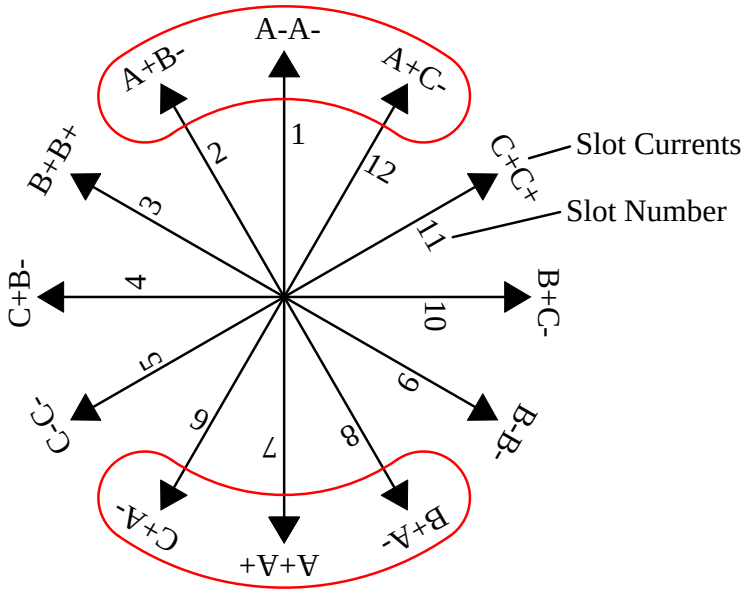

(a) Winding arrangements of 12/10 machine

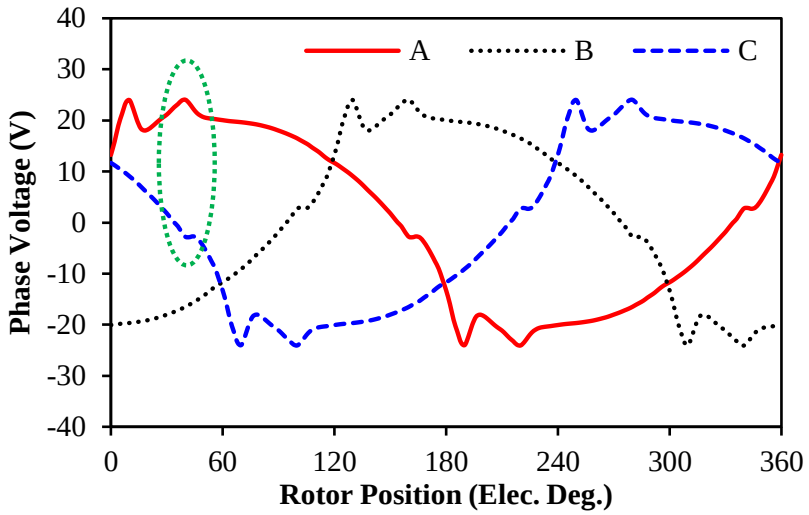

(b) Terminal phase voltages (I_{max}=10A, β=0°, 400rpm).

Fig. 3.5 Winding arrangements and their influence on voltage ripples occurring positions for 12/10 machine.

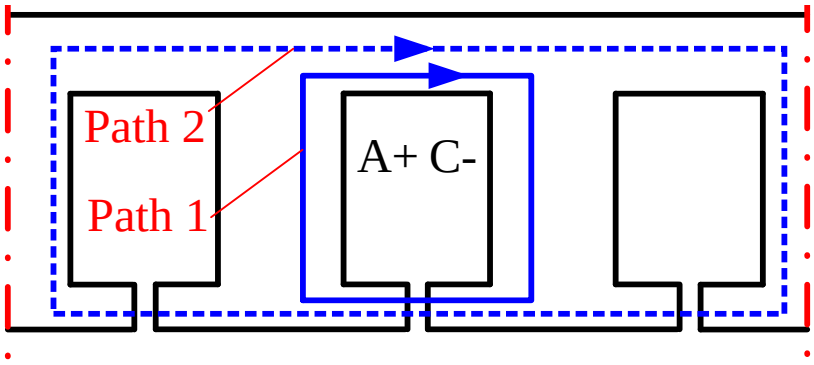

Fig. 3.6 Leakage flux circulating paths for slot currents of a single slot.

For a single slot, the tooth-tip leakage flux of the slot current could circulate through the tooth-tips belonging to the slot itself, e.g. Path 1 in Fig. 3.6, or by-pass of tooth-tips from other slots, e.g. Path 2 in Fig. 3.6. Since the tooth-tips are normally saturated under load operation, the value of leakage flux circulating through Path 2 is very limited compared with the one through Path 1. Assuming the tooth body and back iron to be infinitely permeable, the armature tooth-tip leakage flux by Path 1 in a single slot can be expressed by

$$\Phi_{tip\sigma}^{k}(\theta_r) = N_c i^{k}(\theta_r)[\Lambda_{b0} + \Lambda^{k}(\theta_r)] \tag{3.1}$$

where k is the slot number, N_c is the turns per coil, $i^k(\theta_r)$ is the instantaneous slot current which consists of the currents of two coil sides within the same slot, Λ_{b0} is the constant permeance for slot openings, $\Lambda^k(\theta_r)$ is the permeance of the tooth-tips belonged to slot k,

which changes with different rotor positions. Therefore, the leakage flux linked with one coil side can be calculated as

$$\psi_{tip\sigma}^{k}(\theta_r) = N_c^2 i^k(\theta_r)[\Lambda_{b0} + \Lambda^k(\theta_r)] \tag{3.2}$$

Since the coil sides of phase A are distributed in different slots, the tooth-tip leakage flux linkage for one phase can be calculated by summing up the leakage fluxes linked with each coil sides as

$$\psi_{tip\sigma}^{a}(\theta_r) = \sum_{k=1}^{N_s} jN_c^2 i^k(\theta_r)[\Lambda_{b0} + \Lambda^k(\theta_r)] \tag{3.3}$$

where j=2 when the slot numbered k is a Type I slot containing phase A, j=1 when the slot numbered k is a Type II slot containing phase A, otherwise j=0 if it does not contain phase A. It can be seen from (3.3) that the winding arrangement directly influences the leakage flux linkage and thereafter the voltage distortion. Meanwhile, the voltage ripples only occur when i^k crosses zero, since the sudden rise of Λ^k opens a high permeance channel for the pulsation of leakage flux. Thus, the voltage distortion pattern (*VDP*) can be further introduced to describe the phenomenon only considering the winding configurations.

$$VDP(\theta_r) = \sum_{k=1}^{N_s} n_i \delta^k(\theta_r) \tag{3.4}$$

$$n_i = \begin{cases} 2j\ , & k \text{ is Type I slot} \\ \sqrt{3}j\ , & k \text{ is Type II slot} \end{cases} \tag{3.5}$$

$$\delta^k(\theta_r) = \begin{cases} 1\ , & i^k \text{ positive zero-crossing} \\ -1, & i^k \text{ negative zero-crossing} \\ 0\ , & \text{otherwise} \end{cases} \tag{3.6}$$

where n_i represents the relative amplitudes of i^k. δ^k is a unit pulsation function which indicates the relative slot current zero-crossing rotor positions. When slot k is Type I slot, the slot current amplitude would be twice of the phase current amplitude. When slot k is Type II slot, the slot current is line current, which is sqrt(3) times of the amplitude of phase current. By

applying (3.4) to the 12/10 machine, the per-unit *VDP* can be calculated in Fig. 3.7(a), in which the pulses contributed by each slot current have been illustrated. The phase terminal voltage for the 12/10 machine is obtained by FEA for comparison, Fig. 3.7(b). Considering the influence of fundamental voltage, the voltage ripples occurring positions and relative amplitudes between each voltage ripple can be explained by *VDP* as marked in the figure.

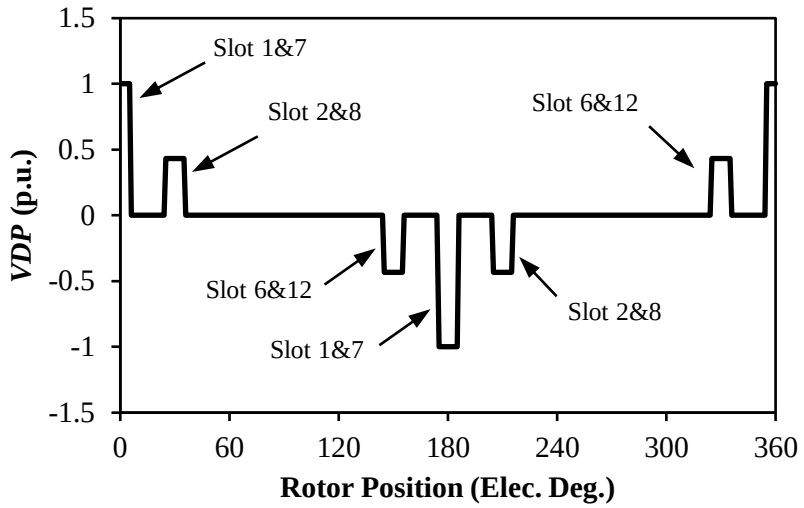

(a) *VDP*

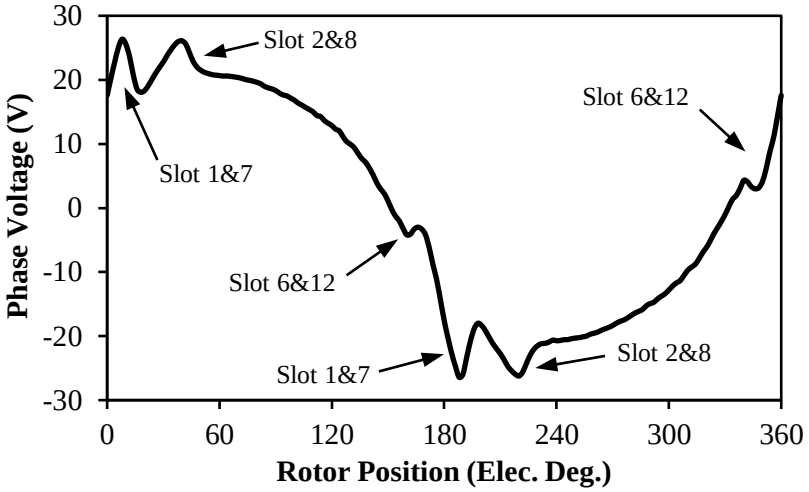

(b) Terminal phase voltage

Fig. 3.7 Comparison of *VDP* and on-load phase terminal voltage distortion for 12/10 machine (I_{max}=10A, β=0°, 400rpm).

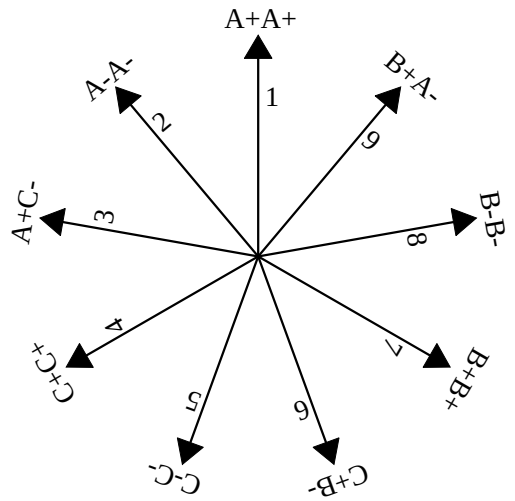

(a) 9/8 and 9/10

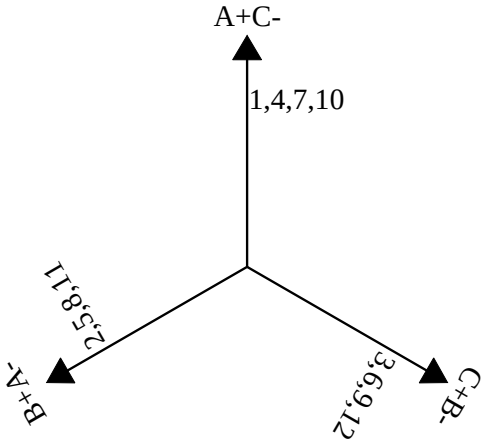

(b) 12/8 and 12/16

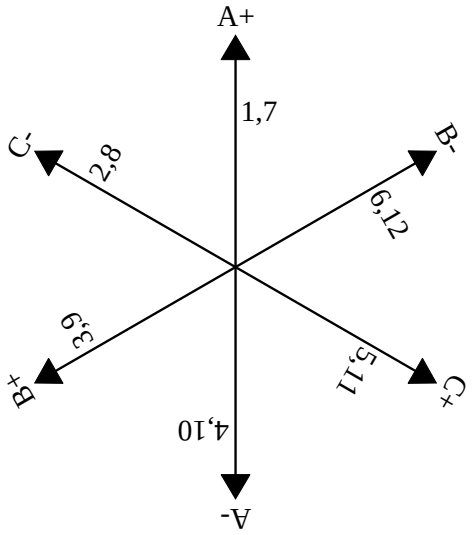

(c) 12/4

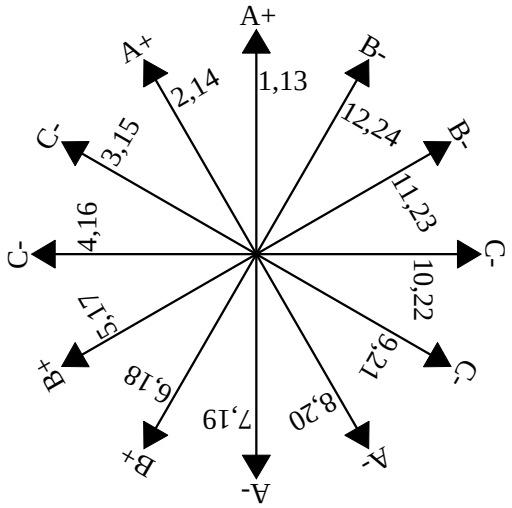

(d) 24/4

Fig. 3.8 Winding arrangements for other investigated machines.

3.3.2 Voltage Distortion Patterns

For the fractional slot machines with the same slot number, the pole number can be in pairs, e.g. $N_s \pm 2 = 2p$, which have the same winding arrangement with only different phase sequences. Thus, the machines appearing in pairs also share the same *VDP* such as 12/14 and 12/10 machines. The winding connections of other machines are shown in Fig. 3.8. It is noted that both the two integer slot machines, e.g. 12/4 and 24/4 machines, have Type I slots only. Thus their voltage ripples will only appear when phase currents cross zero, which makes their *VDP* the same as well. Following this principle and the method above, the *VDP* for all machines to

be analysed can be calculated and shown in Fig. 3.9. It can be observed that the ripples occurring positions for the first two curves are the same. However, the amplitudes of the centre ripples are much more obvious in the second curve. This is because there are more Type I slots in N_s±1=2p machines than that in N_s±2=2p machines. Meanwhile, since the N_s/2=3/2 (3/4) machines only contain Type II slot, the number of ripples reduces as well.

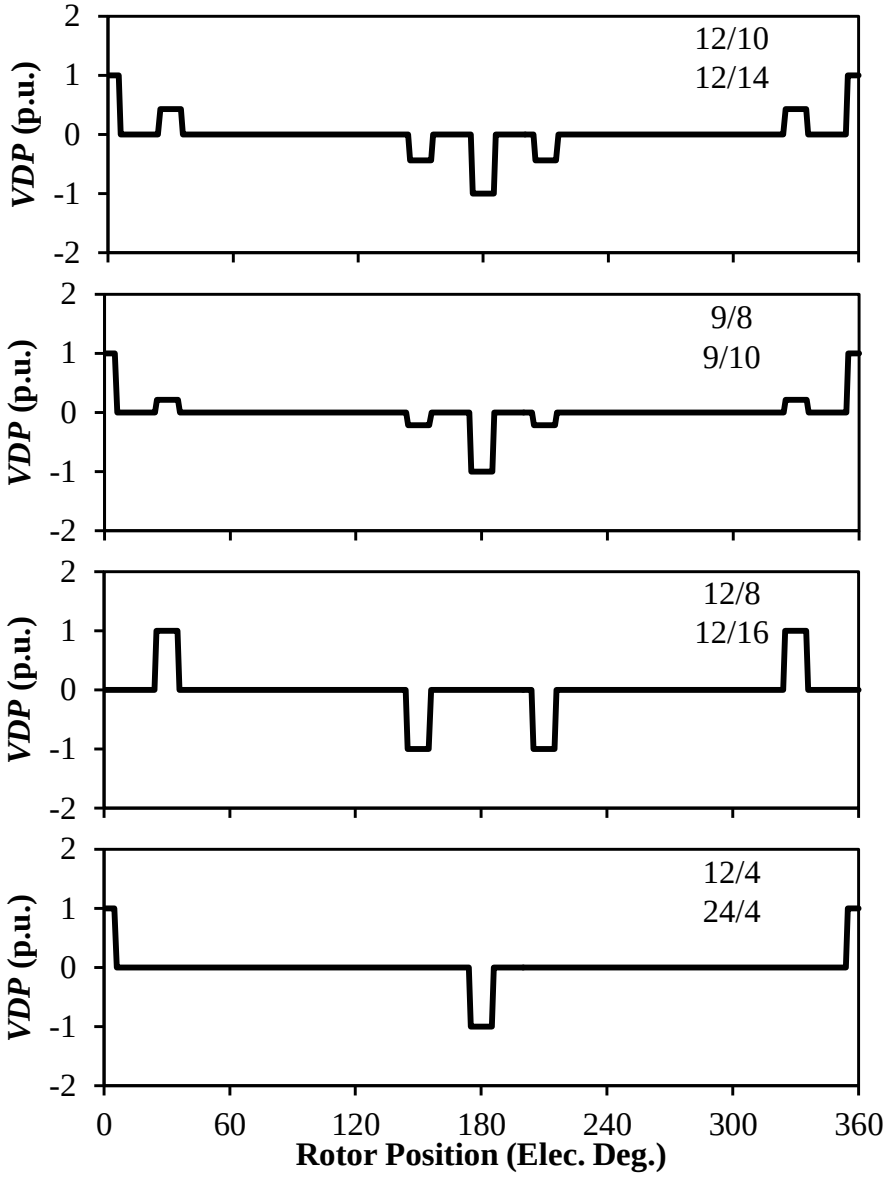

Fig. 3.9 *VDP* for machines with different slot and pole number combinations (β=0°).

3.3.3 Influence of PM Tooth-Tip Leakage Flux

According to the aforementioned analyses, if PM and armature tooth-tip leakage fluxes cross zero at the same time, the worst voltage distortion could be expected under the same driving

current. When the inter-pole boundaries of rotor PM cross a slot opening, the PM leakage flux will cross zero and reverse its direction. Thus, by investigating the relative positions between slot openings and PM inter-pole boundaries, the influence of PM tooth-tip leakage flux could be revealed. For example, the relative positions between slot openings and PM inter-pole boundaries in the 12/10 machine are illustrated in Fig. 3.10(a) with θ_r=0°. It can be seen that one PM boundary line is aligned with the slot containing slot current of -2i_A. Thus, the armature tooth-tip leakage flux of this slot will cross zero together with the PM leakage flux, which generates voltage ripples at θ_r =0° and 180° as predicted by *VDP*. Meanwhile, the two adjacent slots are 30° in advance or lagging behind the relative slot openings as marked in Fig. 3.10(a). Fig. 3.10(b) illustrates that the slot currents i_A-i_B and i_A-i_C also cross zero at 30° in advance or lagging behind the zero position, which have the same zero-crossing positions with their relative PM leakage fluxes. Thus, the PM leakage flux will contribute together with armature leakage flux to all voltage ripples. By adopting the same analysis method, the tooth-tip PM leakage fluxes in 12/14, 12/8, 12/16, and 12/4 machines all cross zero at the same positions when their relative slot currents cross zero, which enhances the voltage distortion.

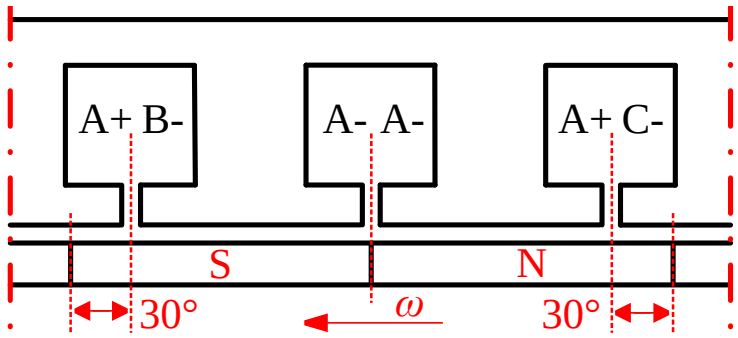

(a) Positions for inter-pole boundaries at θ_r=0°

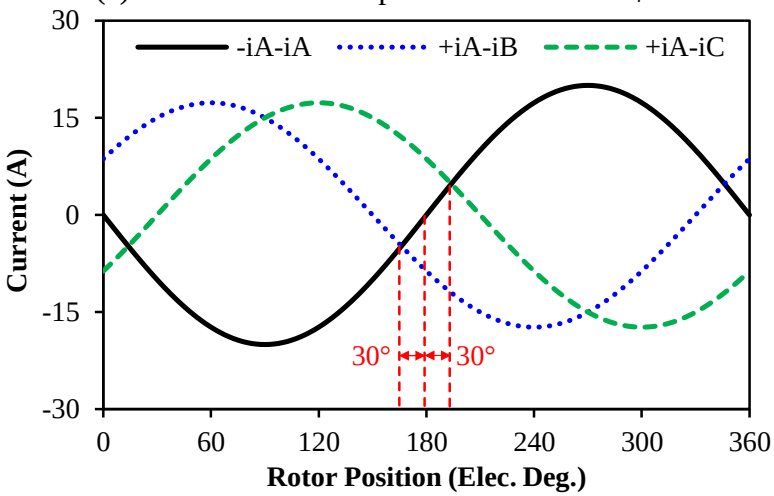

(b) Slot currents zero-crossing positions, I_{max}=10A, β=0°

Fig. 3.10 Relations between inter-pole boundaries and slot currents zero-crossing positions for 12/10 machine (marked with electric degree).

The influences of tooth-tip PM leakage flux in different machines may differ due to different winding arrangements. The relative inter-pole boundaries of 9/8 machine are shown in Fig. 3.11(a), which could not align with the slot openings at the same time. However, the two Type II slots with $-i_A+i_B$ and $-i_A+i_C$ are still 30° in advance or lagging behind the relative PM boundaries, which still enhance the voltage ripples, Fig. 3.11(b). Due to the above influences, the amplitude differences between voltage ripples caused by Type I and Type II slots are slightly smaller as predicted by *VDP* shown in Fig. 3.9. By adopting the virtual detecting coil marked in Fig. 3.11(a), the tooth-tip leakage can be shown in Fig. 3.12(a). Clearly, the crossing zero points of PM and armature leakage fluxes are different, which reduce the resultant voltage ripple, Fig. 3.12(b).

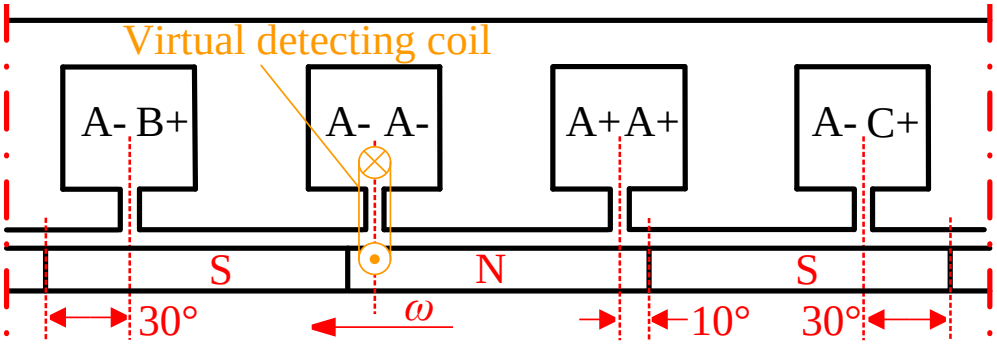

(a) Relative positions for inter-pole boundaries θ_r=0°,

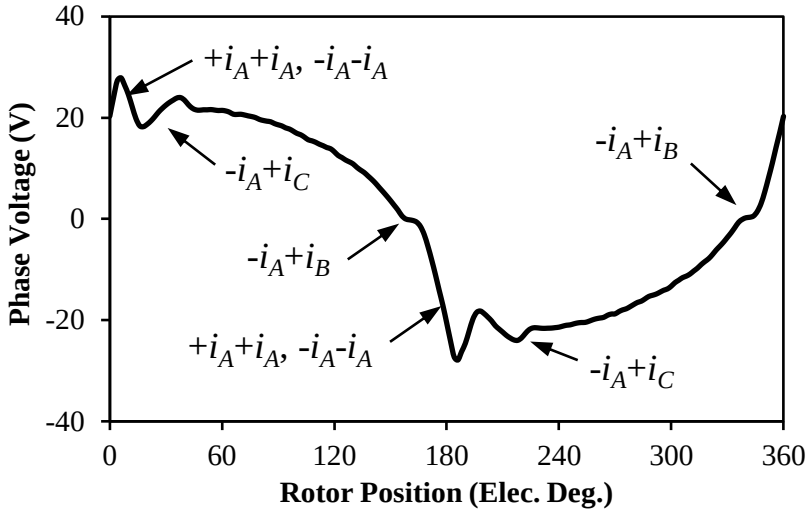

(b) Terminal phase voltage, I_{max}=10A, β=0°, 400rpm.

Fig. 3.11 Illustration of influence of PM leakage flux on voltage distortion in 9/8 machine.

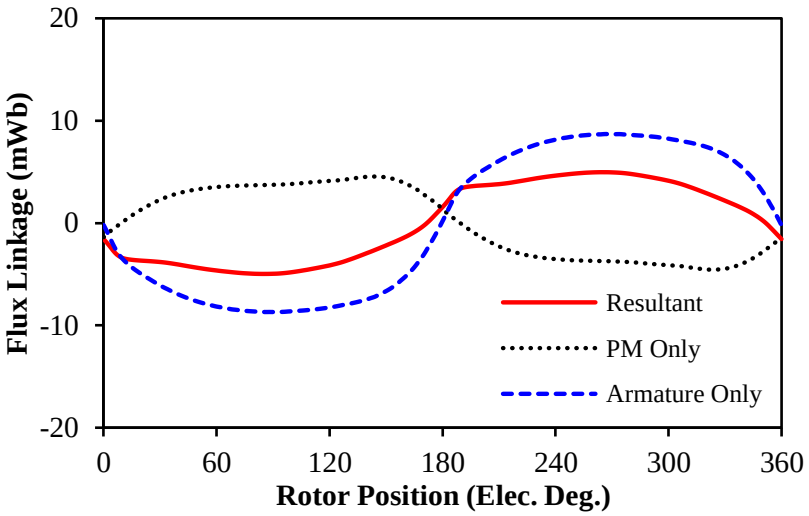

(a) Flux linkages

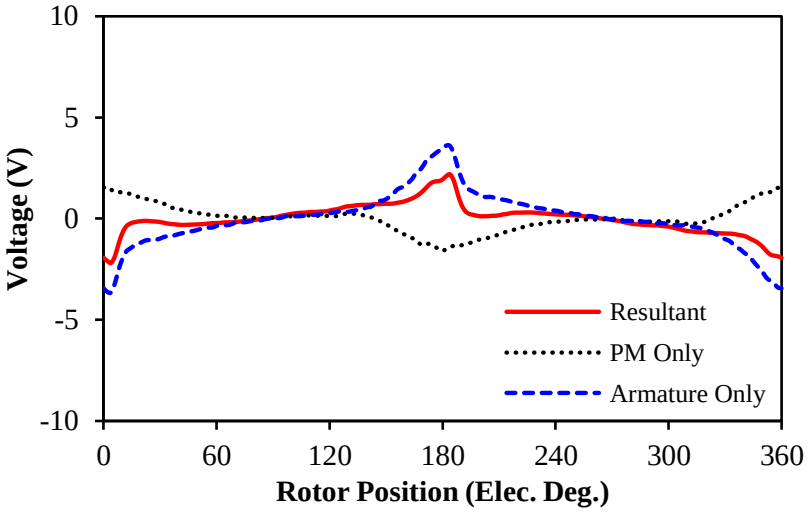

(b) Voltages

Fig. 3.12 Tooth-tip leakage fluxes and voltage in virtual detecting coil by FP method for 9/8 machine (I_{max}=10A, β=0°, 400rpm).

Since the 9/10 machine has the same winding arrangements as the 9/8 machine, the PM leakage flux also reduces the amplitudes of potential voltage ripples. Similarly, for the machines with more than two adjacent Type I slots from the same phase, the PM inter-pole boundaries could not be aligned with the relative slot openings at the same time, which will reduce the potential voltage ripples. According to [HUT05], the slot number of a unit machine can be defined as (3.7), while the number of adjacent Type I slots from the same phase in a unit fractional slot machine with concentrated winding can be defined as (3.8).

$$N_{s0} = N_s / GCD(N_s, 2p) \tag{3.7}$$

$$q_e = \begin{cases} \dfrac{N_{s0}}{m} - 1, & N_{s0} \in \text{odd} \\ \dfrac{N_{s0}}{2m} - 1, & N_{s0} \in \text{even} \end{cases} \tag{3.8}$$

where m is the phase number. Thus, for fractional slot machines with q_e>2, the PM leakage flux will reduce the fluctuation of potential voltage ripples.

Since the fractional slot machines with concentrated windings prefer to have N_s close to $2p$ in order to gain high winding factor [BIA02], the PM boundaries are physically quite close to slot openings at θ_r =0°. Therefore, the voltage ripple reduction by PM leakage fluxes is usually limited in these machines. However, such an influence may become more obvious in integer slot machines with q≥2. For example, the relative positions between PM inter-pole boundaries and slot openings in the 24/4 machine are shown in Fig. 3.13(a), which show that the inter-pole boundary is aligned with the stator tooth instead of the slot opening. Thus, the PM leakage fluxes will significantly reduce the potential voltage ripples, Fig. 3.13(b). By adopting the virtual detecting coil, the tooth-tip leakage fluxes in 24/4 machine can be observed in Fig. 3.14(a). The fluctuations are not obvious compared with other machines, which lead to small voltage ripples, Fig. 3.14(b).

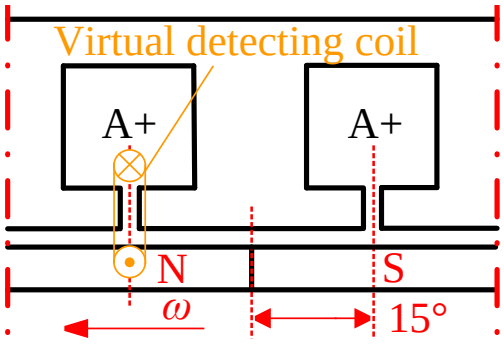

(a) Relative positions for inter-pole boundaries θ_r=0°

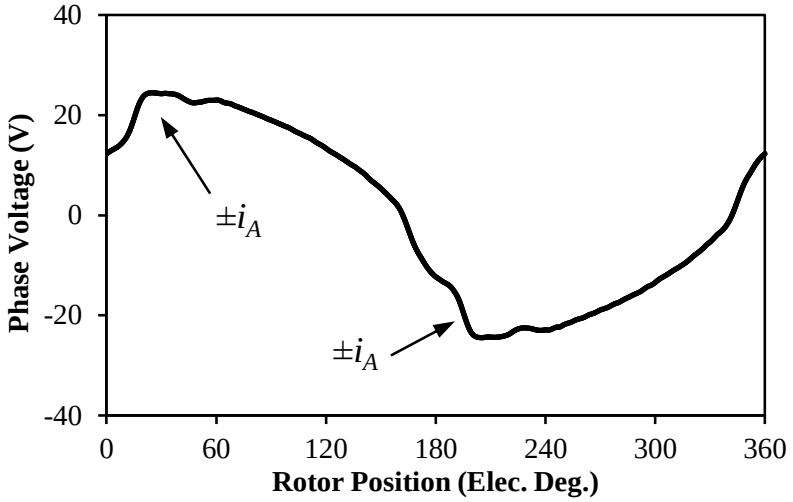

(b) Terminal phase voltage, I_{max}=10A, β=0°, 400rpm.

Fig. 3.13 Illustration of influence of PM leakage flux on voltage distortion in 24/4 machine.

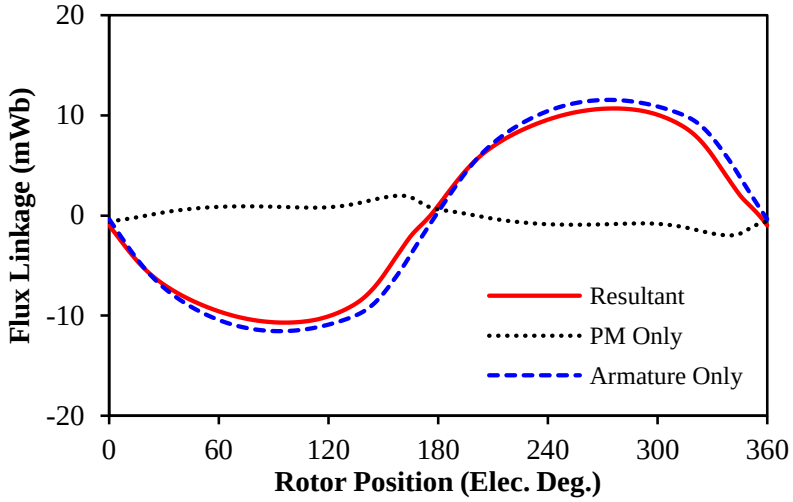

(a) Flux linkages

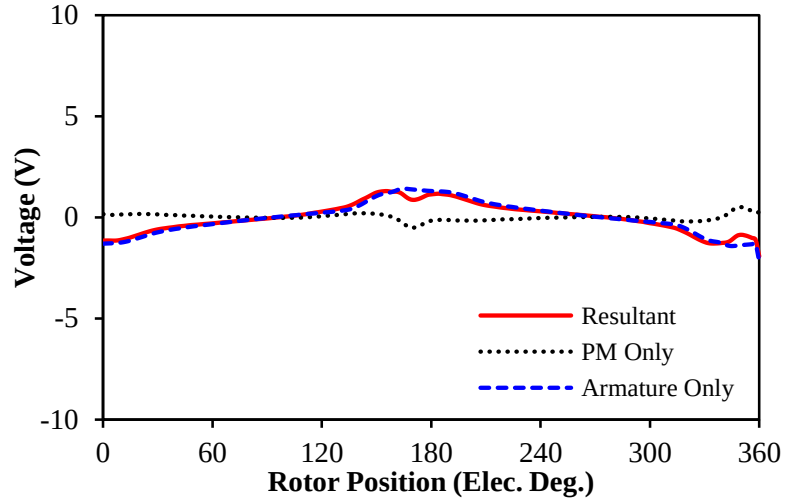

(b) Voltages

Fig. 3.14 Tooth-tip leakage fluxes and voltage in virtual detecting coil by FP method for 24/4 machine (I_{max}=10A, β=0°, 400rpm).

3.4 Comparison of Terminal Voltage Distortions for Different Slot and Pole Number Combinations

3.4.1 Under Constant Torque Operation

For constant torque operation, the machines operate under fixed current angle, e.g. β=0°. Thus, the comparison in this section can also be utilized to validate the *VDP*s as predicted in Fig. 3.9. Since 3*n* times phase voltage harmonics will be cancelled in the line voltage with Y-connection, which would not influence the control performance if the conventional three phase inverter is adopted. A new evaluation standard is demanded to reflect the real influence of terminal voltage distortion considering limited DC link voltage. Therefore, line voltage distortion ratio (*LVDR*) can be introduced as

$$LVDR = \frac{U_{peak}^{line} - U_{fund}^{line}}{U_{fund}^{line}} \times 100\% \tag{3.9}$$

where U^{line}_{peak} and U^{line}_{fund} refer to the peak and fundamental values of line voltages. Meanwhile, total harmonic distortion (*THD*) can also be adopted to describe the voltage waveform quality for comparison.

$$THD = \frac{\sqrt{U_2^2 + U_3^2 + \cdots + U_n^2 + \cdots}}{U_1} \times 100\% \tag{3.10}$$

where U_n is the amplitude of n^{th} harmonic voltage. Fig. 3.15(a) compares the on-load voltage distortion for 12/10 and 12/14 machines. It can be seen that there are three adjacent voltage ripples for both machines at similar positions, which validate the relative positions and amplitudes predicted by *VDP*. Although the 3*n* times harmonics can be cancelled in line voltages, Fig. 3.15(b), the 12/14 machine still has higher voltage distortion than the 12/10 machine, which can be reflected in the FFT results and *LVDR* as shown Fig. 3.15(c). Since the tooth-tip armature leakage flux-linkage has been defined in (3.3), the voltage distortion due to the armature leakage flux can be expressed as

$$u_{tip}^{a} = p\omega_m \frac{d\psi_{tip\sigma}^{a}(\theta_r)}{d\theta_r} \tag{3.11}$$

where ω_m represents the mechanical speed. For the two fractional slot machines in pairs, their winding arrangements as well as b_0 and h_t are the same, which lead to similar leakage flux paths. Since the 12/14 machine has larger number of turns per phase than the 12/10 machine, it will obtain higher $\psi^a_{tip\sigma}$ at the same current condition. Meanwhile, since the 12/14 machine also has larger p, its voltage distortion level will be higher according to (3.11). Furthermore, for all the machines appearing in pairs, the ones with $N_s<2p$ would be expected to have higher voltage distortion level than their counterparts with $N_s>2p$, which can be validated by other two pairs of machines as compared in Fig. 3.16 and Fig. 3.17 respectively. Besides, according to (3.11), more obvious voltage distortion difference would be expected for machines appearing in pairs with larger difference between the pole pairs, such as 12/8 and 12/16 machines.

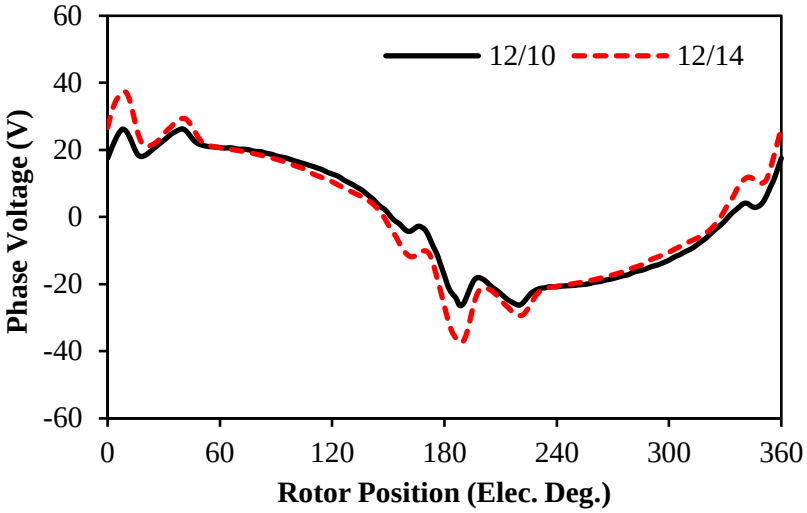

(a) Terminal phase voltages

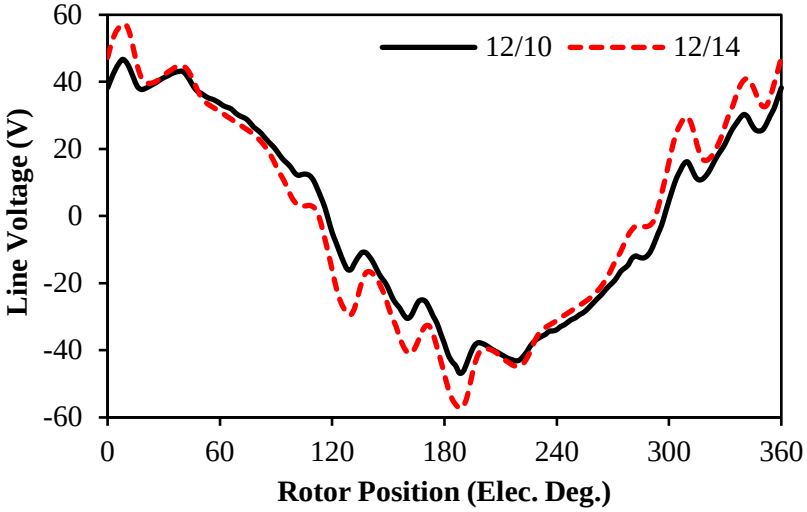

(b) Terminal line voltages

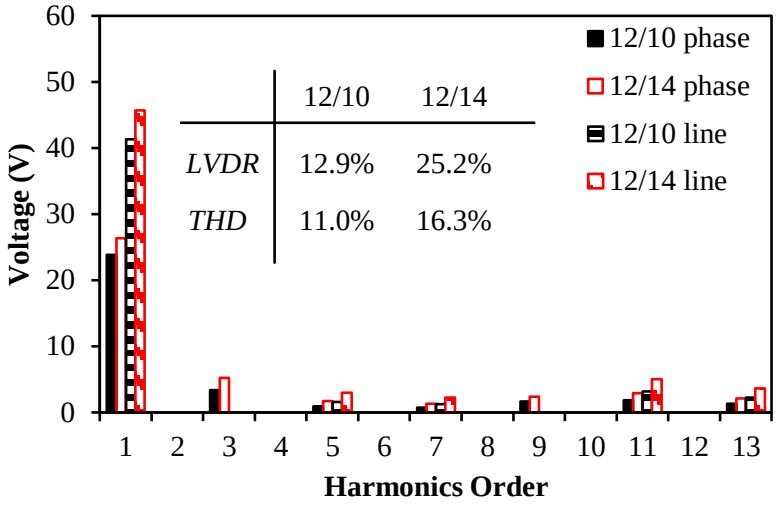

(c) Harmonic components and *LVDRs*

Fig. 3.15 On-load voltage distortion of 12/10 and 12/14 machines (I_{max}=10A, β=0°, 400rpm).

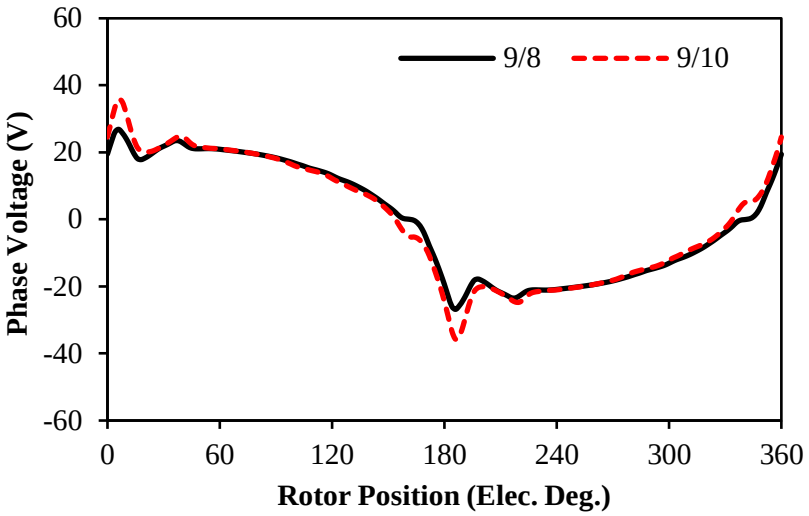

(a) Terminal phase voltages

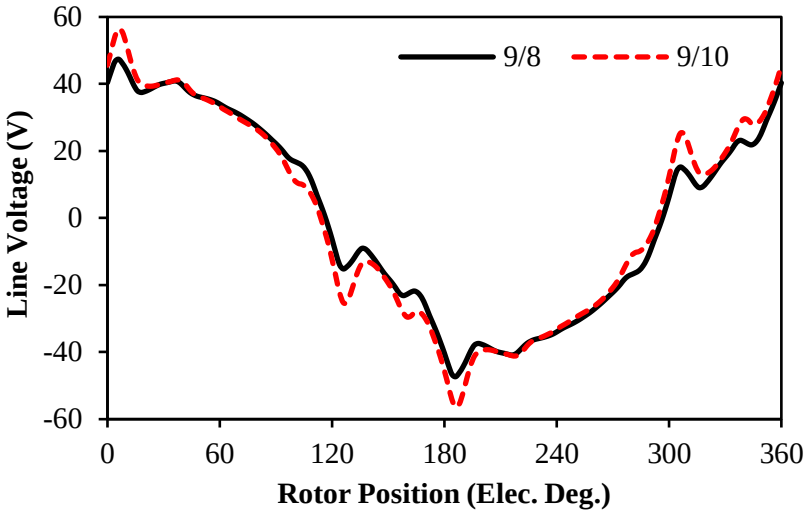

(b) Terminal line voltages

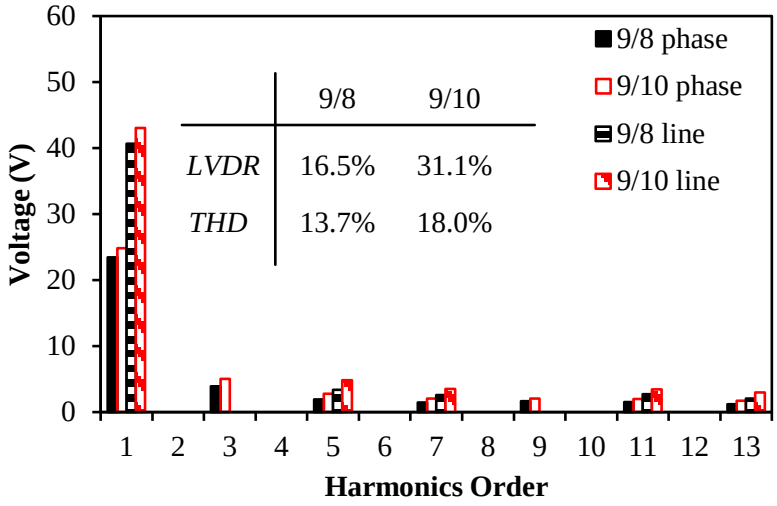

(c) Harmonic components and *LVDRs*

Fig. 3.16 On-load voltage distortion of 9/8 and 9/10 machines (I_{max}=10A, β=0°, 400rpm).

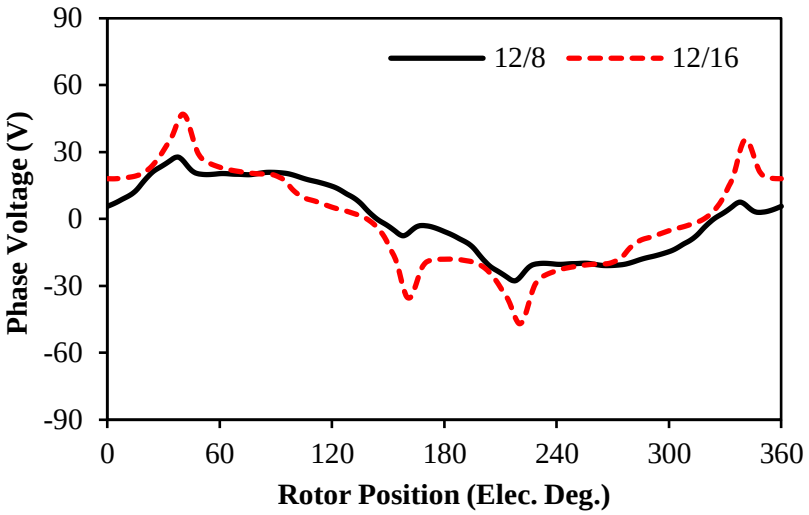

(a) Terminal phase voltages

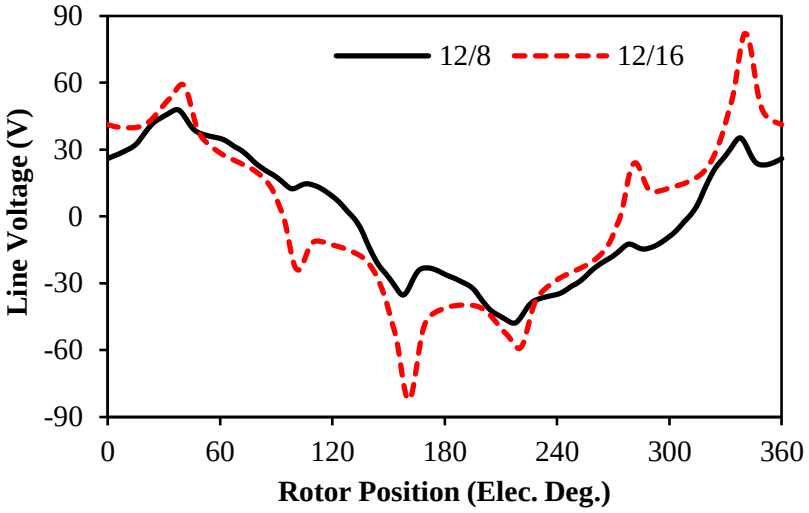

(b) Terminal line voltages

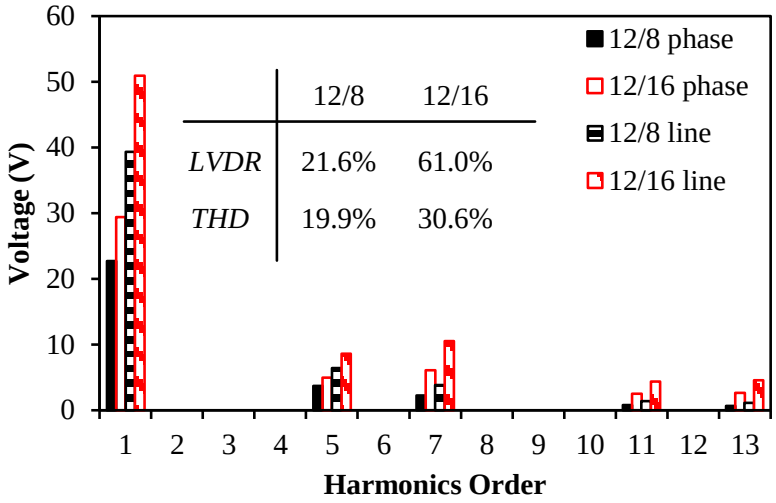

(c) Harmonic components and *LVDRs*

Fig. 3.17 On-load voltage distortion of 12/8 and 12/16 machines (I_{max}=10A, β=0°, 400rpm).

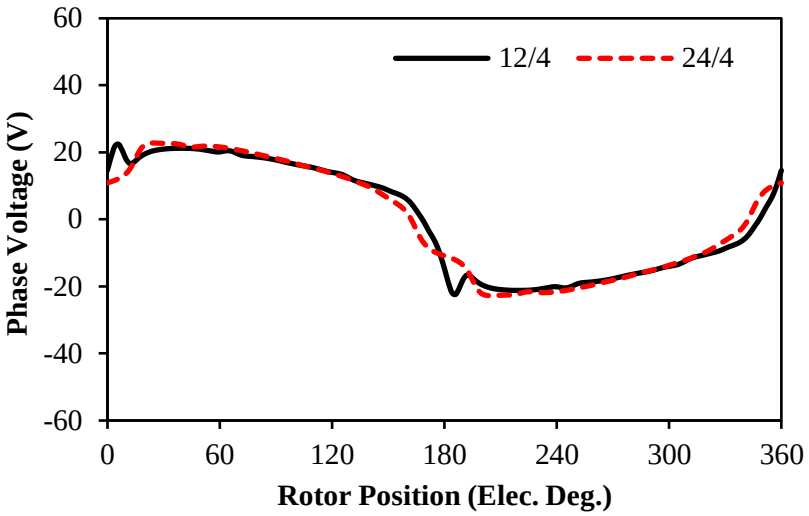

(a) Terminal phase voltages

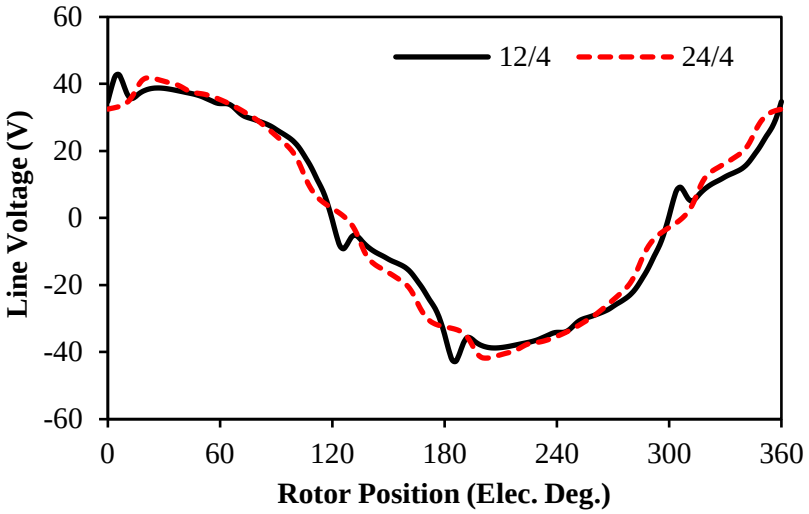

(b) Terminal line voltages

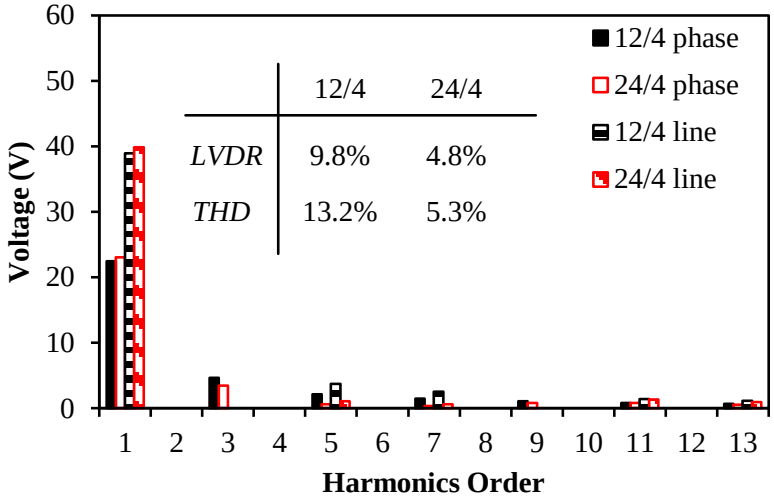

(c) Harmonic components and *LVDRs*

Fig. 3.18 On-load voltage distortion of 12/4 and 24/4 machines (I_{max}=10A, β=0°, 400rpm).

Fig. 3.18(a) compares two integer machines at the same driving current. As predicted by *VDP*, the voltage ripples would only occur at θ_r=0° and 180°. According to the discussions in the aforementioned sections, the PM inter-pole boundaries will not align with any slot openings when phase current crosses zero in the 24/4 machine. Thus, its voltage distortion level will be much smaller compared with the 12/4 machine, Fig. 3.18(b).

All the *LVDR* results can be summarized in Fig. 3.19(a), which reveal that under I_d=0 control, all fractional slot SPM machines with N_s>2p have relative lower voltage distortion level than their counterparts with N_s<2p. Fig. 3.19(b) illustrates that under the same comparison conditions, the integer machines would suffer less from on-load voltage distortion compared with fractional slot machines, especially when q=2. Although the discussion could not include all the possible slot and pole combinations for SPM machines, the investigated results and analysis method could be equally adopted for all SPM machines with small or closed slot openings.

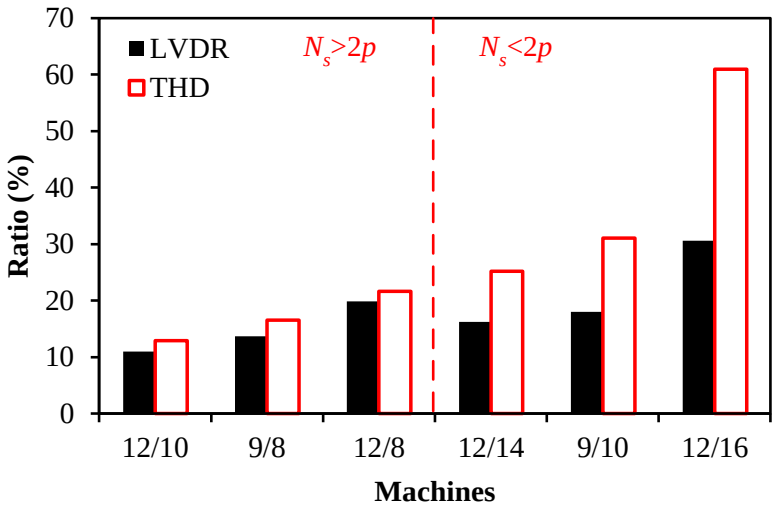

(a) Fractional slot machines in pairs

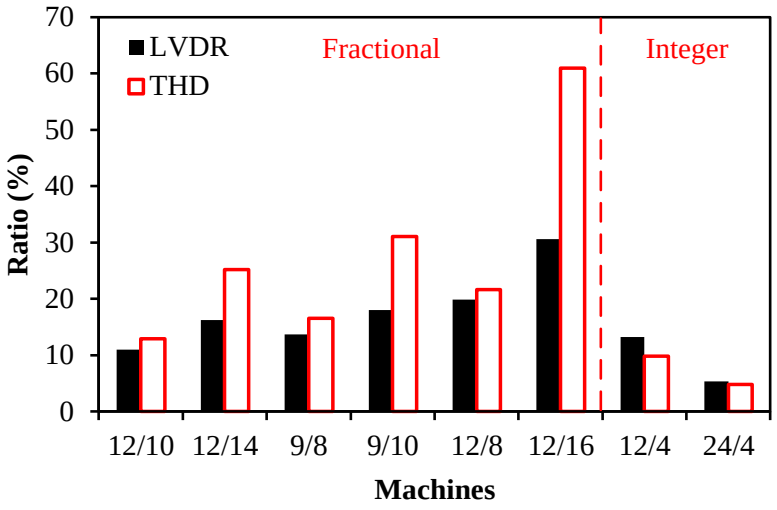

(b) All machines

Fig. 3.19 Comparison of *LVDRs* in all investigated machines (I_{max}=10A, β=0°, 400rpm).

3.4.2 Under Flux Weakening Operation

When considering the flux weakening operation, the voltage distortion for different β will be investigated. Fig. 3.20 (a) shows the variation of *LVDR* and *THD* for the 12/10 machine with different β. Since the local magnetic saturation releases with the increases of β, *LVDR* reduces at first. However, the voltage ripples occurring positions also change with β, the negative voltage ripples make *LVDR* increase again when β approaches 90°, which can be seen clearly in Fig. 3.21(a). When β=90°, the fundamental voltage is relative small. Thus, only tiny distorted voltage will generate obvious *LVDR*. This phenomenon can be reflected more clearly in the 12/14 machine, Fig. 3.20(b). Since two machines have similar flux paths, the relative less flux per pole in the 12/14 machine enhances its flux weakening performance. Thus, when β=90°, the armature field completely cancels the PM field and generates negative terminal phase voltage in Fig. 3.21(b). Due to negative voltage ripples at the same time, the overall *LVDR* becomes even more obvious than the 12/10 machine.

Fig. 3.22 compares voltage distortion levels for 9/8 and 9/10 machines. With the increase of β, *LVDR* for both machines decrease. As analysed in Section 3.3.3, the 9/8 and 9/10 machines suffer less from terminal voltage distortion due to higher q_e. Thus, the influence of negative voltage ripples when β=90° could be negligible, as can be revealed in Fig. 3.23.

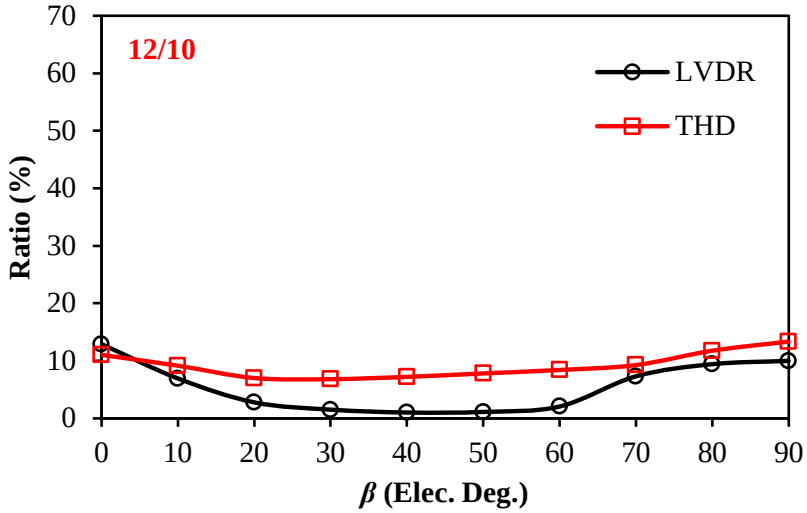

(a) 12/10 machine

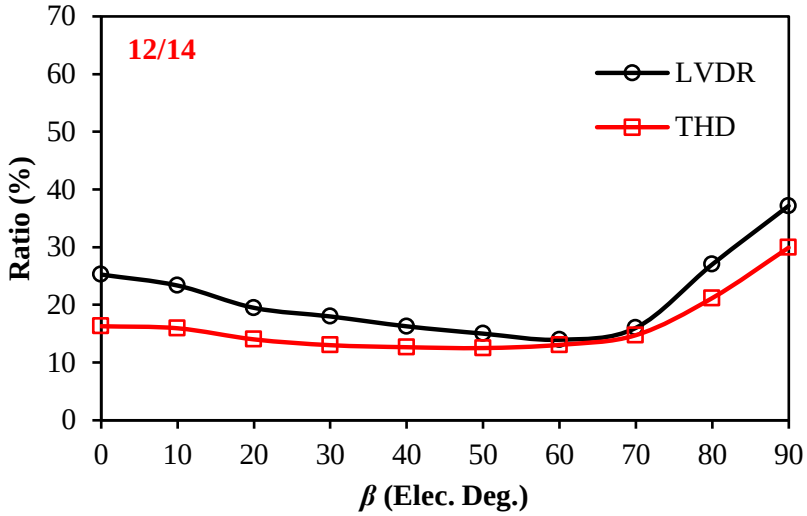

(b) 12/14 machine

Fig. 3.20 Comparison of *LVDR* and *THD* for 12/10 and 12/14 machines (I_{max}=10A, 400rpm).

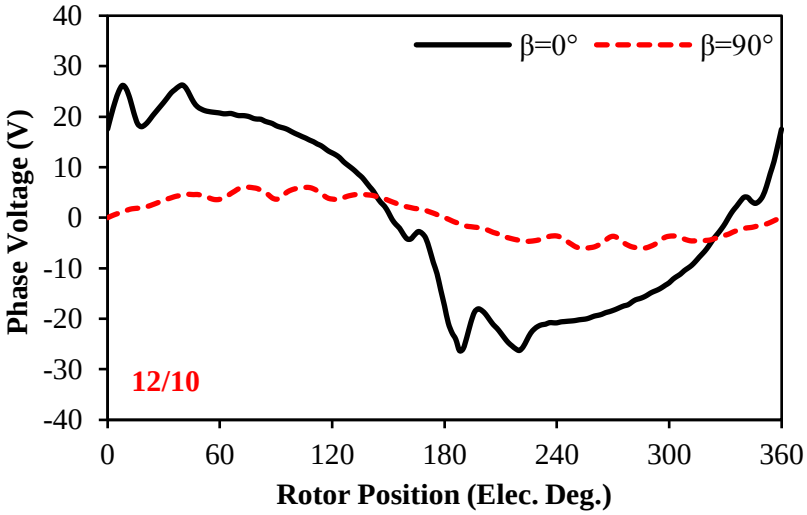

(a) 12/10 machine

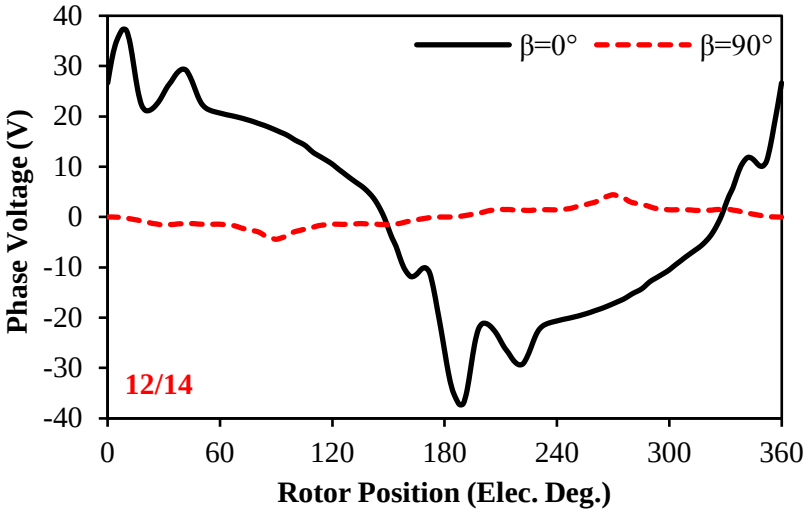

(b) 12/14 machine

Fig. 3.21 Comparison of terminal phase voltage waveforms under different current conditions (I_{max}=10A, 400rpm).

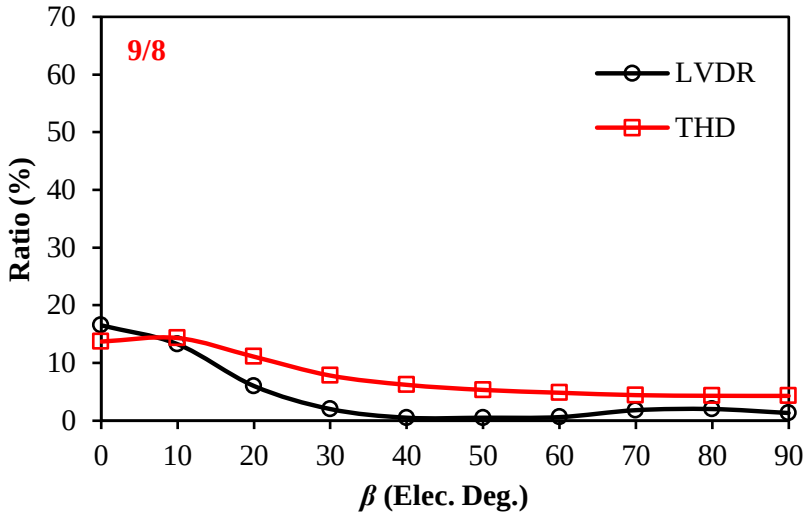

(a) 9/8 machine

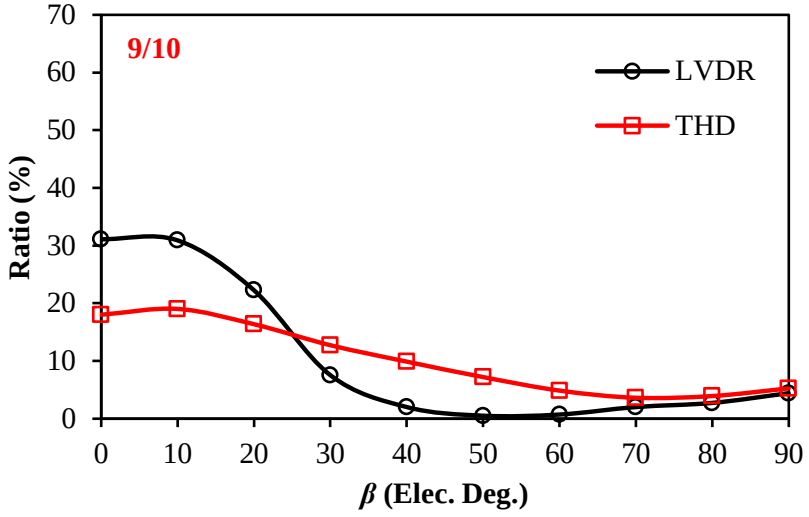

(b) 9/10 machine

Fig. 3.22 Comparison of *LVDR* and *THD* for 9/8 and 9/10 machines (I_{max}=10A, 400rpm).

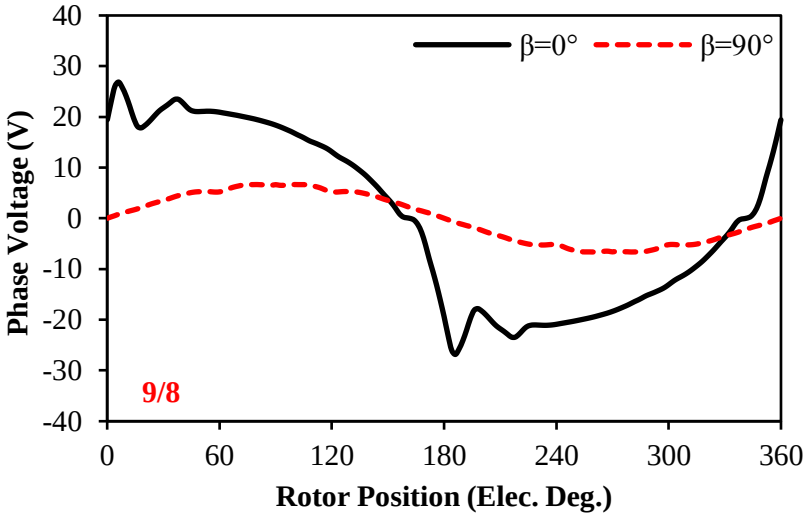

(a) 9/8 machine

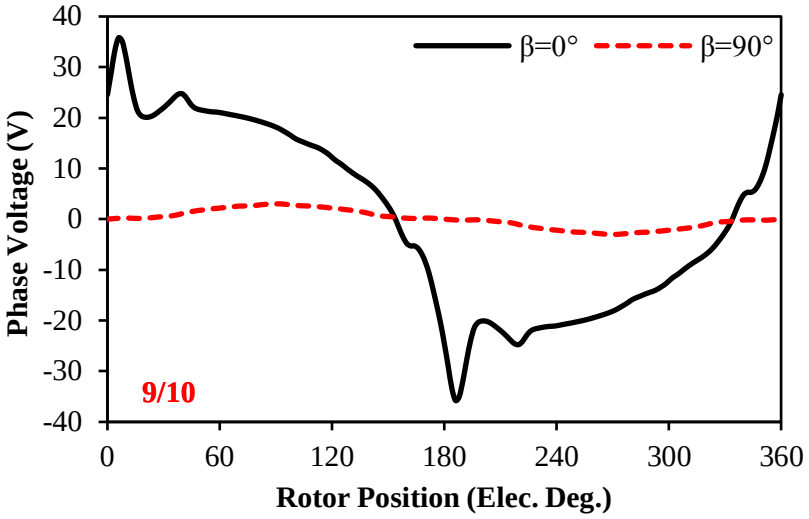

(b) 9/10 machine

Fig. 3.23 Comparison of terminal phase voltage waveforms under different current conditions (I_{max}=10A, 400rpm).

Fig. 3.24(a) shows the voltage distortion level against β of the 12/8 machine. Similar to that in the 12/10 machine, *LVDR* will reduce firstly, and then increase when β approaches 90°. Since the 12/8 machine suffers more from on-load voltage distortion due to local magnetic saturation, its negative voltage ripples, i.e. the voltage drops, when β=90° are more obvious as revealed in Fig. 3.25(a), which leads to higher *THD* compared with the aforementioned four machines. Although the voltage distortion for the 12/16 machine is the highest compared with other machines when β=0°, its *LVDR* and *THD* are relatively small when β=90°, Fig. 3.24(b). When θ_r=60° and β=90°, the slot current (i_A-i_C) crosses zero, which generates a voltage ripple for both 12/8 and 12/16 machines. As shown in Fig. 3.26(a), the relative tooth-

tips (marked with arrow) in the 12/8 machine are at low saturation level, which increases the variation of leakage flux and generates significant negative voltage ripple at θ_r=60°, Fig. 3.25(a). However, in the 12/16 machine in Fig. 3.26(b), the associated tooth-tips (marked with arrow) for the same slot are highly saturated by PM leakage flux, which reduces the fluctuation of tooth-tip leakage fluxes and results in small voltage ripples, Fig. 3.25(b). Therefore, such negligible voltage ripples lead to small *LVDR* and *THD* for the 12/16 machine when β approaches 90°.

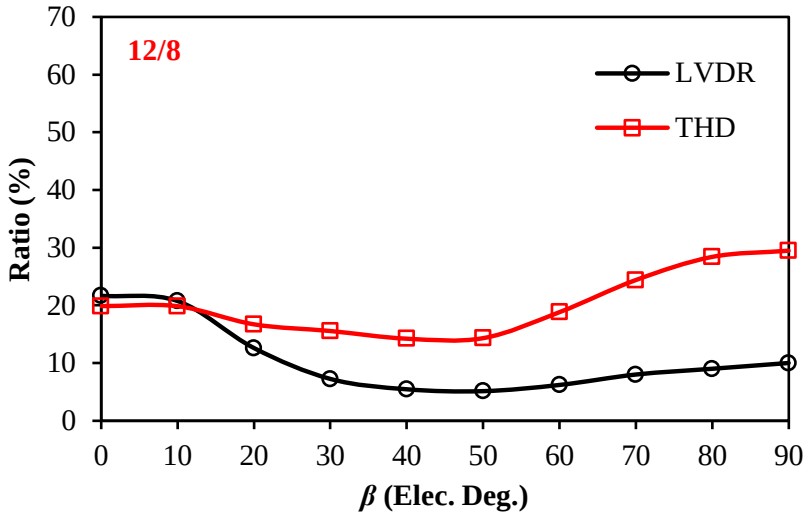

(a) 12/8 machine

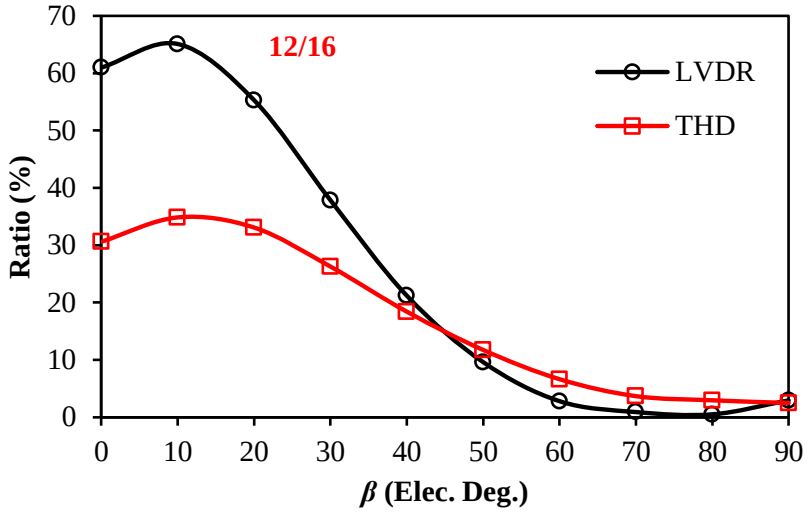

(b) 12/16 machine

Fig. 3.24 Comparison of *LVDR* and *THD* for 12/8 and 12/16 machines (I_{max}=10A, 400rpm).

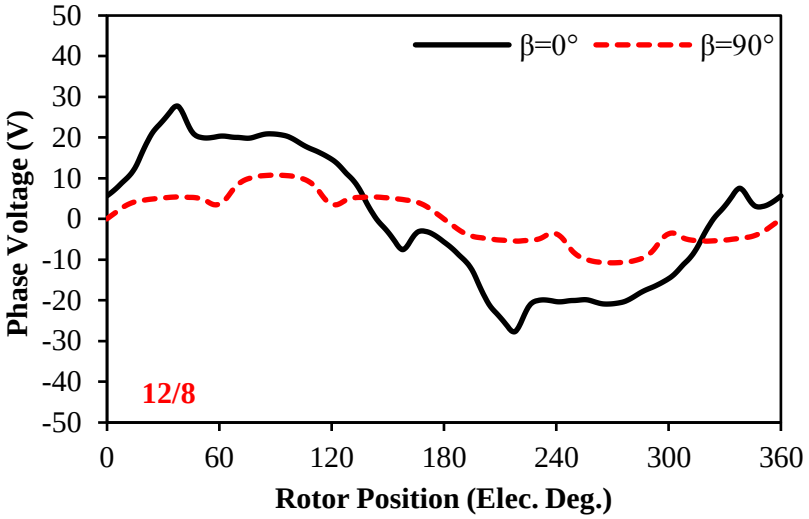

(a) 12/8 machine

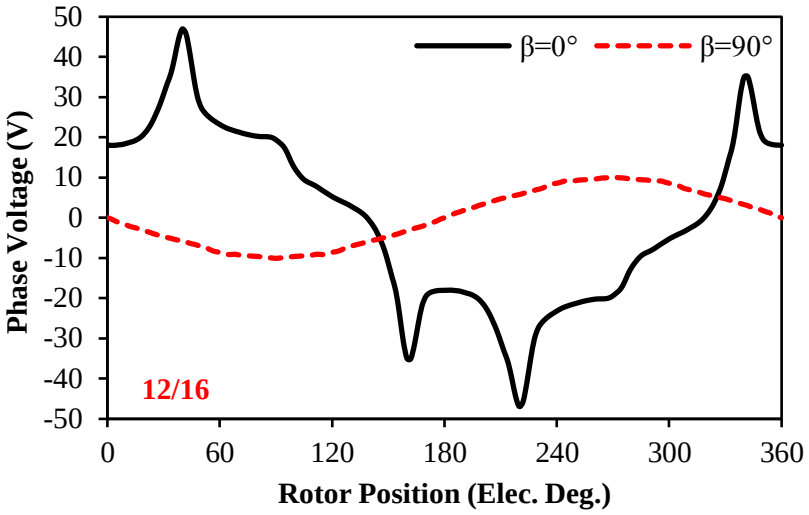

(b) 12/16 machine

Fig. 3.25 Comparison of terminal phase voltage waveforms under different current conditions (I_{max}=10A, 400rpm).

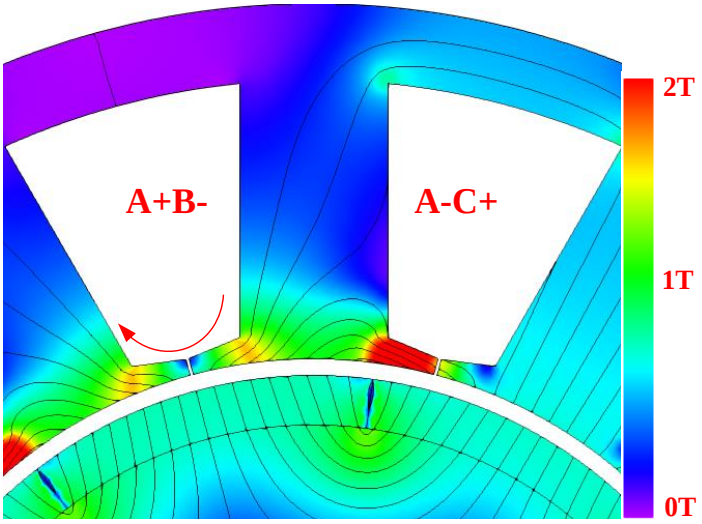

(a) 12/8 machine

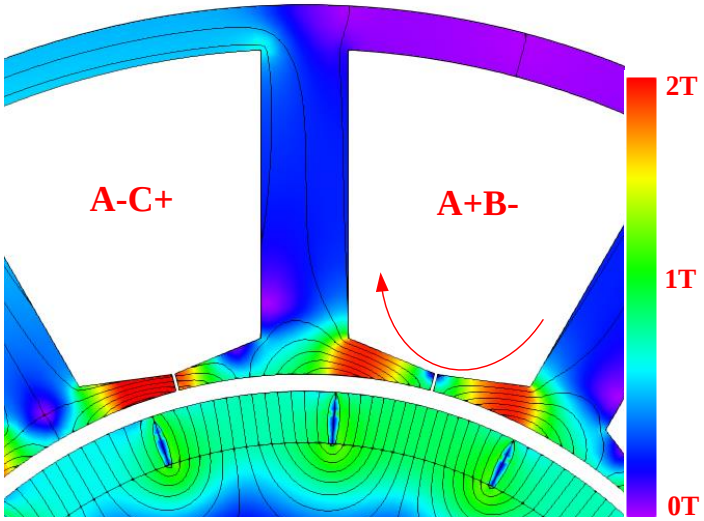

(b) 12/16 machine

Fig. 3.26 Comparison of tooth-tip saturation when slot current reversing (I_{max}=10A, β=90°, θ_r=60°)

Fig. 3.27 shows the *LVDR* and *THD* of the 12/4 and 24/4 machines. Unlike fractional slot machines, the *LVDR* of two integer slot machines reaches the peaks around β=60°, and then reduces to almost zero when β reaches 90°. Since there are only Type I slots in the 12/4 and 24/4 machines, all coil sides in the same phase will generate voltage ripples at the same time. Thus, with the increase of β, the amplitudes of voltage ripples do not significantly reduce as that in the fractional slot machines. Meanwhile, the *LVDR* of the integer slot machines are significantly influenced by the positions where the voltage ripples occur, which can be seen in Fig. 3.28 and Fig. 3.29. Due to this reason, the variation trend of *LVDR* in the 24/4 machine is similar as that in the 12/4 machine, although its local magnetic saturation and voltage distortion levels are much smaller.

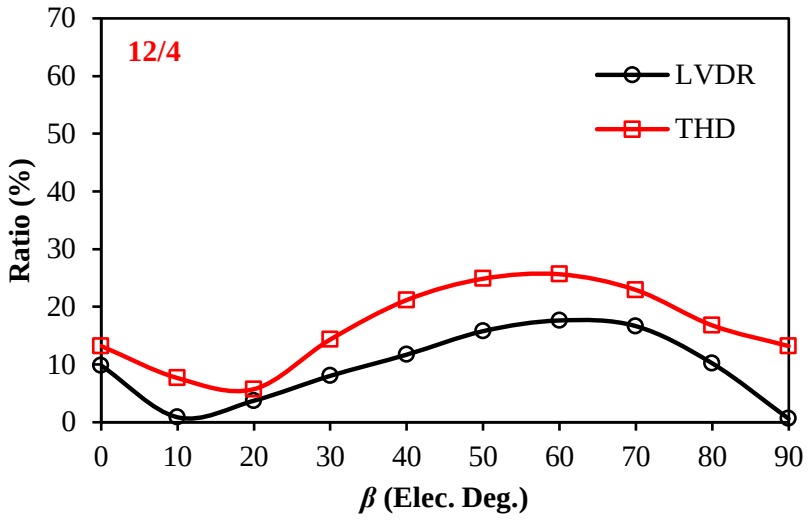

(a) 12/4 machine

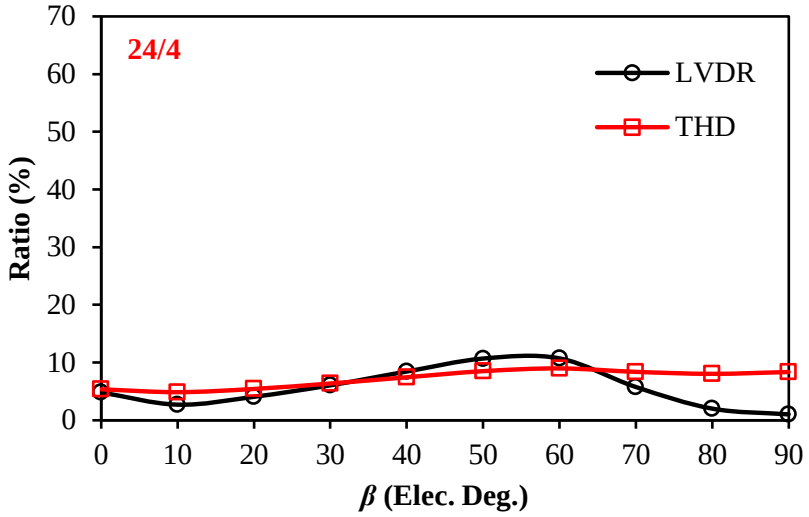

(b) 24/4 machine

Fig. 3.27 Comparison of *LVDR* and *THD* for 12/8 and 12/16 machines (I_{max}=10A, 400rpm).

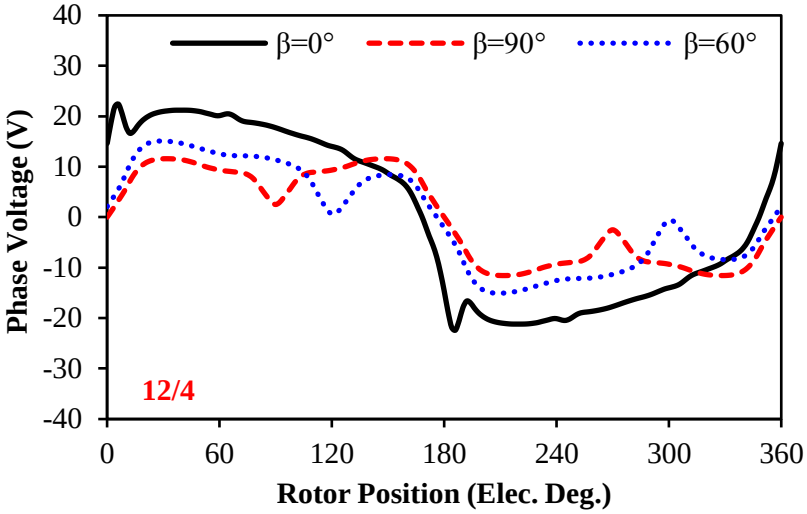

(a) Phase voltages

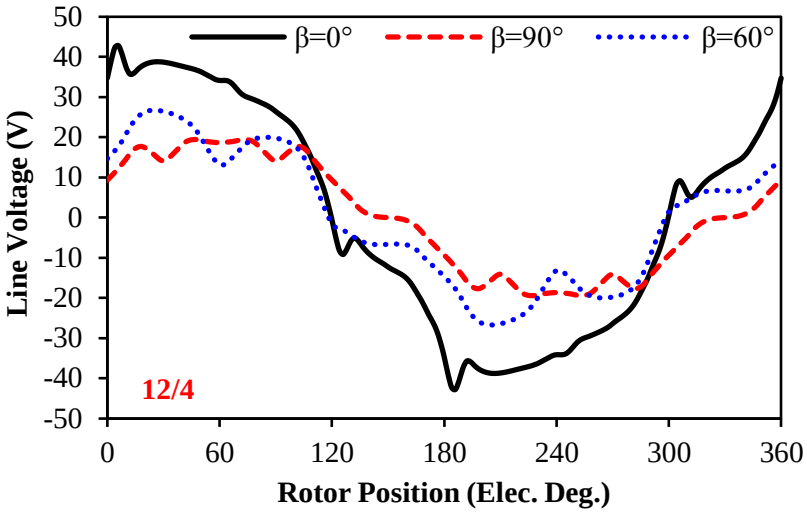

(b) Line voltages

Fig. 3.28 Comparison of terminal phase voltage waveforms of 12/4 machine at different current conditions (I_{max}=10A, 400rpm).

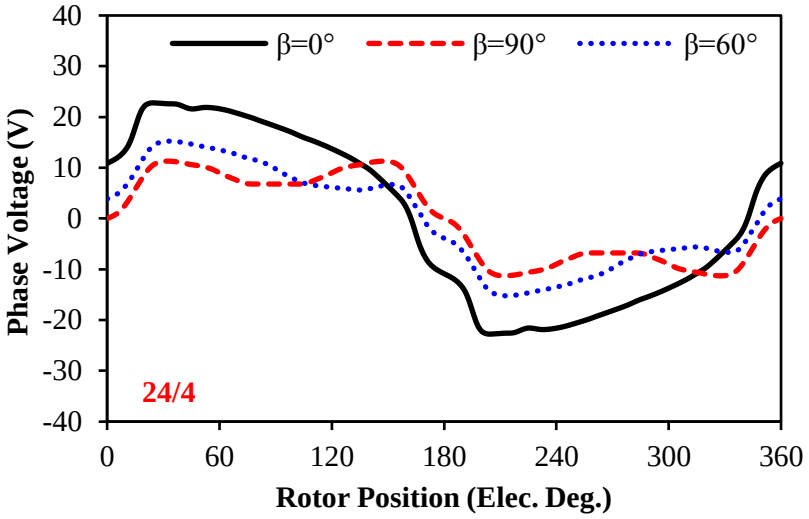

(a) Phase voltages

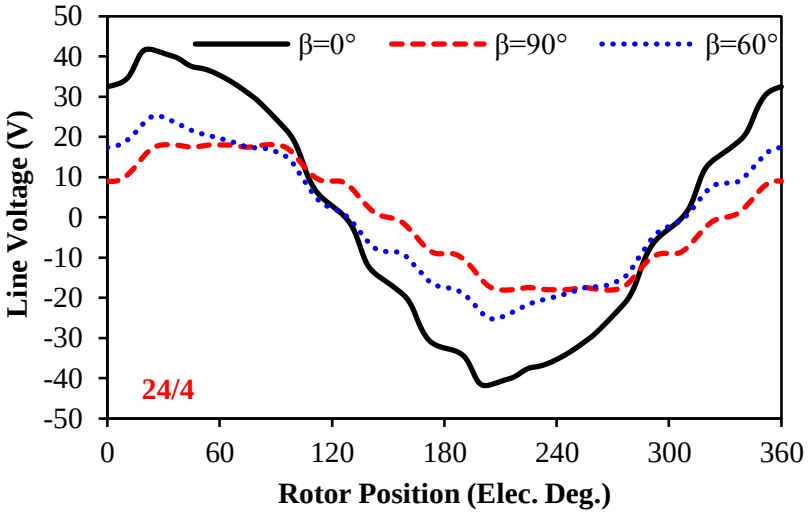

(b) Line voltages

Fig. 3.29 Comparison of terminal phase voltage waveforms of 24/4 machine at different current conditions (I_{max}=10A, 400rpm).

The *LVDR* for all machines can be compared in Fig. 3.30 under the rated current. It can be seen that the machines appearing in pairs, e.g. sharing the same winding arrangement and *VDP*, have the same variation trend of *LVDR*. For fractional slot machines, the one with N_s>2p has higher *LVDR* in the flux weakening region than their counterparts with N_s<2p, which is similar to that for constant torque operation. Meanwhile, the integer slot machines may suffer more from voltage distortion in flux weakening regions compared with fractional slot machines. The influence of voltage distortion on the machine performance will be investigated in the next section.

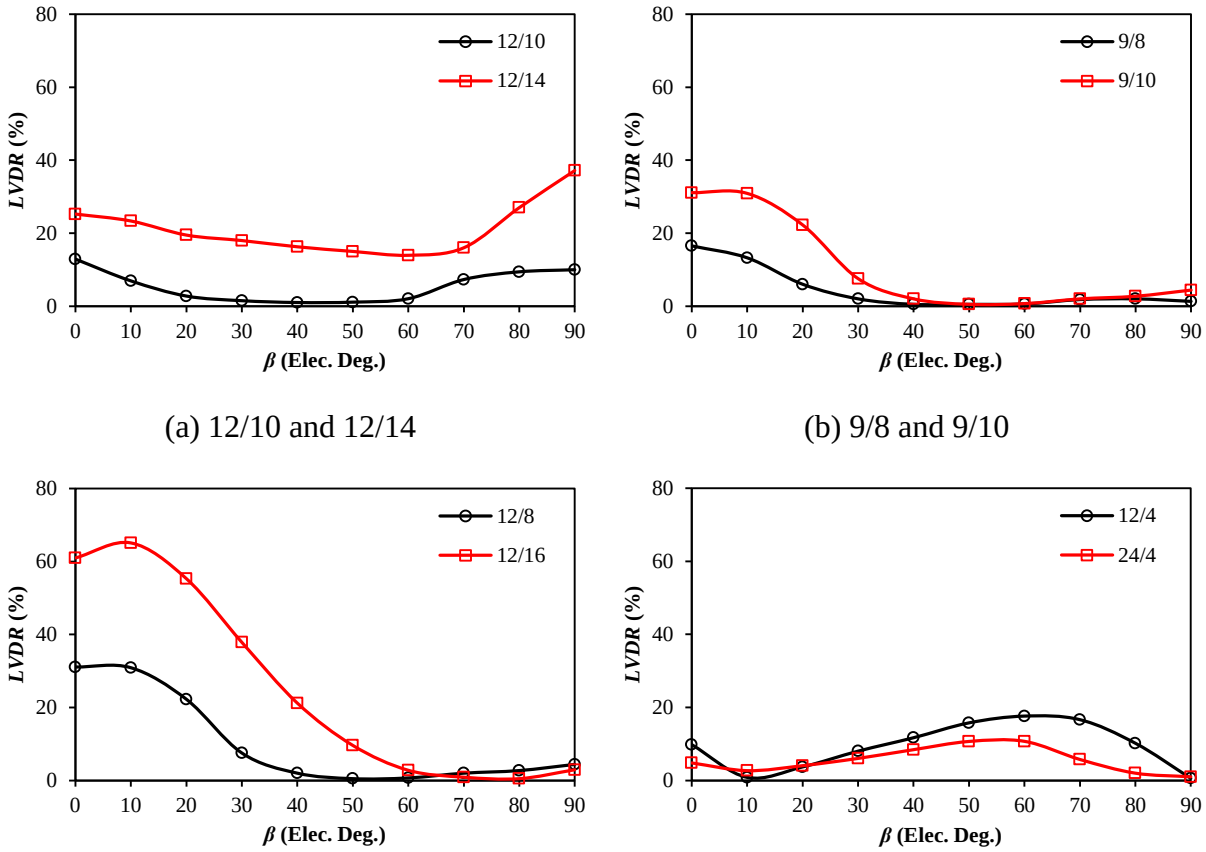

(a) 12/10 and 12/14

(b) 9/8 and 9/10

(c) 12/8 and 12/16

(d) 12/4 and 24/4

Fig. 3.30 Comparison of *LVDR* against β for different slot and pole number combinations (I_{max}=10A, 400rpm).

3.5 Comparison of Electromagnetic Performance Influenced by Voltage Distortion and Local Magnetic Saturation

3.5.1 On-Load Back-EMF

As shown in Section 3.2, all investigated machines are adjusted to obtain the same fundamental value of open-circuit back-EMFs at rated speed. Thus, the difference between on-load and open-circuit back-EMFs could reflect the voltage distortion level and local magnetic saturation for a specific machine. By FP method, the on-load back-EMFs for all machines could be calculated and compared in Fig. 3.31, in which the OC refers to open-circuit. When β=0°, the 12/16 machine has the most significant difference between on-load and open-circuit back-EMFs both in shape and fundamental value, which validate its most significant voltage distortion level under the same current, Fig. 3.19. Since the 24/4 machine has the smallest *LVDR* under the rated current, its on-load back-EMF is almost the same as the open-circuit one. Meanwhile, the harmonic winding factors also influence the harmonics

on on-load back-EMFs, since 5th and 7th harmonics in the 12/8, 12/16 and 12/4 machines are much higher than other machines, their 5th and 7th harmonics in the on-load back-EMFs are relatively larger as well.

On the other hand, the fundamental back-EMFs for β=90° condition are higher than the open-circuit values for all machines. Under flux weakening operation, the *d*-axis armature flux becomes more dominant for the local magnetic saturation due to large equivalent air-gap in SPM machines, which consequently reduces the tooth-tip PM leakage flux. Further, with the increase of β, the saturation in major flux paths also reduces. Thus, the amplitudes of on-load back-EMFs in flux weakening operation are higher than the values under open-circuit condition based on these two reasons. Since the on-load back-EMFs represent the variation of PM flux linkages under load condition, the torque ripples will be influenced as well, which will be investigated later. In order to evaluate the fluctuation of on-load back-EMFs, the *THDs* of on-load line back-EMFs for all machines are compared in Fig. 3.32. It can be seen that besides the 12/8 and 12/16 machines, the *THDs* of other machines do not significantly change with β. Due to small fundamental winding factor for the $N_s/2p$=3/2 (3/4) machines, i.e. 0.866, their winding turns have been increased to maintain the same fundamental back-EMF as other machines. Thus, the more severe local magnetic saturation will be generated under the same currents. Meanwhile, the high harmonic winding factors (0.866 for all $6n\pm1$ harmonics) in the 12/8 and 12/16 machines also increase the harmonics in back-EMFs. Therefore, the *THDs* in the two machines change more obviously than other machines.

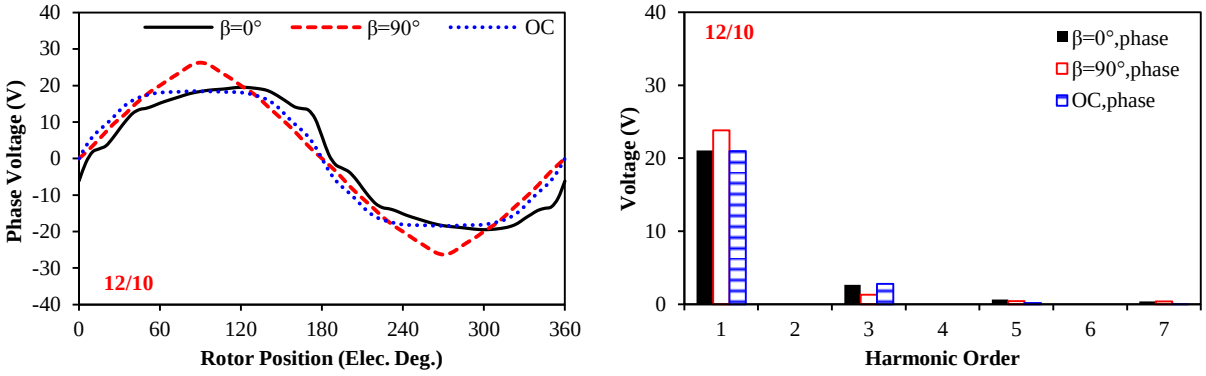

(a) 12/10 machine

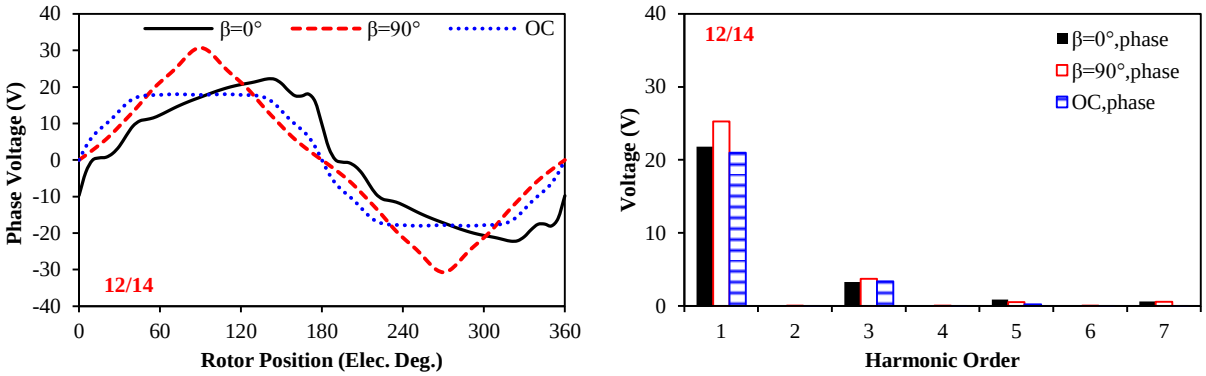

(b) 12/14 machine

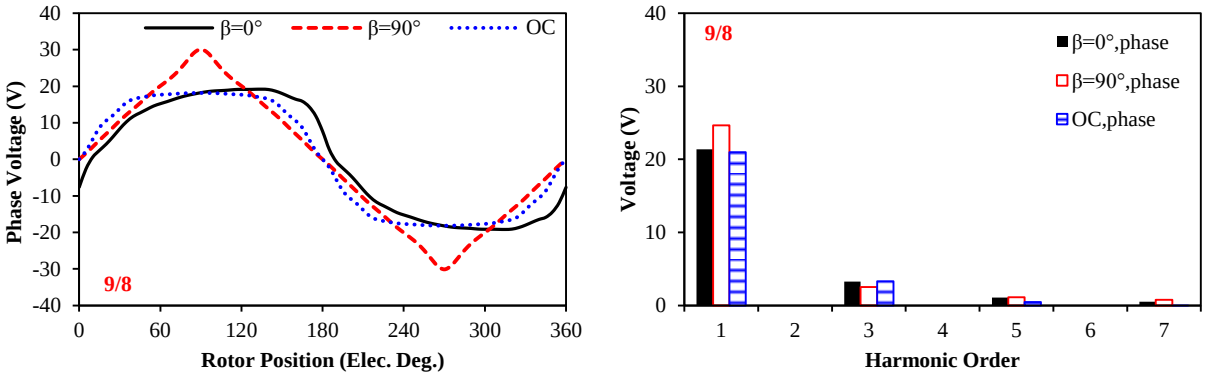

(c) 9/8 machine

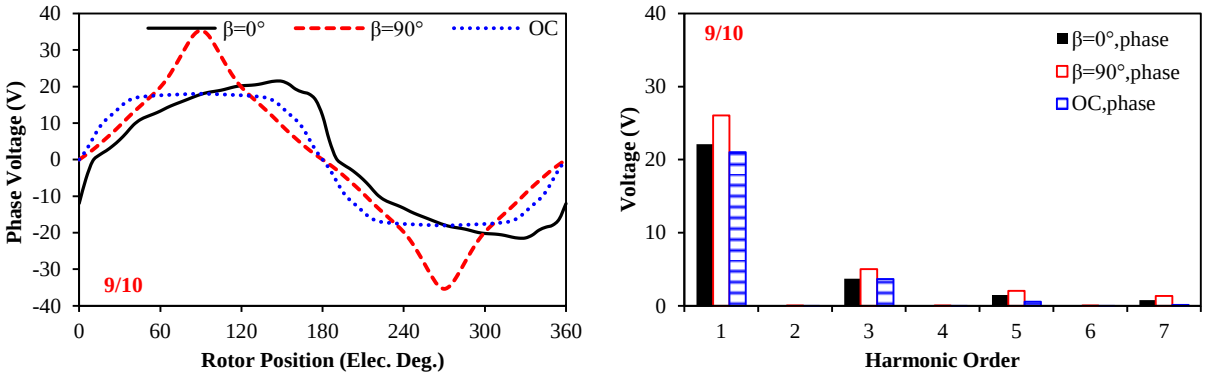

(d) 9/10 machine

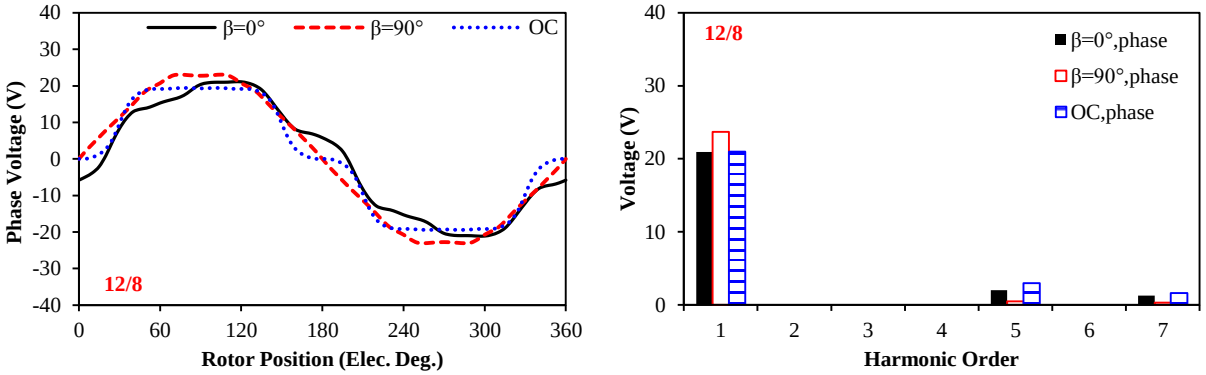

(e) 12/8 machine

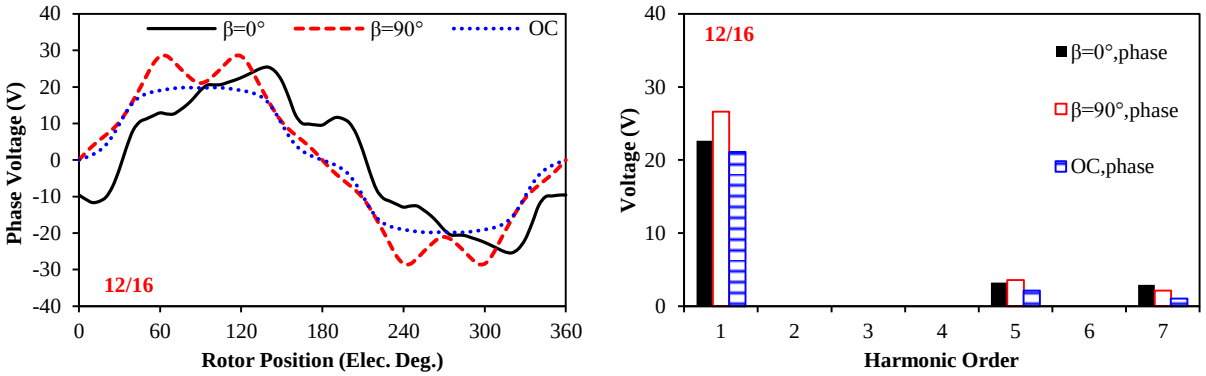

(f) 12/16 machine

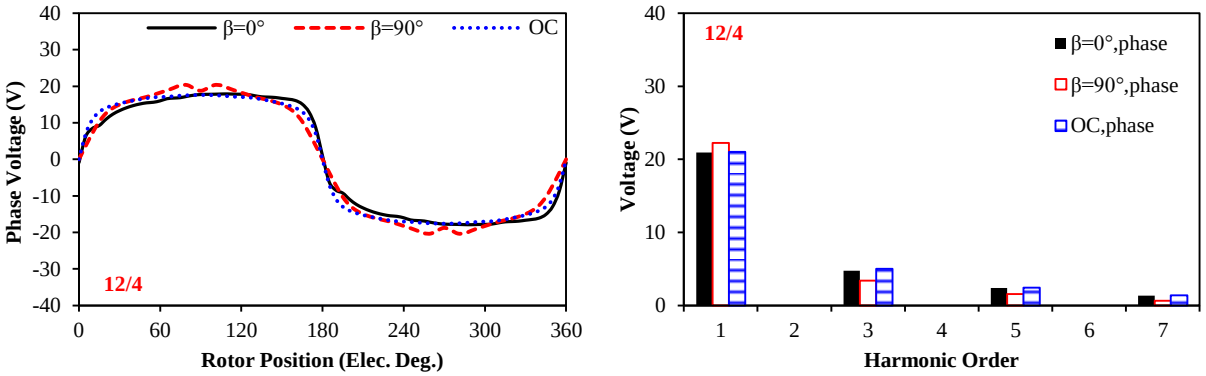

(g) 12/4 machine

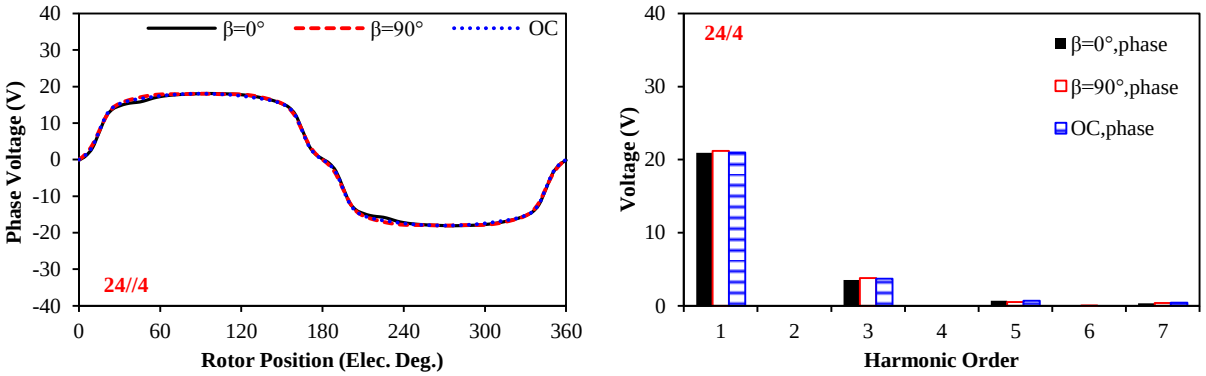

(h) 24/4 machine

Fig. 3.31 Comparison of on-load phase back-EMFs for machines with different slot and pole number combinations (I_{max}=10A, 400rpm).

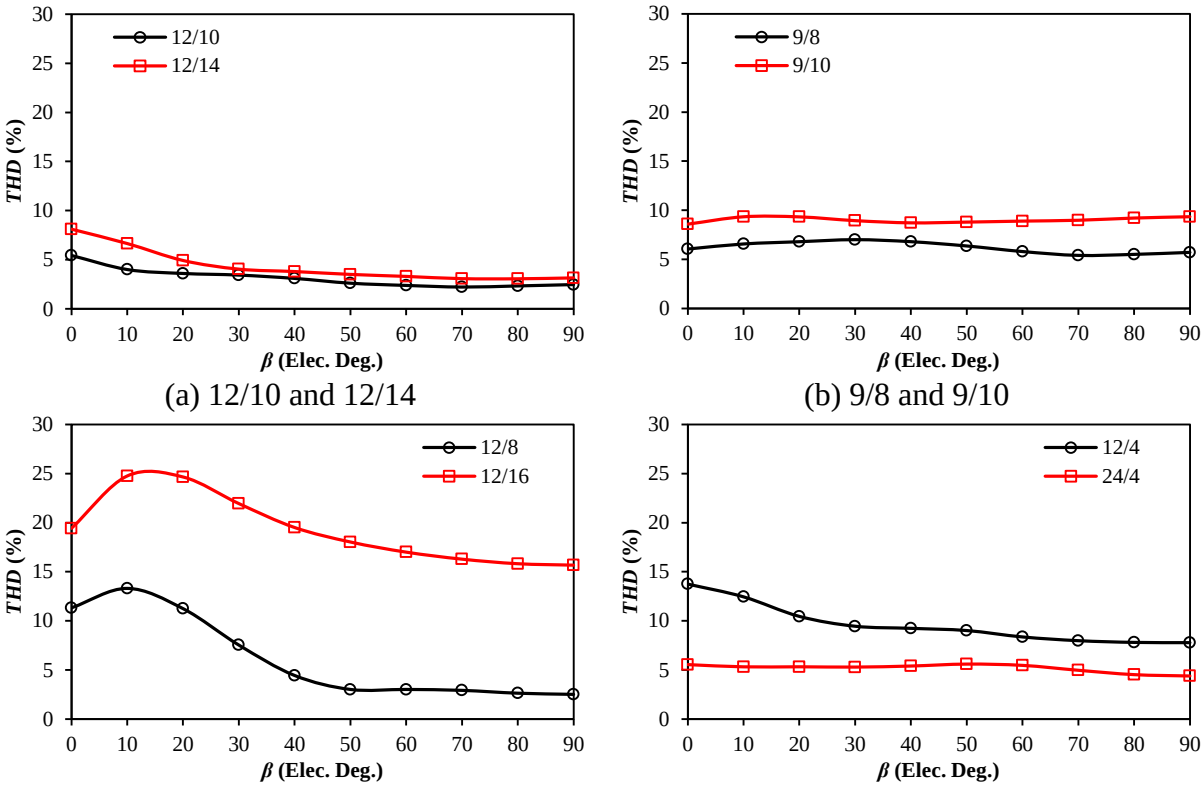

(a) 12/10 and 12/14 (b) 9/8 and 9/10

(c) 12/8 and 12/16 (d) 12/4 and 24/4 machine

Fig. 3.32 Comparison of on-load line back-EMF *THD* against β for machines with different slot and pole number combinations (I_{max}=10A).

3.5.2 On-Load Cogging Torque

With the aid of FP method, the on-load cogging torque can be calculated for all investigated machines under different current conditions in Fig. 3.33. Clearly, the on-load cogging torques are much higher than the open-circuit values especially when β=0°. With the increase of β, the local magnetic saturation also changes, which make peaks of on-load cogging torques occur at different positions as well. According to [ZHU00], machines with different slot and pole number combinations will lead to different cogging torque periods over an electric cycle. However, due to the local magnetic saturation, the on-load cogging torque waveforms for all machines mainly have 6 ripples over an electric period, which do not obey the principle for the open-circuit condition. Meanwhile, if the machine has higher level of local magnetic saturation such as the 12/16 machine, the amplitudes of on-load cogging torque will also be much higher than other machines. This can be revealed more clearly from Fig. 3.34, in which the 24/4 machine has the lowest value similar to that for *LVDR* illustrated in Fig. 3.19. Fig. 3.35 compares the pk-pk cogging torque against β for all investigated machines, which also follow the same trends as their on-load voltage distortion and local magnetic saturation levels.

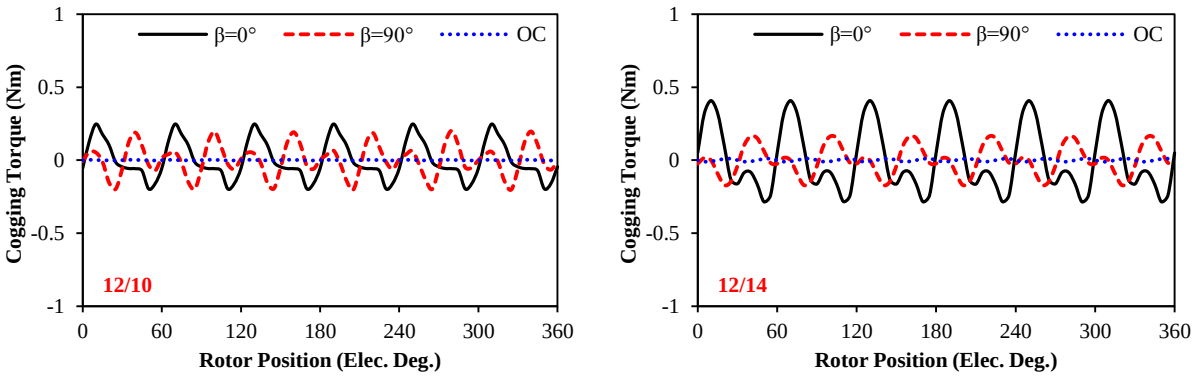

(a) 12/10 machine

(b) 12/14 machine

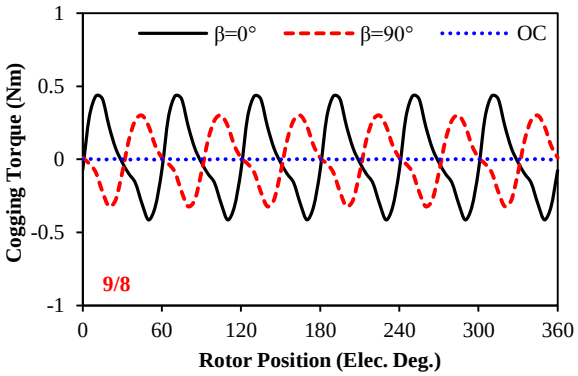

(c) 9/8 machine

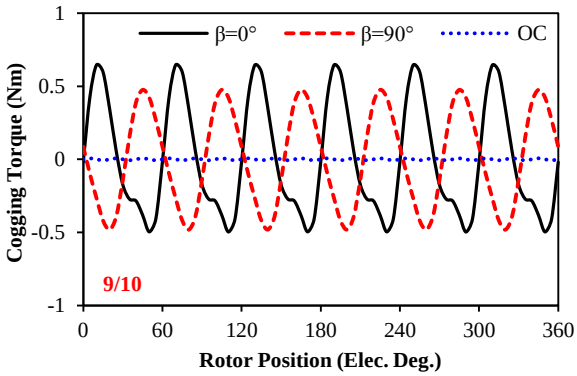

(d) 9/10 machine

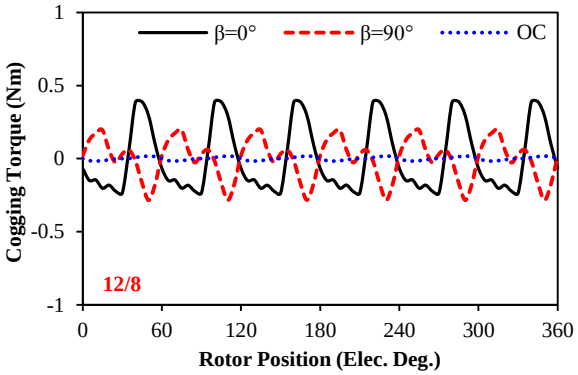

(e) 12/8 machine

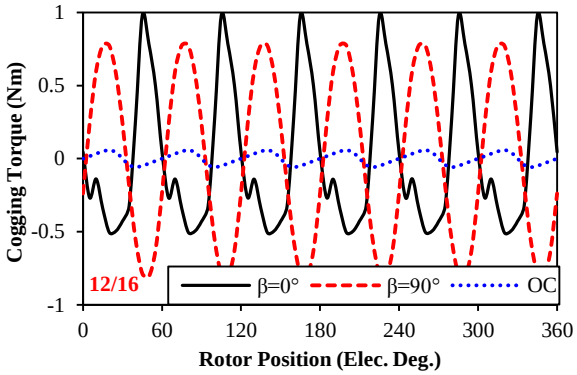

(f) 12/16 machine

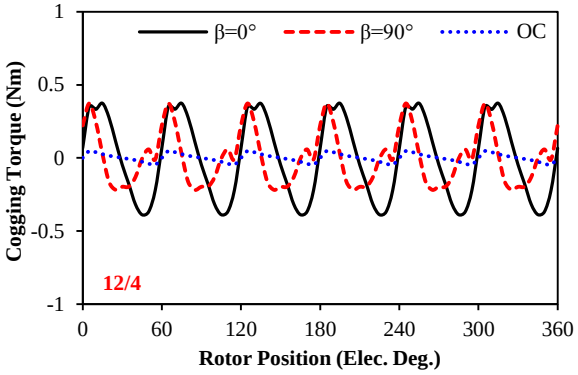

(g) 12/4 machine

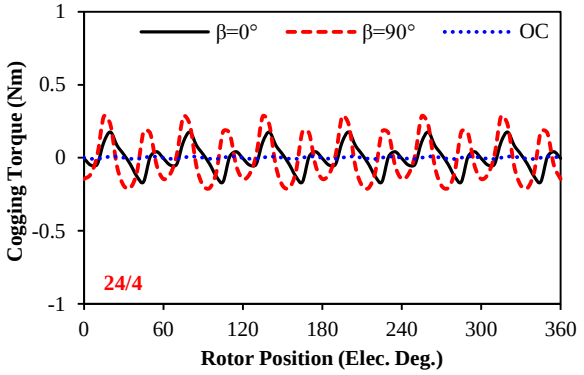

(h) 24/4 machine

Fig. 3.33 Comparison of on-load cogging torque for machines with different slot and pole number combinations (I_{max}=10A).

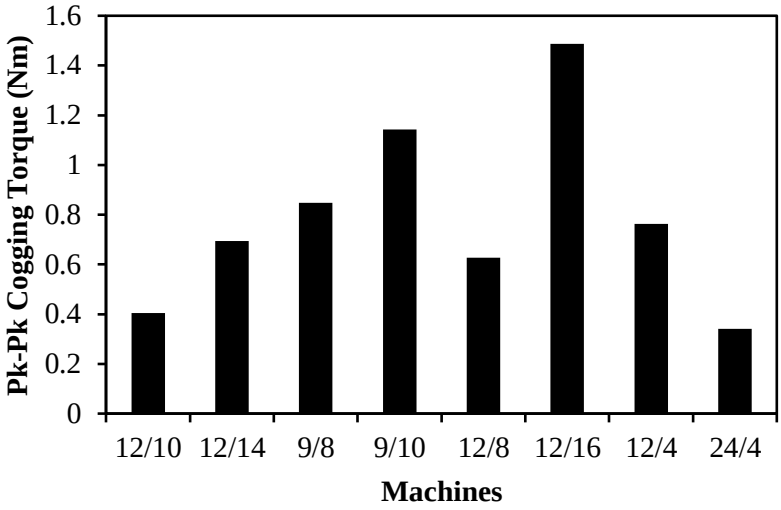

Fig. 3.34 Comparison of on-load cogging torque amplitudes for machines with different slot and pole number combinations (I_{max}=10A, β=0°).

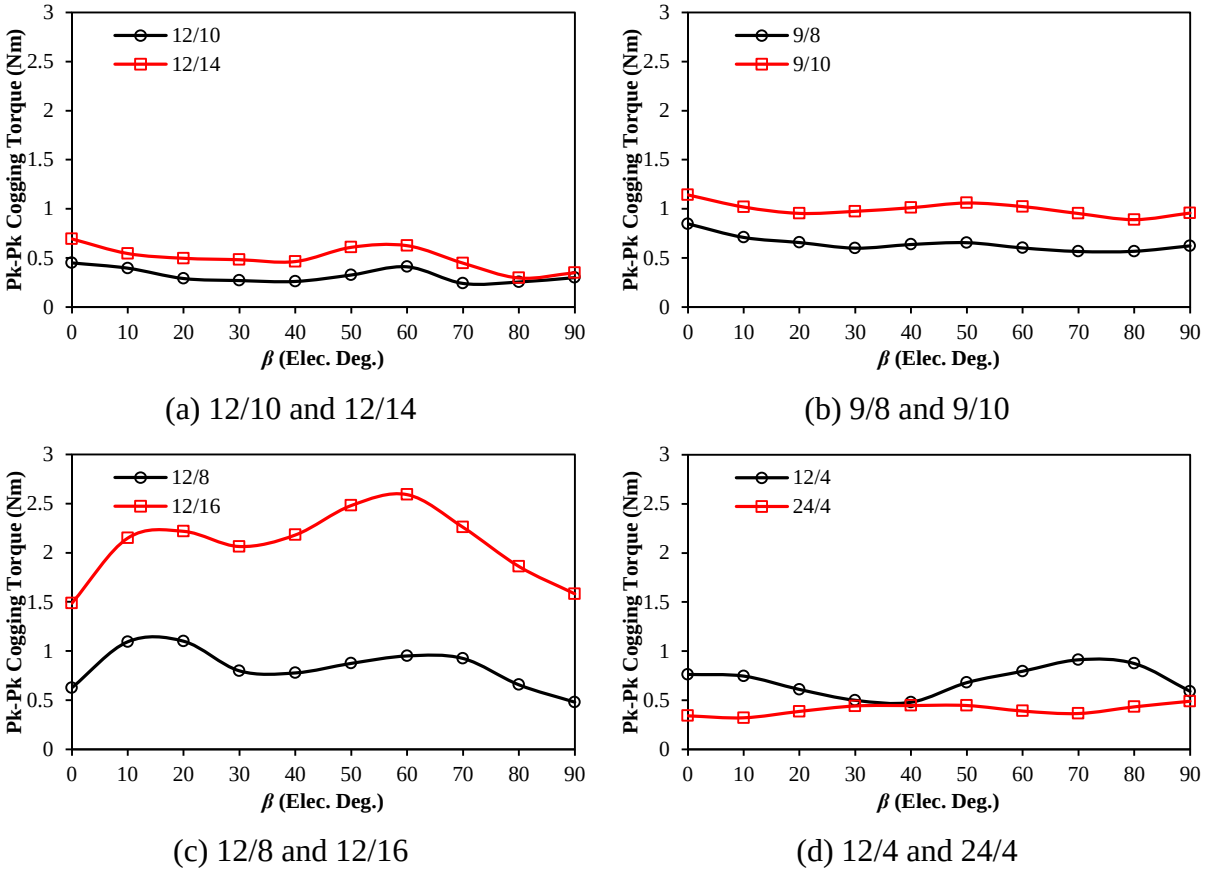

(a) 12/10 and 12/14

(b) 9/8 and 9/10

(c) 12/8 and 12/16

(d) 12/4 and 24/4

Fig. 3.35 Comparison of pk-pk on-load cogging torques against β for machines with different slot and pole number combinations (I_{max}=10A).

3.5.3 DQ-Axis Inductances

By FP method, the *dq*-axis inductance waveforms under different load conditions are calculated in Fig. 3.36. When β=0°, the *q*-axis current saturates the *q*-axis flux paths, which makes the average values of L_q smaller than L_d in all investigated machines. At the same time, there are the obvious 6^{th} inductances ripples which exist in L_q due to the fluctuation of local magnetic saturation, which represent the armature components of terminal voltage distortion as analysed in Chapter 2. With the increase of β, the local magnetic saturation shifts from *q*-axis to *d*-axis, which reveals the tooth-tip saturation time and relative rotor positon will change with β. Therefore, when β=90°, the average values of L_d becomes smaller than L_q. Meanwhile, there are the 6^{th} inductances ripples for L_q when β=90°, which reflect the voltage ripples shift to *q*-axis as well. Since the global saturation is reduced with the increase of β, while the voltage distortion level also reduces with β, the inductance ripples when β=90° are smaller than that for β=0°. Fig. 3.37 illustrates the variation of inductance ripples against β for all investigated machines, which clearly reflect that the shifting process of local magnetic saturation from *d*-axis to *q*-axis. Since the inductance ripples can reflect the terminal voltage distortion, the machine which suffers from higher *LVDR*, e.g. the 12/16 machine, will have higher inductance ripples, while the machine with low *LVDR*, e.g. the 24/4 machine, will have negligible inductance ripples consequently, which are both validated by the inductance ripples, Fig. 3.37.

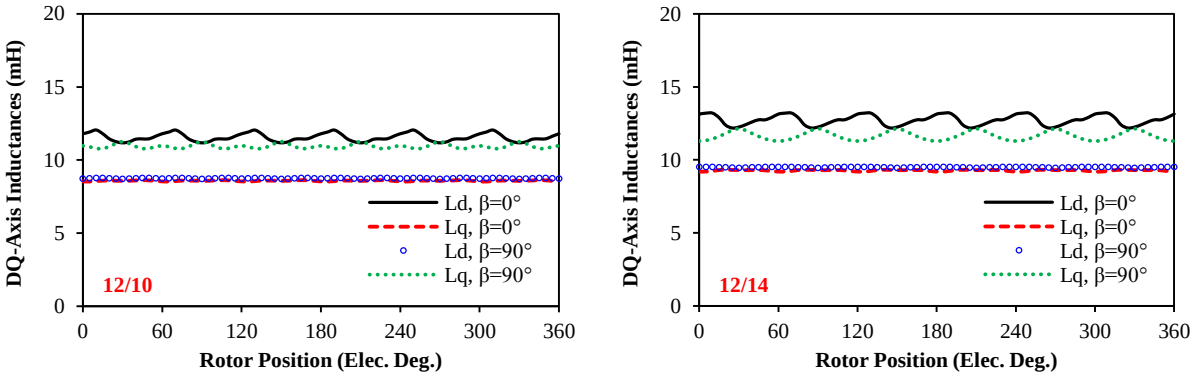

(a) 12/10 machine

(b) 12/14 machine

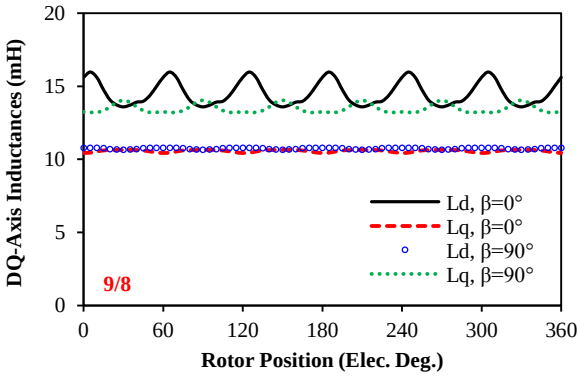

(c) 9/8 machine

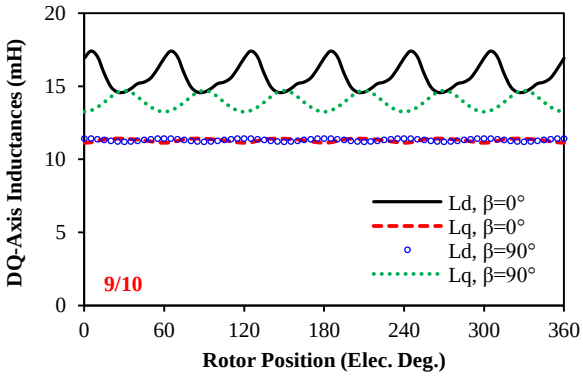

(d) 9/10 machine

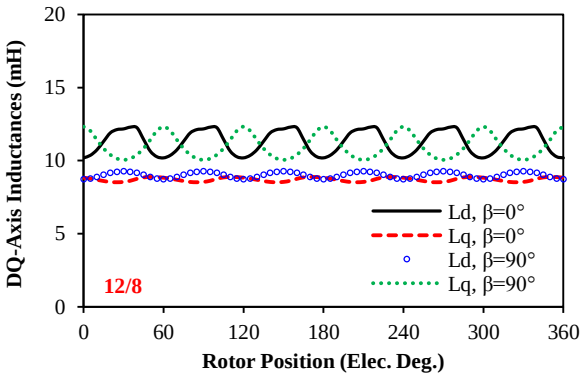

(e) 12/8 machine

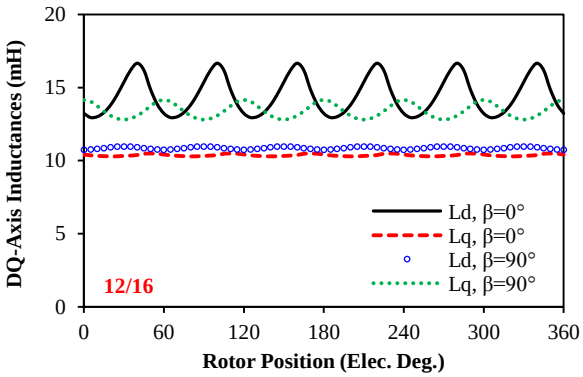

(f) 12/16 machine

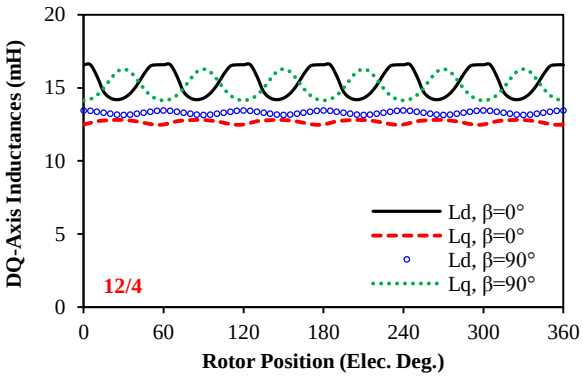

(g) 12/4 machine

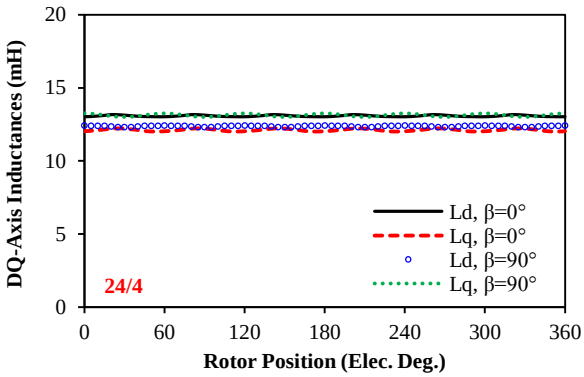

(h) 24/4 machine

Fig. 3.36 Comparison of *dq*-axis inductances waveforms for machines with different slot and pole number combinations (I_{max}=10A).

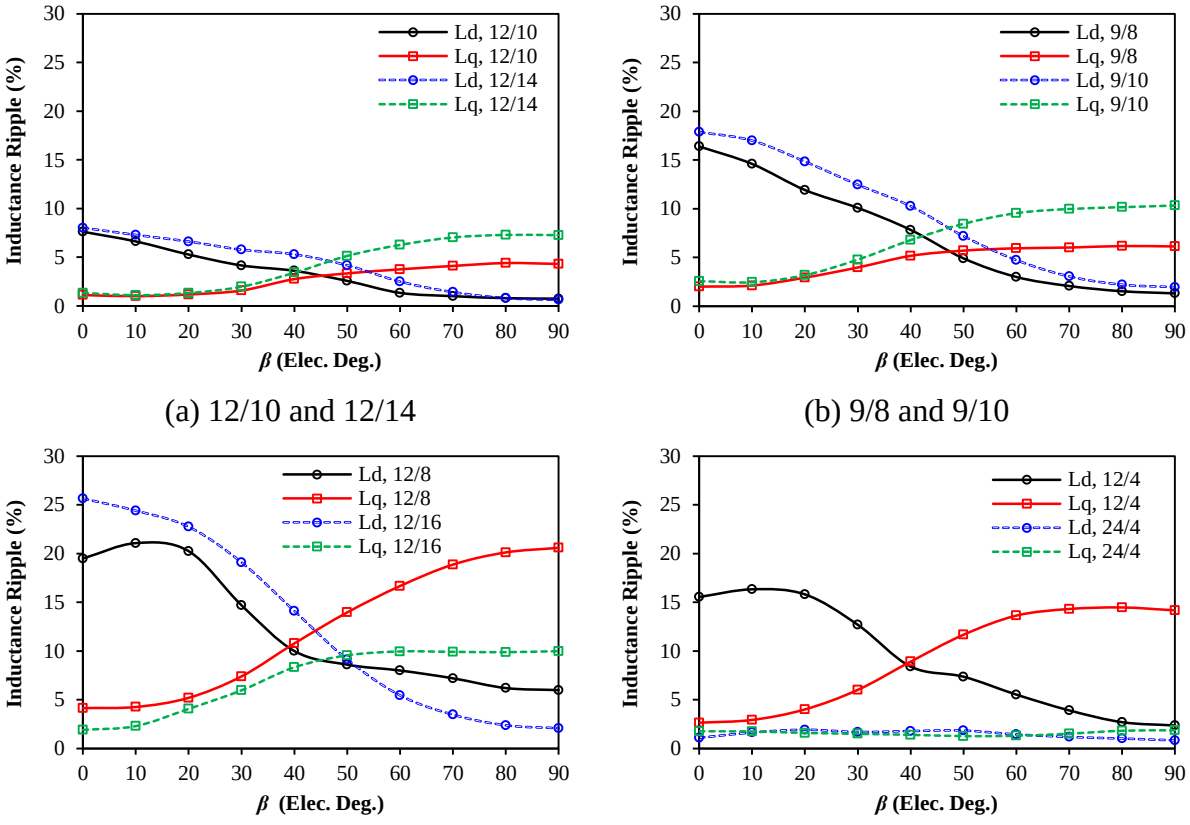

(a) 12/10 and 12/14

(b) 9/8 and 9/10

(c) 12/8 and 12/16

(d) 12/4 and 24/4

Fig. 3.37 DQ-axis inductance ripples against β for machines with different slot and pole number combinations (I_{max}=10A).

3.5.4 Average Torque and Torque Ripple

All the investigated machines are designed to obtain the same fundamental open-circuit back-EMF, their torque capabilities under the same driving current are expected to be the same as well. However, since the rotor inter-pole leakage, such as zigzag leakage [QU04], increases with the pole numbers especially under load operation, the investigated machines with higher pole numbers will obtain lower average torque under I_d=0 control, which can be shown in Fig. 3.38. Meanwhile, the reluctance torque in SPM machines could be negligible, which makes the relation between average torques for different β similar, Fig. 3.39.

As investigated in Section 2.4.3, the torque ripples consist of components of PM torque, reluctance torque, as well as on-load cogging torque. The distortion of PM torque can be represented by the distortion of on-load back-EMF, while the distortion of reluctance torque can be represented by the fluctuation of *dq*-axis inductances. According to the aforementioned analyses, all these components will increase with the increase of voltage

distortion and local magnetic saturation. Thus, the torque ripples can also reflect the level of voltage distortion and local magnetic saturation. Fig. 3.40 shows the variation of pk-pk torque ripple against β for all investigated machines. The machines appearing in pairs have the similar variation trend of torque ripples, while the fractional slot machines with $N_s<2p$ have larger torque ripples at the same β than their counterparts with $N_s>2p$, which is similar to that for on-load voltage distortion. With the increase of β, the 12/16 machine has the largest torque ripple as expected since it suffers most from the local magnetic saturation and voltage distortion. However, the torque ripples for the integer slot machines increase with β, which do not behave like that for *LVDR*. Take the 12/10 and 12/4 machines for examples to explain this phenomenon. Fig. 3.41(a) and Fig. 3.41(b) show the torque waveforms of the 12/10 machine under two different β. Although the torque ripples for each component are large, the resultant torque ripple is small, since the on-load cogging torque are always in opposite phase angle with the PM and reluctance torques, which can be revealed by Fig. 3.41(c) and Fig. 3.41(d). On the contrary, the phase angles between torque components change more significantly with β in the 12/4 machine in Fig. 3.42. When β=0°, the on-load cogging torque in the 12/4 machine still has opposite phase angle with other torque components. However, the phase angles of the PM and reluctance torque change from positive to negative when β=60°. Therefore, all the torque ripples will be added together, which generate large resultant torque ripples.

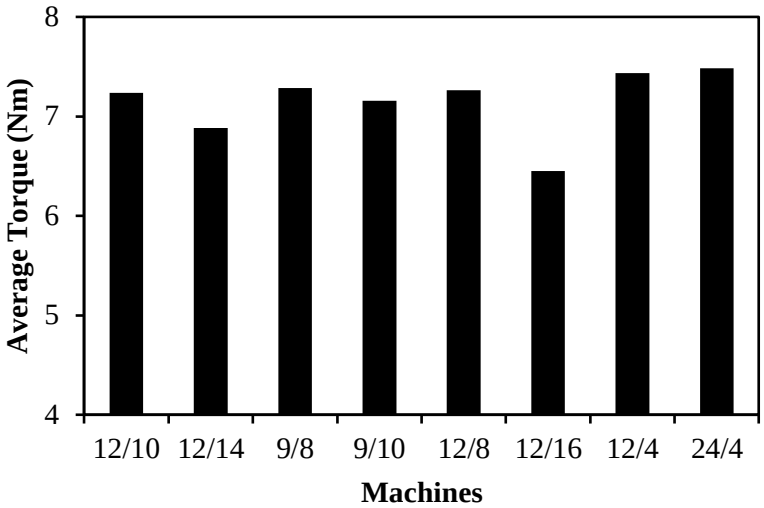

Fig. 3.38 Comparison of average torque for machines with different slot and pole number combinations (I_{max}=10A, β=0°).

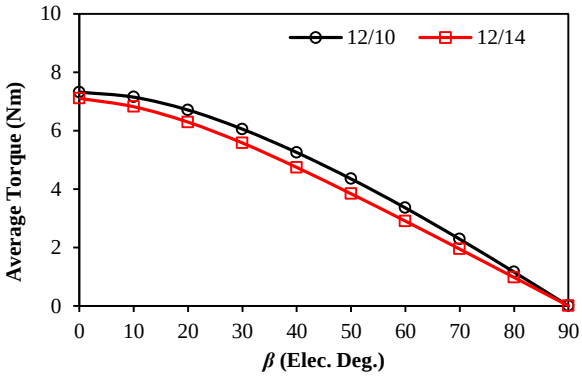

(a) 12/10 and 12/14

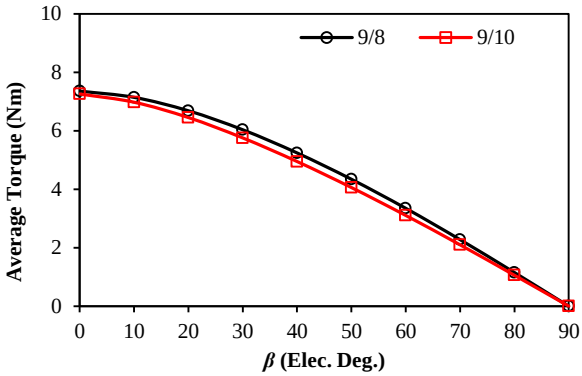

(b) 9/8 and 9/10

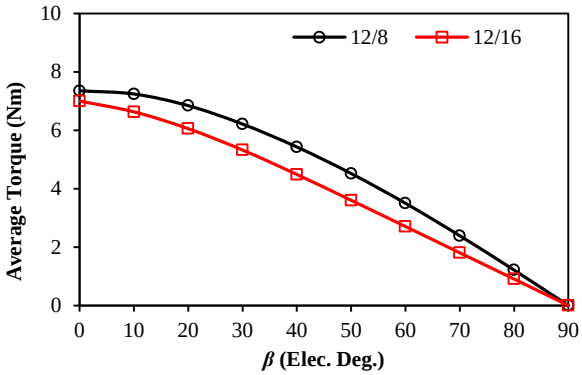

(c) 12/8 and 12/16

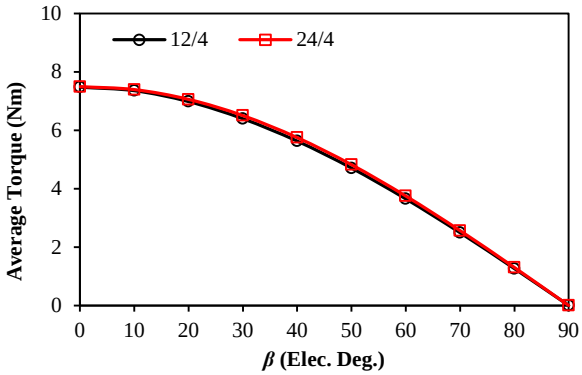

(d) 12/4 and 24/4

Fig. 3.39 Comparison of average torque against β for machines with different slot and pole numbers (I_{max}=10A).

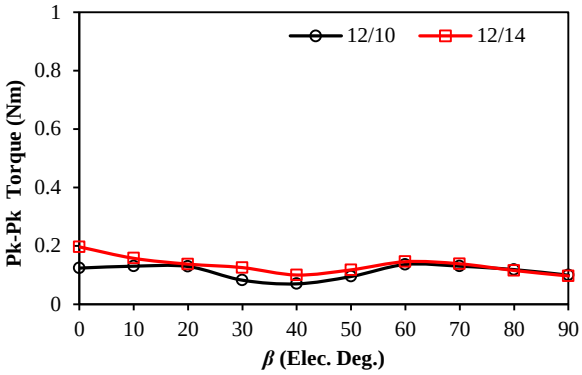

(a) 12/10 and 12/14

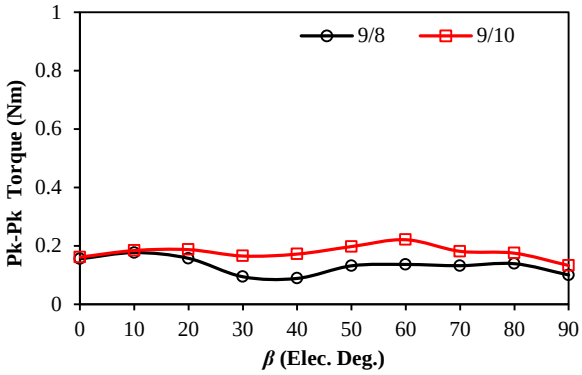

(b) 9/8 and 9/10

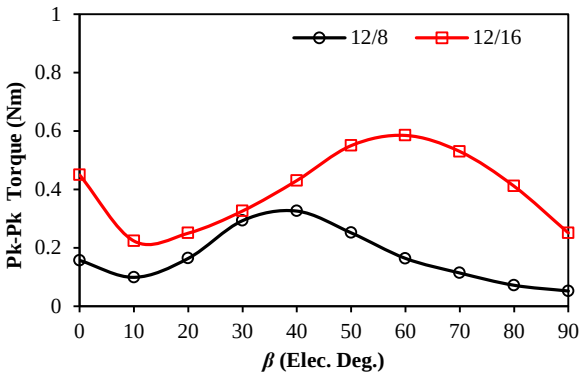

(c) 12/8 and 12/16

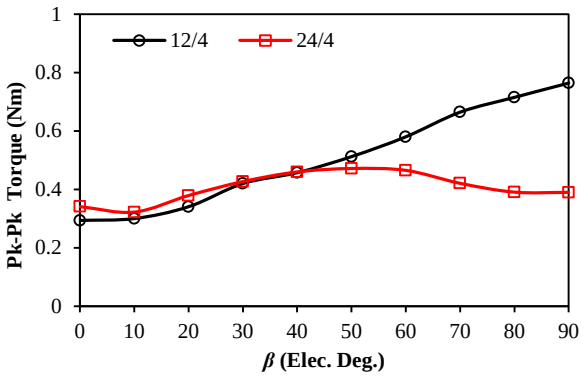

(d) 12/4 and 24/4

Fig. 3.40 Comparison of pk-pk torques for machines with different slot and pole number combinations (I_{max}=10A).

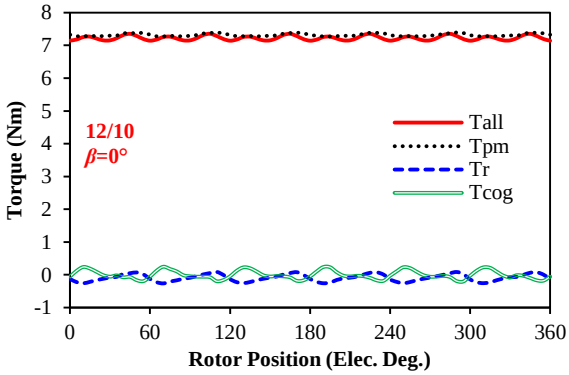

(a) waveforms β=0°

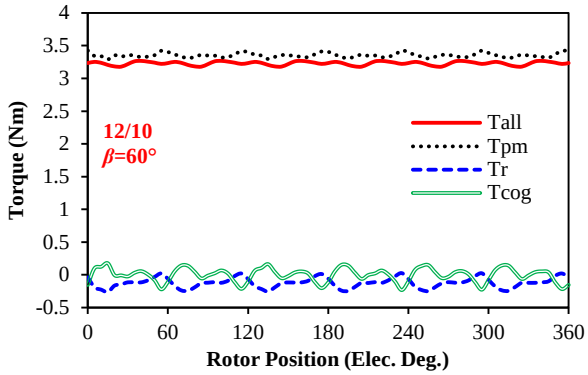

(b) waveforms β=60°

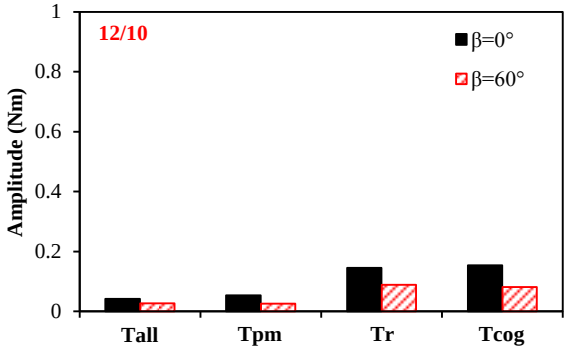

(c) 6th ripple amplitudes

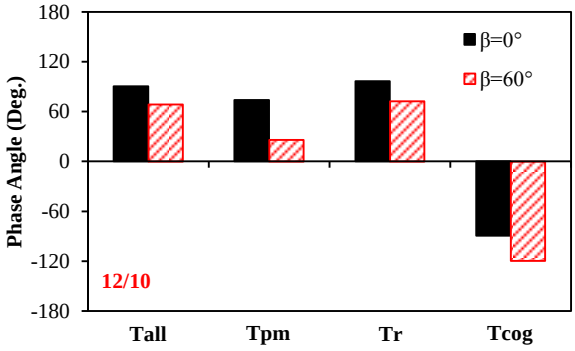

(d) 6th ripple phase angles

Fig. 3.41 Torque ripple components in 12/10 machine with different β (I_{max}=10A).

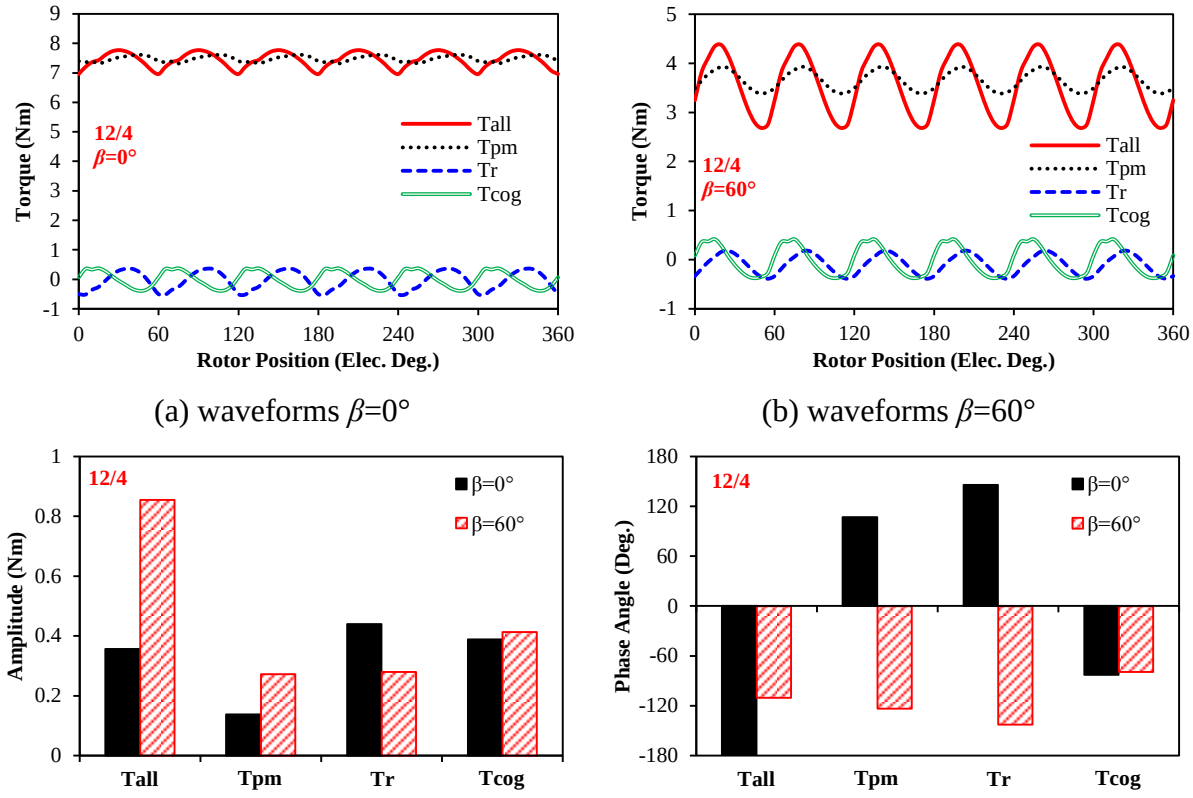

(a) waveforms β=0°

(b) waveforms β=60°

(c) 6th ripple amplitudes

(d) 6th ripple phase angles

Fig. 3.42 Torque ripple components in 12/4 machine with different β (I_{max}=10A).

3.5.5 Iron Loss

Fig. 3.43 compares the iron loss of different lamination parts for all machines at rated speed and current. With the increase of β, the major flux path becomes less saturated, which reduces the resultant iron losses. However, due to local magnetic saturation, the iron losses in tooth-tips do not significantly change with β. Since the stator tooth and back iron of all machines have been adjusted to have similar flux density under rated currents with I_d=0 control, the iron losses largely depend on the operation frequency of the machine. Thus, the machine with higher pole numbers will exhibit larger iron loss, which can also be reflected in the iron loss density of tooth-tips, Fig. 3.44.

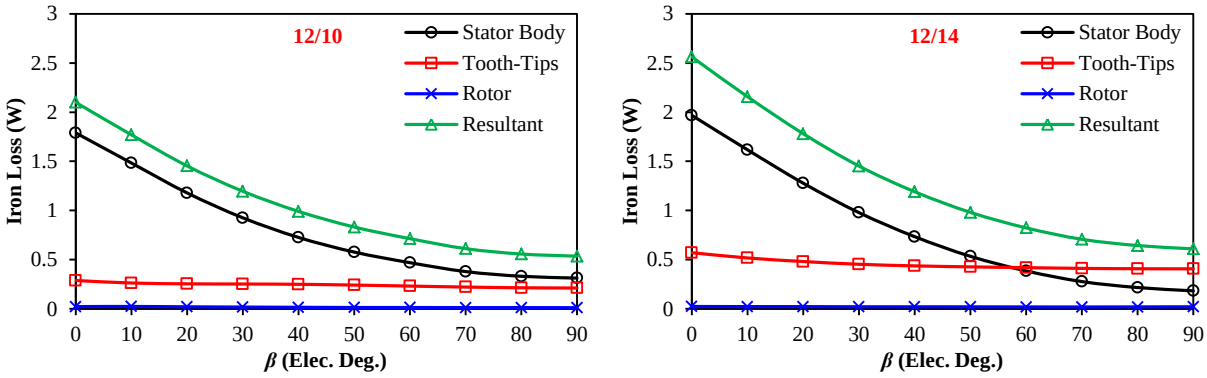

(a) 12/10 machine

(b) 12/14 machine

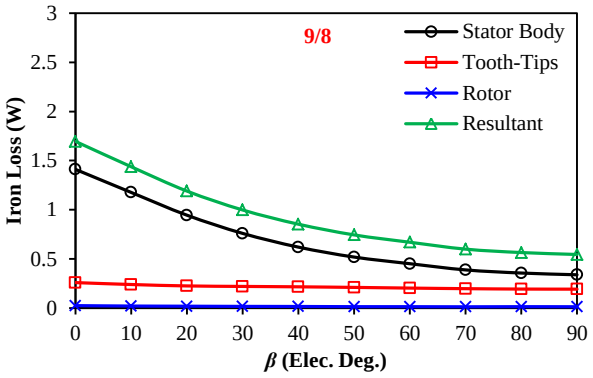

(c) 9/8 machine

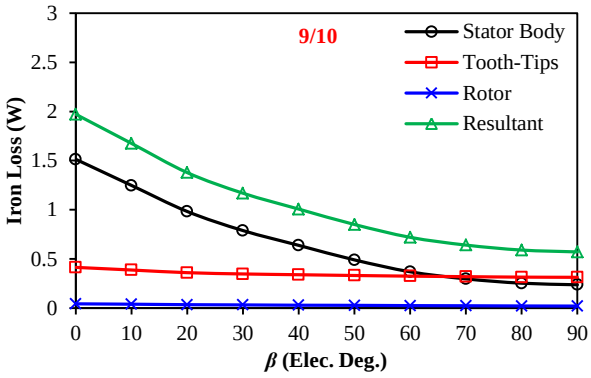

(d) 9/10 machine

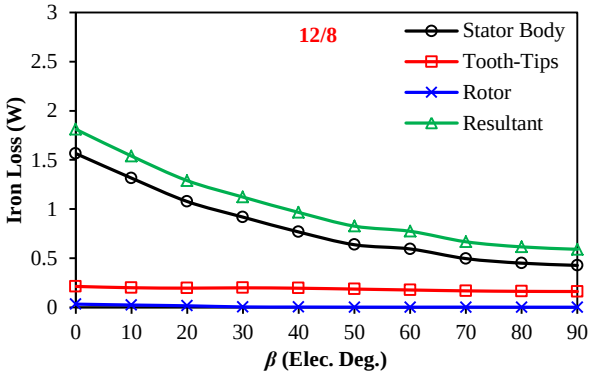

(e) 12/8 machine

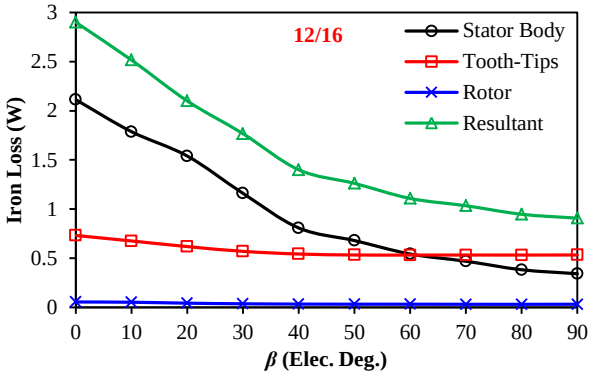

(f) 12/16 machine

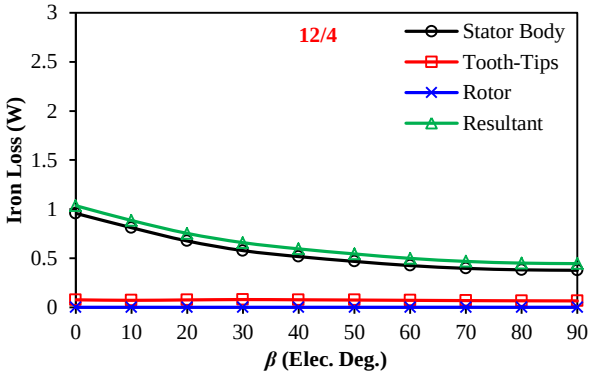

(g) 12/4 machine

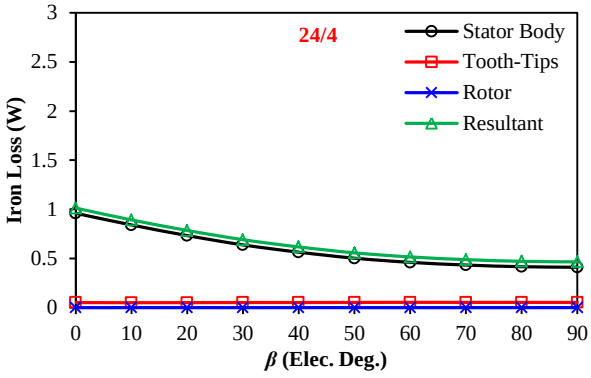

(h) 24/4 machine

Fig. 3.43 Comparison of iron loss against β for machines with different slot and pole number combinations (I_{max}=10A, 400rpm).

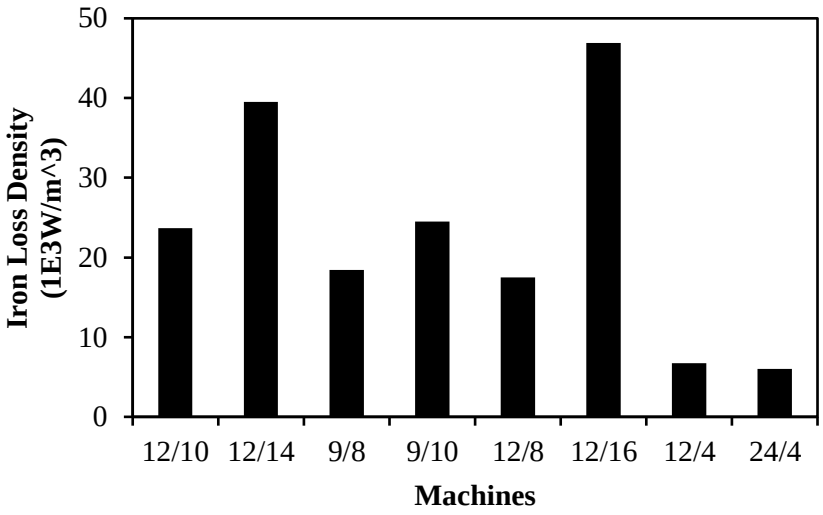

Fig. 3.44 Comparison of tooth-tip iron loss densities for machines with different slot and pole numbers (I_{max}=10A, β=0°, 400rpm).

3.5.6 PM Eddy Current Loss

Fig. 3.45 compares the PM eddy current losses in all the machines at rated speed and current. Since the operation frequencies are different for all the machines due to different rotor pole numbers, their PM eddy current losses under the same speed differ significantly. However, it still can be observed that the machines appearing in pairs obtain the same variation trend of PM eddy current losses due to similar winding arrangements. Meanwhile, since all space harmonics for the 12/8 machine are mainly slot harmonics, it suffers most from PM eddy current loss when β=0°. With the increase of β, the influence of local magnetic saturation on PM loss reduces, which makes the PM loss more dependent on the operating frequency. Thus, the PM loss of the 12/8 machine is less than that of the 12/16 machine in the flux weakening regions. Further, due to low space harmonics as well as low operation frequencies, the PM losses for the integer slot machines could be negligible at rated speed.

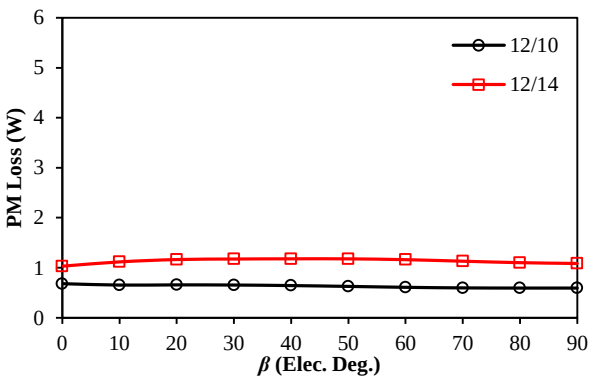

(a) 12/10 and 12/14

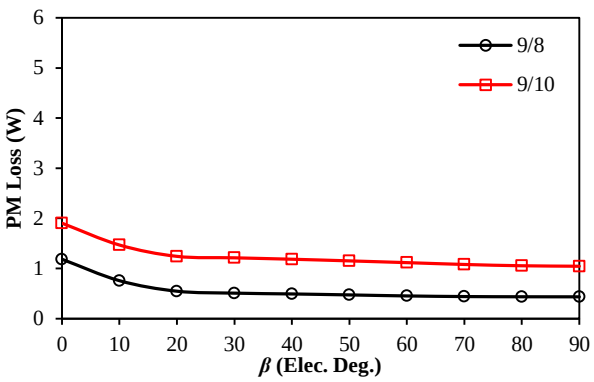

(b) 9/8 and 9/10

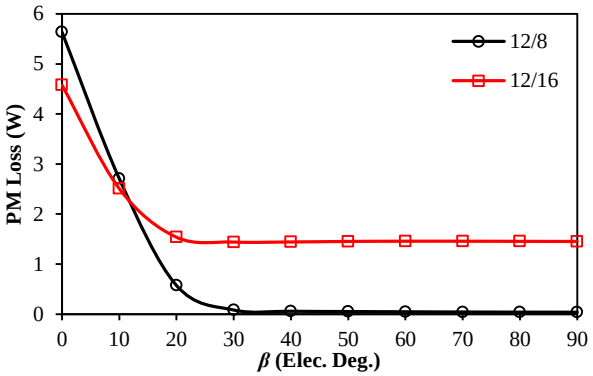

(c) 12/8 and 12/16

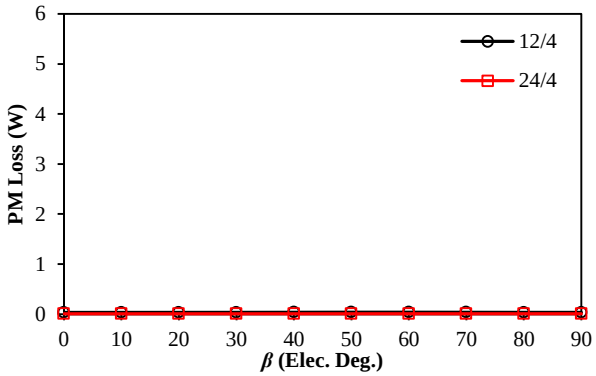

(d) 12/4 and 24/4

Fig. 3.45 Comparison of PM eddy current losses for machines with different slot and pole numbers (I_{max}=10A, 400rpm)

3.5.7 Flux Weakening Performance

As investigated in Section 3.4, the investigated machines have different *LVDR* with different β, which also influence their flux weakening performances. Assuming U_{DC} is 42V, the torque speed and torque ripple speed curves for all machines are calculated and compared in Fig. 3.46. For simplicity, the maximum torque per volt (MTPV) operation is not considered for comparison. In the fractional slot machines, the *LVDR*s are all obvious when β=0°, which significantly reduce the base speed compared with the values calculated by fundamental voltages. Meanwhile, since the fractional slot machines with N_s<2p suffer more from voltage distortion than their counterparts with N_s>2p, their torque speed curves calculated by peak voltages are much different from the ideal curves especially around the base speed. When the average torque falls to zero, the torque ripples will soar up, which can be observed in the 12/8 and 12/16 machines. As shown in Fig. 3.24, the 12/8 machine obtains higher *LVDR* when β approaches 90°, while the 12/16 machine has low *LVDR* at the same time. Based on this, the difference between curves calculated by the fundamental and peak voltages are enlarged in the deep flux weakening region for the 12/8 machine, but diminished in the 12/16 machine. On the other hand, the *LVDR*s for two integer slot machines are small when β=0°. Thus, their base speeds are quite close to the ideal values calculated by fundamental voltages. However, the *LVDRs* for both machines increase with β in Fig. 3.27, which results in larger differences in flux weakening regions.

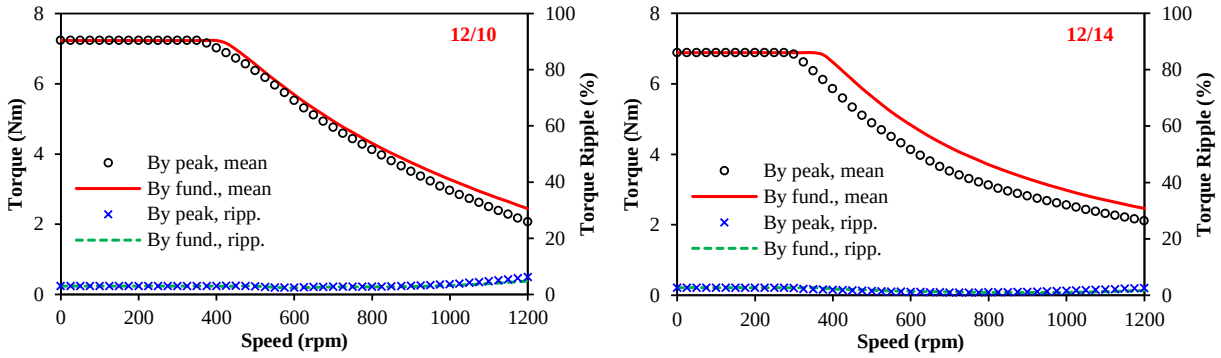

(a) 12/10 machine

(b) 12/14 machine

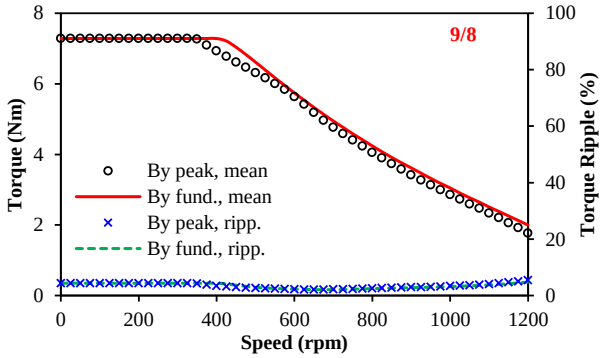

(c) 9/8 machine

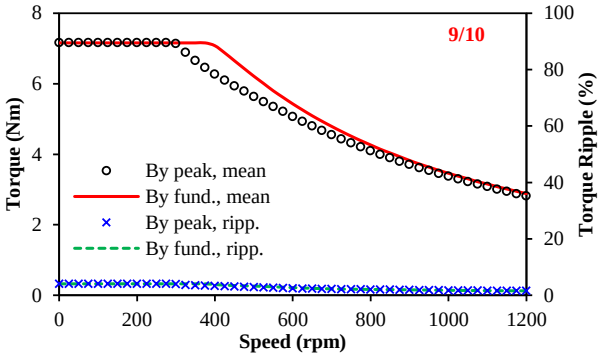

(d) 9/10 machine

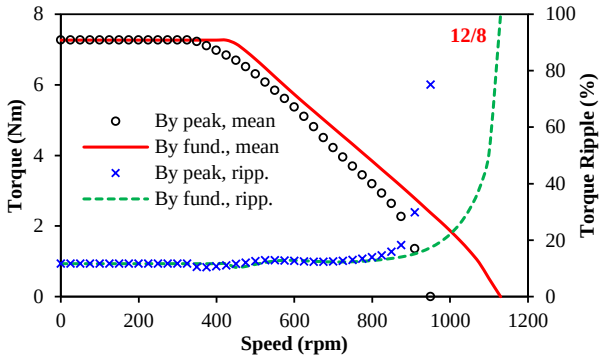

(e) 12/8 machine

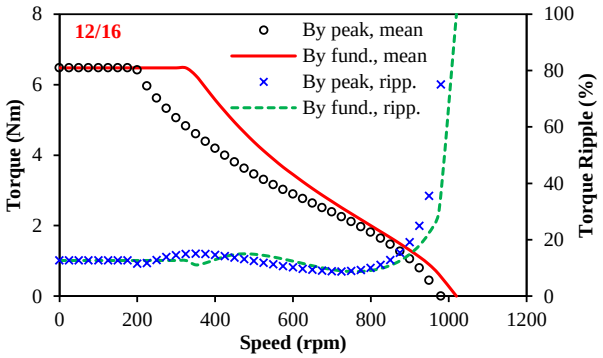

(f) 12/16 machine

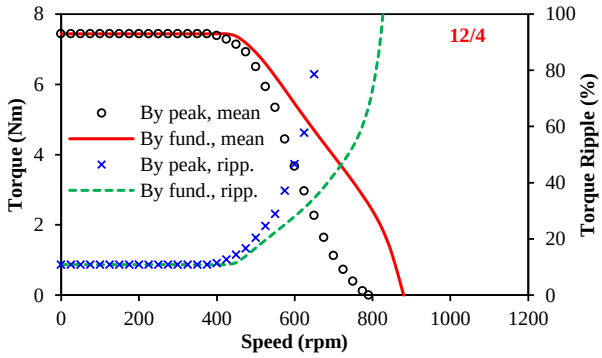

(g) 12/4 machine

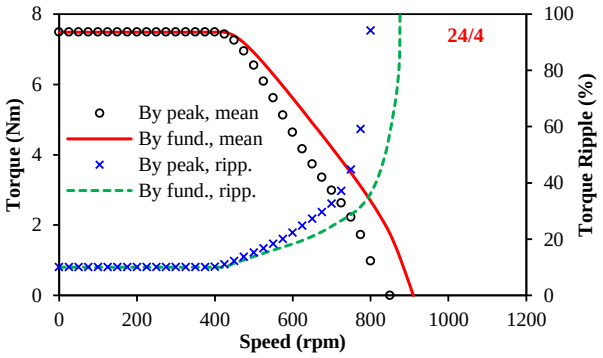

(h) 24/4 machine

Fig. 3.46 Comparison of flux weakening performance for machines with different slot and pole number combinations (I_{max}=10A, U_{DC}=42V).

3.6 Experimental Validation

3.6.1 Prototype Machines

The 12/8 and 12/10 machines with closed slot openings are adopted for validation. In order to ease the fabrication and save the cost, the 12/8 machine is the same as that in Chapter 2, while only a 10-pole rotor is made for the 12/10 prototype. The differences of two rotors can be found in Table 3.3. The photos of the prototypes are shown in Fig. 3.47, while the measured phase resistance under room temperature is 0.64Ω. The test rig is similar as that in Chapter 2, Fig. 2.38(c). The DC generator is adopted as the load, while the PWM frequency for all load tests is 10kHz. Due to the inverter limitation, the maximum driving current for dynamic test is reduced to 8A.

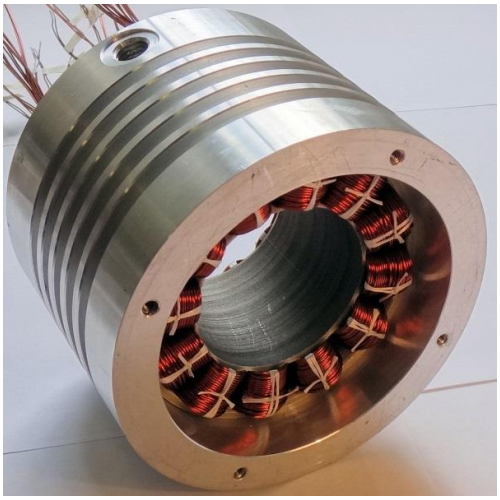

(a) Stator

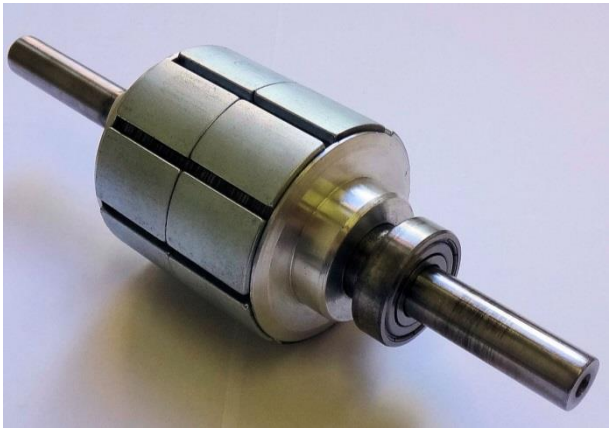

(b) 8-pole rotor

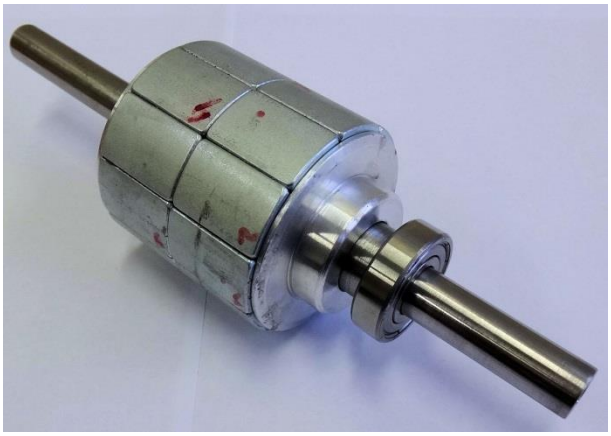

(c) 10-pole rotor

Fig. 3.47 Prototype machines.

Table 3.3 Basic parameters of prototype machines

Parameters	***Prototype 1***	***Prototype 2***
Slot number	12	
Pole number	8	10
Stator out diameter	50mm	
Axial length	50mm	
Stator inner diameter	57mm	
Rotor outer diameter	55mm	
Slot bridge thickness	0.6mm	
Turns per phase	184	
Rated current	$5.66A_{rms}$	
Rated speed	200rpm	
PM thickness	3mm	
Rotor PM pole arc	155°	180°

3.6.2 Back-EMFs

The comparison of measured and predicted open-circuit line back-EMFs are shown in Fig. 3.48, which reveal both machines have almost sinusoidal back-EMFs. Considering about the end-effect of small sized machines, as well as the manufacturing tolerance and measuring error, the fundamental values of the measured results are ~5% less than the predictions.

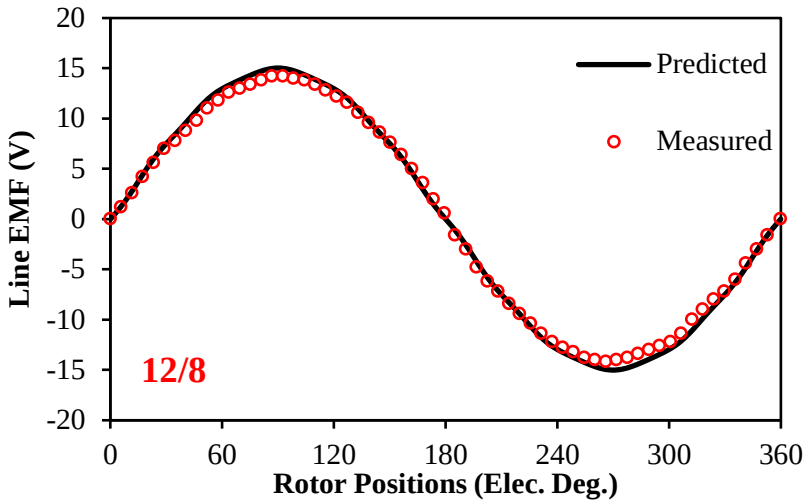

(a) 12/8 waveforms

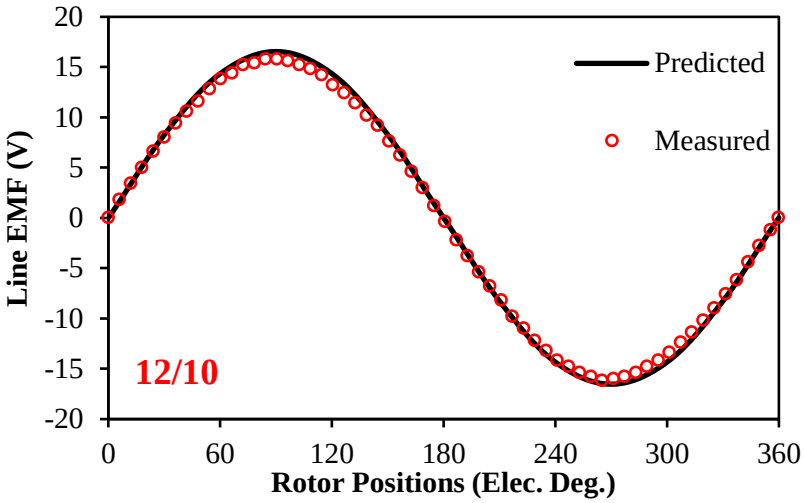

(b) 12/10 waveforms

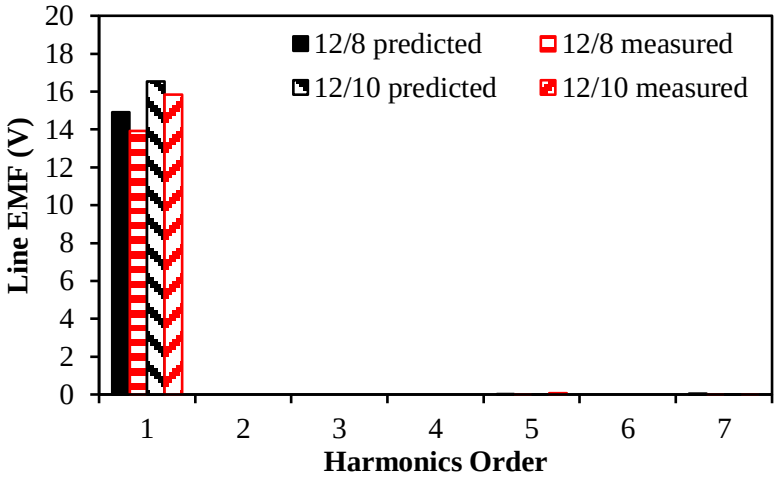

(c) Harmonics

Fig. 3.48 Comparison of measured and predicted line back-EMFs (400rpm).

3.6.3 Torque Waveforms

Fig. 3.49 compares the measured and predicted torque waveforms under I_d=0 control. Although the both machines have the same stator and rated current, as well as sinusoidal back-EMFs, the 12/8 machine suffers more voltage ripples compared with the 12/10 machine due to voltage distortion and local magnetic saturation. Meanwhile, since the local magnetic saturation level is less than the full load condition, the torque ripple will be smaller as well.

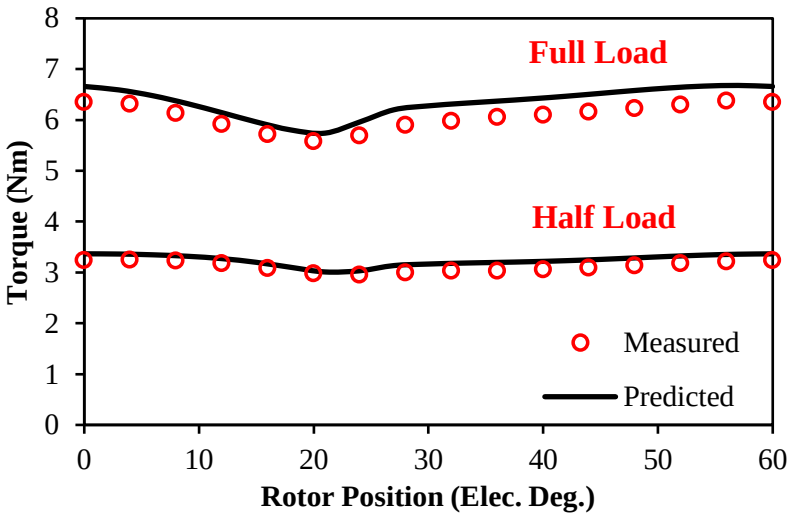

(a) 12/8 machine

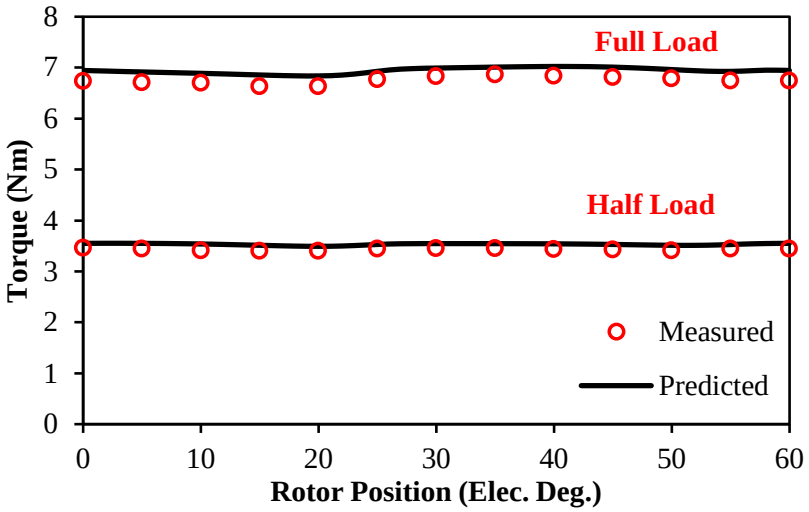

(b) 12/10 machine

Fig. 3.49 Comparison of predicted and measured torque waveforms (I_{max}=10A, β=0°).

3.6.4 Voltage Distortion Patterns

To validate the *VDP*, the machines are tested without rotors first. In order to observe the distorted terminal voltage clearly, a low pass filter with cut-off frequency about 1.5 kHz is adopted to filter out the PWM. When the machines are injected with I_q=2A under 11Hz, the response phase voltage (V_a) and current (I_a) are measured in Fig. 3.50. It can be seen that the currents are maintained as sinusoidal as possible, in which the disturbances are caused by high voltage pulsation. Considering the fundamental voltages due to inductance and resistance of the windings, the two ripples appearing in Fig. 3.50(a) have almost the same amplitude. Meanwhile, their occurring positions are symmetric around the position (about 30°) when I_a crosses zero, which validate the *VDP* of 12/8 machine in Fig. 3.9. On the other

hand, there are three adjacent voltage ripples in the phase voltage of the 12/10 machine in Fig. 3.50(b). Their relative amplitudes and occurring positions also validate the *VDP* predicted in Fig. 3.9.

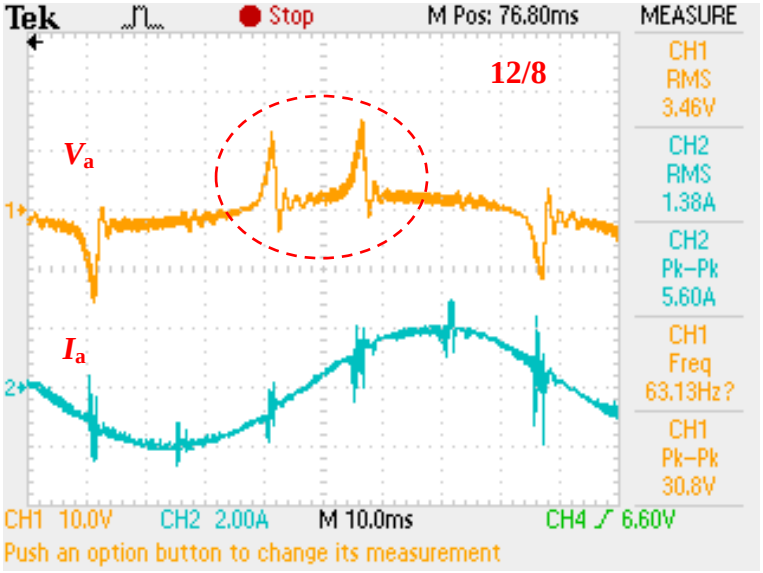

(a) 12/8 machine

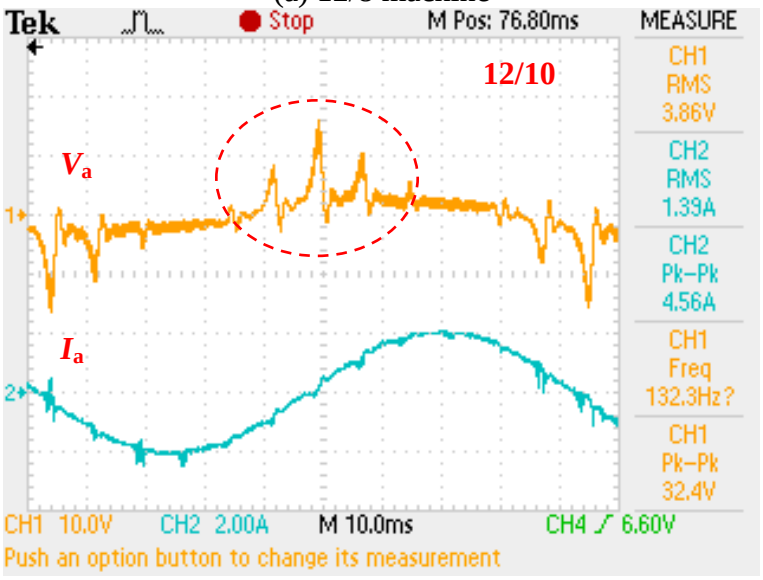

(b) 12/10 machine

Fig. 3.50 Phase voltage and current without rotor (I_q=2A, 11Hz, U_{DC}=80V).

3.6.5 On-Load Voltage Distortion

The terminal voltage distortions under rated current with β=0° and β=60° are illustrated for examples. Fig. 3.51 shows the measured line voltages with and without PWM for two prototypes under rated current with β=0°. It can be observed that the phase current I_a is quite sinusoidal, while obvious voltage ripples appears in the terminal voltages. Fig. 3.52 compares the measured terminal voltages with the prediction by FEA, which shows good agreement.

Since the PWM harmonics could not be totally filtered out by the low-pass filter, the measured *THD* are higher than predictions. Meanwhile, Fig. 3.53 shows the measured line voltages with and without PWM for two machines with β=60° under the same current amplitude, while Fig. 3.54 compares the measured results with the predictions. Due to the control error as well as the PWM harmonics, the differences between measured and prediction are slightly higher than those for β=0°. However, the reductions of *LVDR* and *THD* under β=60° are still significant compared with β=0°, which validates that the voltage distortion level reduces with the increase of β.

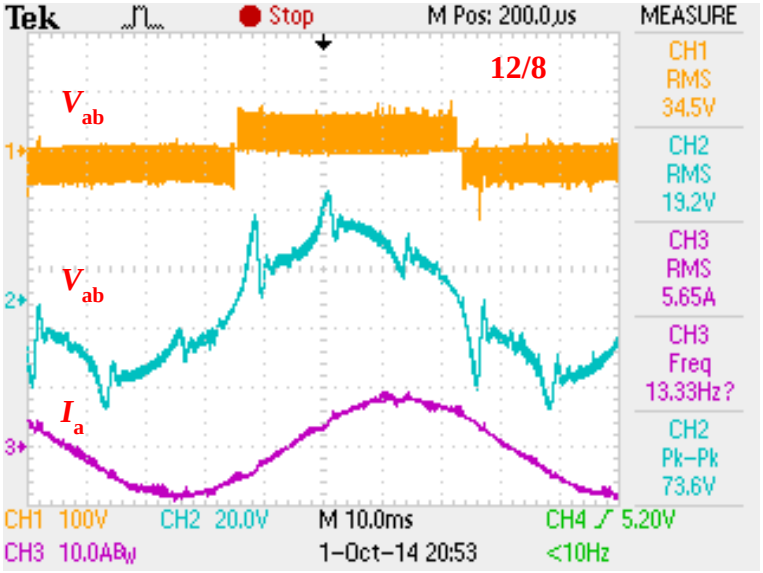

(a) 12/8, β=0°

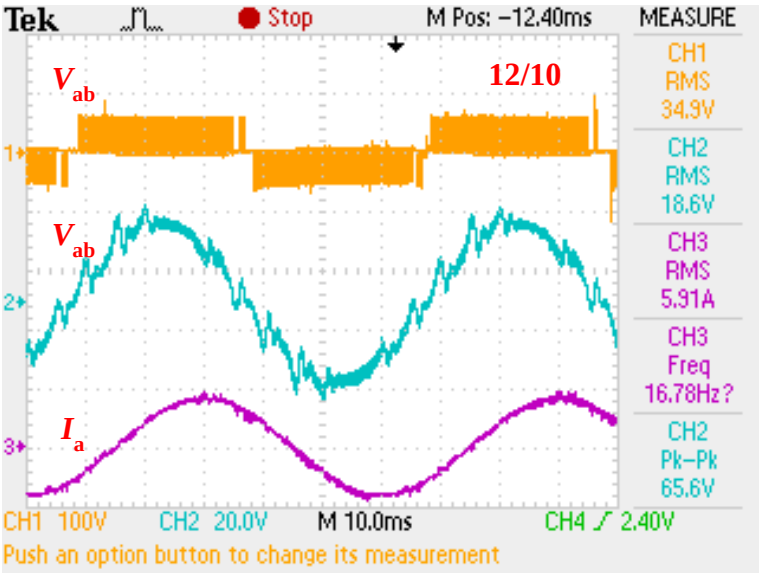

(b) 12/10, β=0°

Fig. 3.51 Comparison of measured terminal line voltages of two prototypes with rotor (I_{max}=8A, β=0°, U_{DC}=60V, 200rpm)

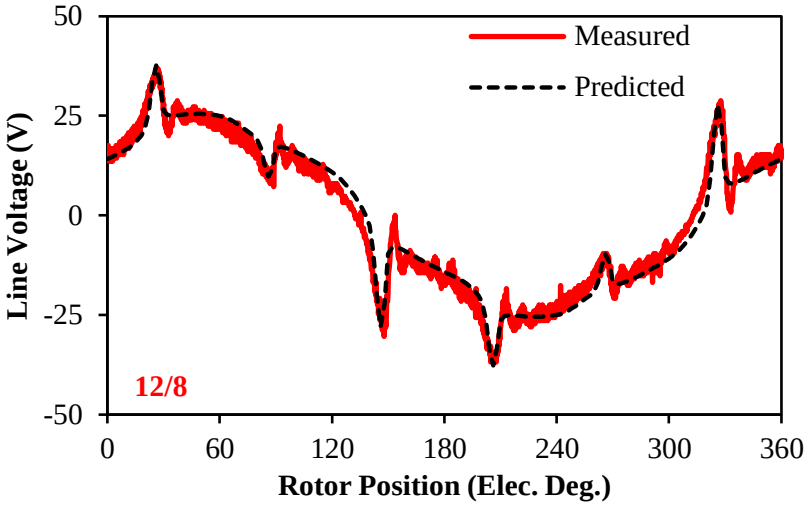

(a) 12/8, β=0°

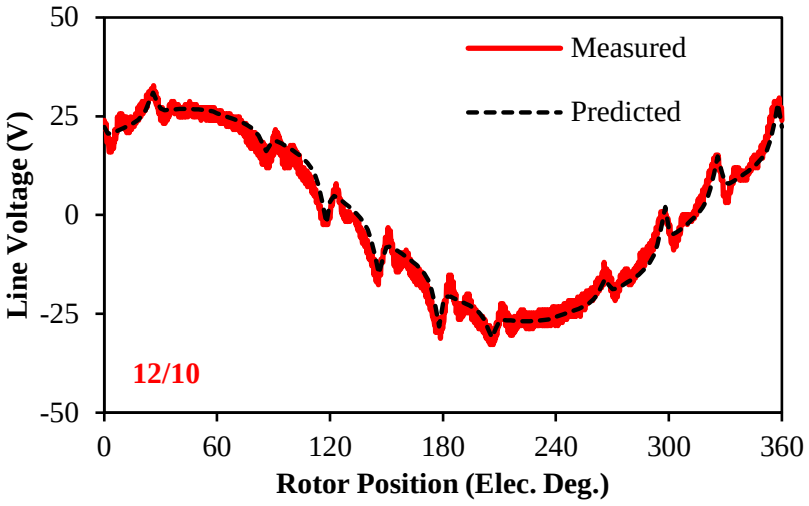

(b) 12/10, β=0°

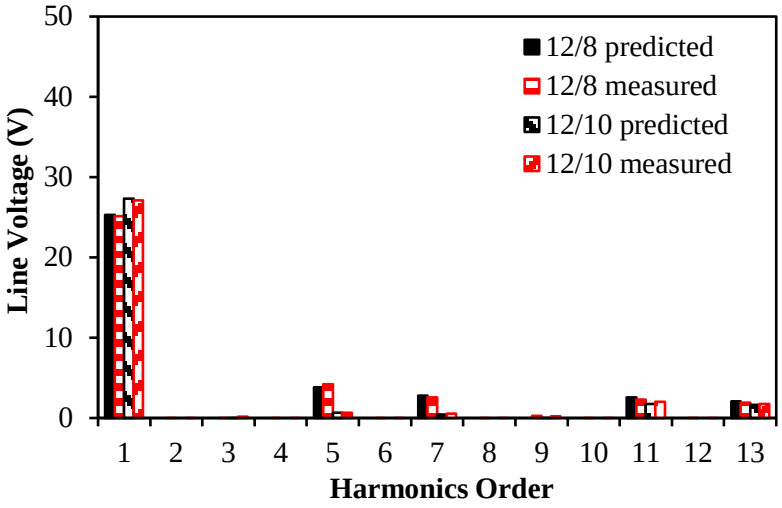

(c) Harmonic components, β=0°

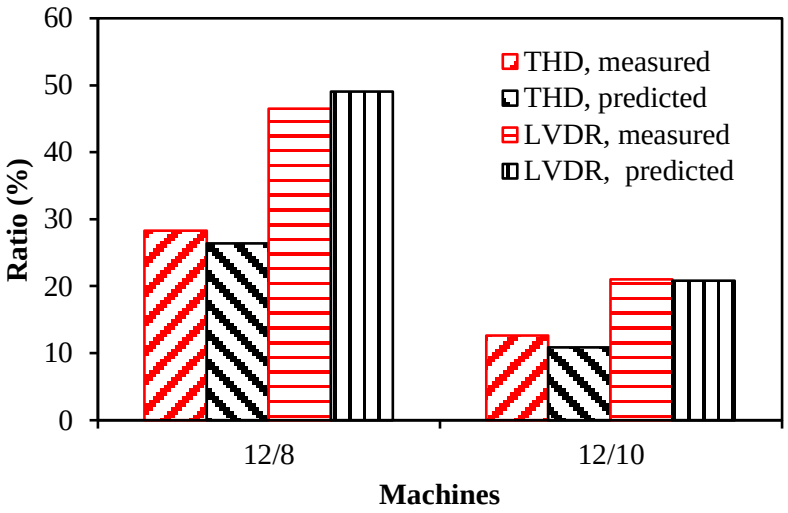

(d) *LVDR* and *THD*, β=0°

Fig. 3.52 Comparison of measured and predicted terminal line voltages (I_{max}=8A, β=0°, U_{DC}=60V, 200rpm)

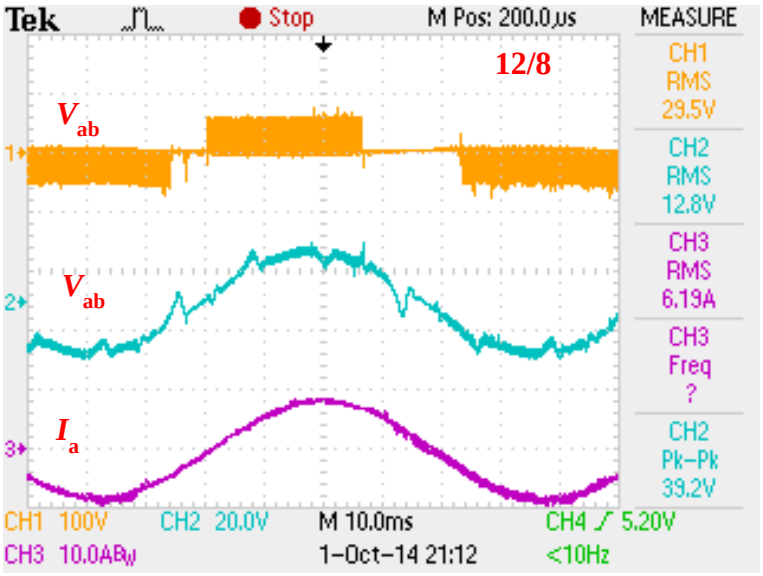

(a) 12/8, β=60°

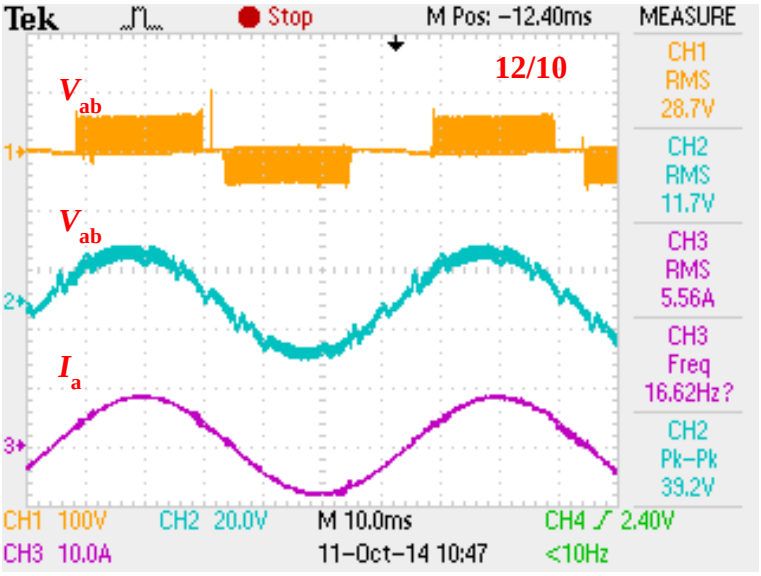

(b) 12/10, β=60°

Fig. 3.53 Comparison of measured terminal line voltages of two prototypes with rotor (I_{max}=8A, β=60°, U_{DC}=60V, 200rpm)

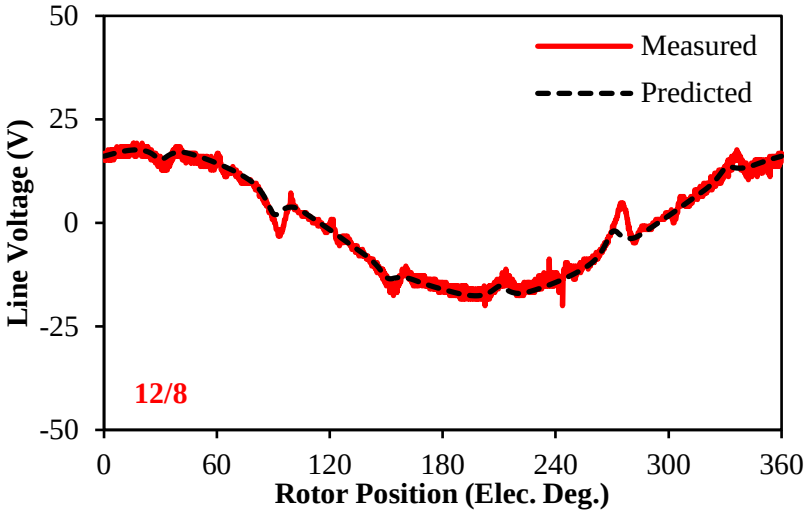

(a) 12/8, β=60°

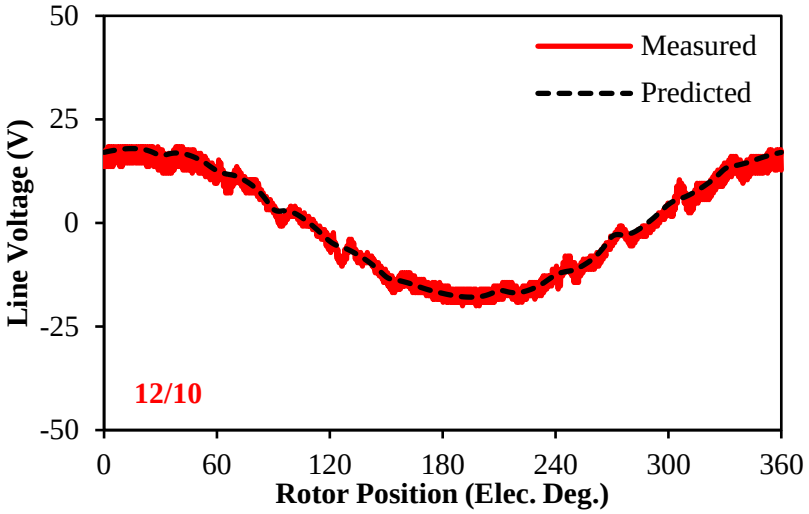

(b) 12/10, β=60°

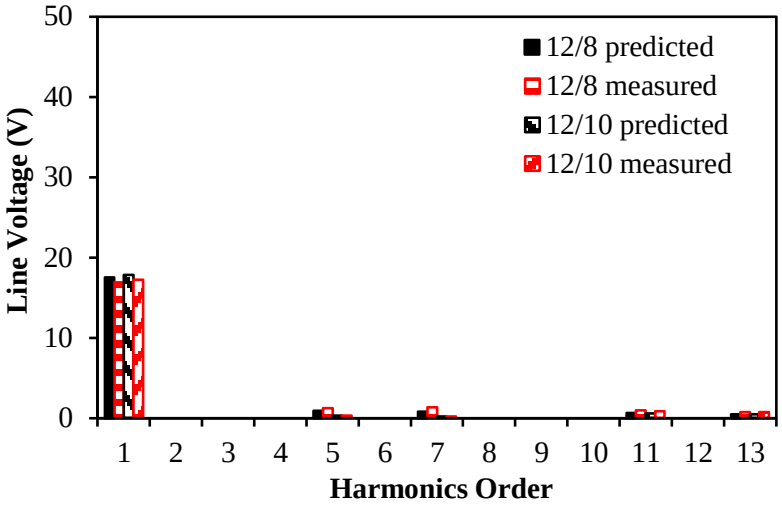

(c) Harmonic components, β=60°

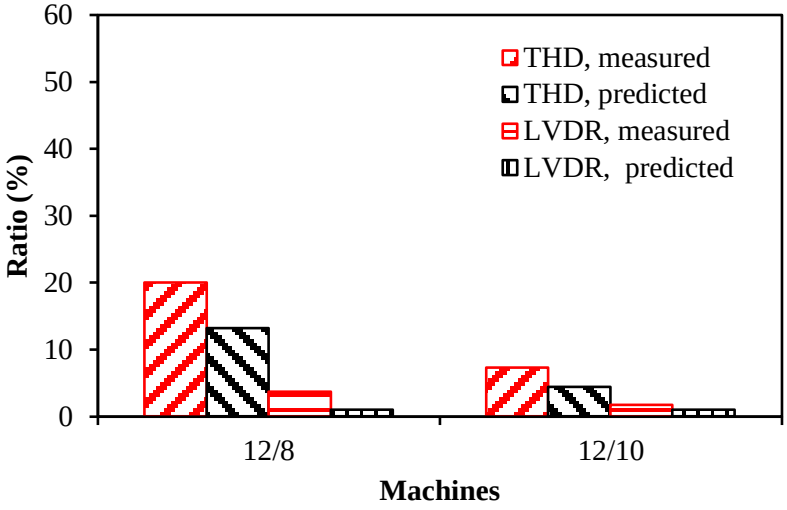

(d) *LVDR* and *THD*, β=60°

Fig. 3.54 Comparison of measured and predicted terminal line voltages (I_{max}=8A, β=60°, U_{DC}=60V, 200rpm)

3.6.6 Torque Speed Characteristics

Feedback voltage regulation method developed in [KIM97] is adopted for the flux weakening control in the experiments. Therefore, the measured torque-speed characteristics for two machines under the same U_{DC} and I_{max} can be shown as the circle-dotted lines in Fig. 3.55. The dashed lines in the figure is the ideal torque-speed curve calculated by only considering the fundamental voltage in 2D FEA, while the predicted lines with the same method as measured curve are shown as the cross-dotted lines. Although the 12/10 machine suffers less from terminal voltage distortion, the measured torque speed curve is still lower than the ideal curve around the base speed, where the largest *LVDR* occurs. However, due to much smaller voltage distortion compared with the 12/8 machine, the measured result for the 12/10 machine is closer to the prediction, which can be explained by considering the controller band width limitation, as well as the end-effect and measuring error. Overall, the experimental results have validated the prediction.

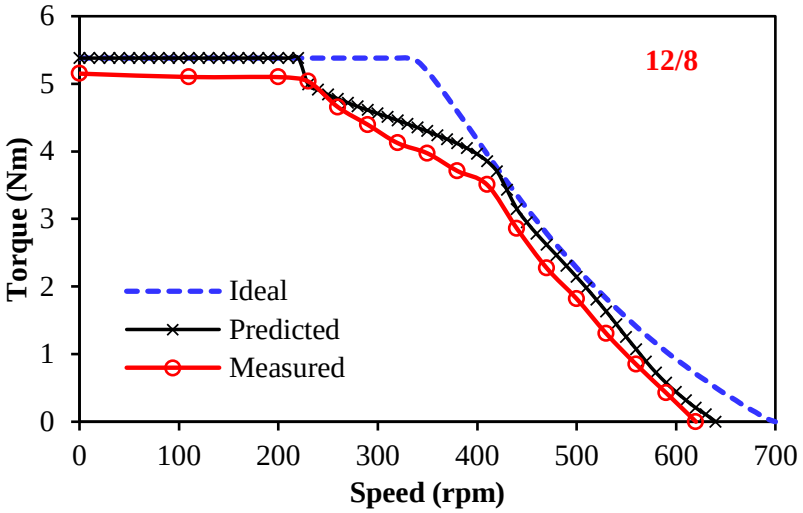

(a) 12/8 machine

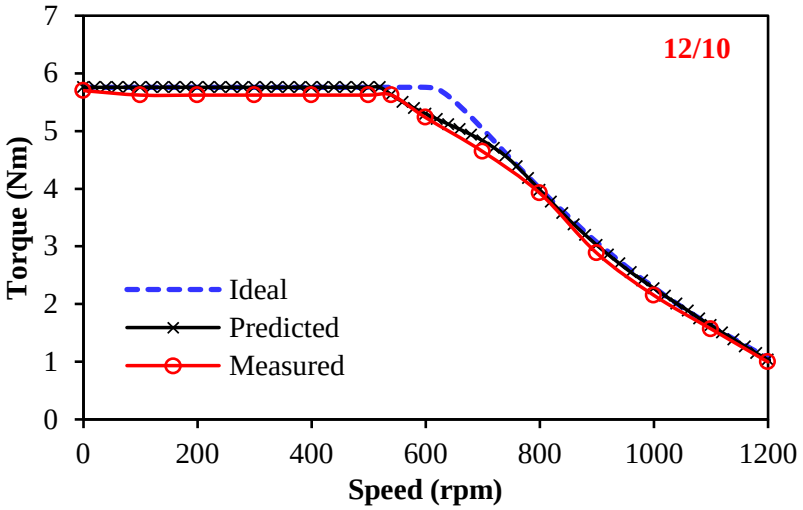

(b) 12/10 machine

Fig. 3.55 Comparison of measured and predicted torque speed characteristics (I_{max}=8A, U_{DC}=42V).

3.7 Summary

This chapter investigates the influence of slot and pole number combinations on the terminal voltage distortion in SPM machines, focusing on the local magnetic saturation caused by small or closed slot openings. In total, eight machines with alternative slot and pole combinations including both fractional slot and integer slot machines are considered. Moreover, the *VDP* is introduced, which can describe the voltage ripples occurring in time (or rotor position) and relative amplitudes in machines having different slot/pole number combinations. The influences of PM leakage flux for different slot/pole combinations are also investigated, which shows PM leakage flux will reduce the potential voltage ripples in fractional slot machines with $q_e \geq 2$, or in integer slot machines with $q \geq 2$. This reduction is more obvious in integer slot machines. Therefore, integer slot machines have less influence from voltage distortion than fractional slot machines. Meanwhile, the fractional slot machines with $N_s > 2p$ would suffer less than their counterparts with $N_s < 2p$ due to lower working frequency but similar tooth-tip leakage flux. The electromagnetic performances of the machines influenced by voltage distortion and local magnetic saturation are also compared, such as on-load back-EMF and cogging torque, *dq*-axis inductances, torque ripple, iron loss, and torque speed characteristic. The comparison results reveal that the machines which suffer more from voltage distortion normally obtain higher on-load back-EMF and inductance ripples, larger on-load cogging torque and torque ripples, as well as worse flux weakening

performance. Finally, two prototypes with different slot/pole numbers are manufactured and tested to validate all the analyses.

CHAPTER 4

ON-LOAD TERMINAL VOLTAGE DISTORTION IN FRACTIONAL SLOT IPM MACHINES CONSIDERING LOCAL MAGNETIC SATURATION

Due to different rotor topologies and thereafter the rotor flux paths, the local magnetic saturation in IPM machines will be different from the SPM machines. Thus, the mechanism and influence of the on-load terminal phase voltage distortion in fractional-slot IPM machines are investigated in this chapter, by taking a 12-slot/8-pole machine for example, while its influences on other machine performances are also discussed.

4.1 Introduction

Interior permanent magnet (IPM) rotor topology was firstly introduced as a flux focusing method many years ago [STR52]. However, its potential advantages were not fully recognized until the development of more powerful PM materials as well as the power electronics technologies. Recently, IPM machines with fractional-slot concentrated windings have been extensively investigated owing to the merits of high power and torque density, high efficiency, good demagnetization withstand capability, as well as high mechanical rotor robustness [ELR10], [PEL12a], [LEE13], [KIM09], and [SOO02].

In order to fulfil the potential advantages of fractional-slot IPM machines, the field orientation control, e.g. vector control, is usually adopted [VAS90]. With this method, the sinusoidal driving currents with required current advancing angle (β) can be achieved by separately controlling the *dq*-axis voltages, which is particularly suitable for flux weakening operation with IPM machines. Normally, the *dq*-axis voltages are calculated by the *dq*-axis inductances which only consider the fundamental values [SOO02]. Thus, the influences of harmonic voltages are often ignored. However, unlike the surface-mounted permanent magnet (SPM) machine [ZHU10], the IPM machines have lamination regions above the magnets, which offer flux paths with high permeance. Hence, the armature reaction, i.e. the interaction between PM and armature fields, will be much stronger in IPM machines, which may lead to high magnetic saturation and thereafter the voltage distortion [STU03], [YU13].

Therefore, simply ignoring the voltage harmonics may influence the performance of IPM machines such as torque speed curves.

Nevertheless, few papers have focused on the mechanism of such on-load voltage distortion and its influence for fractional-slot IPM machines. [ZHU93], [BOU12] and [LI13] adopt alternative analytical methods to calculate the on-load airgap field, which shows clear process for the armature reaction. However, the analytical methods treat the lamination as linear material, which cannot reflect the influence of saturation. [TAN09], [HAN07] and [KIM14] improve the analytical methods to consider the influence of saturation for armature reaction. However, the phenomenon and influence of voltage distortion have not been investigated further. [COR98], [CHE03] and [CHO13] introduce harmonic inductances to compensate the influence of saturation. However, these inductances may change according to different load conditions due to the variation of saturation, which cannot reflect essential link between armature reaction and on-load voltage distortion.

Since the fractional-slot IPM machines with the number of slot per pole per phase equalling 0.5 are very popular in industrial and domestic applications, a 12-slot/8-pole machine will be taken as an example for the investigation in this chapter and the investigation on influence of slot and pole number combinations will be presented in Chapter 5. Based on the model, the phenomenon of the on-load voltage distortion is introduced firstly. Then, the mechanism of voltage distortion is investigated by the frozen permeability (FP) method. Subsequently, the influences of voltage distortion are investigated in constant torque and flux weakening operation regions respectively, while the influences on other performance are also investigated, such as on-load back-EMF, on-load cogging torque, *dq*-axis inductances. Finally, a prototype with the similar dimensions as the analysis model has been manufactured and tested to validate the analysis results.

4.2 Phenomenon of On-Load Voltage Distortion in IPM Machines

4.2.1 Prototype Model

The investigation is carried out on a 3-phase double-layer winding 12-slot/8-pole fractional slot IPM machine in Fig. 4.1 at zero rotor position (θ_r=0°). All basic parameters of the machine are shown in Table 4.1.

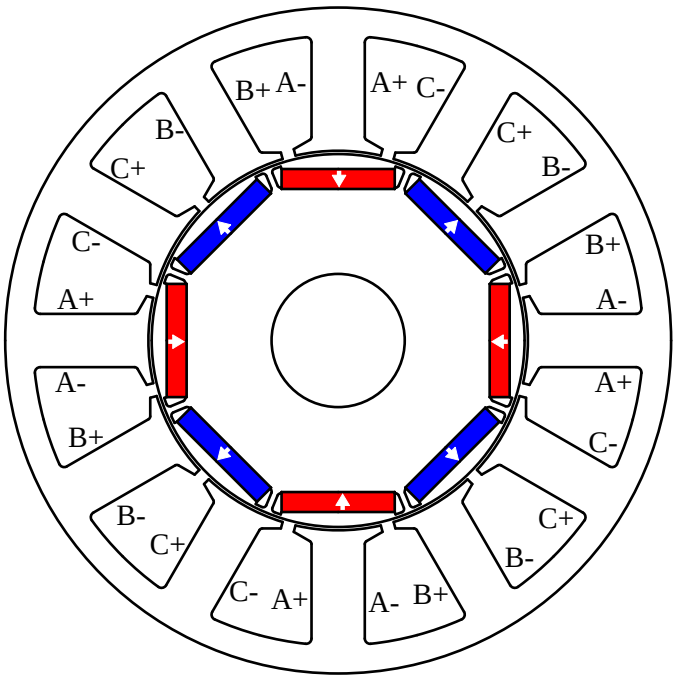

Fig. 4.1 Cross section of 12-slot/8-pole IPM prototype machine (θ_r=0°).

Table 4.1 Basic parameters of 12-slot/8-pole IPM prototype machine

Parameter	***Value***	***Parameter***	***Value***
Stator outer diameter	100mm	Axial length	50mm
Split ratio	0.57	Airgap length	0.5mm
Tooth width	8mm	Back iron thickness	4.2mm
Rotor bridge thickness	0.5mm	Turns per phase	184
Magnet thickness	3.0mm	Pole arc/pitch ratio	0.8
Rated current	$7.1A_{rms}$	Phase resistance	0.5Ω
Magnet permeability	1.05	Magnet remanence	1.2T
Magnet material	N35SH	Lamination material	M300
L_d	7.9mH	L_q	11.4mH

4.2.2 On-Load Voltage Distortion

Fig. 4.2(a) shows the terminal phase voltages of the investigated IPM machine under different current conditions, in which OC stands for open-circuit back-EMF. It can be seen that the on-load phase voltage under rated current with β=0° is distorted compared with the back-EMF due to armature reaction. However, it becomes more problematic when β=60°, since the terminal voltage becomes asymmetric and contains large voltage ripples, which can be reflected by the harmonic components in Fig. 4.2(b). The voltage distortion level in IPM machines could also be evaluated by *VDR* defined in equation (2.1), which can be shown in

Fig. 4.3. Different from the SPM machine, the voltage distortion in the IPM prototype enhances with the increase of β, which indicates the generating mechanism of voltage distortion may also be different from the SPM machines.

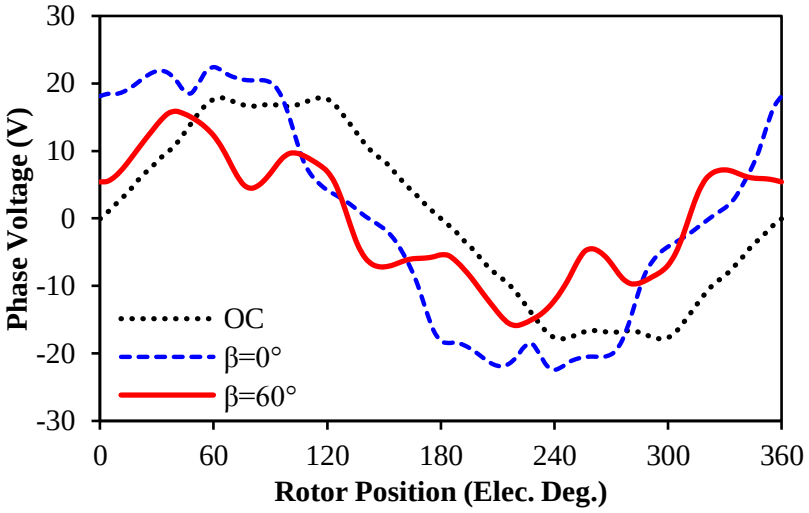

(a) Waveforms

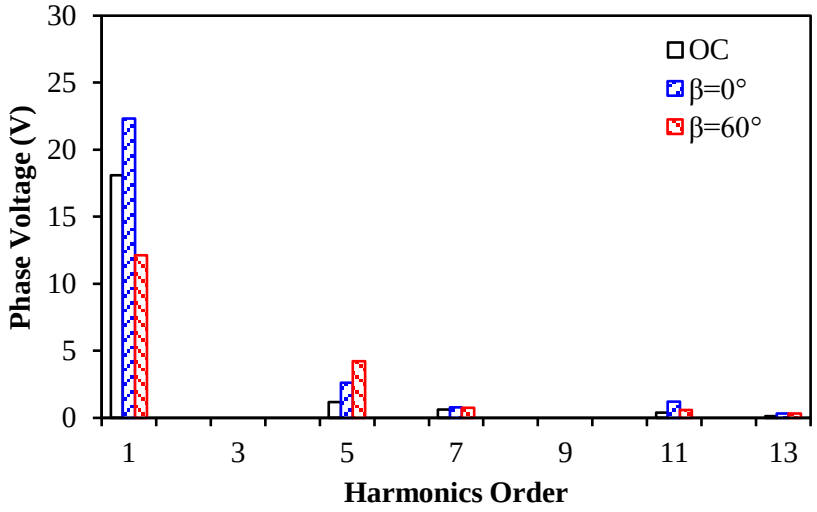

(b) Harmonics

Fig. 4.2 Comparison of phase voltages under different current conditions (I_{max}=10A, 400rpm).

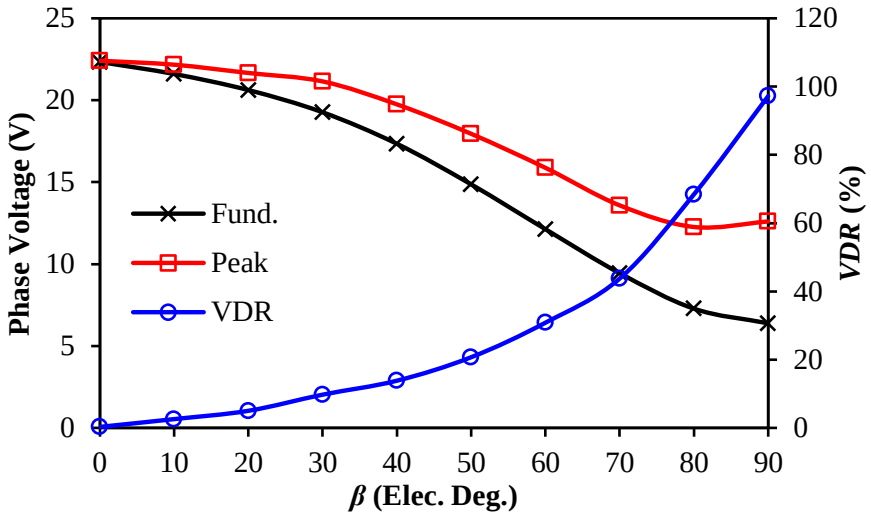

Fig. 4.3 Variation of voltage distortion ratio for different β (I_{max}=10A, 400rpm).

4.3 Mechanism of On-Load Voltage Distortion in IPM machines

4.3.1 Mechanism

The phase voltage equation for IPM machines is the same as that for SPM machines in (2.2). If ignoring the voltage drop on resistance, the distortion must be triggered by the distorted flux linkages. Taking β=60° for example to investigate the phenomenon. With the aid of frozen permeability method [CHU13a], ψ_a^{pm} and ψ_a^{arm} under the same driving current can be separated in Fig. 4.4(a), while the respective voltages are calculated in Fig. 4.4(b). It can be seen that ψ_a^{pm} under load condition is slightly asymmetric, which introduces harmonics to the on-load PM voltage, i.e. the on-load back-EMF [AZA12]. However, more severe distortion exists in the on-load ψ_a^{arm}, which contributes to majority of the overall voltage distortion. Meanwhile, it can be observed the resultant voltage distortion is constituted by a series of voltage ripples which are related with the local distortion of flux linkages at certain positions, e.g. around 80°, 140°, 260°and 320° respectively. The dashed vertical lines in Fig. 4.4 point out the position of the first local voltage ripple, which will be investigated in detail later.

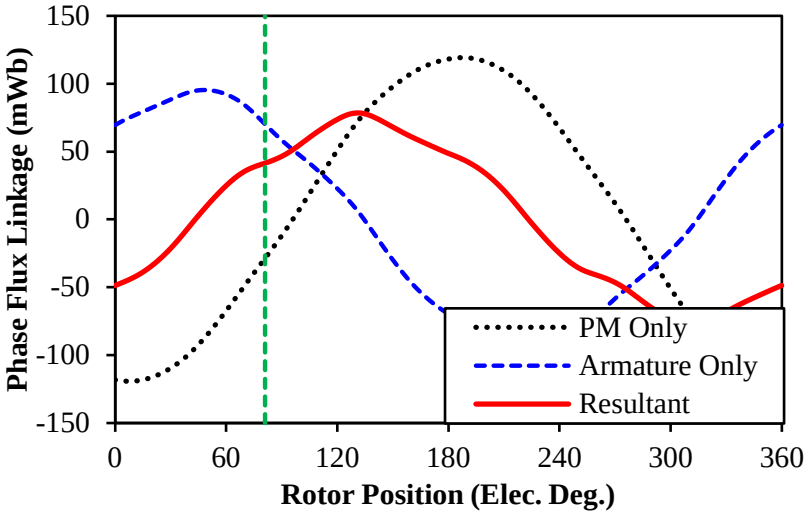

(a) Flux linkages

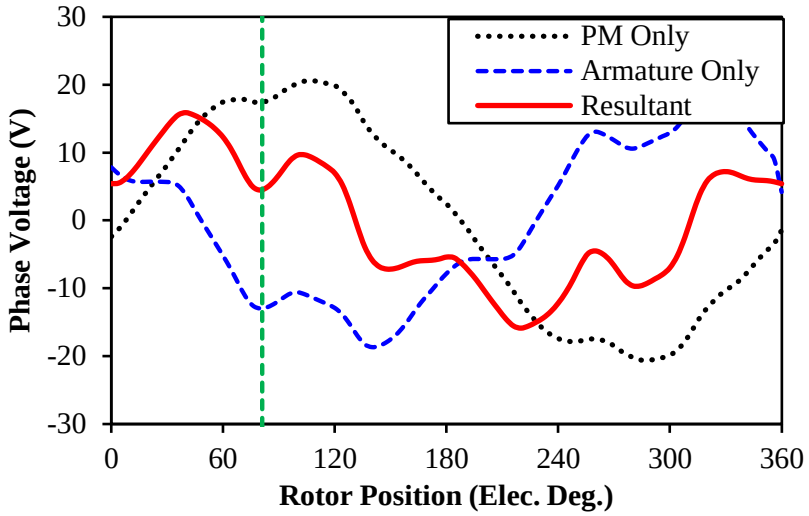

(b) Voltages

Fig. 4.4 On-load phase flux linkage and terminal voltage components by FP method (I_{max}=10A, β=60°, 400rpm).

Since armature reaction contributes to most of the voltage distortion, it is worth investigating the variation of armature reaction field when the voltage ripple occurs. With the aid of FP method, the process of the first voltage ripple can be illustrated in Fig. 4.5. The left column shows the real flux density distribution of each rotor position, while the right column shows the equipotential distribution of only armature field by FP method. When θ_r=60°, the armature flux generated by coil A tries to circulate through teeth B and C respectively, Fig. 4.5(a) and (b). However, due to the saturated iron ribs, the lamination rotor is separated as the isolated high permeance regions on the top of each magnet. Thus, the armature flux between teeth A and C can only circulate through leakage flux paths related with the tooth-tips in the

circle, which reduce the potential flux linkage of phase A, and enhance the local magnetic saturation in such tooth-tips and the rotor iron region around the related rotor ribs. Moreover, the flux in tooth B reduces to zero when θ_r=75°, Fig. 4.5 (c) and (d), and the tooth-tips and the lamination region around the rotor ribs become the only way for coil A flux to circulate, which significantly enhance their saturation levels. Therefore, the flux linkage in phase A is influenced most at such position, which generates the bottom of local voltage ripple, Fig. 4.4(b). After that, the highly saturated rotor flux barrier gradually rotates away, while the flux paths recover to normal, which reduce the saturation in the tooth-tip and end the process of one typical local voltage distortion, Fig. 4.5 (e) and (f).

The aforementioned process reveals the rotor ribs will significantly influence the armature flux paths and contribute to voltage distortion. Due to the geometric feature of IPM rotor topology, the rotor lamination regions are separated by saturated ribs and air flux barriers, which influence both major and leakage flux paths, and can be designated as ***the rotor segmentation effect***. Under load operation, this effect will push the armature reaction flux to circulate through leakage flux paths or highly saturated flux paths at some rotor positions, which distort the phase flux linkage and lead to the significant distortion of on-load armature voltage. Meanwhile, the undesired armature leakage flux will further increase the tooth-tip local magnetic saturation, which results in the distortion of on-load PM voltage, and further aggravates the overall on-load voltage distortion.

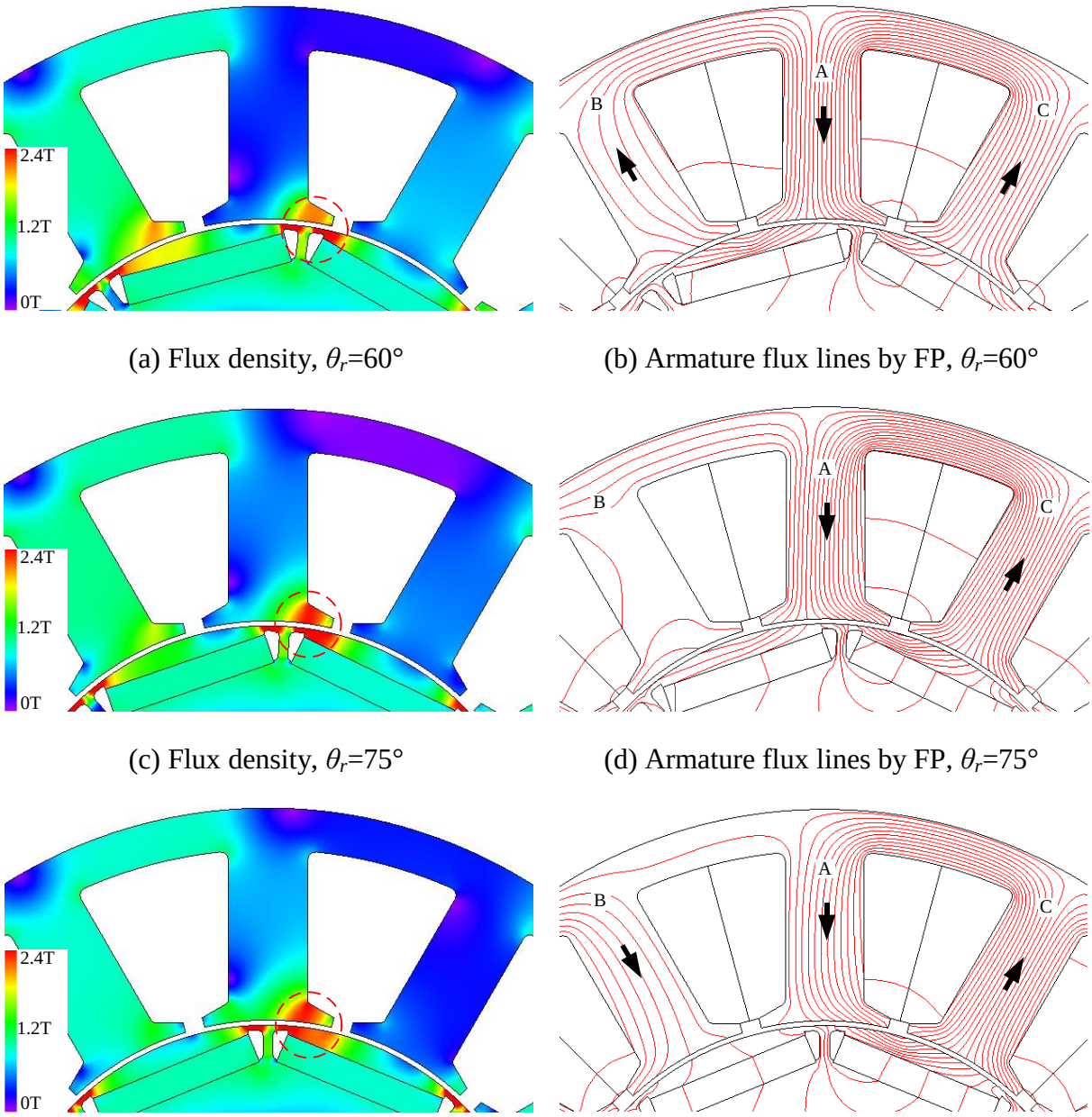

(a) Flux density, θ_r=60° (b) Armature flux lines by FP, θ_r=60°

(c) Flux density, θ_r=75° (d) Armature flux lines by FP, θ_r=75°

(e) Flux density, θ_r=90° (f) Armature flux lines by FP, θ_r=90°

Fig. 4.5 Variation of armature reaction flux distribution by FP method (I_{max}=10A, β=60°).

4.3.2 Influence of Current Advance Angle and Current Amplitude

Compared with the voltage distortion mechanism of SPM machine, it can be found that the local magnetic saturation in IPM machine is more complicated due to the rotor lamination. Since the voltage distortion increases with β in Fig. 4.3, the influence of rotor segmentation effect may increase with β as well. Fig. 4.6 illustrates the differences of flux paths between β=0° and β=90°. When β=0°, the typical flux paths circulate through the lamination region on the top of PMs following the arrowed line shown in Fig. 4.6(a). Beside the airgap, all other

parts are lamination, which offers high permeance flux paths for armature reaction flux. When β=90°, the relative rotor position for the same instantaneous armature current with β=0° is shifted by 90°, Fig. 4.6(b). In order to weaken the PM field, the armature flux is expected to go through PMs as the arrowed line. However, due to the very low permeance of PMs and saturated ribs, the majority of armature flux could only circulate through leakage flux paths when β=90°, which leads to strong voltage distortion according to the mechanism analysis. Therefore, with the increasing of β, the rotor segmentation effect will gradually become more problematic, which consequently leads to the increasing of voltage distortion level.

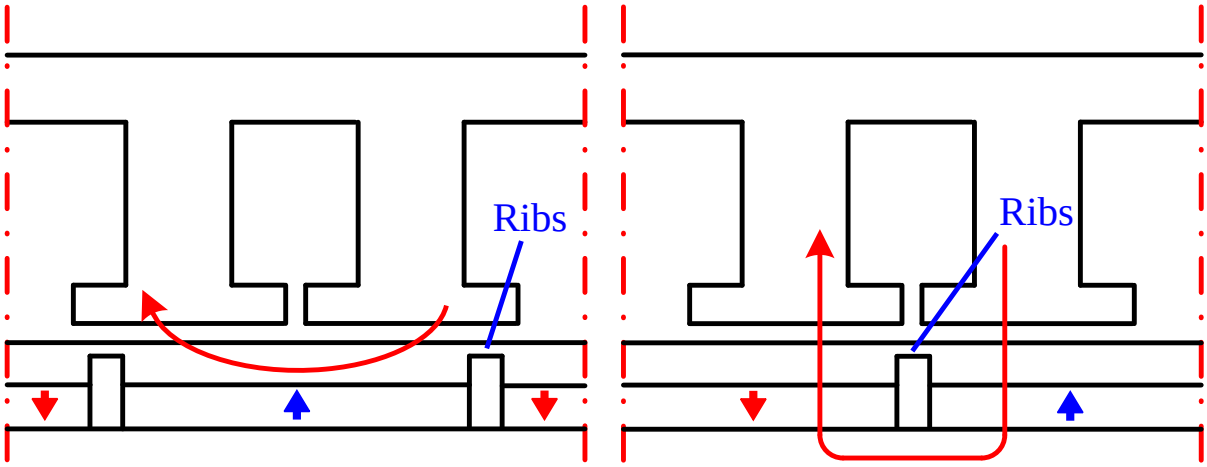

(a) β=0° (b) β=90°.

Fig. 4.6 Illustration of differences in flux paths for different β.

Meanwhile, I_{max} will also determine the levels of armature reaction and magnetic saturation, which will influence the on-load voltage distortion as well. In order to reflect this, the on-load voltage distortion presented by *VDR* with different I_{max} and β have been calculated and shown in Fig. 4.7. Clearly, when I_{max} is small, *VDR* is relatively small due to less magnetic saturation caused by armature reaction. With the increase of I_{max}, the maximum *VDR* increases as well. Meanwhile, for a certain I_{max}, the *VDR* is always higher when β approaches 90°, which has already been explained by the aforementioned analyses. Meanwhile, it is noticed that there is a nonlinear process with the increase of I_{max} when β=0°. When I_{max}=0, i.e. open-circuit, the back-EMF approaches sinusoidal as shown in Fig. 4.2(a). With the increase of I_{max}, the armature reaction flux quickly enhances the local magnetic saturation in tooth-tips and rotor iron region near airgap, which results in the increase of peak voltage and *VDR*. Nevertheless, if I_{max} continually increases, such local magnetic saturation will stop the peak

voltage to proportionally increase with I_{max}. But the fundamental phase voltage will be less influenced since the working points of the major flux paths were designed to be around the knee point of lamination material under rated current. Therefore, the *VDR* changes nonlinearly with the increase of I_{max} when β=0°.

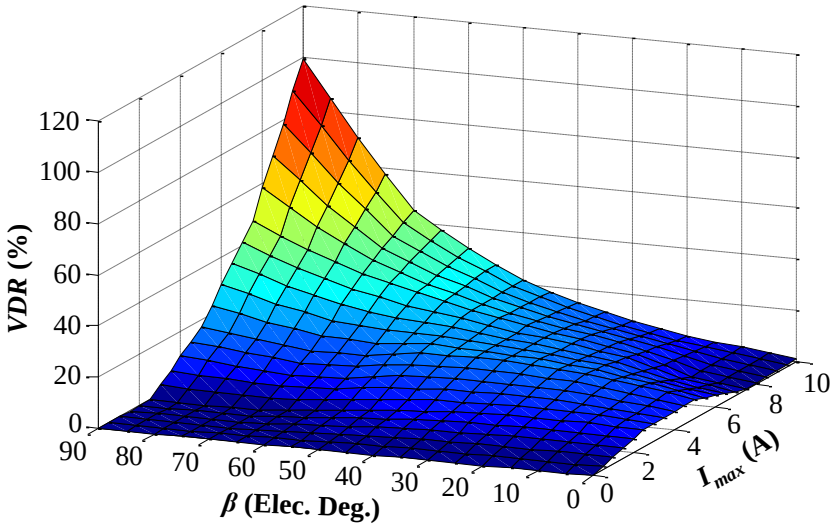

Fig. 4.7 Variation of *VDR* with different β and I_{max}.

4.3.3 Influence of Tooth-Tips Geometric Parameters

As shown in the analysis, the tooth-tips are one of the key geometric components to determine the local magnetic saturation and thereafter the voltage distortion. Therefore, this section will try to find out the relation between tooth-tip designs and on-load voltage distortion. Fig. 4.8 illustrates the main geometric parameters of the stator, which are the same as that for the SPM machines. When b_0=0, closed slot opening will be generated. As shown in the introduction part, the closed slot or alternative closed slot designs in IPM machines become more popular recently. Thus, an IPM machine with closed slot design is introduced for comparison in Fig. 4.9. The tooth-tip geometric parameters are listed in Table 4.2, while other major parameters are kept the same as Table 4.1.

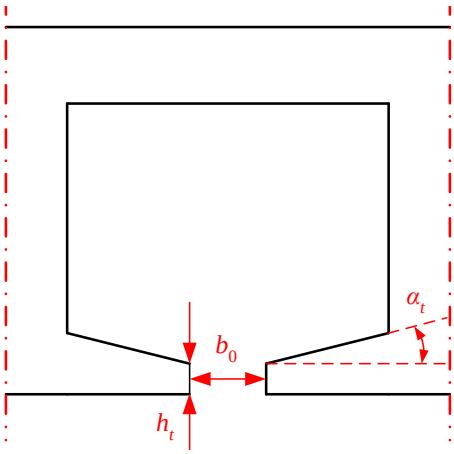

Fig. 4.8 Illustration of main geometric parameters of the tooth-tips.

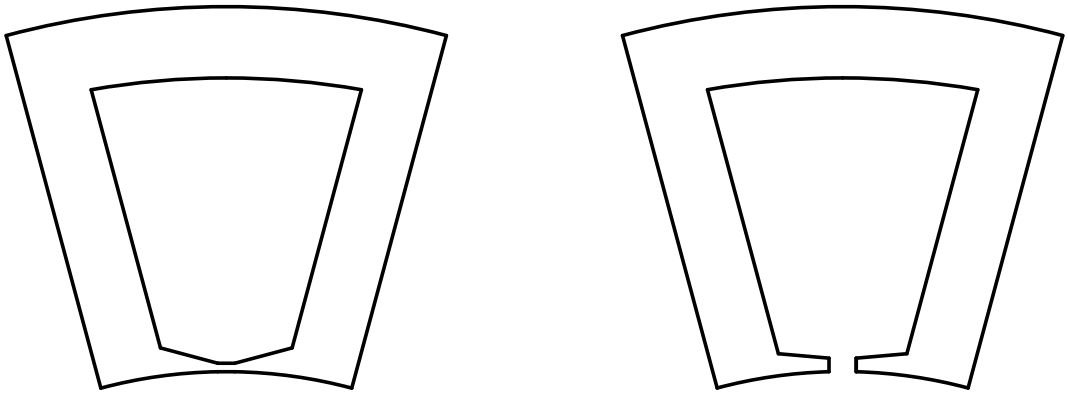

(a) Closed slot opening (b) Normal slot opening

Fig. 4.9 Comparison of stator lamination of closed and normal slot designs.

Table 4.2 Differential tooth-tip parameters for closed slot and normal slot openings.

Parameters	***Closed Slot Design***	***Normal Slot Design***
b_0	0mm	2mm
h_t	0.6mm	1mm
α_t	15°	10°

The terminal phase voltages for two models under different current conditions are compared in Fig. 4.10. For the closed slot design, the open-circuit back-EMF becomes more sinusoidal, although the fundamental value reduces due to higher tooth-tip leakage flux. More importantly, the closed slot design significantly increases the voltage distortions especially for β=0° due to more severe local magnetic saturation by tooth-tip leakage fluxes similar to that for the closed slot SPM machines. The *VDRs* for different β are calculated and compared in Fig. 4.11. Although the value of the closed slot opening design increases when β=0°, the

overall variation trend of *VDRs* still increases with β, which shows rotor segmentation effect plays more dominant role in the voltage distortion of IPM machines. Compared with the normal slot opening design, the *VDR* for closed slot design is almost doubled since the local magnetic saturation is more serious due to both leakage flux and rotor segmentation effect.

By taking β=60° for example, the *VDRs* for different tooth-tip designs can be reflected in Fig. 4.12, in which the *VDR* always increases when b_0 approaches zero, which is similar to the SPM machine since the variation of local magnetic saturation becomes more significant for small or closed slot openings. For fixed h_t and α_t, *VDR* slightly reduces with the reduction of b_0 first, since the increased length of tooth-tips widens the flux paths and compensates for the rotor segmentation effect to some extent. However, if b_0 continuously reduces, the variation of local magnetic saturation caused by leakage fluxes will become more dominant, which quickly enhances the *VDR* when b_0 approaches zero. Meanwhile, if h_t or α_t is too small, the flux through tooth-tips will be limited. Thus, the amount of fluxes influenced by the variation of local magnetic saturation will be relatively small compared with the main flux, which also limits the maximum value of *VDR*.

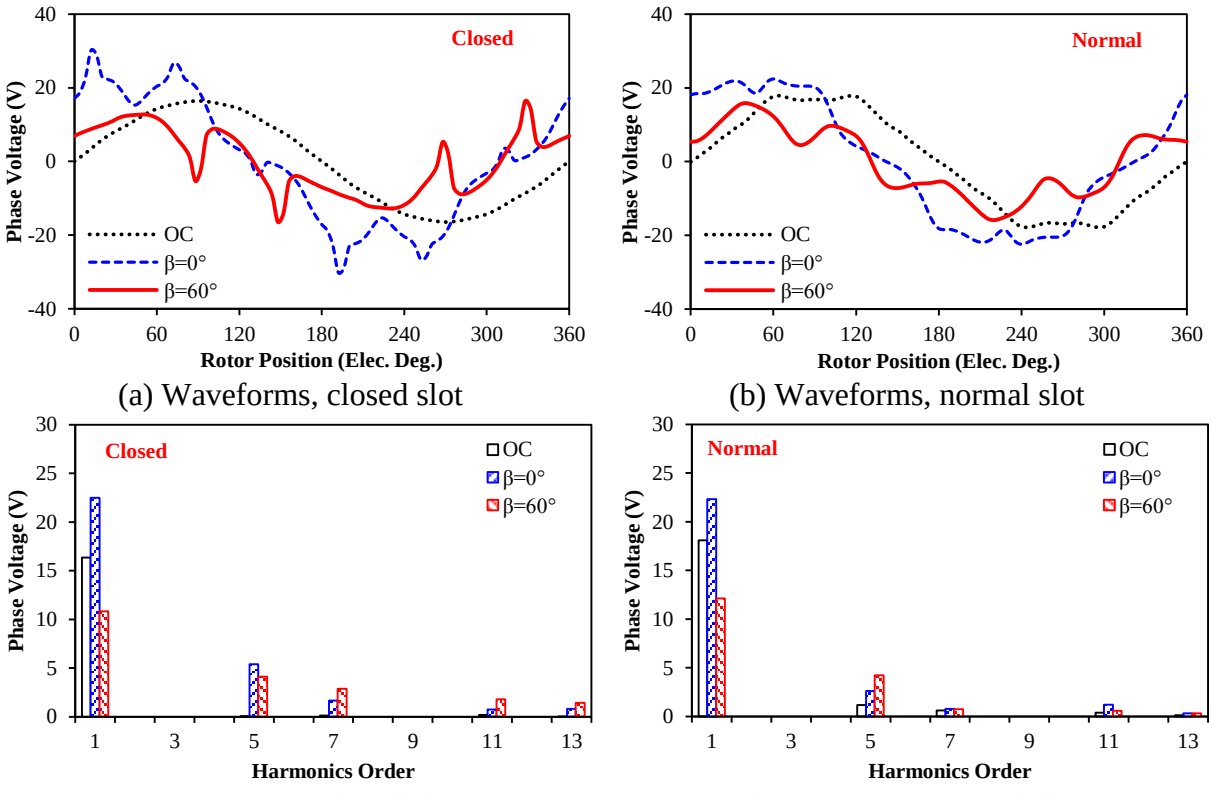

(a) Waveforms, closed slot (b) Waveforms, normal slot

(c) Harmonics, closed slot (d) Harmonics, normal slot

Fig. 4.10 Comparison of phase voltages for different tooth-tip designs (I_{max}=10A, 400rpm).

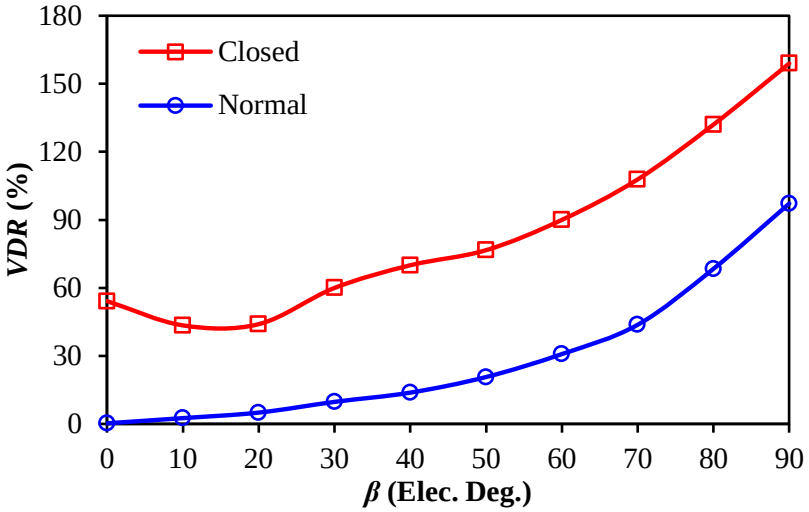

Fig. 4.11 Comparison of *VDR* for different tooth-tip designs (I_{max}=10A, 400rpm).

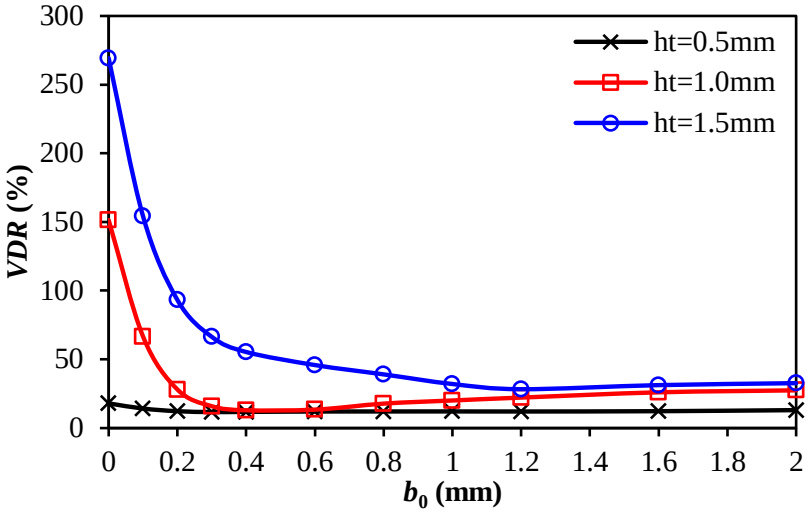

(a) *VDR* against b_0 and h_t, α_t=10°

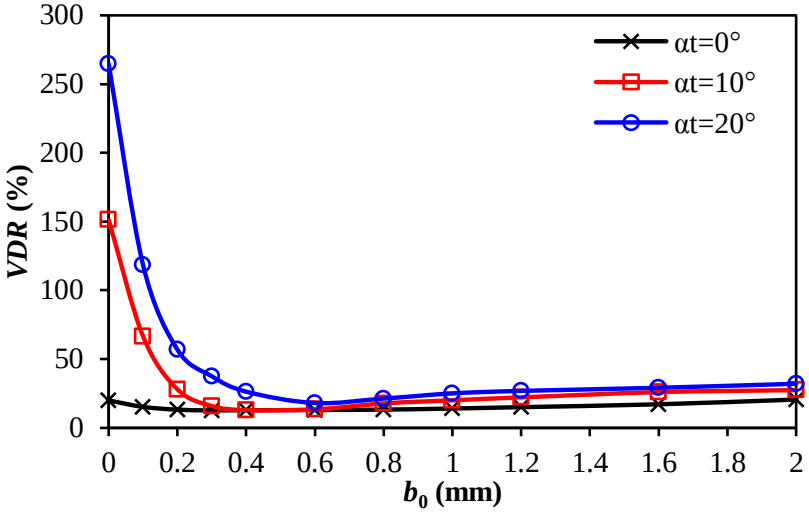

(b) *VDR* against b_0 and α_t, h_t=1mm

Fig. 4.12 Variation of *VDR* against tooth-tip geometric parameters (I_{max}=10A, β=60°, 400rpm).

4.3.4 Influence of Rotor Geometric Parameters

The aforementioned local magnetic saturation will be influenced by the iron region near the rotor surface as well, which could be majorly influenced by the rotor pole arc angle α_p, the step length of iron region above magnets h_r, and the width of rotor central beam w_r as defined in Fig. 4.13. In order to describe the influence of pole arc, the pole arc / pole pitch ratio $k_{\alpha p}$ could be adopted. Due to the feature of IPM rotor, $k_{\alpha p}$ could not reach 1, which is limited by the iron bridge and magnet thickness. By taking β=60° as example, the variation of *VDR* against $k_{\alpha p}$ could be reflected in Fig. 4.14(a) with other parameters fixed. With the reduction of $k_{\alpha p}$, the magnet length significantly reduced, which can be reflected as the decreasing of open-circuit back-EMF shown in Fig. 4.14(b). Thus, both peak and fundamental voltages reduce with $k_{\alpha p}$ as well. Meanwhile, *VDR* reduces with $k_{\alpha p}$ firstly, but then rises up again when $k_{\alpha p}$ is small.

In order to explain this, the terminal phase voltages for three typical $k_{\alpha p}$ are compared in Fig. 4.15, in which the dashed circle indicates the first local voltage ripple within an electric period. The aforementioned analysis reveals that this voltage ripple is caused by the rotor segmentation effect. With the reduction of $k_{\alpha p}$, the flux paths become even narrow in Fig. 4.16, which makes the armature flux still difficult to change smoothly. Thus, the minimum values of the local voltage ripples are almost the same for three machines with different $k_{\alpha p}$. Meanwhile, it also can be seen from Fig. 4.15 that the variation of *VDR* with $k_{\alpha p}$ is more relevant with the reduction of peak voltages instead of the voltage ripples. Actually, the open-circuit back-EMF shapes could be changed significantly by adjusting the rotor pole arc [KIM07] as shown in Fig. 4.17. With the reduction of $k_{\alpha p}$, e.g. 0.7, the back-EMF becomes more sinusoidal, which reduces the harmonics and leads to smaller *VDR*. However, if $k_{\alpha p}$ reduces further, e.g. 0.5, the back-EMF shape becomes less sinusoidal again, which makes the peak value higher than fundamental value. Considering about the barely changed amplitudes of voltage ripples, *VDR* will increase again if $k_{\alpha p}$ is too small.

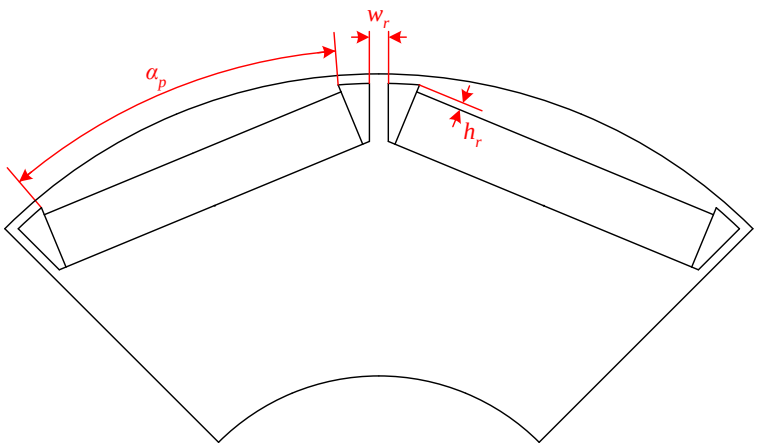

Fig. 4.13 Illustration of major rotor geometric parameters for IPM machine.

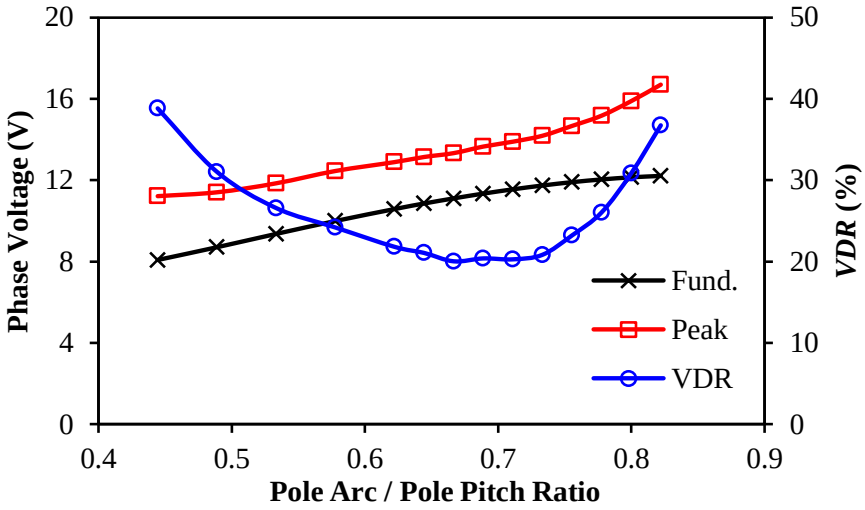

(a) *VDR* against $k_{\alpha p}$

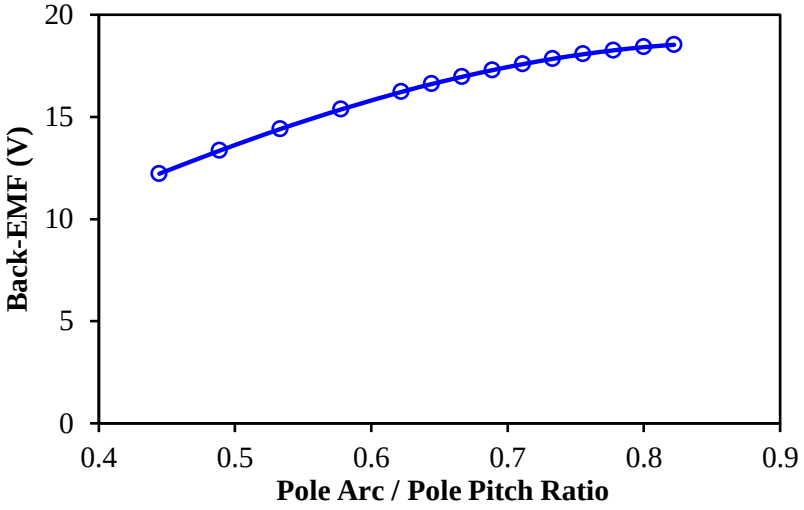

(b) Back-EMF against $k_{\alpha p}$

Fig. 4.14 Variation of *VDR* for different $k_{\alpha p}$ (I_{max}=10A, β=60°, w_r=0.5mm, h_r=0.4mm).

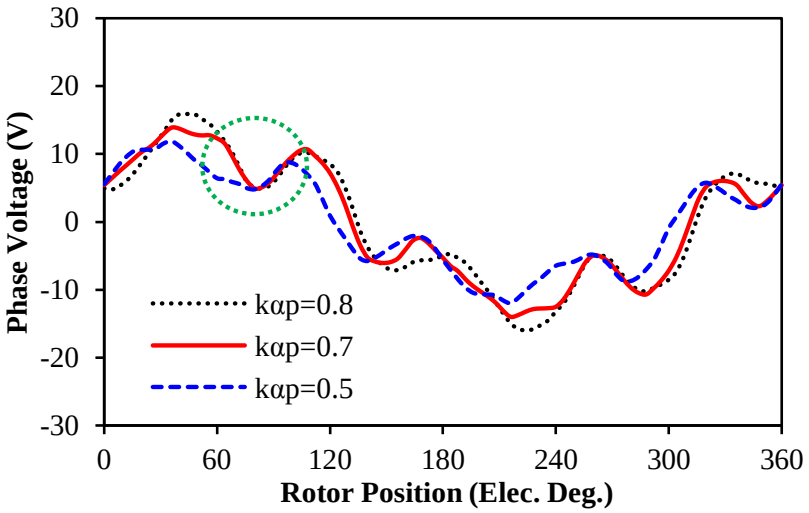

(a) Waveforms

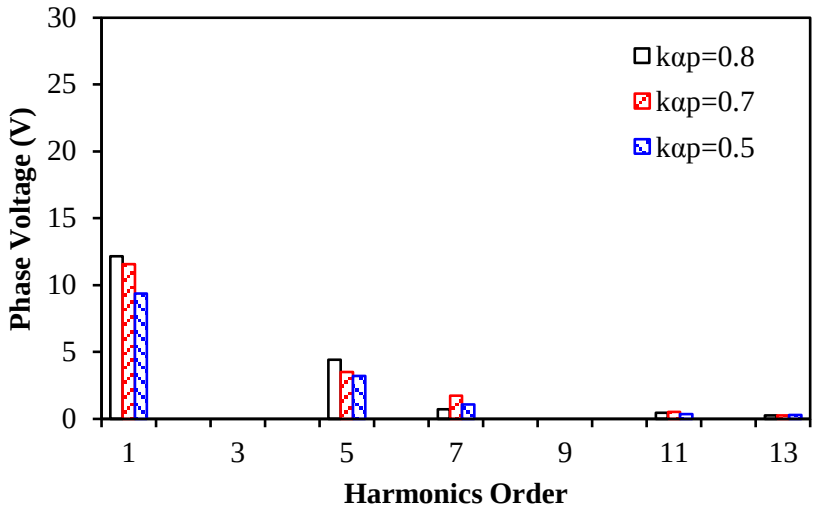

(b) Harmonics

Fig. 4.15 Comparison of terminal phase voltages for different $k_{\alpha p}$ (I_{max}=10A, β=60°, w_r=0.5mm, h_r=0.4mm, 400rpm).

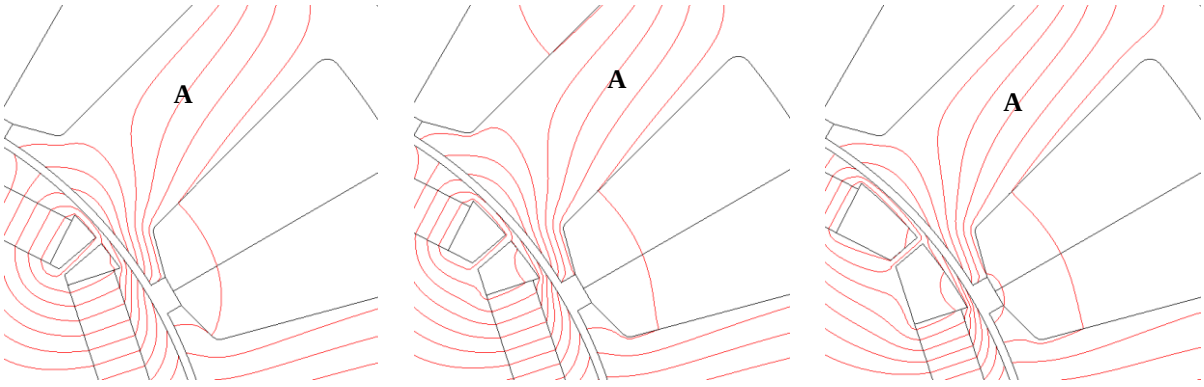

(a) $k_{\alpha p}$=0.8 (b) $k_{\alpha p}$=0.7 (c) $k_{\alpha p}$=0.5

Fig. 4.16 Comparison of equipotential distribution for different $k_{\alpha p}$ (I_{max}=10A, β=60°, θ_r=75°, w_r=0.5mm, h_r=0.4mm).

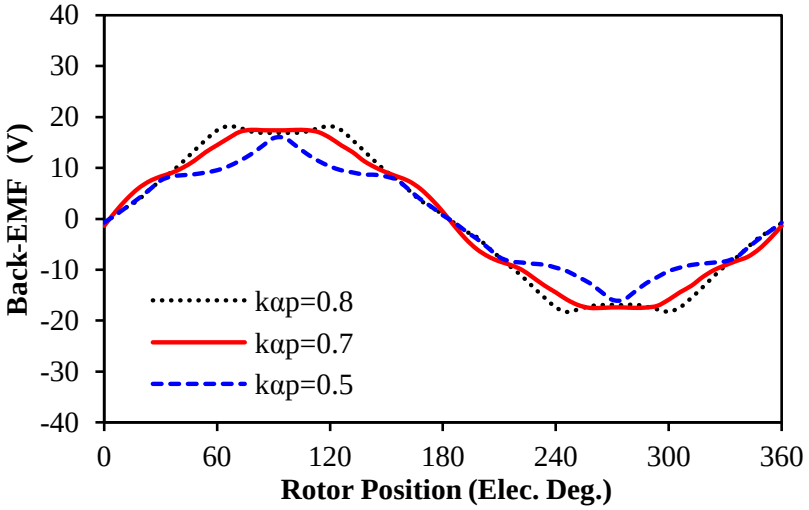

(a) Waveforms

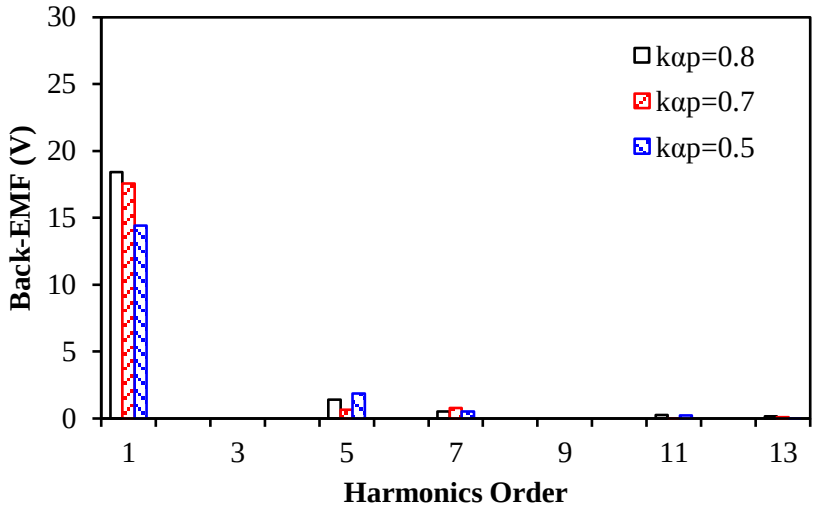

(b) Harmonics

Fig. 4.17 Comparison of open-circuit back-EMFs for different $k_{\alpha p}$ (400rpm, w_r=0.5mm, h_r=0.4mm).

The variation of *VDR* against w_r for the fixed $k_{\alpha p}$ and h_r are calculated and shown in Fig. 4.18(a), while the variation of fundamental back-EMF is shown in Fig. 4.18(b). Due to the reduction of flux bridge length the inter-pole leakage flux increases, which reduces the fundamental back-EMF. However, due to the extra flux paths offered by the centre rib, Fig. 4.19, *VDR* will reduce with the increase of w_r. Normally, w_r will not be too wide in fractional slot machines since it will reduce the length of rotor flux bridges and influences the maximum pole arc, but it still offers an option to reduce the voltage distortion level.

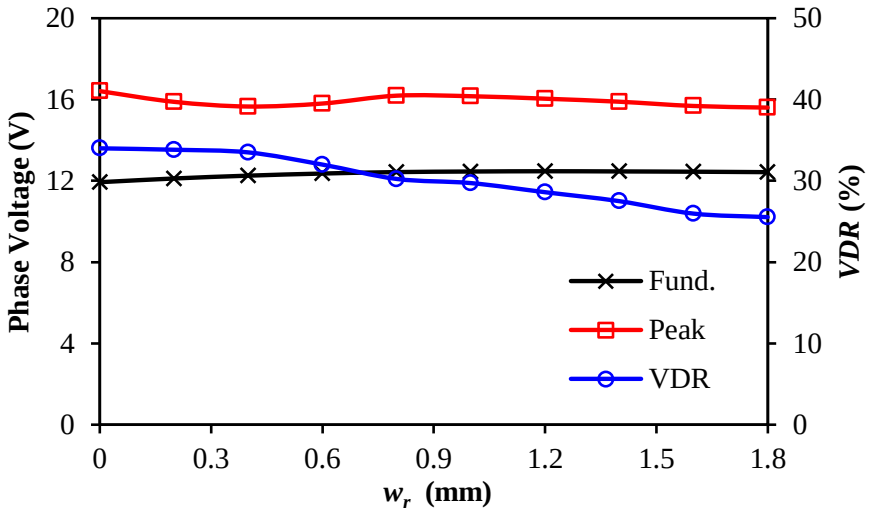

(a) *VDR* against w_r

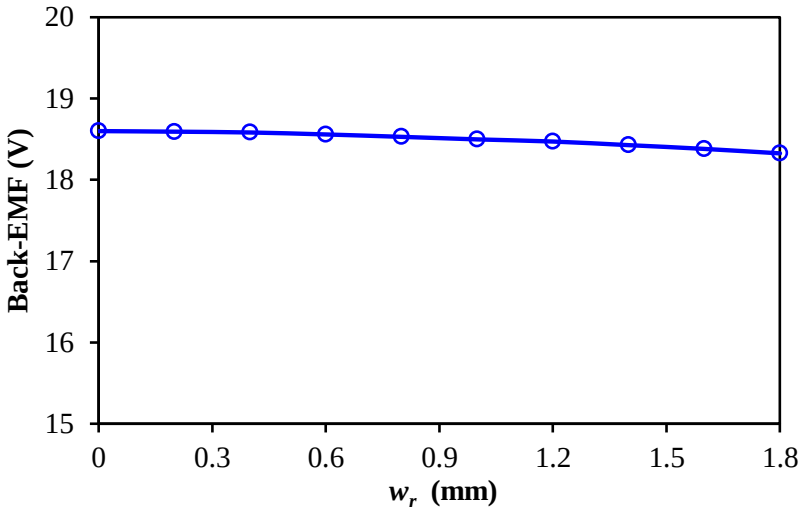

(b) Back-EMF against w_r

Fig. 4.18 Variation of *VDR* for different w_r (I_{max}=10A, β=60°, 400rpm, $k_{\alpha p}$=0.8, h_r=0.4mm).

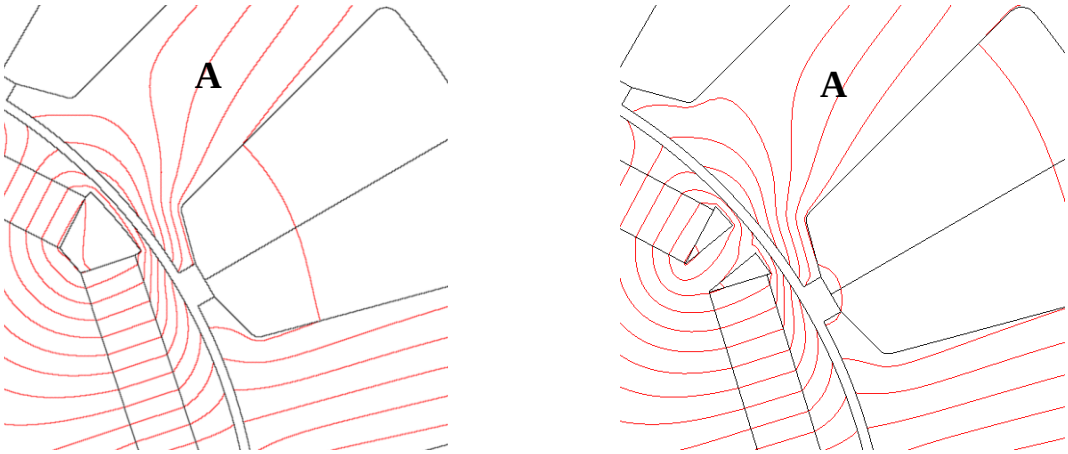

(a) w_r=0mm, θ_r=75° (b) w_r=1.8mm, θ_r=75°

Fig. 4.19 Comparison of equipotential distribution for different w_r (I_{max}=10A, β=60°, 400rpm, $k_{\alpha p}$=0.8, h_r=0.4mm).

Fig. 4.20(a) shows the variation of *VDR* for machines with different h_r. With the increase of h_r, *VDR* increases at first. However, the increasing trend becomes saturated if h_r is larger than 0.6mm. Meanwhile, with the increase of h_r, the two adjacent PMs become closer physically, which increases the inter-pole leakage and reduces the fundamental back-EMF, Fig. 4.20(b). Fig. 4.21 compares the terminal phase voltages for different h_r at the same current condition. Due to more iron region above the magnet, the local magnetic saturation in rotor iron region is released, which can be reflected in Fig. 4.22. Based on this, the voltage harmonics, e.g. 7^{th} and 11^{th}, reduce with the increase of h_r. However, the peaks of the voltages are almost unchanged during the variation process, which lead to the increase of *VDR* since the fundamental voltages reduce. Fig. 4.23 compares the phase flux linkages for the three different w_r. Clearly, when the flux linkages cross zero, the phase voltages reach the peaks at the same time. Since the tooth body is unsaturated during the flux linkage zero-crossing period, the zero-crossing speed rates of the flux linkages are determined by the design of major flux paths, as well as the excitation sources, e.g. PM and armature current. Since all these conditions are the same for three different machines, their flux linkage zero-crossing speeds will be the same, which leads to the same on-load peak voltages as well.

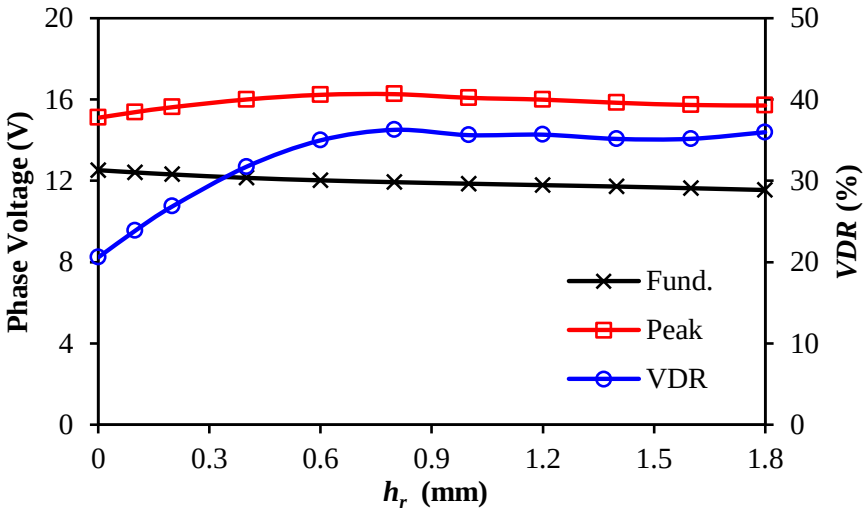

(a) *VDR* against h_r

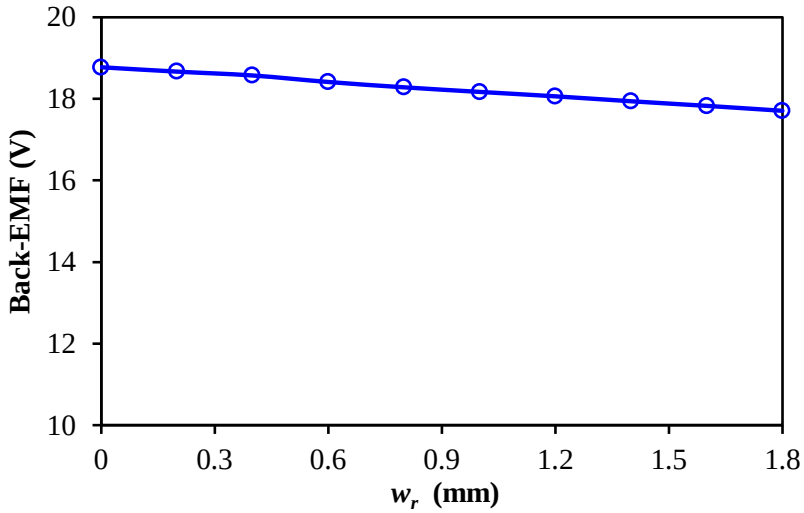

(b) EMF against h_r

Fig. 4.20 Variation of *VDR* for different h_r (I_{max}=10A, β=60°, 400rpm, k_{ap}=0.8, w_r=0.5mm).

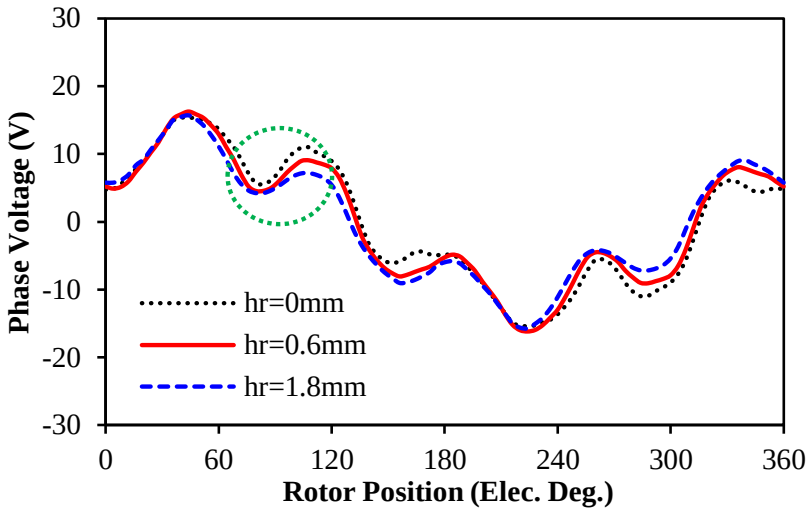

(a) Waveforms

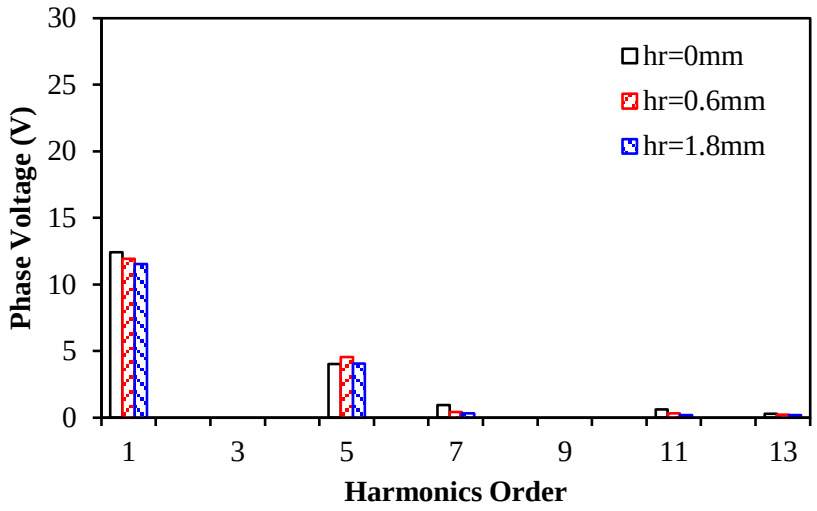

(b) Harmonics

Fig. 4.21 Comparison of terminal phase voltages for different h_r, (I_{max}=10A, β=60°, 400rpm, $k_{\alpha p}$=0.8, w_r=0.5mm).

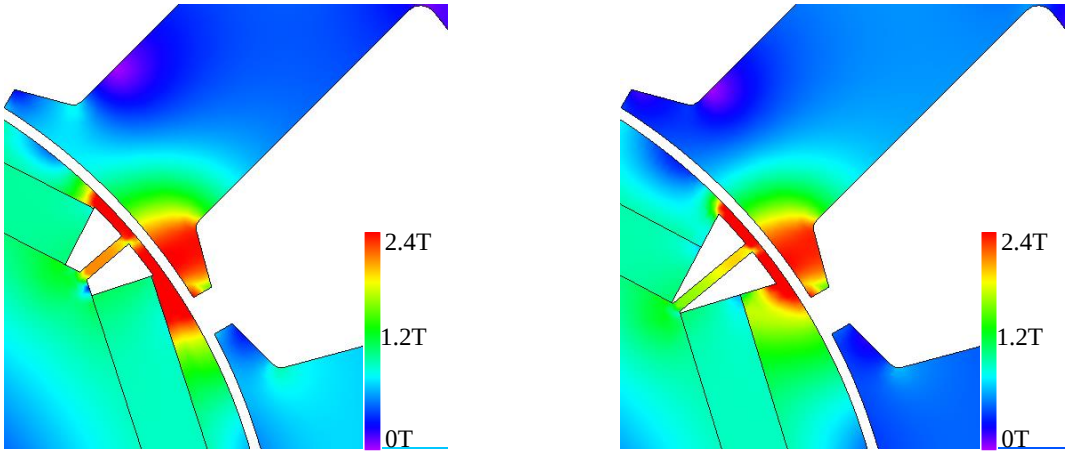

(a) h_r=0mm, θ_r=75° (b) h_r=1.8mm, θ_r=75°

Fig. 4.22 Comparison of flux density distributions for different h_r (I_{max}=10A, β=60°, $k_{\alpha p}$=0.8, w_r=0.5mm).

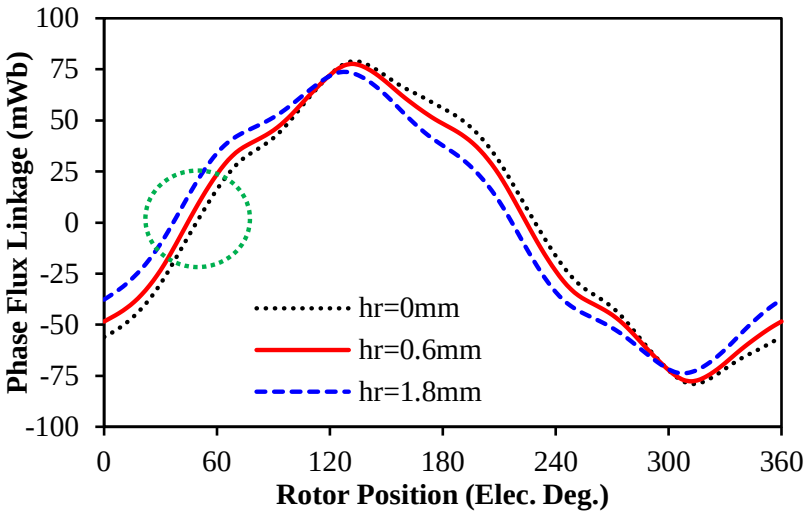

Fig. 4.23 Comparison of phase flux linkages for different h_r, (I_{max}=10A, β=60°, 400rpm, $k_{\alpha p}$=0.8, w_r=0.5mm).

4.4 Electromagnetic Performance Influenced by Voltage Distortion and Local Magnetic Saturation

According to the aforementioned analyses, the on-load voltage distortion represents the variation of local magnetic saturation as well as the rotor segmentation effect. Therefore, other electromagnetic performance may change accordingly, which will be investigated in this section.

4.4.1 On-Load Back-EMF

The on-load back-EMF is the voltage induced by the PM magnetic field only with consideration of the saturation in lamination on load. According to the mechanism of terminal voltage distortion, the local magnetic saturation changes the on-load PM flux linkage, which influences the on-load back-EMF as well. The three-phase on-load back-EMFs at rated current with β=60° can be calculated by FP method in Fig. 4.24(a), while the comparison with open-circuit condition is illustrated in Fig. 4.24(b) and (c). Since the PM leakage fluxes through flux bridges are reduced by armature reaction, the fundamental on-load back-EMF is larger than the open-circuit condition. With the increase of β, the on-load back-EMF continuously increases, Fig. 4.25. Although *VDR* rises with β, the peak of on-load back-EMF is higher than the fundamental value when β is small due to relative higher global magnetic saturation. However, the difference between peak and fundamental voltages reduces with the growing of β, which makes the peak values almost the same as the fundamental results when

β approaches 90°, which also reveals that the influence of rotor segmentation effect on armature field is more dominant for the voltage distortion in flux weakening region.

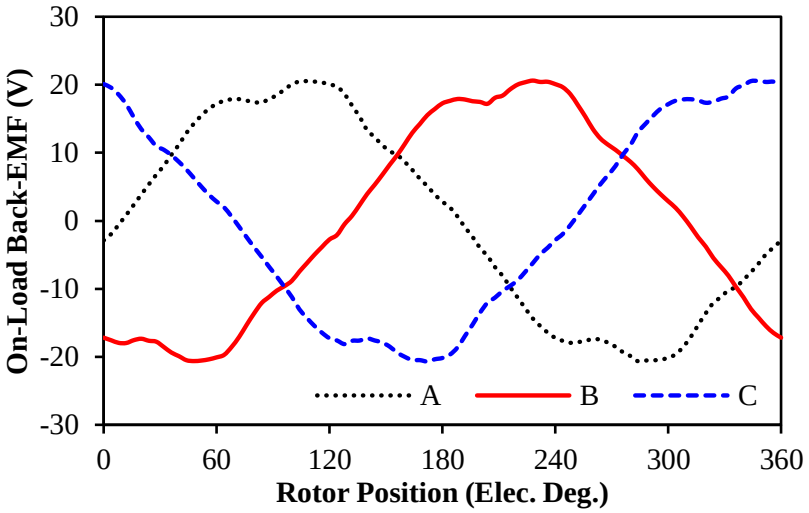

(a) Three phase on-load back-EMF

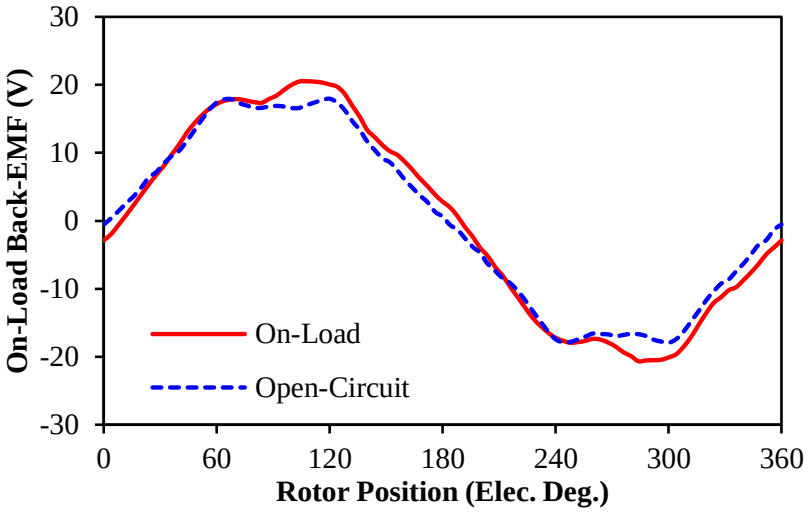

(b) Comparison with open-circuit condition

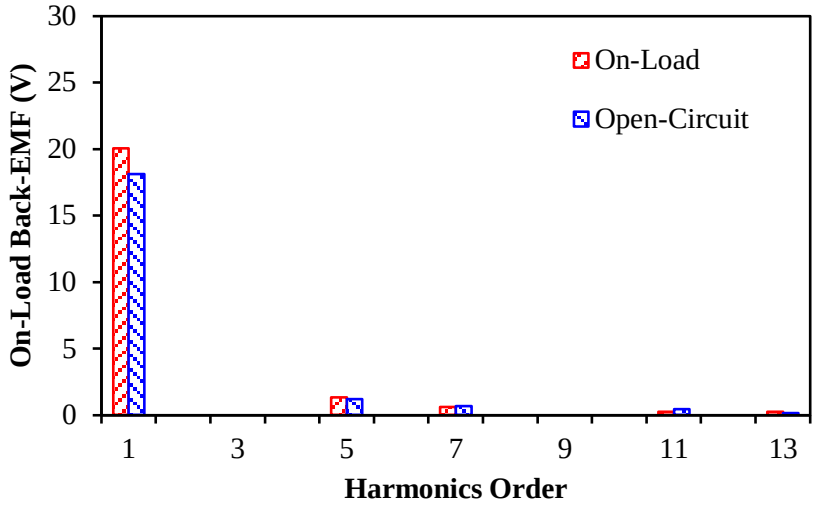

(c) Harmonic components

Fig. 4.24 Comparison of open-circuit and on-load back-EMFs (I_{max}=10A, β=60°, 400rpm)

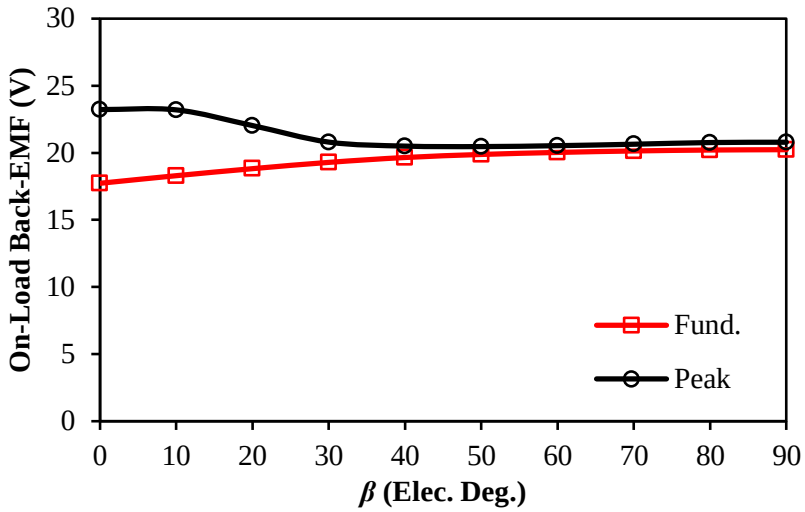

Fig. 4.25 Variation of peak and fundamental on-load back-EMFs against β (I_{max}=10A, 400rpm).

4.4.2 DQ-Axis Inductances

When β=0°, the variation of *dq*-axis flux linkage components are shown in Fig. 4.26. The PM flux linkages can represent the on-load back-EMF, while the armature flux linkages can represent the voltage drop on armature winding inductances. All waveforms significantly change every 60°, even for the *d*-axis armature flux linkage with zero average value. Normally, it is expected that there is no *q*-axis armature PM linkage since the rotor pole centre is aligned with armature *d*-axis under vector control. However, the cross saturation effect between *dq*-axes shifts the real *d*-axis of PM field [YAM14], which leads to nonzero on-load *q*-axis PM flux linkage. With the increase of β, the saturation in main flux paths reduces due to the flux weakening effect, which can be reflected as the smooth *dq*-axis PM flux linkages when β=90°, Fig. 4.27. The increase of *VDR* can be reflected as the obvious ripples in *dq*-axis armature flux linkages due to rotor segmentation effect.

With the aid of FP method, the *dq*-axis inductances waveforms under different β can be calculated in Fig. 4.28, in which the average values of L_q are always larger than L_d due to the saliency of IPM rotors. Similar to the variation of *dq*-axis flux linkages, the *dq*-axis inductances fluctuate simultaneously when β=0°. With the increase of β, the saturation in main flux paths releases, which makes the fluctuation of L_d reduce. However, the rotor segmentation effect increases with β, which causes ripples of L_q even when β=90°. This can be reflected more clearly in Fig. 4.29. With the increase of β, the gap between peak and fundamental values of L_d gradually reduces due to the reduction of global saturation.

However, the gap between peak and fundamental values of L_q slightly reduces initially, but then increases continuously due to the increasing rotor segmentation effect.

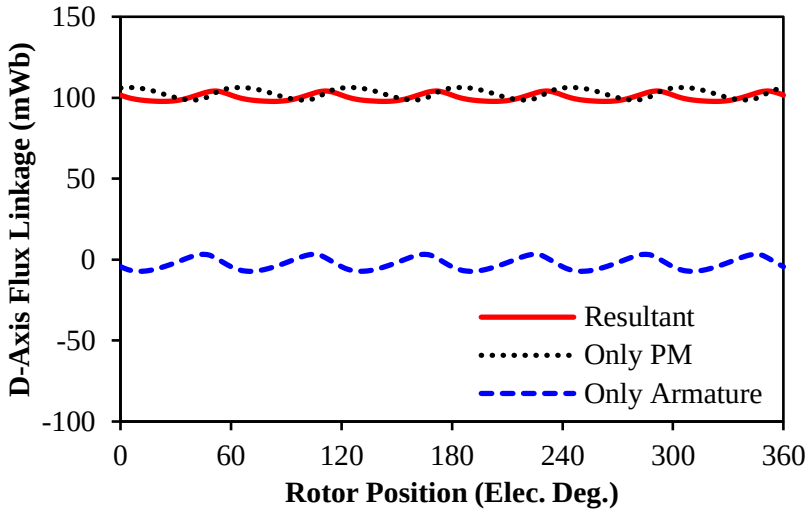

(a) D-axis flux linkages, β=0°

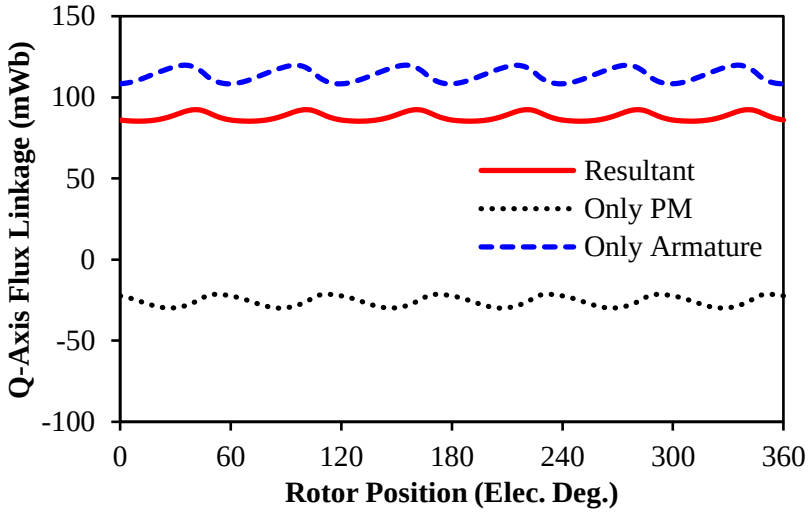

(b) Q-axis flux linkages, β=0°

Fig. 4.26 Variation of *dq*-axis flux linkages by FP method for β=0° (I_{max}=10A, β=0°)

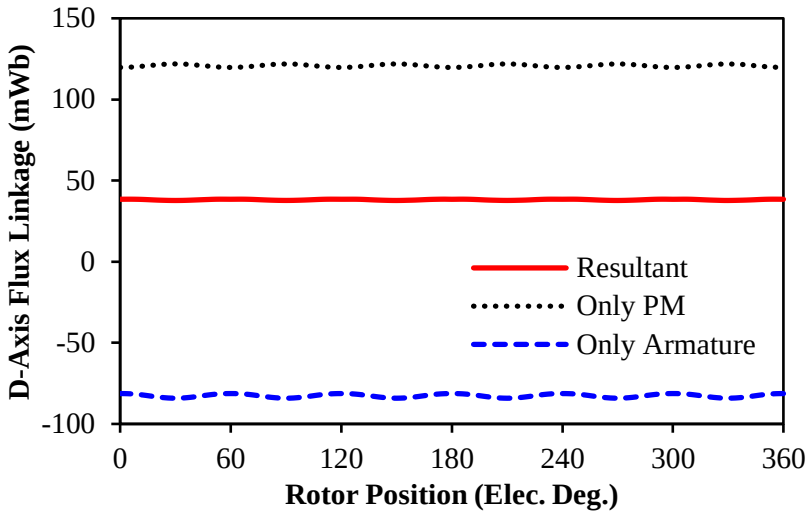

(a) D-axis flux linkages, β=90°

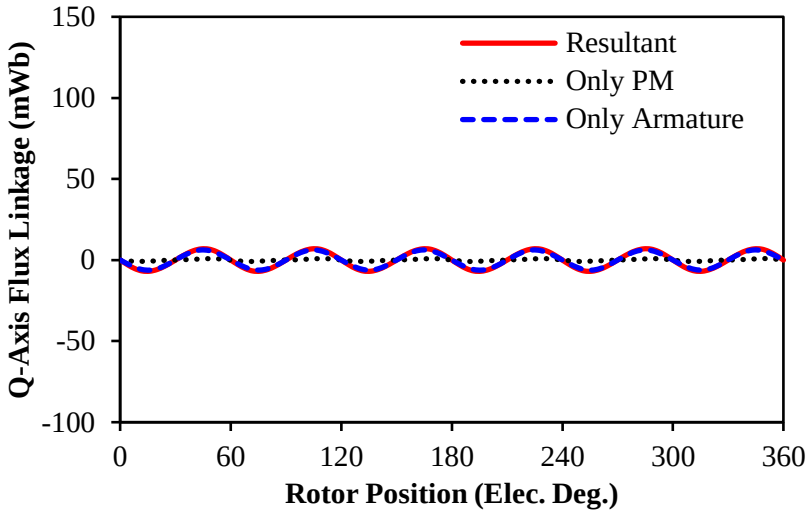

(b) Q-axis flux linkages, β=90°

Fig. 4.27 Variation of *dq*-axis flux linkages by FP method for β=90° (I_{max}=10A, β=90°)

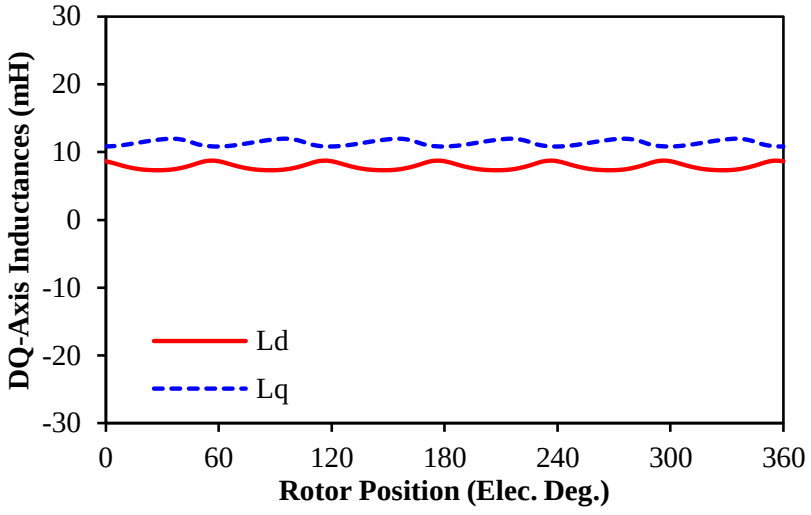

(a) β=0°

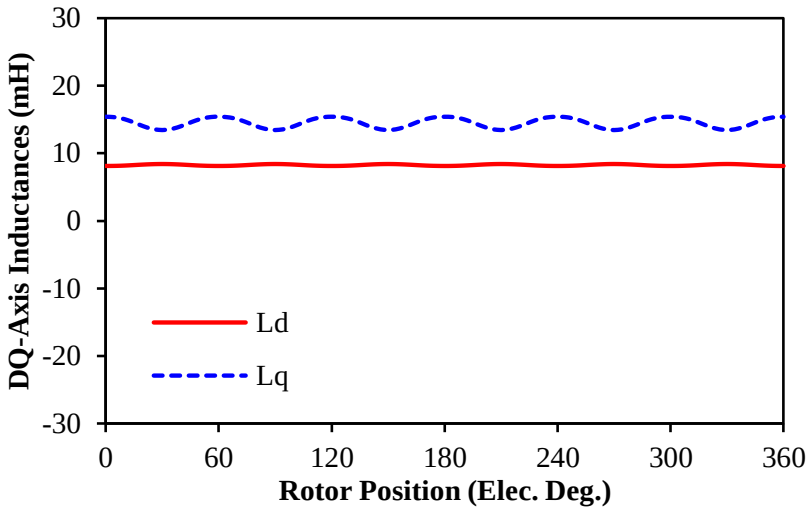

(b) β=90°

Fig. 4.28 Waveforms of *dq*-axis inductances by FP method (I_{max}=10A).

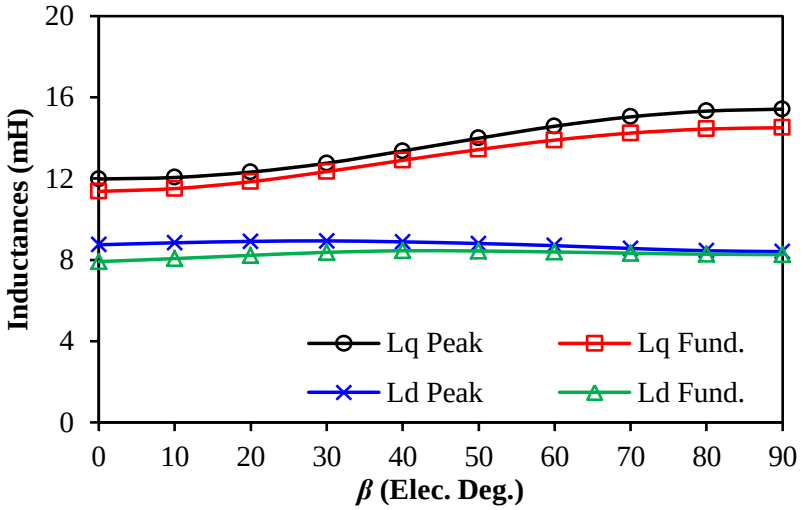

Fig. 4.29 Variation of *dq*-axis inductances against β by FP method (I_{max}=10A).

4.4.3 On-Load Cogging Torque and Torque Ripple

By FP method, the on-load cogging torque could be calculated in Fig. 4.30 together with the open-circuit cogging torque. Since the highly saturated rotor ribs increase the variation of airgap permeance compared with SPM machines, the open-circuit cogging torque is also more obvious. Due to the magnetic saturation, the on-load cogging torque is still much higher than the open-circuit condition. The pk-pk on-load cogging torque with different β is shown in Fig. 4.31. With the increase of β, the global saturation has been released, which reduces the on-load cogging torque at first. However, the rotor segmentation effect also increases with β, which gradually enhances the local magnetic saturation in tooth-tips and leads to the increase of on-load cogging torque.

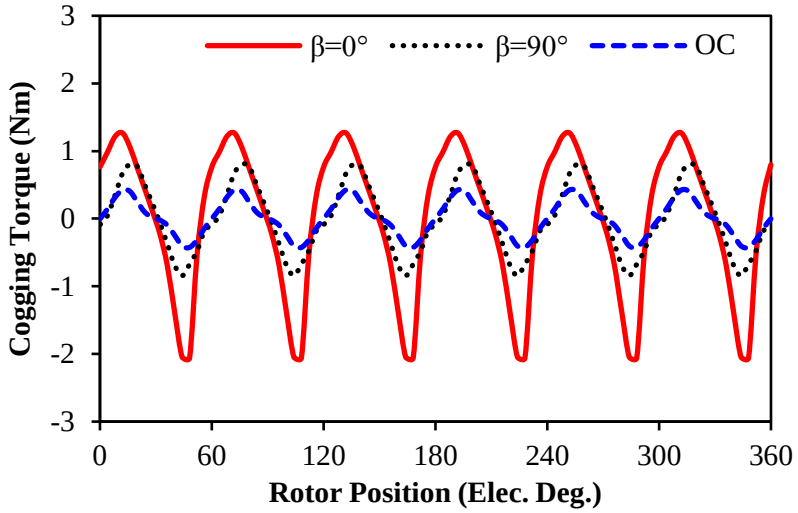

Fig. 4.30 Comparison of open-circuit and on-load cogging torques (I_{max}=10A, β=0°).

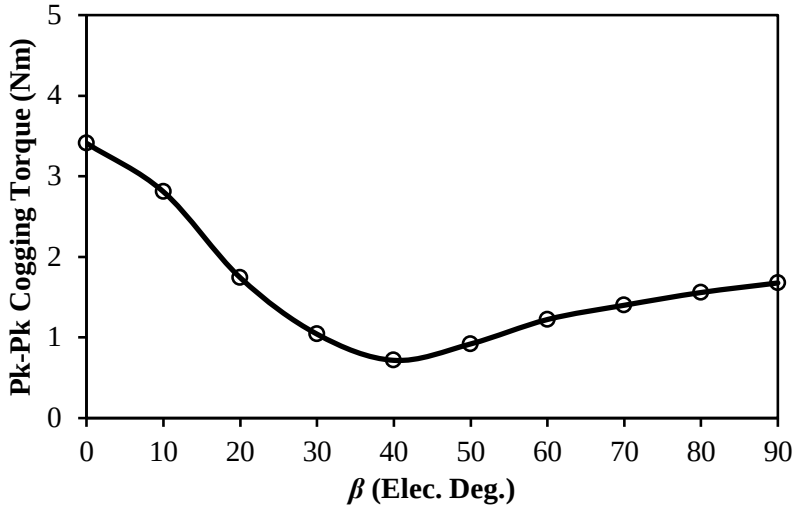

Fig. 4.31 Variation of pk-pk on-load cogging torque against β (I_{max}=10A).

The torque components for β=0° can be calculated in Fig. 4.32(a). It can be observed that all components fluctuate significantly, which leads to significant resultant 6n times ripples in the resultant torque (T_{all}). Fig. 4.32(b) shows the harmonics of each torque components, in which the zero order harmonic refers to average torque. Due to the cross saturation, there is slight negative T_r even under I_d=0 control. When β=90°, the torque components are shown in Fig. 4.33. Although the average torques for all components are zero, the 6n times torque ripples are still significant due to the local magnetic saturation.

The variation of torque ripple against different β can be calculated and shown in Fig. 4.34. Since the global saturation reduces with β but rotor segmentation effect increases with β,

T_{ripple} does not change obviously at first. However, the rotor segmentation effect plays more dominant role in flux weakening regions while the average torque reduces with β, T_{ripple} rises quickly after β=50°.

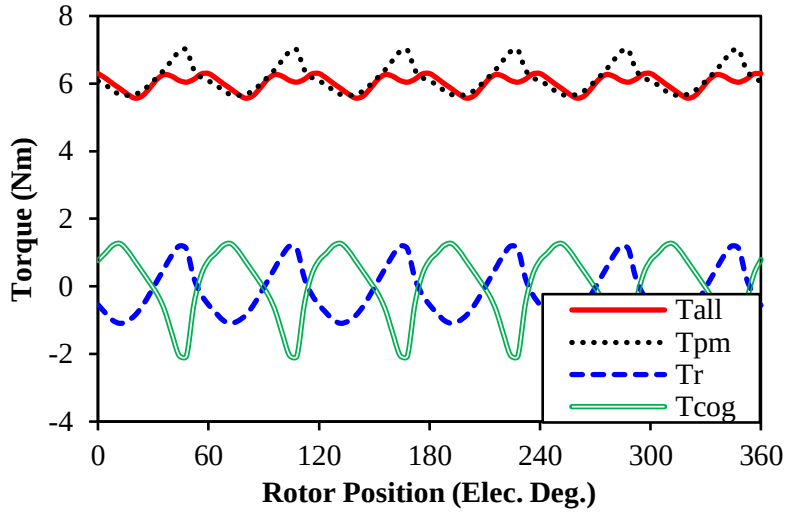

(a) Waveforms, β=0°

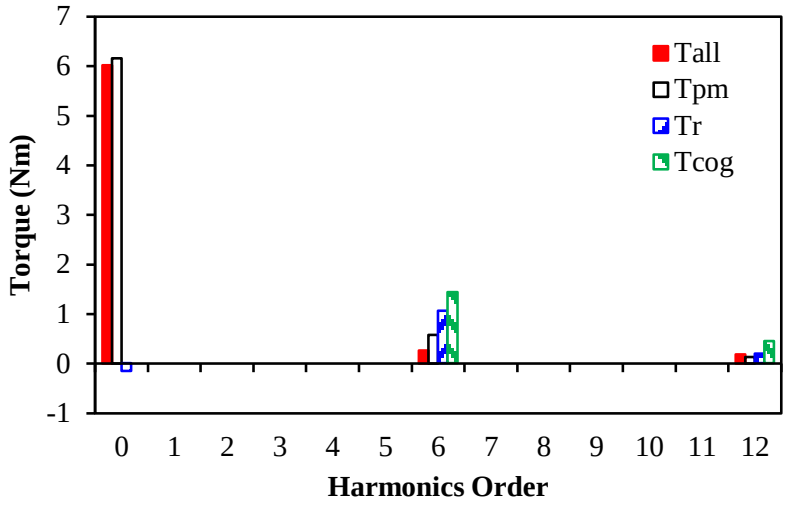

(b) Harmonics, β=0°

Fig. 4.32 Variation of torque components by FP method for β=0° (I_{max}=10A, β=0°).

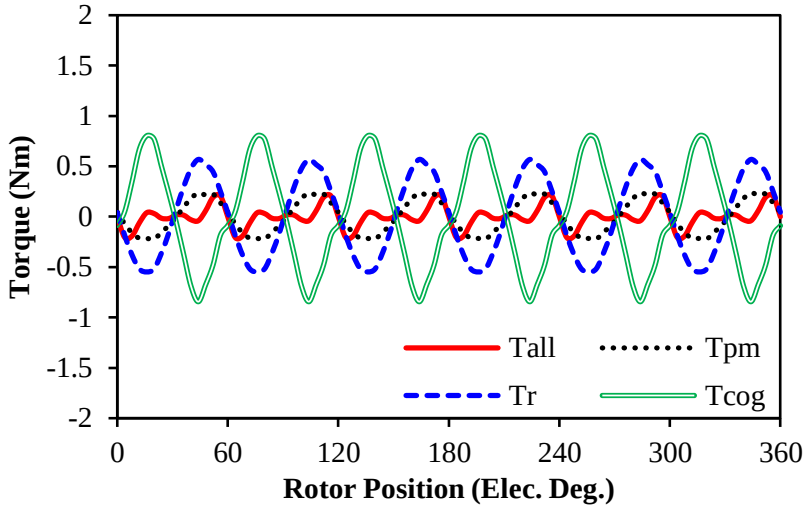

(a) Waveforms, β=90°

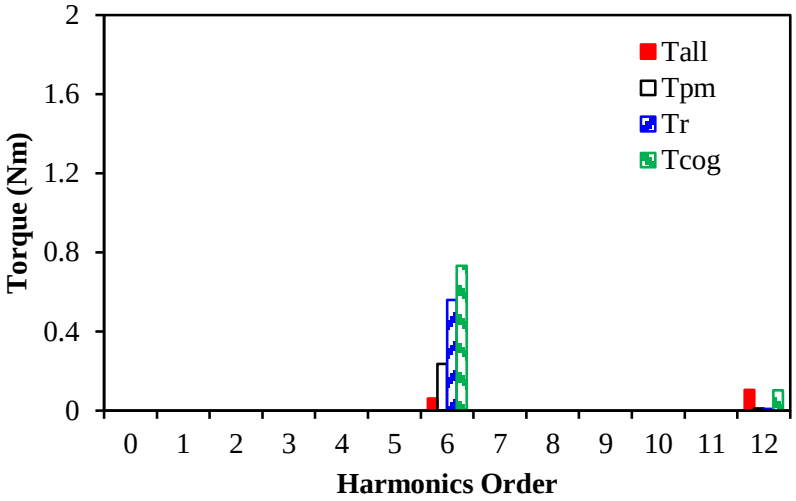

(b) Harmonics, β=90°

Fig. 4.33 Variation of torque components for β=90° (I_{max}=10A, β=90°).

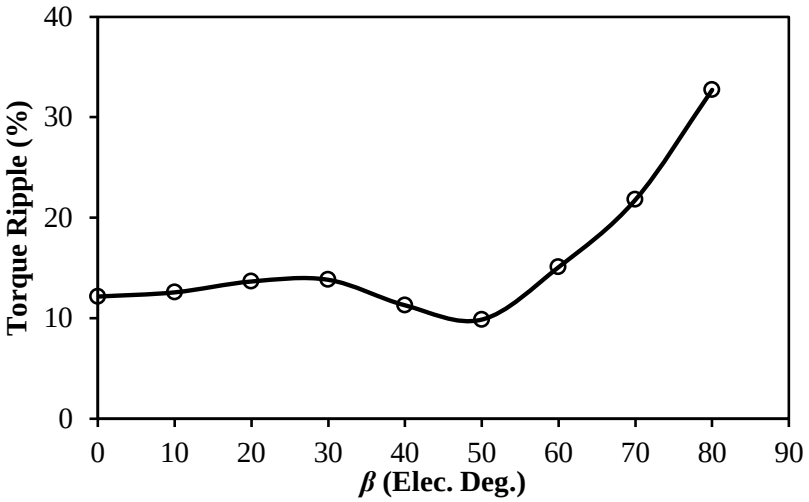

Fig. 4.34 Variation of torque ripple against β (I_{max}=10A).

4.4.4 Iron Loss

Similar to the investigation in SPM machines, the iron loss could be calculated according to different parts of the lamination as defined in Fig. 4.35. In order to reflect local magnetic saturation on the rotor, the rotor lamination has been divided into two parts as well, e.g. the "Rotor-Cap" referring to the region above the PMs and "Rotor Body" referring to the region at the back of PMs. Fig. 4.36 illustrates the flux density distributions for different β. Although the tooth body and back iron are saturated when β=0°, the tooth-tips and rotor-cap are still the most saturated iron region. With the increase of β, the saturation in main flux path alleviates significantly, but the local magnetic saturation in tooth-tips and rotor-cap are still significant even when β=90°**.** At the rated speed, the iron loss of the investigated model can be calculated and compared in Fig. 4.37(a), which shows the iron loss in stator-body takes the dominant role but reduces quickly with the increase of β. However, the iron losses in tooth-tips and rotor-cap barely change since the local magnetic saturation does not significantly change with β as illustrated in Fig. 4.36. Although the areas of tooth-tip and rotor-cap are much smaller compared with stator body and rotor core, they form a considerable part of the resultant iron loss especially in flux weakening regions. Considering the geometric area of each lamination region, the iron loss densities in tooth-tips and rotor-cap are higher than the other parts, which can be revealed in Fig. 4.37(b).

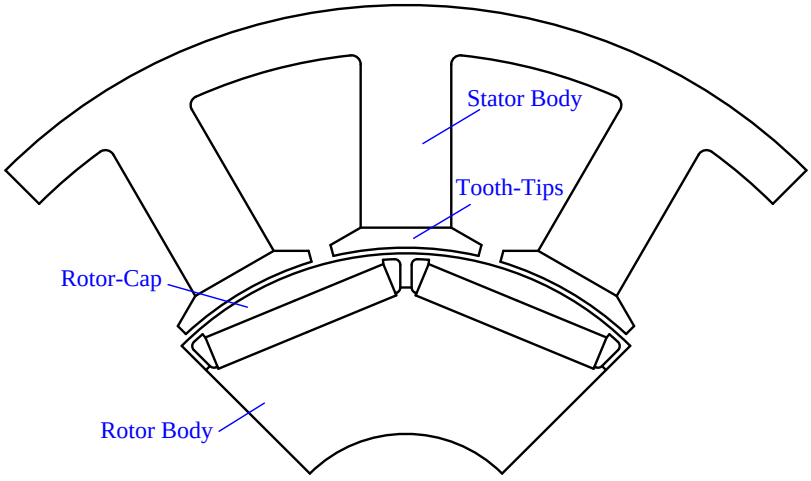

Fig. 4.35 Region separation of the investigated model.

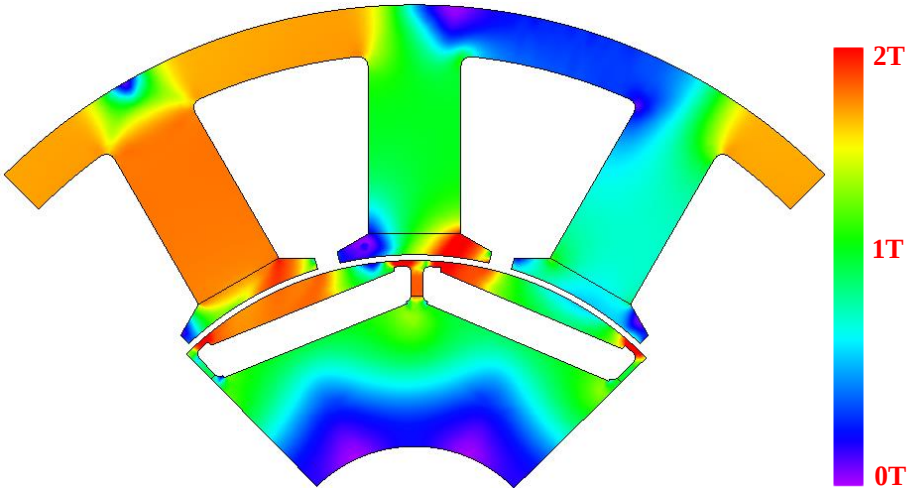

(a) β=0°

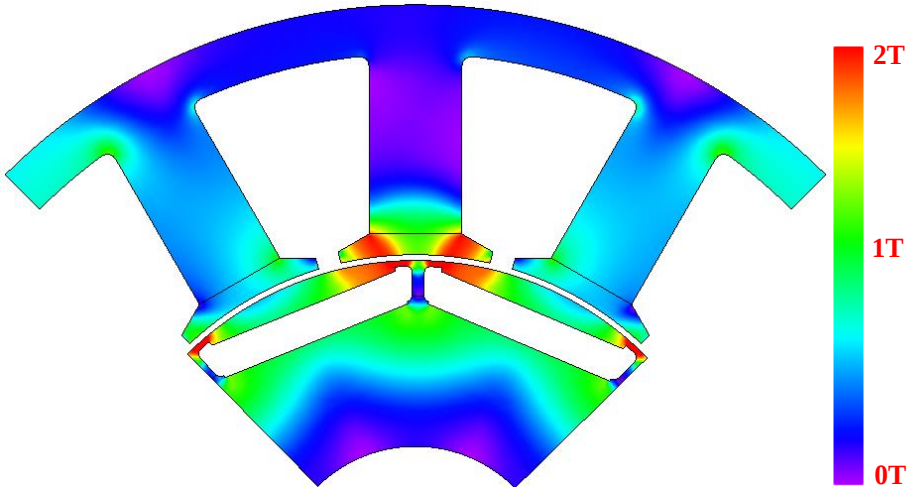

(b) β=90°

Fig. 4.36 On-load flux density distribution for lamination (I_{max}=10A, θ_r=90°).

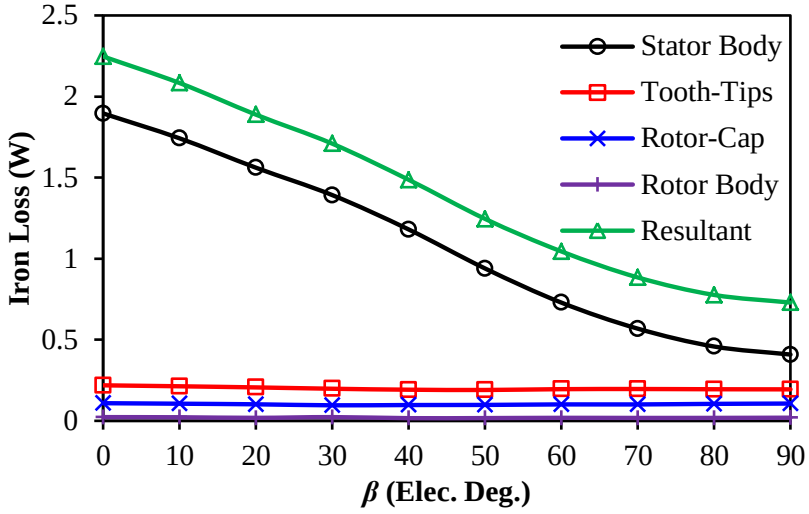

(a) Iron loss

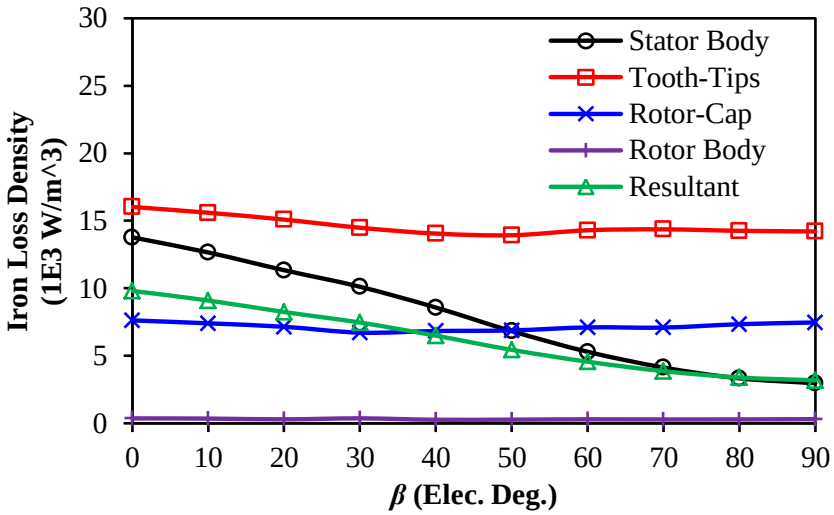

(b) Iron loss density

Fig. 4.37 Iron loss components against β (I_{max}=10A, 400rpm).

4.4.5 Flux Weakening Performance

When U_{DC} is not sufficient, the machine will enter flux weakening operation under vector control by increasing β. Normally, the length of dq-axis voltage phasor, which is calculated by only considering the fundamental voltage, will be maintained within DC limitation in such a situation. However, considering the on-load voltage distortion, the peak voltage should be maintained within the DC limitation as well, Fig. 4.38. Thus, the flux weakening performance by these two methods will be different as well.

Assuming the phase resistance (r_a) is 0.6Ω at 20°C and U_{DC} equals 42V, the torque speed characteristics calculated only by fundamental or peak voltage are shown in Fig. 4.39(a). It can be seen that the expected torque calculated by fundamental voltage is still 0.8Nm at 1200rpm. However, due to the voltage distortion, the real torque speed curve calculated by peak voltage drops to zero at about 750rpm. Due to the increases of β, the torque ripple slightly drops firstly, and then rises quickly, Fig. 4.39(b) since the average torque will reduce to zero when β approaches 90°. Considering voltage distortion, the machine will enter flux weakening faster, which consequently leads to faster increase of torque ripple. Meanwhile, the influences can also be reflected in the dq-axis currents in Fig. 4.39(c). Owing to the voltage distortion, the negative I_d begins to increase earlier with the falling of I_q accordingly, which reduces the average torque earlier than expected.

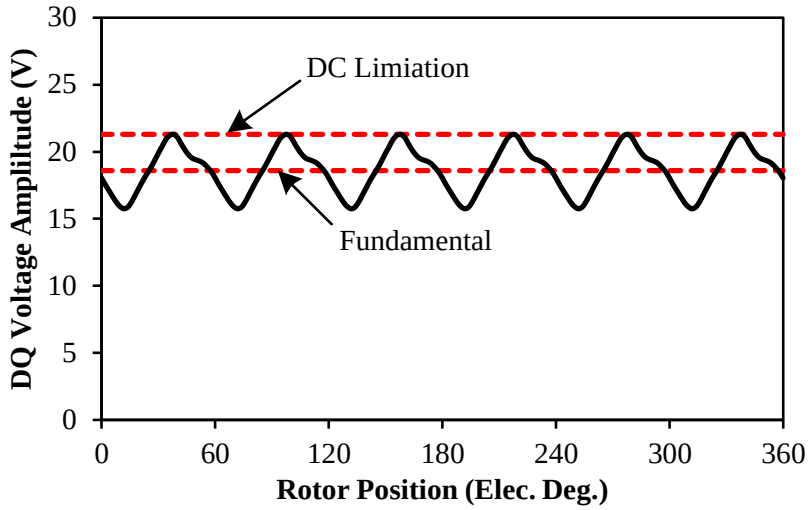

Fig. 4.38 Illustration of voltage distortion in *dq*-axis (I_{max}=10A, β=60°, 400rpm, 'fundamental' refers to the *dq*-axis voltage phasor calculated by only fundamental phase voltages).

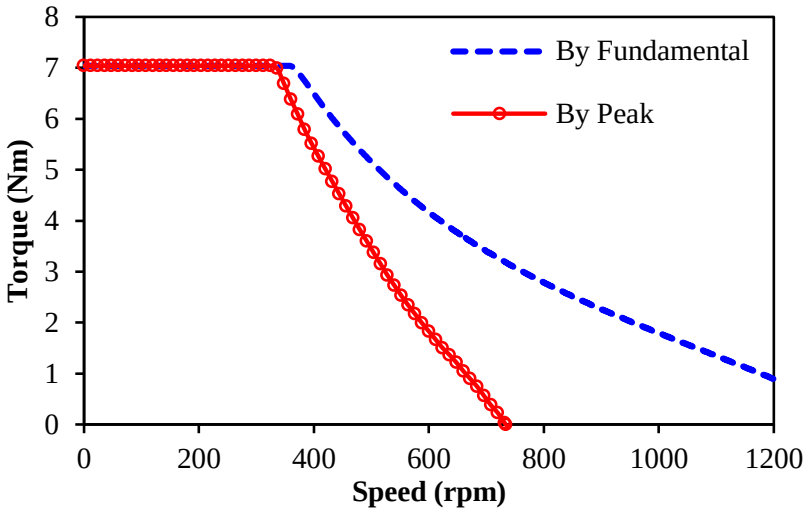

(a) Torque speed curves

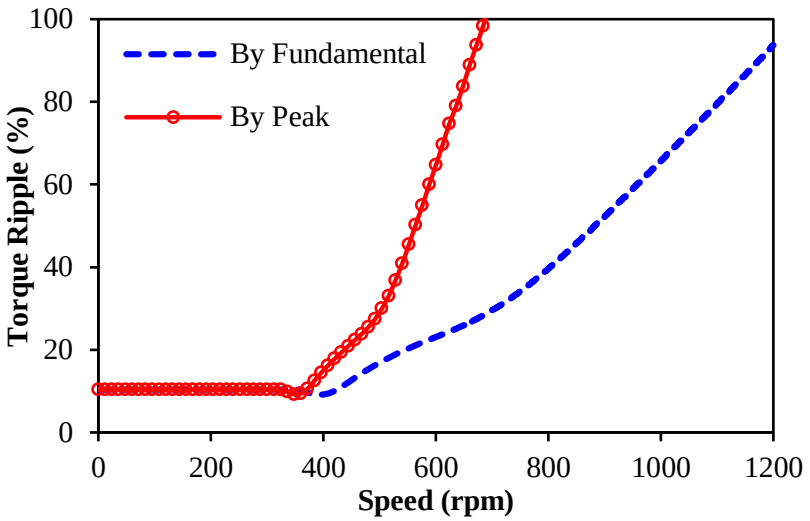

(b) Torque ripple speed curves

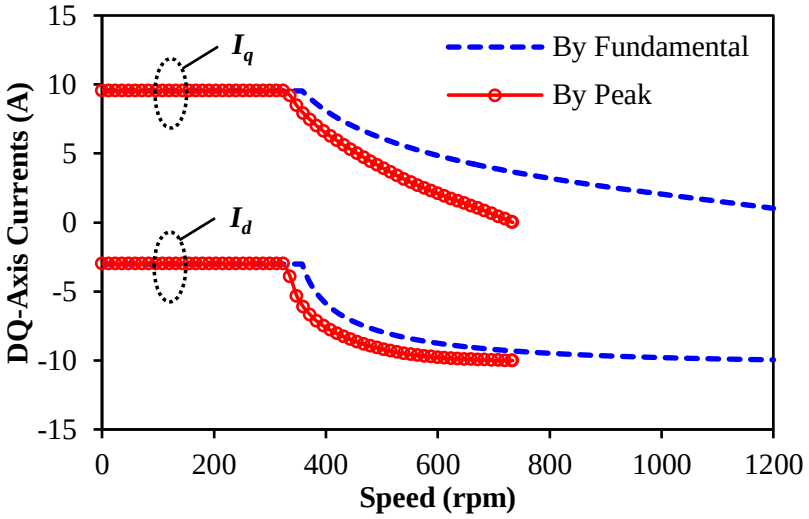

(c) Corresponding currents

Fig. 4.39 Influence of on-load voltage distortion on flux weakening performances (U_{DC}=42V, r_a=0.6Ω, I_{max}=10A).

4.5 Experimental Validation

4.5.1 Prototype Machine

The prototype machine is manufactured as shown in Fig. 4.40(a) and Fig. 4.40(b). In order to save the fabrication cost, the stator is shared with other machines. Thus, the tooth width and back iron thickness are adjusted to 8mm and 4.2mm respectively, while the other parameters are still the same as the investigated model. The measured phase resistance at 20°C is 0.62Ω. Meanwhile, the test rig arrangement is similar to that for SPM machines, Fig. 2.38(c). A DC generator is adopted as the load, while the torque is measured by a torque transducer. Due to the inverter limitation, the rated peak current is reduced to 9A, while the PWM frequency is 10kHz. The measured and predicted phase back-EMFs are shown in Fig. 4.41(a), which shows good agreement in shape. Due to slight manufacturing error, the measured fundamental voltage is 3.3% lower than the FEA prediction, Fig. 4.41(b).

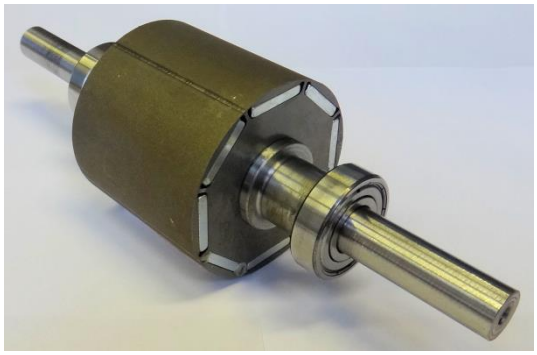

(a) Stator (b) Rotor

Fig. 4.40 Photos of prototype machine.

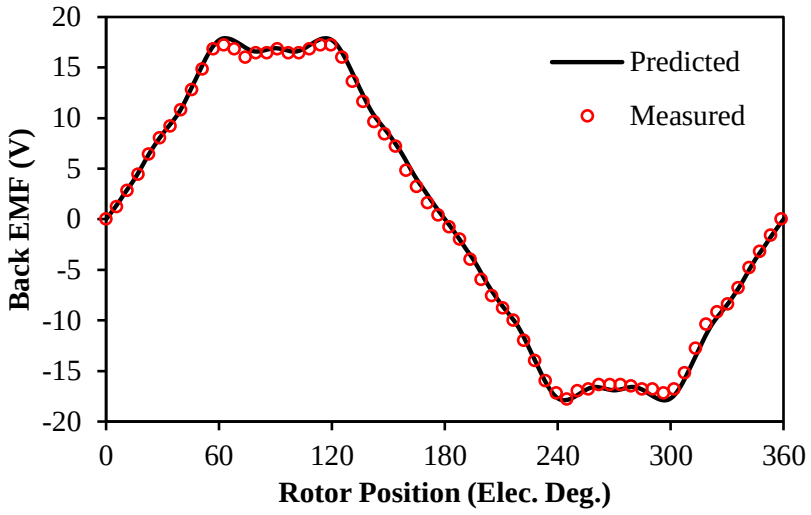

(a) Waveforms

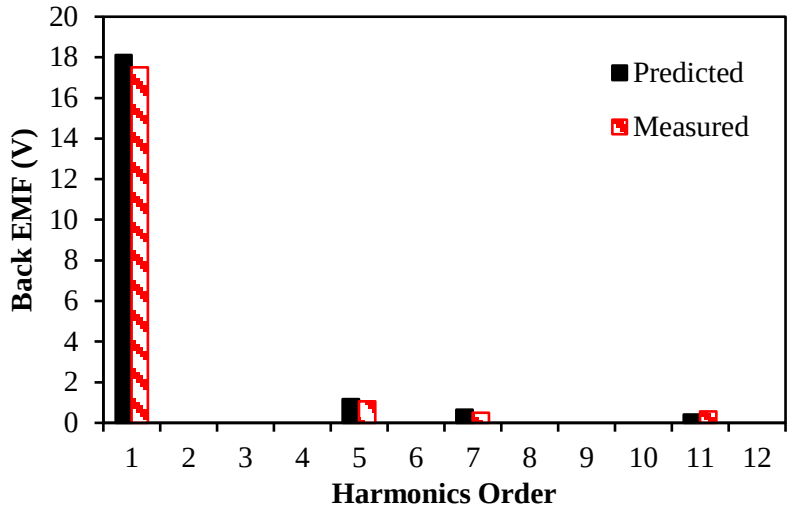

(b) Harmonics

Fig. 4.41 Comparison of measured and predicted phase back-EMF (400rpm).

4.5.2 Torque Waveforms

The measuring method of open-circuit cogging torque and on-load torque waveforms has been introduced in the appendix in detail. With this method, the measured cogging torque is compared with the FEA prediction in Fig. 4.42, which shows good agreement. By taking β=0° for example, the measured and predicted torque waveforms under rated current and half of the rated current are shown in Fig. 4.43, which also show good agreement.

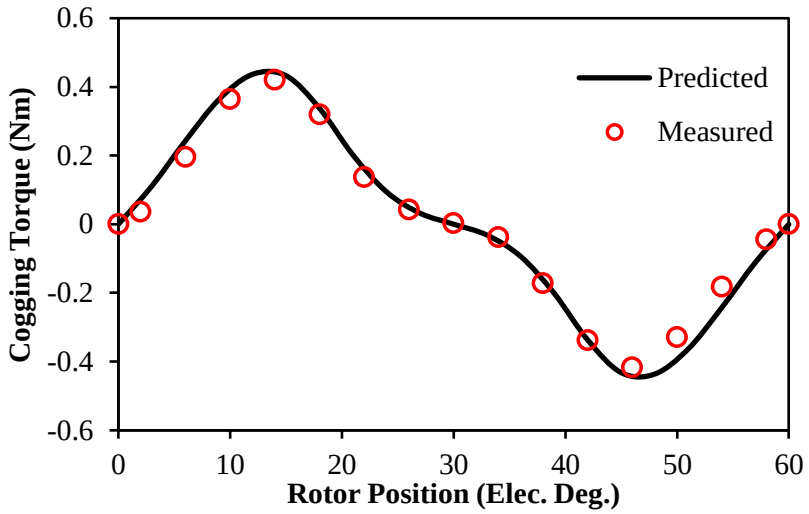

Fig. 4.42 Comparison of measured and predicted cogging torque.

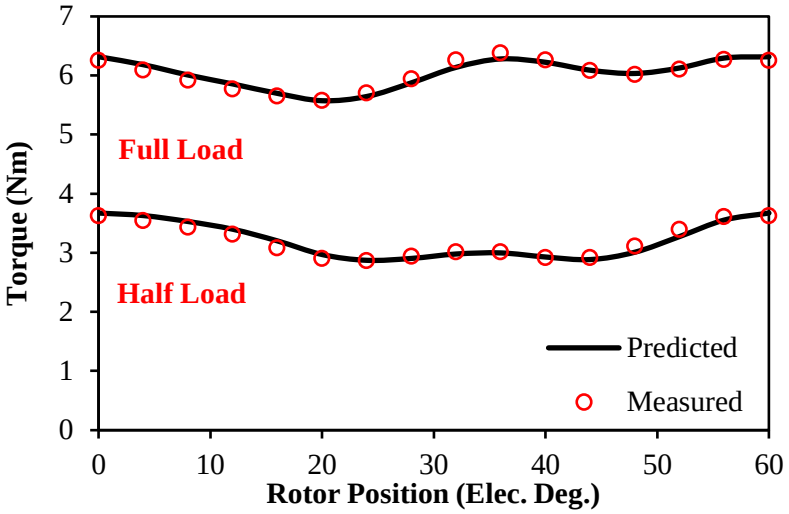

Fig. 4.43 Comparison of measured and predicted torque waveforms (I_{max}=10A, β=0°).

4.5.3 Phenomenon of Voltage Distortion

Since the PWM harmonics influence the observation of on-load terminal voltage, a low pass filter with the cut-off frequency of about 1.5kHz is adopted for measuring the phase voltage.

As represented for the constant torque operation, the measured on-load terminal phase voltage with β=20° is shown in Fig. 4.44(a), which is clearly distorted when sinusoidal current is injected. However, as represented for flux weakening operation, the on-load voltage with β=60° is much more distorted, Fig. 4.44 (b). The comparison between prediction and measured results for both current angles are shown in Fig. 4.45(a) and Fig. 4.45 (b). It can be seen that the measured results validate the prediction very well, which can also be observed from the harmonic components in Fig. 4.45 (c).

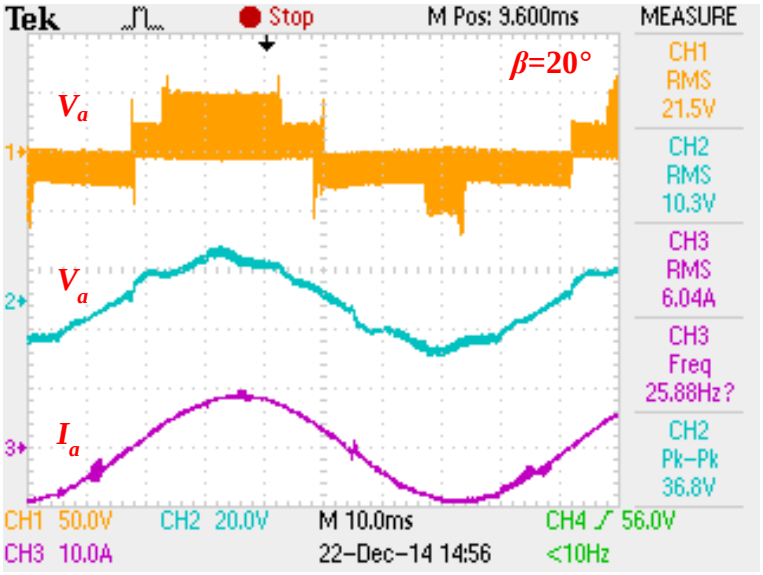

(a) β=20°

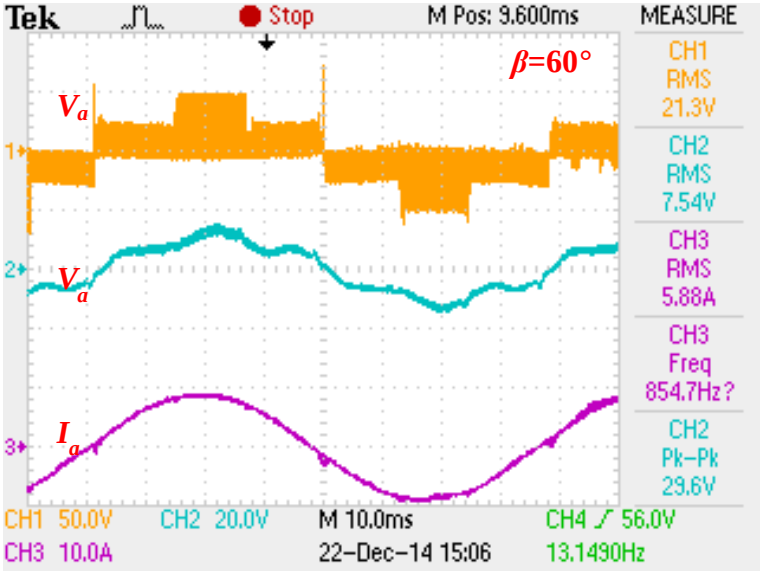

(b) β=60°

Fig. 4.44 Measured on-load terminal phase voltages (200rpm, U_{DC}=80V, I_{max}=9A),

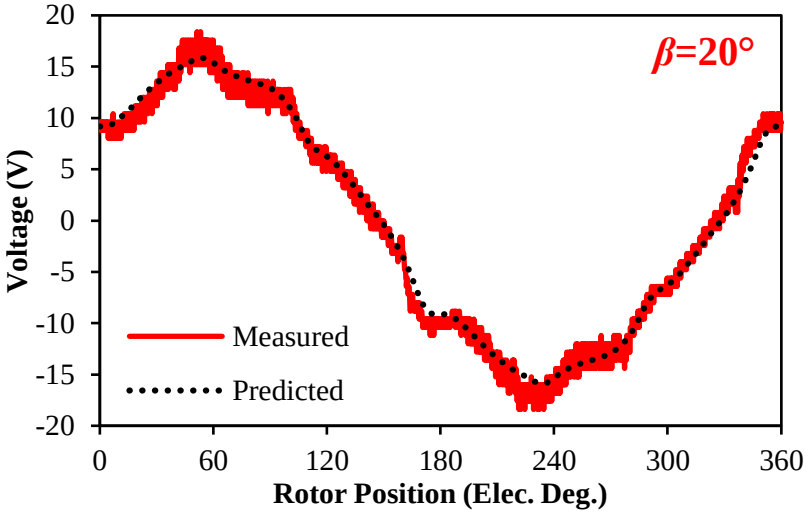

(a) Waveforms, β=20°

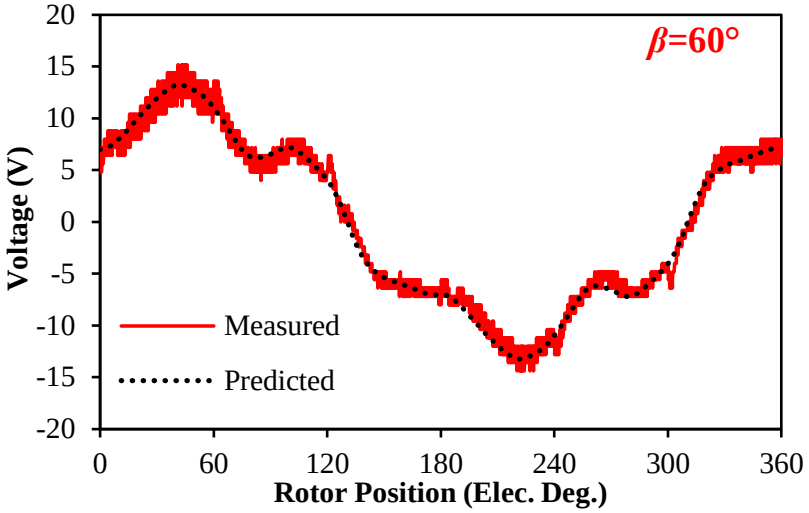

(b) Waveforms, β=60°

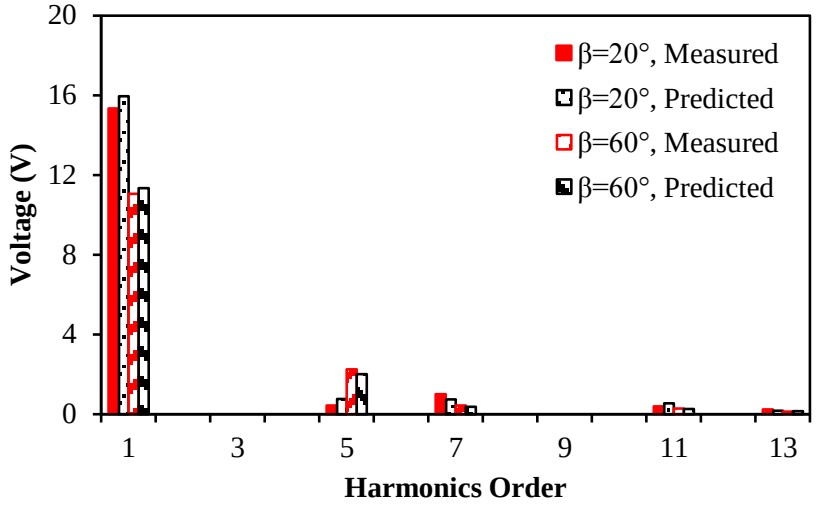

(c) Harmonics

Fig. 4.45 Comparison of predicted and measured terminal voltages (I_{max}=9A, U_{DC}=80V, 200rpm).

4.5.4 Torque Speed Characteristics

Feedback voltage regulation method developed in [KIM97] is adopted for the flux weakening experiment. If the command voltage vector length exceeds the DC link limitation, the controller will make the machine enter flux weakening operation. Based on this, the measured and predicted torque speed characteristics are shown as the circle and cross line in Fig. 4.46. As comparison, the ideal torque-speed curve calculated by the fundamental voltage under the same current condition is shown as the dashed line in the figure. It can be seen that the measured flux weakening performance agrees with the prediction by peak voltage, which is much different from the expected ideal curve. Overall, the experiment validates the prediction.

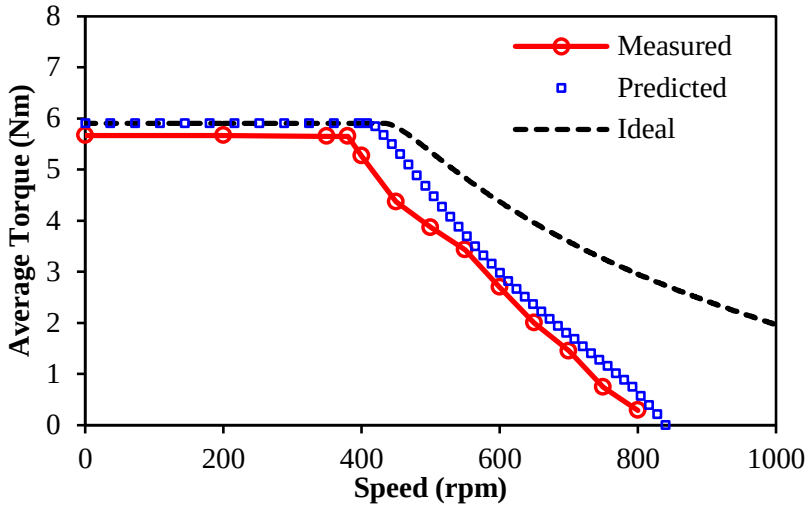

Fig. 4.46 Comparison of predicted and measured torque speed characteristics (U_{DC}=48V, I_{max}=9A).

4.6 Summary

This chapter focuses on the on-load voltage distortion in fractional-slot IPM machines by taking a 12-slot/8-pole prototype as example. The phenomenon of the voltage distortion is presented firstly, which shows the higher the current angle, the higher voltage distortion will be. Then, the mechanism of this phenomenon is investigated with the aid of frozen permeability method. Due to the rotor segmentation effect in IPM machines, the armature reaction flux can only circulate through leakage flux paths or highly saturated flux paths in some rotor positions, which significantly change the flux linkages and leads to voltage distortion. With the increase of current advancing angle, this effect becomes more obvious

and results in higher distortion level. Meanwhile, the influence of on-load voltage distortion on machine performance has also been investigated. Under constant torque region, the on-load voltage distortion only contributes to the torque ripple. However, it will largely reduce the flux weakening operation region compared with the ideal one calculated by fundamental voltages. The influences on other performance are also investigated, such as on-load back-EMF, on-load cogging torque, *dq*-axis inductances, and iron loss. Finally, a prototype machine has been manufactured and tested. The experimental results validate the analyses. The influence of slot and pole number combinations on the terminal voltage distortion in IPM machines will be investigated in next chapter.

CHAPTER 5

INFLUENCE OF SLOT AND POLE NUMBER COMBINATIONS ON TERMINAL VOLTAGE DISTORTION IN IPM MACHINES CONSIDERING LOCAL MAGNETIC SATURATION

The aforementioned chapter investigates the mechanism of terminal voltage distortion in IPM machines. This chapter focuses on the influence of slot and pole number ($N_s/2p$) combinations in both fractional slot and integer slot IPM machines. Meanwhile, the electromagnetic performance of the investigated machines influenced by voltage distortion and local magnetic saturation are also compared.

5.1 Introduction

Interior permanent magnet (IPM) machines have gained extensive research interests in the last three decades with the development of novel permanent magnet materials and power electronics technologies [JAH86], due to the inherent advantages such as high torque and power density, high efficiency, good demagnetization withstand capability, as well as good flux weakening performance [WAN14], [RED12], [PEL11], [ELR06]. In order to realize the potential merits of IPM machines, vector control is usually adopted [VAS90]. Within limited DC link voltage (U_{DC}), the control method can separately adjust the *dq*-axis currents to maintain the terminal voltage and output torque. Many papers in literature investigate the flux weakening issues of fractional slot concentrated windings (FSCW) IPM machines, which have the advantage of short end windings, they only consider the fundamental inductances and voltages as for the conventional overlapping distributed IPM machines [JAH86], [PEL11], [ELR06], [VAS90], [DUE08], [HAN10], [BAR12]. However, in actual applications, the terminal voltages are usually distorted due to the nonlinearity of both machines and drives, which consequently could influence the torque and flux weakening performance.

Although harmonic voltages could be generated from the drive side, such as inverter nonlinearity [GON11], PWM dead time [HWA10], as well as DC link voltage disturbance [SIL11] etc., more obvious terminal voltage distortion is contributed by the nonlinear nature of machines [FUL05], [MOR92]. Due to armature reaction, the magnetic saturation in machines will aggravate, which consequently distorts the terminal voltages. However, since

the flux paths in FSCW IPM machines also change significantly with different rotor positions due to rotor saliency [BIA06a], the terminal voltage distortion could be deteriorated further, which needs to be investigated.

Nevertheless, as mentioned in the previous chapter, few papers have investigated the terminal voltage distortion considering the rotor saliency and local magnetic saturation. [CHO13] adopts distorted terminal voltage to explain the torque ripples in IPM machines through calculating the instantaneous power by terminal voltages and currents. However, the origins of distorted voltage are directly ascribed to the magnetic saturation, which does not point out the influence of local magnetic saturation and the influence of rotor saliency. [LEE11] finds that the local magnetic saturation in tooth-tips will influence the peak value of the on-load line voltages. But its relations with rotor saliency and influences on other machine performances have not been investigated further. [YU13] introduces spatial harmonic inductances to compensate the *dq*-axis inductance ripples according to different rotor positions in order to enhance the machine control performance. But the influences of local magnetic saturation and rotor saliency on such inductances are not presented.

Due to alternative physical positions, the armature flux paths and PM flux paths in FSCW IPM machines are influenced by rotor saliency, respectively [HAN07]. In order to separate their contributions on voltage distortion, as in the previous chapter, the frozen permeability (FP) method [CHU13a], [YAM14] is also adopted as the basic analysis method in this chapter. Based on a 12-slot/10-pole machine, the phenomenon and mechanism of terminal voltage distortion are investigated by FP method firstly, focusing on the influence of rotor saliency. By comparing the voltage distortions for several typical slot and pole numbers ($N_s/2p$) combinations, a design trade-off will be proposed, which can minimize the influence of terminal voltage distortion by selecting proper $N_s/2p$ combinations. Finally, two prototypes are manufactured to validate the analysis results, while the influences of terminal voltage distortion on flux weakening performance are investigated as well.

5.2 Investigated IPM Machines

All machines to be investigated have the same machine size, i.e. the same stator lamination outer diameter and axial length, as well as the same rated current and the stator inner diameter. Meanwhile, for fair comparison, the numbers of turns per phase are adjusted to

maintain the same back-EMF under rated speed, while their tooth width and back iron thickness are adjusted to keep the typical flux density of stator lamination around 1.5T at rated current with I_d=0 control. In order to reflect the influence of local magnetic saturation in tooth-tips, all machines adopt similar slot opening designs. Due to much higher slot numbers, the slot opening width of the 24/4 machine has been adjusted to 1mm to maintain proper tooth width. Other main parameters are listed in Table I and Table II respectively.

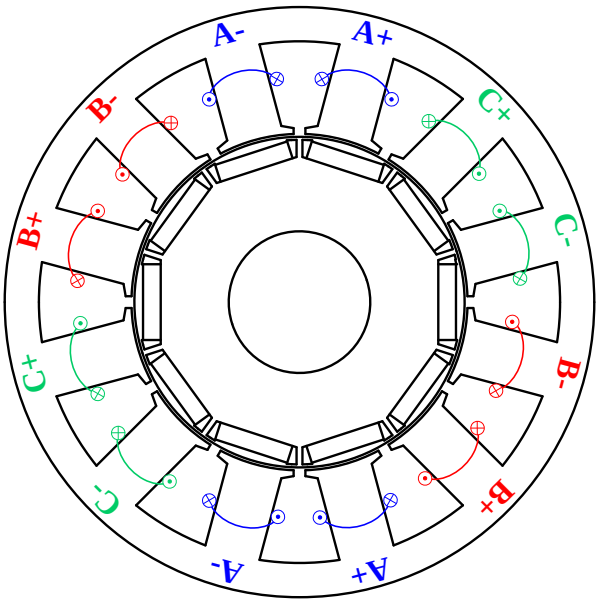

(a) 12/10

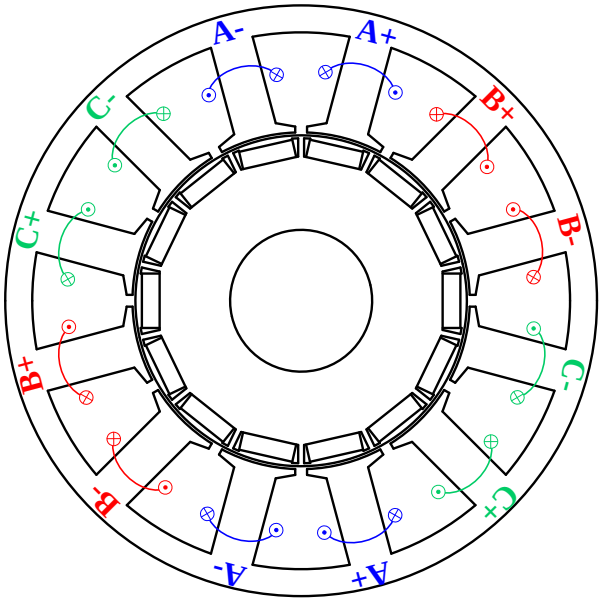

(b) 12/14

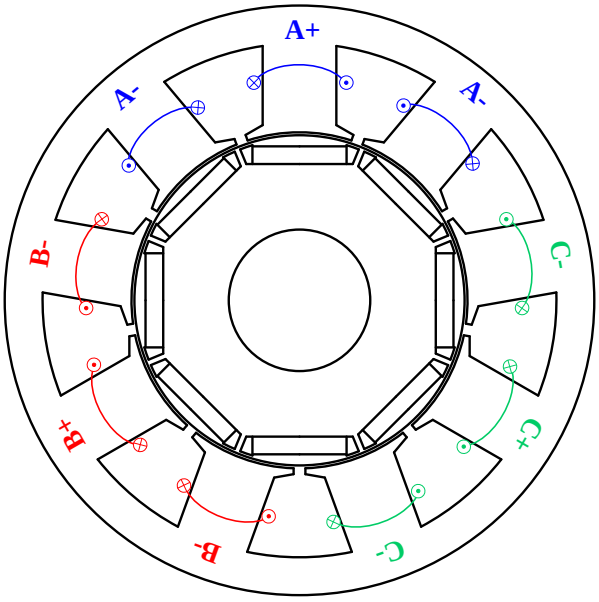

(c) 9/8

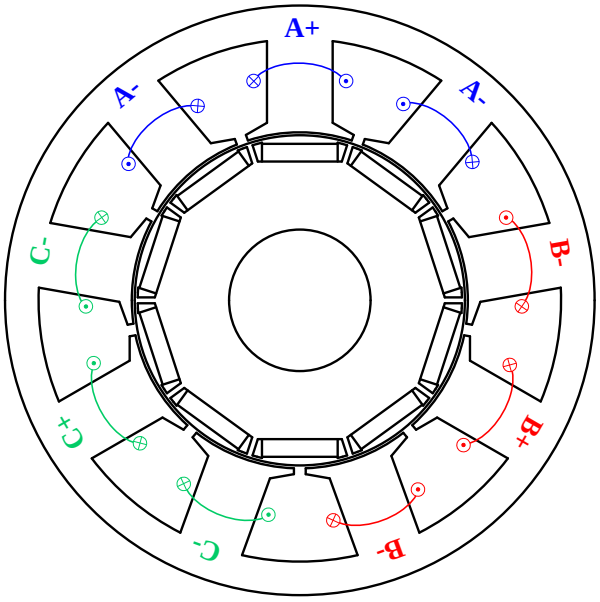

(d) 9/10

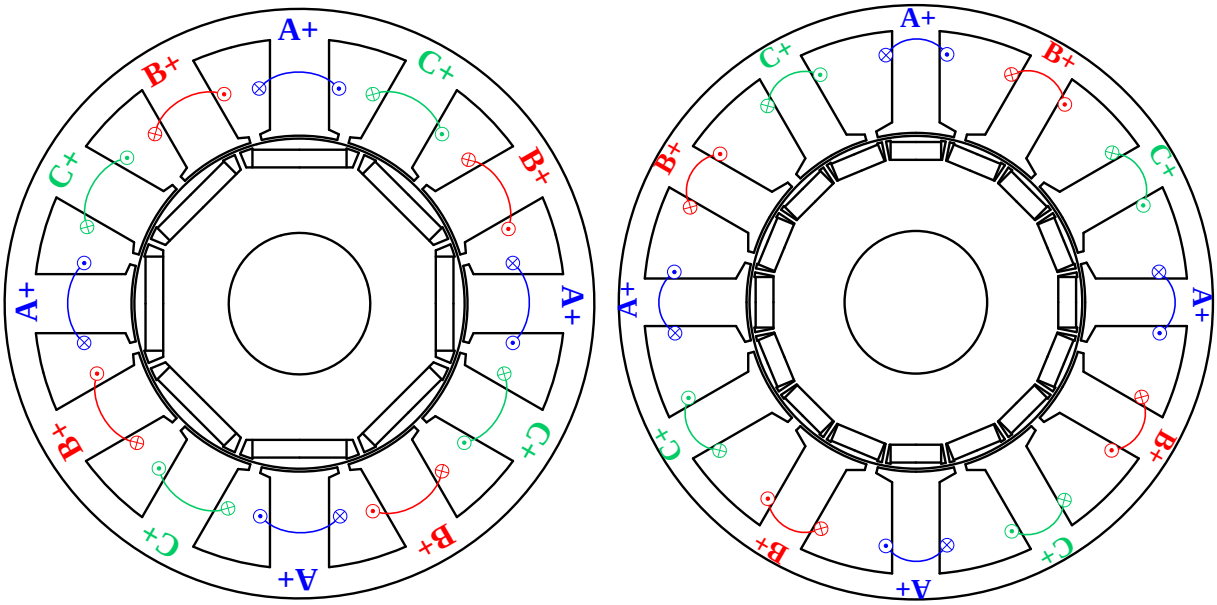

(e) 12/8 (f) 12/16

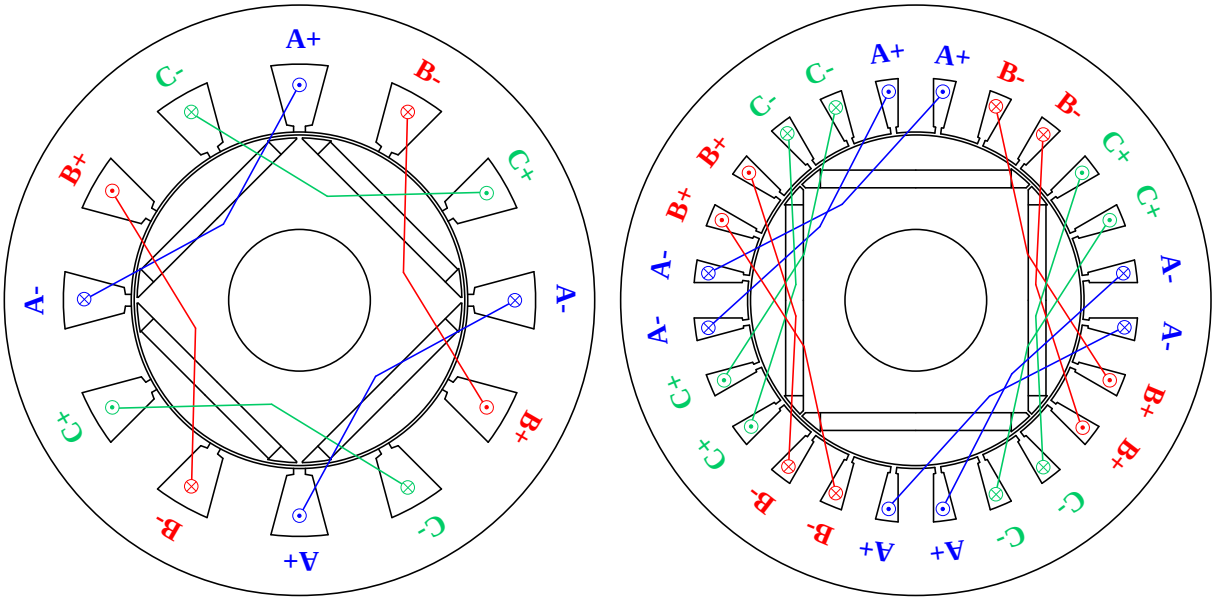

(g) 12/4 (h) 24/4

Fig. 5.1 Configurations of IPM machines with different slot/pole number combinations (Phase A at *d*-axis, θ_r=0°).

Table 5.1 Basic Common Parameters of the Investigated Models

Parameter	***Value***	***Parameter***	***Value***
Stator outer diameter	100mm	Axial length	50mm
Split ratio	0.57	Airgap length	1.0mm
Rated speed	400rpm	Rated current	$7.1A_{rms}$
Magnet thickness	3.0mm	Pole arc/pitch ratio	0.75
Slot opening width	2mm	Tooth-tip thickness	1mm
Tooth-tip slot	10°	Lamination material	M300
Magnet permeability	1.05	Magnet remanence	1.2T

Table 5.2 Basic Different Parameters of the Investigated Models

Machine	***A***	***B***	***C***	***D***	***E***	***F***	***G***	***H***
Slot number	12	12	9	9	12	12	12	24
Pole number	10	14	8	10	8	16	4	4
Tooth width, mm	9.5	7.7	13.1	11.1	10.3	6.3	9.9	6.5
Yoke height, mm	5.2	4.3	6.7	5.7	5.1	3.2	10.8	10.3
Turns per phase	160	178	150	159	168	192	148	146

5.3 Influence of Slot and Pole Number Combinations on Terminal Voltage Distortion

5.3.1 Rotor Segmentation Effect

The mechanism of on-load voltage distortion in IPM machines reveals that the magnetic saturation and the rotor segmentation effect are the major reasons especially under flux weakening operation. Since the maximum flux density in stator tooth and back iron of the investigated machines have been adjusted to be ~1.5T, which is the knee point of the lamination material adopted. Thus, the rotor segmentation and local magnetic saturation become dominant for the voltage distortion, which will be compared in this section.

In order to better understand the rotor segmentation effect from the armature reaction point of view, the 12/10 machine shown in Fig. 5.1(a) has been adopted for the illustration. Although *dq*-axis armature reactions cannot be ideally separated due to cross saturation, the comparison of models operated under β=0° and β=90° can still be adopted to reflect the mechanism of rotor segmentation effect, and explain the increasing of *VDR* when β increases. By FP method, the PM and armature reaction flux linkages for β=0° and β=90° can be separated and

shown in Fig. 5.2. It can be observed that the PM flux linkages are similar in shape although a phase shift exists under β=0° condition due to cross saturation [YAM14]. Nevertheless, the shapes of armature flux linkages are significantly differed although they are generated by the same amplitude of sinusoidal currents. When β=0°, the armature flux linkage is almost sinusoidal except slight distortion due to saturation. However, the armature flux linkage for β=90° nearly becomes trapezoidal, which will lead to strong phase voltage distortion for *d*-axis armature reaction.

The different flux paths for different β can explain this phenomenon. Fig. 5.3(a) and Fig. 5.3(b) compare the equipotential distributions only excited by PMs between β=0° and 90° by FP method. Except for some tiny differences caused by different saturation level, they are nearly the same, which result in similar PM flux linkages in Fig. 5.2 (a). Meanwhile, Fig. 5.3 (c) and Fig. 5.3(d) illustrate obvious difference for armature reaction flux paths. When β=0°, the armature field is perpendicular with PM field, which makes the *q*-axis armature reaction flux always circulate through the relative high permeance lamination regions above or below the PMs, Fig. 5.4(a). However, when β=90°, the *d*-axis armature reaction flux is forced to circulate through PMs for flux weakening, Fig. 5.4(b). Since the PMs have relative low permeance, the armature flux linkage will be reduced and distorted, Fig. 5.2(b). Meanwhile, the low permeance in main flux path increases the leakage flux consequently, which further increases the harmonics in terminal phase voltages. Therefore, with the increase of β under fixed I_{max}, more current will be allocated to increase the *d*-axis armature reaction, which leads to the increasing of *VDR*.

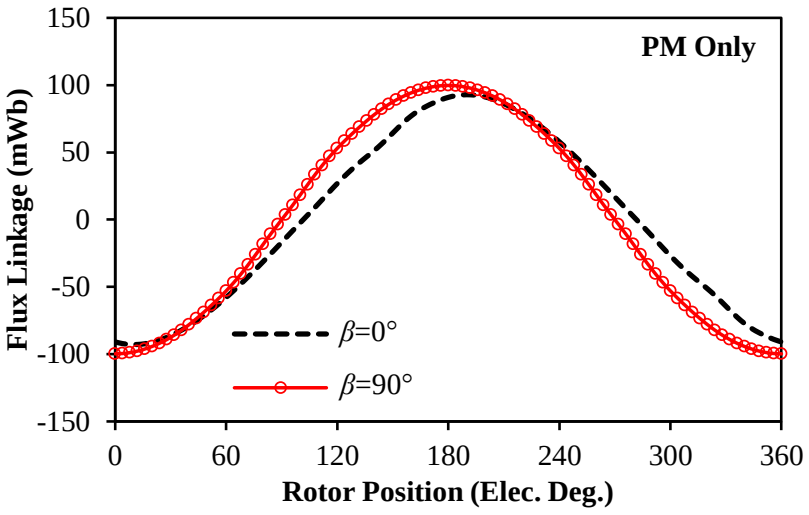

(a) PM flux linkages

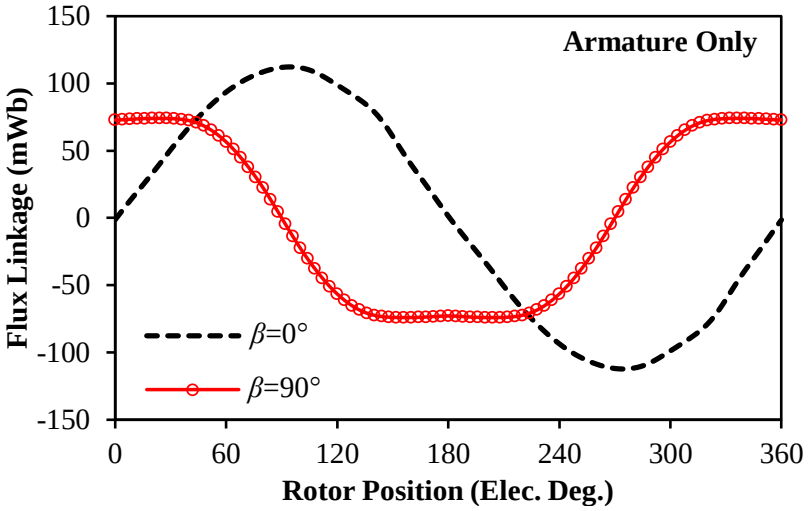

(b) Armature flux linkages

Fig. 5.2 Comparison of flux linkage components by FP method for different β (I_{max}=10A).

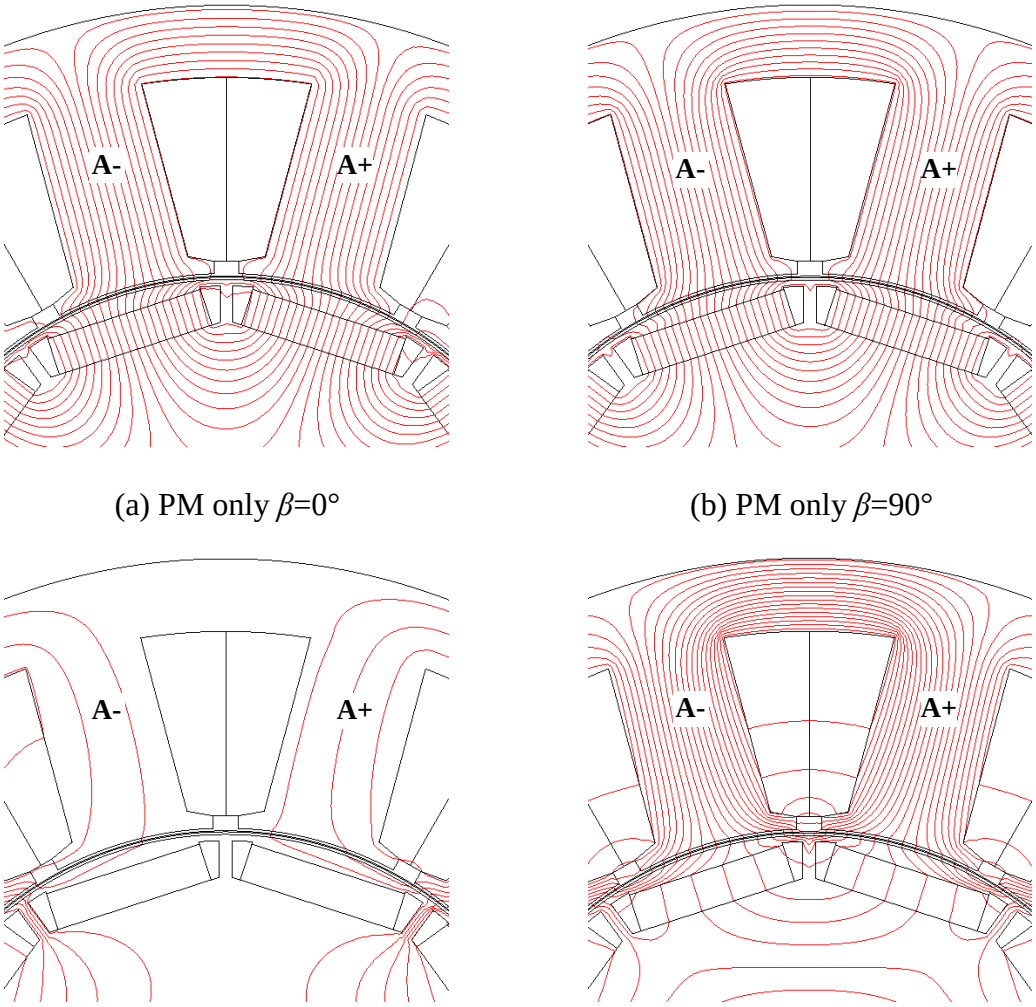

(a) PM only β=0°

(b) PM only β=90°

(c) Armature only β=0°

(d) Armature only β=90°

Fig. 5.3 Equal potential differences by FP method for different β (I_{max}=10A, θ_r=0°).

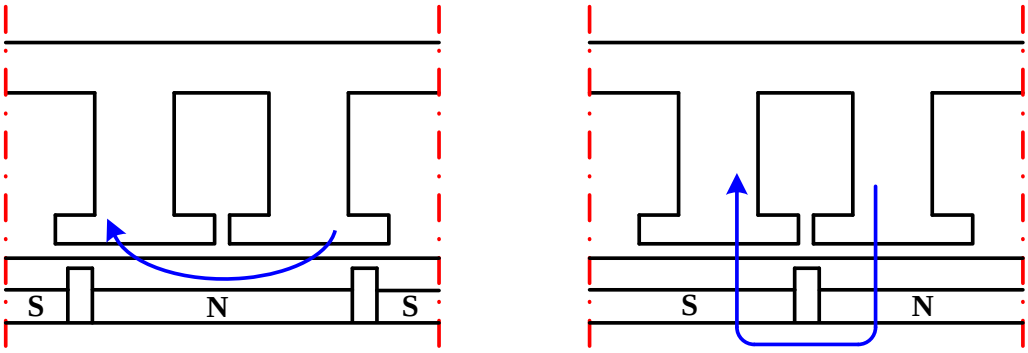

(a) β=0° (b) β=90°

Fig. 5.4 Illustration of different flux paths for different β.

5.3.2 Machines with N_s±1=2p and N_s±2=2p

The aforementioned analysis shows that the flux paths for *d*-axis armature reaction will determine the terminal voltage distortion level, which provides a key to analyse the influence of N_s/2p combinations. The difference in flux paths for different FSCW machines can be reflected as the relation between stator slot pitch (τ_s) and rotor pole pitch (τ_r), which can be described by the number of slot per pole per phase (q). In a three phase FSCW machine, when q=1/3, τ_s and τ_r will be equal. Normally, when *d*-axis aligned, the *d*-axis armature flux can still circulate through the rotor surface, Fig. 5.5(a). However, when q approaches 1/3, the rotor ribs will align with stator slot opening, and *d*-axis armature flux could only circulate though leakage flux paths, Fig. 5.5 (b). Therefore, the machine's q value is closer to 1/3, the worse terminal voltage distortion could be expected.

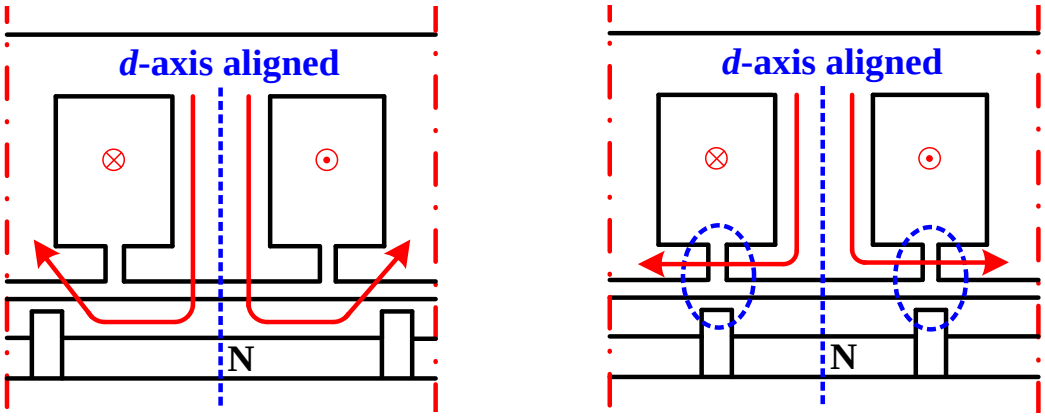

(a) q is different from 1/3 (b) q approaches 1/3

Fig. 5.5 Influence of q on major *d*-axis flux paths for FSCW IPM machines.

Take 9-slot/8-pole and 12-slot/10-pole machines for examples since they have q equal 3/8 and 2/5 respectively. Under I_{max}=10A and β=60°, the comparison of phase flux linkages are shown in Fig. 5.6(a). Clearly, the 9/8 machine has more obvious distortion due to the influence of d-axis flux paths according to the aforementioned prediction. In consequence, the 9/8 machine has higher voltage distortion than the 12/10 machine, although their fundamental voltages are similar, Fig. 5.6(b) and Fig. 5.6(c).

By adopting *LVDR* and *THD* defined in (3.9) and (3.10), the voltage distortions for typical N_s±1=2p and N_s±2=2p machines can be compared together in Fig. 5.7, which proves the 9/8 machine suffers more from voltage distortion than the 12/10 machine. Meanwhile, since the 9/10 machine has q more close to 1/3 than the 12/14 machine (3/10 and 2/7 respectively), it has worse *VDR* as well, which obeys the analysis result. Nevertheless, for the machines having the same slot number, the ones with N_s<2p will have much worse voltage distortion than their counterparts with N_s>2p, which needs to be explained.

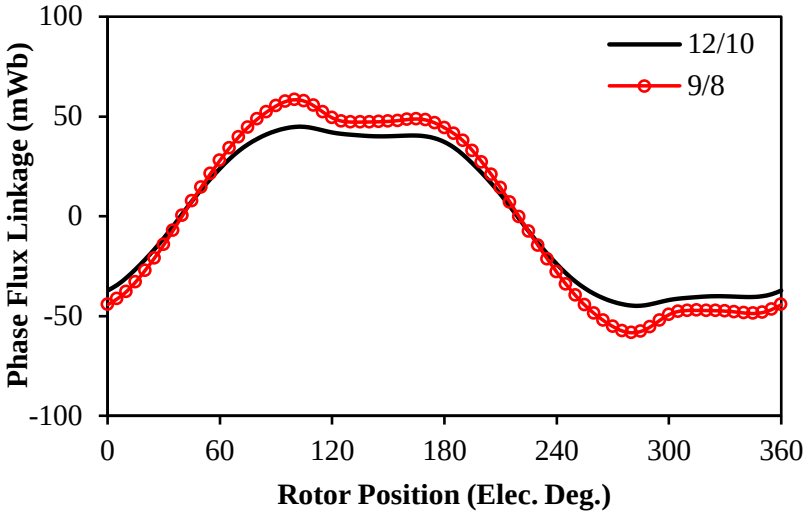

(a) Flux linkages

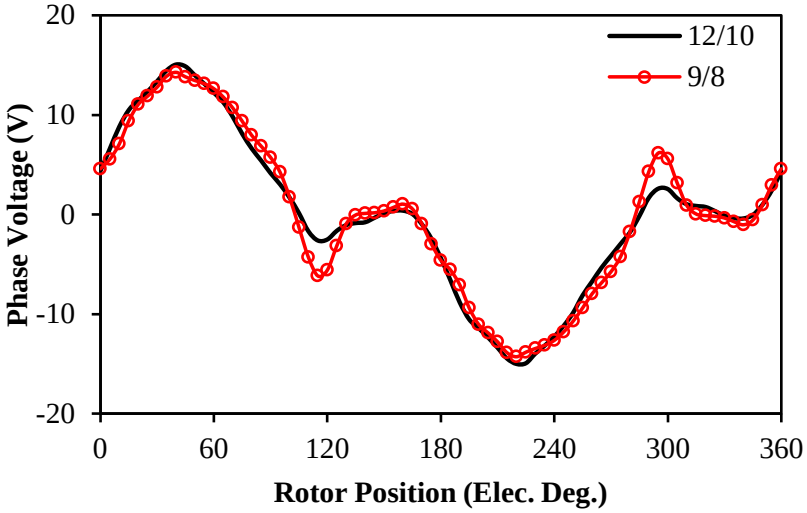

(b) Voltages waveforms

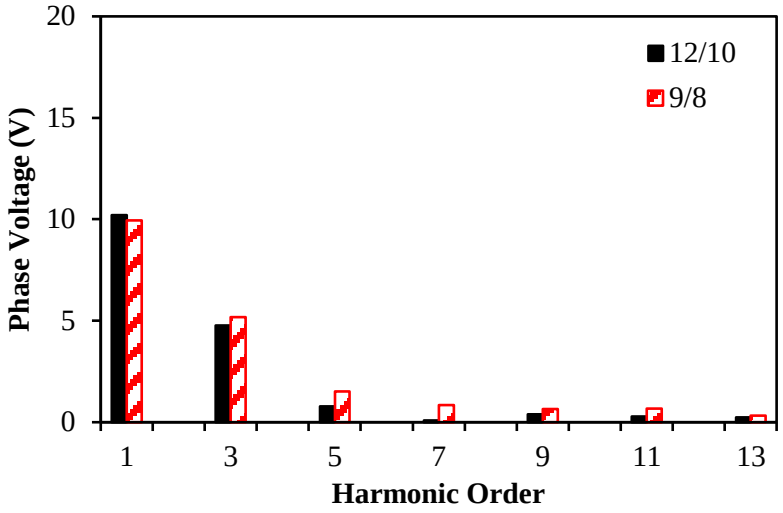

(c) Voltage harmonics

Fig. 5.6 Comparison of phase flux linkages and phase voltages between 12/10 and 9/8 machines (I_{max}=10A, β=60°, 400rpm).

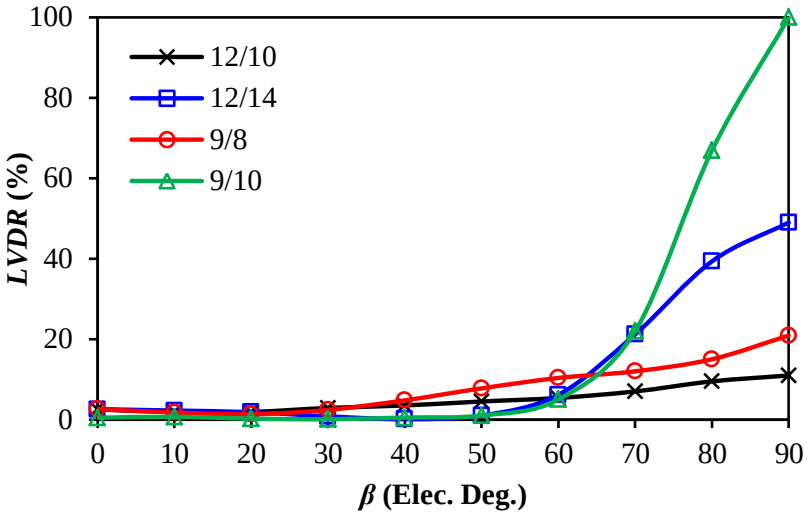

(a) *LVDR*

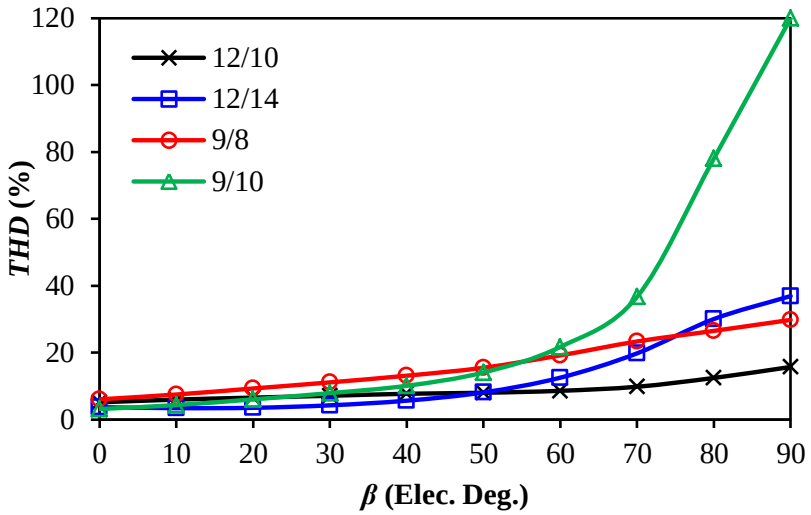

(b) *THD*

Fig. 5.7 Comparison of voltage distortion for typical N_s±1=2p and N_s±2=2p machines (I_{max}=10A, 400rpm).

In order to explain this, the N_s±2=2p machines are taken as examples. The *d*-axis armature flux equipotential distributions for the two machines are compared in Fig. 5.8 by FP method. Since τ_s is larger than τ_r, the *d*-axis armature flux in the 12/14 machine is easily circulated with the aid of tooth-tips through rotor ribs or directly through the adjacent pole surface, which is marked with dashed circles. However, this kind of flux paths is highly dependent on tooth-tips and rotor ribs, which also enhance their saturation level compared with the 12/10 machine in Fig. 5.9. This influence can be reflected on the terminal phase voltages in Fig. 5.10 and Fig. 5.11. Although the 3rd harmonics reduces due to the extra flux paths when *d*-axis aligned, the saturation in the flux paths largely increases the 5th and 7th harmonics which makes the voltage distortion worse.

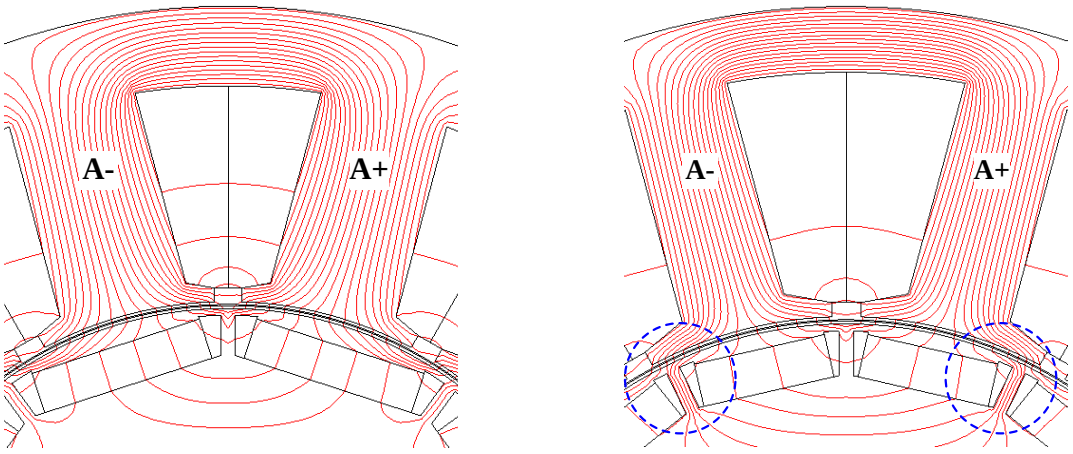

(a) 12/10 (b) 12/14

Fig. 5.8 Comparison of *d*-axis current armature flux paths for two machines by FP method (I_{max}=10A, β=90°)

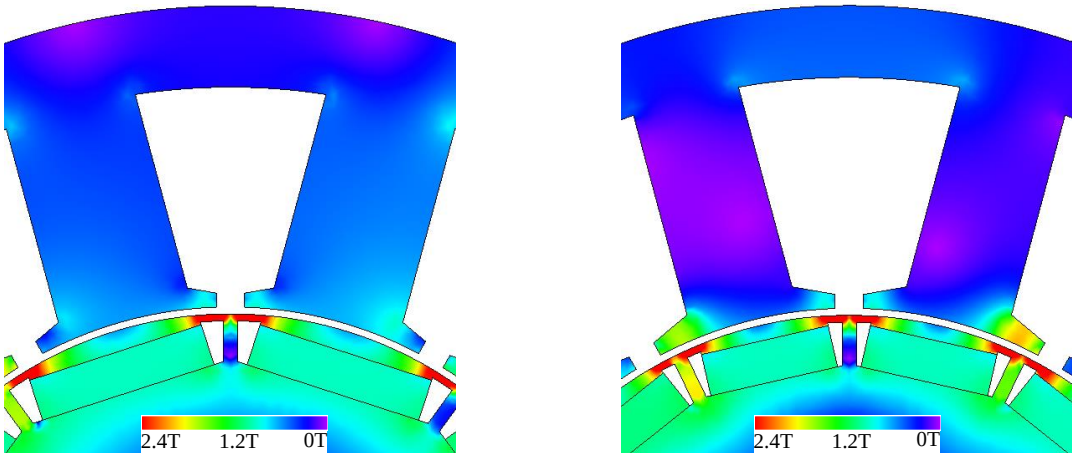

(a) 12/10 (b) 12/14

Fig. 5.9 Comparison of tooth-tips local magnetic saturation for two machines (I_{max}=10A, β=90°).

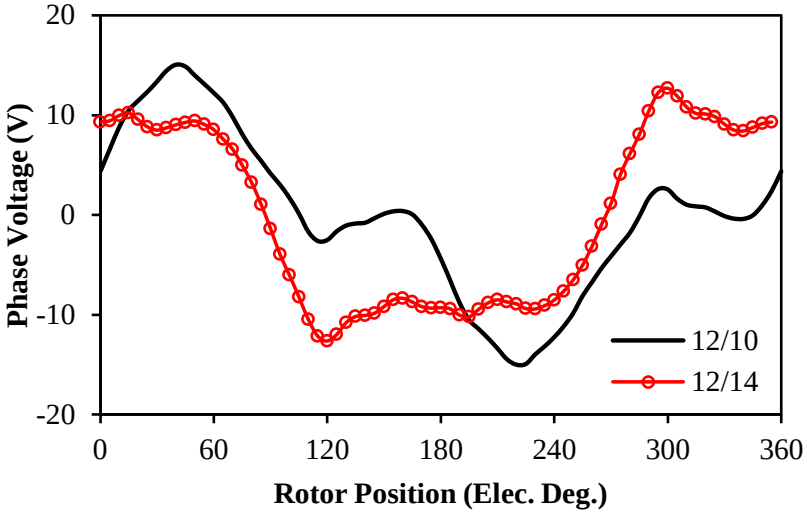

(a) Waveforms

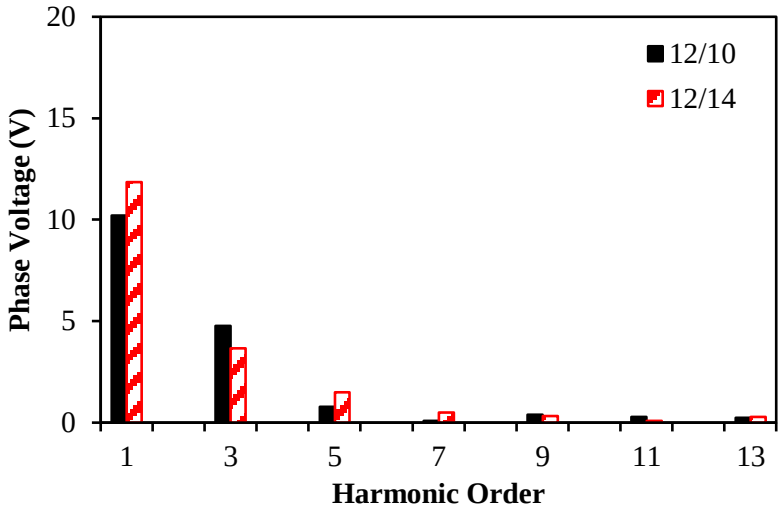

(b) Harmonics

Fig. 5.10 Comparison of terminal phase voltages for 12/10 and 12/14 machines (I_{max}=10A, β=60°, 400rpm).

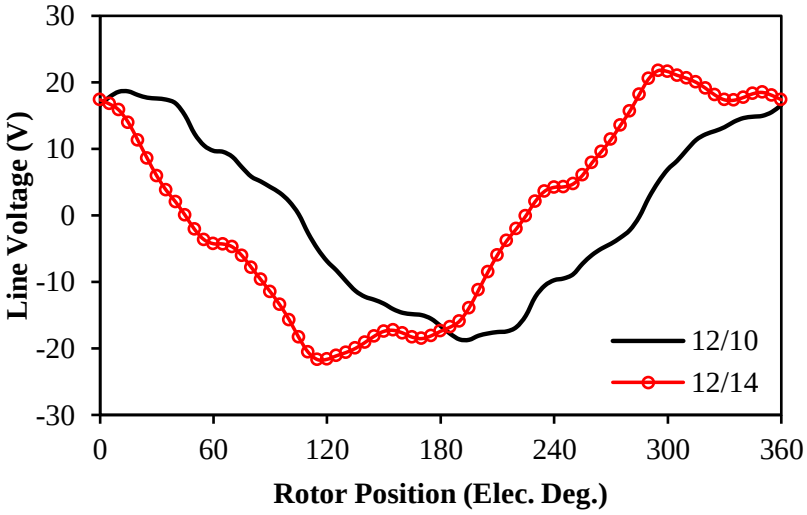

(a) Waveforms

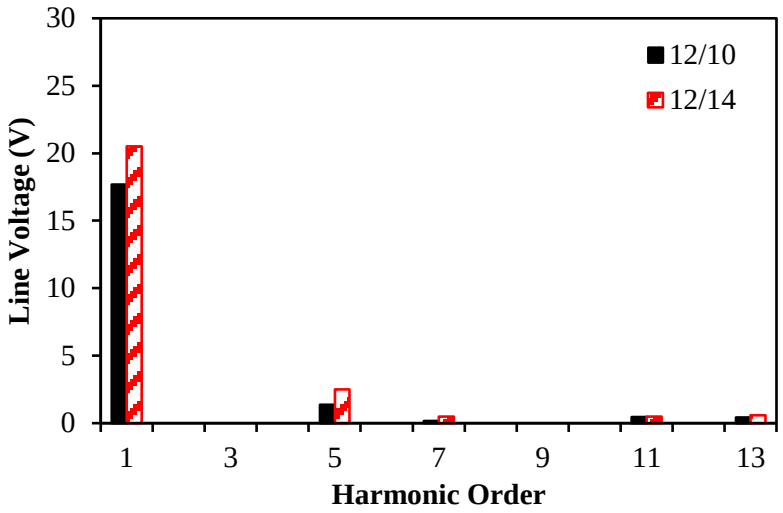

(b) Harmonics

Fig. 5.11 Comparison of terminal line voltages for 12/10 and 12/14 machines (I_{max}=10A, β=60°, 400rpm).

5.3.3 Machines with $N_s/2p$=3/2 and 3/4

According to the aforementioned results, when q is less close to 1/3 and $N_s>2p$, the alleviative voltage distortion would be expected. Nevertheless, if q is too far away from 1/3, i.e. τ_s and τ_r differ significantly, the voltage distortion could deteriorate as well. For example, the 12/8 and 12/16 machines with q equal to 1/2 and 1/4 respectively are analysed and compared in Fig. 5.12. It can be observed that the maxim *VDR* for the 12/8 machine is nearly 70%, which is three times higher than the maximum value for the 12/10 machine.

Fig. 5.13(a) shows the equipotential distribution excited by only armature current I_d when the rotor inter-pole line aligns with stator tooth A. Different from other $N_s/2p$ combinations, the armature fluxes of phases B and C will circulate through tooth-tips belonged to phase A due to large difference between τ_s and τ_r. This by-pass flux will largely increase the local saturation of these tooth-tips, Fig. 5.13(b), and influence the armature flux linkage when it is crossing zero, Fig. 5.13(c). When τ_r is much larger than τ_s, the armature flux linkage would not be influenced at *d*-axis aligned positions as the 12/10 machine. However, it will be largely influenced when *q*-axis is aligned, which contributes to more terminal voltage distortions. The even worse voltage distortion in the 12/16 machine can be explained similarly as the aforementioned result for the 12/14 machine.

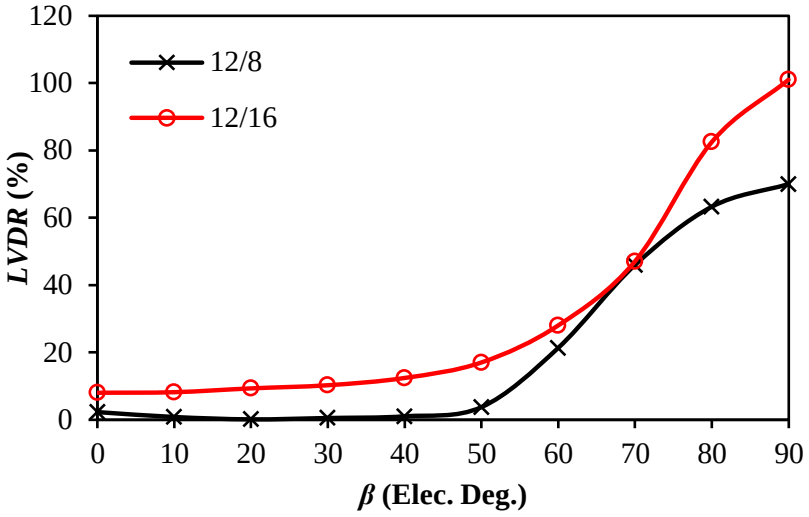

(a) *LVDR*

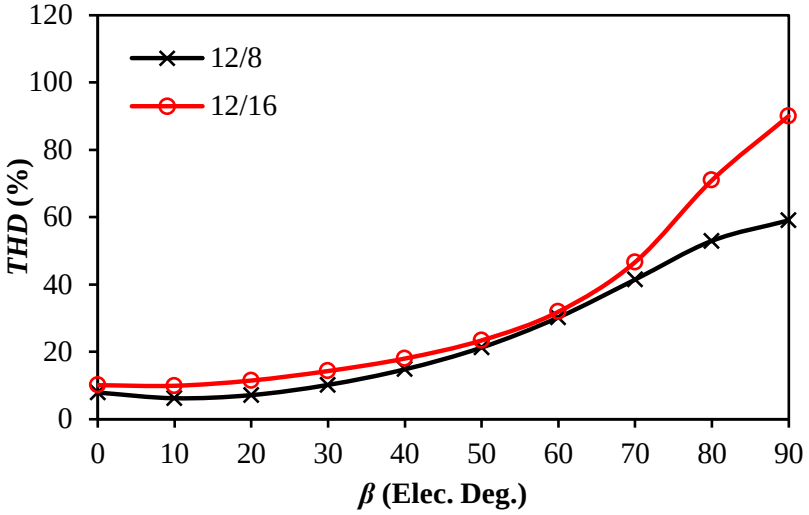

(b) *THD*

Fig. 5.12 Comparison of *VDR* for 12/8 and 12/16 machines (I_{max}=10A, 400rpm).

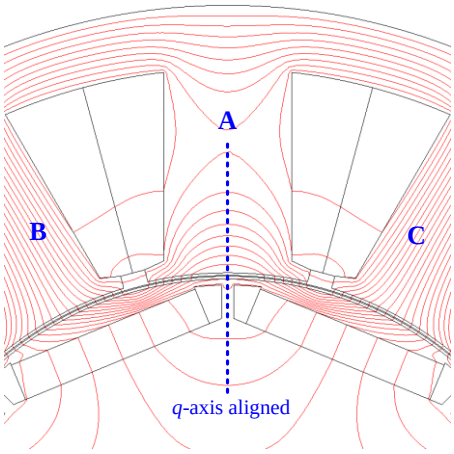

(a) Armature flux path by FP method

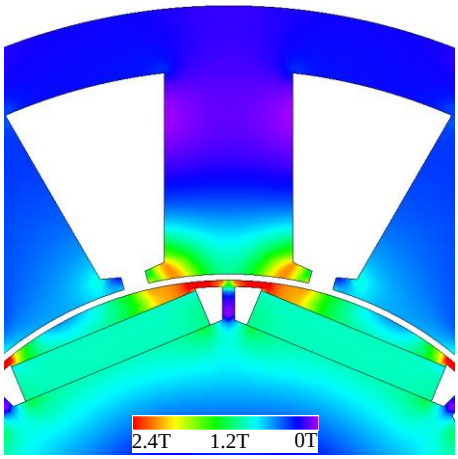

(b) Local magnetic saturation

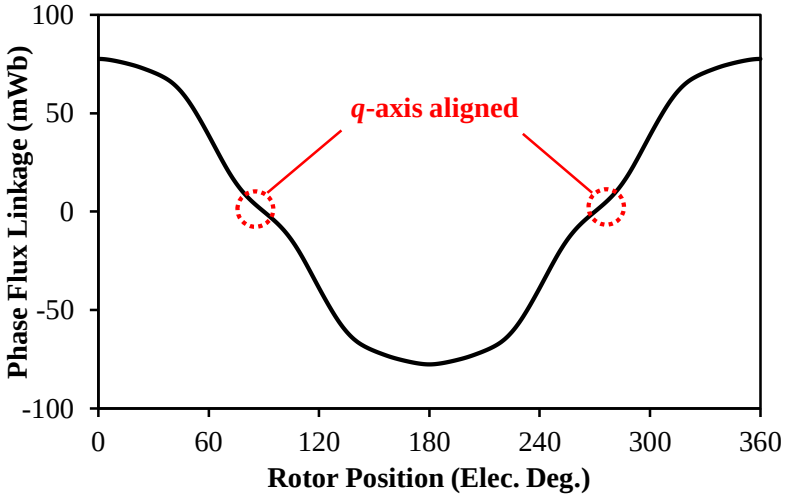

(c) Armature flux linkage by FP method

Fig. 5.13 Illustration of *d*-axis armature flux path and armature phase flux linkage by FP method in 12/8 machine (I_{max}=10A, β=90°).

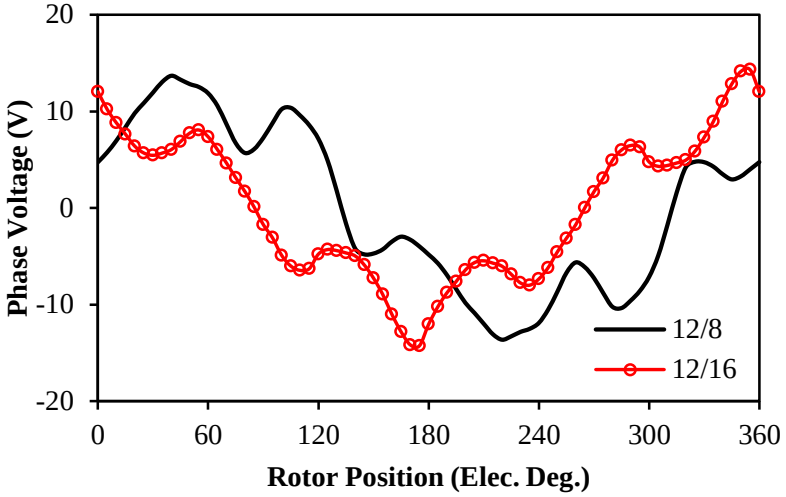

(a) Waveforms

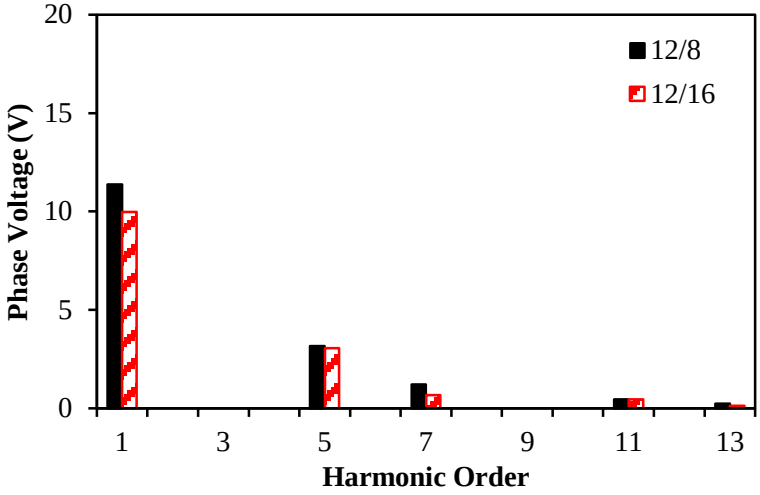

(b) Harmonics

Fig. 5.14 Comparison of terminal phase voltages for 12/8 and 12/16 machines (I_{max}=10A, β=60°, 400rpm).

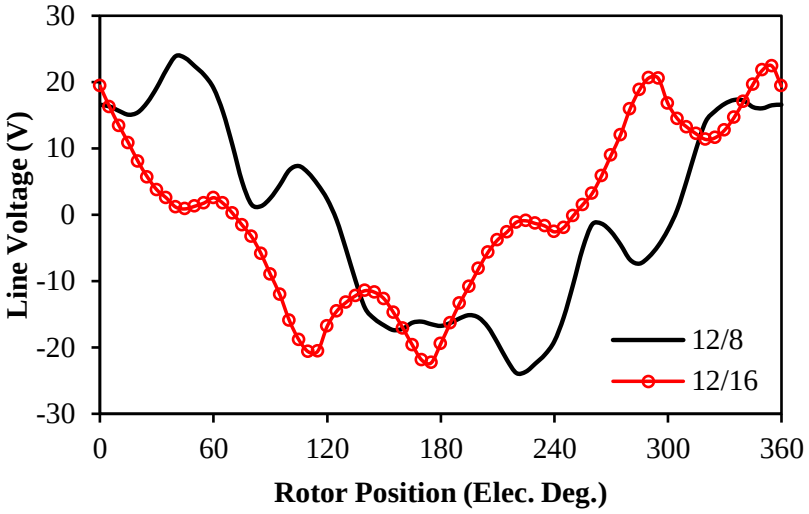

(a) Waveforms

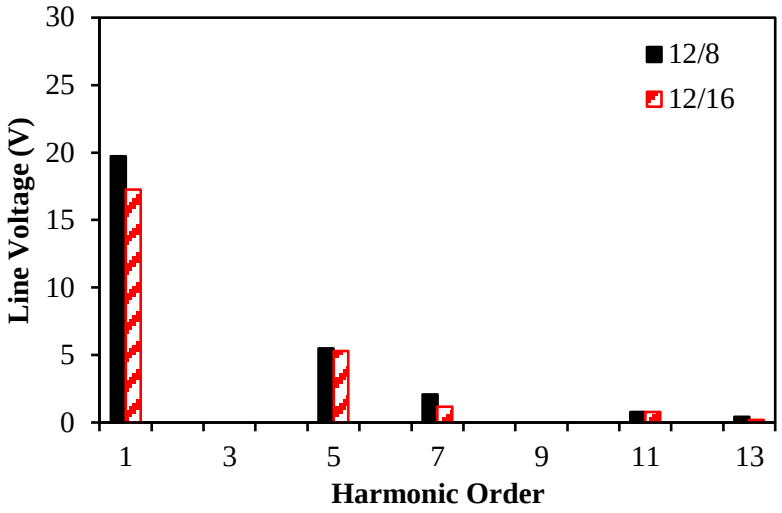

(b) Harmonics

Fig. 5.15 Comparison of terminal line voltages for 12/8 and 12/16 machines (I_{max}=10A, β=60°, 400rpm).

5.3.4 Integer Slot Machines

Fig. 5.16 compares *LVDR* and *THD* for the two integer slot machines, which show large voltage distortion especially for the 12/4 machine. Since winding coil pitch and rotor pole pitch in integer slot machines equal, they suffer more from rotor segmentation effect than other fractional slot machines. As shown in Fig. 5.17, the *d*-axis armature flux has to cross the magnet or circulate from the leakage flux paths, which largely increases the local magnetic saturation, as can be reflected in the terminal voltages in Fig. 5.18 and Fig. 5.19. Since the armature winding of the 24/4 machine distributes in more slots, its relative low

harmonic winding factor helps to cancel parts of the voltage harmonics. Thus, the voltage distortion in the 24/4 machine is lower than that in the 12/4 machine.

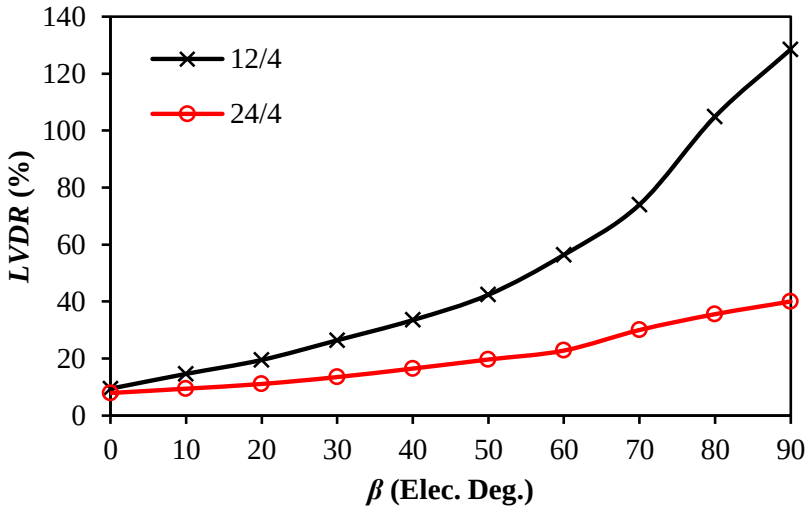

(a) *LVDR*

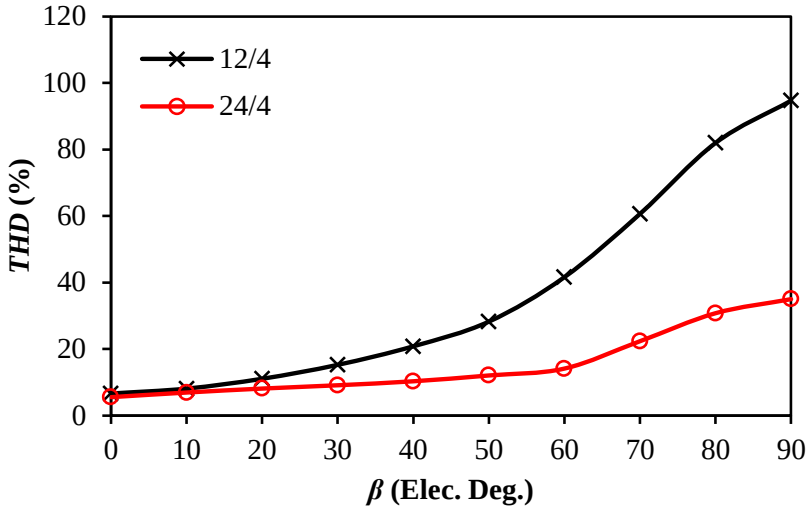

(b) *THD*

Fig. 5.16 Comparison of *VDR* for 12/4 and 24/4 machines (I_{max}=10A, 400rpm).

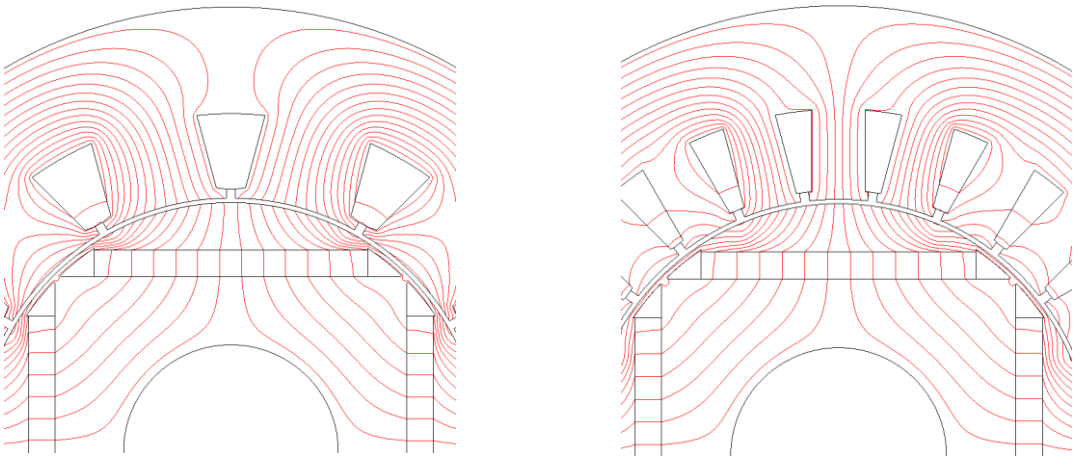

(a) 12/4 (b) 24/4

Fig. 5.17 Comparison of *d*-axis current armature flux paths for two machines by FP method (I_{max}=10A, β=90°)

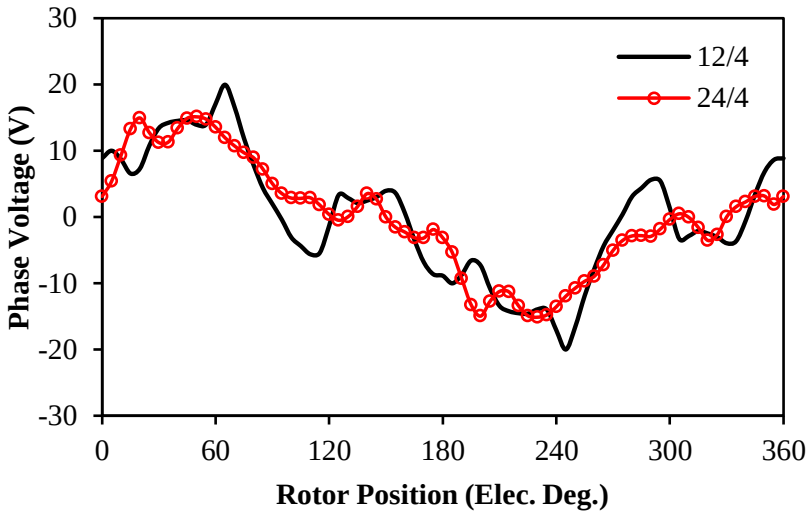

(a) Waveforms

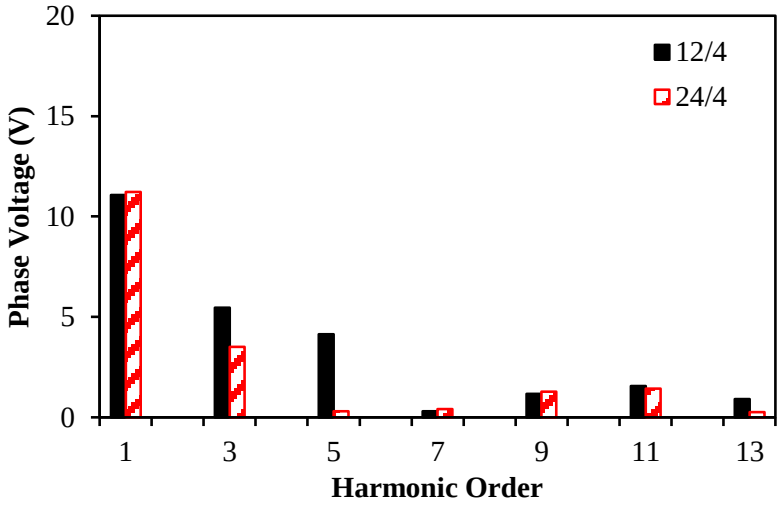

(b) Harmonics

Fig. 5.18 Comparison of terminal phase voltages for the integer slot machines (I_{max}=10A, β=60°, 400rpm).

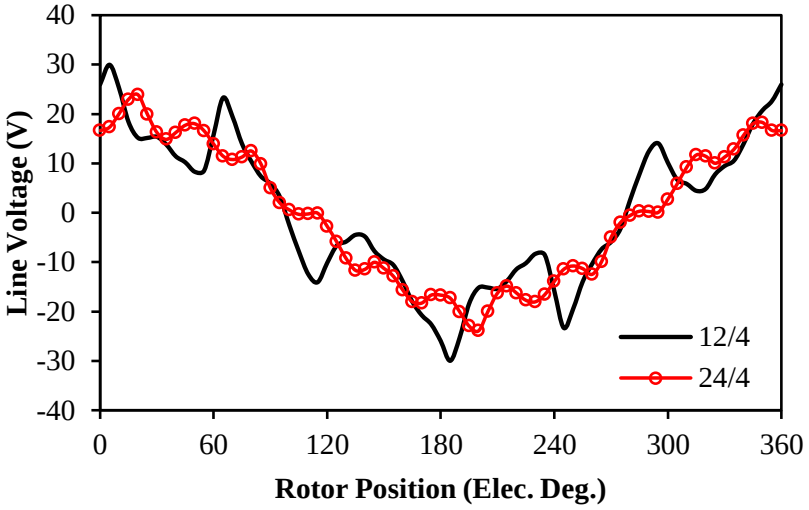

(a) Waveforms

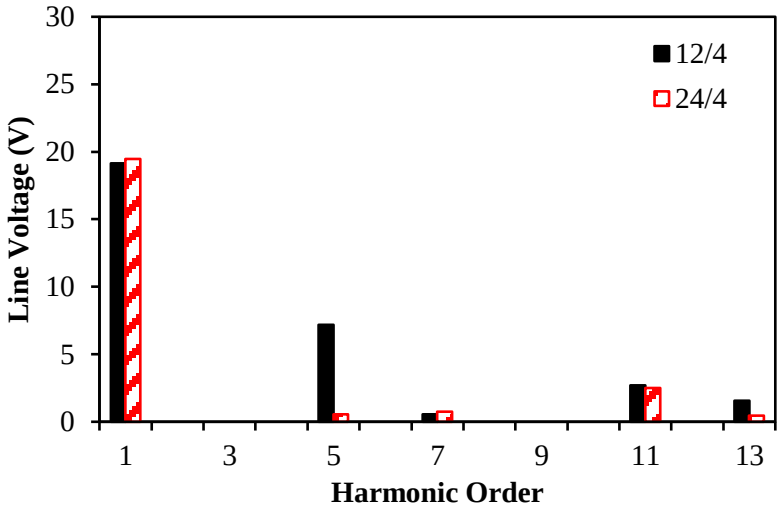

(b) Harmonics

Fig. 5.19 Comparison of terminal line voltages for the integer slot machines (I_{max}=10A, β=60°, 400rpm).

5.3.5 Comparison of Maximum Terminal Voltage Distortion

According to the analysis above, the influence of slot and pole number combinations on terminal voltage distortion could be summarized in Fig. 5.20(a). Since the armature coil pitch is the same as the rotor pole pitch in integer slot machines, they suffer more from voltage distortion than fractional slot machines, especially for the integer slot machines with q=1 due to high harmonic winding factors. Meanwhile, the fractional slot machines could be re-arranged according to their q in Fig. 5.20(b). Clearly, all fractional slot machines with N_s>2p have much lower *LVDR* and *THD* than their counterparts with N_s<2p. Further, when q is too

close to or too far away from 1/3, the voltage distortion could both become worse according to the analyses.

Since the relation between τ_s and τ_r is really important for the voltage distortion in fractional slot IPM machines, the harmonic pitch factor could be adopted as an evaluation tool, which specifically describes the relation between τ_s and τ_r for each machine.

$$k_{p\nu} = \sin\left(\frac{\nu p\pi}{N_s}\right) \tag{5.1}$$

where ν is the time of harmonics. Therefore, the 3rd, 5th and 7th harmonic winding pitch factors can be shown in Fig. 5.21. It can be observed that the 12/10 machine is located at q=0.4, which has both small 5th and 7th harmonic pitch factors. Although the 3rd harmonic may be still strong in the terminal phase voltage due to armature reaction, it will not influence the control performance in a symmetric 3-phase machine. Thus, the machines having smaller 5th and 7th harmonic winding factors will definitely reduce the influence of armature reaction and terminal voltage distortion. The preferred $N_s/2p$ region can be chosen as the shadowed part in Fig. 5.21. In this way, the machines belonged to the region, e.g. the 12/10 machine, or at least close to the region, e.g. the 9/8 machine, will suffer relatively less influence from on-load terminal voltage distortion than other $N_s/2p$ combinations machines.

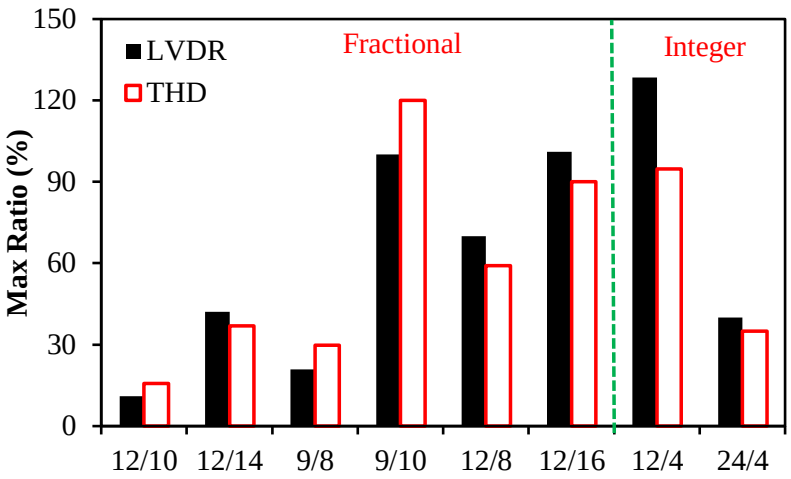

(a) All machines

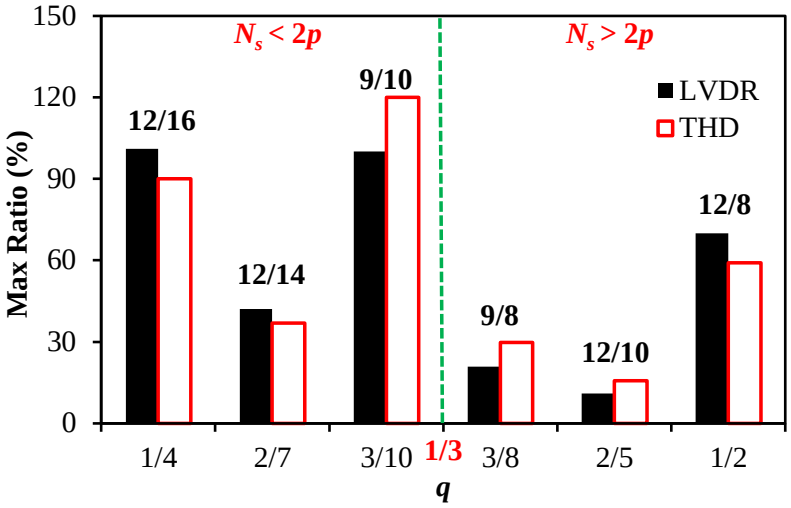

(b) Fractional slot machines

Fig. 5.20 Comparison of maximum *LVDR* and *THD* in all investigated machines (I_{max}=10A, β=90°, 400rpm).

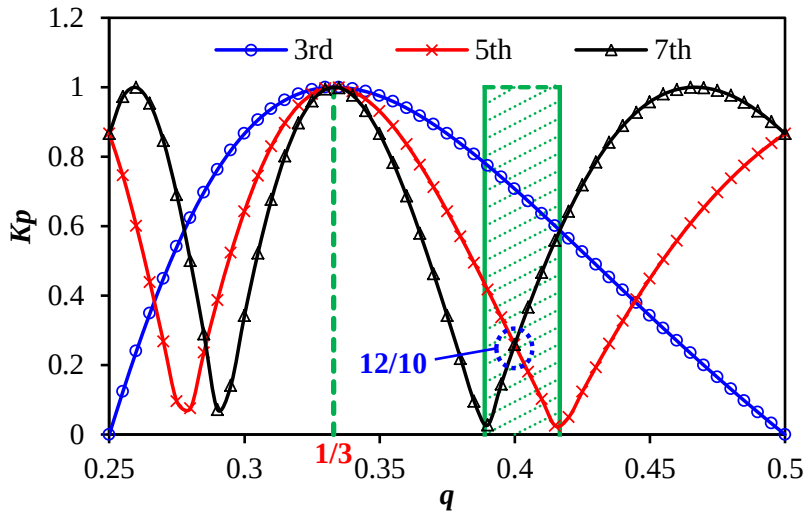

Fig. 5.21 Variation of harmonic pitch factors against q (showing the optimal $N_s/2p$ combination regions to minimize the influence of voltage distortion).

5.4 Comparison of Electromagnetic Performance Influenced by Voltage Distortion

5.4.1 On-Load Back-EMF

As shown in Section 5.2, all investigated machines are adjusted to obtain the same fundamental value of open-circuit back-EMFs at rated speed. Thus, the difference between on-load and open-circuit back-EMFs could reflect the on-load local magnetic saturation. By FP method, the on-load back-EMFs for all machines could be calculated and compared in Fig. 5.22, in which the OC refers to open-circuit condition. Although the typical flux densities of

the stator tooth body and back iron have been adjusted to the knee point of the lamination material, the local magnetic saturation still exists in tooth-tips and rotor lamination region above the magnets. Thus, the distortion of on-load back-EMF for β=0° is more obvious compared with β=90° and open-circuit condition. According to the aforementioned analysis, the magnetic saturation for all machines will reduce with the increase of β, which result in the reduction of voltage distortion level, Fig. 5.23. Due to the same reason, the fundamental value of the on-load back EMF will increase with β as well, which can be reflected in the FFT results, Fig. 5.22.

Meanwhile, the integer slot machines have higher on-load back-EMF distortions than the fractional slot machines especially for the 12/4 machine. Since two integer slot machines have smaller pole pair numbers, their fluxes per pole will be higher, which enhance the local magnetic saturation in tooth-tips and rotor lamination regions above the magnet. Meanwhile, compared with fractional slot machines, the 12/4 integer slot machine has much higher harmonic winding factors (all equal to 1), while it suffers more from rotor segmentation effect according to the aforementioned analyses. Thus, the 12/4 machine has the worst distortion level of on-load back-EMF among the investigated machines.

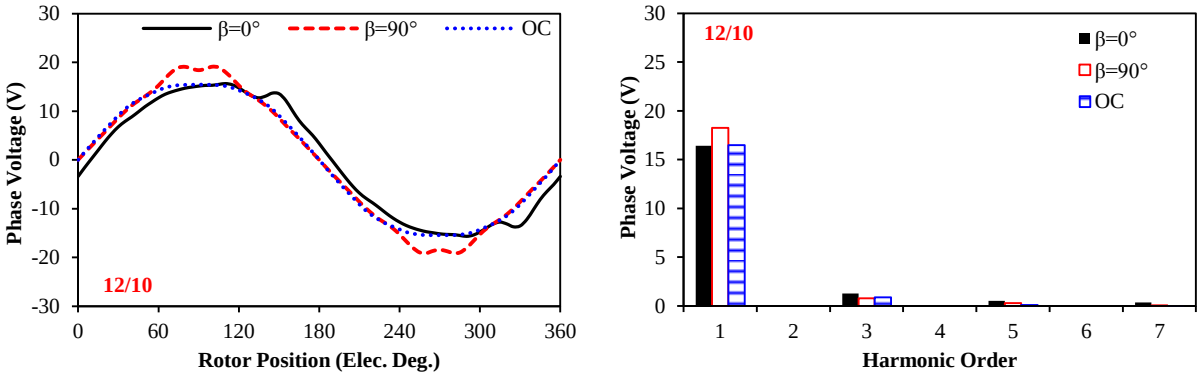

(a) 12/10 machine

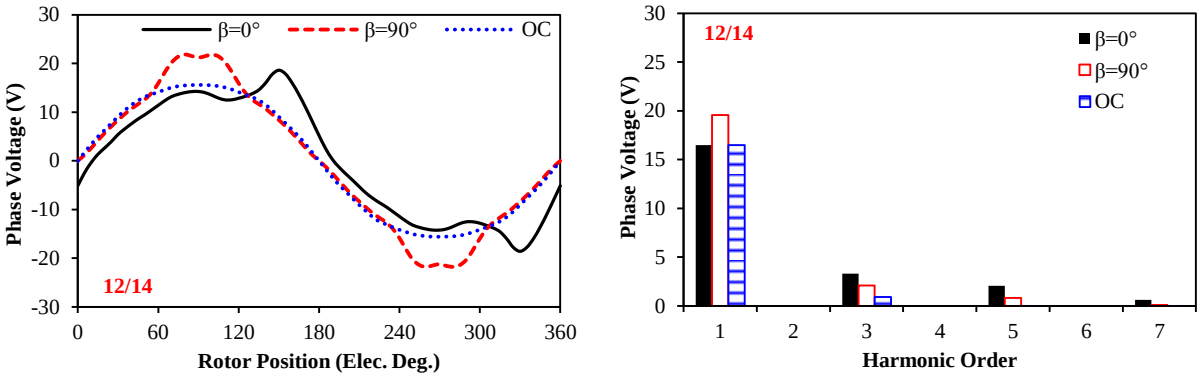

(b) 12/14 machine

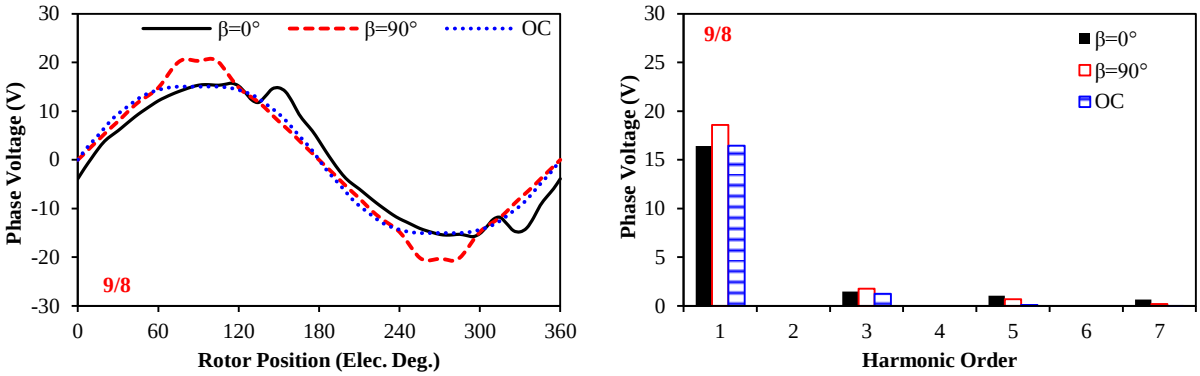

(c) 9/8 machine

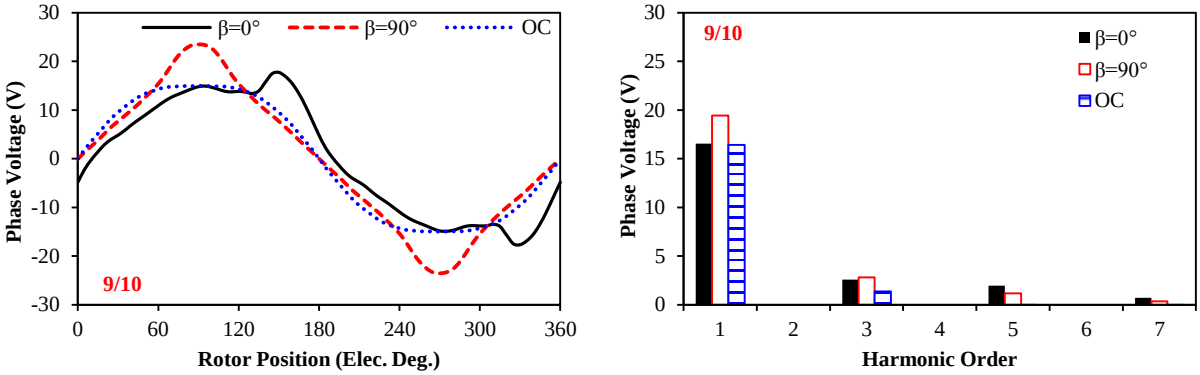

(d) 9/10 machine

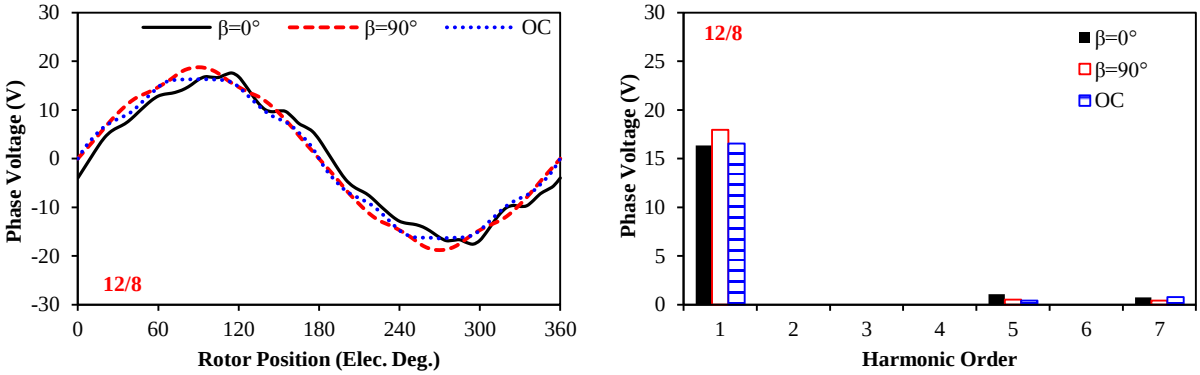

(e) 12/8 machine

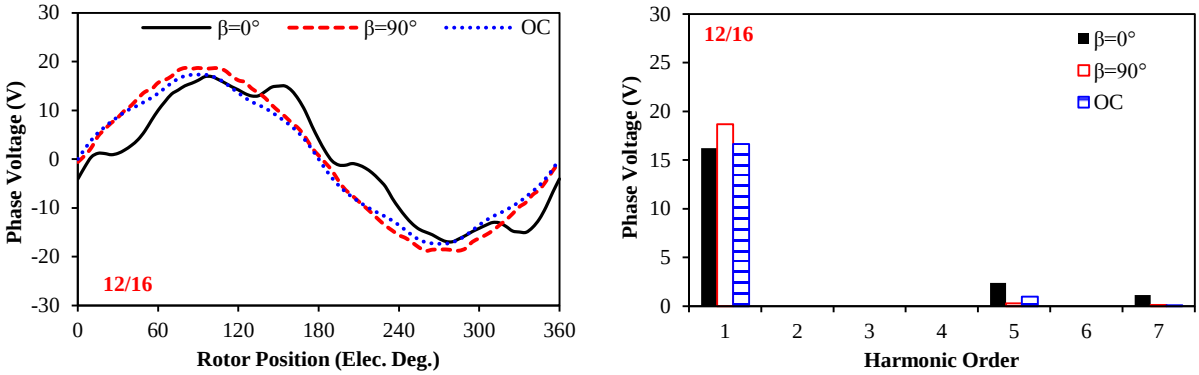

(f) 12/16 machine

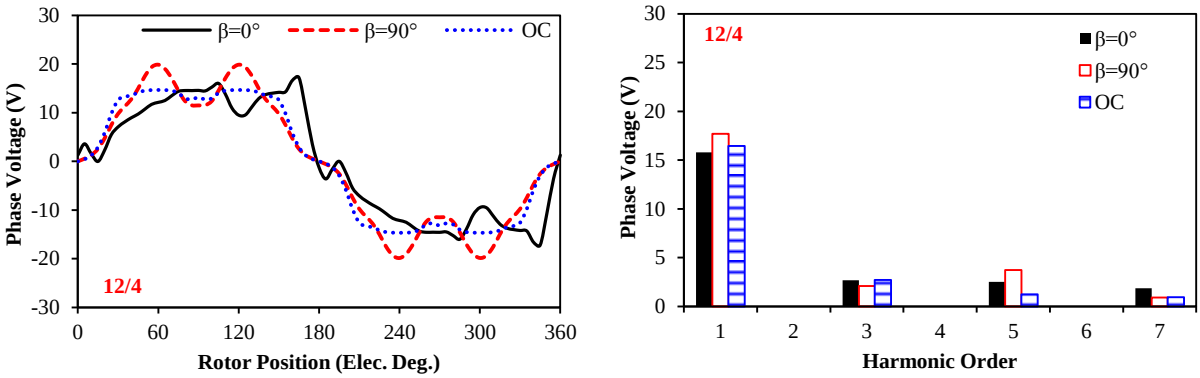

(g) 12/4 machine

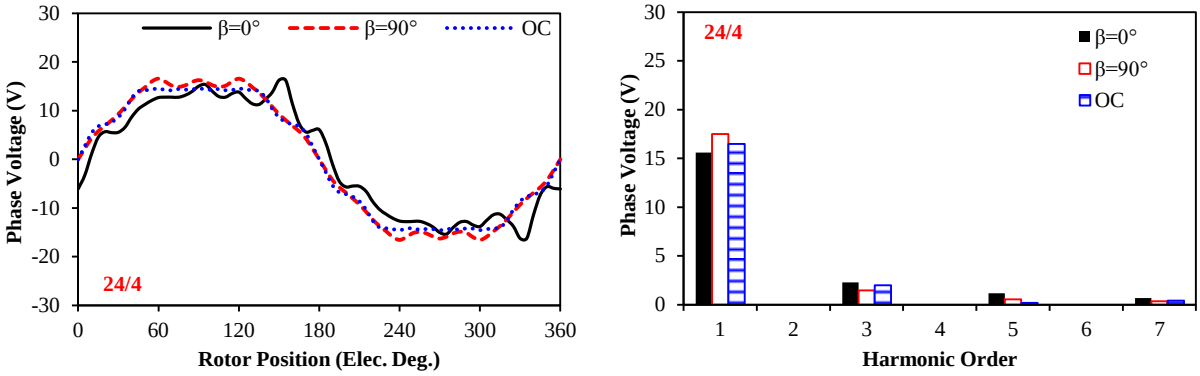

(h) 24/4 machine

Fig. 5.22 Comparison of on-load phase back-EMFs for machines with different slot and pole number combinations (I_{max}=10A, 400rpm).

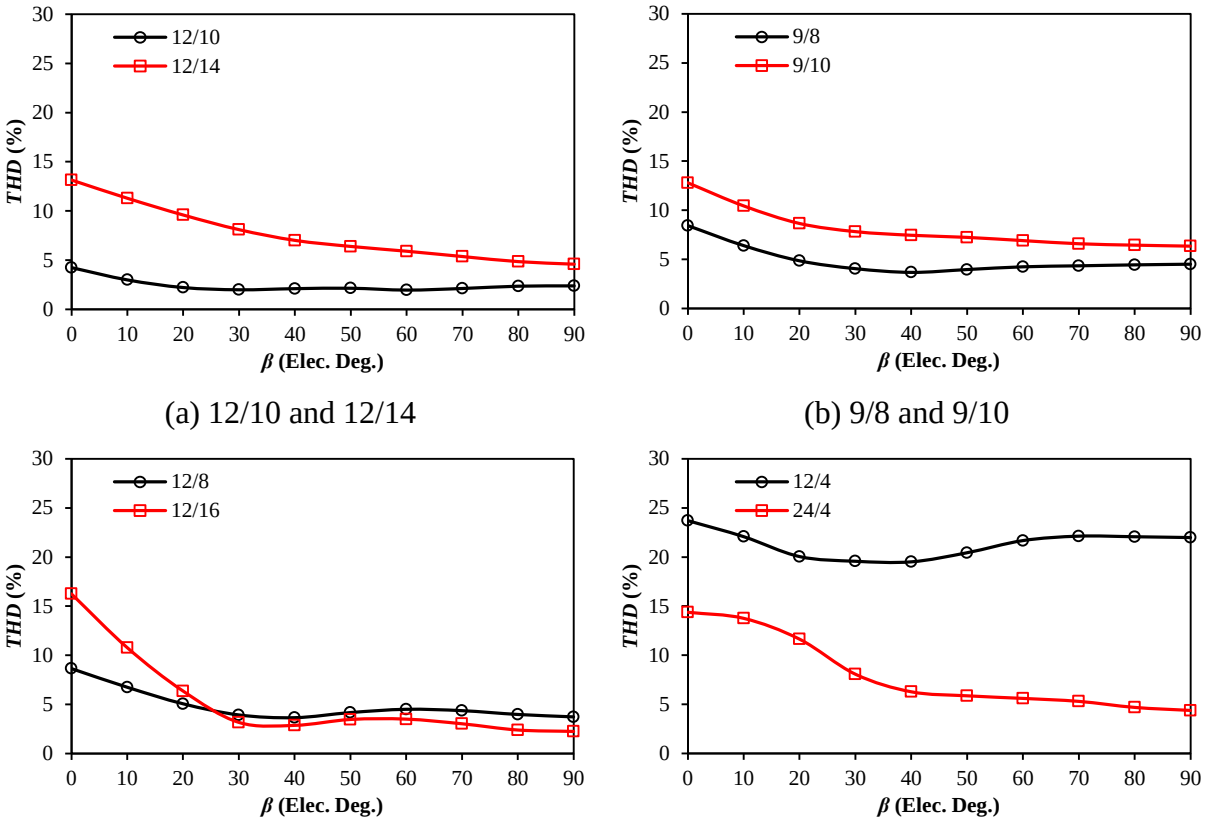

(a) 12/10 and 12/14

(b) 9/8 and 9/10

(c) 12/8 and 12/16

(d) 12/4 and 24/4 machine

Fig. 5.23 Comparison of on-load line back-EMF *THD* against β for machines with different slot and pole number combinations (I_{max}=10A).

5.4.2 On-Load Cogging Torque

With the aid of FP method, the on-load cogging torque can be calculated for all investigated machines under different current conditions in Fig. 5.24. According to [ZHU00], machines with different slot and pole number combinations will lead to different number of cogging torque periods over an electric cycle. However, since the on-load saturation conditions are much more complicated, the on-load cogging torque waveforms for all machines majorly have 6 ripples over an electric period, which does not obey the principle for the open-circuit condition. Meanwhile, since the investigated machines are not optimized for minimal cogging torque, the open-circuit cogging torque for some investigated machines are not as small as others, such as the 12/10 machine. However, due to the local magnetic saturation caused by armature reaction, it can still be observed that the on-load cogging torques have higher amplitudes than the values for open-circuit conditions in all investigated machines. The variation of on-load cogging torque amplitudes according to different β can be summarized in Fig. 5.25. Besides 12/8 and 12/16 machines, other machines in pairs all follow

the same variation trend, while the one suffers more from voltage distortion will have higher on-load cogging torque as well. Due to high rotor pole number of 12/16 machine, the saturation in tooth-tips and iron region above the magnets are always saturated although the tooth body and back iron are not saturated. Thus, the on-load cogging torque for the 12/16 machine only slightly reduces with the increase of β. More analysis about the local saturation in the 12/16 machine will be presented combined with the torque ripple section.

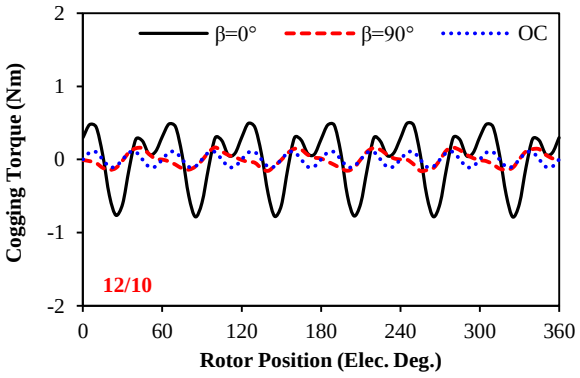

(a) 12/10 machine

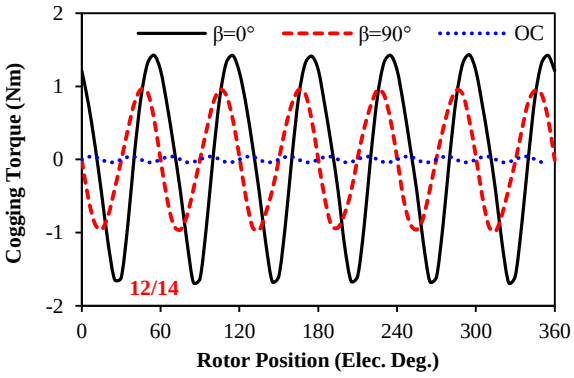

(b) 12/14 machine

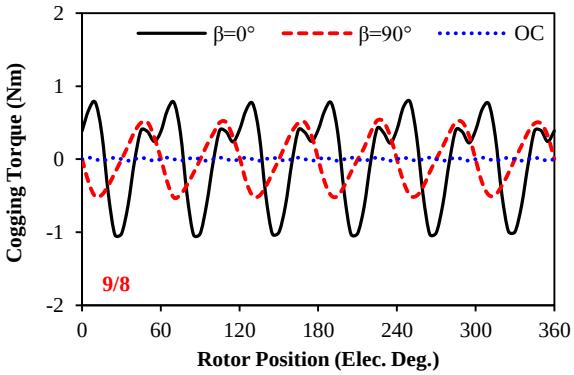

(c) 9/8 machine

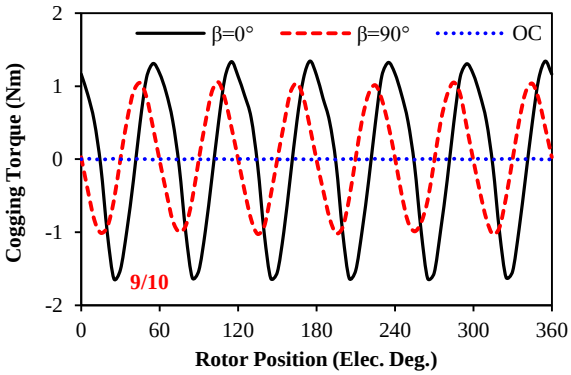

(d) 9/10 machine

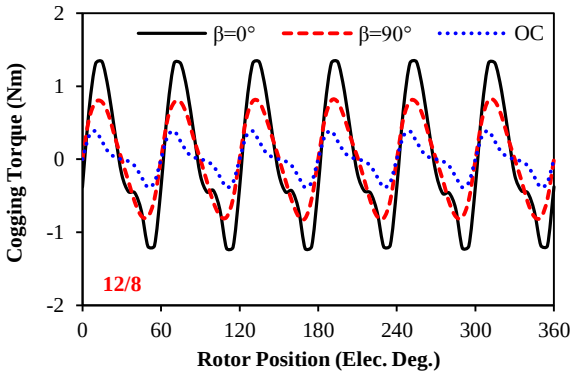

(e) 12/8 machine

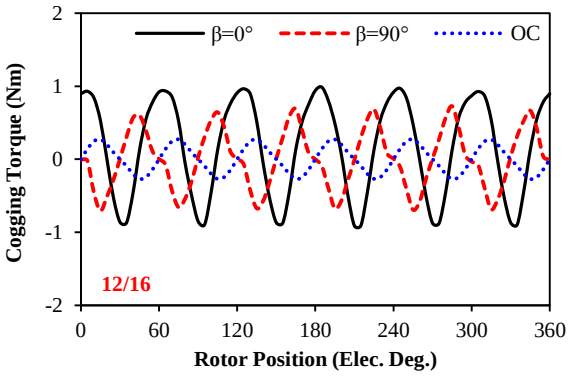

(f) 12/16 machine

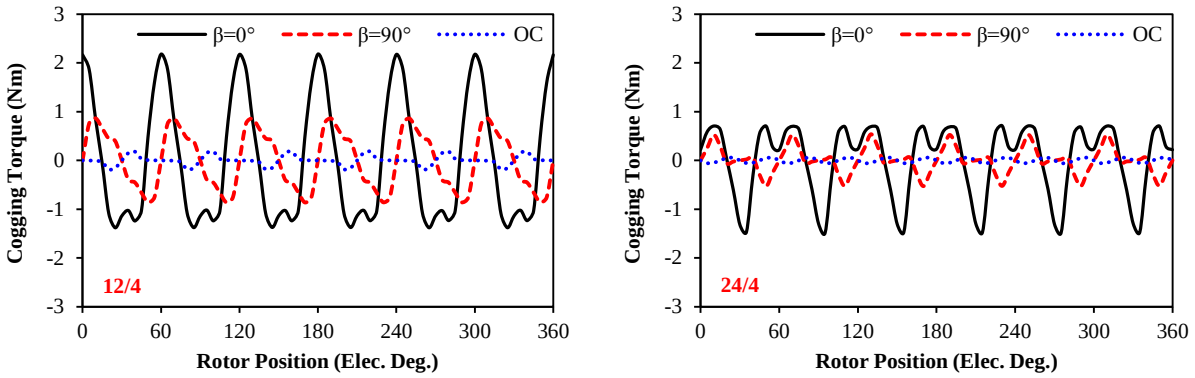

(g) 12/4 machine (h) 24/4 machine

Fig. 5.24 Comparison of on-load cogging torque for machines with different slot and pole number combinations (I_{max}=10A).

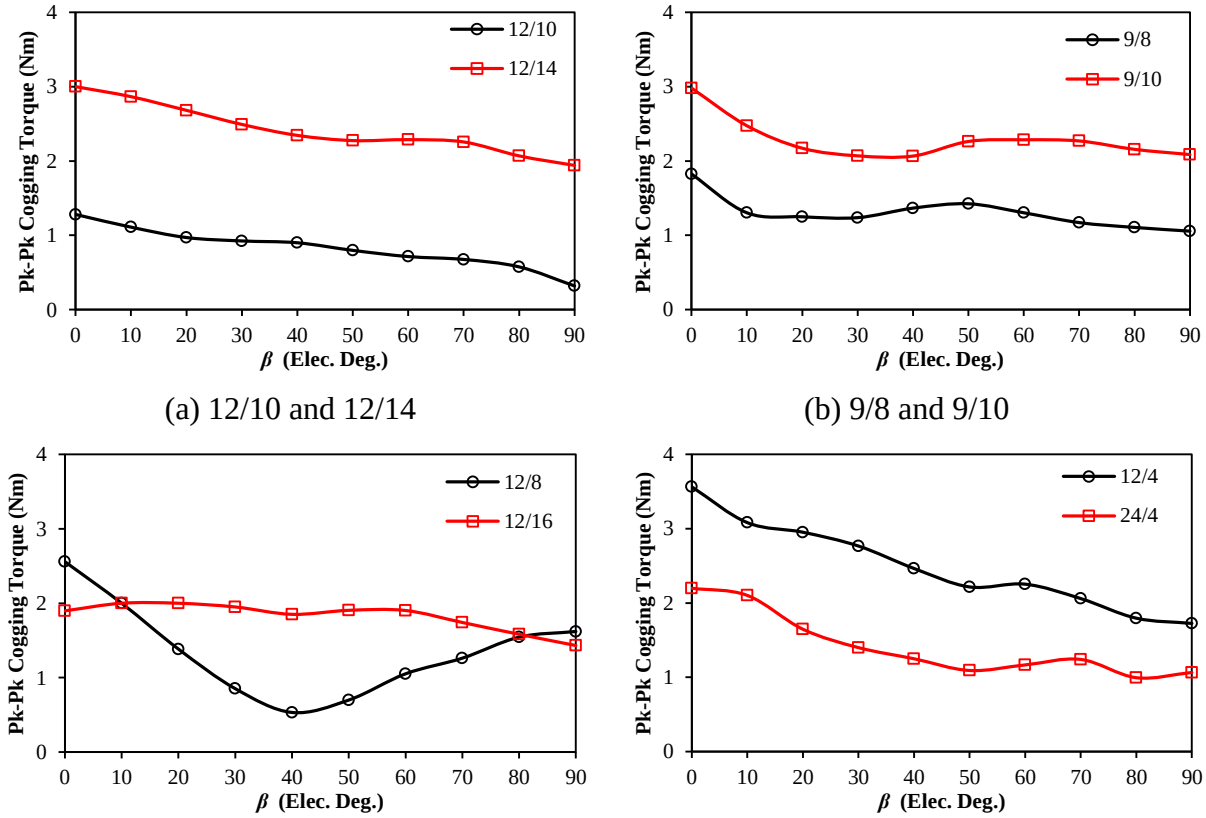

(a) 12/10 and 12/14 (b) 9/8 and 9/10

(c) 12/8 and 12/16 (d) 12/4 and 24/4

Fig. 5.25 Comparison of pk-pk on-load cogging torques against β for machines with different slot and pole number combinations (I_{max}=10A).

5.4.3 DQ-Axis Inductances

By FP method, the *dq*-axis inductance waveforms under different load conditions are calculated in Fig. 5.26. Since the reluctance torque are always negligible in fractional slot

machines, the differences between average values of L_d and L_q in the fractional slot machines are not obvious compared with the integer slot machines. When β=0°, the flux paths of all investigated machines are saturated by both PM and armature fluxes, which lead to the ripples of both L_d and L_q. With the increase of β, the flux weakening effect releases the saturation of main flux paths. However, the ripples of inductances begin to be dominated by the increase of rotor segmentation effect with the increase of β. This can be reflected more clearly from the variation of inductance ripples in Fig. 5.27. Take the 12/10 and 12/14 machines for examples, Fig. 5.27(a), the ripples of L_d continuously reduce with the increase of β, but the ripples of L_q firstly increase but then reduce with β due to the balance between the rotor segmentation and the reduction of saturation by flux weakening effect. This can be seen more clearly in 9/8 and 9/10 machines, Fig. 5.27(b). Since the 9/10 machine suffers more from voltage distortion, its stronger rotor segmentation effect makes the ripples of L_q continually increase. However, due to less voltage distortion caused by rotor segmentation effect, the ripples of L_q in the 9/8 machine firstly increase but then reduces similar as the 12/10 machine. With the same rotor diameters, the 12/16 machine has much higher pole numbers, which limits the iron region above the PMs and suffers more from local magnetic saturation in these regions. Thus, the reduction of inductances of L_d is not as obvious as other machines, but the rotor segmentation effect still increase its ripples of L_q with the increase of β. Further, with higher rotor segmentation effect, the inductances ripples in the two integer slot machines are higher than other fractional slot machines. Although their curves are more fluctuated, the overall variation trend of inductance ripples of the 12/4 and 24/4 machines still follows the principles similar to the fractional slot machines.

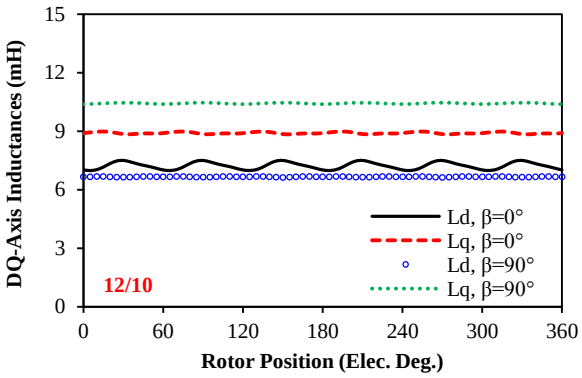

(a) 12/10 machine

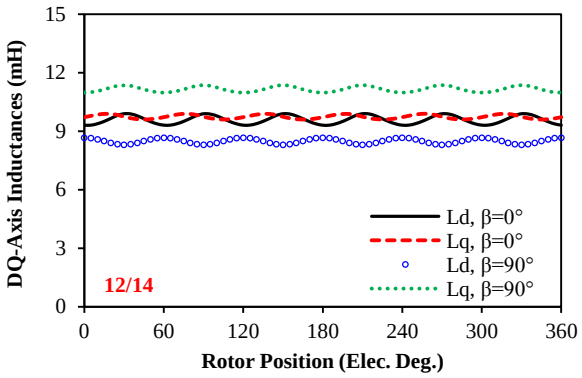

(b) 12/14 machine

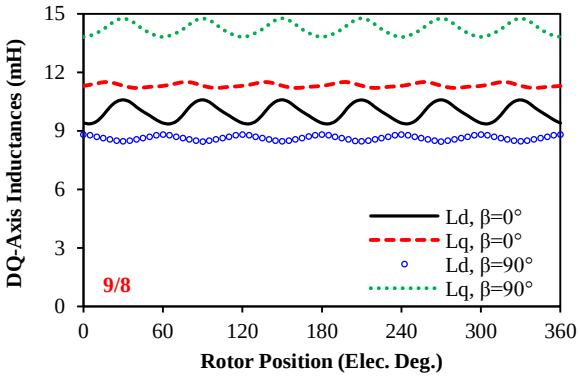

(c) 9/8 machine

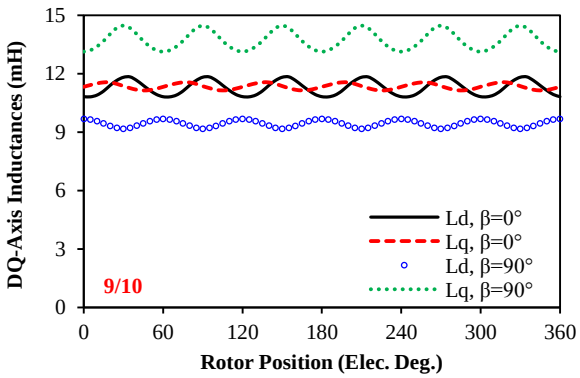

(d) 9/10 machine

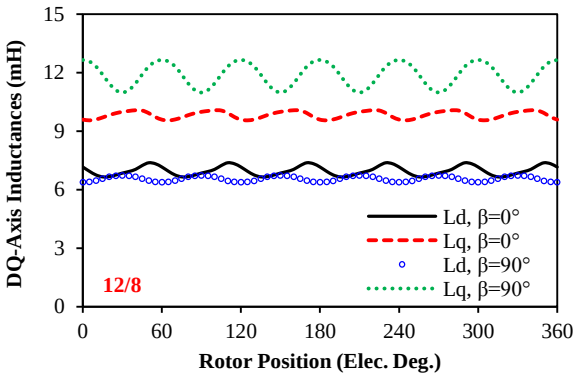

(e)12/8 machine

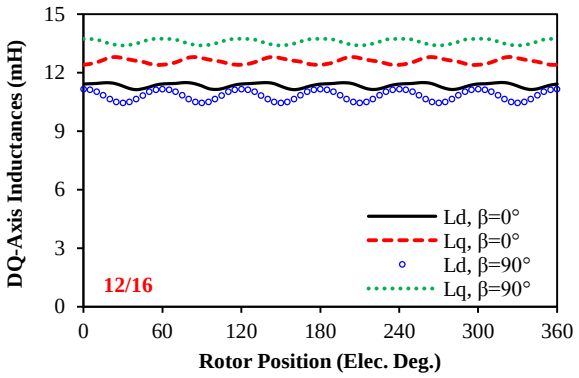

(f) 12/16 machine

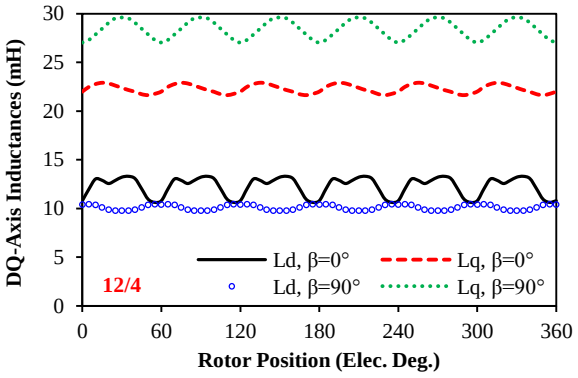

(g) 12/4 machine

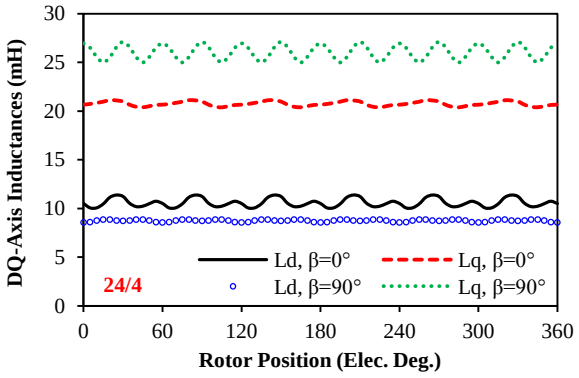

(h) 24/4 machine

Fig. 5.26 Comparison of *dq*-axis inductances waveforms for machines with different slot and pole number combinations (I_{max}=10A).

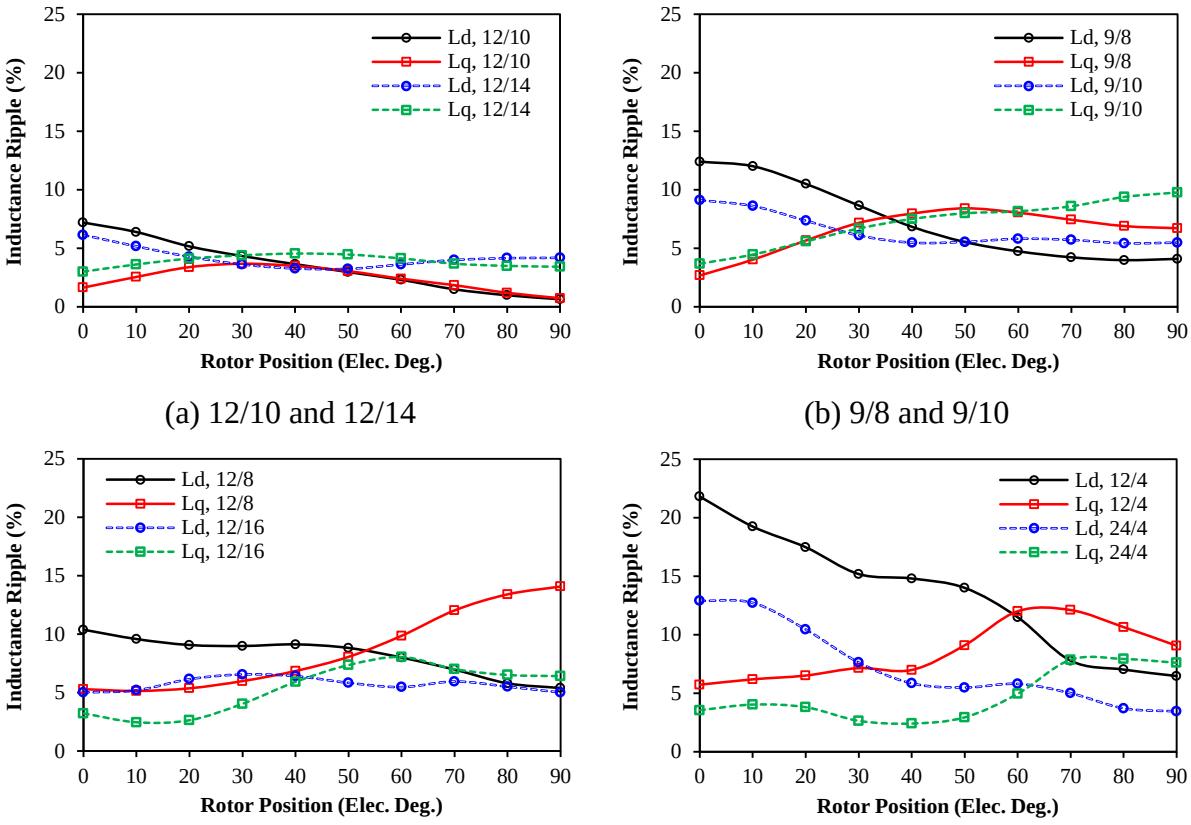

(a) 12/10 and 12/14

(b) 9/8 and 9/10

(c) 12/8 and 12/16

(d) 12/4 and 24/4

Fig. 5.27 DQ-axis inductances ripple against β for machines with different slot and pole number combinations (I_{max}=10A).

5.4.4 Average Torque and Torque Ripple

All the investigated machines are designed to obtain the same fundamental open-circuit back-EMF. Thus, their torque capabilities under I_d=0 control are expected to be the same as well, which is reflected in Fig. 5.28. However, considering the reluctance torque contributed by the IPM rotor saliency, their maximum torque capability will be different. Since the integer slot machines have much higher rotor saliency, which have been proved by the *dq*-axis inductances, their peak torques are also higher than the values under I_d=0 condition.

As shown in the aforementioned analyses, the torque ripples consists of the components associated with PM torque, reluctance torque, as well as on-load cogging torque. The distortion of PM torque can be represented by the distortion of on-load back-EMF, while the distortion of reluctance torque can be represented by the fluctuation of *dq*-axis inductances. According to the aforementioned analyses, all these components will change with the

variation of voltage distortion and local magnetic saturation. Thus, the torque ripples can also reflect the level of voltage distortion and local magnetic saturation.

Fig. 5.29 shows the variation of pk-pk torque ripples against β for all investigated machines, which shows similar variation trends as the on-load cogging torque shown in Fig. 5.25. Similar to the performance of on-load cogging torques and *dq*-inductances, the torque ripple performance for the 12/8 and 12/16 machines are also different. In order to explain this, the torque components of the two machines under β=0° and β=90° are compared in Fig. 5.30. It can be observed that the on-load cogging torques and the reluctance torques fluctuate in opposite directions, while the on-load cogging torque contributes significantly to the resultant torque ripples. The variations of torque ripples against β are compared in Fig. 5.31. With the increase of β, the flux weakening effect reduces the on-load back-EMF harmonics and leads to the torque ripple reduction of T_{pm} for both machines. In the 12/8 machine, the ripples of T_r also reduce with β, which can also be validated by the *dq*-axis inductance shown in Fig. 5.27.

Due to the influence of both flux weakening effect and rotor segmentation effect, the on-load cogging torque of the 12/8 machine firstly reduces and then rises, which makes the resultant torque ripples change in the same way. However, due to more severe local magnetic saturation, the on-load cogging torque in the 12/16 machine does not change obviously at first, but then reduces due to the significant reduction of global saturation in deep flux weakening regions. Since the on-load cogging torque plays the dominant role while other torque ripple components are in opposite directions, the resultant torque ripples of the 12/16 machine reduces with the increasing of β. The differences of saturation conditions for two machines can be reflected in Fig. 5.32. When β=0°, both 12/8 and 12/16 machines are influenced by the local magnetic saturation.

Due to less flux per pole, the tooth width of the 12/16 machine is less than that in the 12/8 machine, which makes tooth-tip region of the 12/16 machine much larger. Although their tooth body and back iron are at the same saturation level, the local magnetic saturation in the 12/16 influences the major flux path more significantly. Meanwhile, since the length of rotor flux bridges in the 12/16 machine is shorter, while the thickness of the iron region above magnets is small, the local magnetic saturation in the rotor of the 12/16 machines are more significant than the 12/8 machine even when β=90°. Therefore, the values of pk-pk on-load cogging torque of the 12/16 machine does not change as obvious as the 12/8 machine due to

the more severe local magnetic saturation, which leads to the difference of their resultant torque ripples.

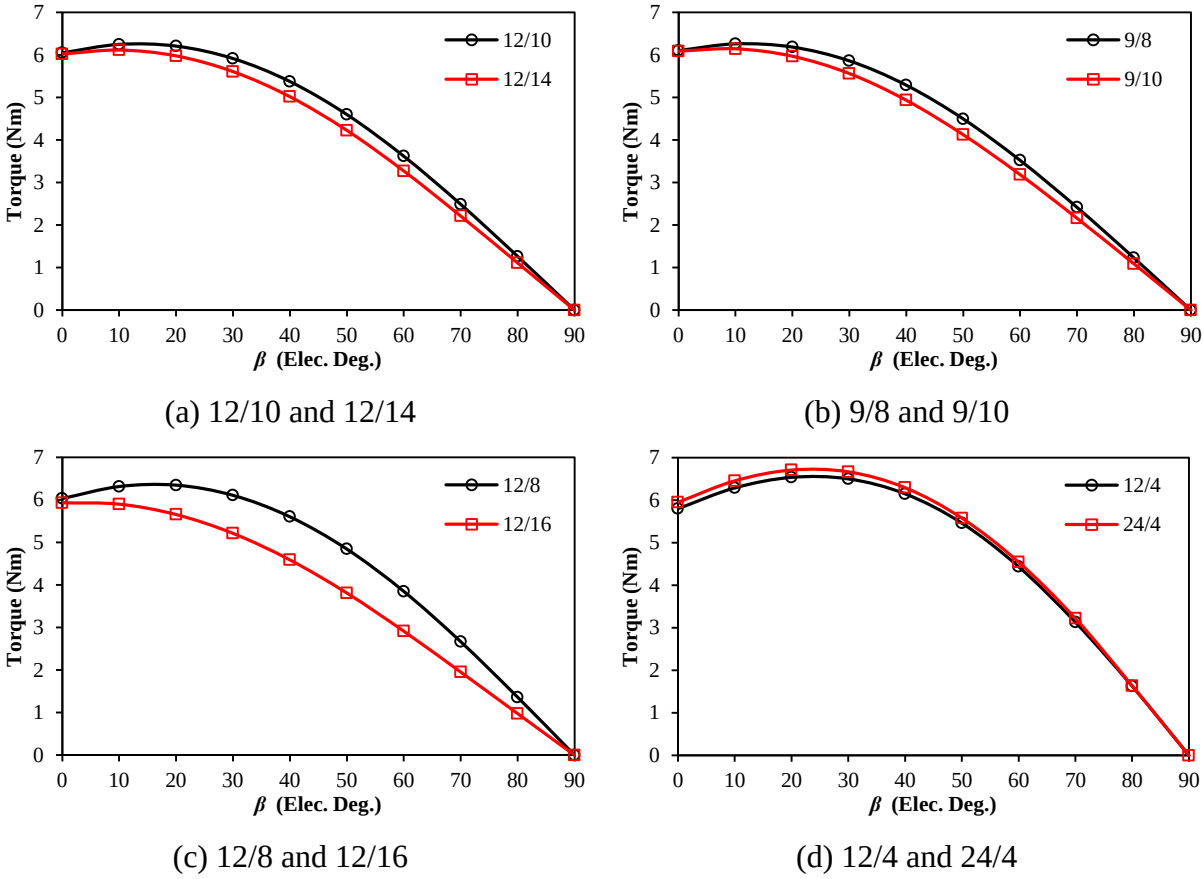

(a) 12/10 and 12/14

(b) 9/8 and 9/10

(c) 12/8 and 12/16

(d) 12/4 and 24/4

Fig. 5.28 Comparison of average torque against β for machines with different slot and pole numbers (I_{max}=10A).

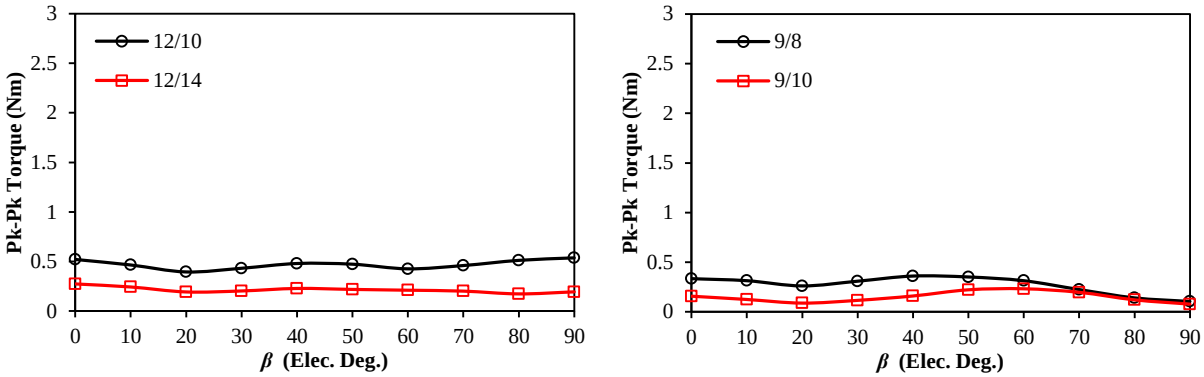

(a) 12/10 and 12/14

(b) 9/8 and 9/10

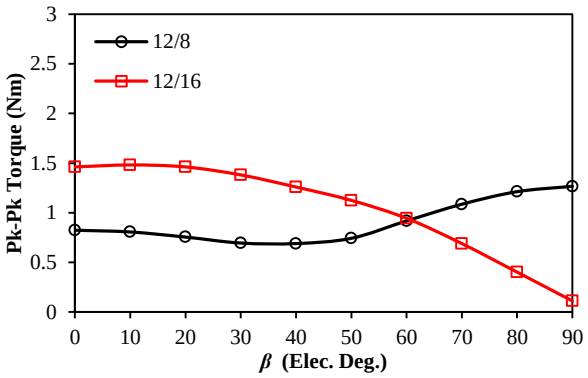

(c) 12/8 and 12/16

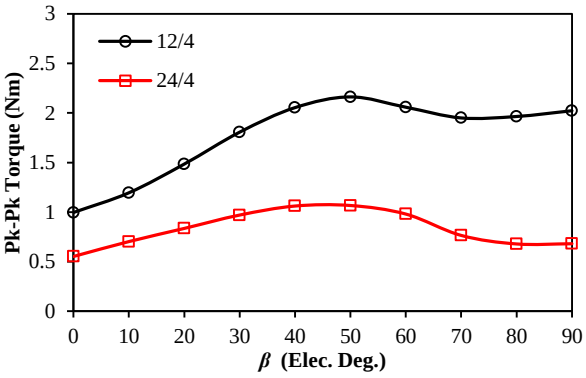

(d) 12/4 and 24/4

Fig. 5.29 Comparison of pk-pk torques for machines with different slot and pole number combinations (I_{max}=10A).

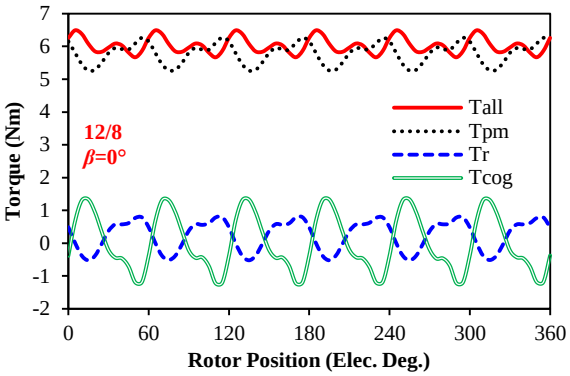

(a) 12/8, β=0°

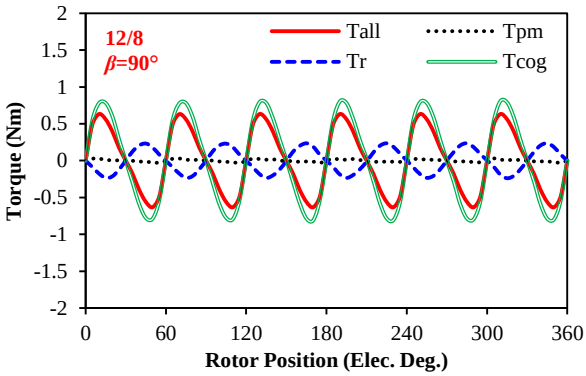

(b) 12/8, β=90°

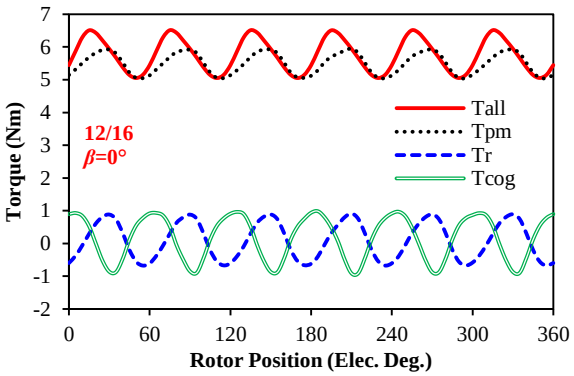

(c) 12/16, β=0°

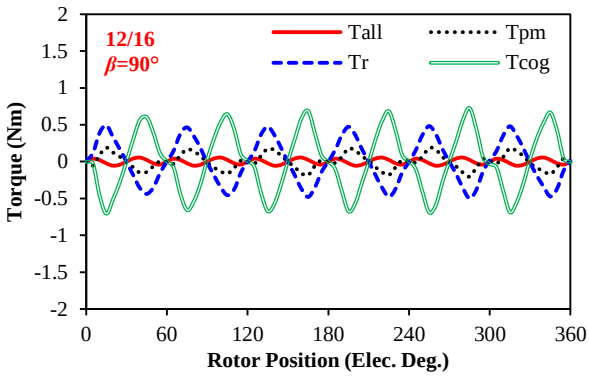

(d) 12/16, β=90°

Fig. 5.30 Comparison of torque components for the 12/8 and 12/16 machines (I_{max}=10A).

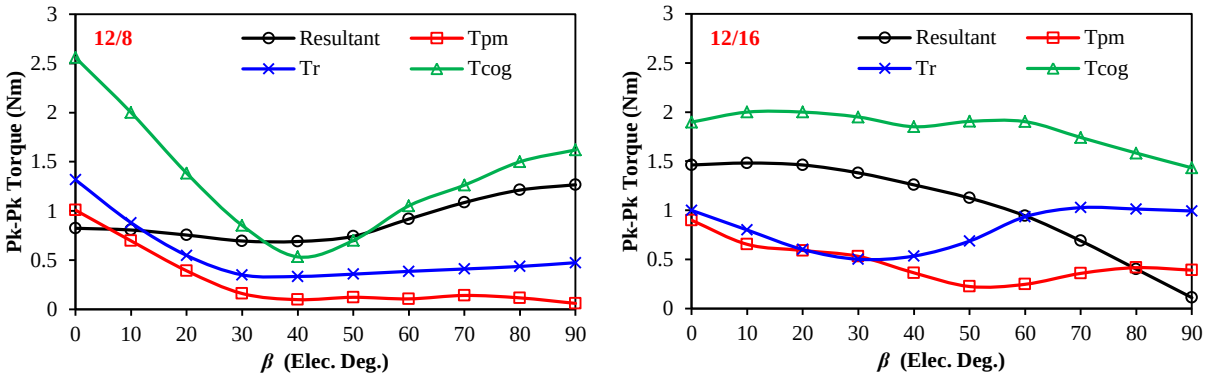

(a) 12/8 (b) 12/16

Fig. 5.31 Comparison of torque ripple components of 12/8 and 12/16 machines (I_{max}=10A).

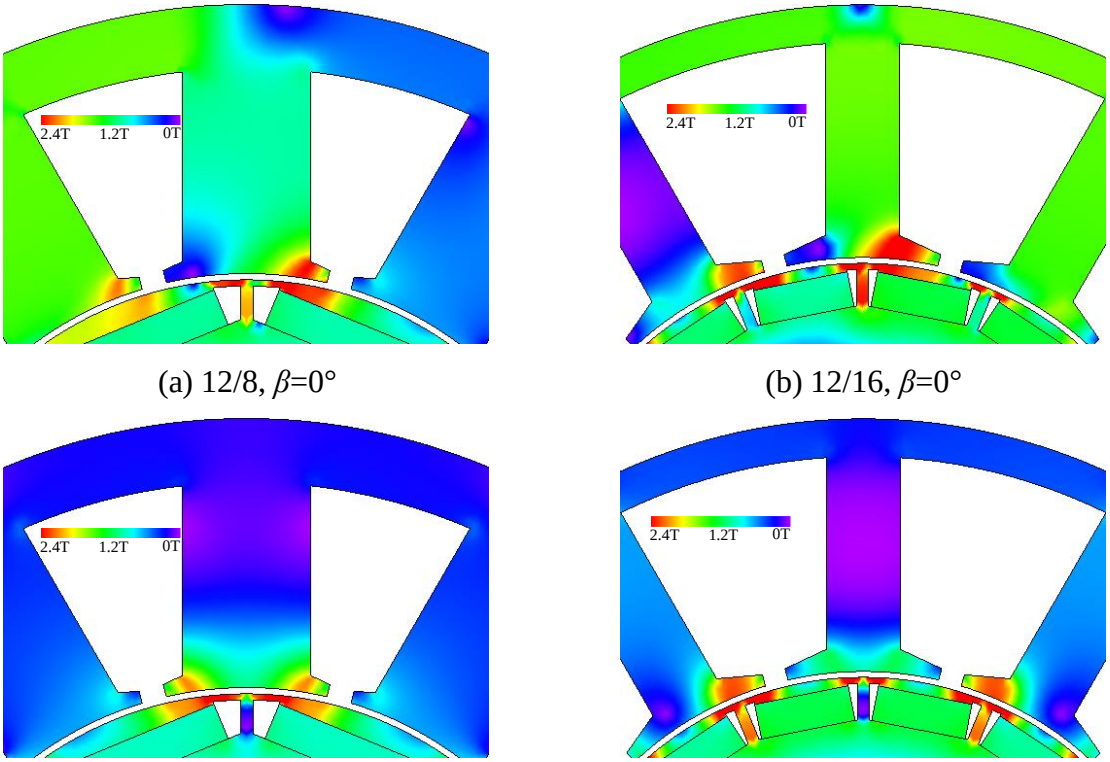

(a) 12/8, β=0° (b) 12/16, β=0°

(c) 12/8, β=90° (d) 12/16, β=90°

Fig. 5.32 Comparison of flux density distribution for different β (I_{max}=10A, θ_r=90°).

5.4.5 Iron Loss

Fig. 5.33 compares the iron loss of different lamination parts for all machines at rated speed and current, in which the lamination parts are defined in Fig. 4.35. With the increase of β, the major flux path becomes less saturated, which reduces the resultant iron losses. However, due to local magnetic saturation, the iron losses in tooth-tips and rotor caps do not significantly change with β. Since the stator tooth and back iron of all machines have been adjusted to

have similar flux density under rated currents with I_d=0 control, the iron losses largely depend on the operation frequency of the machine. Thus, the machine with higher pole numbers will obtain larger iron loss, which can also be reflected in the iron loss density of tooth-tips, Fig. 5.34.

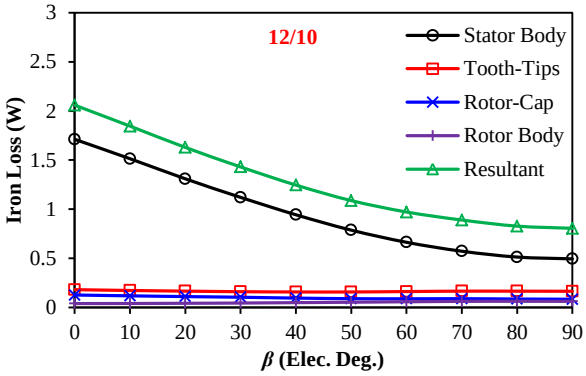

(a) 12/10 machine

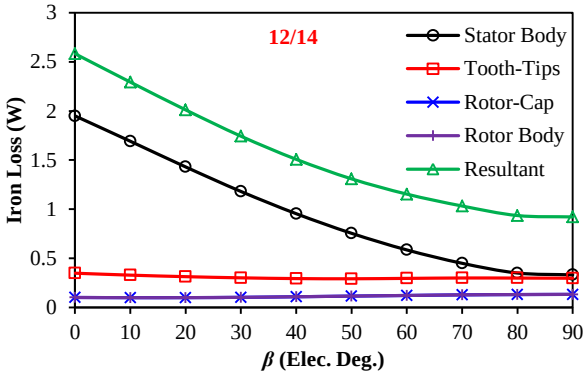

(b) 12/14 machine

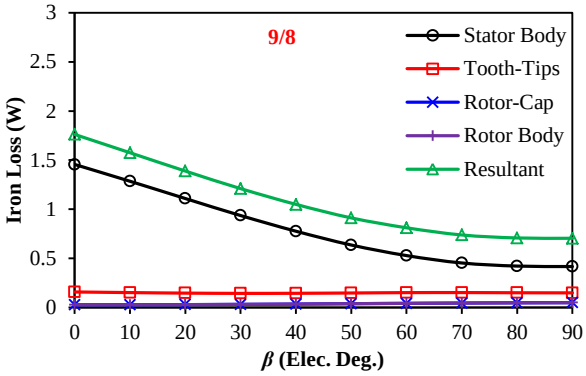

(c) 9/8 machine

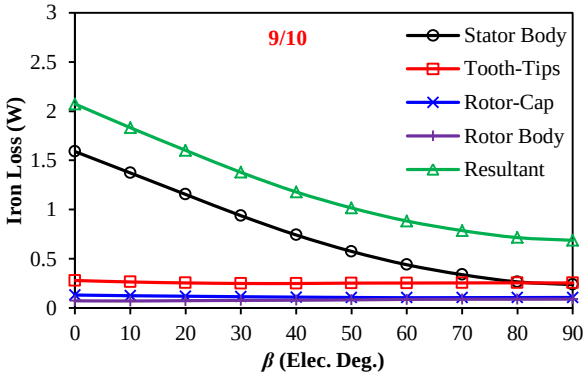

(d) 9/10 machine

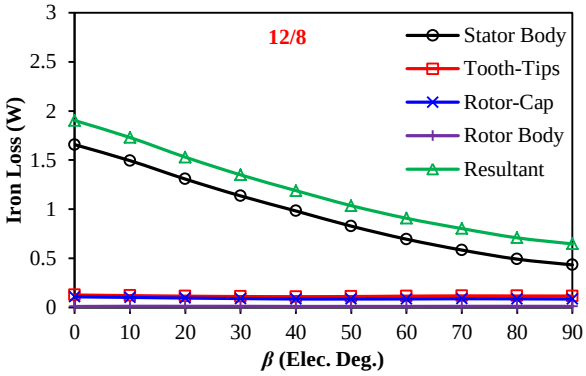

(e) 12/8 machine

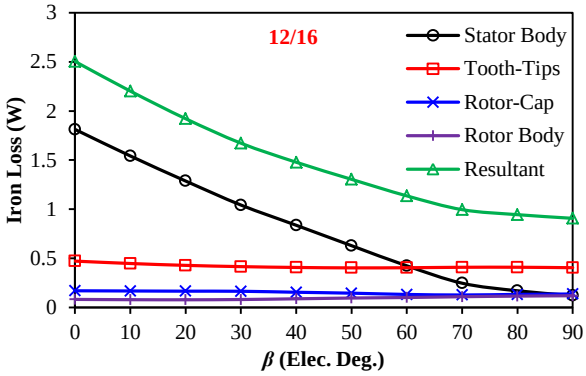

(f) 12/16 machine

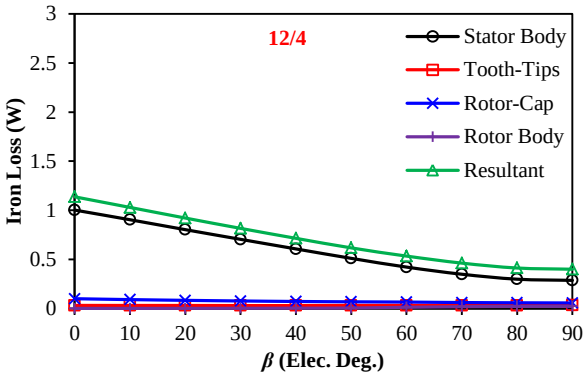

(g) 12/4 machine

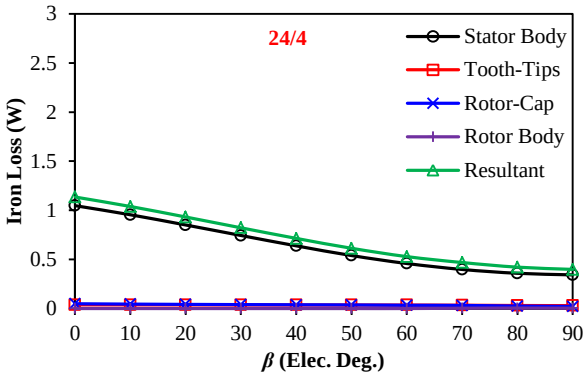

(h) 24/4 machine

Fig. 5.33 Comparison of iron loss against β for machines with different slot and pole number combinations (I_{max}=10A, 400rpm).

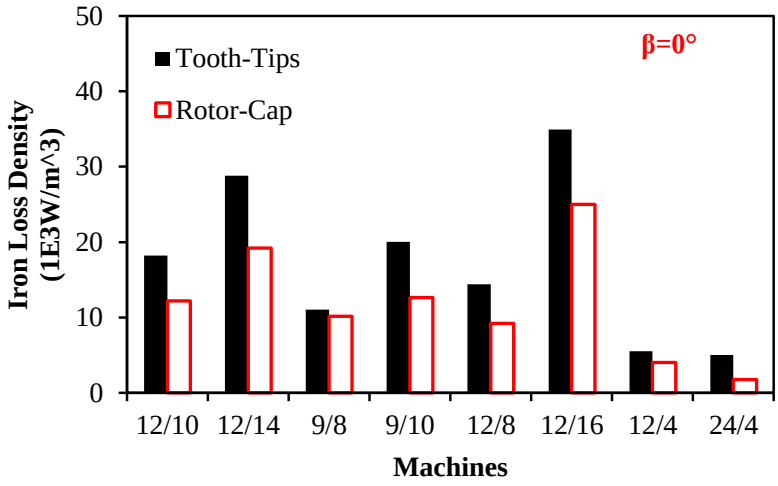

(a) β=0°

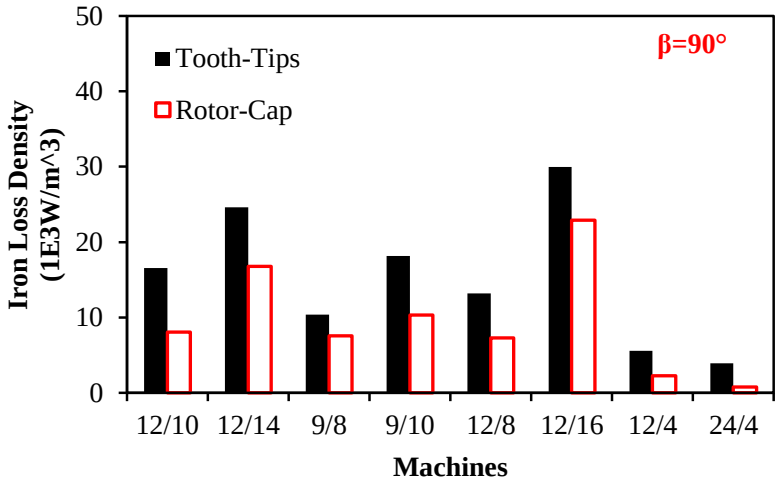

(b) β=90°

Fig. 5.34 Comparison of tooth-tip iron loss densities for machines with different slot and pole numbers (I_{max}=10A, 400rpm).

5.4.6 Flux Weakening Performance

According to the aforementioned analyses, the investigated machines have different *LVDR* with different β, which also influence their flux weakening performances. Assuming U_{DC} is 42V, the torque speed and torque ripple speed curves for all machines are calculated and compared in Fig. 5.35. For simplicity, the MTPV operation is not considered for the comparison.

The low *LVDR* and *THD* of the 12/10 machine make its torque speed performance only slightly differ from the ideal curves predicted by fundamental voltages. Since the 12/14 and 9/8 machines both have higher voltage distortion levels compared with the 12/10 machine, their real torque speed curves are obviously lower than expected. Although the 9/10 machine has high *LVDR* when β=90°, its *LVDR* only soaring up after β>70° in Fig. 5.7. Thus, under the same comparison conditions, its torque speed curves differ slightly from its ideal curves. Due to higher on-load voltage distortion level, the torque speed curves for both 12/8 and 12/16 machines reduce to zero within the investigated speed range, while their torque ripple soaring up due to zero average torque when β=90°. Further, in order to track the maximum torque per ampere for the constant torque operation, the integer slot machine work with a relative high β. Thus, the voltage distortion in constant regions results in much lower base speed compared with their ideal values. With the increase of β, the voltage distortion level of two integer slot machines deteriorates, which quickly reduces their torque speed curves to zero. Overall, the on-load voltage distortion will significantly reduce the flux weakening operation compared with the expected performance calculated only by fundamental voltages.

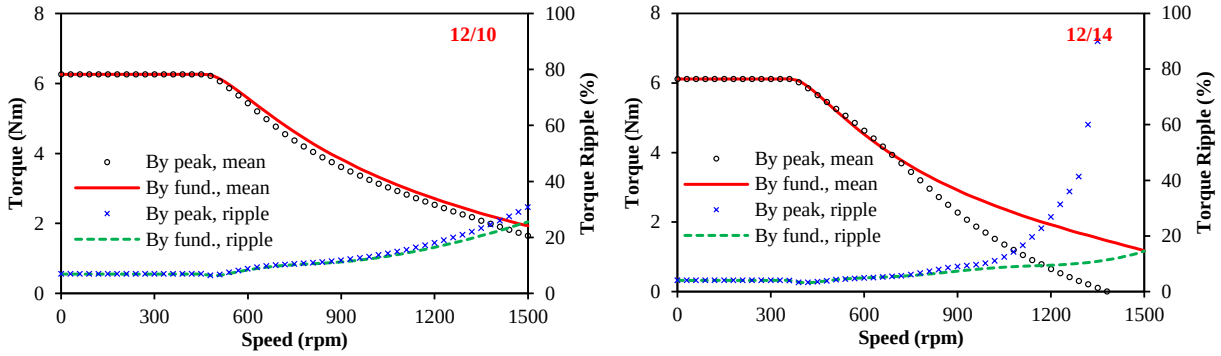

(a) 12/10 machine

(b) 12/14 machine

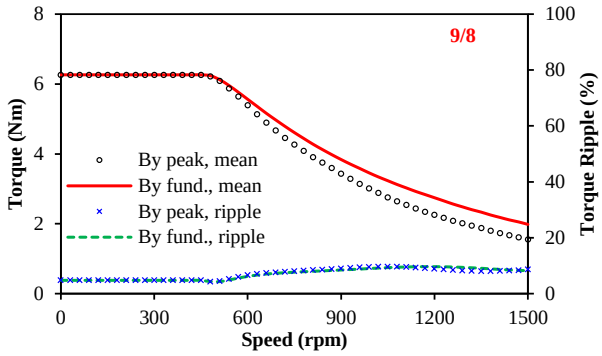

(c) 9/8 machine

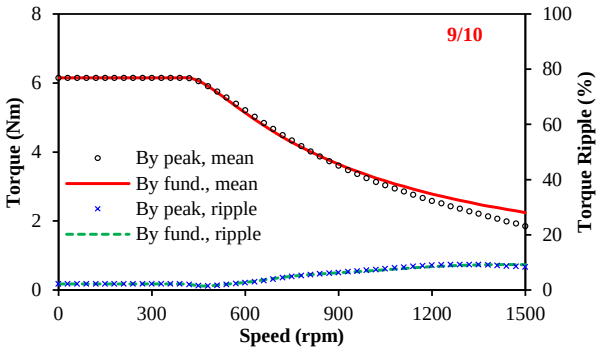

(d) 9/10 machine

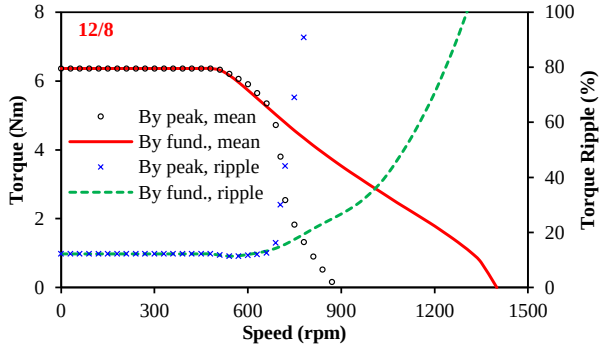

I 12/8 machine

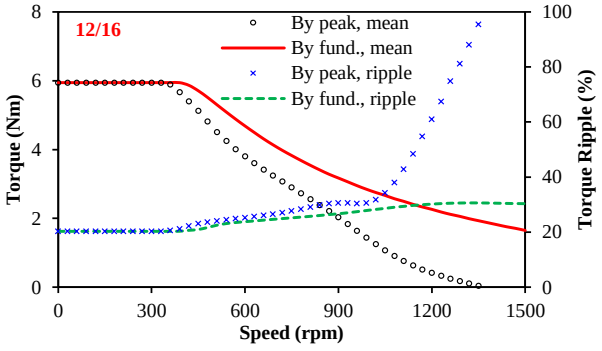

(f) 12/16 machine

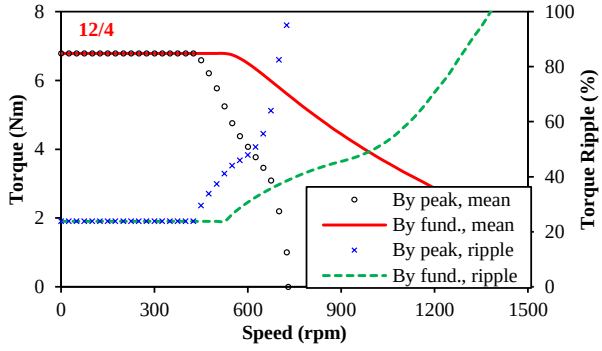

(g) 12/4 machine

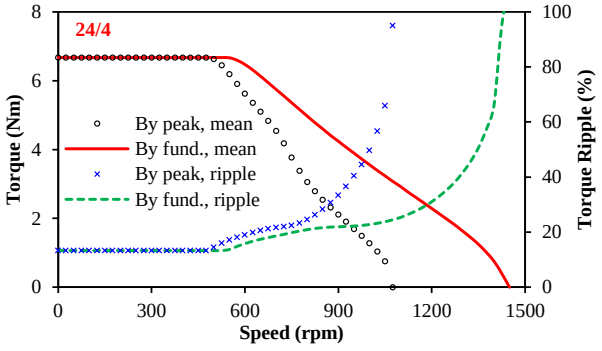

(h) 24/4 machine

Fig. 5.35 Comparison of flux weakening performance for machines with different slot and pole number combinations (I_{max}=10A, U_{DC}=42V).

5.5 Experimental Validation

5.5.1 Prototype Machines

Two prototype IPM machines with $N_s/2p$ equal to 12/10 and 12/8 are adopted to validate the analysis results. In order to ease the fabrication and save the cost, the 12/8 prototype machine is the same as that in Chapter 4, while the 12/10 prototype shares its stator. The rotor of the 12/10 prototype is the same as that in Fig. 5.1 and Table 5.1. The photos of the prototypes are shown in Fig. 5.36. The measured phase resistance under room temperature is 0.62Ω. Meanwhile, the test rig is the same as that for the aforementioned chapters. Due to the inverter limitation, the maximum driving current has been reduced to 9A. The PWM frequency for all experiments will be 10kHz.

(a) Stator

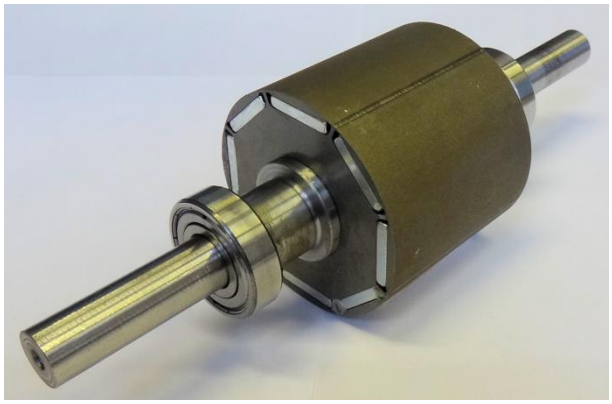

(b) 8-pole rotor

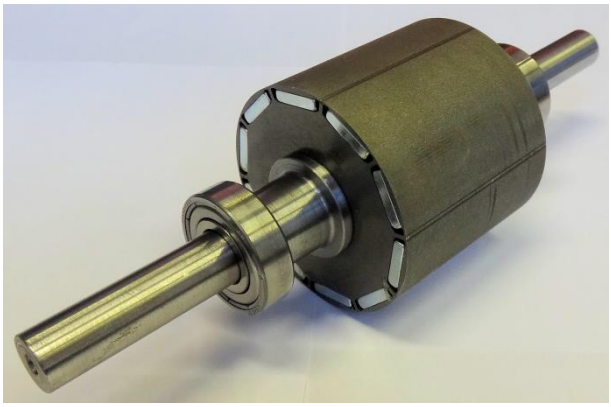

(c) 10-pole rotor

Fig. 5.36 Prototype IPM machines.

5.5.2 Back-EMFs

The measured and predicted open-circuit back-EMFs are shown in Fig. 5.37(a) and (b). Due to the end-effect and manufacturing tolerance, the fundamental values of the prototypes are slightly smaller than the predicted. Beside the 3rd harmonic, the back-EMF of the 12/10 machine is almost sinusoidal. However, more 5th and 7th harmonics exist in the back-EMF of the 12/8 machine.

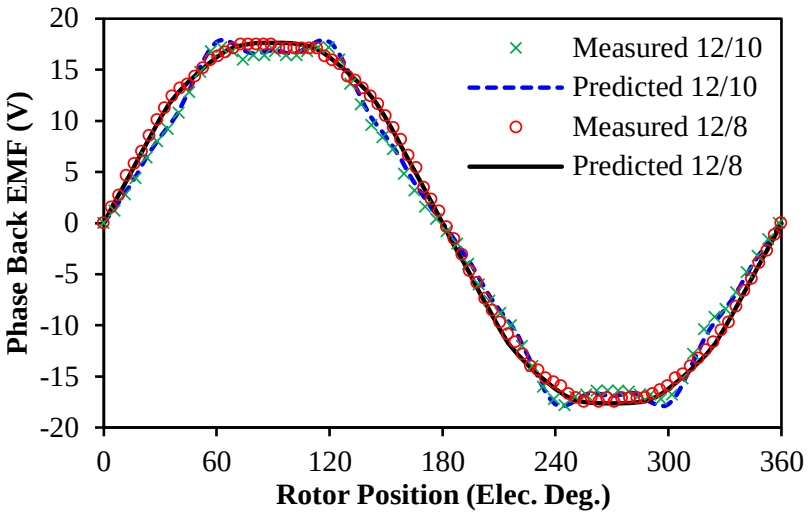

(a) Waveforms

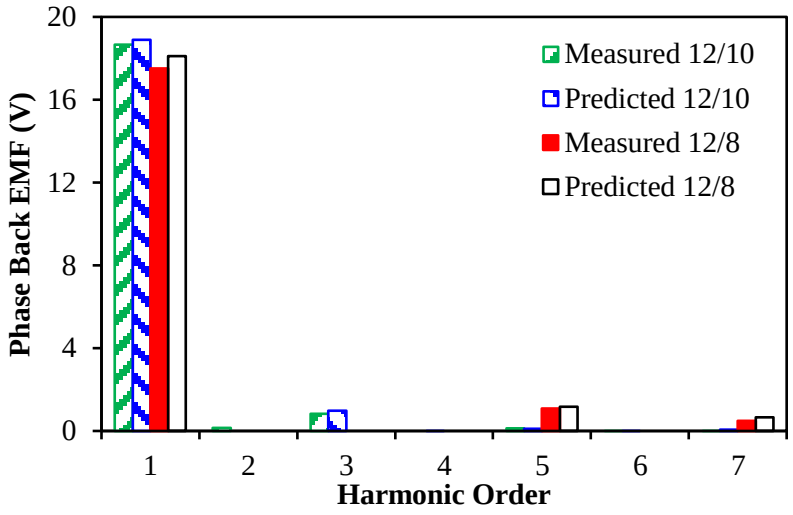

(b) Harmonics

Fig. 5.37 Comparison of predicted and measured open-circuit back-EMFs (400rpm).

5.5.3 Torque Waveforms

Fig. 5.38 compares the predicted and measured cogging torque of both machines. Due to different slot and pole numbers, their cogging torque period will also be different [ZHU00].

Considering the measuring error, the measured results agree with the prediction well. Meanwhile, the measured and predicted torque waveforms for full load and half load under β=0° are shown in Fig. 5.39, which also shows good agreement.

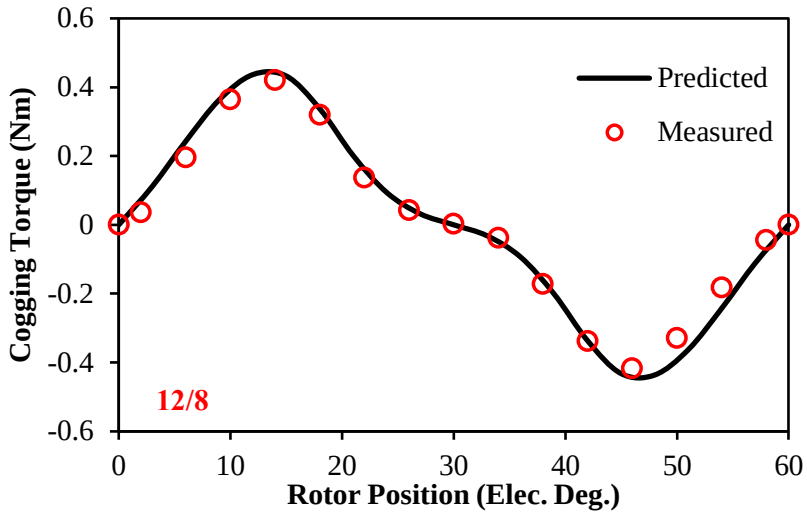

(a) 12/8

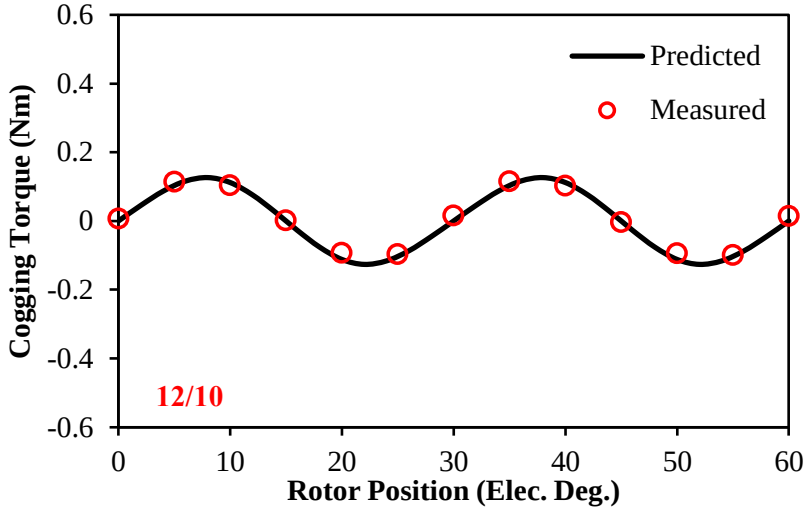

(b) 12/10

Fig. 5.38 Comparison of measured and predicted cogging torque.

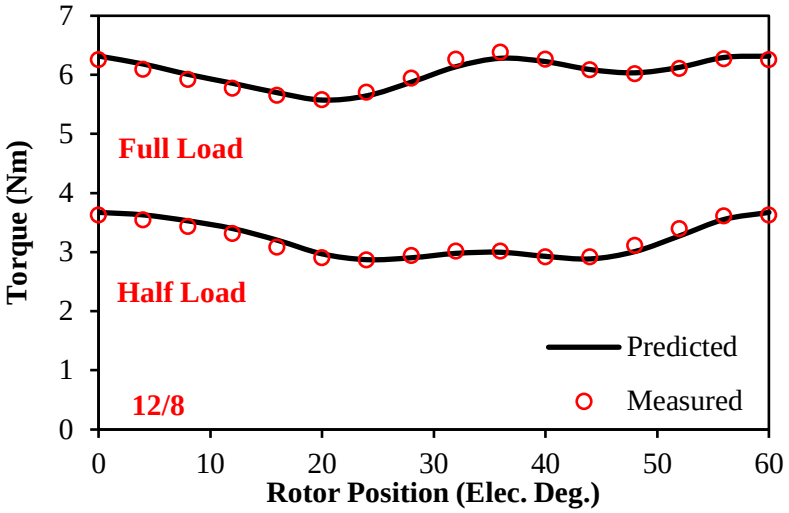

(a) 12/8

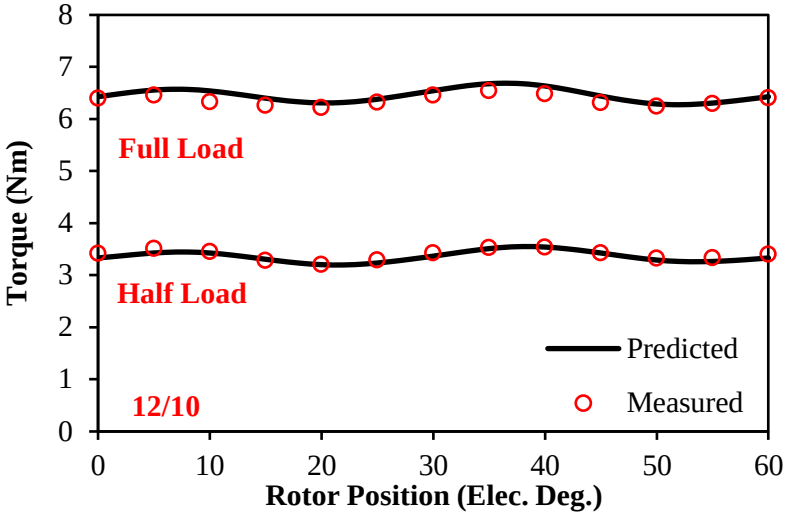

(b) 12/10

Fig. 5.39 Comparison of predicted and measured torque waveforms (I_{max}=10A, β=0°).

5.5.4 On-Load Voltage Distortion

In order to observe the terminal voltage clearly, a low pass filter with the cut-off frequency about 1.5kHz is adopted. Both the terminal phase voltages with and without PWM will be shown on the scope together with the phase current waveform. In example, the measured results for both machines driven by currents with I_{max}=9A and β=60° are shown in Fig. 5.40. It can be seen that both phase currents are sinusoidal but the phase voltages are distorted obviously. Fig. 5.41 (a) and (b) compares the predicted and measured phase voltages at the same current condition, which shows good agreement. Meanwhile, the comparisons of harmonics in Fig. 5.41(c) reveal the significant increase of harmonics compared with open-circuit back-EMFs.

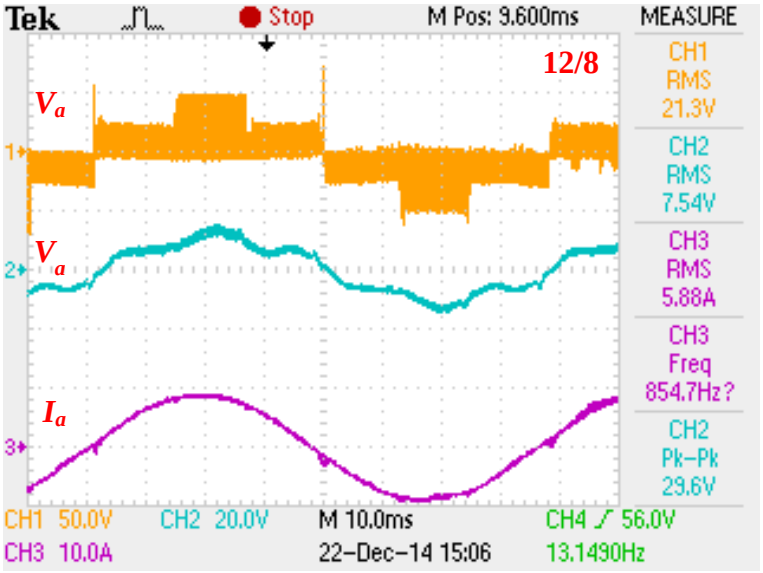

(a) 12/8

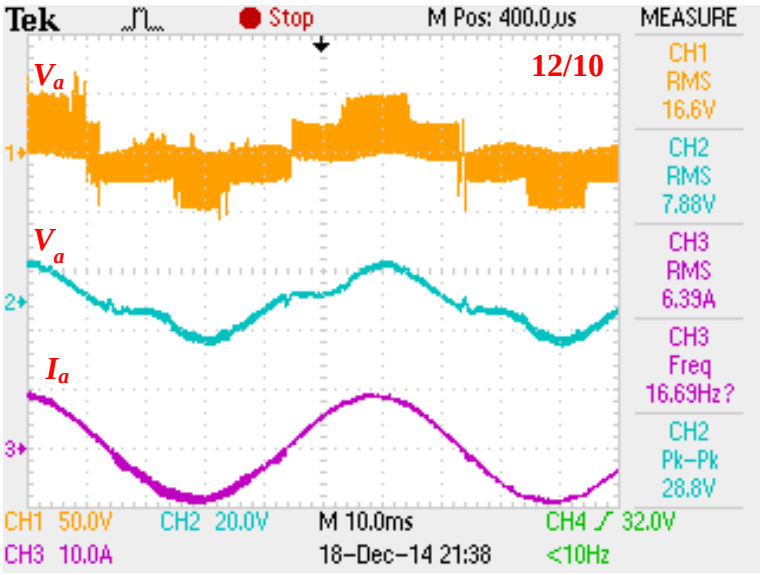

(b) 12/10

Fig. 5.40 Measured terminal phase voltages and phase currents (I_{max}=9A, β=60°, 200rpm, U_{DC}=80V).

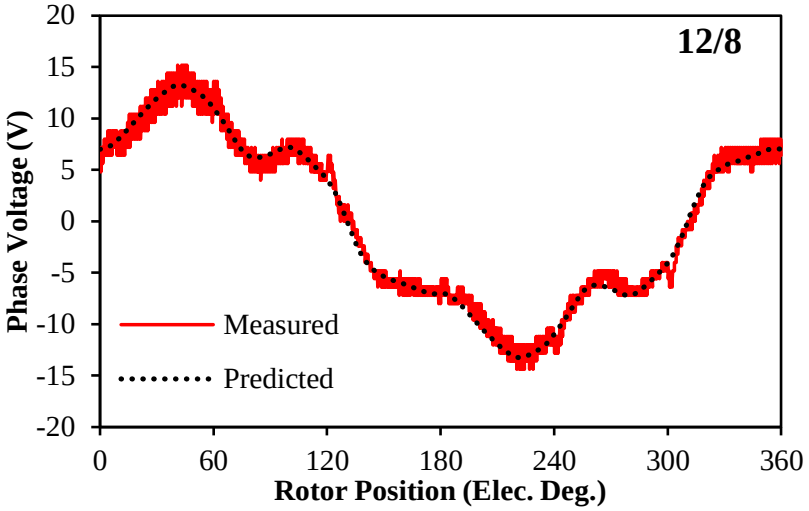

(a) Waveforms, 12/8

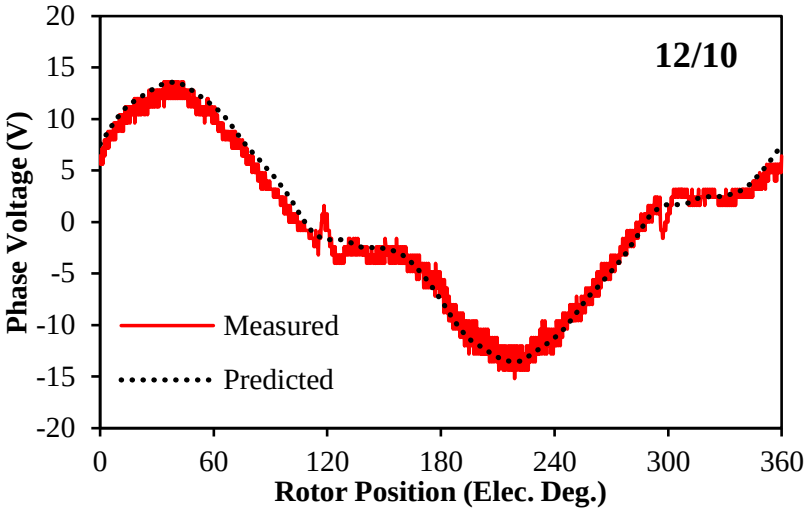

(b) Waveforms, 12/10

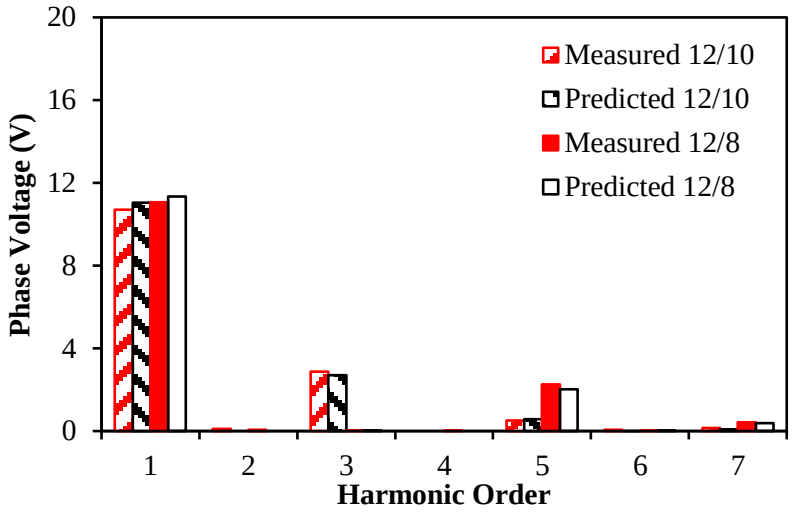

(c) Harmonics

Fig. 5.41 Comparison of measured and predicted terminal phase voltages (I_{max}=9A, β=60°, 200rpm, U_{DC}=80V).

5.5.5 Torque Speed Characteristics

The feedback voltage regulation method is adopted for the flux weakening operation [KIM97], in which the output voltage of PI controller is compared with the reference voltage of the inverter to generate negative *d*-axis current. The measured and predicted torque speed characteristics are shown in Fig. 5.42, in which the ideal curves are calculated by only the fundamental voltages for comparison. It can be seen that, due to the terminal voltage distortion, the real torque speed curve of the 12/10 machine is slightly lower than the ideal curve, and the measured result can validate the prediction considering measuring error. However, the 12/8 machine suffers much more from terminal voltage distortion, since the strong 5^{th} and 7^{th} voltage harmonics will largely increase the peak voltage value especially under flux weakening operation according to the aforementioned analyses. Overall, the experimental results validate the prediction, and illustrate the deterioration of flux weakening performance due to terminal voltage distortion for different $N_s/2p$ combinations.

5.6 Summary

This chapter focuses on the on-load terminal voltage distortion in IPM machines with fractional slot concentrated windings, with particular emphasis on the influence of slot and pole number combinations. Due to the salient feature of IPM rotor, the *dq*-axis armature reaction flux paths are largely different, which causes significant distortion of armature reaction voltage if *d*-axis current is injected. As consequence, the leakage flux as well as tooth-tip saturation will also increase, which distorts the PM flux linkage and further aggravates the overall voltage distortion. For the same rotor topology, the *d*-axis armature reaction flux paths will be determined by the relation between stator slot pitch and rotor pole pitch, which can be described by *q*. When *q* is too close to 1/3 or too far away from it, the voltage distortion could deteriorate in both cases. Meanwhile, for the machines with $N_s>2p$, the voltage distortion is always less than their counterparts with $N_s<2p$. According to the aforementioned conclusions, the design trade-off of slot and pole combinations to minimize the influence of voltage distortion has been proposed. Finally, two prototypes have been built and tested to validate the analyses. Although the investigation is carried out on small power rating machines with concentrated windings, the mechanism and analyses methods could be applied to machines with distributed windings as well, which can be validated by the case study of two high power rating traction machines with distributed windings in Appendix C.

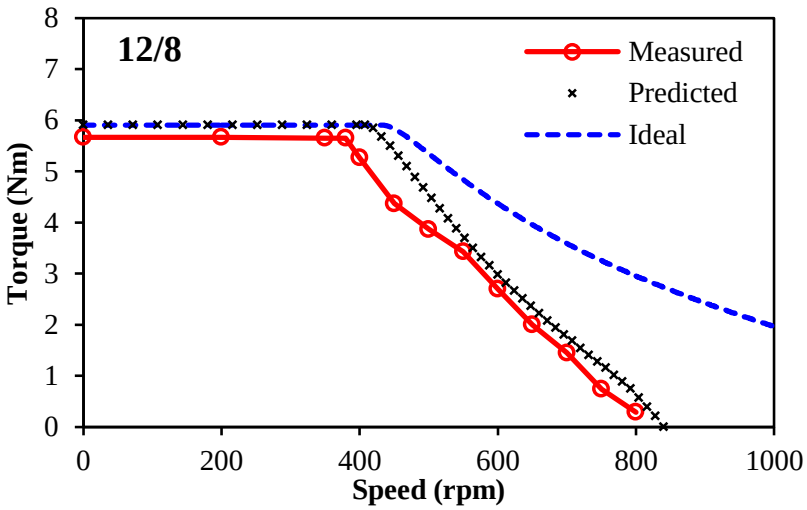

(a) 12/8

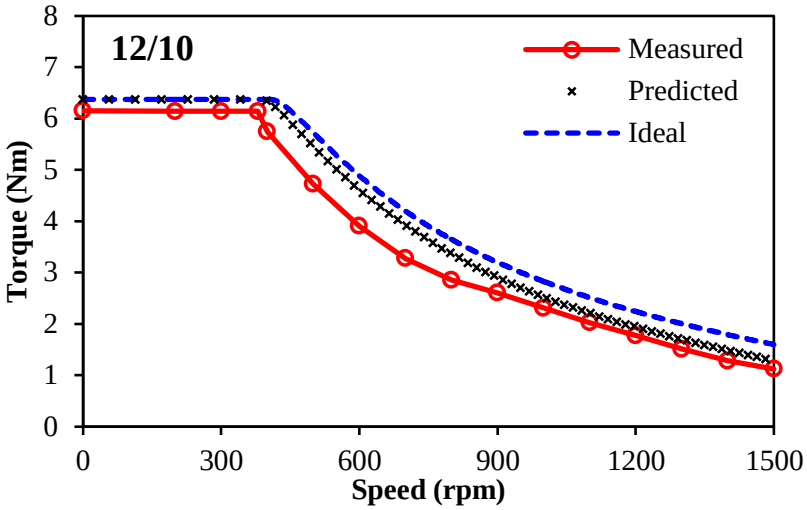

(b) 12/10

Fig. 5.42 Comparison of measured and predicted torque speed characteristics (I_{max}=9A, U_{DC}=48V).

CHAPTER 6

MINIMIZATION OF ON-LOAD TERMINAL VOLTAGE DISTORTION IN FRACTIONAL SLOT SPM AND IPM MACHINES

The aforementioned four chapters illustrate the influences of local magnetic saturation and voltage distortion in both fractional slot SPM and IPM machines. Thus, the minimization of voltage distortion should be considered at the design stage. Traditionally, rotor skewing and non-uniform airgap are the most common techniques to reduce the back-EMF harmonics and cogging torque. Their effectiveness about the minimization of on-load terminal voltage distortion will be investigated in this chapter based on the 12-slot/8-pole SPM and IPM machines for examples.

6.1 Introduction

According to the aforementioned analyses, the local saturation represented by the on-load voltage distortion will introduce many drawbacks to the machine performance, which needs to be reduced during the design stage. Within all popular harmonics reduction methods, skewing is the most common one which can significantly reduce the cogging torque [LI88], [ZHU00], back-EMF harmonics [SEB96], as well as torque ripple [JAN96], etc. However, most of the references have not considered the magnetic saturation of on-load operations. Even for the papers investigating the influence of skewing on pulsation torques, the reduction of torque ripple is mainly ascribed to the reduction of cogging torque and back-EMF harmonics [CHE10], [JAH96], [DEL89], [CAR89]. In fact, the on-load saturation may influence the effectiveness of skewing on the reduction of torque ripple. [WIL99] pointed out that the magnetic saturations differ in axial direction due to rotor skewing. However, it only concerns about the inductances in induction machines. [AZA12] investigated the cogging torque and torque ripple considering magnetic saturation with the aid of FP method. The results show that the on-load cogging torque is much different from the open-circuit condition due to saturation, which makes the skewing designed for open-circuit less effective for reducing the on-load torque ripple. However, it only focuses on torque ripple, which does not consider other on-load performance such as terminal voltages. In fact, the most significant feature for the rotor skewing is the different current angles for different rotor

segmentations [ISL09]. Thus the phase angles of torque ripples generated by different segment are different as well, which reduces the effectiveness of skewing even for the linear case [CHU13b]. Although improved skewing method was proposed based on the on-load saturation [CHU13c], the influences on other machine performance are still missing. Therefore, a further step will be carried out in this chapter focusing on the effectiveness of skewing about on-load terminal phase voltages for both fractional slot SPM and IPM machines.

On the other hand, rotor pole shaping is another popular method to reduce the cogging torque and back-EMF harmonics [SCH60], [KIM03], [LI08], [ISL09], [EVA10]. Due to more sinusoidal airgap field contributed by rotor shaping, the reduced cogging torque and back-EMF harmonics also reduce the torque ripple [ISL09]. Normally, sinusoidal shaping is adopted [LI08], [ISL09] since it can directly generate the sinusoidal airgap field. However, with the same total magnet thickness, sinusoidal shaping will reduce the magnet volume in SPM machines [WAN14a], or increase the equivalent airgap in IPM machines [EVA10], [WAN14b], which both reduce the average toque of machines. In order to compensate such drawback, inverse cosine shaping [ISL05], [EVA10] and third harmonics shaping [WAN14a], [WAN14b] were proposed. However, all these papers focus on the torque issue of the machines, while other performances, such as the on-load terminal voltage, have not been paid enough attention.

As another way to generate non-uniform airgap, stator tooth shaping could also be adopted to reduce the torque ripples since it reduce the area of highly saturated tooth-tips. [JUN10] introduced Monte-Carlo method to optimize the tooth-tips shape in order to reduce torque ripple. [SEO14] also adopted tooth-tip shaping to reduce torque ripple, and finds this method will increase cogging torque since the equivalent slot opening width increases. [LEE11] claimed that stator shaping will reduce the peak line voltage under load operation since the saturation area has been reduced. However, it has not given the details about how to shape the rotor, which could be further investigated.

In this chapter, the effectiveness of rotor skewing and non-uniform airgap in SPM machines will be investigated firstly. Then, the design trade-off about voltage distortion and other performance is discussed since small and closed slot opening can bring many advantages according to the aforementioned review and investigations. Then, the effectiveness of rotor

skewing and non-uniform airgap in IPM machines is investigated. Finally, two SPM machines and two IPM machines are manufactured and tested to validate the analyses.

6.2 Minimization of Terminal Voltage Distortion in SPM machines

6.2.1 Rotor Skewing

When the number of rotor segments increases, the effect of step skewing will approach ideal rotor skewing for the same skewing angle [CHU13b]. Considering the real application, four steps skewing will be adopted to illustrate the method, while the influence of step numbers will also be discussed, Fig. 6.1. According to the aforementioned analyses, the on-load voltage distortion in SPM machines will appear as the $6n\pm1$ times harmonics in the terminal voltages, and $6n$ times harmonics in dq-axis frame. Thus, the skewing angle of 60 electrical degrees is the best choice to eliminate such harmonics [CHU13b], which will be adopted to illustrate the effectiveness of skewing.

Fig. 6.2 compares the open-circuit back-EMF with and without skewing. Since the back-EMF of the original model is already quite sinusoidal due to the closed slot design, the skewing mainly reduces the amplitude of fundamental back-EMF. When driving by rated current, the terminal phase voltages are compared in Fig. 6.3. Clearly, the peaks of the voltage ripples are reduced by skewing, which has also been reflected as the reduction of harmonic voltages in Fig. 6.3(b). If each segment is numbered according to the number marked on Fig. 6.1, the on-load phase voltage generated by different segments can be calculated in Fig. 6.4. Since all rotor segments are shifted away from the rotor d-axis, the current angles for each section are also different. Consequently, the voltage ripples amplitudes and appearing times will be different according to the aforementioned analyses, which can be reflected clearly in Fig. 6.4(a). Based on that, the amplitude and phase angle of each section are also different in Fig. 6.4(b) and (c), which result in the un-cancelled harmonics in the resultant phase voltage.

Since the local magnetic saturations of each segment in axial direction are different, the number of steps may also influence the effect of skewing. Fig. 6.5 shows the peak and fundamental voltages for different step numbers, in which step number of one refers to the original model without skewing. For the same skewing angle, i.e. 60°, the fundamental voltages after skewing are almost the same. However, their peak values change with the number of steps. For odd number of steps, e.g. 3 and 5, the centre magnet still locates at the

original position similar to the non-skewing rotor, Fig. 6.1(a), which leads to higher peak voltages. However, for even number of steps, e.g. 2 and 4, all the magnets have been shifted away from the original position of the non-skewing rotor, Fig. 6.1(b), which improves the effectiveness of rotor skewing.

Further, the influences of different skewing angles can be reflected in Fig. 6.6. With the increase of skewing angle, the voltage ripples appearing rotor positions for each section will be much different, which results the smaller resultant voltage ripple, and leads to the reduction of *VDR*. However, *THD* does not proportionally reduce with *VDR*, which means strong voltage distortion still exists in tooth-tips. Meanwhile, the relative current angle for each segment will be more different from 0° with the increase of skewing angle. Thus, *VDR* for each section will also reduce according to the aforementioned analyses. Although the skewing can reduce *VDR*, it also significantly reduces the average torque as well. Therefore, this technique needs to be carefully considered during the machine design stage.

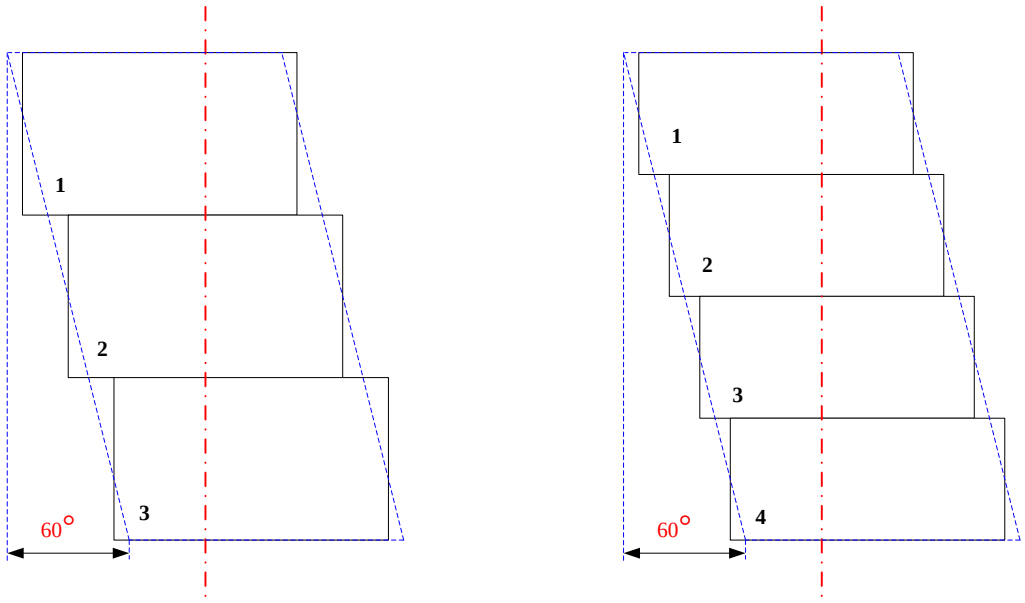

(a) 3-step skewing (b) 4-step skewing

Fig. 6.1 Illustration of step skewing.

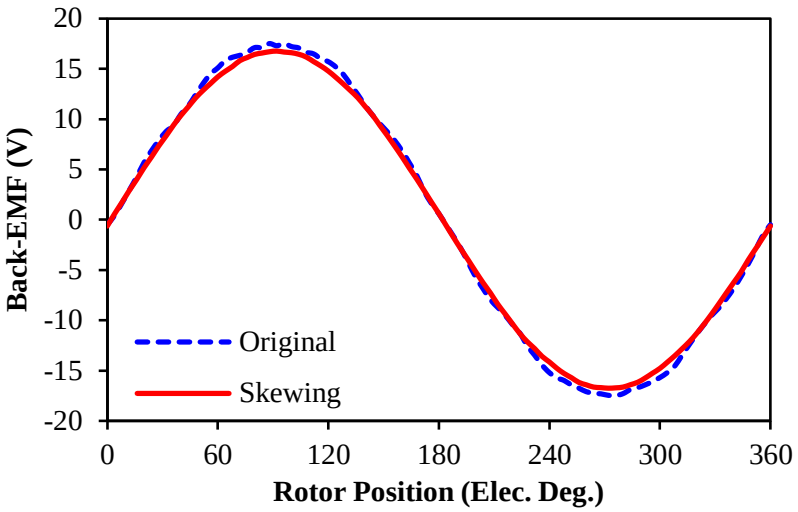

(a) Waveforms

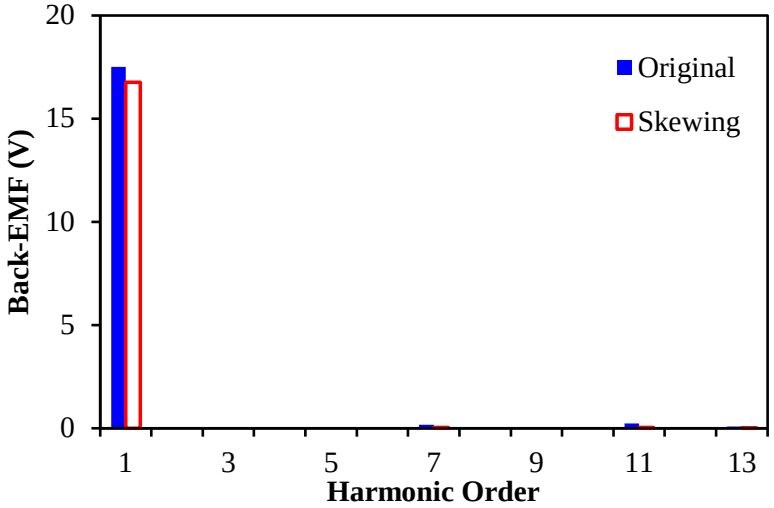

(b) Harmonics

Fig. 6.2 Comparison of open-circuit back-EMFs without and with skewing (400rpm).

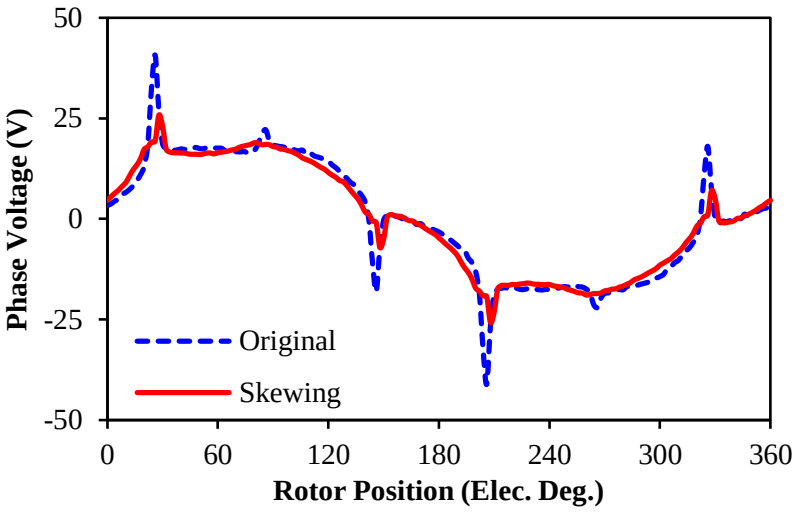

(a) Waveforms

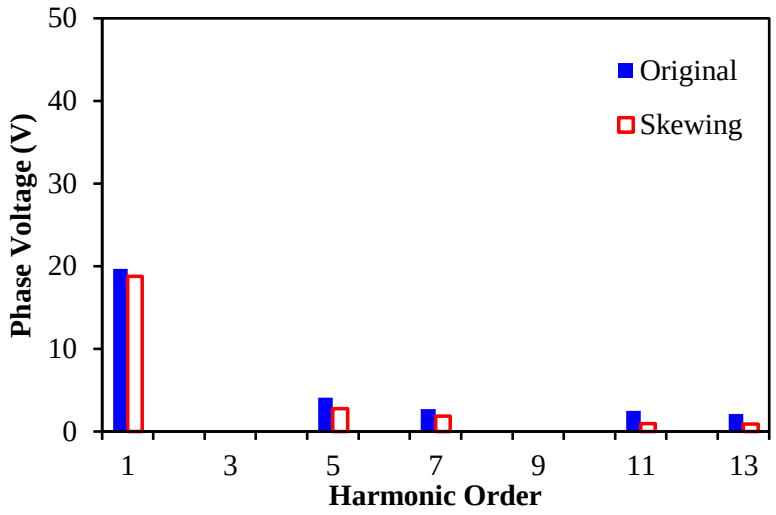

(b) Harmonics

Fig. 6.3 Comparison of phase voltages without and with skewing (I_{max}=10A, β=0°, 400rpm).

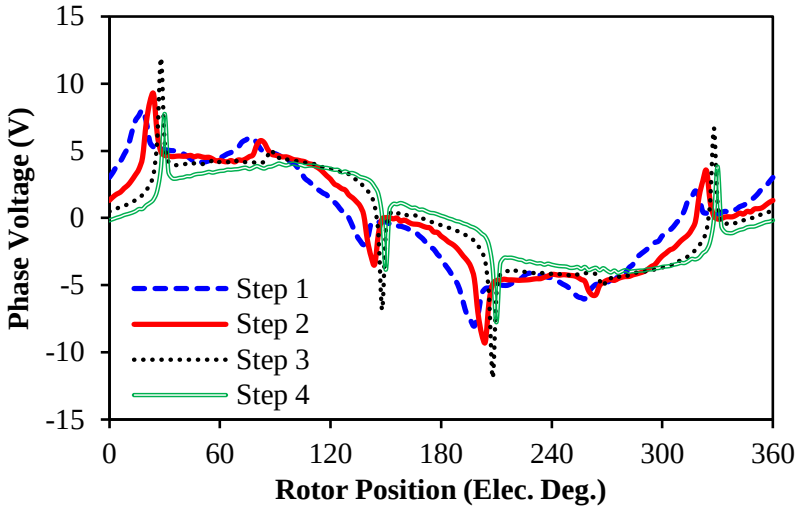

(a) Waveforms

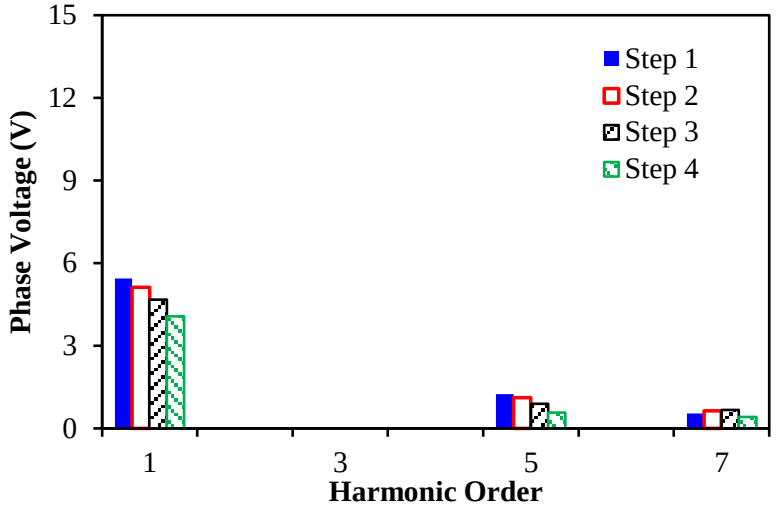

(b) Harmonics

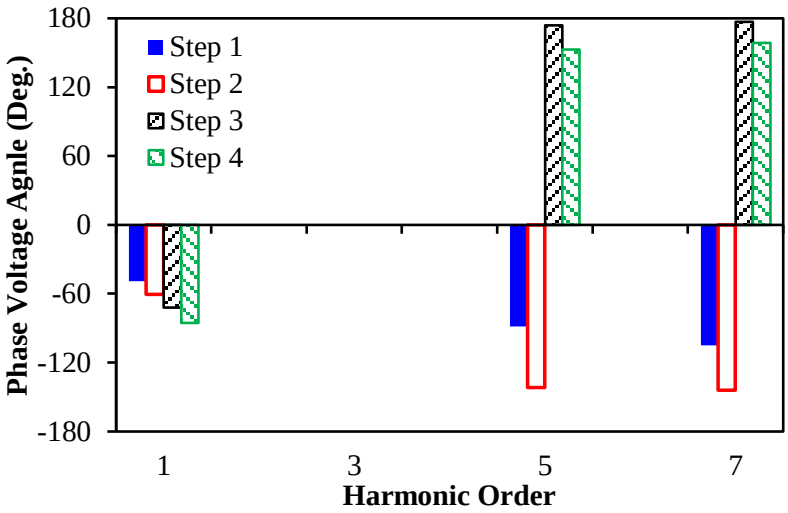

(c) Harmonics phase angles

Fig. 6.4 Comparison of terminal phase voltages of each rotor step (I_{max}=10A, β=0°, 400rpm).

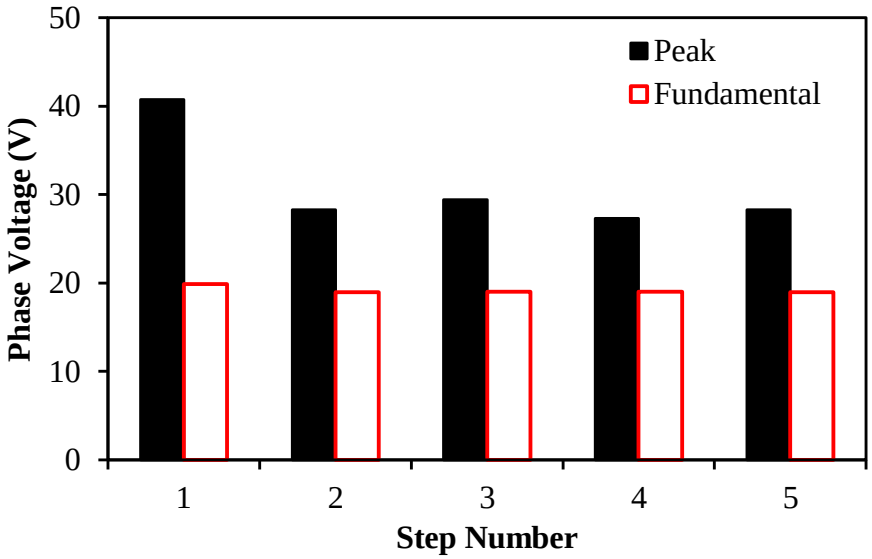

Fig. 6.5 Influence of step-skewing numbers (I_{max}=10A, β=0°, 400rpm).

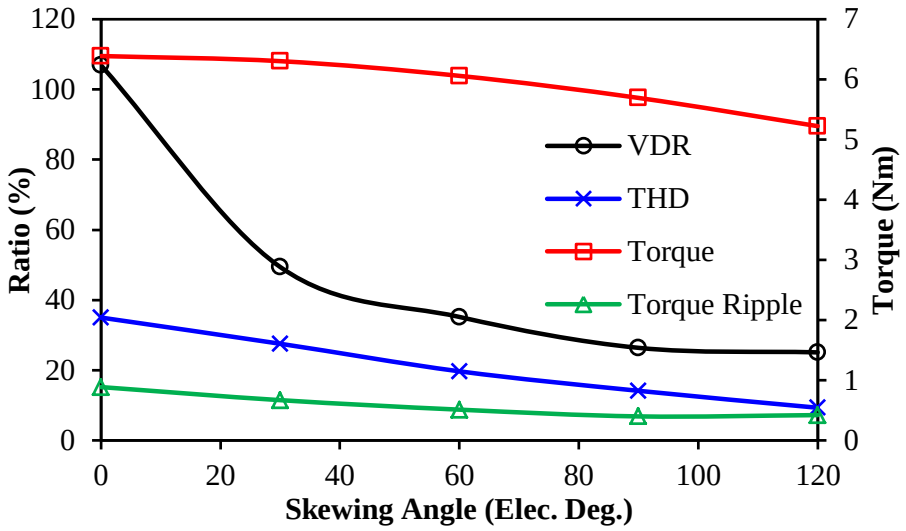

Fig. 6.6 Variation of voltage distortion level and torque against skewing angle (I_{max}=10A, β=0°, 400rpm).

6.2.2 Rotor Shaping

Rotor shaping technique can make the airgap flux density more sinusoidal, which leads to small harmonics in the terminal voltages. Within various shaping methods, inverse cosine shaping is an effective technique which has been investigated intensively recently [EVA10], [WAN14a]. Thus, this section will adopt this method to investigate the effectiveness of rotor shaping on terminal voltage distortion. With such method, the airgap length can be expressed by

$$g(\theta) = \frac{k_a g_0}{\cos(\pi / \tau_r \theta)} \tag{6.1}$$

where g_0 is the minimum airgap length, i.e. the normal airgap length in non-shaping SPM machines, k_a is the shaping depth factor, which controls the rotor shaping level. Fig. 6.7 illustrates magnet shapes for different k_a, in which k_a =0 refers to the original prototype without shaping. When adopting the same stator and winding arrangement, the comparison of open-circuit back-EMFs of the three models can be shown in Fig. 6.8. By adopting the proper rotor pole arc, the original design can have almost sinusoidal back-EMF, which makes the rotor shaping not obvious on the reduction of harmonics. Since the magnet volume has been reduced in the shaped rotor, the fundamental back-EMFs reduce with the increase of k_a. Driven by the same current, the terminal phase voltages of three models are compared in Fig. 6.9. Considering the reduction of back-EMF, the voltage harmonics in the shaped models are

even higher, which reveal that rotor magnet shaping could not reduce the voltage distortion. Due to magnet shaping, the effective pole arc has been reduced, while the tooth-tip PM leakage reduce as well. According to Fig. 2.17, the reduction of tooth-tip leakage flux will make armature tooth-tip leakage dominate the tooth-tip local saturation, which leads to even higher voltage distortion level.

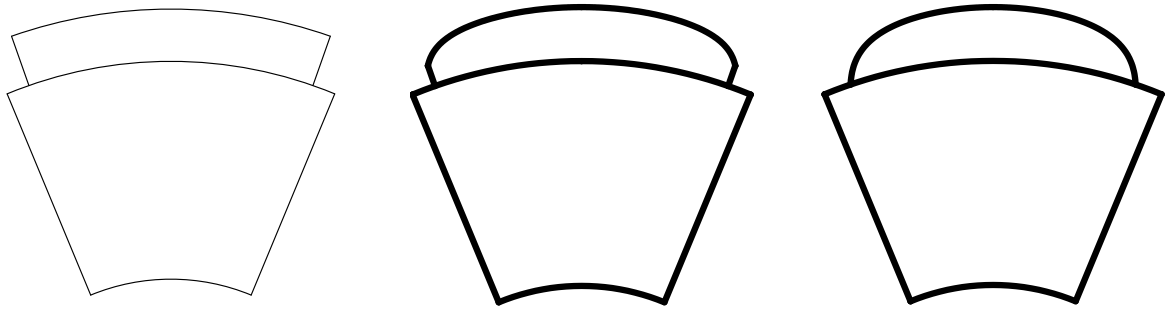

(a) k_a=0 (b) k_a=0.5 (c) k_a=1

Fig. 6.7 Illustration of magnet shapes for different k_a.

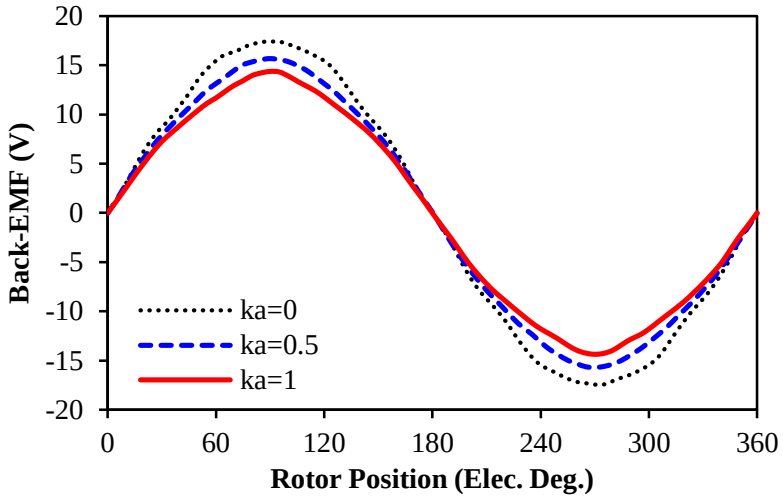

(a) Waveforms

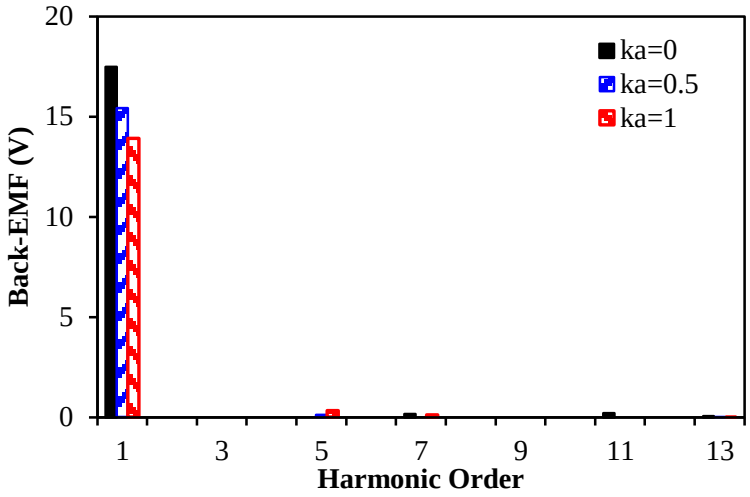

(b) Harmonics

Fig. 6.8 Comparison of open-circuit back-EMF for different k_a (400rpm).

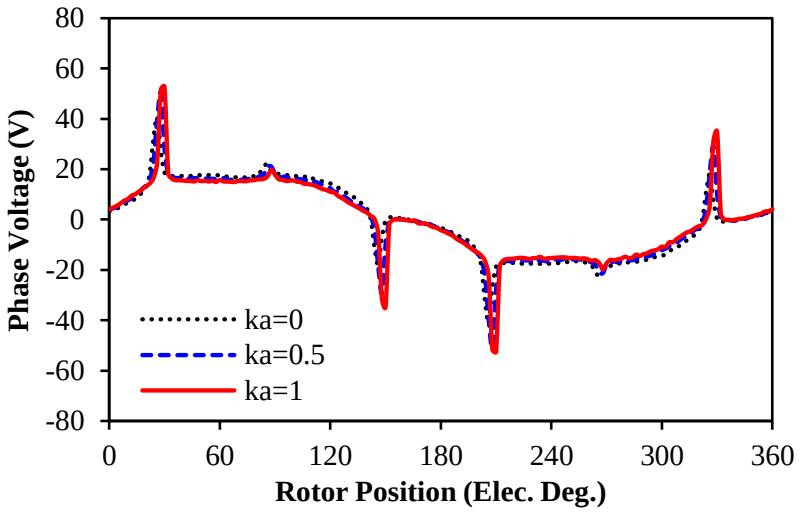

(a) Waveforms

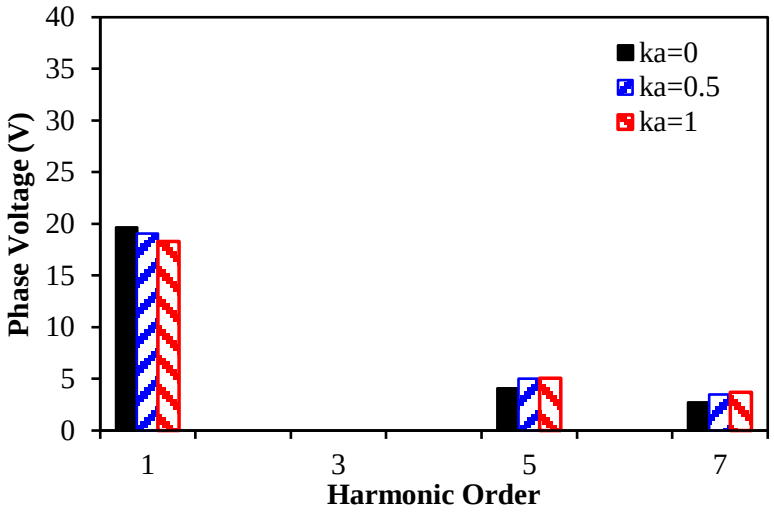

(b) Harmonics

Fig. 6.9 Comparison of on-load phase voltages for different k_a (I_{max}=10A, β=0°, 400rpm).

6.2.3 Stator Shaping

Stator shaping is another way to generate non-uniform airgap, which can be illustrated in Fig. 6.10(a) with shaping depth d_s defined in the figure. The slot bridge thickness for the original closed slot model is 0.6mm. Thus, if d_s=0.3mm, half of the slot bridge is cut off, Fig. 6.10(b). When d_s=0.6mm, all the slot bridge has been removed by the shaping as shown in Fig. 6.10(c). Fig. 6.11 compares the open-circuit back-EMFs for different shaping depth, in which d_s=0mm refers to the original model as investigated in Chapter 2. With the increase of d_s, the tooth-tip thickness reduces, which lead to less tooth-tip leakage flux as well as higher fundamental back-EMF. However, the harmonics in the back-EMF will increase with the decrease of d_s, since the tooth-tips become more saturated by the PM leakage fluxes. Driven

by the same current, the terminal phase voltages for different d_s can be compared in Fig. 6.12. When d_s=0.3mm, the voltage ripples are still as obvious as the original model. Although the leakage flux paths have been narrowed, the PM leakage fluxes also become less influenced on the variation of local magnetic saturation since the airgap length around slot bridge increases. When d_s=0.6mm, the voltage ripples finally disappear. However, all the slot bridge has been removed under such condition, which means the equivalent slot opening width b_0 has been increased as a consequence. Thus, the contribution is not due to the stator shaping but more relevant with b_0, which has already been proved in Fig. 2.15. Overall, stator shaping is not an effective method to reduce the voltage distortion in SPM machines if small or closed slot openings are demanded.

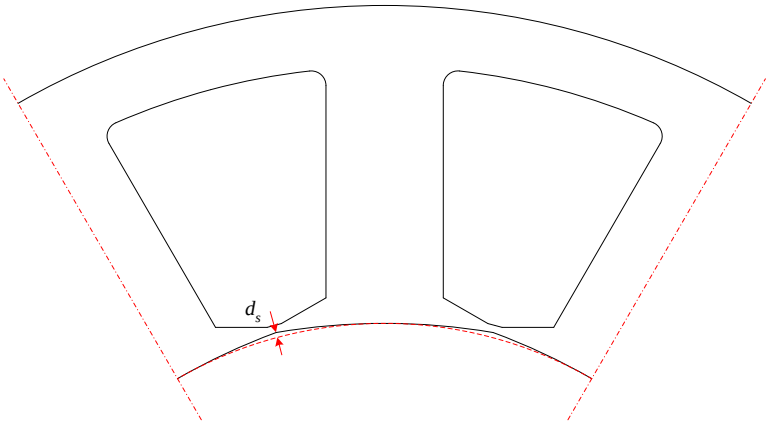

(a) Definition of d_s

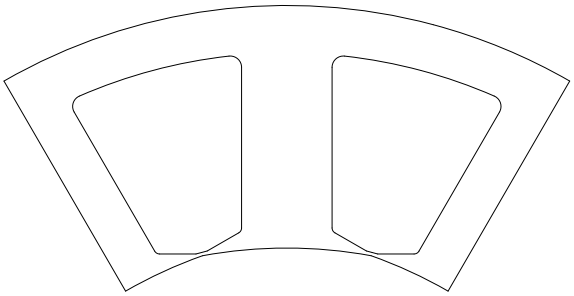

(b) d_s=0.3mm

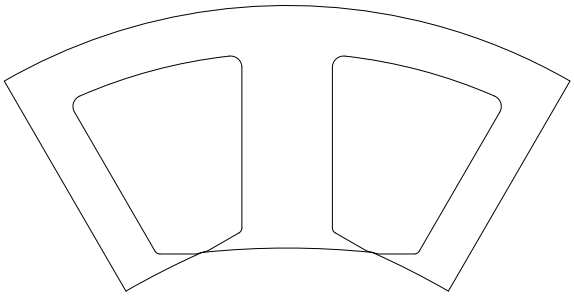

(c) d_s=0.6mm

Fig. 6.10 Illustration of stator shaping depth.

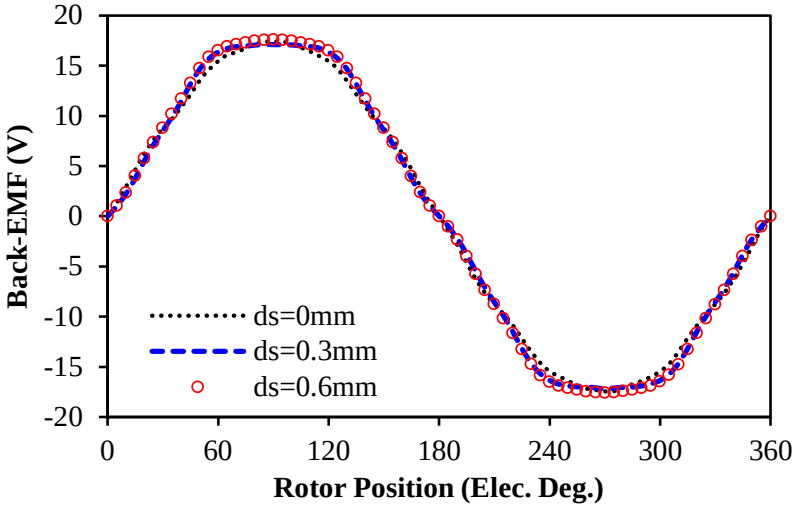

(a) Waveforms

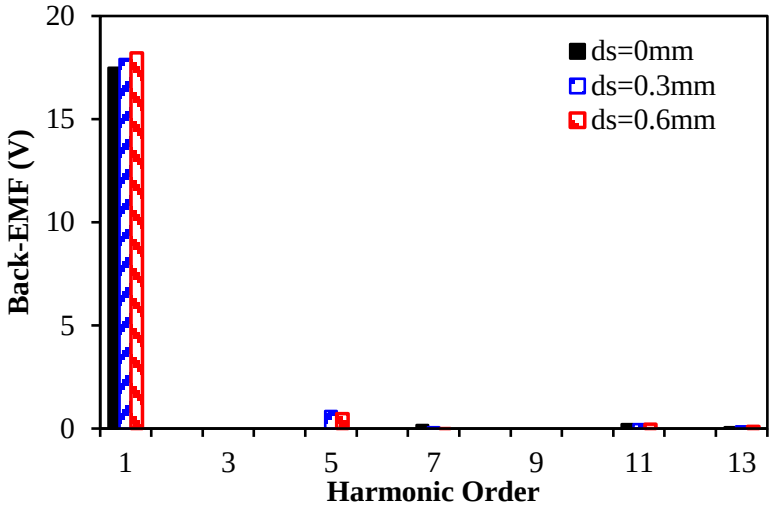

(b) Harmonics

Fig. 6.11 Comparison of back-EMFs without and with stator shaping (400rpm).

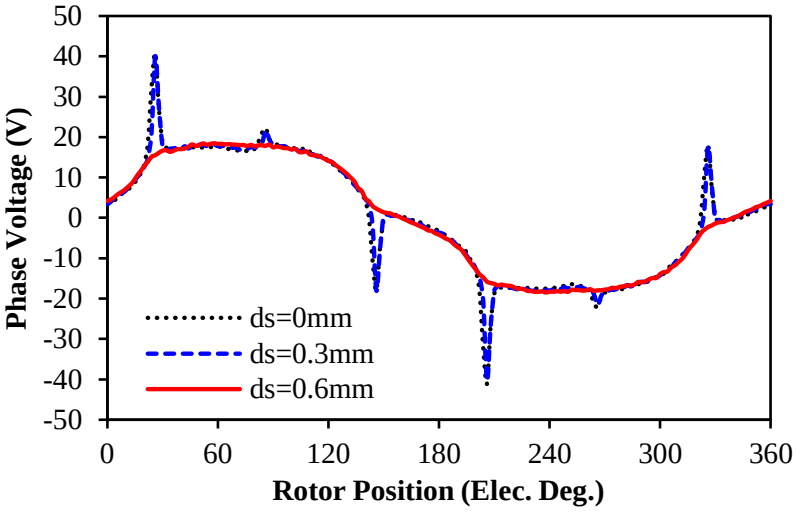

(a) Waveforms

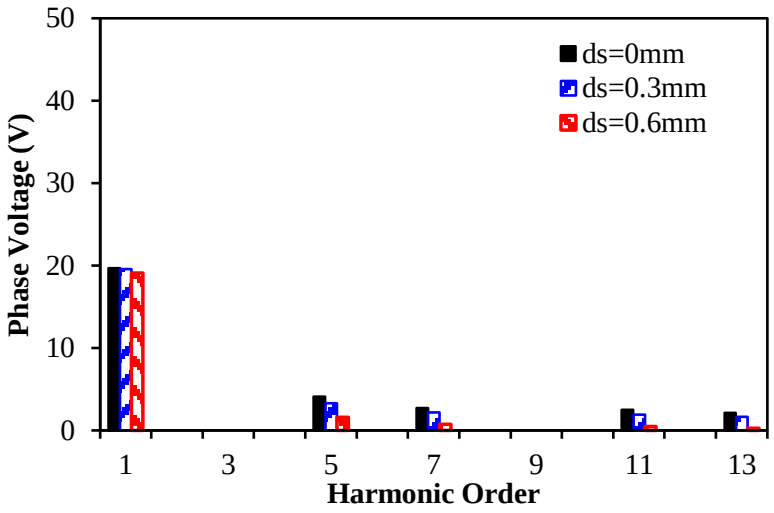

(b) Harmonics

Fig. 6.12 Comparison of on-load terminal phase voltages without and with stator shaping (I_{max}=10A, β=0°, 400rpm).

6.2.4 Design Trade-off of Slot Opening Width

According to the aforementioned discussions, the conventional harmonics minimization method could not efficiently eliminate the voltage distortion since the tooth-tip local magnetic saturation is always strong if small or closed slot openings are adopted. Therefore, this section tries to analyse the merits and demerits with different slot opening designs, in order to achieve a design trade-off between machine performances in terms of the torque performance and voltage distortion. The basic parameters of the investigated machine are b_0 and h_t, Fig. 6.13, while other parameters are kept the same as Table 2.1. Fig. 6.14 shows the back-EMF waveforms of two typical tooth-tip designs, which reveal that both shape and amplitudes of back-EMFs are different for different tooth-tip designs. Fig. 6.15 illustrates the fundamental back-EMFs for different b_0 and h_t. It can be observed that the back-EMF increases with the decrease of b_0 at first due to the increase of flux focusing effect by tooth-tips. However, after reaching the peak, the tooth-tip leakage flux becomes more dominated, which results in the reduction of back-EMF when b_0 approaches 0. Meanwhile, h_t is not sensitive for the fundamental back-EMF since the tooth-tips are not highly saturated on open-circuit condition. However, the on-load voltage distortion will largely differ by different tooth-tip designs, since there is obvious local saturation in tooth-tips for on-load conditions, which has been discussed clearly in Chapter 2. Thus, the results are simply shown in Fig. 6.16.

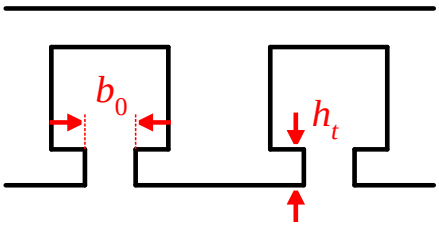

Fig. 6.13 Basic parameters of tooth-tips.

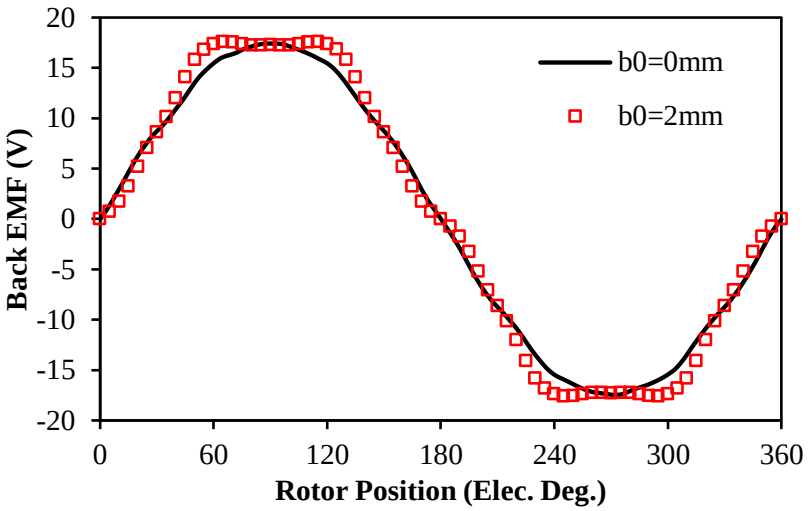

(a) Waveforms

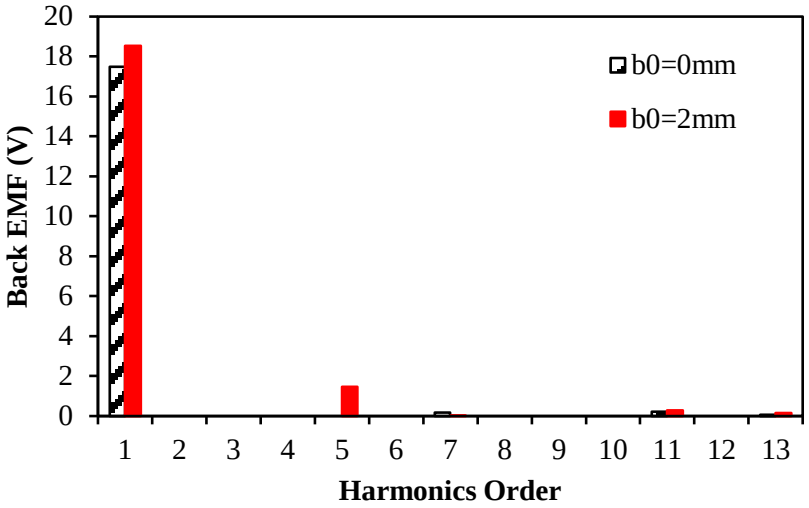

(b) Harmonics

Fig. 6.14 Back-EMFs for different tooth-tip designs (h_t=1mm, 400rpm).

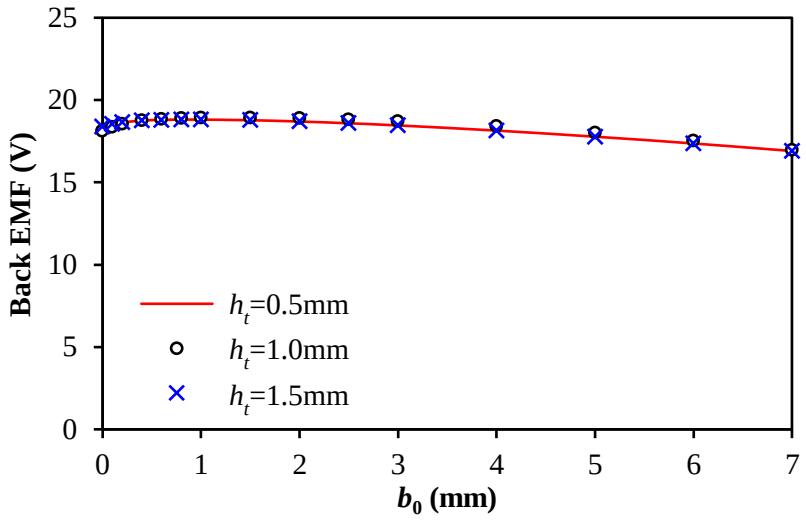

Fig. 6.15 Variation of fundamental back-EMF against different tooth-tip designs (400rpm).

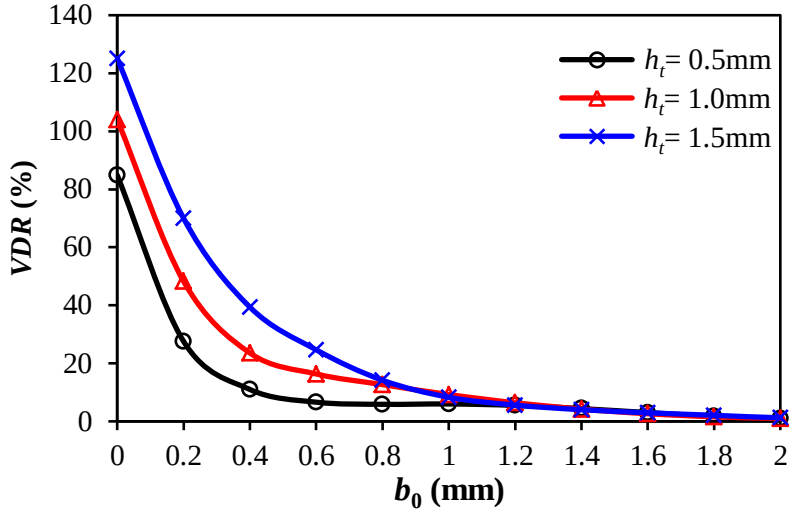

Fig. 6.16 Variation of on-load terminal voltage distortion by *VDR* (I_q=10A, I_d=0, 400rpm).

Cogging torque is mainly generated by the variation of air-gap permeance [ZHU00]. Therefore, small and closed slot opening design can smooth such variation, which leads to small cogging torque as well. Fig. 6.17 illustrates the peak to peak (pk-pk) cogging torque against different tooth-tip designs. It can be observed that the cogging torque is not sensitive with h_t due to low open-circuit local saturation as well. With the reduction of b_0, the amplitude of cogging toque reduces significantly, which approaches zero together with b_0. Similar to the back-EMF, the average torque also has maximum value according to different tooth-tip designs, which occurs at the balance between flux focusing effect and tooth-tip leakage flux, Fig. 6.18. Meanwhile, the torque ripple also has minimum design since it has complicated relation with saturation and harmonics, Fig. 6.19. In fact, different loads will lead to different local magnetic saturation conditions, which make the optimal design for

minimum full load torque ripple different from the optimal design for minimum open-circuit cogging torque. Thus, design trade-offs should be made according to the machine most frequent operating load condition, which has been discussed in Appendix D.

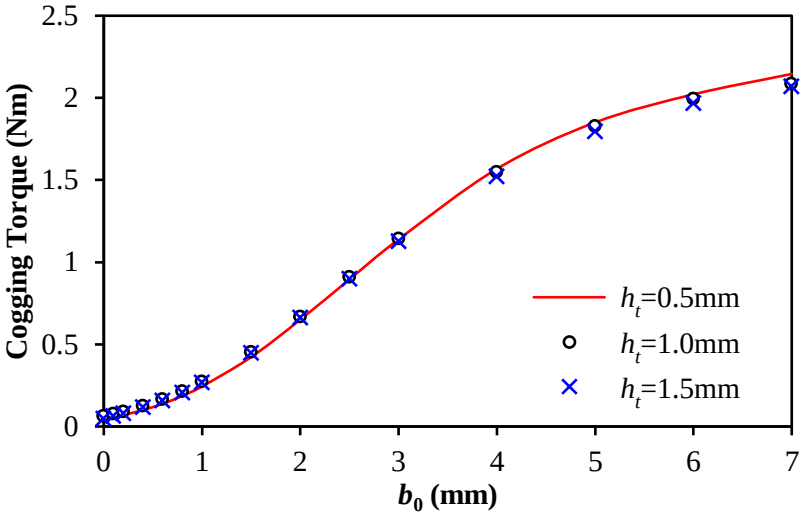

Fig. 6.17 Variation of pk-pk cogging torque against different tooth-tip designs.

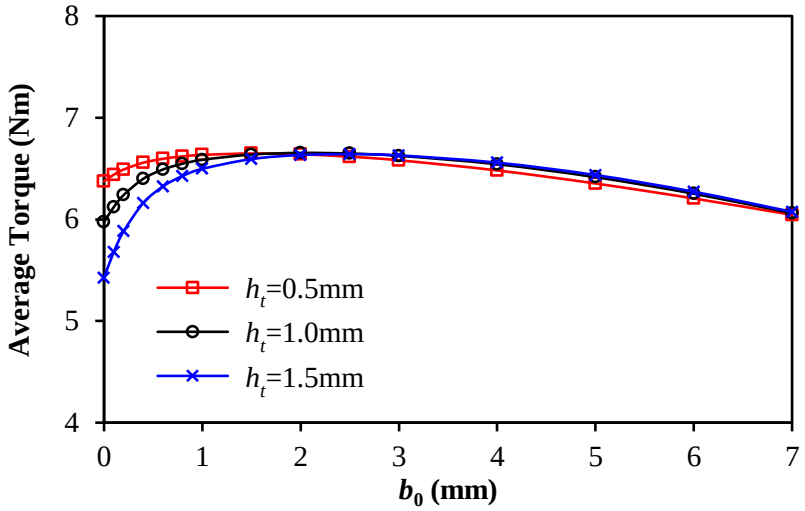

Fig. 6.18 Variation of average torque against different tooth-tip designs (I_q=10A, I_d=0).

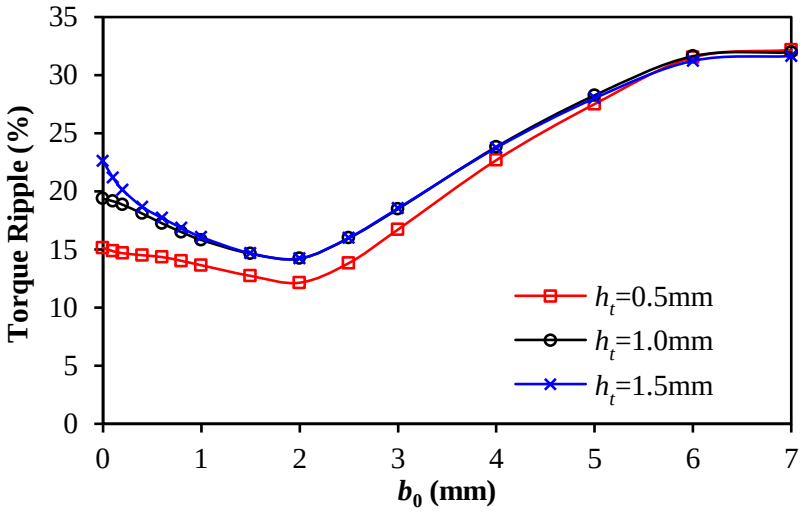

Fig. 6.19 Variation of torque ripple against different tooth-tip designs (I_q=10A, I_d=0).

Since torque speed characteristic is another important issue of machine torque performance, it needs to be discussed as well. Due to large equivalent air-gap, the slot leakage inductances take important role for the overall winding inductances [ELR08]. Therefore, the *dq*-axis inductances and the flux weakening performance will be influenced as well. Since the tooth-tip design significantly influences the tooth-tip leakage flux, it also influences the *dq*-axis inductances, Fig. 6.20. With the increase of b_0, the tooth-tip leakage fluxes reduce, which lead to the reduction of both L_d and L_q. Meanwhile, when b_0 is fixed, higher h_t will result in higher *dq*-axis inductance due to the increase of tooth-tip leakage flux. Although L_d is slightly larger than L_q when b_0 is small, this saliency will not contribute to the reluctance torque since the armature leakage flux does not enter the air-gap and contribute to the air-gap field. Therefore, the optimal β for maximum torque per ampere is still 0°, which has already been analysed in Chapter 2.

In order to evaluate the flux weakening performance for different tooth-tip designs, the flux weakening factor (K_w) could be introduced.

$$K_w = \frac{-L_d I_{\max}}{\psi_{PM}} \tag{6.2}$$

As shown in (6.2), K_w represents the maximum flux weakening capability of one machine. If K_w<1, its flux weakening performance is limited, since the armature flux could not fully counteract the PM flux linkage. Thus, the smaller the K_w, the worse the flux weakening performance could be expected. On the contrary, if $K_w \geq 1$, the infinite flux weakening

operation could be achieved, since the PM field could be fully counteracted by the armature field. By adopting such evaluation method, the flux weakening capabilities according to different tooth-tip designs can be shown in Fig. 6.21. Similar to the *dq*-axis inductances, K_w also reduces with b_0, while increases with h_t. Therefore, for the machines with small or closed slot openings, the relatively better flux weakening performances could be expected. It has to be noted that, when h_t=1.5mm while b_0 approaches 0, K_w is larger than 1, which means infinite flux weakening operation could be realized in SPM machines if the application demands [ELR05].

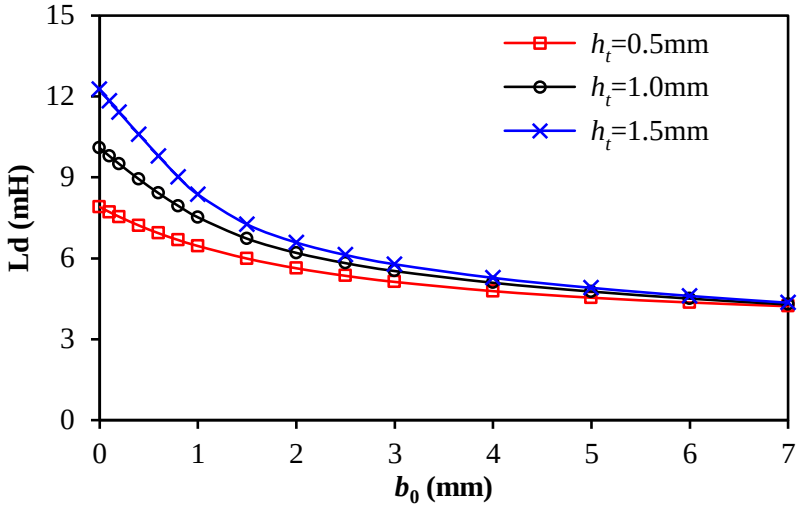

(a) L_d, *d*-axis inductances

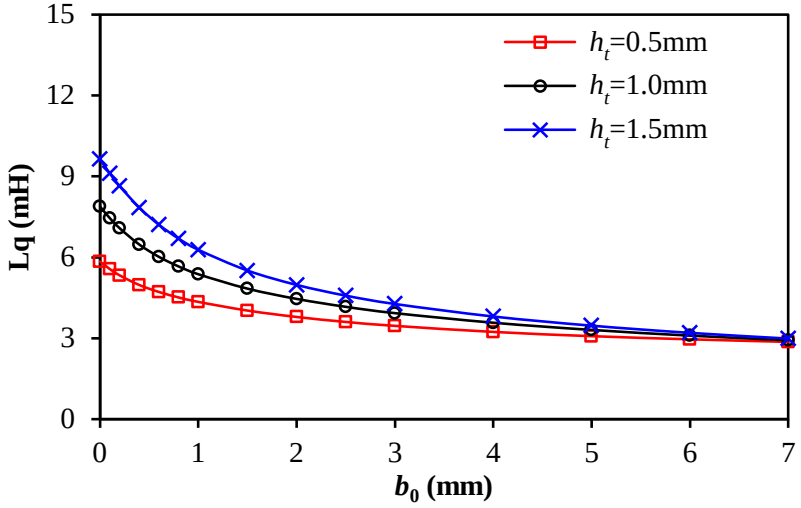

(b) L_q, *q*-axis inductances

Fig. 6.20 DQ-axis inductances against different tooth-tip designs (I_{max}=10A).

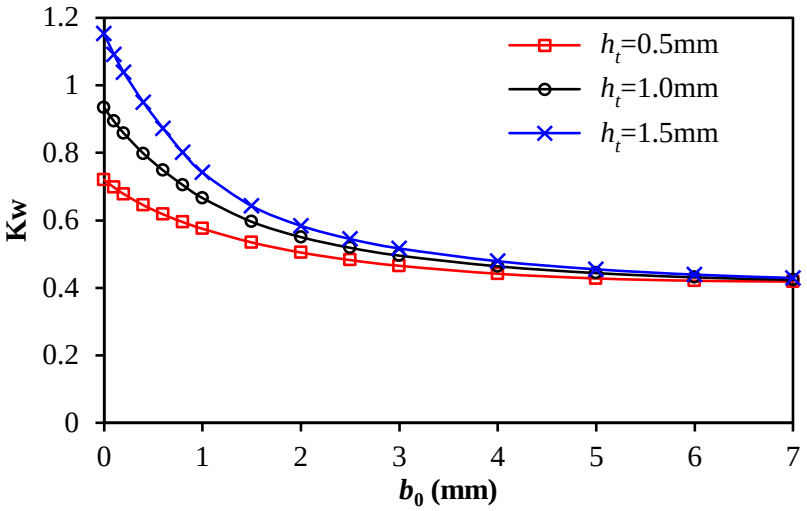

Fig. 6.21 Variation of flux weakening capability against different tooth-tip designs (I_{max}=10A).

The trade-offs should be made considering the machine most frequently operation conditions. For a heavy duty oil pump or ventilation fan, the machines always work under rated load, which makes the on-load torque ripple the key design specification. On the other hand, for an electric vehicle or wind turbine, the direct-drive machines frequently work under half load or even idle condition, while the full load operation only takes a small percentage of a typical driving cycle. Thus, the open-circuit cogging torque and torque ripple under half load condition are more important during design. Meanwhile, if a machine works under strictly limited DC link voltage, the voltage distortion should be seriously considered. However, if the DC link voltage has enough margins, or if the machine only works at fixed speed, the voltage distortion becomes a less important consideration.

For example, two 12-slot/8-pole machines with different tooth-tip designs are compared in this section, which are designated as Machine A and Machine B, respectively, Fig. 6.22. The main design purposes for Machine A are negligible cogging torque and low torque ripple for low load operation, while there is no strict DC-link voltage limitation. On the contrary, the main design purposes for Machine B are maximum average torque and strict limitation for DC-link voltage. The major parameters are kept the same as Table 2.1, while parameters for different tooth-tip designs are listed in Table 6.1.

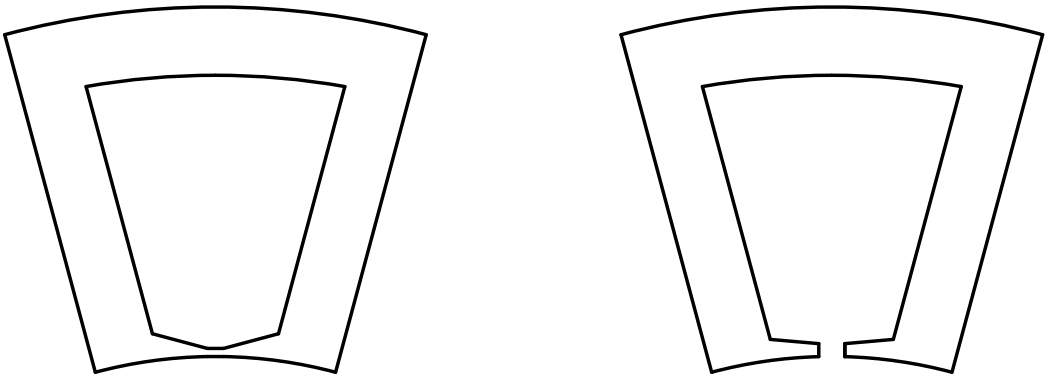

(a) Machine A (b) Machine B

Fig. 6.22 Comparison of lamination of two different designs.

Table 6.1 Differential parameters of two different designs

Parameters	***Machine A***	***Machine B***
Slot opening	0mm	2mm
Tooth-tip thickness	0.6mm	1mm
Tooth-tip slot	15°	10°

Fig. 6.23 compares the cogging torques of two machines. Due to closed slot opening, Machine A has negligible cogging torque amplitude compared with Machine B, which illustrates one of the design purposes for Machine A. Due to the same reasons, the open-circuit back-EMF for Machine A is much more sinusoidal although the fundamental value is smaller due to larger tooth-tip leakage flux, Fig. 6.24. On the other hand, the torque waveforms for two machines are compared in Fig. 6.25. Since the back-EMF of Machine B is larger than Machine A, its average torque is larger as well, since relatively higher b_0 is adopted to reduce the tooth-tip leakage flux. Meanwhile, it can be seen that Machine A has much smaller torque ripple than Machine B under half load operation, although its torque ripple on full load is slightly higher.

Fig. 6.26 shows the comparison of terminal phase voltages for two machines at rated currents. It can be seen that the voltage distortion in Machine A is quite obvious due to the closed slot which it adopts. However, Machine B has negligible voltage distortion since the local saturation variation due to tooth-tip leakage flux is unobvious for large b_0. This difference can be observed more clearly from the variation of *VDR* for different current advance angle in Fig. 6.27, which reveals that the *VDR* for Machine B is nearly unchanged for different β.

However, the *VDR* of Machine A reaches maximum value at β=10°, which has already been explained in Chapter 2.

Although two SPM machines are designed for constant torque operation only, the torque speed curves considering flux weakening can still be calculated in Fig. 6.28. Due to significant voltage distortion, the base speed of Machine A is largely reduced. However, the differences between base speeds calculated by peak or fundamental voltages in Machine B are quite small, which realizes the design purpose. Due to large b_0, the flux weakening performance of Machine B deteriorates similarly, Fig. 6.21. If further flux weakening operation is demanded, h_t could be increased to compensate the drawback due to large b_0.

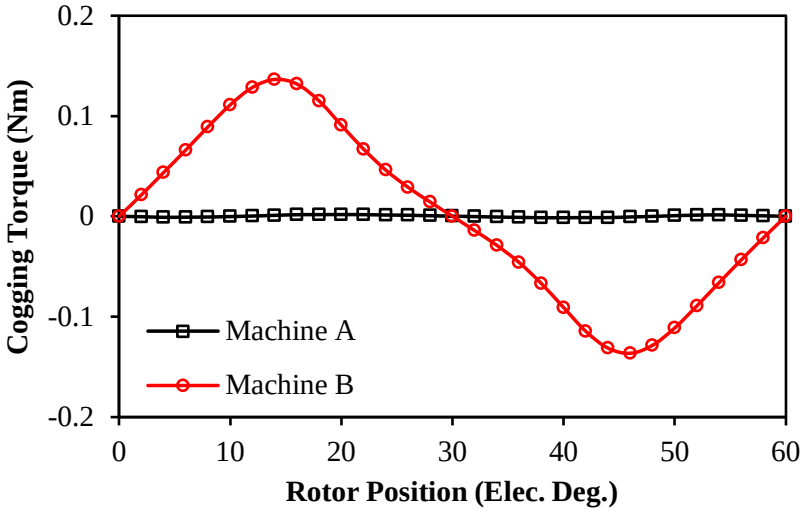

Fig. 6.23 Comparison of cogging torque waveforms.

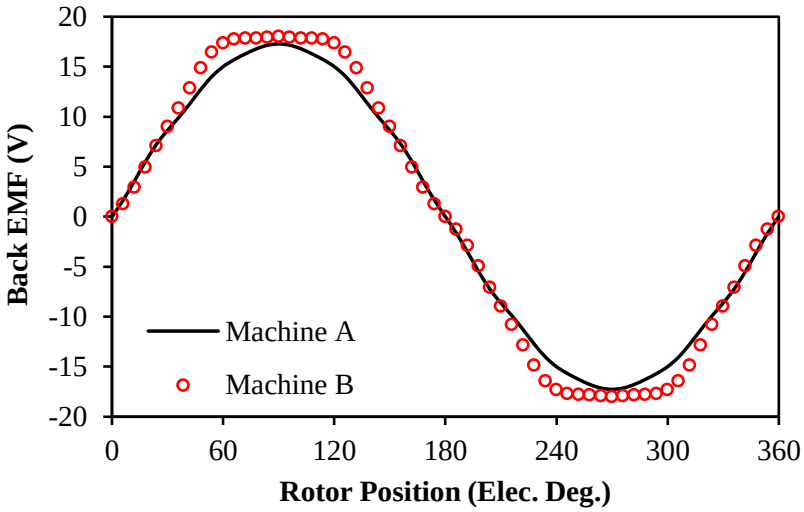

(a) Waveforms

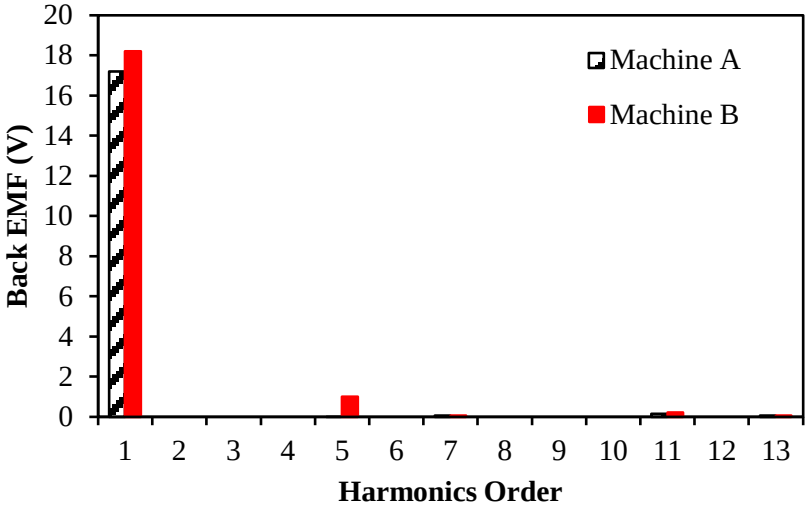

(b) Harmonic components

Fig. 6.24 Comparison of open-circuit back-EMFs (400rpm).

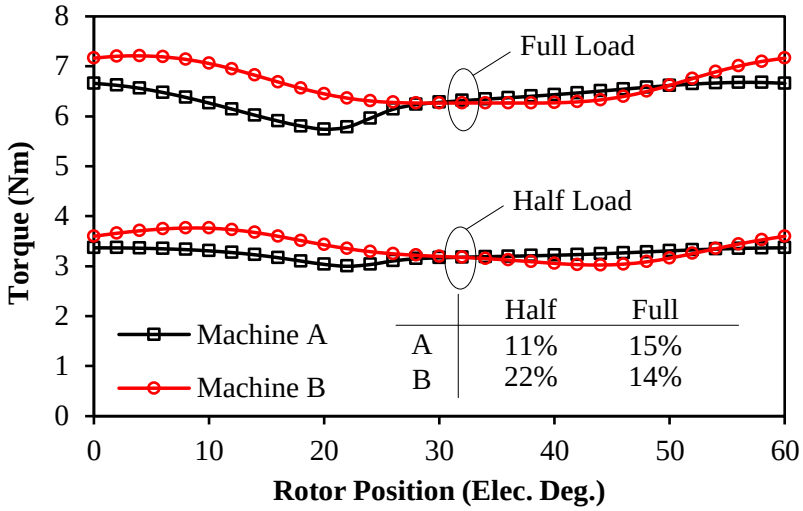

Fig. 6.25 Comparison of torque waveforms (for full load I_q=10A, I_d=0, showing the torque ripple values)

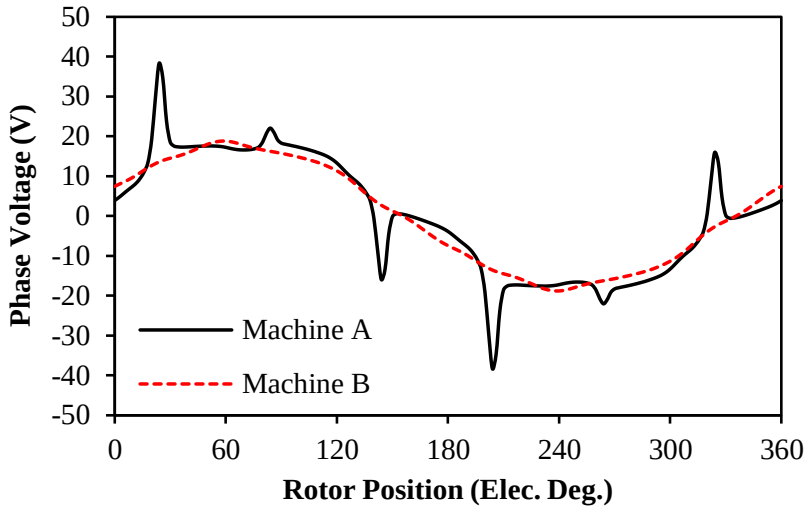

(a) Waveforms

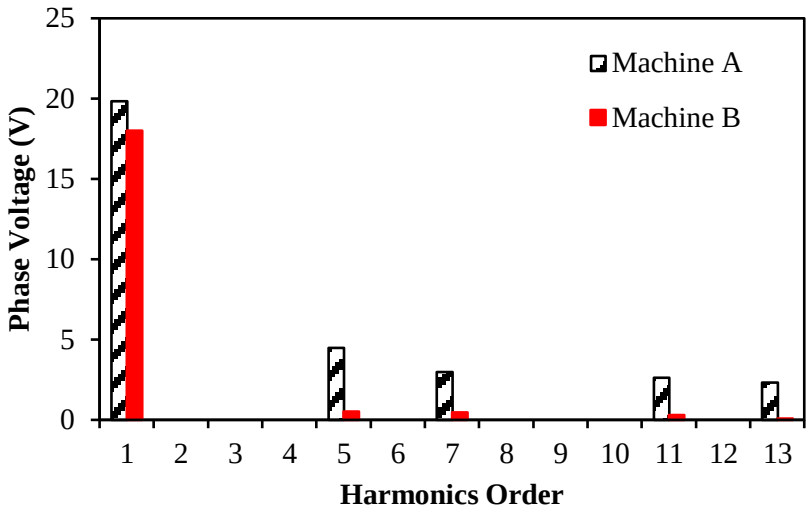

(b) Harmonics

Fig. 6.26 Comparison of terminal phase voltages (I_q=10A, I_d=0, 400rpm).

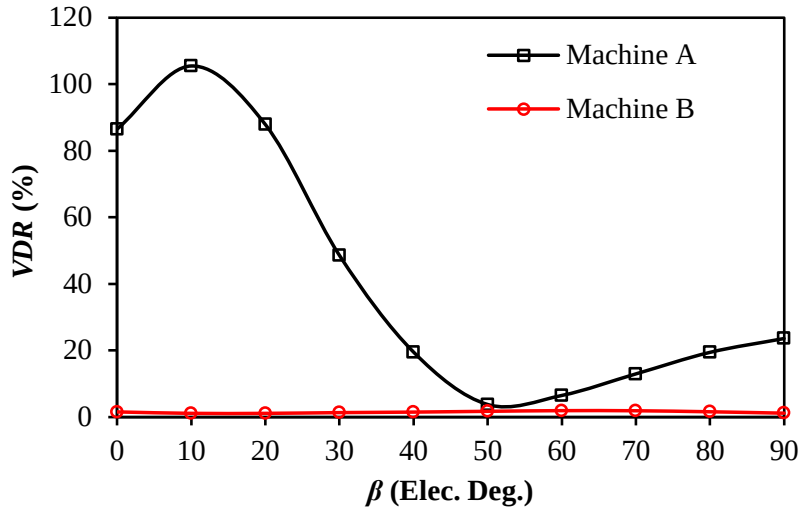

Fig. 6.27 Comparison of voltage distortion ratios (I_{max}=10A, 400rpm).

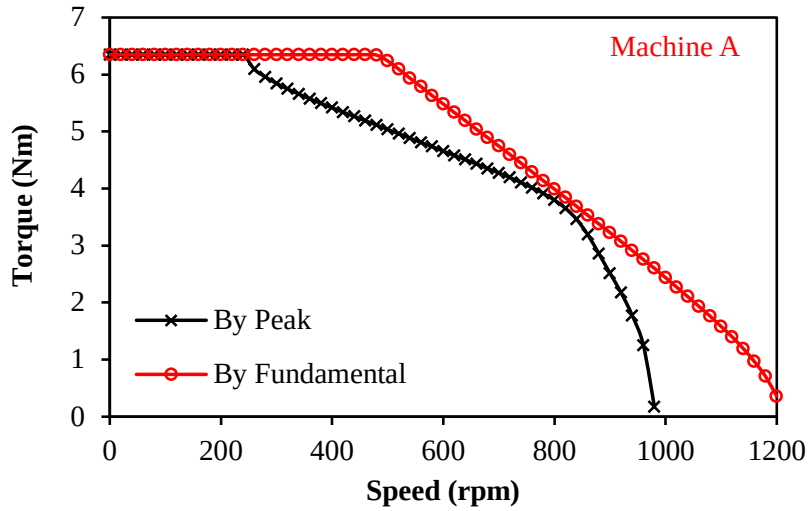

(a) Machine A

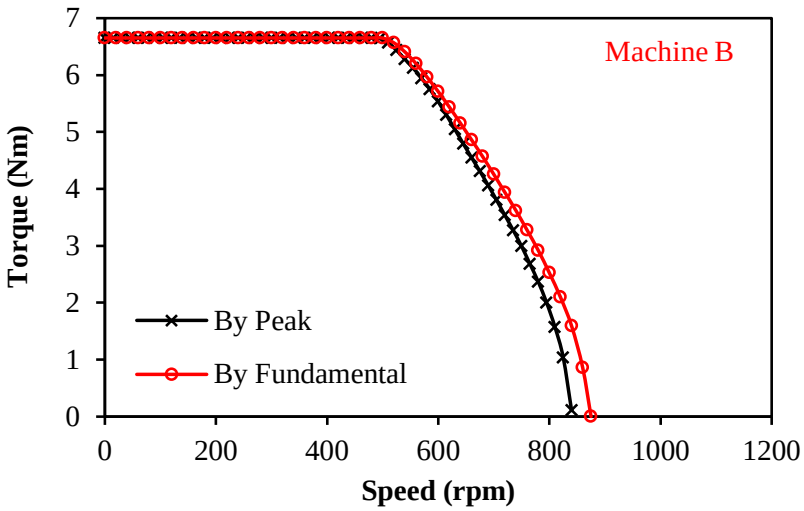

(b) Machine B

Fig. 6.28 Comparison of torque speed characteristics (I_{max}=10A, U_{DC}=42V).

6.3 Minimization of Terminal Voltage Distortion in IPM machines

According to the analyses in Chapter 4 and Chapter 5, rotor segmentation effect plays more dominant role for the voltage distortion in IPM machines especially under flux weakening operation. Thus, this section tries to investigate the voltage distortion minimization methods from the rotor segmentation point of view.

6.3.1 Rotor Skewing

Similar to the analysis in SPM machine, 4-step skewing with 60° skewing angle will be adopted for the IPM skewing model since the voltage ripples are also represented as 6n±1 times harmonics in the terminal voltages. Fig. 6.29 compares the open-circuit back-EMF without and with skewing, which shows the back-EMF harmonics have been significantly reduced. When driven by rated current with β=60°, the comparison of terminal voltages for different models is shown in Fig. 6.30(a). Although the peak voltage are slightly reduced, the voltage ripples in the skewing model are still significant, which can be reflected more clearly by the harmonics in Fig. 6.30(b). In order to investigate the mechanism of such phenomenon, the terminal phase voltage of different rotor segments are calculated in Fig. 6.31(a). Due to different current angle for each rotor segment, the influences of local magnetic saturation and rotor segmentation effect are different, which lead to different voltage distortion levels as reflected in Fig. 6.31(b). More importantly, as shown in Fig. 6.31(c), the harmonics phase angles are not in opposite directions, which make the harmonics not be totally cancelled

between segments, although the peak phase voltage could be reduced due to voltage ripple appearing at different rotor positions.

Fig. 6.32 illustrates the influence of step numbers for skewing, in which step number of one refers to the original model without skewing. It can be seen that when number of steps is larger than three, both peak and fundamental voltages become almost constants. Due to less local magnetic saturation compared with that in the aforementioned SPM machines, the influence of even or odd number of steps also becomes less obvious. Meanwhile, the variations of voltage distortion with different skewing angles are shown in Fig. 6.33. Although *VDR* of the resultant terminal phase voltage reduces with the increase of skewing angle and reaches minimum value when the skewing angle equals 90°, *THD* of terminal voltage is only slightly reduced, which reveals the voltage distortion due to rotor segmentation effect has not been alleviated. Meanwhile, considering the significant reduction of average torque, rotor skewing is not an effective way to reduce the on-load terminal voltage distortion in IPM machines.

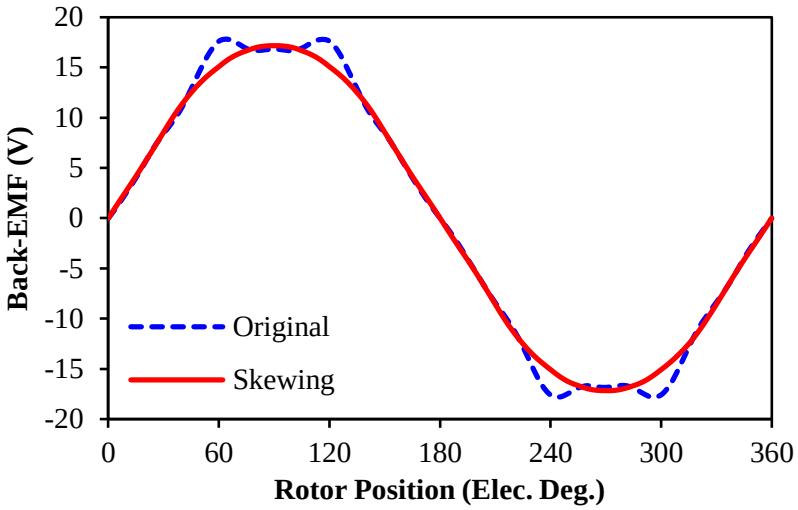

(a) Waveforms

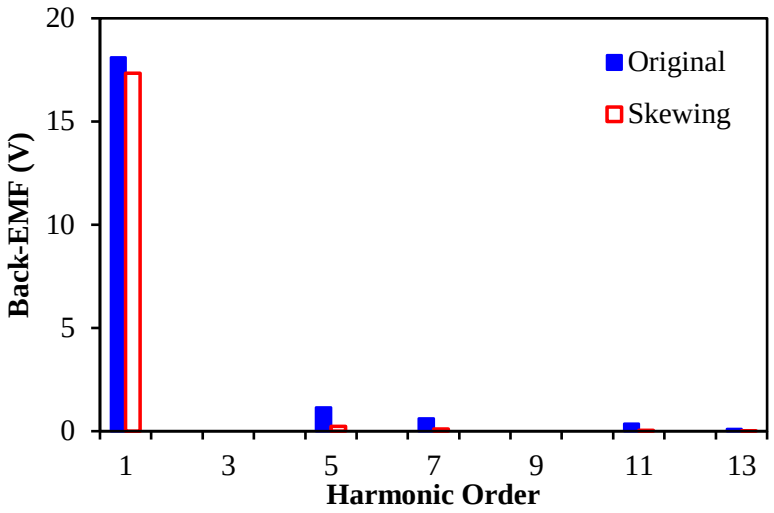

(b) Harmonics

Fig. 6.29 Comparison of open-circuit back-EMFs without and with skewing (400rpm).

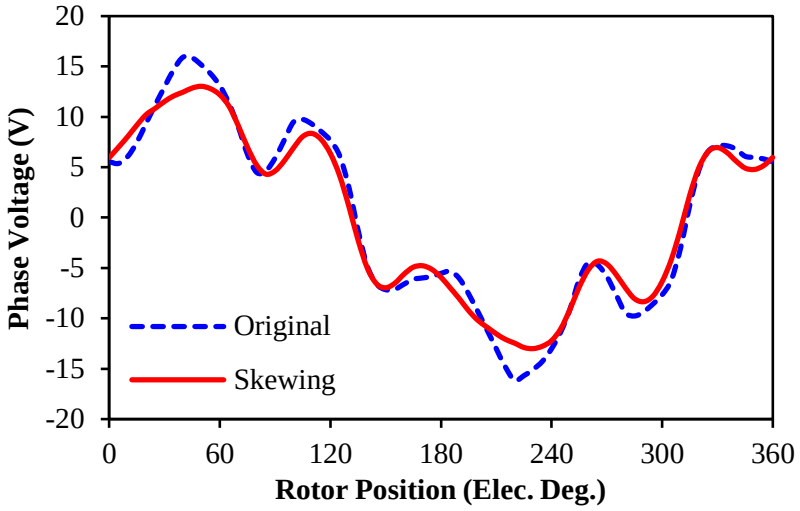

(a) Waveforms

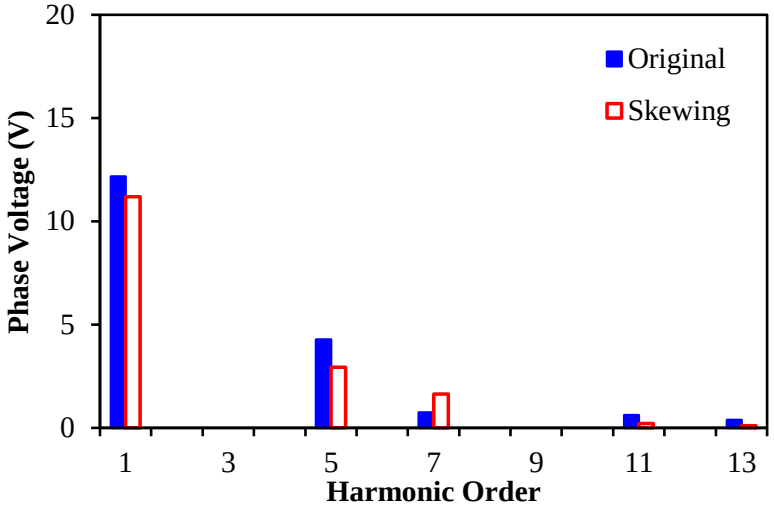

(b) Harmonics

Fig. 6.30 Comparison of voltages without and with skewing (I_{max}=10A, β=60°, 400rpm).

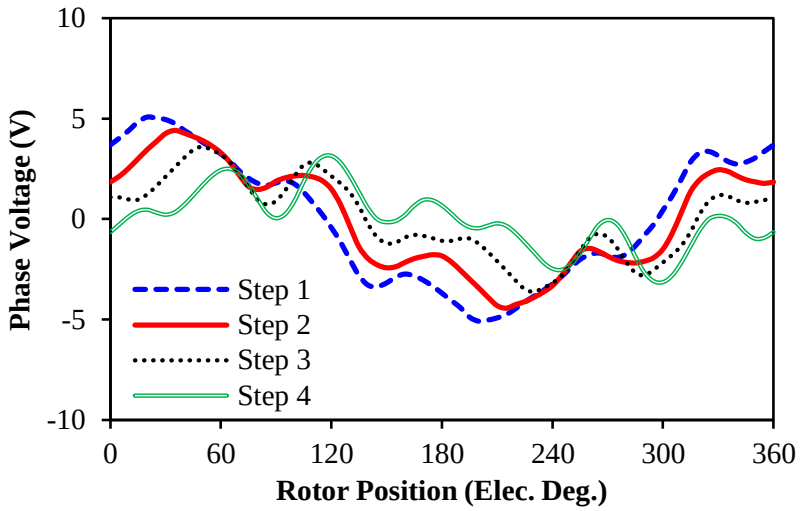

(a) Waveforms

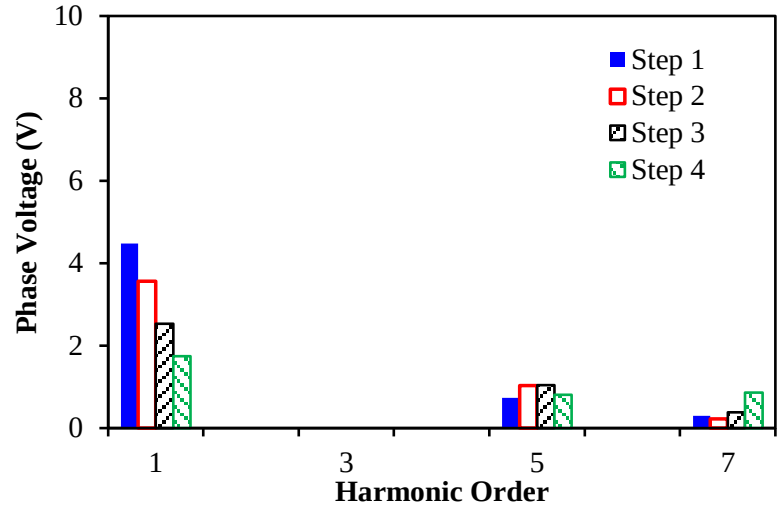

(b) Harmonics

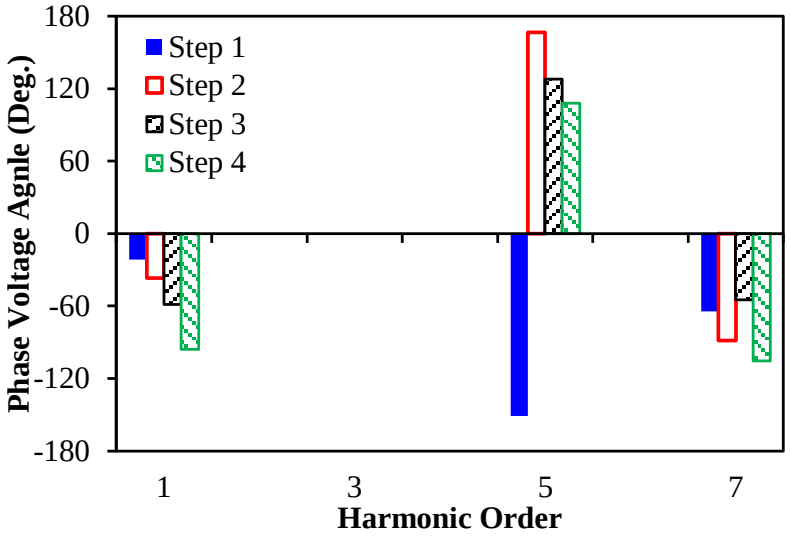

(c) Harmonics phase angles

Fig. 6.31 Comparison of phase voltages of each rotor step (I_{max}=10A, β=0°, 400rpm).

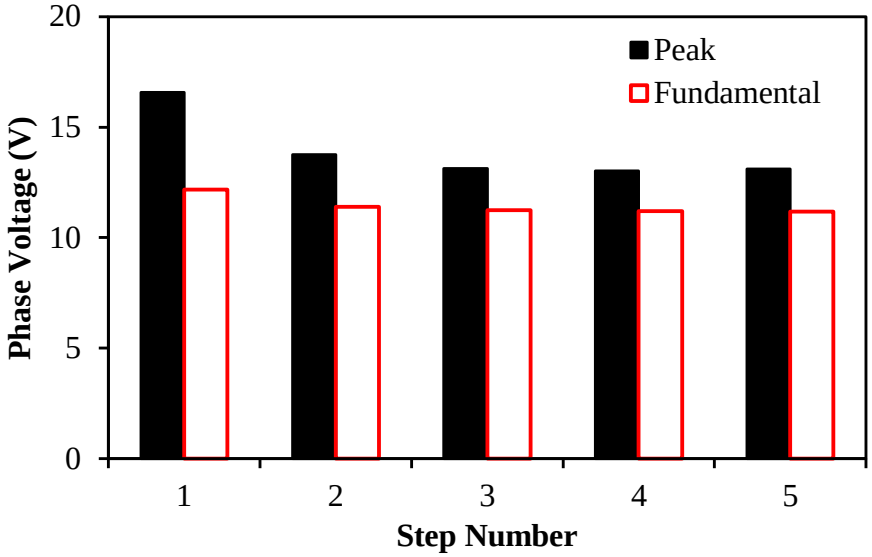

Fig. 6.32 Influence of step-skewing number (I_{max}=10A, β=0°, 400rpm).

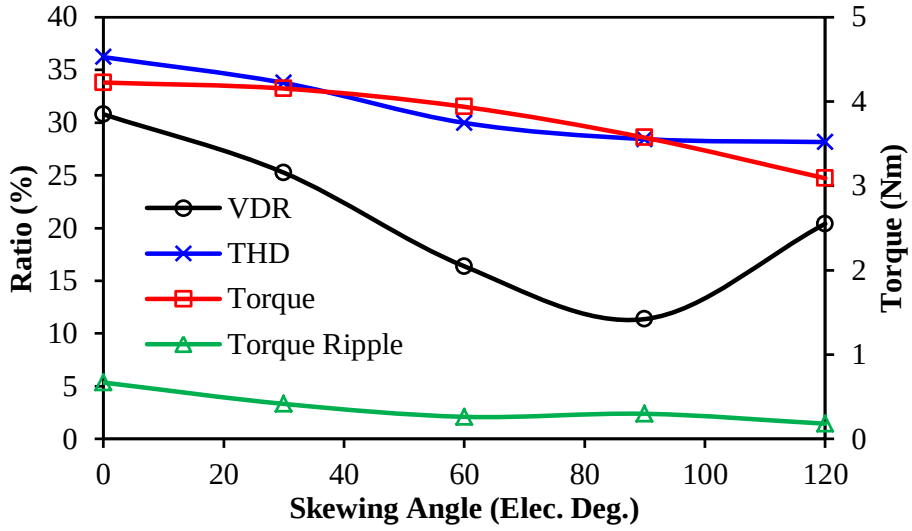

Fig. 6.33 Variation of voltage distortion level and torque against skewing angle (I_{max}=10A, β=60°, 400rpm).

6.3.2 Rotor Shaping

Since the rotor segmentation effect originates from the discontinuous rotor permeance due to IPM rotor topology, the non-uniform airgap method could be a viable solution to release such effect and thereafter the voltage distortion. The inverse cosine shaping is also adopted for the investigation in this section, which has already been defined as (6.1). The model with k_a=1 is introduced for example, Fig. 6.34, while the influence of different k_a will be presented later.

Fig. 6.35(a) compares the open-circuit back-EMFs of the models without and with rotor shaping. It can be seen that the waveform of the shaping rotor is much more sinusoidal than

the original design, which can be reflected more clearly from the harmonic components in Fig. 6.35(b). Fig. 6.36 compares the terminal voltages under the same current conditions. Clearly, the voltage ripples in the shaping rotor are much smaller compared with the original design, which reveals that the rotor segmentation effect has been released. From the FFT results, *VDR* has been reduced from 25.2% to 11.6%, while *THD* has been reduced from 32.2% to 15.7%.

In order to illustrate this phenomenon clearly, the flux density distributions for θ_r=0° are compared in Fig. 6.37. Clearly, the original design is more saturated in tooth-tips and rotor iron region compared with the rotor shaping model. By FP method, the armature flux paths of two machines can be compared in Fig. 6.38. Due to larger airgap in the rotor inter-pole area, the armature fluxes through leakage flux paths when rotor poles and stator teeth aligned together reduce in the shaped rotor. According to the mechanism of voltage distortion of IPM machine, this reduction obviously reduces the local magnetic saturation caused by rotor segmentation effect, which results in less voltage distortion level. Fig. 6.39 shows the variation of voltage distortion level against different k_a. With the increase of k_a, both *VDR* and *THD* reduce significantly. Meanwhile, the torque ripple also reduces, while the average torque reduces less than that for the rotor skewing. Therefore, rotor shaping is a more efficient way to reduce voltage distortion compared with rotor skewing.

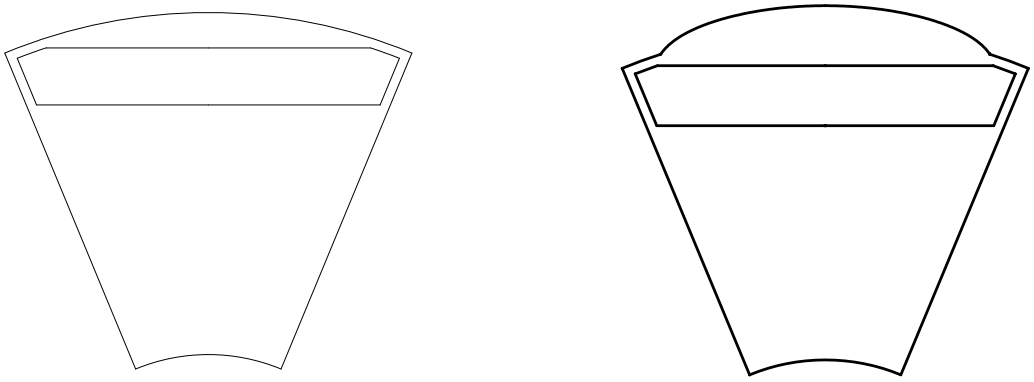

(a) Original, without shaping (b) With shaping, k_a=1

Fig. 6.34 Comparison of rotor laminations without and with shaping.

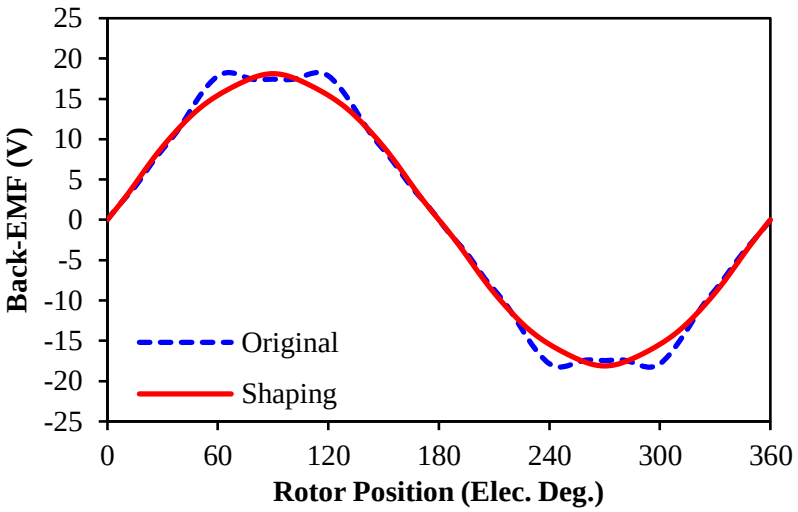

(a) Waveforms

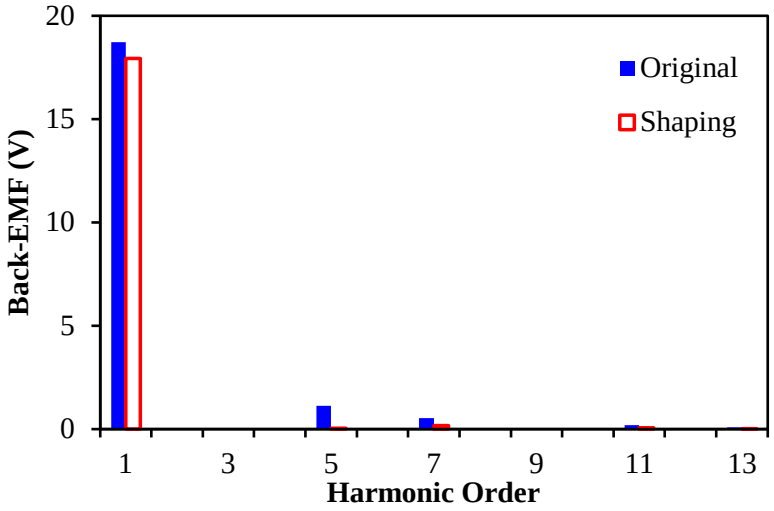

(b) Harmonics

Fig. 6.35 Comparison of open-circuit back-EMF without and with shaping (400rpm).

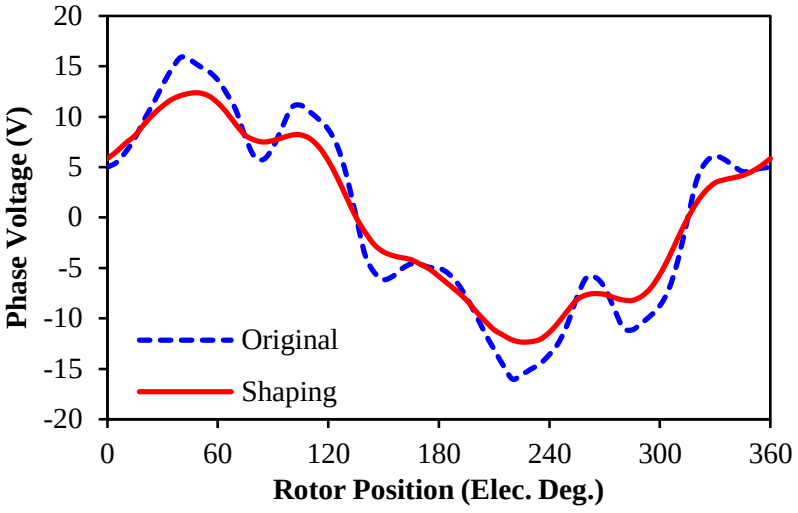

(a) Waveforms

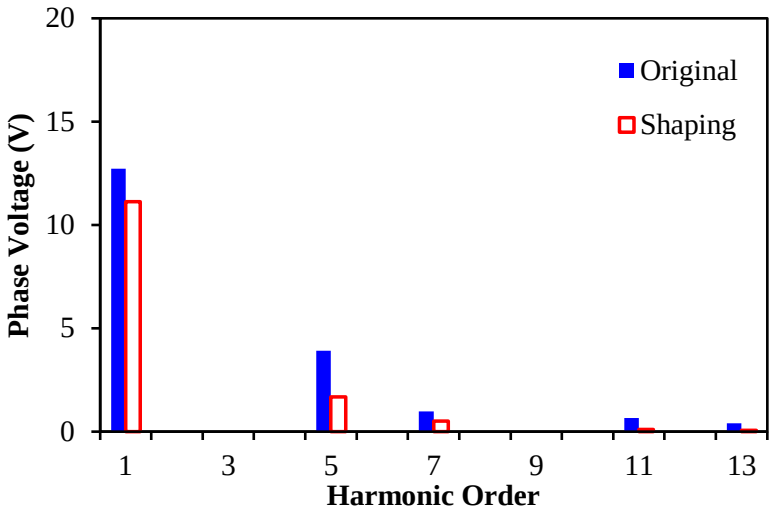

(b) Harmonics

Fig. 6.36 Comparison of terminal phase voltages without and with shaping (I_{max}=10A, β=60°, 400rpm).

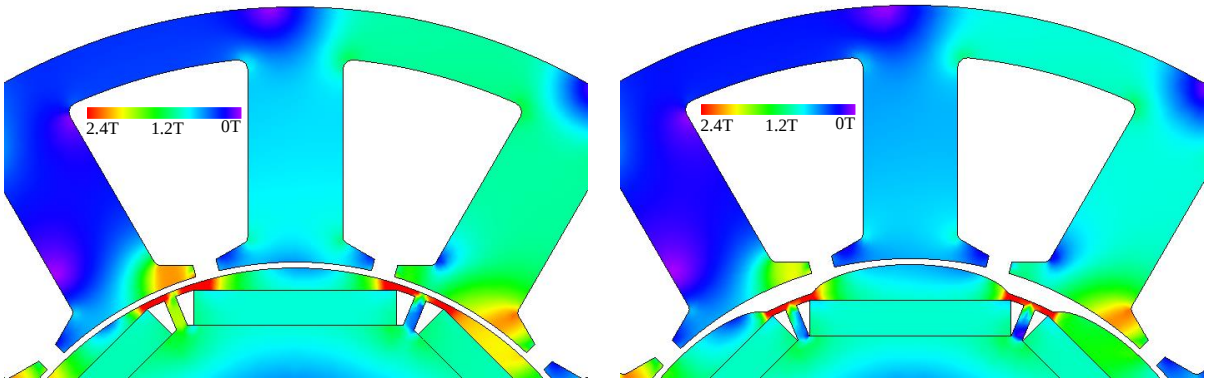

(a) Without shaping (b) With shaping, k_a=1

Fig. 6.37 Comparison of flux density distribution of models without and with shaping (I_{max}=10A, β=60°, 400rpm, θ_r=0°).

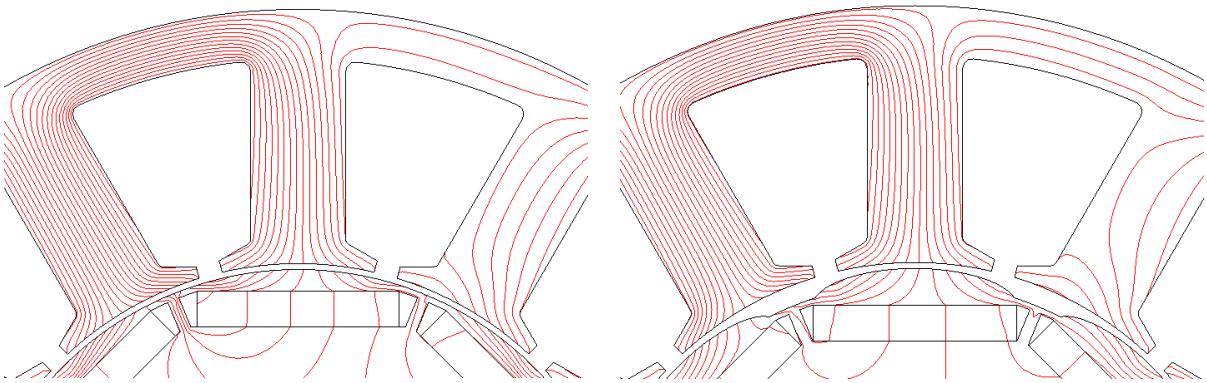

(a) Without shaping (b) With shaping, k_a=1

Fig. 6.38 Comparison of equipotential distribution with only armature excitation by FP method (I_{max}=10A, β=60°, 400rpm, θ_r=0°).

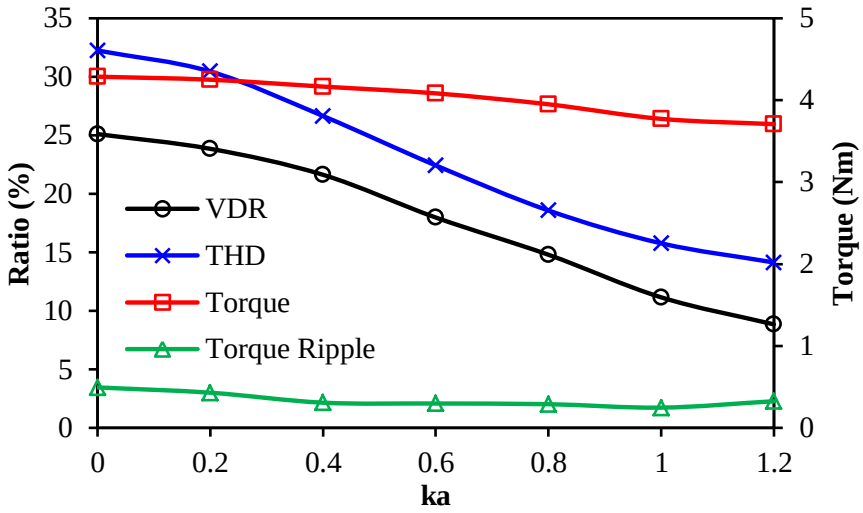

Fig. 6.39 Variation of voltage distortion level and torque against k_a (I_{max}=10A, β=60°, 400rpm).

6.3.3 Stator Shaping

Stator shaping is another way to generate non-uniform airgap, which has already been illustrated in Fig. 6.10. The minimum airgap length is still kept the same as the original model, while the maximum airgap length appears at the end of tooth tips. The difference between maximum and minimum airgap length can be designated as the shaping depth d_s. In example, d_s=0.5mm is selected to illustrate the effectiveness of stator shaping. Fig. 6.40 compares the open-circuit back-EMFs of the original model and the stator shaping model, which shows the harmonics are not significantly reduced by stator shaping. Since the airgap length around tooth-tips increases, the flux focusing effect by the tooth-tips are also reduced, which leads to the reduction of fundamental back-EMF. Fig. 6.41 compares the on-load terminal phase voltages for two models. Although their fundamental voltages are similar, the harmonics of the shaping model are much lower. Due to the increased airgap length, as well as the reduction of tooth-tip area, the local magnetic saturation in tooth-tips has been alleviated, which can be observed from Fig. 6.42. By FP method, the equipotential distributions excited by only armature current are compared in Fig. 6.43, in which the leakage flux through tooth-tips reduces. Thus, the reduction of rotor segmentation effect and local magnetic saturation by stator shaping can reduce the on-load terminal voltage distortion in IPM machines. Further, the variation of voltage distortion levels against d_s is calculated in Fig. 6.44. Clearly, with the increase of d_s, both *VDR* and *THD* proportionally reduce, while the average torque only slightly decreases. For the same reduction of *VDR*, e.g. from 25% to

15%, stator shaping will cause less average torque drop compared with rotor shaping, but its improvement on back-EMF is not as obvious as rotor shaping.

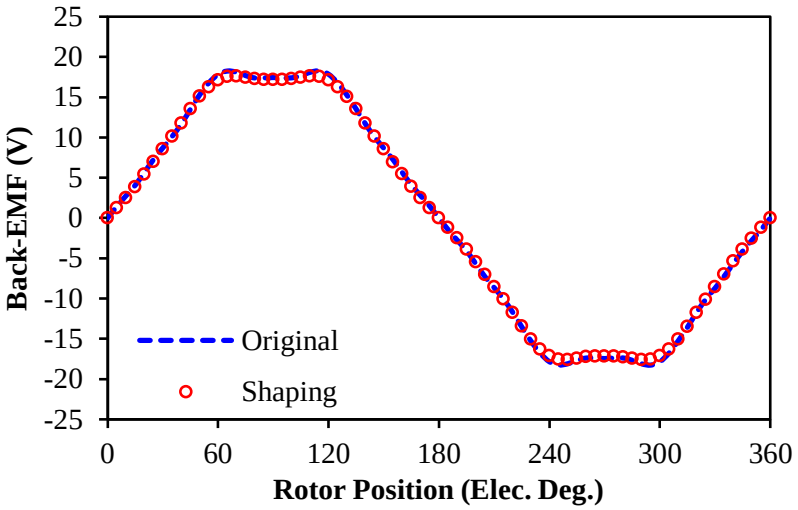

(a) Waveforms

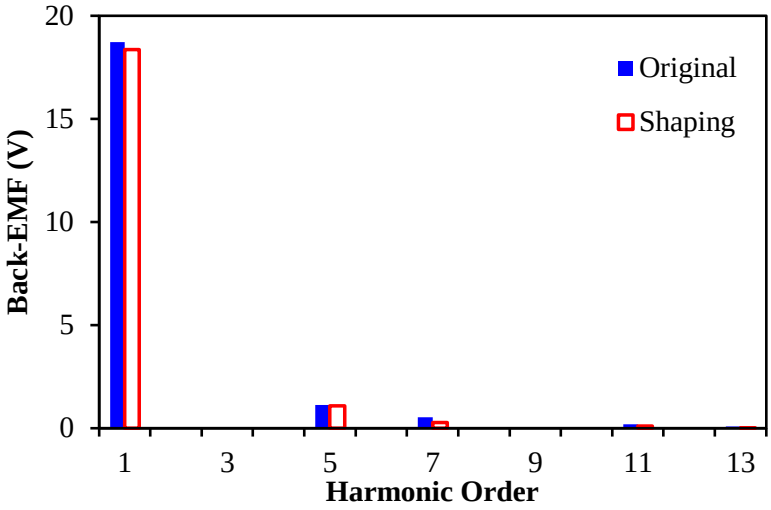

(b) Harmonics

Fig. 6.40 Comparison of open-circuit back-EMF without and with shaping (400rpm, d_s=0.5mm).

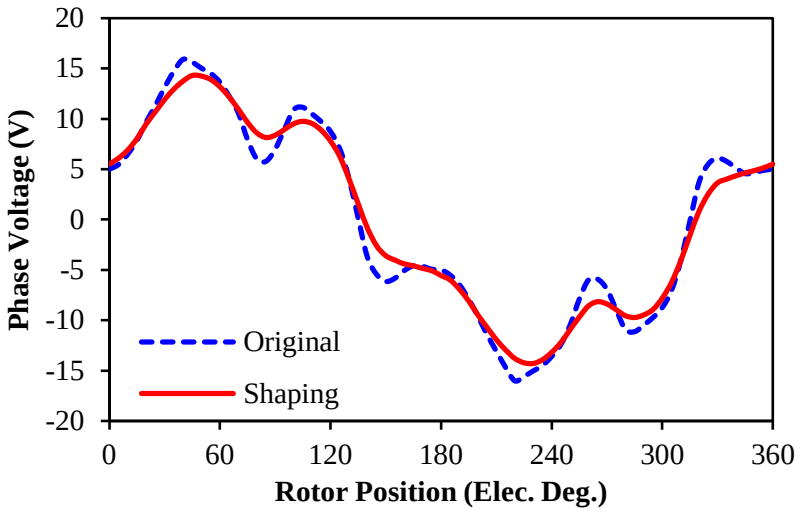

(a) Waveforms

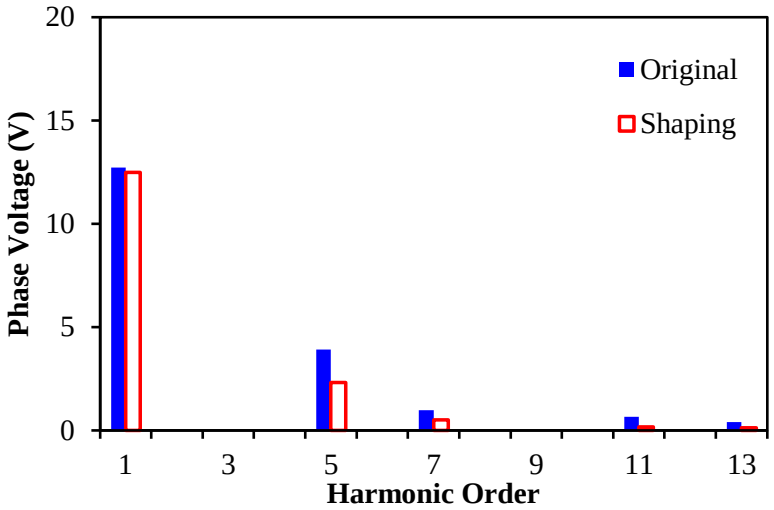

(b) Harmonics

Fig. 6.41 Comparison of terminal phase voltages without and with shaping (I_{max}=10A, β=60°, 400rpm, d_s=0.5mm).

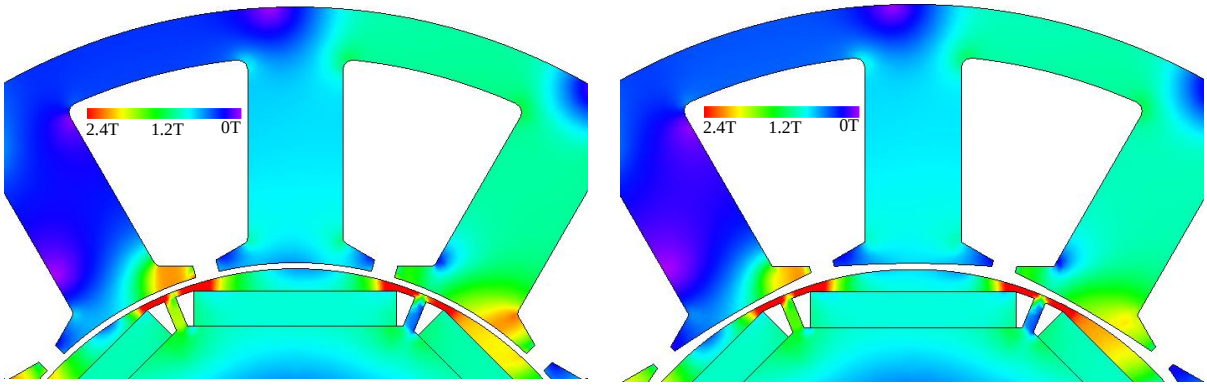

(a) Without shaping (b) With shaping, d_s=0.5mm

Fig. 6.42 Comparison of flux density distribution of models without and with shaping (I_{max}=10A, β=60°, 400rpm, θ_r=0°).

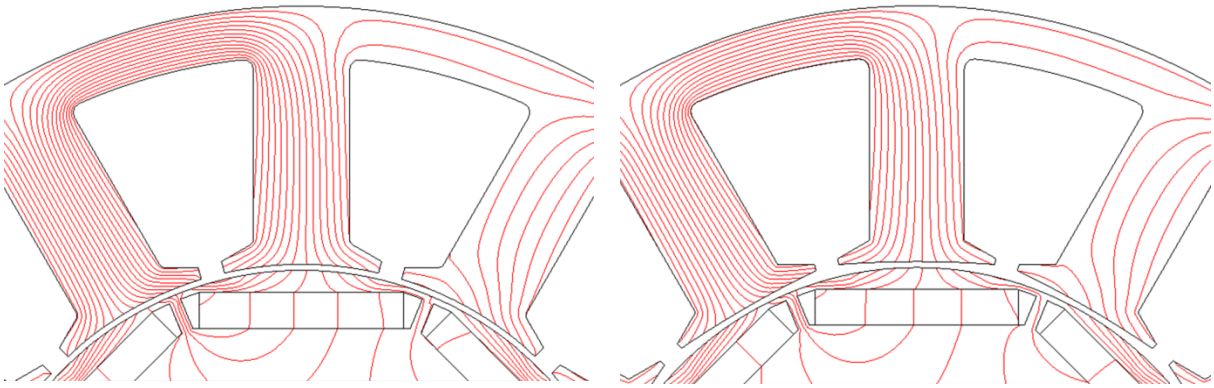

(a) Without shaping (b) With shaping, d_s=0.5mm

Fig. 6.43 Comparison of equipotential distribution with only armature excitation by FP method (I_{max}=10A, β=60°, 400rpm, θ_r=0°).

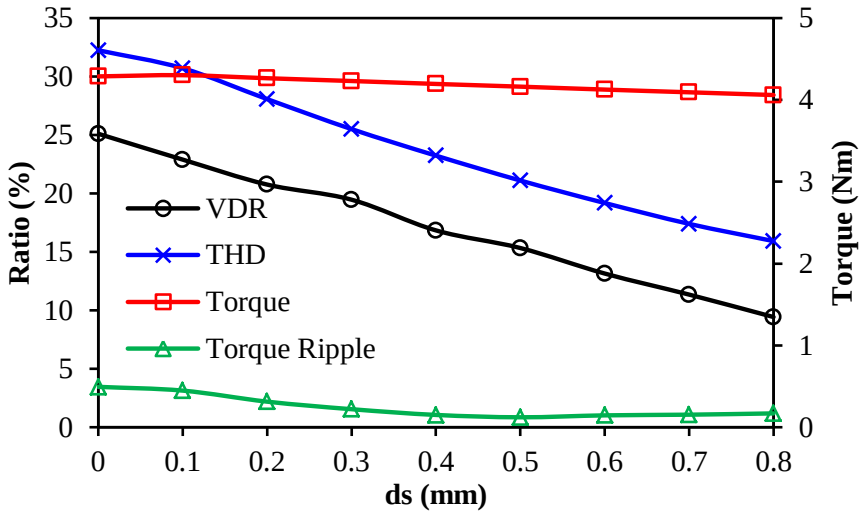

Fig. 6.44 Variation of voltage distortion level and torque against shaping depth (I_{max}=10A, β=60°, 400rpm).

6.4 Experimental Validation

6.4.1 SPM Machines

The trade-off of slot opening width for SPM machines will be validated by experiments in this section. Two prototypes according to the dimensions of the investigated models illustrated in Fig. 6.22 and Table 6.1 are built, Fig. 6.45. The test rig is the same as the aforementioned chapters. The measured phase resistances for two machines are 0.64Ω and 0.62Ω, which are quite closed due to the same winding design.

Fig. 6.47 shows the comparison of predicted and measured open-circuit back-EMFs of two machines. Due to end-effect as well as manufacturing tolerance, the measured results are

slightly smaller than the prediction. Fig. 6.48 compares the measured and predicted cogging torques of two machines. Since the cogging torque for Machine A is too small due to closed slot opening, it is difficult to measure it accurately. However, the measured amplitudes still proves the small amplitude of predicted cogging torque. The measured result in Machine B validates the prediction well due to much higher amplitudes. Fig. 6.48 compares the measured and predicted torque waveform under I_d=0 control, which also shows good agreement considering end-effect and measuring error.

When driven by the same current, the measured terminal phase voltages are compared in Fig. 6.49. It can be seen that all the phase currents are kept as sinusoidal as possible, but phase voltages reveal different distortion level. When β=0°, the voltage distortion in Machine B is much smaller than in Machine A. With the increase of β, the voltage distortion will be alleviated according to the analysis, which leads to almost sinusoidal phase voltage for Machine B when β=60°, but the voltage ripples are still obvious in Machine A. The comparison of predicted and measured terminal voltages is shown in Fig. 6.50, which shows good agreement.

Under the same U_{DC} and driven currents, the comparison of measured and predicted torque speed curves are shown in Fig. 6.51, in which the ideal curves are calculated by only fundamental voltages for comparison. Considering the different between predicted and measured back-EMF and torque waveform, the torque difference between measured and predicted torque waveforms could be explained. Overall, the experimental results agree with the prediction well.

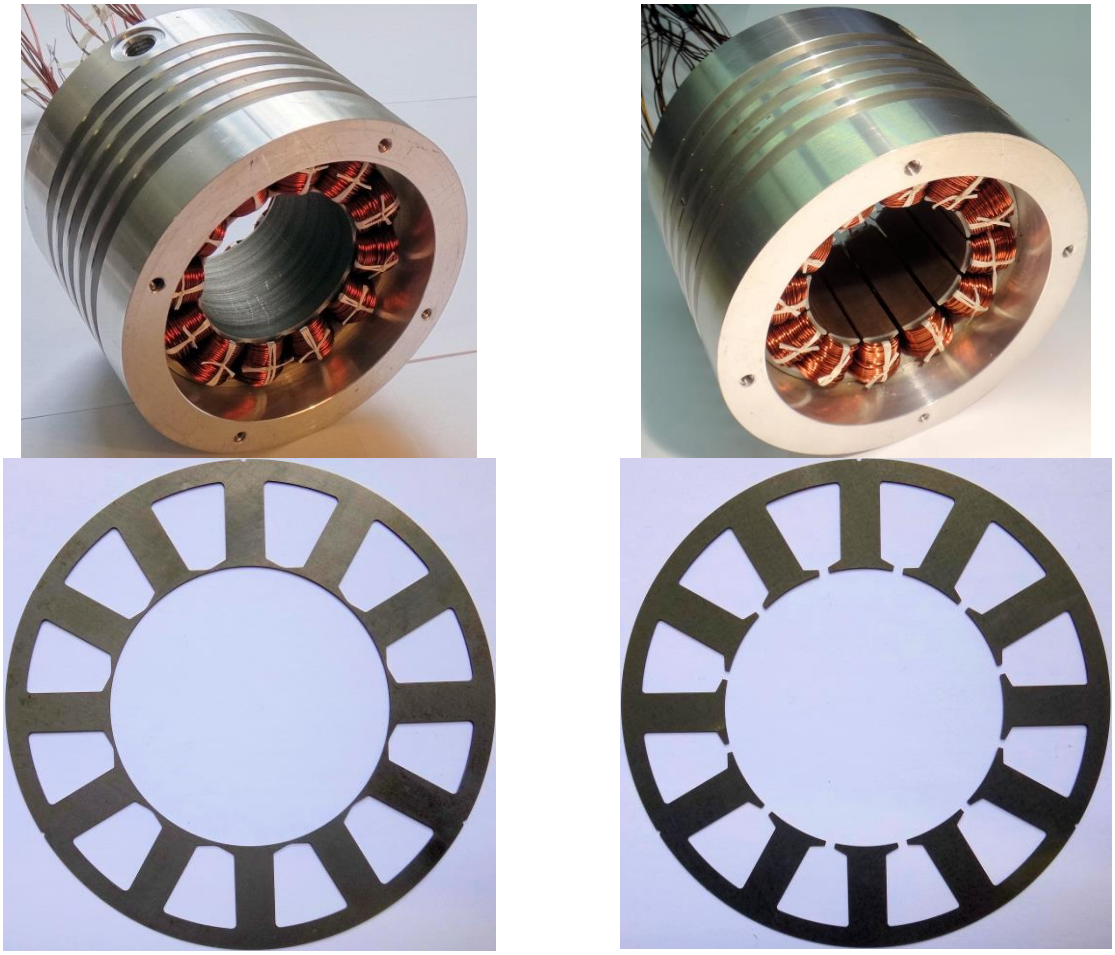

(a) Stator Machine A

(b) Stator Machine B

(c) Rotor

Fig. 6.45 Prototype photos.

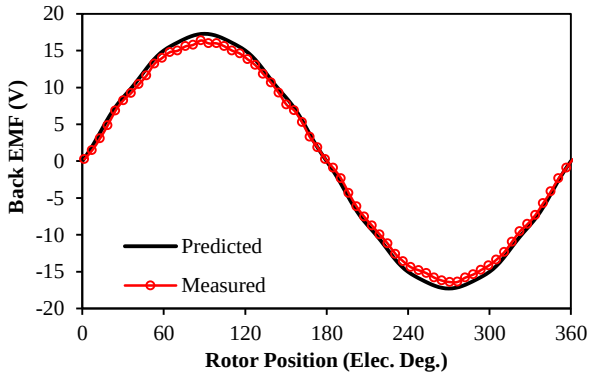

(a) Waveforms, Machine A

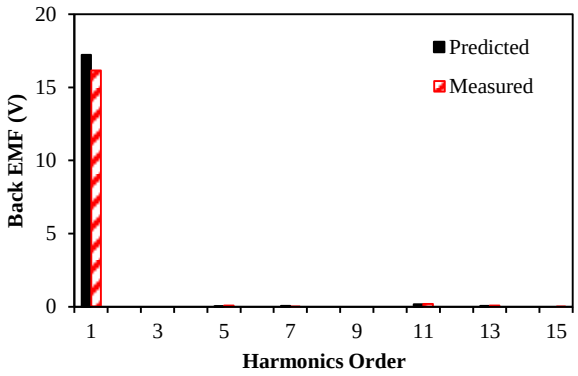

(b) Harmonics, Machine A

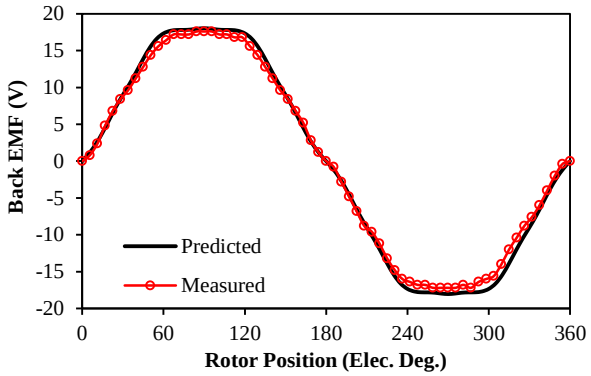

(c) Waveforms, Machine B

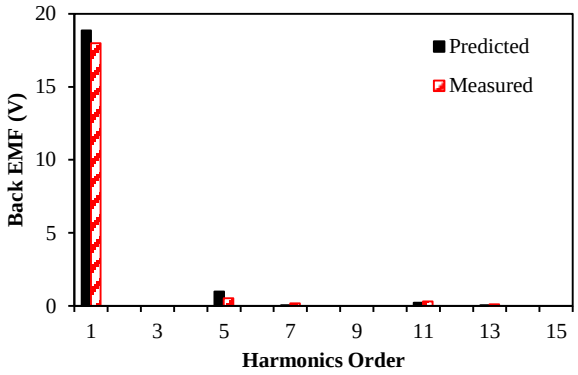

(d) Harmonics, Machine B

Fig. 6.46 Comparison of measured and predicted open-circuit back-EMFs (400rpm).

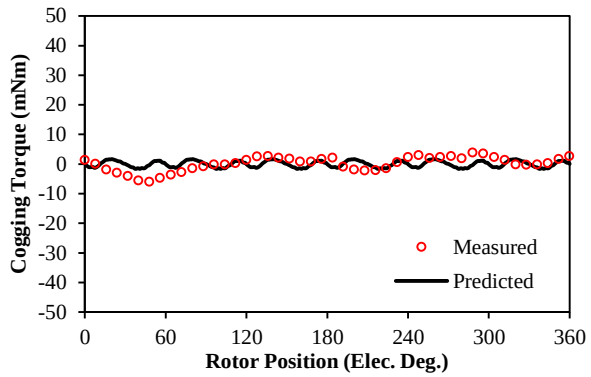

(a) Machine A

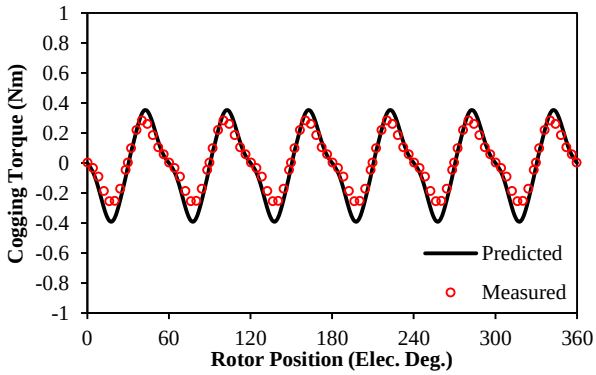

(b) Machine B

Fig. 6.47 Comparison of measured and predicted cogging torques.

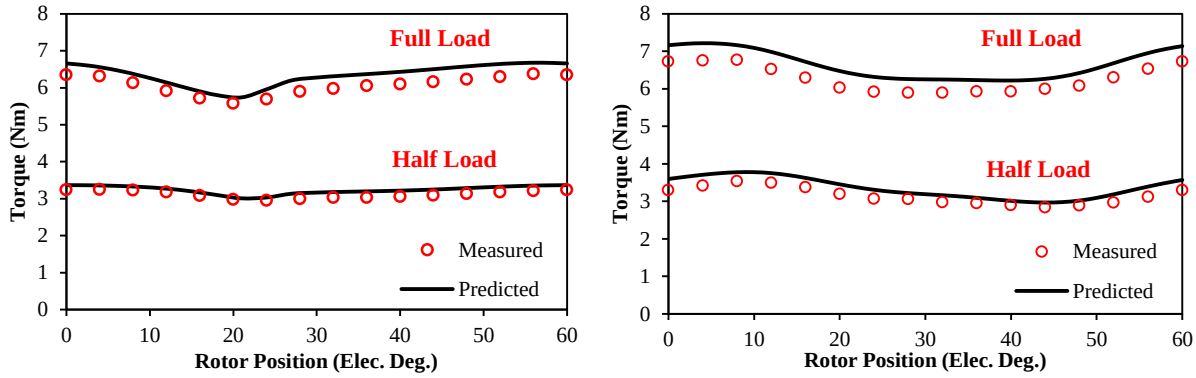

(a) Machine A (b) Machine B

Fig. 6.48 Comparison of measured and predicted torque waveforms (I_{max}=10A, β=0°).

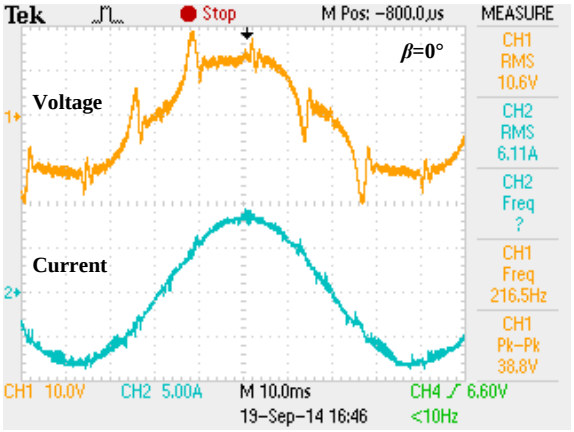

(a) Machine A, β=0°

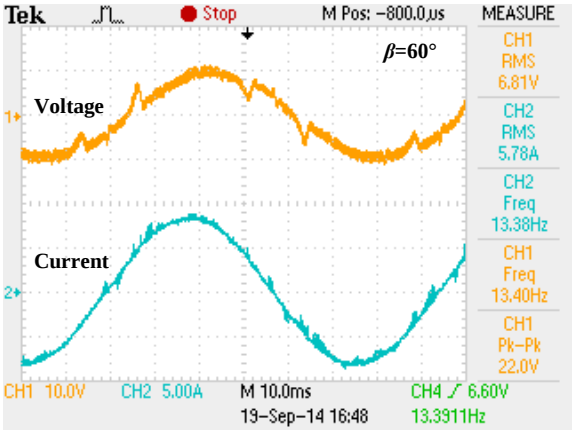

(b) Machine A, β=60°

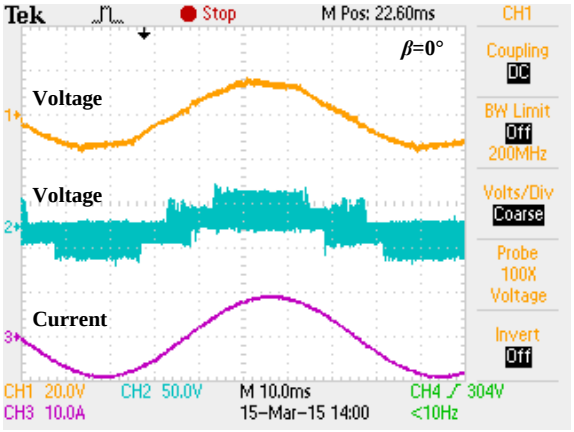

(c) Machine B, β=0°

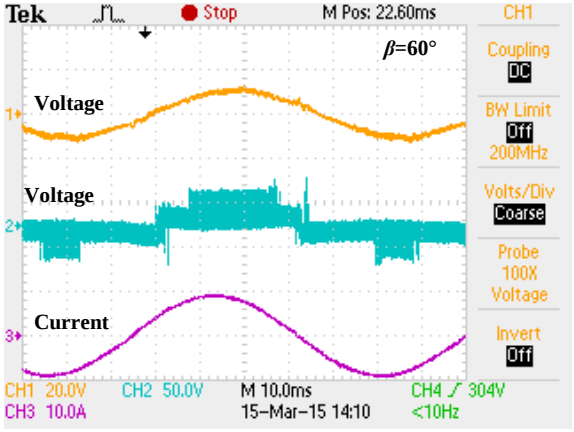

(d) Machine B, β=60°

Fig. 6.49 Comparison of measured on-load terminal voltages (I_{max}=8A, 200rpm, U_{DC}=60V).

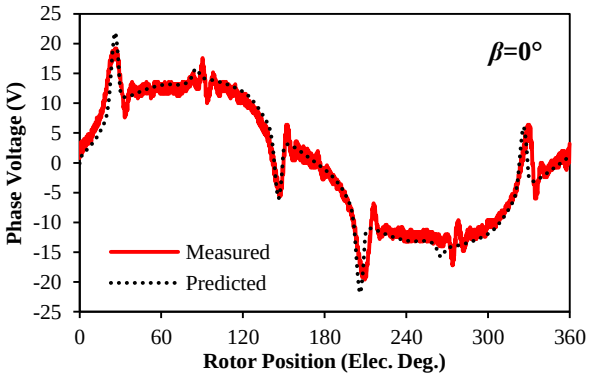

(a) Machine A, β=0°

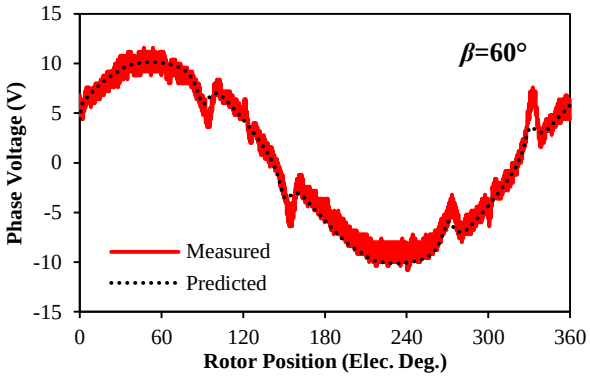

(b) Machine A, β=60°

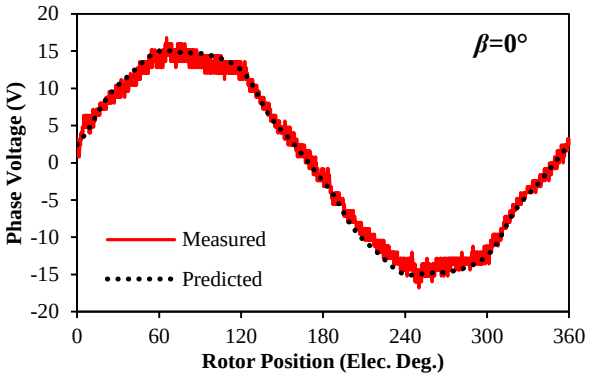

(c) Machine B, β=0°

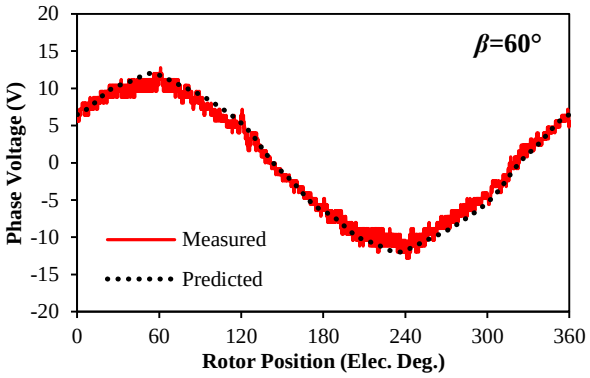

(d) Machine B, β=60°

Fig. 6.50 Comparison of measured and predicted on-load terminal voltages (I_{max}=8A, 200rpm, U_{DC}=60V).

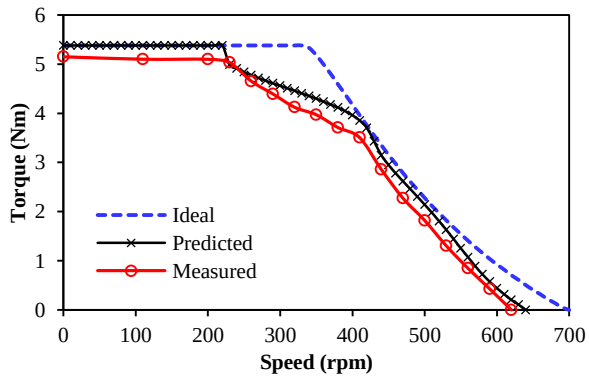

(a) Machine A

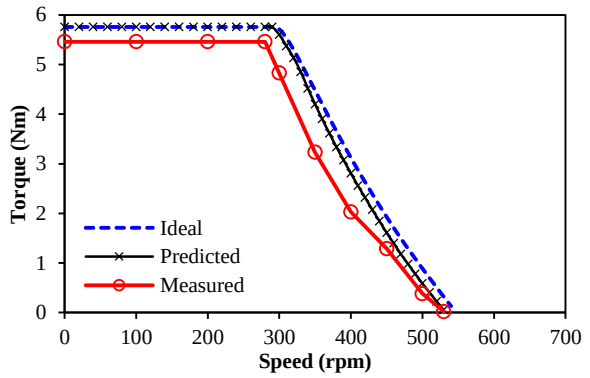

(b) Machine B

Fig. 6.51 Comparison of the measured and predicted torque speed curves (I_{max}=8A, U_{DC}=42V).

6.4.2 IPM Machines

Considering the manufacturing cost, only the rotor shaping is selected to be validated in this section. Fig. 6.52 shows the photos of the prototype machines. All parameters of the stator

and non-shaping rotor are the same as shown in Chapter 4, while the shaping rotor has shaping factor k_a=1. The measured phase resistance at 20°C is 0.62Ω. The test rig is the same as that in the aforementioned analyses.

Fig. 6.53 compares the open-circuit back-EMFs for two machines, which shows the shaping rotor has much more sinusoidal back-EMF. Due to manufacturing tolerance, the measured result of the shaping rotor is more closed to the prediction compared with the original rotor. Fig. 6.54 and Fig. 6.55 compare the open-circuit cogging torque and on-load torque waveforms for both rotors under the same current condition, which show good agreement. It can be observed that both the ripples of cogging torque and load torque for the shaping rotor are much smooth compared with the original rotor due to more sinusoidal airgap field and back-EMF waveforms. Under the same I_{max} and β, the measured terminal phase voltages and phase currents are compared in Fig. 6.56, in which all the phase currents are controlled as sinusoidal as possible. According to the aforementioned analyses, the voltages ripples for the shaping rotor are much smoother compared with the original one, which can also be reflected from the comparison with predictions shown in Fig. 6.57. The smaller voltage distortion is also influenced in the torque speed characteristics, Fig. 6.58. Due to less voltage distortion ratio, the peak voltages of the shaping rotor are more closed to the fundamental voltages, which make the real torque speed curve closer to the ideal curve predicted by fundamental voltage. Overall, the experimental results agree with the predictions.

(a) Stator

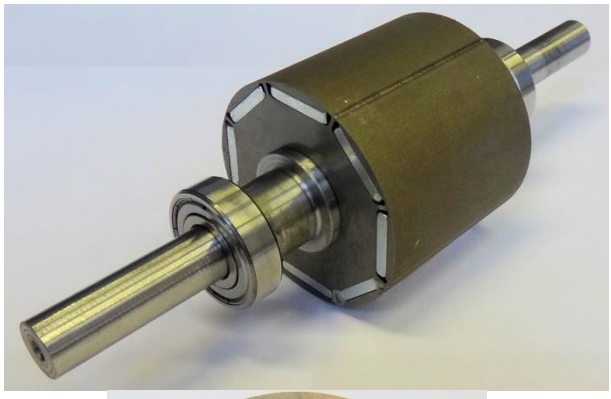

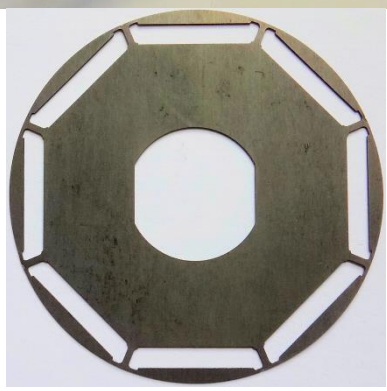

(b) Original rotor

(c) Shaping rotor

Fig. 6.52 Prototype photos.

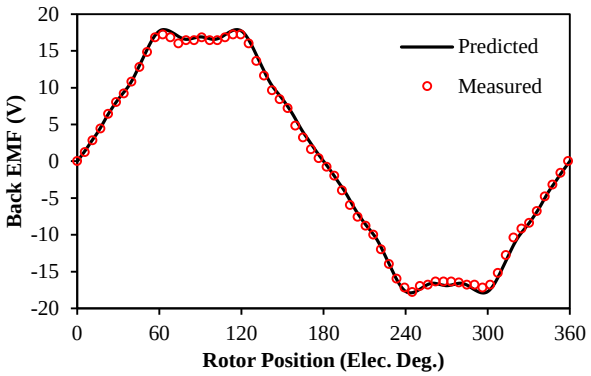

(a) Waveforms, Original

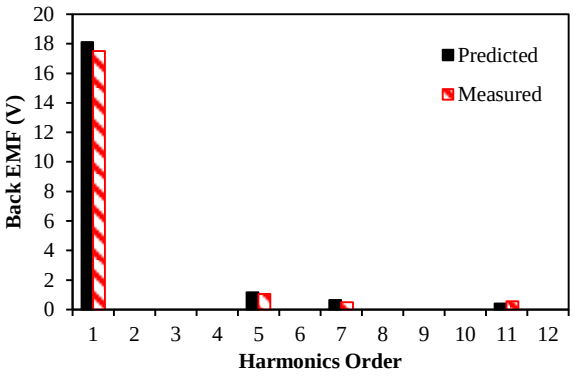

(b) Harmonics, Original

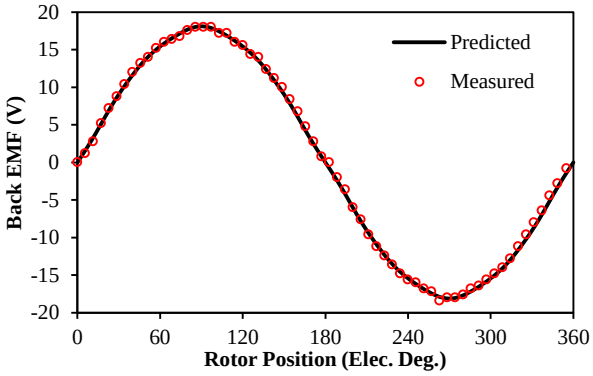

(c) Waveforms, Shaping

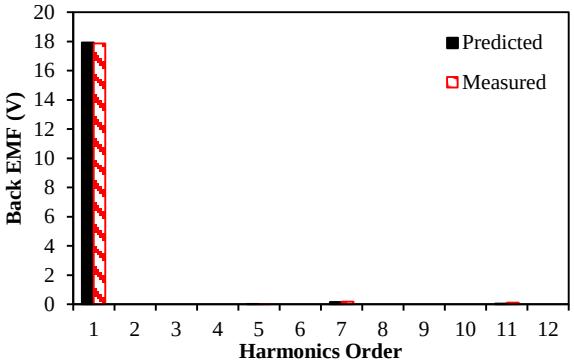

(d) Harmonics, Shaping

Fig. 6.53 Comparison of measured and predicted open-circuit back-EMFs (400rpm).

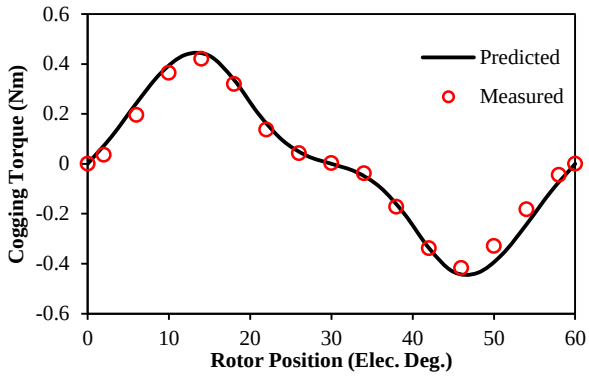

(a) Original rotor

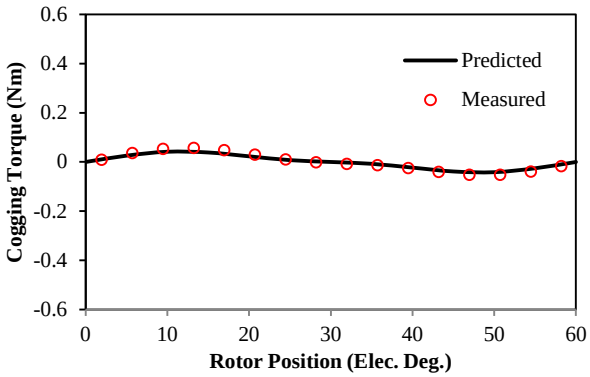

(b) Shaping rotor

Fig. 6.54 Comparison of measured and predicted cogging torques.

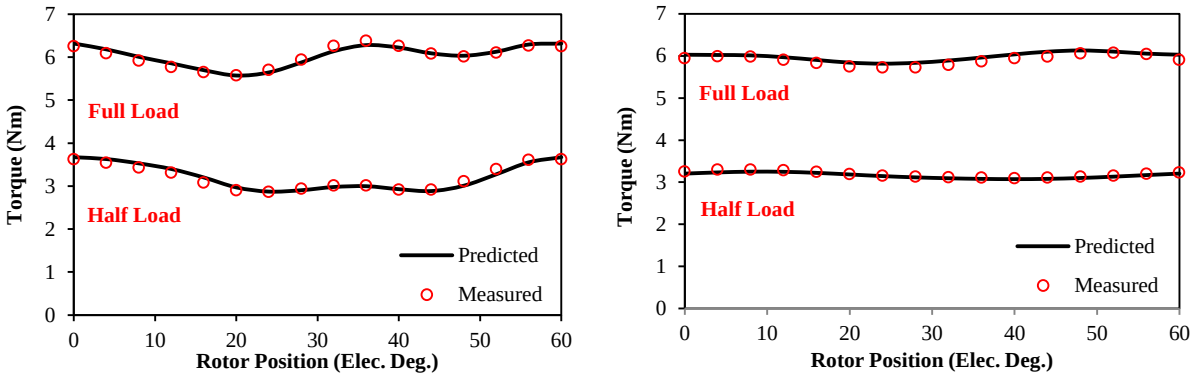

(a) Original rotor (b) Shaping rotor

Fig. 6.55 Comparison of measured and predicted torque waveforms (I_{max}=10A, β=0°).

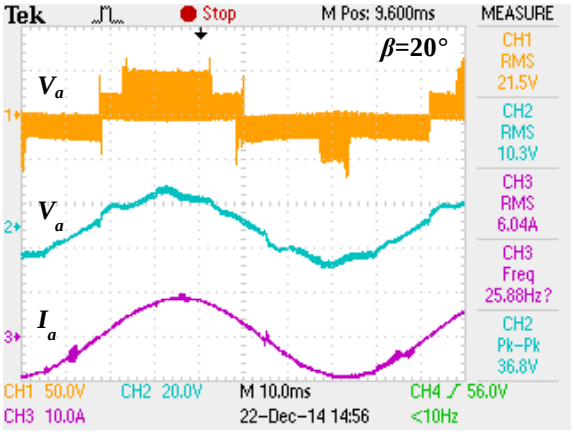

(a) Original, β=20°

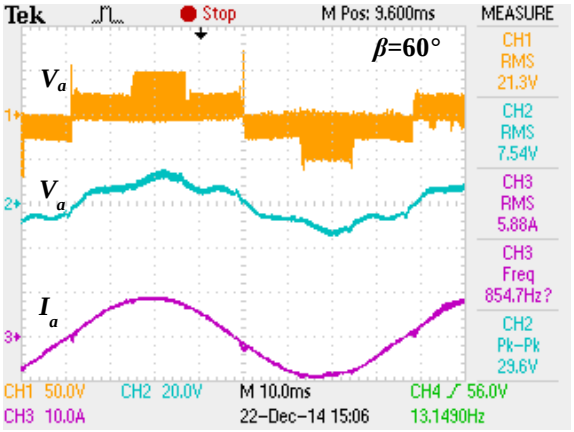

(b) Original, β=60°

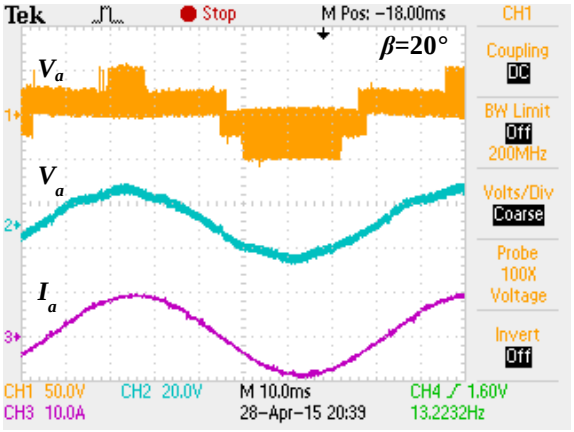

(c) Shaping, β=20°

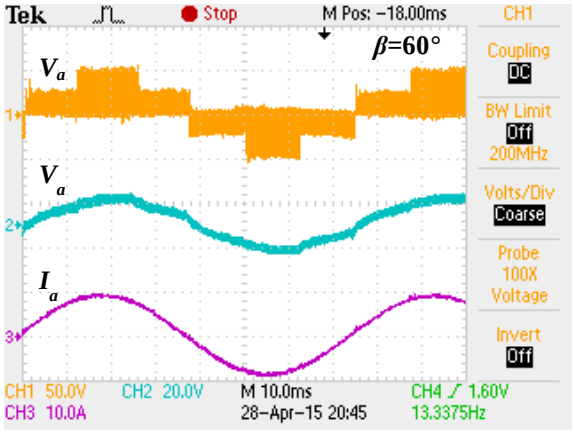

(d) Shaping, β=60°

Fig. 6.56 Comparison of measured on-load terminal voltages (I_{max}=9A, 200rpm, U_{DC}=80V).

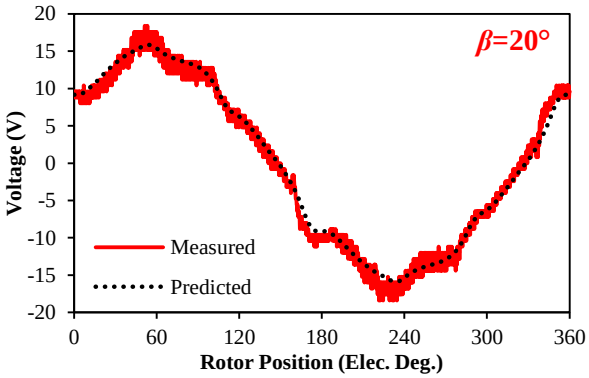

(a) Original, β=20°

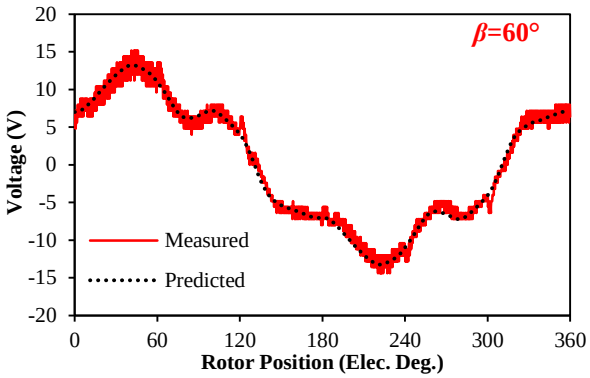

(b) Original, β=60°

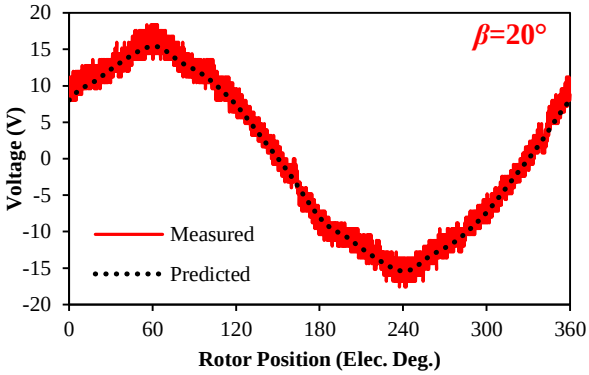

(c) Shaping, β=20°

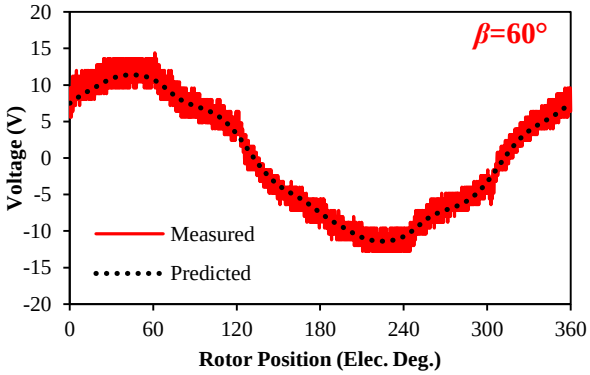

(d) Shaping, β=60°

Fig. 6.57 Comparison of measured and predicted on-load terminal voltages (I_{max}=9A, 200rpm, U_{DC}=80V).

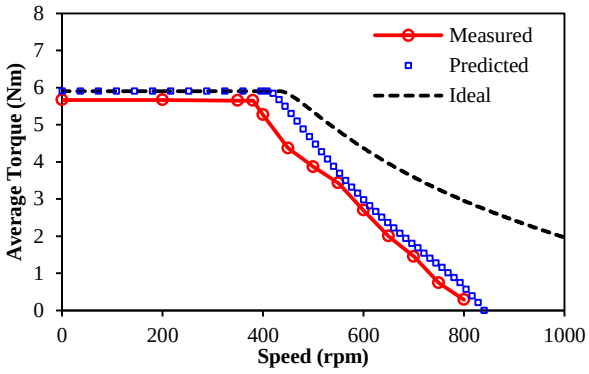

(a) Original rotor

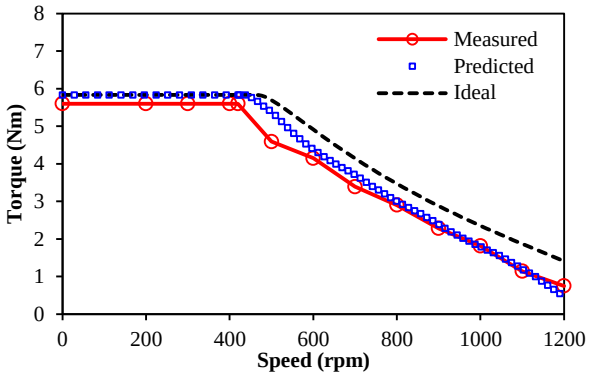

(b) Shaping rotor

Fig. 6.58 Comparison of torque speed characteristics for different rotors (I_{max}=9A, U_{DC}=48V).

6.5 Summary

The aforementioned four chapters have illustrated the influences of local magnetic saturation and voltage distortion in both SPM and IPM machines. Thus, the voltage distortion should be

paid enough attention during the design stage. This chapter investigates the effectiveness of several methods to reduce the voltage distortion. It is found that both rotor skewing and non-uniform airgap are not ideal methods to eliminate the voltage distortion in SPM machines with small and closed slot opening, since the local saturation in tooth-tips still exist. Therefore, the most essential method for SPM machine is the proper slot opening design. However, the increasing of slot opening width will lose many advantages contributed by small and closed slot opening designs, such as small cogging torque and back-EMF harmonics, good flux weakening performance, etc. Thus, it needs a careful design trade-off according to the machine most frequently operation condition. On the other hand, rotor skewing can reduce the *VDR* of IPM machine, but the less reduction of *THD* shows rotor segmentation effect has not been alleviated. In order to release the rotor segmentation effect, non-uniform airgap methods, e.g. rotor shaping and stator tooth-tip shaping, are investigated, which show effectiveness to reduce both *VDR* and *THD* of the terminal voltages at the same time. Finally, the experiments of the prototype SPM and IPM machines validate the analysis results.

CHAPTER 7

GENERAL CONCLUSIONS AND FUTURE WORKS

7.1 General Conclusions

7.1.1 Mechanism of On-Load Terminal Voltage Distortion in FSCW SPM and IPM Machines

For SPM machines with small or closed slot opening design, the local magnetic saturation in the tooth-tips could not be ignored. When the direction of resultant *tooth-tip leakage* flux reverses, the local magnetic saturation also changes significantly. This change generates the distortion of both PM and armature reaction flux linkages, and leads to terminal voltage distortion especially around β=0°. With the increase of β, the armature and PM tooth-tip leakage fluxes cross zero at different time, which reduces the amplitude of voltage ripples.

If IPM machines adopting small or closed slot opening design, they also suffer from the terminal voltage distortion around β=0° due to the same reason as that in SPM machines. Although larger slot opening may reduce the tooth-tip leakage flux compared with closed slot design, the high permeance rotor in IPM machines still retains relative high tooth-tip leakage fluxes, which leads to the voltage distortion around β=0°. Nevertheless, due to the geometric feature of IPM rotor topology, the rotor lamination regions are separated by saturated ribs and air flux barriers, which influence both main and leakage flux paths, and can be designated as *rotor segmentation effect*. Since the rotor segmentation effect mainly influences the *d*-axis armature reaction, the most significant voltage distortion in IPM machines will appear when β approaches 90°, which is opposite to the voltage distortion caused by tooth-tip leakage fluxes. Overall, the voltage distortion levels according to different origins could be summarized in Fig. 7.1.

It is worth mentioning that all the investigations are carried out based on the fixed airgap length. With the increase of airgap length, the rotor PM leakage fluxes will less influence the local magnetic saturation of tooth-tips, which reduces the voltage distortion level for SPM machines. Nevertheless, since the increasing of airgap length will alleviate the influence of rotor segmentation effect, it will consequently result in smaller voltage distortion level for IPM machines.

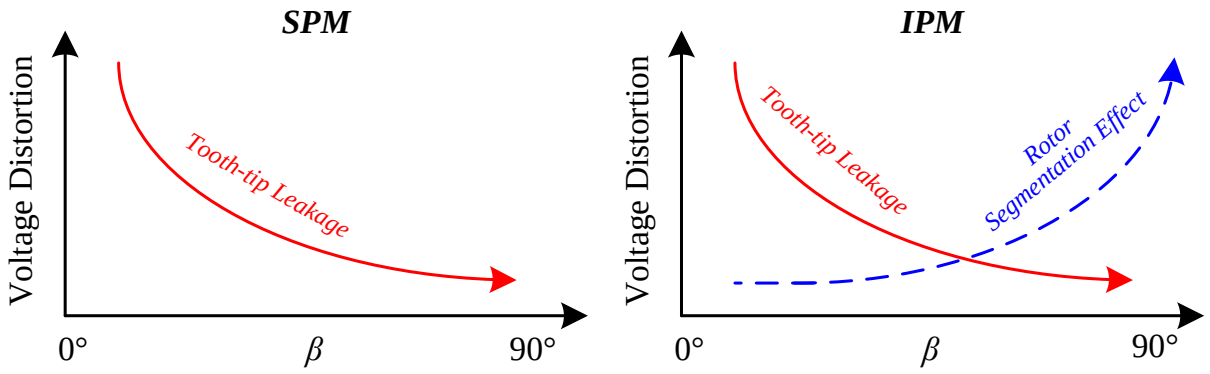

(a) SPM (b) IPM

Fig. 7.1 Summary of mechanisms for terminal voltage distortions in SPM and IPM machines.

7.1.2 Influence of Slot and Pole Number Combinations on Voltage Distortion in FSCW SPM and IPM Machines

Eight typical $N_s/2p$ combinations for both SPM and IPM machines are investigated and compared in this thesis, as summarized in Fig. 7.2. All fractional slot SPM machines obtain higher voltage distortion levels than integer slot SPM machines especially when $q \geq 2$, Fig. 7.2(a). On the contrary, all fractional slot IPM machines suffer less voltage distortion than integer slot IPM machines especially when $q=1$, Fig. 7.2(b). If only considering FSCW machines, the comparison results could be summarized in Fig. 7.3. For both FSCW SPM and IPM machines appearing in pairs, the ones with $N_s>2p$ always have less voltage distortion than their counterparts with $N_s<2p$. Overall, $2p=N_s-2$ machines, e.g. 12-slot/10-pole machines, have the least terminal voltage distortion for both IPM and SPM designs. Meanwhile, the machines suffer more from voltage distortion will have more ripples or higher fluctuation of on-load back-EMF, on-load cogging torque, dq-axis inductances, torque ripple, iron loss, while the torque speed characteristics will be more deteriorated from the ideal curves calculated by the fundamental voltage only.

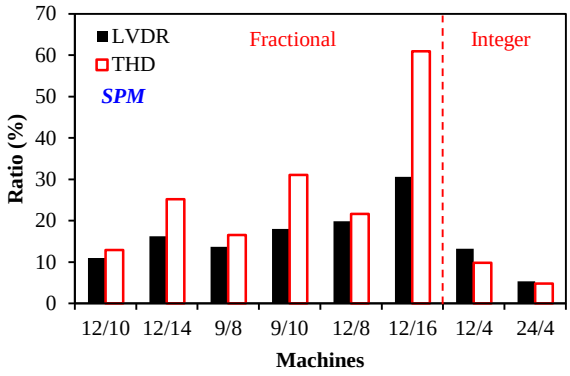

(a) SPM, I_{max}=10A, β=0°

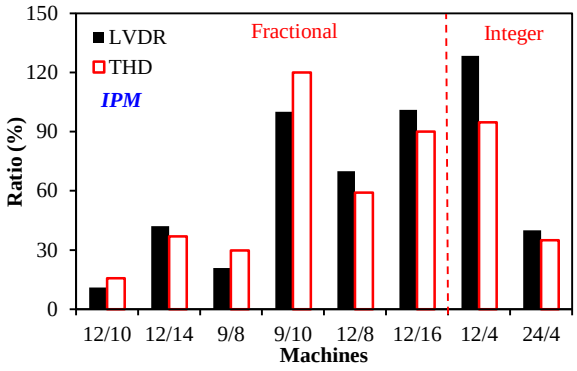

(b) IPM, I_{max}=10A, β=90°

Fig. 7.2 Comparison of influences of $N_s/2p$ combinations on all SPM and IPM machines.

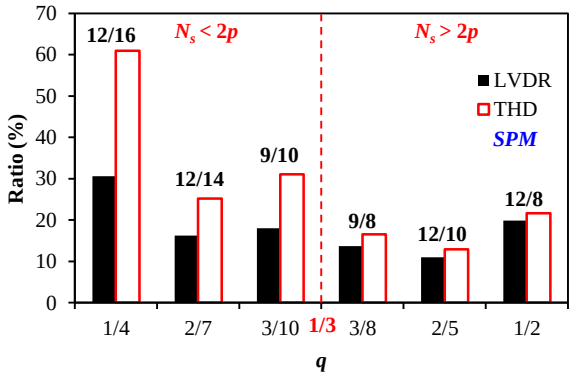

(a) SPM, β=0°

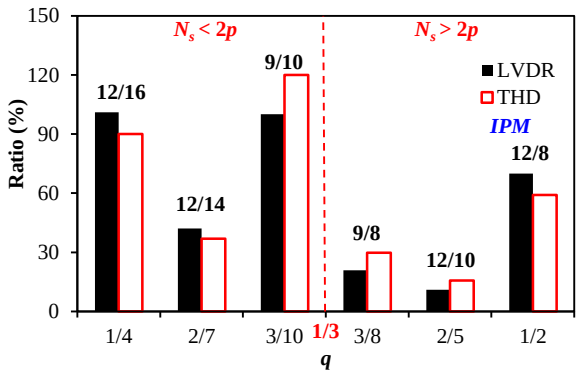

(b) IPM, β=90°

Fig. 7.3 Comparison of influences of $N_s/2p$ combinations on FSCW SPM and IPM machines.

7.1.3 Voltage Distortion Minimization Methods

Both rotor skewing and non-uniform airgap are not ideal methods to eliminate the voltage distortion in SPM machines with small and closed slot opening, since the local saturation in tooth-tip still exists. Therefore, the most appropriate method for SPM machine is the proper slot opening design. However, the increasing of slot opening width will loss many advantages of small and closed slot opening designs, such as small cogging torque and back-EMF harmonics, good flux weakening performance, etc. Thus, it needs a careful design trade-off according to the machine most frequent operation condition. On the other hand, rotor skewing can reduce *VDR* of IPM machines, but the less reduction of *THD* shows rotor segmentation effect will not be alleviated. In order to release the rotor segmentation effect, non-uniform airgap methods, e.g. rotor shaping and stator tooth-tip shaping, are investigated, which are shown to be effective to reduce both *VDR* and *THD* of the terminal voltages at the same time.

7.2 Future Works

Due to time limit, more investigations could be carried out in the future as follows:

- Using control methods to eliminate the influence of voltage distortion to improve the flux weakening performance, such as open-winding control method.

- Investigating the influence of 3D effect on terminal voltage distortion, particularly for the machines with large diameter but short axial length.

- Investigating the influence of manufacturing tolerance on terminal voltage distortion.

- Investigating the terminal voltage distortion and its influences for other special BLAC machine types, such as synchronous reluctance machine, switched flux machine, etc.

- Investigating the voltage distortion and its influences for machines under BLDC operation.

REFERENCES

[AKA07] K. Akatsu, M. C. Harke, and R. D. Lorenz, "SPMSM design considerations for initial position and magnet polarity estimation using carrier signal injection," in *Proc. IEEE IAS Annual Meeting*, New Orleans, LA, Sep. 2007, pp. 2393-2398.

[AKI03] H. Akita, Y. Nakahara, N. Miyake, and T. Oikawa, "New core structure and manufacturing method for high efficiency of permanent magnet motors," in *Conf. Rec. IEEE IAS Annu. Meet.*, Salt Lake City, U.S., Oct. 2003, pp. 367-372.

[ALB12] L. Alberti, E. Fornasiero, and N. Bianchi, "Impact of the rotor yoke geometry on rotor losses in permanent magnet machines," *IEEE Trans. Ind. Appl.*, vol. 48, no. 1, pp. 98-105, Jan./Feb. 2012.

[ALB13] L. Alterti, and N. Bianchi, "Theory and design of fractional-slot multilayer windings," *IEEE Trans. Ind. Appl.*, vol. 49, no. 2, pp. 841-849, Mar./Apr. 2013.

[AZA12] Z. Azar, Z. Q. Zhu, and G. Ombach, "Influence of electric loading and magnetic saturation on cogging torque, back-EMF and torque ripple of PM machines," *IEEE Trans. Magn.*, vol. 48, no. 10, pp. 2650-2658, Oct. 2012.

[AZA12a] Z. Azar, Z. Q. Zhu, and G. Ombach, "Investigation of torque speed characteristics and cogging torque of fractional-slot IPM brushless AC machines having alternative slot openings," *IEEE Trans. Ind. Appl.*, vol. 48, no. 3, pp. 903-912, May/Jun. 2012.

[BAR12] M. Barcaro, N. Bianchi, and F. Magnussen, "Permanent-magnet optimization in permanent-magnet-assisted synchronous reluctance motor for a wide constant-power speed range," *IEEE Trans. Ind. Electron.*, vol. 59, no. 6, pp. 2495-2502, Jun.2012.

[BIA98] N. Bianchi, and S. Bolognani, "Magnetic models of saturated interior permanent magnet motors based on finite element analysis," in *IEEE IAS Annu. Meet.*, St. Louis, U.S., Oct. 1998, pp. 27-34.

[BIA02] N. Bianchi, and S. Bolognani, "Design techniques for reducing the cogging torque in surface-mounted PM motors," *IEEE Trans. Ind. Appl.*, vol. 38, no. 5, pp. 1259-1265, Sep./Oct. 2002.

[BIA06] N. Bianchi, S. Bolognani, and P. Frare, "Design criteria for high-efficiency SPM synchronous motors," *IEEE Trans. Energy Convers.*, vol. 21, no. 2, pp. 396-404, Jun. 2006.

[BIA06a] N. Bianchi, S. Bolognani, M. D. Pre, and G. Grezzani, "Design considerations for fractional-slot winding configurations of synchronous machines," *IEEE Trans. Ind. Appl.*, vol. 42, no. 4, pp. 997-1006, Jul./Aug. 2006.

[BIA08] N. Bianchi, S. Bolognani, and M. D. Pre, "Magnetic loading of fractional-slot three-phase PM motors with nonoverlapped coils," *IEEE Trans. Ind. Appl.*, vol.

44, no. 5, pp. 1513-1521, Sep./Oct. 2008.

[BIA10] N. Bianchi, S. Bolognani, and E. Fornasiero, "An overview of rotor losses determination in three-phase fractional-slot PM machines," *IEEE Trans. Ind. Appl.*, vol. 46, no. 6, pp. 2338-2345, Nov./Dec. 20110.

[BOA14] B. Boazzo, G. Pellegrino, and A. Vagati, "Multipolar SPM machines for direct-drive application: a general design approach," *IEEE Trans. Ind. Appl.*, vol. 50, no. 1, pp. 327-337, Jan./Feb. 2014.

[BOU12] K. Boughrara, R. Ibtiouen, and T. Lubin, "Analytical prediction of magnetic field in parallel double excitation and spoke-type permanent-magnet machines accounting for tooth-tips and shape of polar pieces," *IEEE Trans. Magn.*, vol. 48, no. 7, pp. 2121-2137, Jul. 2012.

[CAL38] J. F. Calvert, "Amplitudes of magnetomotive force harmonics for fractional slot windings-I," *Trans. AIEE*, vol. 57, no. 2, pp. 777-785, Dec. 1938.

[CAR89] R. Carlson, A. Tavares, J. Bastons, and M. Lajoie-Mazenc, "Torque ripple attenuation in permanent magnet synchronous motors," in *Rec. IEEE Ind. Appl. Soc. Annu. Meet.*, San Diego, CA, Oct. 1989, pp. 57-62.

[CAS09] B. N. Cassimere, and S. D. Sudhoff, "Population-based design of surface-mounted permanent-magnet synchronous machines," *IEEE Trans. Energy Convers.*, vol. 24, no. 2, pp. 338-346, Jun. 2009.

[CHE03] Z. Chen, M. Tomita, S. Doki, and S. Okuma, "An extended electromotive force model for sensorless control of interior permanent-magnet synchronous motor," *IEEE Trans. Ind. Electron.*, vol. 50, no. 2, pp. 288-295, Apr. 2003.

[CHE06] Y. S. Chen, Z. Q. Zhu, and D. Howe, "Vibration of PM brushless machines having a fractional number of slots per pole," *IEEE Trans. Magn.*, vol. 42, no. 10, pp. 3395-3397, Oct. 2006.

[CHE10] H. S. Chen, D. G. Dorrell, and M. C. Tsai, "Design and operation of interior permanent-magnet motors with two axial segments and high rotor saliency," *IEEE Trans. Magn.*, vol. 46, no, 9, pp. 3664-3657, Sep. 2010.

[CHO99] H. S. Cho, H. R. Cho, and H. S. Lee, "Effect of pole and slot number ratio on back-EMF constant of BLDC motor with nonoverlapping stator winding," in *Int. Conf. Electric Machines and Drives*, Seattle, U.S., May 1999, pp. 54-56.

[CHO09] L. Chong, and M. F. Rahman, "Saliency ratio derivation and optimization for an interior permanent magnet machine with concentrated windings using finite-element analysis," *IET Trans. Electric Power Appl.*, vol. 4, no. 4, pp. 249-258, Apr. 2010.

[CHO10] J. H. Choi, Y. D. Chun, P. W. Han, M. J. Kim, D. H. Koo, J. Lee and J. S. Chun, "Design of high power permanent magnet motor with segment rectangular copper wire and closed slot opening on electric vehicles," *IEEE Trans. Magn.*, vol. 46, no. 9, pp. 3701-3704, Sep. 2010.

[CHO13] M. Chowdhury, A. Gebregergis, M. Islam, and T. Sebastian, "Analysis of harmonic contents in induced voltage and electromagnetic torque in interior permanent magnet synchronous machines under load condition," in *Proc. Int. Electric Mach. And Drives Conf.*, Chicago, IL, May 2013, pp. 260-267.

[CHU13] W. Q. Chu, and Z. Q. Zhu, "On-load cogging torque calculation in permanent magnet machines," *IEEE Trans. Magn.*, vol. 49, no. 6, pp. 2982-2989, Jun. 2013.

[CHU13a] W. Q. Chu, and Z. Q. Zhu, "Average torque separation in permanent magnet synchronous machines using frozen permeability," *IEEE Trans. Magn.*, vol. 49, no. 3, pp. 1202-1210, Mar. 2013.

[CHU13b] W. Q. Chu, and Z. Q. Zhu, "Investigation of torque ripples in permanent magnet synchronous machines with skewing," *IEEE Trans. Magn.*, vol. 49, no. 3, pp. 1211-1220, Mar. 2013.

[CHU13c] W. Q. Chu, and Z. Q. Zhu, "Reduction of on-load torque ripples in permanent magnet synchronous machines by improved skewing," *IEEE Trans. Magn.*, vol. 49, no. 7, pp 3822-3825, Jul. 2013.

[COR98] M. J. Corley, and R. D. Lorenz, "Rotor position and velocity estimation for a salient-pole permanent magnet synchronous machine at standstill and high speeds," *IEEE Ind. Appl.*, vol. 34, no.4, pp. 784-789, Jul./Aug. 1998.

[CRO02] J. Cros, and P. Viarouge, "Synthesis of high performance PM motors with concentrated windings," *IEEE Trans. Energy Convers.*, vol. 17, no. 2, pp. 248-253, Jun. 2002.

[CVE08] G. Cvetkovski, and L. Petkovska, "Performance improvement of PM synchronous motor by using soft magnetic composite material," *IEEE Trans. Magn.*, vol. 44, no. 11, pp. 3812-3815, Nov. 2008.

[DAJ12] G. Dajaku, and D. Gerling, "A novel 12-teeth/10-poles PM machine with flux barriers in stator yoke," in *Int. Conf. Elect. Mach.*, Ontario, Canada, May 2011, pp. 65-70.

[DAJ12a] G. Dajaku, and D. Gerling, "Low cost and high efficiency electric machines," in *Proc. Elect. Drives Production Conf.*, Nuremberg, Germany, Oct. 2012, pp. 1-7.

[DEL89] J. De La Ree, and N. Boules, "Torque production in permanent-magnet synchronous motors," *IEEE. Trans. Ind. Appl.*, vol. 25, no. 1, pp. 107-112, Jan./Feb. 1989.

[DEO96] R. P. Deodhar, D. A. Staton, T. M. Jahns, and T. J. E. Miller, "Prediction of cogging torque using the flux-MMF diagram techniques," *IEEE Trans. Ind. Appl.*, vol. 32, no. 3, pp. 569-576, May/Jun. 1996.

[DOG11] H. Dogan, F. Wurtz, A. Foggia, and L. Garbuio, "Performance analysis and comparison of three IPMSM with high homopolar inductance for electric vehicle applications," in *Proc. Euro. Conf. Pow. Electron. Appl.*, Birmingham,

U.K., Aug. 2011, pp. 1-10.

[DON12] G. D. Donato, F. G. Capponi, and F. Caricchi, "No-load performance of axial flux permanent magnet machines mounting magnetic wedges," *IEEE Trans. Ind. Electron.*, vol. 59, no. 10, pp. 3768-3779, Oct. 2012.

[DUT08] R. Dutta, and M. F. Rahman, "Design and analysis of an interior permanent magnet machine with very wide constant power operation range," *IEEE Trans. Energy Convers.*, vol. 23, no. 1, pp. 25-33, Mar. 2008.

[DUT12] R. Dutta, M. F. Rahman, and L. Chong, "Winding inductances of an interior permanent magnet machine with fractional slot concentrated winding," *IEEE Trans. Magn.*, vol. 48, no. 12, pp. 4842-4849, Dec. 2012.

[ELR05] A. M. El-Refaie, and T. M. Jahns, "Optimal flux weakening in surface PM machines using fractional-slot concentrated windings," *IEEE Trans. Ind. Appl.*, vol. 41, no. 3, pp. 790-800, May/Jun. 2005.

[ELR06] A. M. El-Refaie, T. M. Jahns, P. J. McCleer, and J. W. McKeever, "Experimental verification of optimal flux weakening in surface PM machines using concentrated windings," *IEEE Trans. Ind. Appl.*, vol. 42, no. 2, pp. 443-453, Mar./Apr. 2006.

[ELR06a] A. M. El-Refaie, and T. M. Jahns, "Scalability of surface PM machines with concentrated windings designed to achieve wide speed ranges of constant-power operation," *IEEE Trans. Energy Convers.*, vol. 21, no. 2, pp. 362-369.

[ELR08] A. M. El-Refaie, Z. Q. Zhu, T. M. Jahns, and D. Howe, "Winding inductances of fractional slot surface-mounted permanent magnet brushless machines," in *Proc. IEEE IAS Annu. Meeting*, Edmonton, Alta, Oct. 2008, pp. 1-8.

[ELR10] A. M. El-Refaie, "Fractional-slot concentrated-windings synchronous permanent magnet machines: opportunities and challenges," *IEEE Trans. Ind. Electron.*, vol. 57, no. 1, pp. 107-121, Jan. 2010.

[ELR14] A. M. El-Refaie, J. P. Alexander, S. Galioto, P. B. Reddy, K. K. Huh, P. de Bock, and X. Shen, "Advanced high-power-density interior permanent magnet motor for traction applications," *IEEE Trans. Ind. Appl.*, vol. 50, no. 5, pp. 3235-3248, Sep./Oct., 2014.

[EVA10] S. A. Evans, "Salient pole shoe shapes of interior permanent magnet synchronous machines," in *Proc. Int. Conf. Electrical Machines*, Rome, Italy, Sep. 2010, pp. 1-6.

[FAG13] A. Faggion, E. Fornasiero, N. Bianchi, and S. Bolognani, "Sensorless capability of fractional-slot surface-mounted PM motors," *IEEE Trans. Ind. Appl.*, vol. 49, no.3, pp. 1325-1332, May/Jun. 2013.

[FOR12] E. Fornasiero, N. Bianchi, and S. Bolognani, "Slot harmonic impact on rotor losses in fractional-slot permanent-magnet machines," *IEEE Trans. Ind. Electron.*, vol. 59, no. 6, pp. 2557-2564, Jun. 2012.

[FUL05] M. Fulczyk, and R. Mydlikowski, "Influence of generator load conditions on third-harmonic voltages in generator stator winding," *IEEE Trans. Energy Convers.*, vol. 20, no. 1, pp. 158-165, Mar. 2005.

[GAN00] J. Gan, K. T. Chau, C. C. Chan, and J. Z. Jiang, "A new surface-inset permanent magnet brushless DC motor drive for electric vehicles," *IEEE Trans. Magn.*, vol. 36, no. 5, pp. 3810-3818, Sep. 2009.

[GON11] L. M. Gong, and Z. Q. Zhu, "A novel method for compensating inverter nonlinearity effects in carrier signal injection-based sensorless control from positive-sequence carrier current distortion," *IEEE. Trans. Ind. Appl.*, vol. 47, no. 3, pp. 1283-1292, May/Jun. 2011.

[HA08] J. I. Ha, "Analysis of inherent magnetic position sensors in symmetric AC machines for zero or low speed sensorless drives," *IEEE Trans. Magn.*, vol. 44, no. 12, pp. 4689-4696, Dec. 2008.

[HAL80] K. Halbach, "Design of permanent magnet multipole magnets with oriented rare earth cobalt material," *Nucl. Instrum. Methods*, vol. 169, pp. 1-10, 1980.

[HAN07] S. H. Han, T. M. Jahns, and W. L. Soong, "A magnetic circuit model for an IPM synchronous machine incorporating moving airgap and cross-coupled saturation effects," in *Proc. Int. Electric Mach. And Drives Conf.*, Antalya, Turkey, May 2007, pp. 21-26.

[HAN10] S. H. Han, T. M. Jahns, and Z. Q. Zhu, "Design tradeoffs between stator core loss and torque ripple in IPM machines," *IEEE Trans. Ind. Appl.*, vol. 46, no. 1, pp. 187-195, Jan./Feb. 2010.

[HEN94] J. R. Hendershot, and T. J. E. Miller, *Design of brushless permanent magnet motors*, Oxford, U.K., Magna Physics & Clarendon Press, 1994.

[HOA86] L. H. Hoang, R. Perret, and R. Feuillet, "Minimization of torque ripple in brushless DC motor drives," *IEEE Trans. Ind. Appl.*, vol. IA-22, no. 4, pp. 748-755, JUL 1986.

[HSI05] M. F. Hsieh, and Y. S. Hsu, "An investigation on influence of magnet arc shaping upon back electromotive force waveforms for design of permanent magnet brushless motors," *IEEE Trans. Magn.*, vol. 41, no. 10, pp. 3949-3951, Mar. 2005.

[HUT05] G. Huth, "Permanent-magnet-excited AC servo motors in tooth-coil technology," *IEEE Trans. Energy Convers.*, vol. 20, no. 2, pp. 300-307, Jun. 2005

[HWA10] S. H. Hwang, and J. M. Kim, "Dead time compensation method for voltage-fed PWM inverter," *IEEE Trans. Energy Convers.*, vol. 25, no. 1, pp. 1-10, Mar. 2010.

[ISH05] D. Ishak, Z. Q. Zhu, and D. Howe, "Eddy-current loss in the rotor magnets of permanent-magnet brushless machines having a fractional number of slots per

pole," *IEEE Trans. Magn.*, vol. 41, no. 9, pp. 2462-2469, Sep. 2005.

[ISH05a] D. Ishak, Z. Q. Zhu, and D. Howe, "Permanent magnet brushless machines with unequal tooth widths and similar slot and pole numbers," *IEEE Trans. Ind. Appl.*, vol. 41, no. 2, pp. 584-590, Mar./Apr. 2005.

[ISH05b] D. Ishak, Z. Q. Zhu, and D. Howe, "Unbalanced magnetic forces in permanent magnet brushless machines with diametrically asymmetric phase windings," in *Proc. IAS Annu. Meet.*, Oct. 2005, pp. 1037-1043.

[ISH06] D. Ishak, Z. Q. Zhu and D. Howe, "Comparison of PM brushless motors, having either all teeth or alternate teeth wound," *IEEE Trans. Energy Convers.*, vol. 21, no. 1, pp. 95-99, Mar. 1996.

[ISL05] M. S. Islam, S. Mir., T. Sebastian, and S. Underwood, "Design consideration of sinusoidal excited permanent-magnet machines for low-torque-ripple applications," *IEEE Trans. Ind. Appl.*, vol. 41, no. 4, pp. 955-962, Jul./Aug. 2005.

[ISL09] R. Islam, I. Husain, A. Fardoun, and K. McLaughlin, "Permanent-magnet synchronous motor magnet designs with skewing for torque ripple and cogging torque reduction," *IEEE Trans. Ind. Appl.*, vol. 45, no. 1, pp. 152-160, Jan./Feb. 2009.

[JAH84] T. M. Jahns, "Torque production in permanent magnet synchronous motor drives with rectangular current excitation," *IEEE Trans. Ind. Appl.*, vol. IA-20, no. 4, pp. 803-813, Jul. 1984.

[JAH86] T. M. Jahns, G. B. Kliman, and T. Neumann, "Interior permanent-magnet synchronous motors for adjustable-speed drives," *IEEE Trans. Ind. Appl.*, vol. IA-22, No. 4, pp. 738-747, Jul./Aug. 1986.

[JAH87] T. M. Jahns, "Flux-weakening regime operation of an interior permanent magnet synchronous motor drive," *IEEE Trans. Ind. Appl.*, vol. 23, no. 4, pp. 681-689, Jul./Aug. 1987.

[JAH96] T. M. Jahns, and W. L. Soong, "Pulsating torque minimization techniques for permanent magnet AC motor drives- a review," *IEEE Trans. Ind. Electron.*, vol. 43, no. 2, pp. 321-330, Apr. 1996.

[JAK00] A. G. Jack, B. C. Mecrow, P. G. Dickinson, D. Stephenson, J. S. Burdess, N. Fawcett, and J. Evans, "Permanent magnet machines with powdered iron cores and pressed windings," *IEEE Trans. Ind. Appl.*, vol. 36, no. 4, pp. 1077-1084, Jul./Aug. 2000.

[JSO14] JSOL Coporation, *JMAG Designer-14 User Help*, Tokyo, Japan, 2014.

[JUN10] J. Junak, and G. Ombach, "Performance optimization of the brushless motor with IPM rotor for automotive applications," in *Proc. Int. Conf. Electrical Machines*, Rome, Italy, Sep. 2010, pp. 1-5

[KIM97] J. M. Kim, and S. K. Sul, “Speed control of interior permanent magnet synchronous motor drive for the flux weakening operation,” *IEEE Trans. Ind. Appl.*, vol. 33, no. 1, pp. 43-38, Jan./Feb. 1997.

[KIM03] D. H. Kim, I. H. Park, J. H. Lee, and C. E. Kim, “Optimal shape design of iron core to reduce cogging torque of IPM motor,” *IEEE Trans. Magn.*, vol. 39, no. 3, pp. 1456-1459.

[KIM05] H. W. Kim, M. J. Youn, and K. Y. Cho, “New voltage distortion observer of PWM VSI for PMSM,” *IEEE Trans. Ind. Electron.*, vol. 52, pp. 4, pp. 1188-1192, Aug. 2005.

[KIM07] K. C. Kim, D. H. Koo, J. P. Hong, and J. Lee, “A study on the characteristics due to pole-arc to pole-pitch ration and saliency to improve torque performance of IPMSM,” *IEEE Trans. Magn.*, vol. 43, no. 6, pp. 2516-2518, Jun. 2007.

[KIM09] K. C. Kim, K. Kim, H. Kim, and J. Lee, “Demagnetization analysis of permanent magnets according to rotor type of interior permanent magnet synchronous motor,” *IEEE Trans. Magn.*, vol. 45, no. 6, pp. 2799-2802, Jun. 2009.

[KIM14] W. Kim, M. Kim, K. Lee, J. Lee, J. Han, T. Jeong, S. Cho, and J. Lee, “Inductance Calculation in IPMSM considering magnetic saturation,” *IEEE Trans. Magn.*, vol. 50, no. 1, pp. 1-4, Jan. 2014.

[KIM14a] H. J. Kim, D. J. Kim, and J. P. Hong, “Characteristic analysis for concentrated multi-layer winding machine with optimal turn ratio,” *IEEE Trans. Magn.*, vol. 50, no. 2, pp. 1-4, Feb. 2014.

[KO04] H. S. Ko, and K. J. Kim, “Characterization of noise and vibration sources in interior permanent-magnet brushless DC motors,” *IEEE Trans. Magn.*, vol. 40, no. 6, pp. 3482-3489, Nov. 2004.

[LEE61] C. H. Lee, “Saturation harmonics of polyphase induction machines,” *Trans. AIEE*, vol. 80, pp. 597-603, Oct. 1961.

[LEE11] H. W. Lee, K. D. Lee, W. H. Kim, I. S. Jang, M. J. Kim, J. J. Lee, and J. Lee, “Parameter design of IPMSM with concentrated winding considering partial magnetic saturation,” *IEEE Trans. Magn.*, vol. 47, no. 10, pp. 3653-3656, Oct. 2011.

[LI88] T. Li, and G. Slemon, “Reduction of cogging torque in permanent magnet motors,” *IEEE Trans. Magn.*, vol. 24, no. 6, pp. 2901-2903, Nov. 1988.

[LI08] Y. Li, J. W. Xing, T. B. Wang, and Y. P. Lu, “Programmable design of magnet shape for permanent magnet synchronous motors with sinusoidal back EMF waveforms,” *IEEE Trans. Magn.*, vol. 44, no. 9, pp. 2163-2167, Sep. 2008.

[LI13] Q. Li, T. Fan, and X. Wen, “Armature-reaction magnetic field analysis for interior permanent magnet motor based on winding function theory,” *IEEE Trans. Magn.*, vol. 49, no. 3, pp. 1193-1201, Mar. 2013.

[LI14] G. J. Li, Z. Q. Zhu, W. Q. Chu, M. P. Foster, and D. Stone, "Influence of flux gaps on electromagnetic performance of novel modular PM machines," *IEEE Trans. Energy Convers.*, vol. 29, no. 3, pp. 716-726.

[LIP04] T. A. Lipo, *Introduction to AC machine design*, Madison, U.S., University of Wisconsin, 2004

[LIU05] Y. Liu, Z. Q. Zhu, and D. Howe, "Direct torque control of brushless DC drives with reduced torque ripple," *IEEE Trans. Ind. Appl.*, vol. 41, no. 2, pp. 599-608, Mar./Apr. 2005.

[MAG05] F. Magnussen, and H. Lendenmann, "Parasitic effects in PM machines with concentrated windings," *IEEE Trans. Ind. Appl.*, vol. 43, no. 5, pp. 1223-1232, Sep./Oct. 2007.

[MEI08] F. Meier, and J. Soulard, "Analysis of flux measurements on a PMSM with non-overlapping concentrated windings," in *Proc. IEEE IAS Annual Meeting*, Edmonton, Alta, Oct. 2008, pp. 1-8.

[MIL92] T. J. E. Miller, *Switched reluctance motors and their control*, Oxford, U.K., Oxford Science Publications, 1992.

[MIT04] A. J. Mitcham, G. Antonopoulos, and J. J. A. Cullen, "Favourable slot and pole number combinations for fault-tolerant PM machines," *IEE Proc. Electric Power Appl.*, vol. 151, no. 5, pp. 520-525, Sep. 2004.

[MOM09] M. F. Momen, and S. Datta, "Analysis of flux leakage in a segmented core brushless permanent magnet motor," *IEEE Trans. Energy Convers.*, vol. 24, no. 1, pp. 77-81, Mar. 2009.

[MOR92] J. C. Moreira, and T. A. Lipo, "Modeling of saturated AC machines including air gap flux harmonics components," *IEEE Trans. Ind. Appl.*, vol. 28, no. 2, pp. 343-349, Mar./Apr. 1992.

[MOR94] S. Morimoto, M. Sanada, and Y. Takeda, "Wide-speed operation of interior permanent magnet synchronous motors with high-performance current regulator," *IEEE Trans. Ind. Appl.*, vol. 30, no. 4, pp. 920-926, Jul./Aug. 1994.

[MUL05] J. Muller, and R. Vollmer, "Stator for a synchronous machine," U.S. Patnet 6858965B2, Apr. 2005.

[OAK11] Oak Ridge National Laboratory, *Evaluation of the 2010 Toyota Prius hybrid synergy drive system*, Oak Ridge, U.S., Mar. 2011.

[ORL11] T. Orlik, M. Lux, and W. Schumacher, "Saturation induced harmonics in permanent magnet synchronous motors," in *Proc. Euro. Conf. Power Electron. & Appl.*, Birmingham, UK, Aug. 2011, pp. 1-9.

[PAP14] L. Papini, T. Raminosoa, D. Gerada, and C. Gerada, "A high-speed permanent-magnet machine for fault-tolerant drivetrains," *IEEE Trans. Ind. Electron.*, vol. 61, no. 6, pp. 3071-3080, Jun. 2014.

[PAR12] K. Park, G. Park, and M. Jung, “Stator and motor comprising same,” US Patent 20120112599A1, May 2012.

[PAP14] L. Papini, T. Raminosoa, D. Gerada, and C. Gerada, “A high-speed permanent-magnet machine for fault-tolerant drivetrains,” *IEEE Trans. Ind. Electron.*, vol. 61, no. 6, pp. 3071-3080, Jun. 2014.

[PAU14] G. T. de Paula, J. R. B. de A. Monteiro, T. E. P. de Almeida, M. P. de Santana, W. C. A. Pereira, and C. M. R. Oliveira, “Evaluation on surface mounted PM machine’s parameters on load conditions using frozen permeability method part II,” in *Int. Conf. on Elect. Mach.*, Berlin, Germany, Sep. 2014, pp. 1-6.

[PEL11] G. Pellegrino, A. Vagati, and P. Guglielmi, “Design tradeoffs between constant power speed range, uncontrolled generator operation, and rated current of IPM motor drives,” *IEEE Trans. Ind. Appl.*, vol. 47, no. 5, pp. 1995-2003, Sep./Oct. 2011.

[PEL12] G. Pellegrino, A. Vagati, P. Guglielmi, and B. Boazzo, “Performance comparison between surface-mounted and interior PM motor drives for electric vehicle application,” *IEEE Trans. Ind. Electron.*, vol. 59, no. 2, pp. 803-811, Feb. 2012.

[PEL12a] G. Pellegrino, A. Vagati, B. Boazzo, and P. Guglielmi, “Comparison of induction and PM synchronous motor drives for EV application including design examples,” *IEEE Trans. Ind. Appl.*, vol. 48, no. 6, pp. 2322-2332, Nov./Dec. 2012.

[PIL91] P. Pillay and R. Krishnan, “Application characteristics of permanent magnet synchronous and brushless dc motors for serve drives,” *IEEE Trans. Ind. Appl.*, vol. 22, no. 5, pp. 986-996, Sep./Oct. 1991.

[PON13] P. Ponomarev, P. Lindh, and J. Pyrhonen, “Effect of slot-and-pole combination on the leakage inductance and the performance of tooth-coil permanent magnet synchronous machines,” *IEEE Trans. Ind. Electron.*, vol. 60, no. 10, pp. 4310-4317, Oct. 2013.

[PON14] P. Ponomarev, I. Petrov, and J. Pyrhonen, “Torque ripple in double-layer 18/16 TC-PMSMs by adjusting teeth widths to minimize local saturation,” in *Proc. Int. Conf. Elect. Mach.*, Berlin, Germany, Sep. 2014, pp. 1461-1467.

[QU04] R. Qu, and T. A. Lipo, “Analysis and modelling of air-gap and zigzag leakage fluxes in a surface-mounted permanent-magnet machine,” *IEEE Trans. Ind. Appl.*, vol. 40, no.1, pp, 121-127, Jan./Feb. 2004.

[RAU10] R. Raute, C. Caruana, C. S. Staines, J. Cilia, M. Sumner, and G. M. Asher, “Analysis and compensation of inverter nonlinearity effect on a sensorless PMSM drive at very low and zero speed operation,” *IEEE Trans. Ind. Electron.*, vol.57, no.12, pp. 4065-4074, Dec. 2010.

[RED09] P. B. Reddy, and T. M. Jahns, “Modelling of stator tooth-tip iron losses in fractional-slot concentrated winding surface PM machines,” in *Proc. Energy*

Conv. Congr. Expo., San Jose, CA, Sep. 2009, pp. 1903-1910.

[RED12] P. B. Reddy, A. M. El-Refaie, K. K. Huh, J. K. Tangudu, and T. M. Jahns, "Comparison of interior and surface PM machines equipped with fractional-slot concentrated windings for hybrid traction applications," *IEEE Trans. Energy Convers.*, vol. 27, no. 3, pp. 593-602, Sep. 2012.

[RIC14] J. Richnow, D. Gerling, P. Stenzel, "Torque ripple reduction in permanent magnet synchronous machines with concentrated windings and pre-wound coils," in *Proc. Int. Conf. Elect. Mach. Sys.*, Hangzhou, China, Oct. 2014, pp. 1-7.

[RUA05] S. Ruangsinchaiwanich, Z. Q. Zhu, and D. Howe, "Influence of magnet shape on cogging torque and back-EMF waveform in permanent magnet machines," in *Proc. Int. Conf. Elect. Mach. Sys.*, Nanjing, China, Sep. 2005, pp. 284-289.

[SAL04] P. Salminen, M. Niemela, J. Pyrhonen, and J. Mantere, "Performance analysis of fractional slot wound PM-motors for low speed applications," *IEEE IAS Annu. Meet.*, vol.2, pp. 1032-1037, Oct. 2004.

[SAU51] R. M. Saunders, and R. H. Weakly, "Design of permanent-magnet alternators," *Trans. AIEE*, vol. 70, no. 2, pp. 1578-1581, Jul. 1951.

[SCH60] W. Schuisky, *Berechnung Elektrischer Machinen*, New York, NY, U.S.: Springer, 1960.

[SEB96] T. Sebastian, and V. Gangla, "Analysis of the induced EMF waveforms and torque ripple in a brushless permanent magnet machine," *IEEE Trans. Ind. Appl.*, vol. 32, no. 1, Jan./Feb. 1996.

[SEO14] K. S. Seo, Y. J. Kim, and S. Y. Jung, "Stator teeth shape design for torque ripple reduction in surface-mounted permanent magnet synchronous motor," in *Proc. Int. Conf. Elect. Mach. Sys.*, Hangzhou, China, Oct. 2014, pp. 387-390.

[SHE13] Y. Shen, and Z. Q. Zhu, "Analysis of electromagnetic performance of Halbach PM brushless machines having mixed grade and unequal height of magnets," *IEEE Trans. Magn.*, vol. 49, no. 5, pp. 1154-1164, Oct. 2012.

[SIL11] C. Silva, L. A. Cordova, P. Lezana, and L. Empringham, "Implementation and control of a hybrid multilevel converter with floating DC links for current waveform improvement," *IEEE Trans. Ind. Electron.*, vol. 58, no. 6, pp. 2340-2312, Jun. 2011.

[SMI16] S. P. Smith, "The theory of armature windings," *Journal of Institution of Electrical Engineers*, vol. 55, no. 261, pp. 18-36, Dec. 1916.

[SOO02] W. L. Soong, and N. Ertugrul, "Field-weakening performance of interior permanent-magnet motors," *IEEE Trans. Ind. Appl.*, vol. 38, no. 5, pp. 1251-1258, Sep./Oct. 2002.

[STA96] D. A. Staton, R. P. Deodhar, W. L. Soong, and T. J. E. Miller, "Torque prediction using the flux-MMF diagram in AC, DC, and reluctance motors,"

IEEE Trans. Ind. Appl., vol. 32, no. 1, pp. 180-188, Jan./Feb. 1996.

[STR52] F. Strauss, "Synchronous machines with rotating permanent-magnet fields," *Trans. AIEE*, vol. 71, no. 1, part III, pp. 887-893, Jan. 1952.

[STU03] B. Stumberger, G. Stumberger, D. Dolinar, A. Hamler, and M. Trlep, "Evaluation of saturation and cross-magnetization effects in interior permanent-magnet synchronous motor," *IEEE Trans. Ind. Appl.*, vol. 39, no. 5, pp. 1264-1271, Sep./Oct. 2003.

[TAN09] J. K. Tangudu, T. M. Jahns, A. El-Refaie, and Z. Q. Zhu, "Lumped parameter magnetic circuit model for fractional-slot concentrated-winding interior permanent magnet machines," in *Proc. Energy Conv. Congr. Expo.*, San Jose, CA, Sep. 2009, pp. 2423-2430.

[TAN10] J. C. Tan, *Technologies of BLDC machines*, Beijing, China, China Machine Press, 2010, (in Chinese).

[TAV10] N. R. Tavana, and A. Shoulaie, "Analysis and design of magnetic pole shape in linear permanent magnet machine," *IEEE Trans. Magn.*, vol. 46, no. 4, pp. 1000-1006, Apr. 2010.

[URA07] N. Urasaki, T. Senjyu, K. Uezato, and T. Funabashi, "Adaptive dead-time compensation strategy for permanent magnet synchronous motor drive," *IEEE Trans. Energy Convers.*, vol. 22, no. 2, pp. 271-280, Jun. 2007.

[VAL14] M. Valavi, A. Nysveen, R. Nilssen, R. D. Lorenz, and T. Rolvag, "Influence of pole and slot combinations on magnetic forces and vibration in low-speed PM wind generators," *IEEE Trans. Magn.*, vol. 50, no. 5, pp. 1-11, May 2014.

[VAS90] P. Vas, *Vector Control of AC Machines*. Oxford, U.K., Oxford Science Publications, 1990.

[WAN14] K. Wang, Z. Q. Zhu, and G. Ombach, "Synthesis of high performance fractional-slot permanent-magnet machines with coil-pitch of two slot-pitches," *IEEE Trans. Energy Convers.*, vol. 29, no. 3, pp. 758-770, May, 2014.

[WAN14a] K. Wang, Z. Q. Zhu, and G. Ombach, "Torque enhancement of surface-mounted permanent magnet machine using third-order harmonic," *IEEE Trans. Magn.*, vol. 50, no. 3, pp. 1-9, Mar. 2014.

[WAN14b] K. Wang, Z. Q. Zhu, G. Ombach, and W. Chlebosz, "Average torque improvement of interior permanent-magnet machine using third harmonic in rotor shape," *IEEE Trans. Ind. Electron.*, vol. 61, no. 9, pp. 5047-5057, Sep. 2014.

[WAN14c] K. Wang, Z. Q. Zhu, and G. Ombach, "Torque improvement of five-phase surface mounted permanent magnet machine using third-order harmonic," *IEEE Trans. Energy Convers.*, vol. 29, no. 3, pp. 735-747, Sep. 2014.

[WIL99] S. Williamson, and C. I. McClay, "The effect of axial variation in saturation due to skew on induction motor equivalent-circuit parameters," *IEEE. Trans.*

Ind. Appl., vol. 35, no. 6, pp. 1323-1331, Nov./Dec. 1999.

[WU13] L. J. Wu, Z. Q. Zhu, and M. L. M. Jamil, "Unbalanced magnetic force in permanent magnet machines having asymmetric windings and static/rotating eccentricities," in *Proc. Int. Conf. Elect. Mach. Sys.*, Busan, Korea, Oct. 2013, pp. 937-942.

[XUA13] H. V. Xuan, D. Lahaye, H. Polinder, and J. A. Ferreira, "Influence of stator slotting on the performance of permanent-magnet machines with concentrated windings," *IEEE Trans. Magn.*, vol. 49, no. 2, pp. 929-938, Feb. 2013.

[YAM14] K. Yamazaki, and M. Kumagai, "Torque analysis of interior permanent-magnet synchronous motors by considering cross-magnetization: variation in torque components with permanent-magnet configuration," *IEEE Trans. Ind. Appl.*, vol. 61, no. 7, pp. 3192-3201, Jul. 2014.

[YAN11] S. C. Yang, T. Suzuzki, R. D. Lorenz, and T. M. Jahns, "Surface-permanent-magnet synchronous machine design for saliency-tracking self-sensing position estimation at zero and low speeds," *IEEE Trans. Ind. Appl.*, vol. 47, no. 5, pp. 2103-2116, Sep./Oct. 2011.

[YU13] C. Y. Yu, J. Tamura, and R. D. Lorenz, "Optimum DC bus voltage analysis and calculation method for inverters/motors with variable DC bus voltage," *IEEE. Trans. Ind. Appl.*, vol. 49, no. 6, pp. 2619-2627, Nov./Dec. 2013

[ZEP05] L. P. Zepp, and J. R. Hendershot, "Electrical machine construction using axially inserted teeth in a stator ring or armature," U.S. Patent 6880229 B2, Arp. 2005.

[ZHU93] Z. Q. Zhu, and D. Howe, "Instantaneous magnetic field distribution in brushless permanent magnet DC motors. II. Armature-reaction field," *IEEE Trans. Magn.*, vol. 29, no.1, pp. 136-142, Jan. 1993.

[ZHU00] Z. Q. Zhu, and D. Howe, "Influence of design parameters on cogging torque in permanent magnet machines," *IEEE Trans. Energy Convers.*, vol. 15, no. 4, pp. 407-412, Dec. 2000.

[ZHU01] Z. Q. Zhu, and D. Howe, "Halbach permanent magnet machines and applications: a review," *IEE Proc. Electric Power Appl.*, vol. 148, no. 4, pp. 299-308, Jul. 2001.

[ZHU07] Z. Q. Zhu, and D. Howe, "Electrical machines and drives for electric, hybrid, and fuel cell vehicles," *Proc. IEEE*, vol. 95, no. 4, pp. 746-765, Apr. 2007.

[ZHU09] L. Zhu, S. Z. Jiang, Z. Q. Zhu, and C. C. Chan, "Analytical methods for minimizing cogging torque in permanent-magnet machines," *IEEE Trans. Magn.*, vol. 45, no. 4, pp. 2023-2031, Apr. 2009.

[ZHU09a] Z. Q. Zhu, Z. P. Xia, L. J. Wu, and G. W. Jewell, "Influence of slot and pole number combination on radial force and vibration modes in fractional slot PM brushless machines having single- and double-layer windings," in *Proc. IEEE Energy Convers. Expo.*, San Jose, U.S., Sep. 2009, pp. 3443-3450.

[ZHU09b] Z. Q. Zhu, “A simple method for measuring cogging torque in permanent magnet machines,” in *IEEE Power & Energy Society General Meeting*, Calgary, U.S., Jul. 2009, pp. 1-4.

[ZHU10] Z. Q. Zhu, L. J. Wu, Z. P. Xia, “An accurate subdomain model for magnetic field computation in slotted surface-mounted permanent-magnet machines,” *IEEE Trans. Magn.*, vol. 46, no. 4, pp. 1100-1115, Apr. 2010.

[ZHU12] Z. Q. Zhu, Z. Azar, and G. Ombach, “Influence of additional air gaps between segments on cogging torque of permanent-magnet machines having modular stator,” *IEEE Trans. Magn.*, vol. 48, no. 6, pp. 2049-2055, Jun. 2012.

[ZHU13] Z. Q. Zhu, M. L. M. Jamil, and L. J. Wu, “Influence of slot and pole number combinations on unbalanced magnetic force in PM machines with diametrically asymmetric windings,” *IEEE. Trans. Ind. Appl.*, vol. 49, no. 1, pp. 19-30, Jan./Feb. 2013.

[ZHU14] Z. Q. Zhu, “Permanent Magnet Machines for Traction Application,” *Encyclopaedia of Automotive Engineering*, New York, U.S., John Wiley & Sons, 2014.

[ZHU14a] Z. Q. Zhu, L. J. Wu, and M. L. M. Jamil, “Influence of pole and slot number combinations on cogging torque in permanent-magnet machines with static and rotating eccentricities,” *IEEE Trans. Ind. Appl.*, vol. 50, no. 5, pp. 3265-3277, Sep./Oct. 2014.

APPENDIX A

FROZEN PERMEABILITY METHOD

The basic principle of frozen permeability (FP) method has been introduced clearly in [BIA98] [AZA12] and [CHU13]. When the machine operates under load condition, the magnetic field in nonlinear lamination materials is excited by two different sources, e.g. armature current and PM, the resultant operating point may enter the saturation region of the material BH curve such as the point A in Fig. A1. In order to separate the magnetic field generated by two excitation sources, the armature current and PM excitations should be applied to the FE model respectively. However, their respective operating points C and B with relative permeability of μ_{arm} and μ_{pm} are much different from the resultant working point A of μ_{all}, which could not reflect the real saturation. In order to solve this problem, FP method was proposed, which can be summarized by the flow chat in Fig. A2. After a normal non-linear operation with both armature currents and PM excitations in FEA, the permeability of each lamination element will be 'frozen', i.e. saved. Then, the armature current and PM excitations will be applied in respective models sharing the same 'frozen' permeability. Thus, their contributions to terminal voltage distortion can be separated.

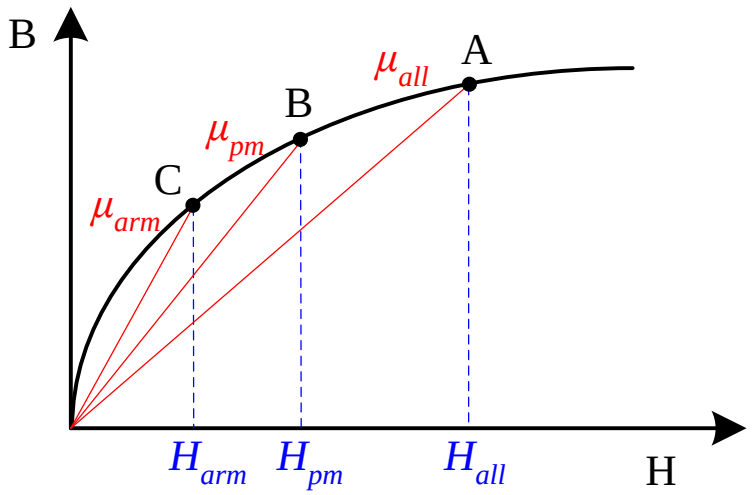

Fig. A1 Principle of frozen permeability method [CHU13].

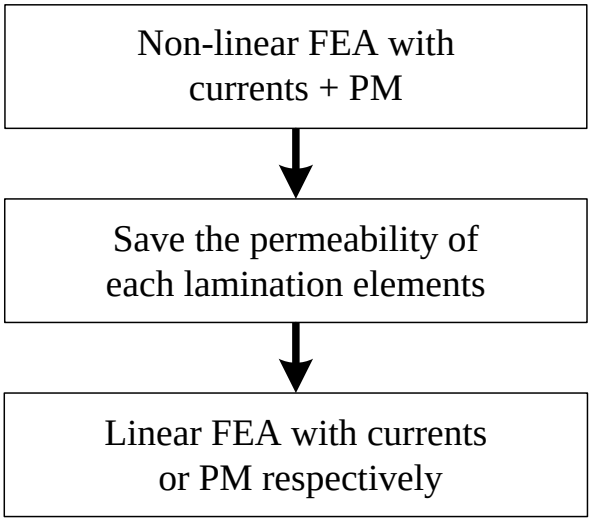

Fig. A2 Process of frozen permeability method [CHU13].

APPENDIX B

COGGING TORQUE AND STATIC TORQUE MEASURING METHOD

The simple cogging torque and static torque measuring method was proposed by Zhu [ZHU09b]. Fig. B1 shows the test rig based on this method. The prototype is mounted on a lathe with a rigid beam fixed on the shaft. The beam is pushed onto a scale by balance weight, which has been adjusted with the aid of surface level. There is a degree calibration on the faceplate of the lathe to indicate the rotor position.

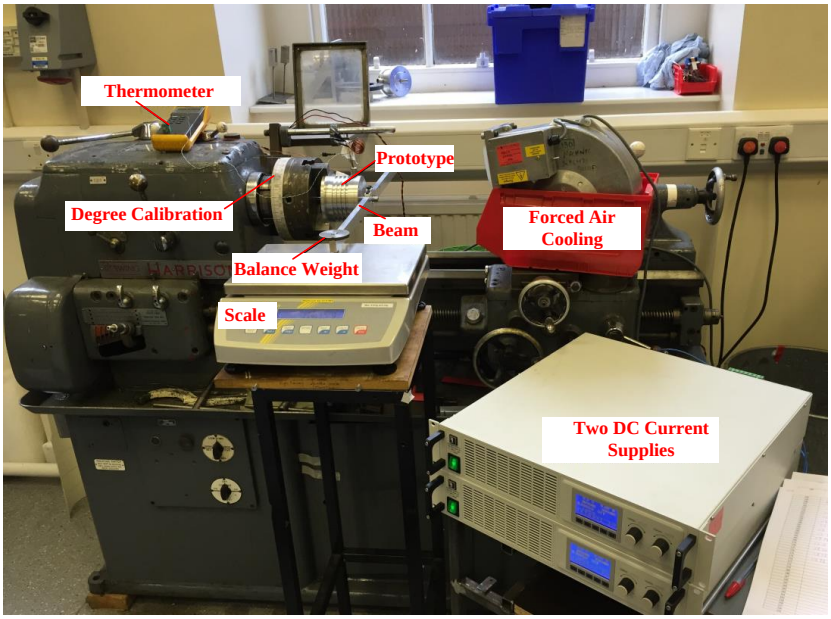

Fig. B1 Test rig for cogging torque and static torque [ZHU09b]

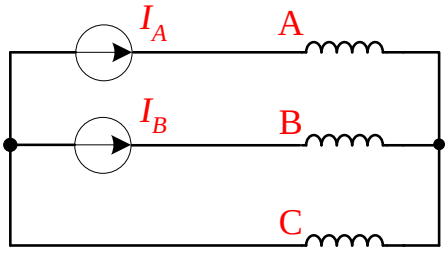

Fig. B2. DC current supplies connection for static torque waveform test.

In order to measure the cogging torque, the lathe is manually rotated within a cogging torque period, while the data appearing on the scale will be recorded and transferred to newton-meter after the test. Further, for static torque waveform test, two DC current supplies will be

connected with the prototype armature following Fig. B2. For each rotor position, the DC current supplies will be adjusted to the simultaneous current values for phase A and phase B respectively, while the scale data will be recorded to reveal the torque waveform. Thermometer and forced air cooling fan are used to keep the temperature of armature winding within the safety limitation.

APPENDIX C

CASE STUDY FOR ON-LOAD VOLTAGE DISTORTION IN HIGH POWER TRACTION MACHINES

The aforementioned chapters have investigated the phenomenon and mechanism of terminal voltage distortion based on low power level machines. This appendix will show that terminal voltage distortion also exists in machines with high power level as will be illustrated by two traction machines with 42-slot/8-pole and 48-slot/8-pole, respectively.

C.1 Investigated Machines

Fig.C1(a) shows the cross-section and winding arrangement of the 42-slot/8-pole machine with q=7/4, which was designed for an EV project. Although it is a fractional slot machine, distributed windings are used to retain enough reluctance torque. Fig.C1(b) shows the well-known Prius 2010 traction machine. In order to obtain high reluctance torque and reduce the PM usage, it adopts integer slot design with q=2. The basic parameters of two machines are listed in Table CI and Table CII respectively.

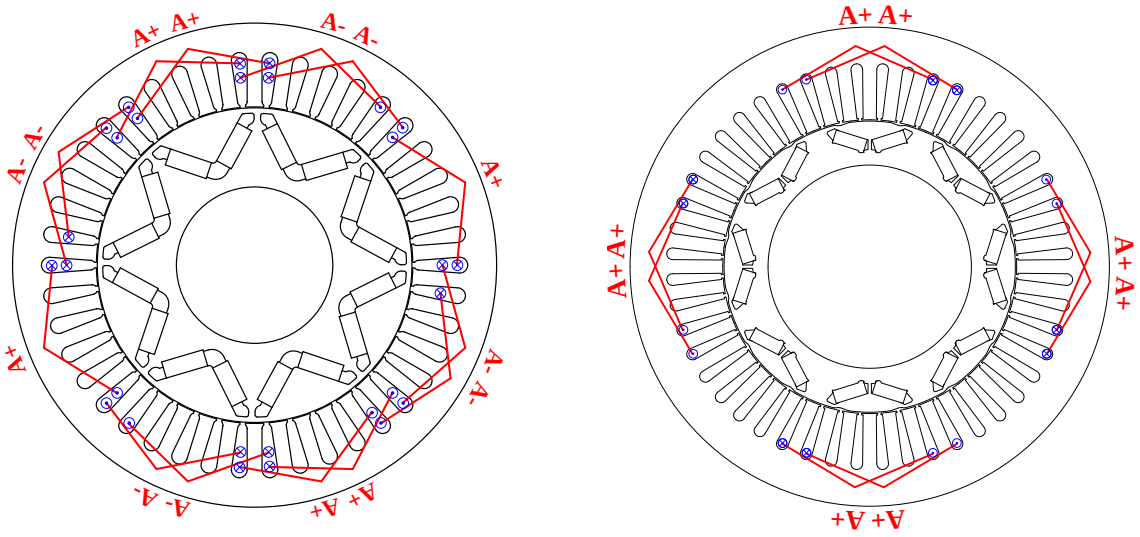

(a) 42-slot/8-pole (b) 48-slot/8-pole

Fig. C1 Cross-sections and winding configurations of the investigated machines.

Table CI Parameters for the 42-slot/8-pole machine

Parameters	***Values***	***Parameters***	***Values***
Number of slots	42	Number of poles	8
Outer diameter	260mm	Inner diameter	84mm
Split ratio	0.65	Airgap length	0.5mm
Axial length	90mm	Phase resistance	0.012Ω
Tooth width	8mm	Yoke thickness	16mm
PM thickness	9mm	PM width	23mm
Number of phases	3	Turns per phase	56
Rated current	$229A_{rms}$	DC-link voltage	300V
PM remanence	1.25T	PM permeability	1.07
PM coercive force	929kA/m	Lamination material	M300

Table CII Parameters for the 48-slot/8-pole machine

Parameters	***Values***	***Parameters***	***Values***
Number of slots	48	Number of poles	8
Outer diameter	264mm	Inner diameter	112mm
Axial length	50.8mm	Phase resistance	0.077Ω
Split ratio	0.61	Airgap length	0.73mm
Tooth width	7.8mm	Yoke thickness	20.0mm
PM thickness	7.2mm	PM width	17.9mm
Number of phases	3	Turns per phase	88
Rated current	$167A_{rms}$	DC-link voltage	650V
PM remanence	1.2T	PM permeability	1.05
PM coercive force	909kA/m	Lamination material	M300

C.2 Phenomenon of Voltage Distortion

Fig.C2 compares the open-circuit phase back-EMFs of two machines under the same speed. Due to higher turns per phase, the 48/8 machine has higher fundamental voltage. However, since the 42/8 machine has lower harmonic winding factors due to fractional slot winding, the harmonic voltages are much lower, which can also be reflected in the line back-EMFs in Fig.C3. Meanwhile, due to the merit of fractional slot winding, the cogging torque of the 42/8 machine is also much lower than the integer slot 48/8 machine, Fig.C4.

Driven by their relative rated currents, the terminal phase voltages of two machines are compared in Fig.C5. Due to much higher turns per phase, the 48/8 machine obtains higher inductance than the 42/8 machine (phase inductances are 1.47mH and 0.53mH respectively by FP method), which leads to much larger fundamental voltage amplitude. Although the back-EMF of the 48/8 machine are relatively sinusoidal, the on-load magnetic saturation as well as the high harmonic winding factors result in much higher voltage harmonics for the

48/8 machine even when β=0°, which is significantly different from the 42/8 machine. With the increase of β, the flux paths of both machines change according to the aforementioned analyses, which leads to higher voltage distortion levels when β=60°. This difference can also be reflected in the terminal line voltages, Fig.C6. Fig.C7 compares the *LVDR*s for two machines under different β. Due to much higher voltage drop on winding inductances, the maximum *LVDR* for the 48/8 machine is much smaller. However, both curves prove that terminal voltage distortion will aggravate when β approaches 90°.

Fig.C8 and Fig.C9 compare the torque waveforms and torque ripples of two machines. Due to higher voltage harmonics as well as higher cogging torque, the torque ripples for the 48/8 machine are higher than the 42/8 machine. Meanwhile, Fig.C10 compares the average torque against β for two machines under rated currents. Compared with their relative torques when β=0°, the peak values for the 48/8 machine are larger due to more significant reluctance torque.

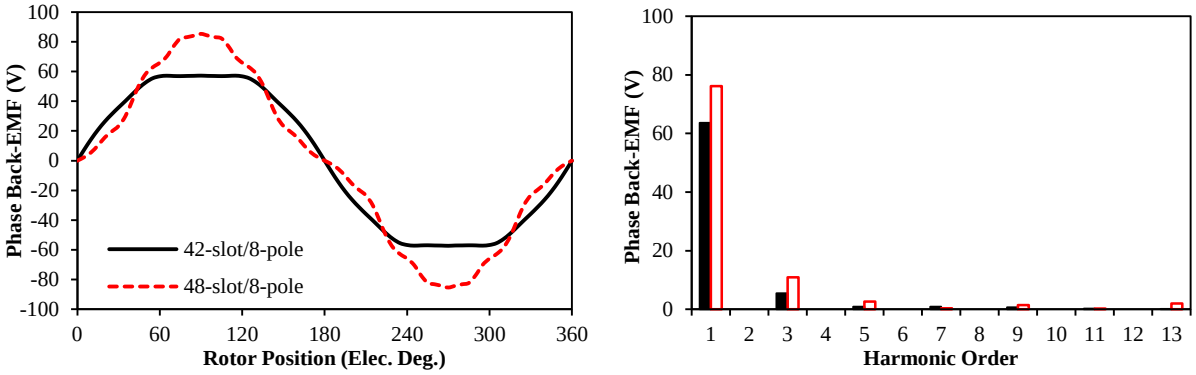

(a) Waveforms (b) Harmonics

Fig. C2 Comparison of open-circuit phase back-EMFs (1500rpm).

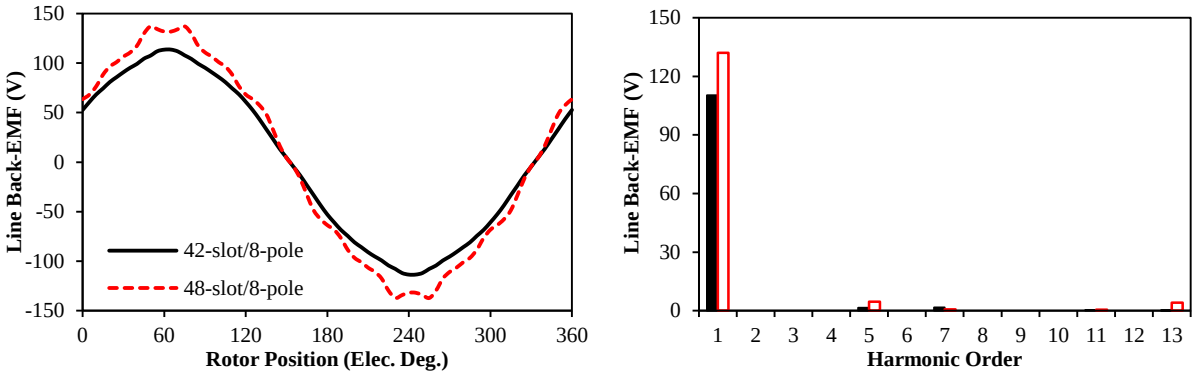

(a) Waveforms (b) Harmonics

Fig. C3 Comparison of open-circuit line back-EMFs (1500rpm).

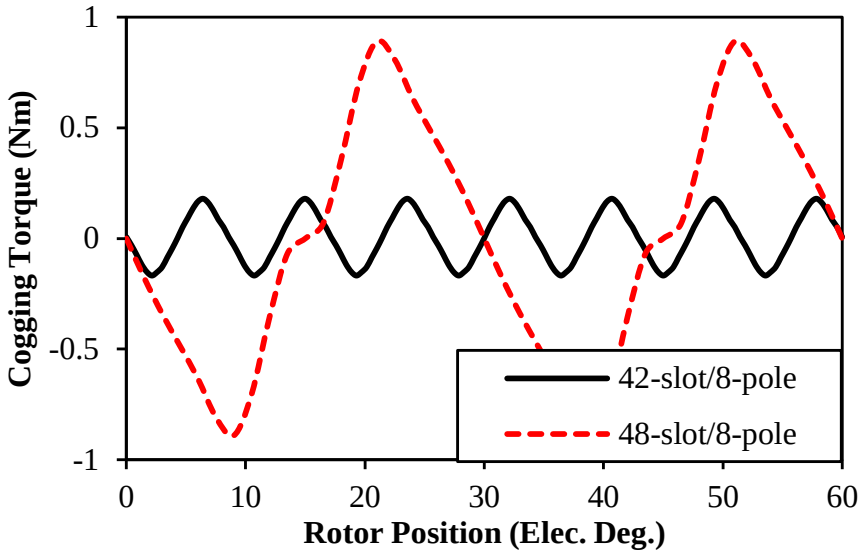

Fig. C4 Comparison of open-circuit cogging torque.

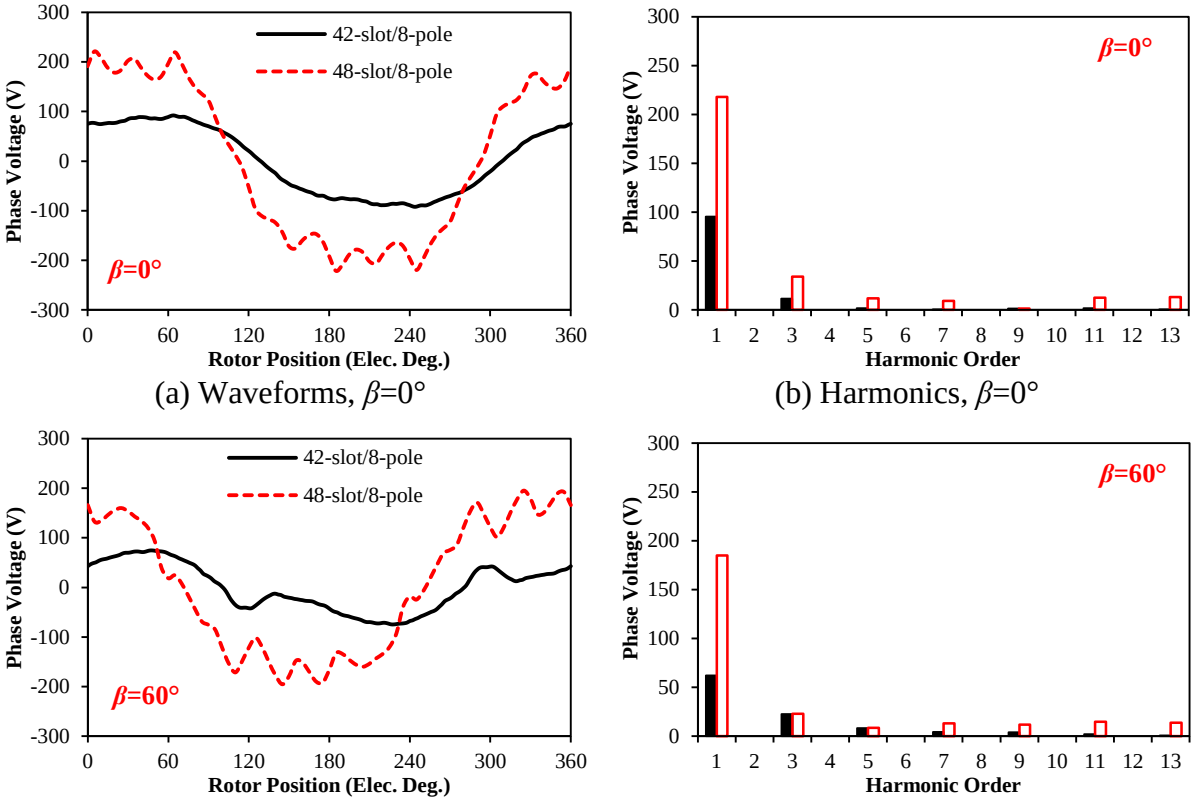

(a) Waveforms, β=0°

(b) Harmonics, β=0°

(c) Waveforms, β=60°

(d) Harmonics, β=60°

Fig. C5 Comparison of on-load terminal phase voltages (1500rpm, I_{max}=300A for 42/8 machine, I_{max}=236A for 48/8 machine).

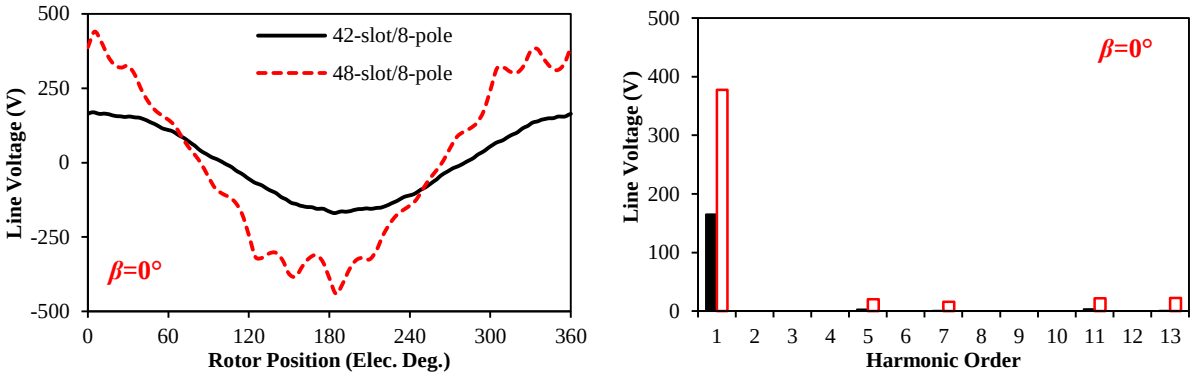

(a) Waveforms, β=0° (b) Harmonics, β=0°

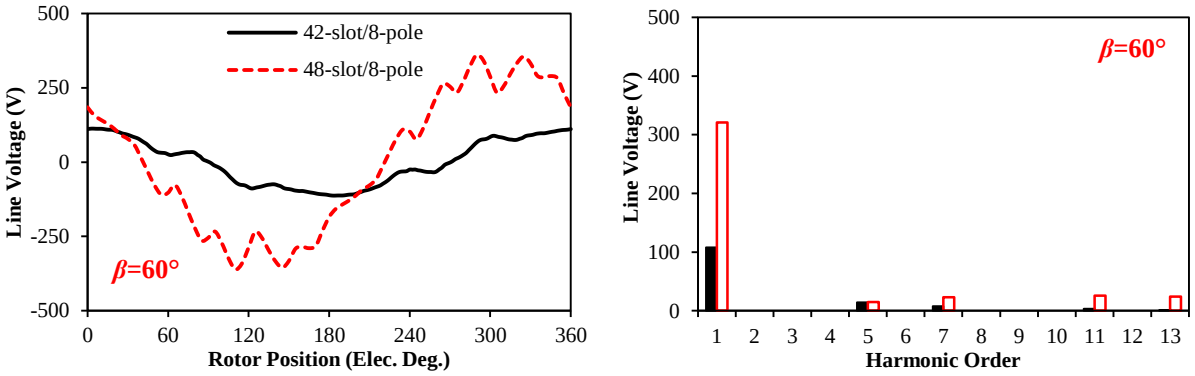

(c) Waveforms, β=60° (d) Harmonics, β=60°

Fig. C6 Comparison of on-load terminal line voltages (1500rpm, I_{max}=300A for 42/8 machine, I_{max}=236A for 48/8 machine).

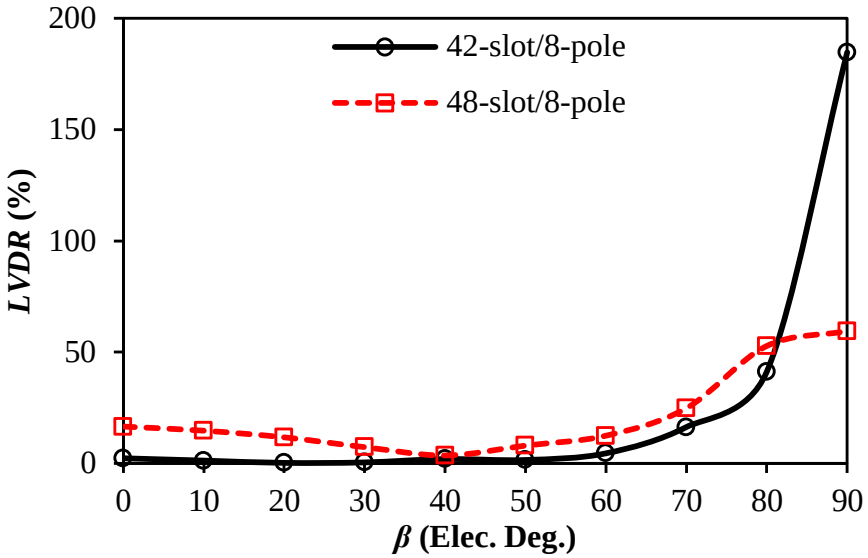

Fig. C7 Comparison of *LVDR* against β (1500rpm, I_{max}=300A for 42/8 machine, I_{max}=236A for 48/8 machine).

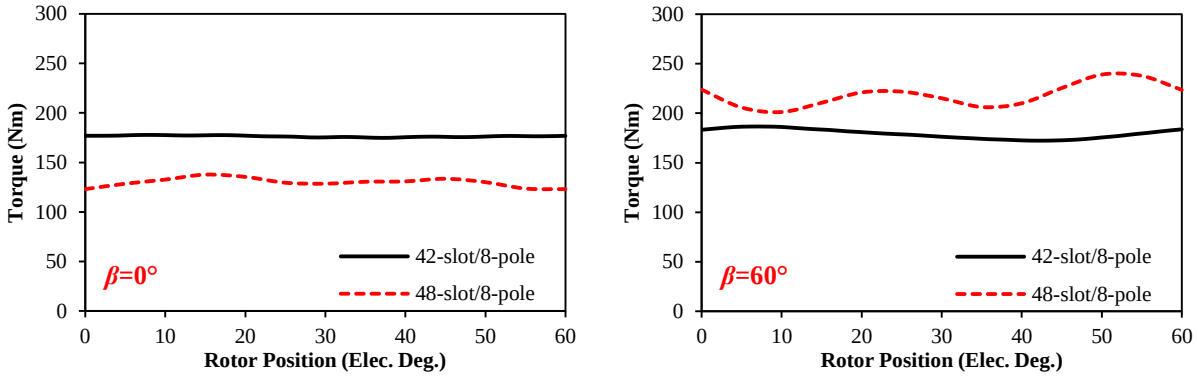

(a) β=0° (b) β=60°

Fig. C8 Comparison of torque waveforms (I_{max}=300A for 42/8 machine, I_{max}=236A for 48/8 machine).

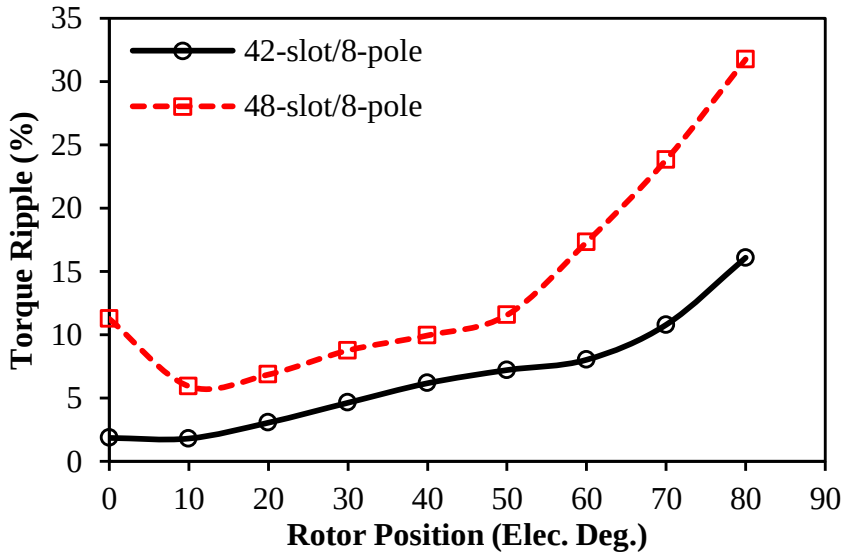

Fig. C9 Comparison of torque ripples against β (I_{max}=300A for 42/8 machine, I_{max}=236A for 48/8 machine).

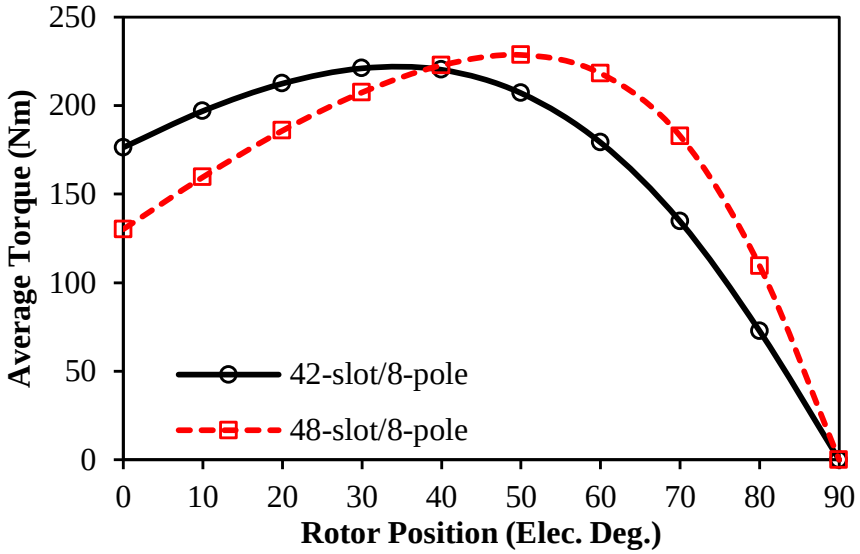

Fig. C10 Comparison of average torque against β (I_{max}=300A for 42/8 machine, I_{max}=236A for 48/8 machine).

In order to simply reflect the influence of voltage distortion on flux weakening operation, MTPV is not considered. Under rated currents and DC link voltages, the torque speed and torque ripple speed curves for two machines are shown in Fig.C11 and Fig.C12, respectively. Clearly, the voltage distortion causes significant difference between the curves calculated by the fundamental or peak voltages especially in the 48/8 machine. In order to explain this, the fundamental and peak line voltages of the two machines are compared in Fig.C13. Due to smaller reluctance torque, β equals 34.5° for constant torque operation in the 42/8 machine. However, in order to achieve maximum torque contributed by high reluctance torque, β equals 49.4° for constant torque operation in the 48/8 machine. Therefore, when entering flux weakening operation after base speed, the 48/8 machine will face much more significant difference between peak and fundamental voltages, Fig.C13(b). Due to high terminal voltage distortion in the flux weakening region for 48/8 machine, the peak voltage only slightly reduces with the increase of β, which results in very limited flux weakening region, Fig.C12. Nevertheless, it is reported that the Prius 48/8 traction machine can achieve wide flux weakening operation range [OAK11]. Thus, special compensation strategy must be adopted from the control side in cooperation with MTPV operation.

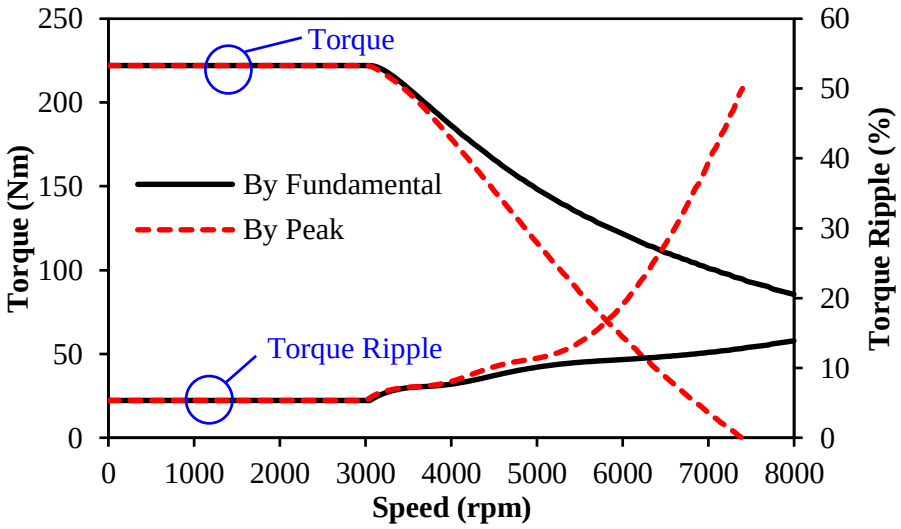

Fig. C11 Torque speed curves for the 42/8 machine (U_{DC}=300V, I_{max}=324A).

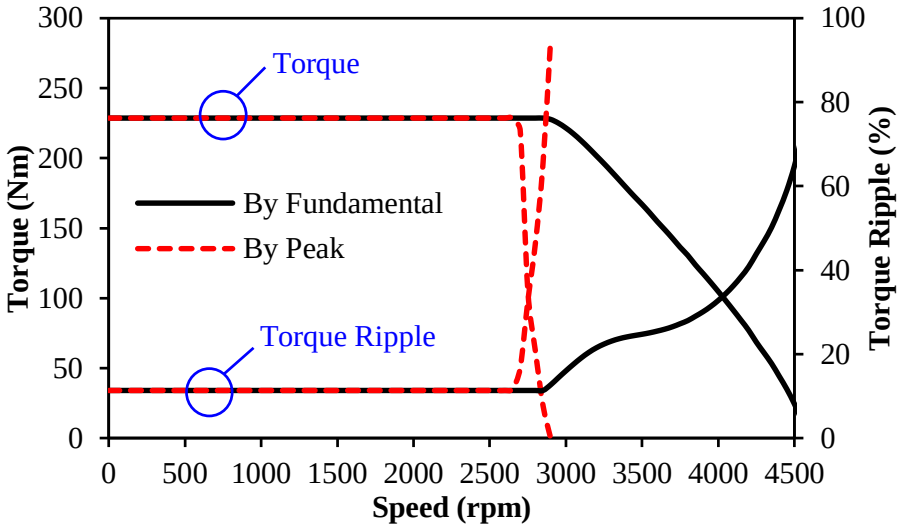

Fig. C12 Torque speed curves for the 48/8 machine (U_{DC}=650V, I_{max}=236A).

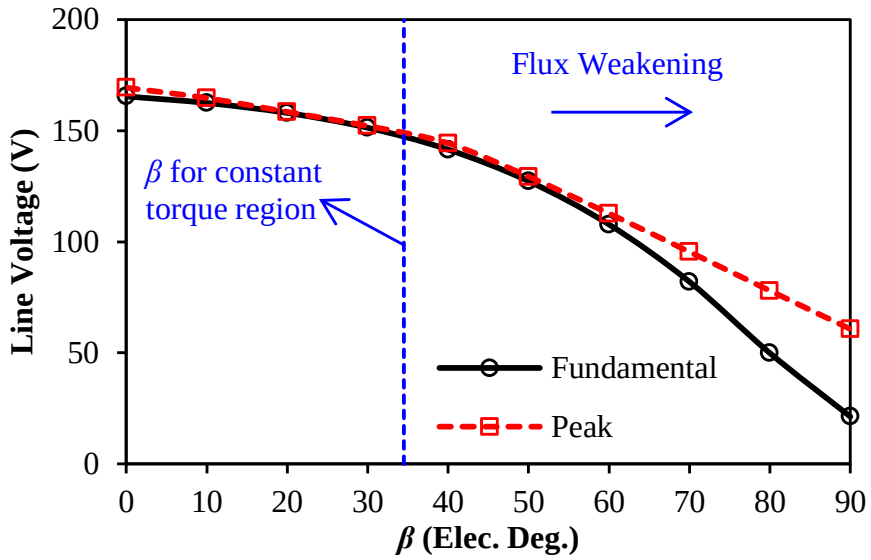

(a) 42-slot/8-pole machine, I_{max}=324A

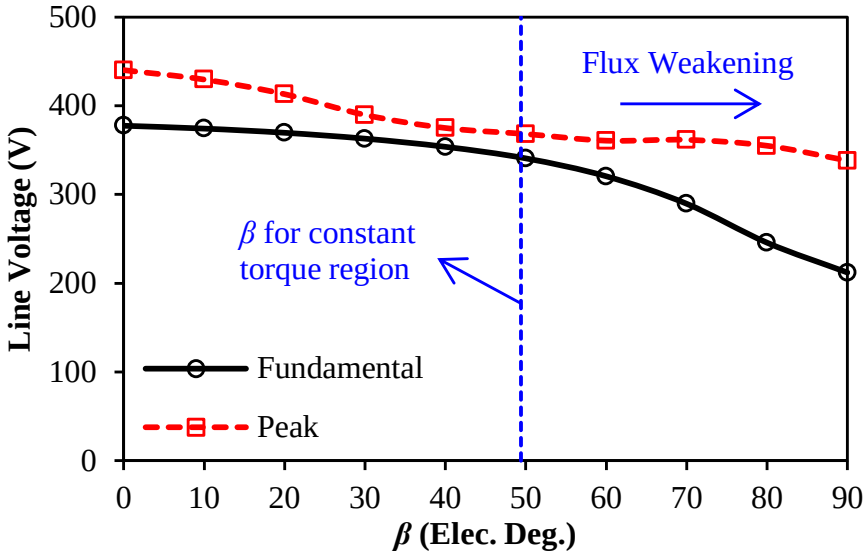

(b) 48-slot/8-pole machine, I_{max}=236A

Fig. C13 Comparison of line voltages against β (1500rpm).

C.3 Experimental Validation

The test results of the 42-slot/8-pole machine are adopted in this section to illustrate the phenomenon and influence of voltage distortion. Since the voltage distortion was not aware during the project over the period of 2011-2012, some experiment data may be insufficient.

Fig.C14 shows the photo of prototype and test rig in which a DC generator is adopted as load. Fig.C15 compares the measured and predicted open-circuit back-EMFs at 1500rpm. Due to manufacture tolerance as well as the measurement error, the measured phase back-EMF is slightly smaller than the predicted value.

It is a pity that the terminal voltages were not captured during the experiment. However, the measured phase currents and torques still prove the influence of terminal voltage distortion. The measured three-phase currents under 1009rpm are shown in Fig.C16(a). Since such an operation point is below the base speed, the voltage distortion will not influence the control performance, which leads to sinusoidal currents. However, under flux weakening operation, such as 5505rpm, the phase currents become less sinusoidal, Fig.C16(b). The measured currents can be summarized as different I_{max} and β in Fig.C17. Clearly, I_{max} was not kept constant in order to maintain the voltage within U_{DC}. This can be further proved by the terminal line voltages calculated from the measured currents, Fig.C18. It can be seen that the fundamental voltages were always kept below the DC limitation, but the peak voltages are

much higher than that due to voltage distortion. For the peak voltages above U_{DC}, the machine may enter generator mode in a short period, which distorts the phase currents.

Fig.C19 compares the measured and predicted torque speed characteristics by different methods. The cross-dot line shows the FEA predicted torque results calculated by the measured currents. Meanwhile, the solid and dashed lines refer to the torque speed performance predicted by fixed I_{max}, which is the same as that in Fig.C11. Although the torque reduction is mainly due to the reduction of I_{max}, the influence of voltage distortion can still be proved from the unstable currents in flux weakening regions.

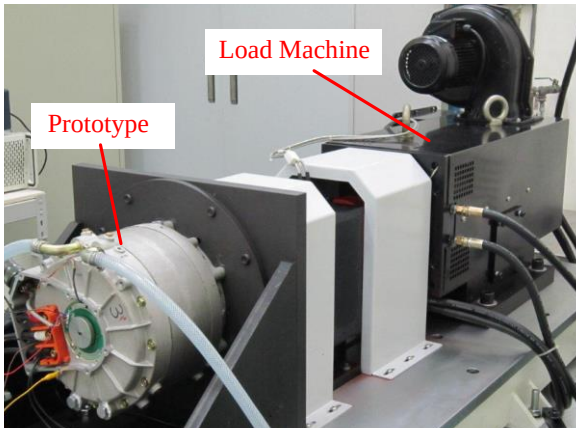

Fig. C14 Prototype and test rig

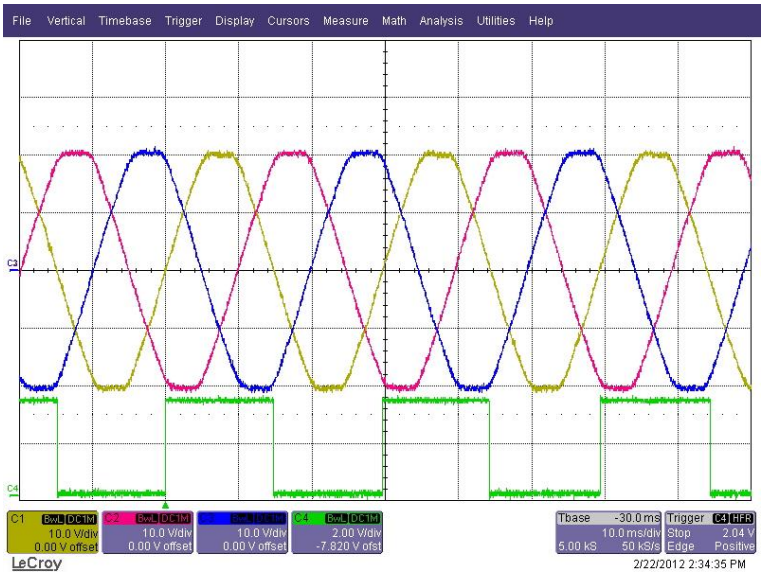

Fig. C15 Three-phase back-EMFs (507rpm, square wave refers to Hall position single).

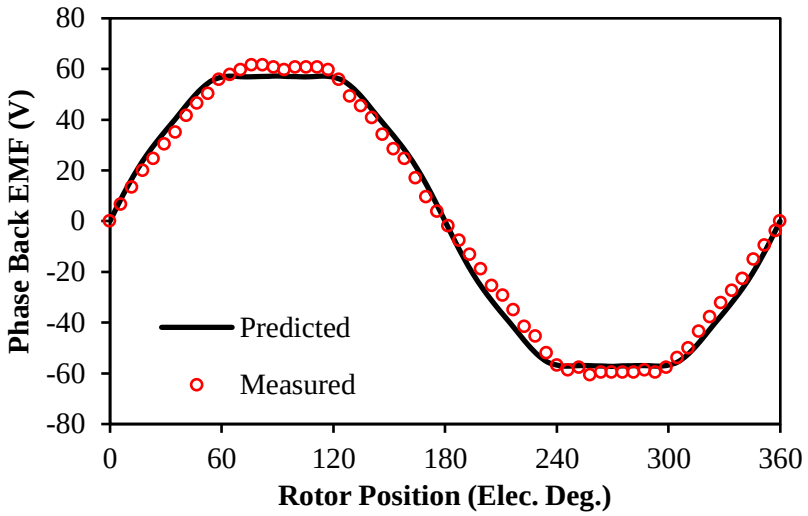

(a) Waveforms

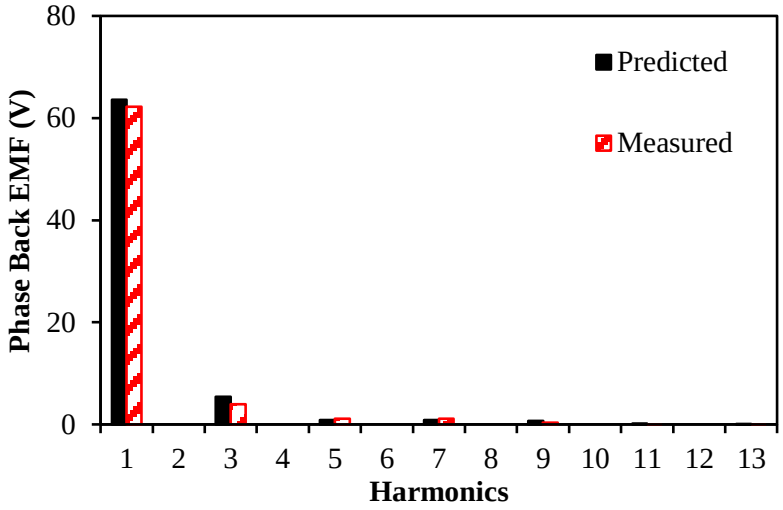

(b) Harmonics

Fig. C16 Comparison of predicated and measured phase back-EMFs (1500rpm).

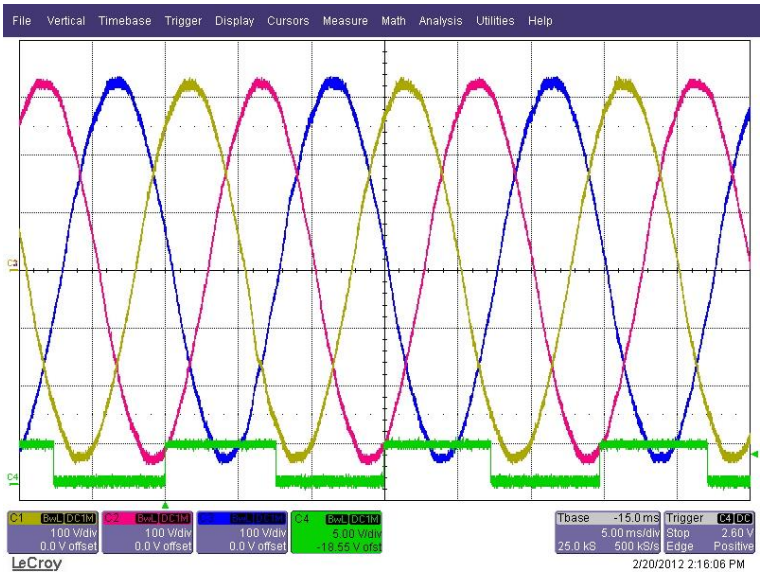

(a) 1009rpm, I_{max}=324A, β=44°

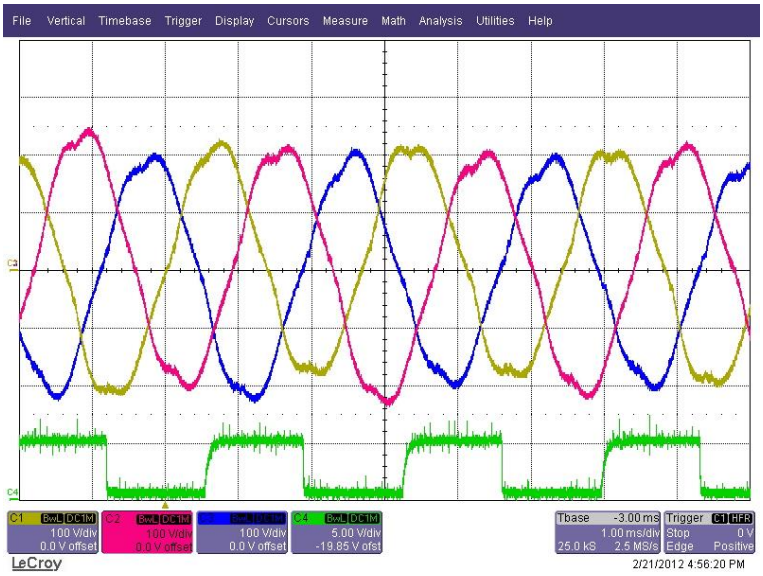

(b) 5505rpm, I_{max}=212A, β=71°.

Fig. C17 Measured phase currents for different speed and load conditions.

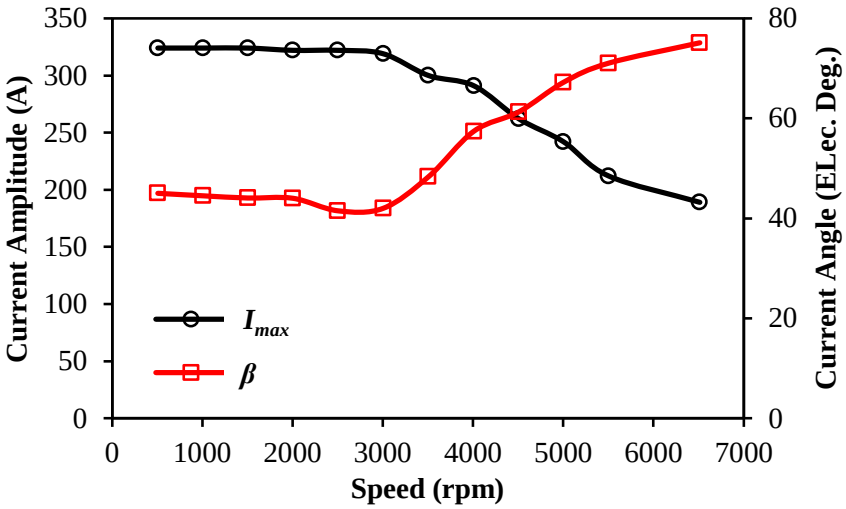

Fig. C17 Measured current amplitudes and current angles against speed.

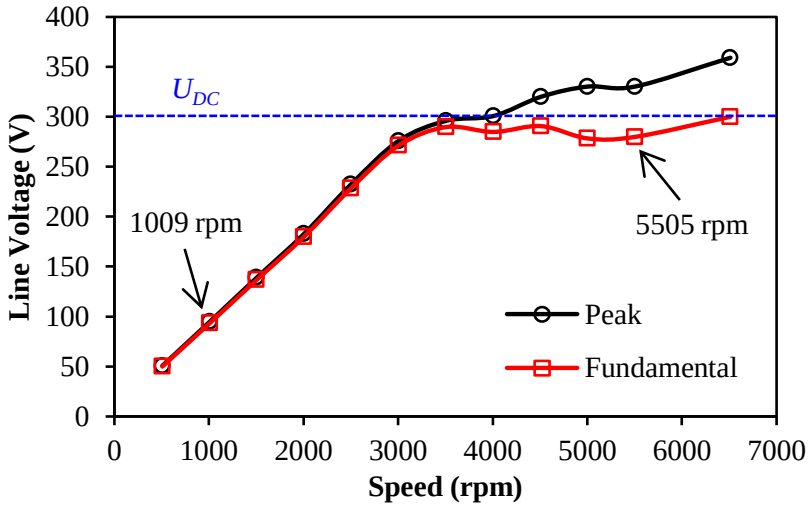

Fig. C18 Terminal line voltages by FEA calculated with measured currents.

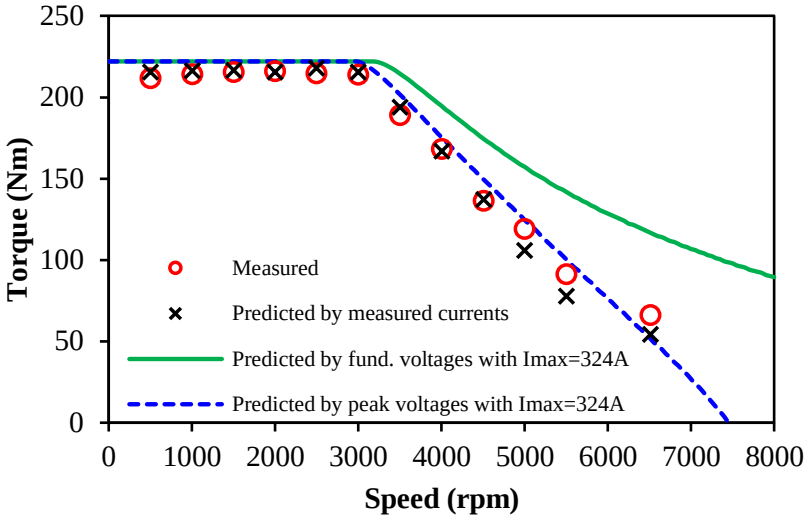

Fig. C19 Comparison of predicted and measured torque speed characteristics (U_{DC}=300V).

C.4 Summary

This appendix investigates two high power rating traction machines with fractional slot and integer slot designs respectively. Both of them suffer from terminal voltage distortion under load operation, especially when β approaches 90°, which reduces the flux weakening operation range similar to the results in Chapter 4 and Chapter 5. Although the experimental data for the 42-slot/8-pole prototype is not sufficient, the measured current waveforms still validate the influence of voltage distortion in flux weakening regions.

APPENDIX D

DESIGN TRADE-OFFS BETWEEN COGGING TORQUE AND TORQUE RIPPLE IN FSCW SPM MACHINES CONSIDERING LOCAL MAGNETIC SATURATION

Due to different magnetic saturation conditions in surface-mounted permanent magnet (SPM) machines operating under different loads, the optimal design to minimize the cogging torque may not be the one to minimize torque ripple as well. This section investigates the design trade-off between open-circuit cogging torque and on-load torque ripple by taking the design of slot opening as an example. With the aid of frozen permeability method, the torque components under different slot opening widths and load conditions are presented based on a 12-slot/8-pole machine firstly. The result reveals that the on-load cogging increases significantly especially when small slot opening width is adopted, which is opposite to the condition for minimizing the open-circuit cogging torque. Then, two machines separately designed for minimum open-circuit cogging torque or minimum on-load torque ripple are compared to illustrate alternative design trade-offs. Finally, a prototype machine is manufactured and tested to validate the analysis results.

D.1 Introduction

The surface-mounted permanent magnet (SPM) machines with fractional slot concentrated non-overlapping windings are widely adopted due to their high torque and power densities, short end-winding, high efficiency and good fault tolerant capability [1]. During the design of SPM machines, cogging torque and torque ripples are normally the main considerations in addition to torque density.

Many papers have paid attention to the influence of design parameters on cogging torque and proposed alternative minimization methods, such as proper tooth-tip design, skewing, rotor shaping, etc. [2]. Nevertheless, due to the influence of saturation, the on-load cogging torque could become much more obvious compared with the open-circuit condition, which may increase the torque ripple [3-4]. Thus, the optimal design for the minimum cogging torque may not result in low torque ripple at the same time. Correspondingly, the design for

minimum torque ripple could have large cogging torque as well. Therefore, a design trade-off exists between minimum cogging torque and torque ripple.

In fact, the most frequent operating conditions for different machines depend on their specific applications. For a heavy duty oil pump or ventilation fan, the machines always work under rated load, which makes the on-load torque ripple prior during design. On the other hand, for an electric vehicle or wind turbine, the direct-drive machines frequently work under half load or idle condition, while the full load operation only takes a small percentage of a typical driving cycle. Thus, the open-circuit cogging torque and torque ripple under half load condition are more important during design.

In this paper, the design trade-off between cogging torque and torque ripple will be presented based on a 12-slot/8-pole machine by taking the slot opening design as an example. The variation of torque components against different slot opening widths with different load currents are investigated by the finite element analysis (FEA) based on the frozen permeability (FP) method [3-5] firstly. Then two machines with similar average torque but different design trade-offs are compared. A prototype machine is manufactured and tested to validate all analyses.

D.2 Influence of Slot Opening Designs on Cogging Torque and Torque Ripple under Different Loads

A 12-slot/8-pole fractional slot SPM machine is adopted to illustrate the design trade-off between cogging torque and torque ripple. The configuration of the model is shown in Fig.D1, while the major parameters except slot opening width (b_0) are listed in Table DI.

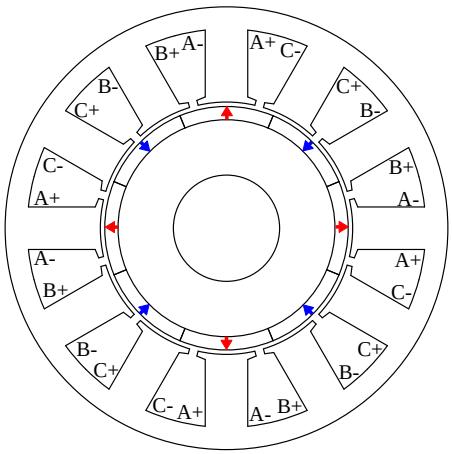

Fig. D1 Configuration of 12-slot/8-pole SPM machine.

Table DI Basic Parameters of the Investigated Machine

Parameter	***Value***	***Parameter***	***Value***
Stator outer diameter	100 mm	Axial length	50 mm
Stator inner diameter	57 mm	Airgap length	1 mm
Tooth width	8 mm	Back iron thickness	4.2 mm
Tooth-tip height	1 mm	Turns per phase	184
Magnet thickness	3 mm	Magnet pole arc	155°
Rated current	7.1 A_{rms}	Lamination	M300
PM remanence	1.2 T	PM permeability	1.05

The open-circuit cogging torque can be directly obtained from FEA, but the calculation of on-load torque components is more complicated. Since SPM machines usually work with zero *d*-axis current, I_d=0, control due to negligible rotor saliency, the on-load torque can be expressed by

$$T_{load} = T_{PM} + T_r + T_{cog} \tag{D1}$$

$$T_{PM} = \frac{3}{2} p(\psi_d^{PM} + \frac{d\psi_q^{PM}}{d\theta}) I_q \tag{D2}$$

$$T_r = \frac{3}{2} p(\psi_d^{arm} + \frac{d\psi_q^{arm}}{d\theta}) I_q \tag{D3}$$

where T_{cog} is the cogging torque for on-load condition, which can be only obtained by the FP method [3-5], p is the pole pair number, $\psi^{PM}{}_d$ and $\psi^{PM}{}_q$ are the *dq*-axis on-load PM flux-linages, $\psi^{arm}{}_d$ and $\psi^{arm}{}_q$ are the *dq*-axis on-load armature flux-linkages. With the aid of FP method, the on-load PM and armature flux-linkages are calculated in Fig.D2(a). Due to the cross saturation between *dq*-axis [5], $\psi^{PM}{}_q$ is not zero anymore, while fluctuation also exists in $\psi^{arm}{}_d$ even with I_d=0 control. Therefore, the fluctuations of different torque components can be calculated in Fig.D2(b). Although the torque ripple for the illustration case is still dominated by PM torque component, the obvious on-load cogging torque and reluctance torque are not negligible, which could be more problematic for other slot opening designs.

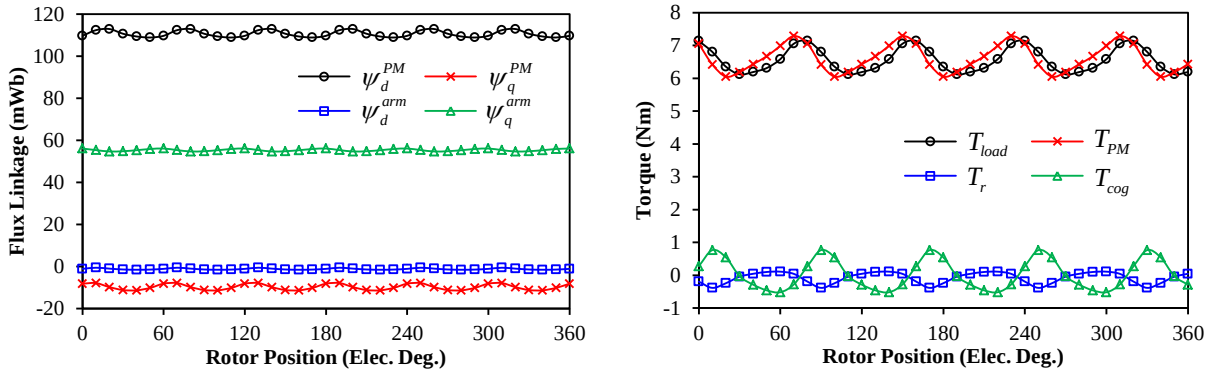

(a) Flux linkages (b) Torque waveforms

Fig. D2 On-load flux linkages and torque components by FP method (I_q=10 A, I_d=0, b_0=1 mm).

The average torque components against different slot opening widths are shown in Fig.D3(a). The PM torque takes the dominant role, which increases with the reduction of b_0 firstly, and begins to reduce after reaching the peak. With the decrease of b_0, the flux focusing effect by tooth-tips enhances, which increase the main flux linkage and thereafter the average torque. However, if b_0 is too small, the slot leakage through tooth-tips rises, which counteracts the advantage of flux focusing effect, and consequently reduce the average torque. The reluctance torque and on-load cogging torque barely contribute to the average torque. Meanwhile, the torque ripple components against different slot opening widths are calculated in Fig.D3(b). All curves vary significantly especially when b_0 approaches zero, since the tooth-tips become highly saturated by slot leakage fluxes.

In fact, the amplitude of on-load cogging torque will be influenced by two different reasons. First, with the decrease of b_0, the stator slotting effect reduces, which smooth the variation of airgap permeance and reduce the cogging torque [2]. On the contrary, with the decrease of b_0, tooth-tip leakage fluxes enhance the local magnetic saturation, which increase the variation of arigap permeance, and may lead to higher cogging torque. Since they influence the amplitude of cogging torque in opposite directions, a balance point will be achieved for minimum on-load cogging torque, Fig.D4(a). Further, since local magnetic saturation change with different load conditions, which results in different balanced points, which can also be observed from Fig.D4(a). Influenced by the on-load cogging torque, the torque ripples under different load conditions have the similar variation trends, Fig.D4(b). Therefore, the optimal design for minimum cogging torque will not be optimal design for on-load torque ripples, in which a design trade-off is demanded considering different load conditions.

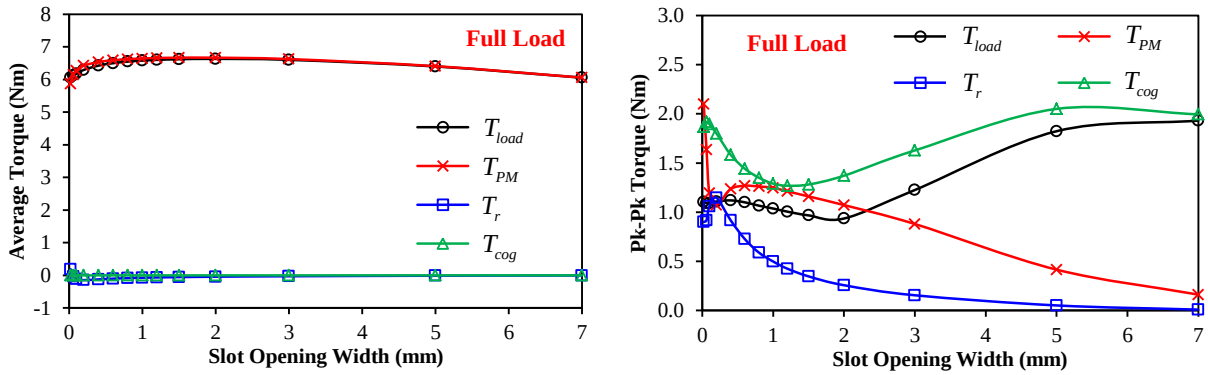

(a) Average torque (b) Torque ripple

Fig. D3 Variation of average toque and torque ripple components against b_0 by FP method (I_q=10 A, I_d=0).

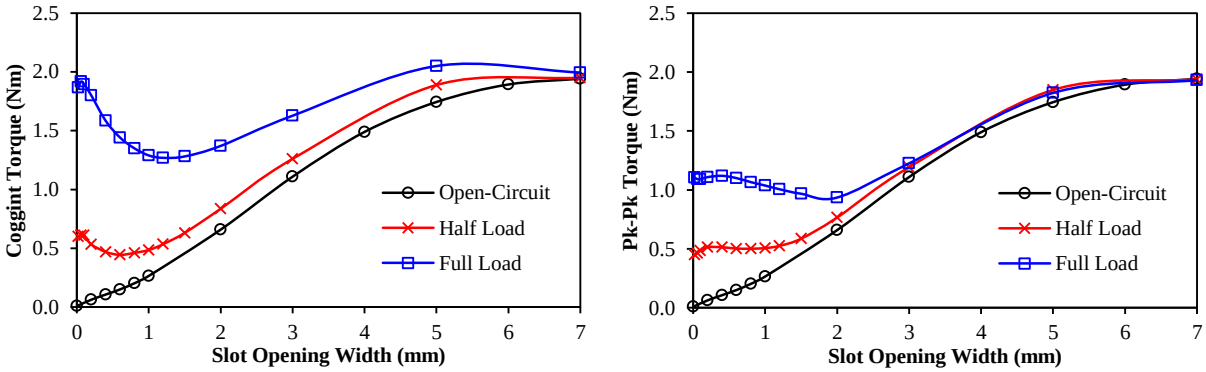

(a) Cogging torque (b) Torque ripple

Fig. D4 Comparison of cogging torque and torque ripple against b_0 under different load conditions (for full load I_q=10 A, I_d=0).

D.3 Comparison of Design Trade-Offs under Different Load Conditions

In example, two 12-slot/8-pole machines which have the similar average torque but different design trade-offs for cogging torques and torque ripples are compared in this section, which are designated as Machine A and Machine B respectively, Fig.D5. The major parameters are kept the same as Table DI, while parameters for different tooth-tip designs are listed in Table DII.

Table DII Tooth-Tips Parameters for Different Design Trade-Offs

Parameters	*Slot opening*	*Tooth-tip height*	*Tooth-tip slop*
Machine A	1.6 mm	1.0 mm	5°
Machine B	0 mm	0.6 mm	15°

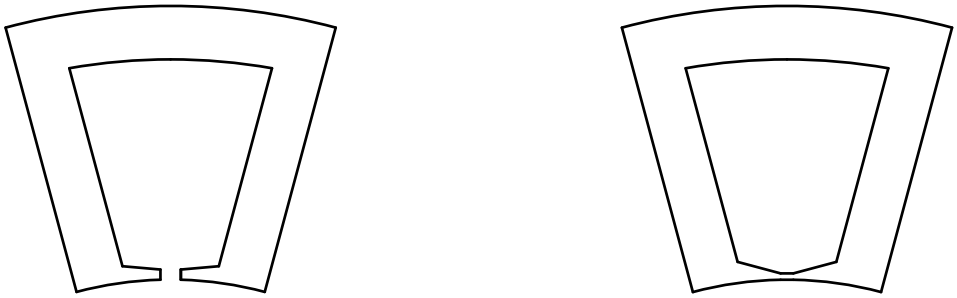

(a) For minimum full load torque ripple (b) For minimum cogging torque

Fig. D5 Comparison of tooth-tip designs for different design trade-offs.

The open-circuit cogging torques of the two machines are compared in Fig.D6(a). With the closed slot openings, the cogging torque of Machine B is almost zero. But the cogging torque of Machine A is much higher due to slot opening effect. Meanwhile, the torque waveforms under different load conditions are compared in Fig.D6(b). Although Machine A has larger cogging torque, its torque ripple under full load condition is much smaller compared with Machine B. Within the full operation range, the torque ripples for Machine A only change slightly, but the values for Machine B vary dramatically, Fig.D7.

This phenomenon can be explained by FP method. Fig.D8(a) shows the torque ripple components of Machine A under different load conditions. All components rise similarly with the increase of load currents, which result in less increasing of resultant torque ripples since they always partly cancelled with each other, Fig.D2(b). However, due to the closed slot design, the tooth-tip leakage fluxes in Machine B will be much stronger compared with that in Machine A, especially with the increase of load currents. Thus, the local magnetic saturation in tooth-tips of Machine B is also much stronger, which leads to the rapidly increasing of on-load cogging torque, Fig.D8(b). Since the on-load cogging torque in Machine B grows much faster than other torque components, the resultant torque ripple in Machine B also significantly increase with load.

According to the aforementioned analyses, Machine A has low full-load torque ripple but very large open-circuit cogging torque, while Machine B has negligible cogging torque but twice the torque ripple under rated load. Due to the saturation changes with different load conditions, the optimal designs for cogging torque and torque ripple are always different.

Therefore, a trade-off is demanded in real applications considering the machine most frequent operation conditions.

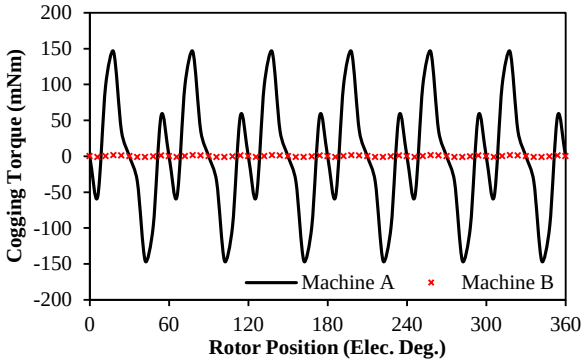

(a) Open-circuit cogging torque

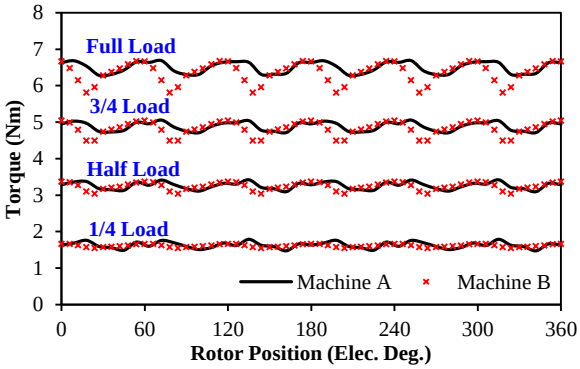

(b) Torque waveforms

Fig. D6 Comparison of cogging torque and torque waveforms between different design trade-offs (for full load I_q=10 A, I_d=0).

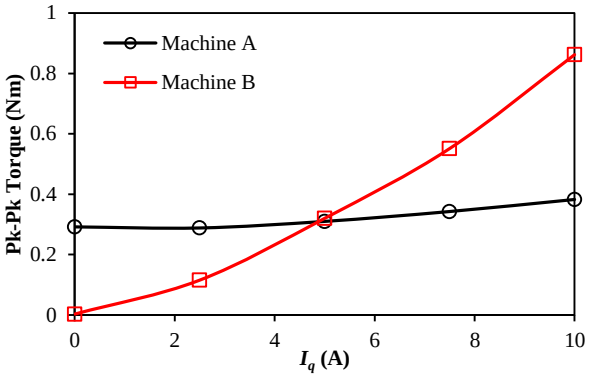

Fig. D7 Comparison of torque ripples against loads for different design trade-offs (I_d=0).

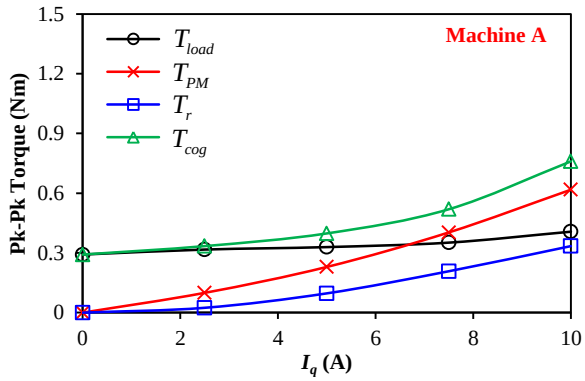

(a) Open-circuit cogging torque

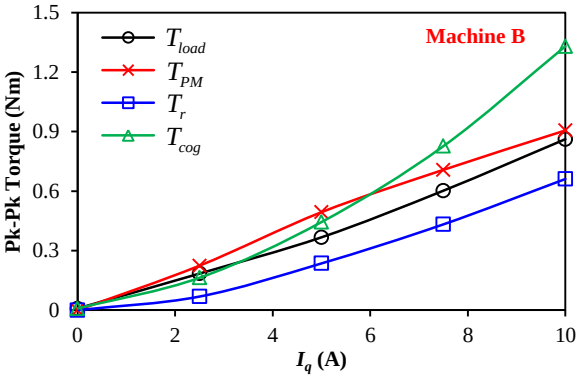

(b) Torque waveforms

Fig. D8 Comparison of torque components for different design trade-offs (I_d=0).

D.4 Experimental Validation

Machine B is manufactured to validate the analyses, Fig.D9. Under open-circuit condition, the comparison of measured and predicted cogging torque is shown in Fig.D10. Since the amplitude of predicted cogging torque is almost zero, it is difficult to measure it accurately. But the amplitude of measured results still proves the negligible cogging torque value. On the other hand, the comparison of torque waveforms under different load conditions is shown in Fig.D11(a), while their corresponding torque ripples are compared in Fig.D11(b). Overall, the experiments validate the analyses for design purposes.

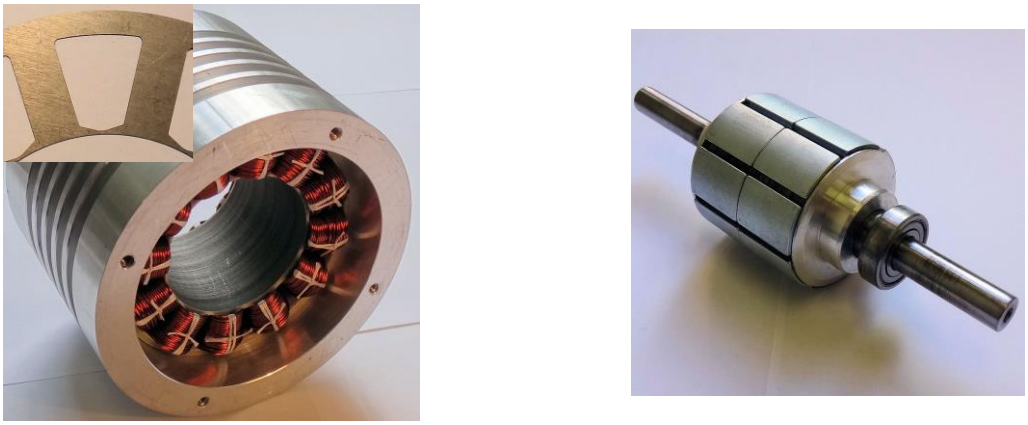

(a) Stator (b) Rotor

Fig. D9 Photos of prototype machine, (a) stator, (b) rotor.

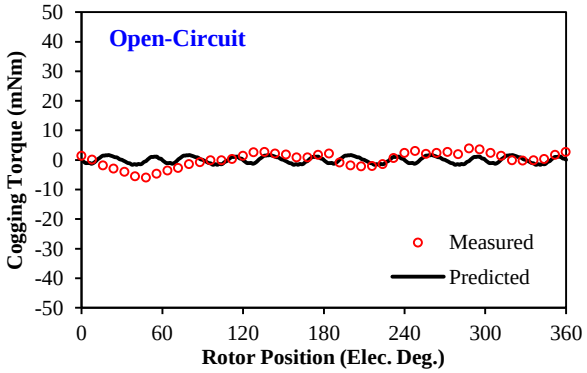

Fig. D10 Comparison of measured and predicted open-circuit cogging torque.

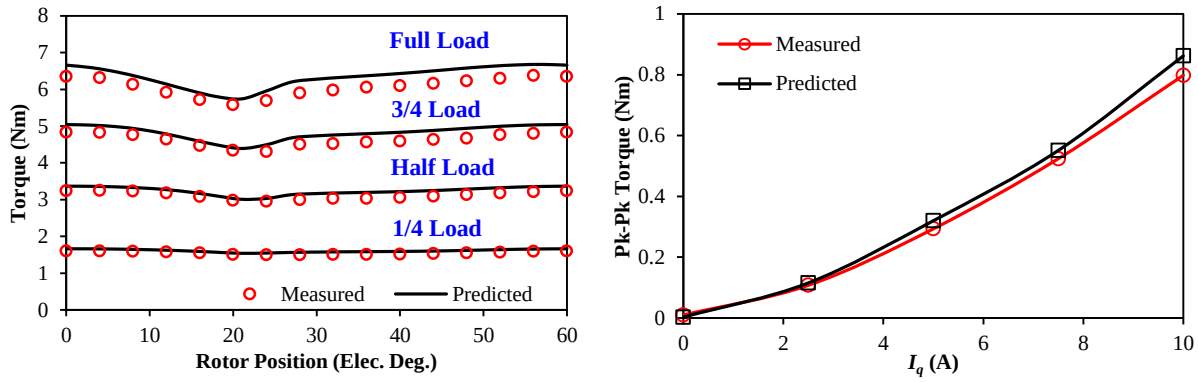

(a) Waveforms (b) Torque ripples

Fig. D11 Comparison of measured and predicted torques (for full load, I_q=10 A, I_d=0).

D.5 Conclusion

The design trade-off between cogging torque and torque ripple in SPM machines operating at different load conditions are presented in this paper. Since the tooth-tip and slot opening mainly determine the cogging torque and torque ripple in SPM machines, they should be carefully chosen according to different applications. With the increase of load currents, the local saturation in tooth-tips also enhances, which consequently lead to the increase of on-load cogging torque and reluctance torque ripples even under I_d=0 control. Two machines with similar average torque are designed and compared to illustrate the design trade-offs, while one prototype machine has been built and tested to validate the analyses. Although this paper only focuses on the design of tooth-tips, all design concepts and analysis methods could be adopted to more systematically optimize the machines under different operation conditions.

REFERENCES

[1] A. M. El-Refaie, "Fractional-slot concentrated-windings synchronous permanent magnet machines: opportunities and challenges," *IEEE Trans. Ind. Electron.*, vol. 57, no. 1, pp. 107-121, Jan. 2010.

[2] Z. Q. Zhu and D. Howe, "Influence of design parameters on cogging torque in permanent magnet machines," *IEEE Trans. Energy Convers.*, vol. 15, no. 4, pp. 407-412, Dec. 2000.

[3] Z. Azar, Z. Q. Zhu, and G. Ombach, "Influence of electric loading and magnetic saturation on cogging torque, back-EMF and torque ripple of PM machines," *IEEE Trans. Magn.*, vol. 48, no. 10, pp. 2650-2658, Oct. 2012.

[4] W. Q. Chu and Z. Q. Zhu, "Average torque separation in permanent magnet synchronous machines using frozen permeability," *IEEE Trans. Magn.*, vol. 49, no. 3, pp. 1202-1210, Mar. 2013.

[5] K. Yamazaki and M. Kumagai, "Torque analysis of interior permanent-magnet synchronous motors by considering cross-magnetization: variation in torque components with permanent-magnet configurations," IEEE Trans. Ind. Electron., vol. 61, no. 7, pp. 3192-3201, Jul. 2014.

APPENDIX E

CAD DRAWINGS OF PROTOTYPES

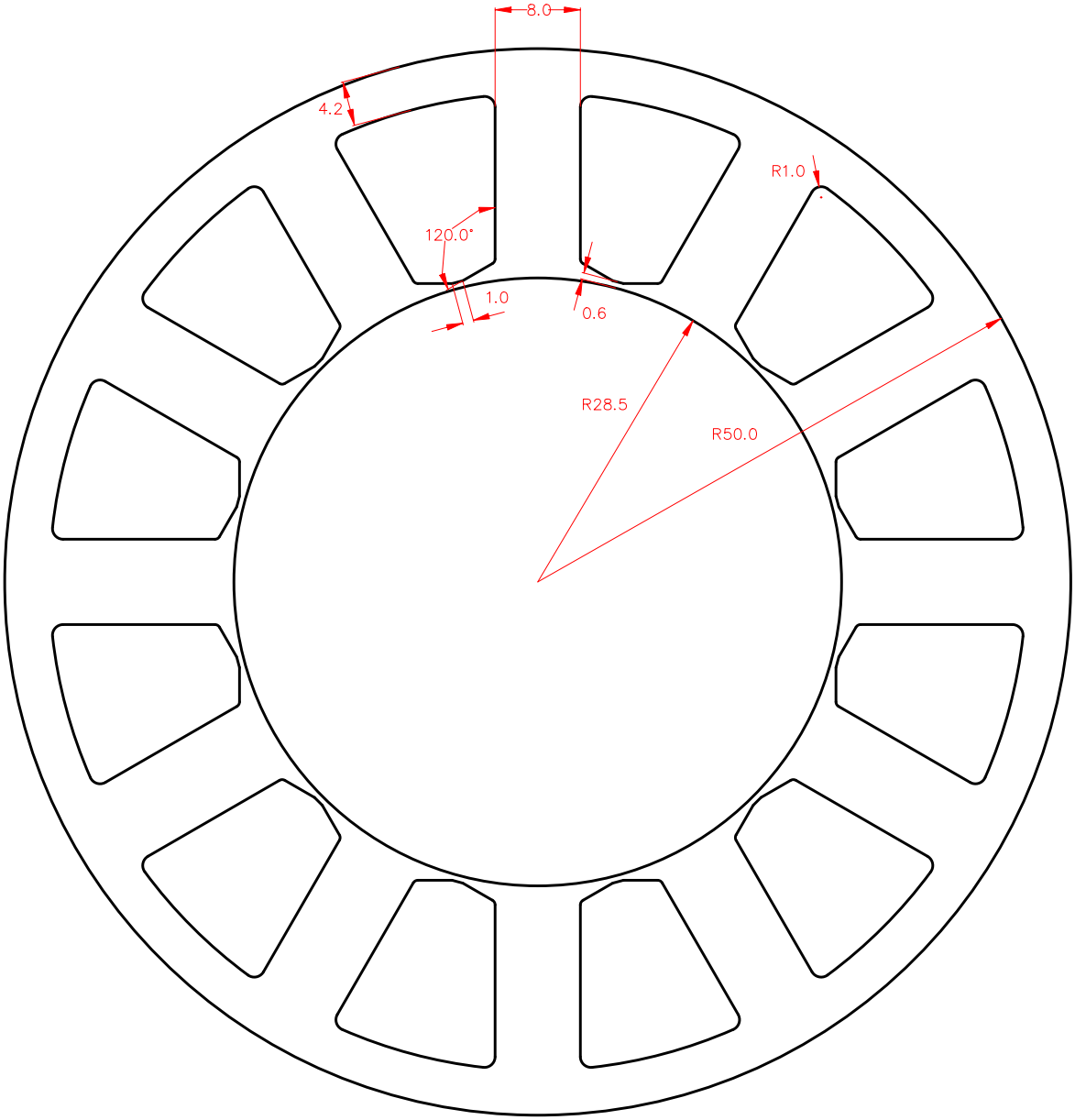

Fig. E1 Dimensions of the 12-slot stator with closed slot openings for SPM machines.

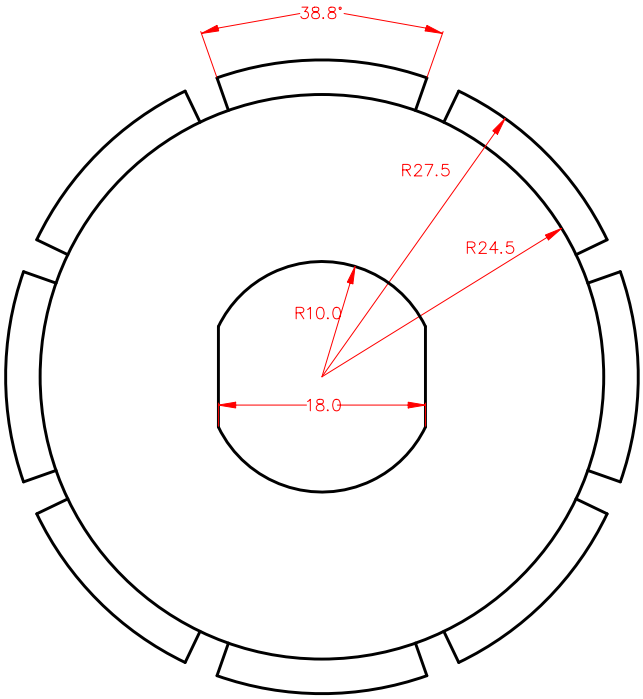

(a) 8-pole

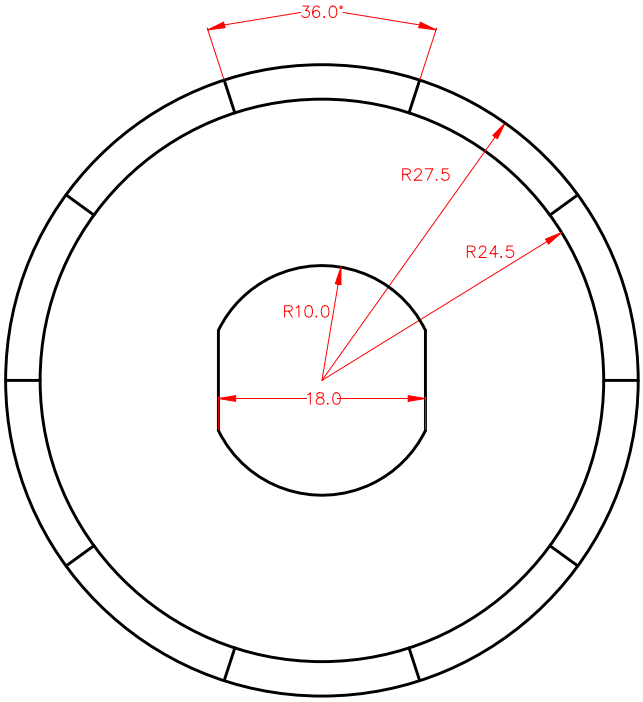

(b) 10-pole

Fig. E2 SPM rotors lamination and PM dimensions.

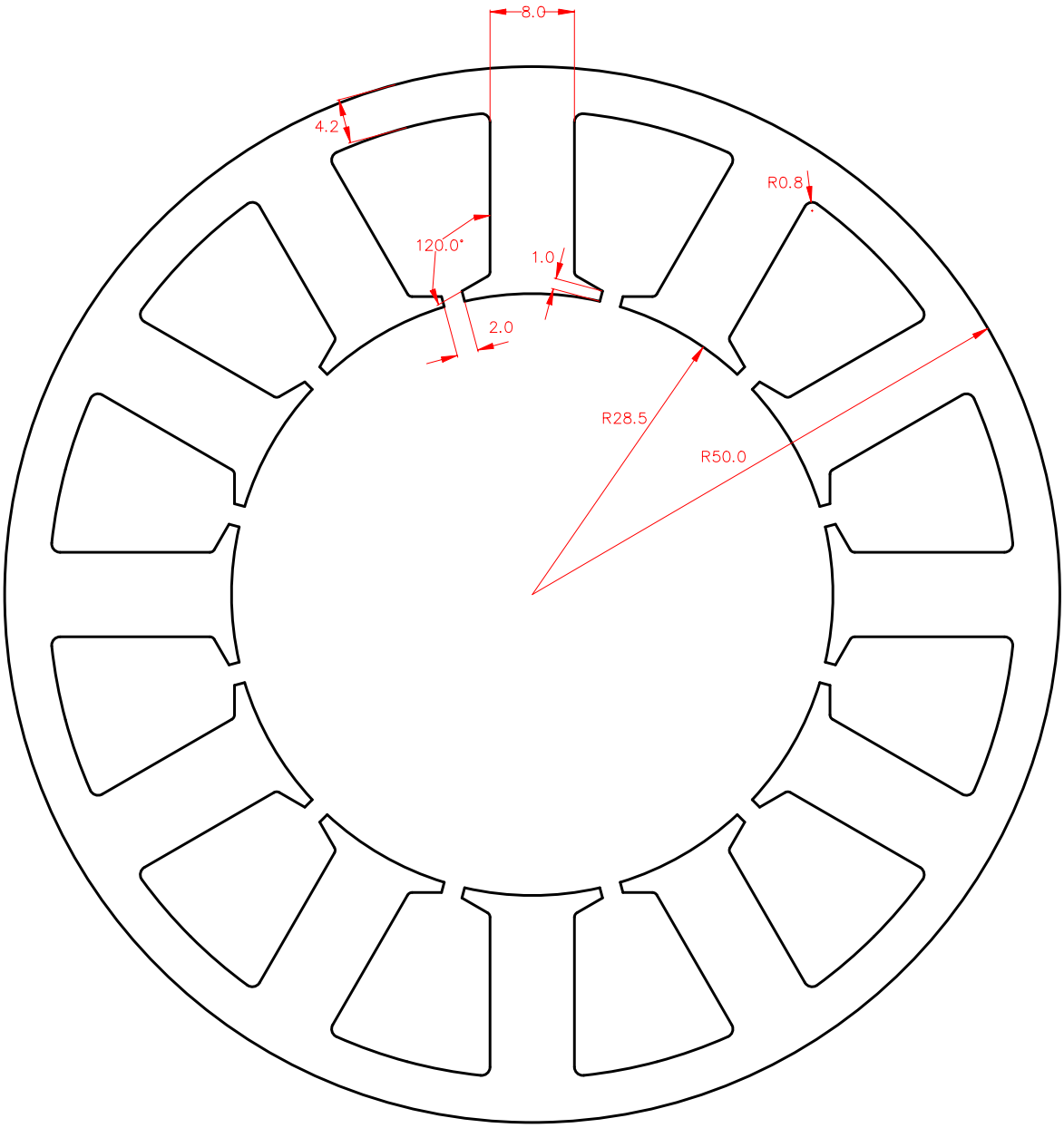

Fig. E3 Dimensions of the 12-slot stator with normal slot openings for both SPM and IPM machines.

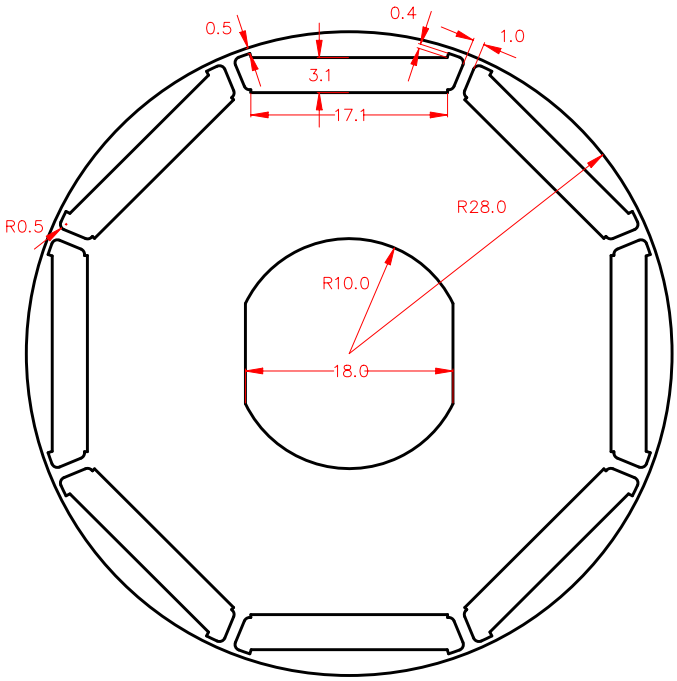

(a) 8-pole

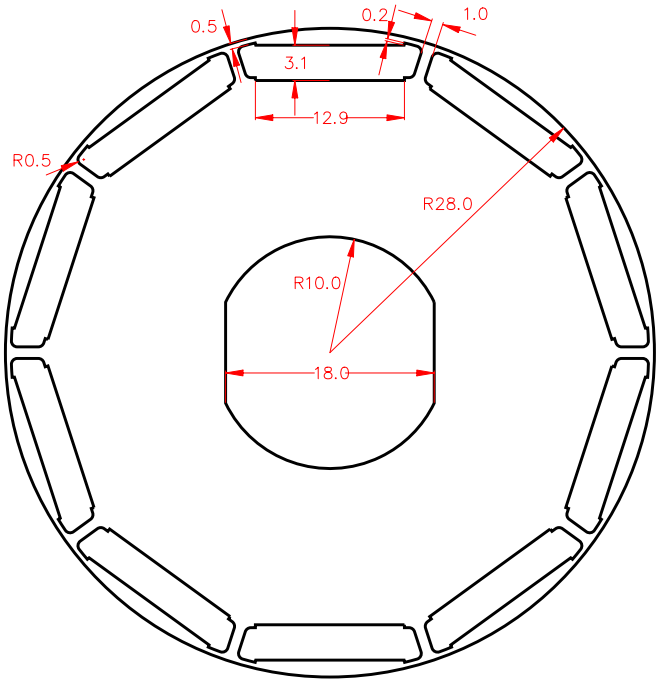

(b) 10-pole

Fig. E4 IPM rotors lamination dimensions.

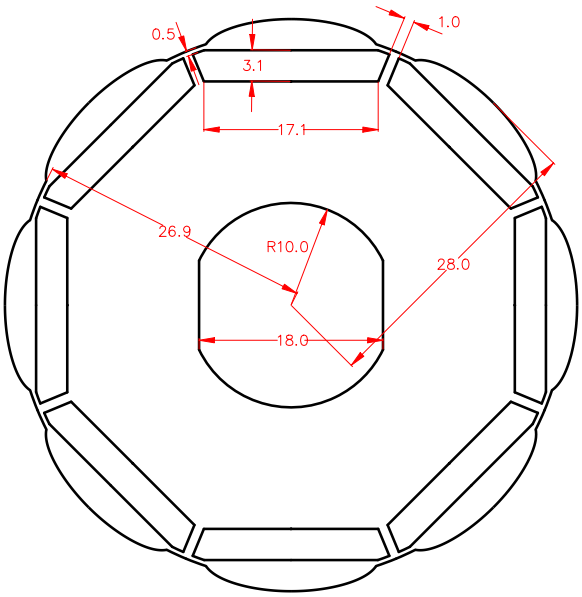

Fig. E5 8-pole shaped IPM rotor lamination dimensions.

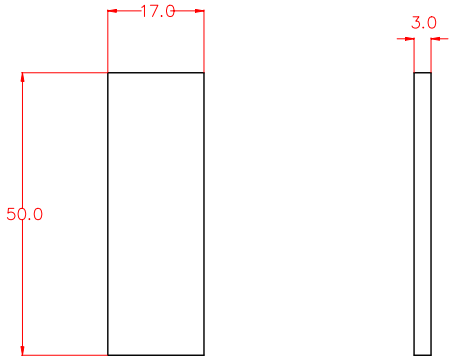

(a) 8-pole

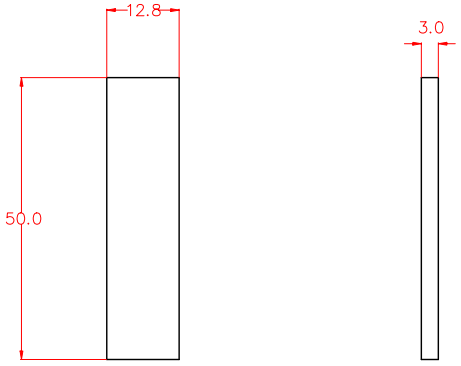

(b) 10-pole

Fig. E6 IPM rotors PM dimensions.

APPENDIX F

PUBLICATION RESULTED FROM PHD STUDY

Journal Publications:

[1] **D. Wu**, and Z. Q. Zhu, "On-load voltage distortion in fractional slot surface-ounted permanent magnet machines considering local magnetic saturation," *IEEE Trans. Magn.*, in Press.

[2] **D. Wu**, and Z. Q. Zhu, "Influence of slot and pole number combinations on voltage distortion in surface-mounted permanent magnet machines with local magnetic saturation," *IEEE Trans. Energy Convers.*, in Press.

[3] **D. Wu**, and Z. Q. Zhu, "Design trade-off between cogging torque and torque ripple in fractional slot surface-mounted permanent magnet machines" *IEEE Trans. Magn*., in Press.

[4] **D. Wu**, X. Liu, Z. Q. Zhu, A. Pride, R. Deodhar, and T. Sasaki, "Switched flux hybrid magnet memory machine," *IET Elect. Pow. Appl.*, vol. 9, no. 2, pp. 160-170, Feb. 2015.

[5] **D. Wu**, J. T. Shi, Z. Q. Zhu, and X. Liu, "Electromagnetic performance of novel synchronous machines with permanent magnet in stator yoke," *IEEE Trans. Magn.*, vol. 50, no. 9, pp. 1-9, Sep. 2014.

[6] **D. Wu**, Z. Q. Zhu, and R. Nilssen, "Development of a segmented linear variable flux reluctance motor with DC-field coil," *Applied Machanics and Materials*, vol. 416-417, pp. 203-208, 2013.

[7] Z. Q. Zhu and **D. Wu**, "On-load voltage distortion in fractional-slot interior permanent magnet machines," *IEEE Trans. Magn*., in Press.

[8] X. Liu, **D. Wu**, Z. Q. Zhu, A. Pride, R. Deodhar, and T. Sasaki, "Efficiency improvement of switched flux PM memory machine over interior PM machine for EV/HEV applications," *IEEE Trans. Magn.*, vol. 50, no. 11, pp. 1-4, Nov. 2014.

[9] J. T. Shi, X. Liu, **D. Wu**, and Z. Q. Zhu, "Influence of stator and rotor pole arcs on electromagnetic torque of variable flux reluctance machines," *IEEE Trans. Magn.*, vol. 50, no. 11, pp. 1-4, Nov. 2014.

[10] Y. X. Li, Q.F. Lu, Z. Q. Zhu, L. J. Wu, G. J. Li and **D. Wu**, "Analytical synthesis of air-gap field distribution in permanent magnet machines with rotor eccentricity by superposition method," *IEEE Trans. Magn.*, in Press.

Journal Papers under Review:

[1] **D. Wu**, Z. Q. Zhu, and X. Liu, "Novel external rotor switched flux memory motor with hybrid magnets," *COMPEL, under Review.*

[2] B. S. Lee, Z. Q. Zhu, and **D. Wu**, "On-load voltage distortion compensation method using disturbance observer for SPM machines with closed slot," *IEEE Trans. Ind. Electron., under Review.*

[3] J. T. Shi, Z. Q. Zhu, **D. Wu**, and X. Liu, "Comparative study of novel biased flux permanent magnet machines with doubly salient permanent magnet machines considering with influence of flux focusing," *Electric Power Systems Research, under Review.*

[4] J. T. Shi, Z. Q. Zhu, **D. Wu**, and X. Liu, "Comparative study of novel synchronous machines having permanent magnet in stator," *Electric Power Systems Research, under Review.*

[5] Y. X. Li, Q. F. Lu, Z. Q. Zhu, **D. Wu**, and G. J. Li, "Superposition method for cogging torque prediction in permanent magnet machines with rotor eccentricity," *IEEE Trans. Magn., under Review.*

Conference Publications:

[1] **D. Wu**, Z. Q. Zhu, and R. Nilssen, "Development of a segmented linear variable flux reluctance motor with DC-field coil," in *LDIA 2013*, vol. 416-417, pp. 203-208, 2013.

[2] **D. Wu**, X. Liu, Z. Q. Zhu, A. Pride, R. Deodhar, and T. Sasaki, "Novel switched flux hybrid magnet memory motor," in *PEMD 2014*, Manchester, U.K. Apr. 2014, pp. 1-6.

[3] **D. Wu**, Z. Q. Zhu, X. Liu, A. Pride, R. Deodhar, and T. Sasaki, "Cross coupling effect in hybrid magnet memory motor," in *PEMD 2014*, Manchester, U.K. Apr. 2014, pp. 1-6.

[4] **D. Wu**, Z. Q. Zhu, and X. Liu, "Novel external rotor switched flux memory motor with hybrid magnets," in *ICEMS 2014*, Hangzhou, China, Oct. 2014, pp. 3324-3330.

[5] **D. Wu**, and Z. Q. Zhu, "Design trade-off between cogging torque and torque ripple in fractional slot surface-mounted permanent magnet machines," in *INTERMAG 2015*, Beijing, China, May 2015, pp. 1-4.

[6] X. Liu, **D. Wu**, Z. Q. Zhu, A. Pride, R. Deodhar, and T. Sasaki, "Efficiency improvement of switched flux PM memory machine over interior PM machine for EV/HEV applications," in *INTERMAG 2014*, Dresden, Germany, May 2014, pp. 1-4.

[7] Z. Q. Zhu, **D. Wu**, M. C. Wu, and I. W. Lan, "Influence of on-load voltage distortion on torque-speed characteristic of interior permanent magnet machines," in *ECCE 2015*, Montreal, Canada, Sep. 2015, pp. 1-8.

[8] J. T. Shi, X. Liu, **D. Wu**, and Z. Q. Zhu, "Influence of stator and rotor pole arcs on electromagnetic torque of variable flux reluctance machines," in *INTERMAG 2014*,

Dresden, Germany, May 2014, pp. 1-4.

[9] J. T. Shi, Z. Q. Zhu, **D. Wu**, and X. Liu, "Influence of flux focusing on electromagnetic torque of novel biased flux PM machines," in *ICEM 2014*, Berlin, Germany, Sep. 2014, pp. 523-529.

[10] J. T. Shi, Z. Q. Zhu, **D. Wu**, and X. Liu, "Comparative study of novel synchronous machines having permanent magnet in stator poles," in *ICEM 2014*, Berlin, Germany, Sep. 2014, pp. 429-435.

[11] X. Liu, Z. Q. Zhu, and **D. Wu**, "Evaluation of efficiency optimized variable flux reluctance machine for EVs/HEVs by comparing with interior PM machine," in *ICEMS 2014*, Hangzhou, China, Oct. 2014, pp. 2648-2654, (***Best Paper Award***).

[12] J. T. Shi, Z. Q. Zhu, **D. Wu**, and X. Liu, "Comparative study of novel biased flux permanent magnet machine with doubly salient permanent magnet machine," in *ICEMS 2014*, Hangzhou, China, Oct. 2014, pp. 415-420.

[13] I. Afinowi, Z. Q. Zhu, **D. Wu**, Y. Guan, J. C. Mipo, and P. Farah, "Flux-weakening performance comparison of conventional and E-core switched-flux permanent magnet machines," in *ICEMS 2014*, Hangzhou, China, Oct. 2014, pp. 522-528.

[14] Z. Q. Zhu, H. Hua, **D. Wu**, J. T. Shi, and Z. Z. Wu, "Comparison of partitioned stator machines with different PM excitation stator topologies," in *EVER 2015*, Monaco, Mar. 2015, pp. 1-7.

[15] P. Xu, Z. Q. Zhu, and **D. Wu**, "Carrier signal injection based sensorless control of permanent magnet synchronous machines without the need of magnetic polarity identification," in *ECCE 2015*, Montreal, Canada, Sep. 2015, pp. 1-8.

[16] Y. X. Li, Z. Q. Zhu, G. J. Li, and **D. Wu**, "Analytical synthesis of air-gap field in permanent magnet machines with rotor eccentricity by superposition method," in *INTERMAG 2015*, Beijing, China, May 2015, pp. 1-4.

[17] C. C. Awah, Z. Q. Zhu, Z. Z. Wu and **D. Wu**, "High torque density magnetically-geared switched flux permanent magnet machines," in *EVER 2015*, Monaco, Mar. 2015, pp. 1-6.

[18] C. C. Awah, Z. Q. Zhu, Z. Z. Wu, J. T. Shi, and **D. Wu**, "Comparison of portioned stator switched flux permanent magnet machines having single- and double-layer windings," in *EVER 2015*, Monaco, Mar. 2015, pp. 1-5.

[19] H. Yang, H. Lin, S. Fang, Y. Huang, Z. Q. Zhu, **D. Wu**, and H. Hua, "Novel alternative switched flux memory machines having hybrid magnet topologies," in *EVER 2015*, Monaco, Mar. 2015, pp. 1-9, (***Best Paper Award***).